

NanoScience and Technology

Srinivasan Gopalakrishnan
Saggam Narendar

Wave Propagation in Nanostructures

Nonlocal Continuum Mechanics
Formulations

 Springer

NanoScience and Technology

Series Editors

Phaedon Avouris

Bharat Bhushan

Dieter Bimberg

Klaus von Klitzing

Hiroyuki Sakaki

Roland Wiesendanger

For further volumes:

<http://www.springer.com/series/3705>

The series NanoScience and Technology is focused on the fascinating nano-world, mesoscopic physics, analysis with atomic resolution, nano and quantum-effect devices, nanomechanics and atomic-scale processes. All the basic aspects and technology-oriented developments in this emerging discipline are covered by comprehensive and timely books. The series constitutes a survey of the relevant special topics, which are presented by leading experts in the field. These books will appeal to researchers, engineers, and advanced students.

Srinivasan Gopalakrishnan
Saggam Narendar

Wave Propagation in Nanostructures

Nonlocal Continuum Mechanics
Formulations

 Springer

Srinivasan Gopalakrishnan
Indian Institute of Science
Bangalore
India

Saggam Narendar
Defence Research and Development
Organisation (DRDO)
Kanchanbagh, Hyderabad
India

ISSN 1434-4904

ISBN 978-3-319-01031-1

ISBN 978-3-319-01032-8 (eBook)

DOI 10.1007/978-3-319-01032-8

Springer Cham Heidelberg New York Dordrecht London

Library of Congress Control Number: 2013942139

© Springer International Publishing Switzerland 2013

This work is subject to copyright. All rights are reserved by the Publisher, whether the whole or part of the material is concerned, specifically the rights of translation, reprinting, reuse of illustrations, recitation, broadcasting, reproduction on microfilms or in any other physical way, and transmission or information storage and retrieval, electronic adaptation, computer software, or by similar or dissimilar methodology now known or hereafter developed. Exempted from this legal reservation are brief excerpts in connection with reviews or scholarly analysis or material supplied specifically for the purpose of being entered and executed on a computer system, for exclusive use by the purchaser of the work. Duplication of this publication or parts thereof is permitted only under the provisions of the Copyright Law of the Publisher's location, in its current version, and permission for use must always be obtained from Springer. Permissions for use may be obtained through RightsLink at the Copyright Clearance Center. Violations are liable to prosecution under the respective Copyright Law. The use of general descriptive names, registered names, trademarks, service marks, etc. in this publication does not imply, even in the absence of a specific statement, that such names are exempt from the relevant protective laws and regulations and therefore free for general use.

While the advice and information in this book are believed to be true and accurate at the date of publication, neither the authors nor the editors nor the publisher can accept any legal responsibility for any errors or omissions that may be made. The publisher makes no warranty, express or implied, with respect to the material contained herein.

Printed on acid-free paper

Springer is part of Springer Science+Business Media (www.springer.com)

S. Gopalakrishnan

*This book is dedicated to my wife Anuradha,
my children Karthik and Keerthana and my
Parents Srinivasan and Saraswathi*

S. Narendar

*This book is dedicated to my parents Saggam
Jagadamba and Saggam Narayana and
my brothers Naveen and Ravinder*

Preface

A material structure assembled from a layer or cluster of atoms with size of the order of nanometers is called a nanostructure. A nanometer is about four atom diameters or 1/50,000 of a human hair. (Our fingernails are growing about a nanometer while reading this). What is so special about nanometer length scales that create so much excitement the world over? To answer this, let us consider a bulk piece of silicon having certain band gap, a feature that is a key property in electronics. If this silicon piece is shrunk to $0.1 \mu\text{m}$ (100 nm) length, the band gap will increase significantly causing silicon to emit visible light. In other words, understanding the physics of a structure at the atomic scale can help us to manipulate its properties in its bulk form. This can result in mind boggling applications that were hitherto not thought of by our research community.

There are many events such as the discovery of scanning electron microscopy that gave fillip to nanotechnology research. However, with the discovery of a new allotrope of carbon in the late 1980s and early 1990s, namely the fullerene, carbon nanotubes and graphene, a new chapter in nanotechnology research has emerged. These have become the basic building blocks for many nanodevices such as nanosensors, nano actuators, nano gyroscopes, etc. All of these devices are packaged under Nano Electro Mechanical Systems (NEMS) or Nano Opto Mechanical Systems (NOMS) devices. The key elements in these devices are the nanobeams, nanorods, nanoplates and nanoshells, respectively. This book deals with mathematical modelling of nanorods, nanobeams, nanoplates and nanoshell, which make up for the bulk of NEMS or NOMS devices.

In the mathematical modelling of physical systems, it is necessary to represent the physics of the system as accurately as possible. Understanding the physics of a material system at nanoscale level is indeed a great challenge. Performing experiments to understand its physics and formulate hypothesis is not an easy task due to extremely small sizes of the nanoscale system. Most of the behaviour has to be understood through mathematical modelling. Any modelling method should account for small-scale effects associated with these nanoscale systems. There are two different modelling methods, one based on atomistic assumptions, and the other based on continuum assumptions. In the former, we consider a group of connected atoms (typically of the order of thousands if not millions) and solve Newton's second law of motion on each atom considered. Here again, we should

make some assumptions to get the interatomic interactions. This approach is computationally prohibitive if we consider a large number of atoms in the modelling. This book mainly deals with modelling using continuum assumptions, wherein the small-scale effects are brought in through the use of non-local elasticity theory. We adopt such a modelling scheme throughout this book to study the wave propagation behaviour in nanostructures. Obviously, such modelling scheme is computationally fast and in fact all the simulations performed in this book are programmed in the general-purpose mathematical code MATLAB.

This book mainly addresses the topic of wave propagation in nanostructures. Most of the nanostructures are subjected to heavy and sometimes violent vibrations at the nanoscale, which sets up stress waves in these structures that propagate and interact with boundaries and create new waves. These waves are in the range of terahertz range and they exhibit band gap behaviour over certain frequency bands. Unlike the bulk structures, these terahertz waves have tremendous energy and their best utilization in the future generation nanodevices requires deep understanding of wave propagation in these structures.

The material developed in this book is the result of sustained research done by the senior author over the last 20 years in the area of wave propagation and the last 5 years in the area of nanostructures by both the authors. A book of this kind is an effort toward filling the need for bringing out a comprehensive textbook on wave propagation in nanostructures that will be helpful to scientists/researchers involved both in basic and applied research in the area of nanoscience and technology.

The book is written in modular form consisting of 11 chapters. [Chapters 1–4](#) present the introductory material on nanostructures, wave propagation, different modelling schemes and a basic introduction to non-local elasticity. These topics form the basis for all the chapters that follow. [Chapter 5](#) deals with nanostructure material property evaluation and small-scale effects parameter determination. [Chapters 6–11](#) deal with core wave propagation problems in different nano waveguides such as nanorods, nanobeams, nanotubes carrying fluids, coupled nano systems, multi-wall nanotubes and graphene structures. The material presented in this book can be used to develop a graduate level course in the topic of wave propagation in nanostructures. Also, this book can form as a reference material on the course of wave propagation in complex mediums. While writing this book, we have assumed that the reader has the basic engineering mechanics and graduate level mathematics background.

The completion of this book would not be possible without the support of the families of the authors. Dr. Gopalakrishnan deeply thanks his wife Anu and his children Karthik and Keerthana for their continuous patience, understanding and support, without which this book would not have been possible. Mr. Narendar thanks his parents and brothers for their constant encouragement and support.

Bangalore, India, March 2013

Srinivasan Gopalakrishnan
Saggam Narendar

Contents

1	Introduction to Nanostructures	1
1.1	Historical Perspectives	3
1.2	Hybridization of Carbon Nanostructures	4
1.2.1	Nanotubes	7
1.2.2	Structure of Carbon Nanotubes	8
1.2.3	Properties of Carbon Nanotubes	10
1.3	Need for Wave Propagation Analysis in Nanostructures	13
1.4	Outline and Scope of the Book	15
1.5	Summary	15
	References	16
2	Introductory Concepts of Wave Propagation Analysis in Structures	19
2.1	Introduction to Wave Propagation	20
2.2	Spectral Analysis	21
2.3	Wave Propagation Terminologies	21
2.4	Spectrum and Dispersion Relations	23
2.4.1	Second-Order PDE	24
2.4.2	Fourth Order PDE	26
2.5	Summary	29
	References	29
3	Various Modeling Techniques for Nanostructures	31
3.1	First-Principles Methods (Atomistic Simulations)	32
3.1.1	Density Functional Theory	34
3.1.2	Ab initio Pseudopotentials	35
3.2	Molecular Dynamics	36
3.2.1	Potential Functions	37
3.3	Molecular Dynamics for Wave Propagation in CNT	38
3.4	Molecular Dynamics Simulation for Wave Propagation in Graphene	41

3.5	Monte Carlo Methods	42
3.5.1	The Metropolis Algorithms	42
3.5.2	Kinetic Monte Carlo Simulations	42
3.6	Continuum Modeling	43
3.7	Methods of Multiscale Modeling	46
3.8	Overview on Length Scales	47
3.9	Nonlocal Theories in Continuum Mechanics	49
3.9.1	Strain-Gradient Elasticity	50
3.9.2	Models with Mixed Spatial-Temporal Derivatives	51
3.9.3	Integral-Type Nonlocal Elasticity	52
3.10	Summary	55
	References	56
4	Theory of Nonlocal Elasticity	59
4.1	Need for Nonlocal Elasticity for Nanostructures	59
4.2	Introduction to Nonlocal Elasticity	60
4.3	Types of Nonlocality	63
4.3.1	Properties of the Kernels	65
4.4	Nonlocal Constitutive Relations	67
4.4.1	Nonlocal Constitutive Relation for 1D Problems	67
4.4.2	Nonlocal Constitutive Relations for 2D Problems	67
4.4.3	Nonlocal Constitutive Relations for 3D Problems	68
4.4.4	Nonlocal Constitutive Relations for Cylindrical Shell Problems	68
4.5	Summary	69
	References	69
5	Material Property and Nonlocal Scale Parameter Estimation for Carbon Nanotubes	71
5.1	Length-Dependent In-plane Stiffness of Carbon Nanotubes	72
5.1.1	Governing Equations for SWCNT	72
5.1.2	Solution of Governing Equations	74
5.1.3	In-plane Stiffness Ratio Estimation	75
5.1.4	Numerical Results and Discussion	77
5.2	Material Property Estimation: A Comparison with Nonlocal Rod Model	79
5.2.1	Numerical Results and Discussions	81
5.3	Prediction of Nonlocal Scale Parameter: A Molecular Structural Mechanics and Nonlocal Elasticity Model	84
5.3.1	Armchair SWCNTs	86
5.3.2	Zigzag SWCNTs	94
5.3.3	Chiral SWCNTs	101
5.4	Summary	117
	References	118

6	Wave Propagation in 1D-Nanostructures: Nanorods	121
6.1	Axial Wave Propagation in NLSGM Nanorod	122
6.1.1	Governing Equations for NLSGM Nanorods	122
6.1.2	Wave Characteristics in NLSGM Nanorods	124
6.2	Axial Wave Propagation NLStGM Nanorods	128
6.2.1	Governing Equations for Second and Fourth-Order NLStGM Nanorods	129
6.2.2	Uniqueness and Stability of Second-Order NLStGM Nanorods	131
6.2.3	Wave Characteristics of Second-Order NLStGM Nanorods	133
6.2.4	Wave Characteristics of Fourth-Order NLStGM Nanorods	134
6.2.5	Numerical Results and Discussion	135
6.3	Axial Wave Propagation in Nanorods with Lateral Inertia	139
6.3.1	NLSGM-Based Governing Equations for Nanorods with Lateral Inertia	139
6.3.2	Wave Characteristics of Nanorods with Lateral Inertia	142
6.4	Torsional Wave Propagation in NLSGM Nanoshafts	147
6.4.1	Numerical Results and Discussion	150
6.5	Spectral Finite Element Formulation	152
6.5.1	Frequency Dependent Shape Functions	154
6.5.2	Dynamic Stiffness Matrix	156
6.5.3	Numerical Results and Discussion	157
6.6	Summary	161
	References	162
7	Wave Propagation in 1D-Nanostructures: Nanobeams	165
7.1	NLSM for Euler–Bernoulli Nanobeams	165
7.1.1	Wave Dispersion Characteristics	167
7.2	NLSGM for Timoshenko Nanobeam	170
7.2.1	Wave Dispersion Characteristics	172
7.3	Rotating Nanotubes: An Introduction	177
7.3.1	Governing Equations for Rotating Nanotube	178
7.3.2	Wave Dispersion Analysis	181
7.4	Fluid Carrying SWCNTs	187
7.4.1	Nonlocal Governing Equations of Motion	187
7.5	Magnetic Field Effects on SWCNT	194
7.5.1	Maxwell’s Relations	195
7.5.2	Nonlocal Governing Equations of Motion Including Magnetic Field Effects	196

7.6	Surface Effects on Flexural Wave Propagation in Nanobeams	201
7.6.1	Governing Equation of Motion Including Surface Residual Stress	204
7.6.2	Wave Propagation Analysis	206
7.7	Summary	211
	References	212
8	Wave Propagation in Multi-Walled Carbon Nanotubes	215
8.1	van der Waals Forces	217
8.2	Governing Equations for NLSGM MWCNT	218
8.2.1	Generalized Wave Dispersion Analysis in MWCNTs	219
8.2.2	Wave Dispersion in SWCNTs	222
8.2.3	Wave Dispersion in DWCNTs	225
8.2.4	Wave Dispersion in TWCNTs	231
8.3	Summary	236
	References	236
9	Wave Propagation in Coupled 1D-Nanosystems	239
9.1	Governing Equations of Motion for Double Nanorod System	240
9.1.1	Wave Propagation Analysis in DNRS	242
9.2	Coupled Nano-Beam System.	248
9.2.1	Wave Propagation in Double Euler–Bernoulli Nanobeam System.	250
9.2.2	Wave Propagation in Coupled Timoshenko Nanobeam System.	254
9.3	Summary	266
	References	266
10	Wave Propagation in 2D-Nanostructures	269
10.1	Flexural Wave Propagation in Monolayer Graphene Sheets	271
10.1.1	Governing Equations for Graphene Structures	271
10.1.2	Wave Dispersion Analysis	273
10.2	Modeling of Graphene Layer on Silicon Substrate.	280
10.2.1	Potential Energy, Equilibrium and Force Constants.	281
10.3	Wave Propagation in Single Graphene Layer on Silicon Substrate.	284
10.3.1	Wave Dispersion Analysis	287
10.4	Temperature Effects on Wave Propagation in Nanoplates.	295
10.4.1	Governing Equations of Motion Including Thermal Effects	297
10.4.2	Thermo-Elastic Flexural Wave Dispersion Analysis	300

- 10.5 Surface Effects on Wave Propagation in Nanoplates 305
- 10.6 Mathematical Modeling of Nanoplate with the
Surface Effects 307
 - 10.6.1 Dispersion Characteristics 309
- 10.7 Summary 317
- References 319

- 11 Wave Propagation in Nanoshells. 323**
 - 11.1 Wave Propagation in Circular Cylindrical Nanoshells 324
 - 11.1.1 Wave Dispersion Analysis 327
 - 11.2 Fluid-Filled Nanoshells 336
 - 11.2.1 Wave Dispersion Analysis 337
 - 11.3 Wave Propagation in Higher Order Nanoshells 341
 - 11.3.1 Governing Nanoshell Equations Including Shear
and Contraction Effects 342
 - 11.3.2 Wave Dispersion Analysis 345
 - 11.4 Summary 352
 - References 353

- Index 355**

Chapter 1

Introduction to Nanostructures

The word *nano* normally signifies one billionth or 10^{-9} part of an unit considered. In terms of length scales, we use meters and hence a *nanometer* normally referred to as 1 nm is equal to 10^{-9} m or 10^{-3} μm or equal to 10 \AA (Angstrom Unit). Nanostructures refers to material system that are in the range of 1–100 nm. In a nanostructures, electrons are normally confined in one of the dimensions while in the other dimensions they are free to move in all directions. Depending upon the nature of confinement, nanostructures can be classified as the following"

- *Quantum Well*: In this type of nanostructures, the electrons are confined in one dimensions and free to move in the other two dimensions.
- *Quantum Wires*: Here, the electrons are confined in two dimensions while they are free to move in the other dimension.
- *Quantum Dots*: In this type of nanostructure, the electrons are confined in all the three dimensions.

Nanostructures have unique properties when compared to their individual atoms or molecules or their bulk macroscopic properties. For example, bulk material such as Copper wire, their intrinsic properties, say density or conductivity, are independent of its size. That is, if a 1 m long Copper wire, when cut into few pieces, and for these pieces, if the density or conductivity is measured, one will find they are same as the original Copper wire. If the dividing process is done indefinitely, then the property invariance will still remain. However, if the division is made at the electron, proton or neutron levels, that is at the nanoscale levels, we can certainly expect significant change in the property of the nanostructures. The properties of the nanoscale material systems can get significantly affected by the following three phenomenon:

- *Quantum Confinement*: The confinement of electrons in the nanoscale dimensions will result in the change in the energy and momentum of the nano material system, which in turn significantly alters its properties.
- *Quantum Coherence*: This phenomenon relates to the phase relation of the wave function in nano material system, that is preserved in the nanomaterial system. The quantum coherence property is well maintained in atoms and molecules but

not always in nanostructures due to inherent defects present in these structures. This results in the change of properties in the nano scale and hence it is necessary to consider both the quantum coherence and de-coherence effects while dealing with nanostructures

- *Surface Effects:* Vast majority of the atoms in a nanostructures are located either at the surfaces or interfaces. The properties of these surface atoms can be quite different than that of those, which are located in the interior.

The above factors significantly alter the properties of the nanostructures as compared to their bulk material. For a nanomaterial systems, both the crystalline state and surface/interface state is very important. These materials are often in metastable state. Their atomic configuration depends on the kinetic process in which they are fabricated or grown. Therefore, the properties of nanostructures can be adjusted or manipulated by changing its size, shape or the process by which it is made, which can often lead to some rich and surprising outcomes.

The potential of nanostructures in various branches of science and engineering is immense. In 1959, physicist and future Nobel Prize winner Richard Feynman gave a lecture to the American Physical Society called "There's plenty of Room at the Bottom". The focus of his speech was about the field of miniaturization and how he believed man would create increasingly smaller, powerful devices [1]. In 1986, K. Eric Drexler wrote 'Engines of Creation' and introduced the term nanotechnology. Scientific research really expanded over the last decade. Inventors and corporations aren't far behind today. More than 13,000 patents registered with the U.S. Patent Office have the word *nano* in them [2].

Nanotechnology is a vast field by itself spread across various disciplines that includes applied physics, materials science, interface and colloid science, device physics, supramolecular chemistry (which refers to the area of chemistry that focuses on the non-covalent bonding interactions of molecules), self-replicating machines and robotics, chemical engineering, mechanical engineering, biological engineering, and electrical engineering. As this is a multidisciplinary field, much speculation exists as to what may result from these lines of research. Can we imagine a thousand machines being able to fit in an area the size of a pinhead, or a spaceship that can repair itself mid-flight? All these are made possible by nanotechnology. Although the research in nanotechnology are in the early stage, nanoscale intelligent materials such as carbon nanotubes, compound nanotubes, nanobelts, and other nanoscale materials have produced great excitement in the research community. These materials have found to have extraordinary mechanical and electrical properties, which have potential for tailorability and it is these features of nanoscale materials that is the cause of excitement among the research community. Currently, most of the focus is on nanotube based nanoscale materials, which are found to have novel strain sensing and force actuation properties. Although nanoscale materials, in particular Carbon Nanotube (CNT) have extraordinary properties, utilizing the properties both at the nano and the macro scale is major challenge that the scientists and engineers have to address.

This chapter deals with the background of the nanostructures and their classification in detail and also the various modelling techniques available to study the static and dynamic response of these materials.

1.1 Historical Perspectives

American physicist Richard Feynman in his talk at the American Physical Society (APS) in the year December 1959 at California Institute of Technology on *There's plenty of room at the bottom*, where he predicted that how one can arrange the atoms/molecules in a way that one wants to get a desired property to achieve some unbelievable applications. This triggered the imagination of scientists and researchers world over. The next major invention that contributed to the growth of nanotechnology is the invention of *Scanning Tunneling Microscope (STM)* in the year 1981 by Gerd Binnig and Heinrich Rohrer at the IBM Zurich Research Laboratory, for which they received the Nobel Prize in the year 1989. The invention of this instrument enabled scientist to image the material at the atomic level. This led to the discovery of CNT and Fullerenes some years later. Binnig, Calvin Quate and Christopher Gerber, in the year 1986, invented the first *Atomic Force Microscope (AFM)*. The word *Nanotechnology* was first used by Nario Taniguchi of the Tokio University of Science in the year 1974, wherein he described the semi conductor processes such as film deposition and ion beam billing, which exhibit the characteristic of the order of nanometers, as an atom-to-atom process. In the year 1991, the first Ph.D thesis in this area was from K. Eric Drexler from the MIT Media Lab. His thesis was titled *Molecular Machinery and Manufacturing with Applications to Computation*. The first real use of STM was demonstrated by IBM researcher Don Eigler, wherein he was the first to manipulate the 35 Xenon atoms.

The real take-off of nanostructures research and technological exploitation started with the accidental discovery of Fullerenes by Richard Smalley and his co workers Harry Kroto and Robert Curl in the year 1985. They received the Nobel prize in the year 1996 for their work. They found strange results in mass spectra of evaporated carbon samples. Fullerenes are large, closed-cage, carbon clusters and have several special properties that were not found in any other compound before. Therefore, fullerenes in general form an interesting class of compounds that surely will be used in future technologies and applications. Before the first synthesis and detection of the smaller fullerenes C₆₀ and C₇₀, it was generally accepted that these large spherical molecules were unstable. However, some Russian scientists already had calculated that C₆₀ in the gas phase was found to be stable and it had a relatively large band gap. With the stability of fullerenes in gas phase proven, the search for other fullerenes started.

The discovery of carbon nanotubes (CNT) is mainly due to Sumio Iijima [3]. However, existence of CNT prior to 1991 is reported in the literature[4]. Iijima initially discovered multi-wall carbon nano tubes (MWCNT) in the insoluble material of arc-burned graphite rods. while Mintmire, Dunlap and White, independently found

that single wall carbon nanotubes (SWCNT) can be made and their initial experiments showed that these exhibited remarkable conducting properties [5]. The works of these two groups created lots of excitement among the research community in the area of CNT's. Subsequent works on SWCNT by Bethune et al. [6] and Iijima et al. [7] greatly accelerated the nanotube research. These research have shown that the CNT's exist in large lengths (up to several microns) and small diameter (a few nanometers), which result in CNT having a large aspect ratio. They can be seen as the nearly one-dimensional form of fullerenes. Therefore, these materials are expected to possess additional interesting electronic, mechanic and molecular properties. Especially in the beginning, all theoretical studies on carbon nanotubes focused on the influence of the nearly one-dimensional structure on molecular and electronic properties.

Today, the nanotechnology is spread across many disciplines. Many unbelievable applications are conceptualized by the scientists and Engineers. For example, in the New York Times article on *Today's Vision of Science of Tomorrow* dated January 4, 2003, the article says that nanotechnology will lead to aerospace vehicles with 98 percent less structural mass. However, it is difficult to speculate the time that aerospace companies will take to meet this prediction. We see that major aircraft and engine companies such as Boeing, Airbus, General Electric and Pratt & Whitney are heavily investing in nanotechnology.

1.2 Hybridization of Carbon Nanostructures

Carbon is a remarkable element that has a unique structures which make it amenable to combine with other elements and compounds to get a new compound. It is said that carbon has the ability for form close to 10 million different compounds. It is present in the food we eat, the clothes we wear, the cosmetics we use and also in the fuel that drives our cars. Carbon exists in four different allotropes, namely the amorphous, the graphite, the diamond and the fullerene. The Amorphous carbon structure is visually a highly disordered structure. It is for this reason that it lacks structural integrity. This carbon structure forms at the edges or is the residue of other elemental compounds. The disorder of this structure allows it to have many available bonds and is responsible for building more complex carbon based molecules. Some of the properties of the carbon are as follows:

- Atomic number is 6
- Atomic mass is 12.011
- Density is 2.267 g/cm^3
- Wave velocity 18, 350 m/s.

Carbon has an atomic number of 6, which means it has 6 electrons out of which 4 of them are on the valance of outer shell as shown in Fig. 1.1a. Out of these 4 electrons, one is called the *s* electron while the other three are called the *p* electrons. The electron configuration shown in Fig. 1.1a can be misleading. It gives the impression that the electrons are circling the nucleus in orbits like planets around the sun. Actually it is

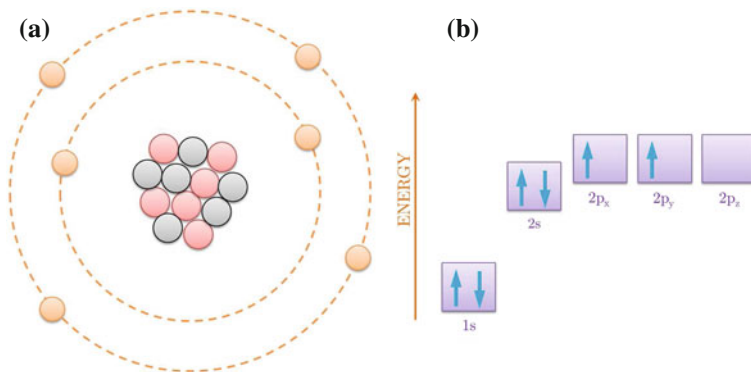


Fig. 1.1 a Structure of carbon atom. b Energy level graph

not possible to know exactly where the electrons are located. Alternatively, one can view the carbon atom by looking at the energy level graph shown in Fig. 1.1b. In this figure, all electrons are represented by arrows and the direction of the arrow represents the direction of the electron spin. From this figure, we see that two electrons are found in the 1s orbital close to the nucleus. The next two will go into the 2s orbital. The remaining ones will be in two separate 2p orbitals. This is because the p orbitals have the same energy and the electrons would rather be in separate orbitals. Hence, the actual location of electrons in a carbon atom cannot be determined with certainty and the electrons appear to be ‘smeared’ into orbitals. The above configuration can be represented as $1s^2 2s^2 2p_x^1 2p_y^1 2p_z^0$. This configuration represents two half-filled orbitals, which makes carbon bivalent. However, it is well known that carbon is tetravalent. In order to account for this tetra valency, one electron from 2s orbital jumps to 2p_z orbital. Thus the electron configuration becomes $1s^2 2s^1 2p_x^1 2p_y^1 2p_z^1$. In addition, it has been observed that carbon atom forms two types of bonds, three of one type (those formed from the three 2p orbitals) and 4th of another type (formed from 2s orbitals), since s and p orbitals are different with respect to energy and shape. However, it is a well-established fact that all the four valencies of carbon are equivalent. Therefore, it has been suggested that all the four orbitals mix together to form new orbitals of equivalent energy. This is the basic concept of hybridization.

Hence, *Hybridization may be defined as the phenomenon of mixing of atomic orbitals of nearly equivalent energy, involving redistribution of energy, to form new orbitals of equal energy known as hybrid orbitals. The number of hybrid orbitals is equal to the number of the orbitals hybridized. The properties of the hybrid orbitals are in between the properties of the orbitals which are hybridized.* The number of p-orbitals that take part in the hybridization is called the *hybridization Index*, normally represented as "m" and it is related to the bond angle (α) as

$$\cos(\alpha) = -\frac{1}{m} \quad (1.1)$$

Based on hybridization index, we can classify hybridization into following three categories.

1. sp^3 or *Tetrahedral Hybridization*: In this hybridization, one $2s$ and three $2p$ orbitals take part resulting in the formation of sp^3 hybridized orbitals. The direction of the orbitals and also the center of mass are to be determined by the specific contributions of the p -orbitals and the s -orbital. A combination of the hybrid orbitals produces a tetrahedral assembly with the center of masses in the corners as shown in Fig. 1.2a. The bond angle as per Eq. 1.1 is equal to $-\cos^{-1}(1/3)$, which is equal to 109.5° . The assembly of many sp^3 hybridized carbon atoms leads to a diamond structure, where the binding strength of each atoms are same and they are very strong. This structure exhibits large band gaps (close to 5 eV) and hence their electrical conductivity is very low. The example compound that came out of this hybridization is Methane CH_4 .
2. sp^2 or *Trigonal Hybridization*: Here, one $2s$ orbital and two $2p$ orbitals, namely p_x and p_y , take part in this hybridization. resulting in three sp^2 orbital. They contribute together to a planar assembly (see Fig. 1.2b) with a characteristic bond angle of 120° ($\alpha = -\cos^{-1}(1/2)$) between hybrid orbitals forming a σ -bond. The additional p_z -orbital is perpendicular to the sp^2 -hybrid orbitals and forms a π -bond. A typical example of a sp^2 -hybridized crystal structure is graphite. It consists of parallel carbon layers. Within a layer the planar sp^2 -hybrid orbitals align themselves to a structure with strong binding. Between the layers the π -orbitals give rise to weak Van-der-Waals-forces. As a result graphite is one of the softest materials known and is used in pencils

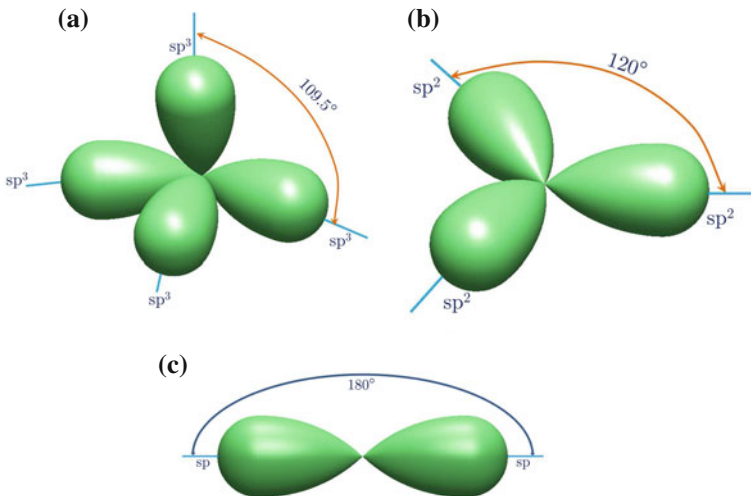


Fig. 1.2 Hybridization of carbon (a) sp^3 -Tetrahedral hybridization (b) sp^2 -Trigonal hybridization (c) sp -Linear hybridization

3. *sp* or *Linear Hybridization*: This hybridization is shown in Fig. 1.2c. Here, one $2s$ and one $2p$ or p_x orbital take part in hybridization, resulting in the formation of two hybrid orbitals known as *sp* hybrid orbitals. The bond angle in this case as per Eq. 1.1 is 180° . The example compound that came from this hybridization is Acetylene (C_2H_2).

With this basic understanding of the carbon hybridization, we will explain the structure of carbon nanotubes in the next subsection.

1.2.1 Nanotubes

There are many definitions to nanotubes. The simplest definition of nanotube is that it is a nanometer scale structure that resembles a tube. There are both organic and inorganic nanotubes. Organic nanotubes are the carbon nanotubes or CNT. With respect to CNT, a nanotube can be defined as a long cylindrical carbon structure consisting of hexagonal graphite molecules attached at the edges. Some nanotubes have a single cylinder while others have two or more concentric cylinders. Nanotubes have several characteristics, namely wall thickness, number of concentric cylinders, cylinder radius, and cylinder length. Some nanotubes have a property called chirality, an expression of longitudinal twisting.

It was mentioned earlier that crystal structure of a graphite is a layered structure and the carbon atoms within a layer are strongly bonded to their neighbors at room temperature. However, the layers are loosely coupled by van-der-Waals forces, which makes graphite highly deformable substance in a particular direction, which is one of the reasons why they are extensively used in pencils. A Single Wall CNT (SWCNT) can be constructed by rolling up the graphite sheet as a tubular shell with carbon atoms covalently bonded to its neighbors. The bonding mechanism in CNT is similar to that of graphite, which is sp^2 hybridization. The characteristic of sp^2 hybridization is the existence of σ -bonds and π -bonds. The σ -bonds are strong covalent bonds that binds the atom in a plane, due to which CNT exhibits high stiffness and strengths. In contrast, the π -bonds is a very weak bond, which represents the inter-layer interaction of atom pairs.

As mentioned earlier, there are also several non carbon nanotubes, which are reported in the literature. The commonly mentioned non-carbon variety are made from boron nitride, or from silicon. These noncarbon nanotubes are most often referred to as nanowires. The dimensions are variable (down to 0.4 nm in diameter) and one can also get nanotubes within nanotubes, leading to a distinction between multi-walled and single-walled nanotubes. Apart from remarkable tensile strength, nanotubes exhibit varying electrical properties (depending on the way the graphite structure spirals around the tube, and other factors, such as doping), and can be superconducting, insulating, semiconducting or conducting (metallic). Nanotubes can be either electrically conductive or semi conductive, depending on their helicity, leading to nanoscale wires and electrical components. These one-dimensional fibers exhibit

electrical conductivity as high as copper, thermal conductivity as high as diamond, strength 100 times greater than that of steel at one sixth its weight, and high strain to failure. A nanotube's chiral angle is the angle between the axis of its hexagonal pattern and the axis of the tube, which determines whether the tube is metallic or semiconducting.

1.2.2 Structure of Carbon Nanotubes

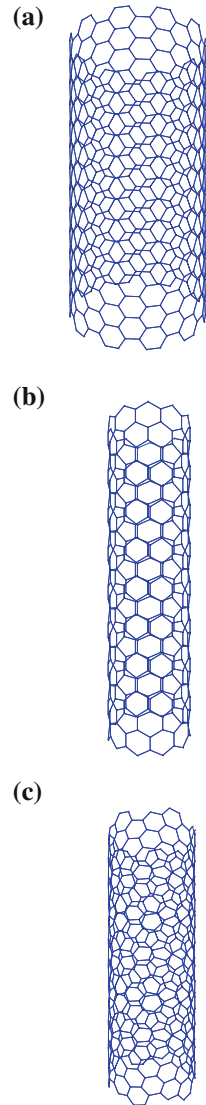
CNT is a cylindrical molecule composed of carbon atoms. Typical single-walled carbon nanotube (SWCNT) structures are illustrated in Fig. 1.3. A major feature of the structure is the hexagon pattern that repeats itself periodically in space. As a result of the periodicity, each atom is bonded to three neighboring atoms. Such structure is mainly due to the process of sp^2 hybridization [8], which was explained earlier. Based on the chirality [9], SWCNTs can have three different configurations. They are armchair (see Fig. 1.3a), zigzag (see Fig. 1.3b) and chiral (see Fig. 1.3c) configurations; denoted as (n, n) , $(n, 0)$ and (n, m) , respectively [9], where n and m represent the number of steps along the carbon bonds of the hexagonal lattice. The Armchair and Zigzag CNTs are generally named as *achiral nanotubes* since they exhibit a mirror symmetry plane, perpendicular to the tube axis [10].

As mentioned earlier, the bonding in carbon nanotubes is sp^2 , with each atom joined to three neighbours, as in graphite. The tubes can therefore be considered as rolled-up graphene sheets (see Fig. 1.4) [11]. The three distinct ways in which a graphene sheet can be rolled into a tube was explained earlier. The armchair and zig-zag CNT have a high degree of symmetry. The terms *armchair* and *zigzag* refer to the arrangement of hexagons around the circumference. The third class of tube, which in practice is the most common, is known as *chiral*, meaning that it can exist in two mirror-related forms. The chiral vector \mathbf{C} , also known as the roll-up vector, can be described by equation $\mathbf{C} = n\mathbf{a} + m\mathbf{b}$, where the integers (n, m) are the number of steps along the zigzag carbon bonds of the hexagonal lattice, \mathbf{a} and \mathbf{b} are unit vectors [12]. The chiral angle determines the amount of twist in the tube.

The chiral angles are 0° and 30° for the two limiting cases which are referred to as zigzag and armchair, respectively. In terms of the roll-up vector, the zigzag nanotube is denoted by $(n, 0)$ and the armchair nanotube as (n, n) . The roll-up vector of the nanotube also defines the nanotube diameter.

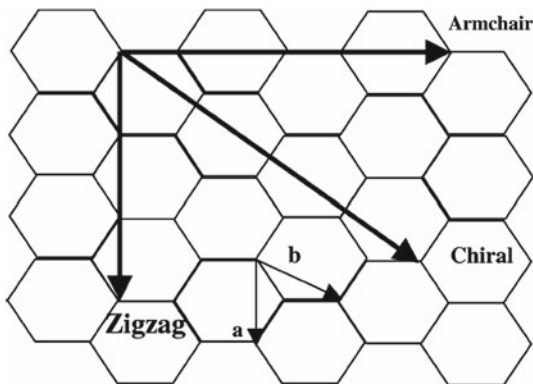
In the coming chapters, we will consider the wave propagation analysis armchair, zig-zag and chiral type of CNTs (see Fig. 1.3). The hexagonal arrangement of carbons in these structures are shown in Fig. 1.4. The physical properties of carbon nanotubes are sensitive to their diameter, length and chirality. In particular, tube chirality is known to have strong influence on the electronic properties of carbon nanotubes. Nanotubes can be either metallic or semiconducting, depending on tube chirality. Single walled carbon nanotube can undergo enormous bending and believed to behave elastically. The common type of CNT is the multi walled carbon nanotube (MWCNT), which is composed of concentric graphitic cylinders and the spacing

Fig. 1.3 **a** (10, 10) arm-chair type of CNT of length 34.6717 nm, consists of 580 carbon atoms, **b** (10, 0) zig-zag type of CNT of length 34.47 nm, consists of 340 carbon atoms, and **c** (10, 5) chiral type of CNT of length 34.563 nm, consists of 450 carbon atoms



between each graphite layer is 0.34 nm. Both single walled and multi walled carbon nanotubes are being used as key components in the production of high strength composites and advanced sensors, electronic and optical devices, catalysts, batteries and fuel cells. For the geometric relations of the structure of SWCNT see Refs. [15, 16].

Fig. 1.4 Definition of roll-up vector as linear combinations of base vectors (**a**) and (**b**)



1.2.3 Properties of Carbon Nanotubes

The strength of the sp^2 carbon-carbon bonds gives carbon nanotubes amazing mechanical properties [15, 16]. The mechanical and electrical properties of carbon nanotubes have been the subject of numerous studies ever since the discovery of nanotubes, largely because of the wide recognition of carbon nanotubes as important nanoscale systems and also because of various envisioned novel applications. Carbon nanotubes which are formed of seamless cylindrical grapheme layers represent the ideal carbon fiber and should presumably exhibit the best mechanical properties. This feature is probably the most promising for applications of nanotubes given the importance of extremely strong lightweight composites. The mechanical stiffness and strength of carbon nanotubes are expected to be very high.

It is remarkably difficult to directly measure the mechanical properties of single nanotubes due to their small diameters and their tendency to form bundles. The stiffness of carbon nanotubes was recently measured by a thermal vibration technique and Young's modulus was reported to be in the range of 1–5 TPa [17]. The Young's modulus of the best nanotubes can be as high as 1,000 GPa which is approximately 5% higher than steel. The tensile strength, or breaking stress of nanotubes can be up to 63 GPa, which is around 50% higher than steel. These properties, coupled with the lightness of carbon nanotubes, give them great potential in applications such as aerospace. The electronic properties of carbon nanotubes are also extraordinary. The unique physical and chemical properties of CNTs, such as structural rigidity and flexibility continue to generate considerable interest. Additionally, CNTs are extremely strong, about 100 times stronger (stress resistant) than steel at one-sixth the weight [16]. CNTs can also act as either conductors or semiconductors depending on their chirality, possess an intrinsic superconductivity, they are ideal thermal conductors, and they can also behave as field emitters. Currently, amazing properties of this material enable us to foresee more than 60 potential applications of carbon nanotubes, in various fields like electronic, aerospace, biomedical etc. (see Refs. [15, 16]). The properties of carbon nanotubes such as the elastic modulus, Poisson's ratio

Table 1.1 Young's modulus and tensile strength of carbon nanotubes compared with some other materials [13]

Material	Young's modulus (TPa)	Tensile strength (GPa)
SWCNT	~1 (from 1 to 5)	13–53
Armchair SWCNT	0.94	126.2
Zig-zag SWCNT	0.94	94.5
Chiral SWCNT	0.92	90
MWCNT	0.82–0.90	150
Stainless steel	~0.2	~0.65–1
Kevlar	~0.15	~0.35

and bulk modulus have been shown to exhibit strong dependence on their helicity and diameter, which in turn influences the stiffness, flexibility and the strength of carbon nanotubes. These aspects have motivated researchers world over to study the fundamentals of this material and explore their applications in different fields. In the next few paragraphs, we will list out the key properties (Mechanical, electrical, thermal, optical etc) of CNT

1. **Mechanical properties:** Following are the key mechanical properties of CNT:

- 100 times stronger than steel (from stress point of view) and 6 times lighter.
- Unlike carbon fibers, CNTs have high flexibility.
- Expansion by charge injection.
- High Young's modulus and tensile strength.
- Large current density and high aspect ratio.

The Young's modulus and tensile strength of carbon nanotubes with the other materials are shown in Table 1.1.

2. **Electrical properties:** Some of the key electrical properties of CNTs are listed below:

- One can tailor the conducting behavior of CNT. That is, CNTs can be made metallic or semiconductor behavior, according to chirality's (way a graphene sheet is rolled on itself). This means that one make CNT as conductive as copper and as insulative as a ceramic. Curvature effects seem to have an effect on its electrical properties.
- CNTs can be made as turnable field emission.

3. **Thermal properties:** The key thermal properties are the following:

- Theoretical work predicts a room-temperature thermal conductivity that is larger than graphite or diamond. Measurements show a room-temperature thermal conductivity over 200 W/m K for bulk samples of SWCNTs and over 3,000 W/m K for MWCNT.
- Addition of epoxy can double the thermal conductivity of CNTs.

- CNTs are stable at very high temperature, which means it can be used for applications such as thermal barrier coatings used in re-entry space vehicles.
 - CNT's are said to be good conductors along the tube axis and good insulators laterally.
 - Carbon nanotubes can resist strong acid effects, especially at high temperature because of their perfect conjugated system. Acid and heat are often applied to purify carbon nanotubes.
4. **Physico-chemical properties:** Some of the important physical and chemical properties of CNTs are the following:
- CNTs high specific area, which means several hundreds of square meters per gram of CNT.
 - They have cavities enabling molecules storage inside the carbon nanotube.
 - Chemical treatment on carbon nanotubes can be done for enabling to fix other molecules of the carbon nanotubes.
 - CNT's have high thermal resistance (up to 1,500°C under vacuum).
5. **Field emission properties:** CNTs have excellent materials properties which make them have attractive field emission characteristics such as
- Large aspect ratio (>1,000)
 - Atomically sharp tips
 - High temperature and chemical stability
 - High electrical and thermal conductivity.

In comparison to usual metallic emitters, the applied voltages needed for field emission were are lower in CNT for a comparable emitted current. Carbon nanotubes can be used as electron sources in two different types of set-ups, namely single and multiple electron beam devices. One possible application of a single electron beam instrument is an electron microscope that uses a single nanotube as a field emission electron gun to produce a highly coherent electron beam. Conversely, flat panel displays are the most popular example of multiple beam instruments where a continuous or patterned film of nanotubes provides a large number of independent electron beams.

6. **Optical Properties:** Some of the key optical properties of CNTs are summarized below:
- Optical properties of the CNT derive from the electronic transitions within the 1-D density of states, which can be assessed by looking at the peaks in the energy levels. These energy levels can be changed by modifying the nanotube structure, which in turn changes the opto-electronic properties of the CNT.
 - CNTs have good Luminescence property, which has applications in the single molecule light emitters.
 - Photoluminescence from SWCNT, as well as optical absorption and Raman scattering, is linearly polarized along the tube axis. This allows monitoring of the SWCNTs orientation without direct microscopic observation.

- A material is said to be perfectly light absorbing material if its emissivity is close to 1.0, which is very difficult to achieve. SWCNT forests also called *buckypaper* is said to have emissivity close to 0.98–0.99 from ultra violet wavelengths (200 nm) to infra red wavelengths (200 μ m)

Here only few important properties is listed for the sake of completeness. As is obvious, the amount of literature available on the various properties of CNTs are plenty. For details on these, the reader is encouraged to see Refs. [15, 16].

1.3 Need for Wave Propagation Analysis in Nanostructures

Increasing emphasis of miniature devices have made the scientists to look for newer and novel materials which can be handled at the atomistic scales. In this regard, Nanoscale materials and structures with nano thicknesses have attracted considerable interest from the scientific community in the fields of microelectronics and nanotechnology. More and more nanostructures, e.g. ultra-thin films, nanowires and nanotubes, have been fabricated and served as the basic building blocks for nano-electro-mechanical-systems (NEMS). For long-term stability and reliability of various devices at nanoscale, researchers should possess a deep understanding and knowledge of mechanical properties of nano-materials and -structures, especially the time dependent or dynamic properties.

Among many techniques, high-frequency acoustic wave technique has been regarded as one of very efficient nondestructive methods to characterize elastic media with nanostructures. Hernaandez et al. [18] used high-frequency laser-excited guided acoustic waves to estimate the in-plane mechanical properties of silicon nitride membranes. Mechanical properties and residual stresses in the membranes were evaluated from measured acoustic dispersion curves. The mean values of the Youngs modulus and density of three nanocrystalline diamond films and a free standing diamond plate were determined by analyzing the dispersion of laser-generated surface waves by Philip et al. [19].

Nanostructures such as CNTs can propagate waves of the order of terahertz (THz). THz waves in nanoscale materials and nano-phonic or nano-phononic devices has opened a new topic on the wave characteristics of nanomaterials [20–22]. They also have applications in CNTs and other applications[23–25]. As dimensions of the material become smaller, however, their resistance to deformation is increasingly determined by internal or external discontinuities (such as surfaces, grain boundary, strain gradient, and dislocation). Although many sophisticated approaches for predicting the mechanical properties of nanomaterials have been reported, few addressed the challenges posed by interior nanostructures such as the surfaces, interfaces, structural discontinuities and deformation gradient of the nanomaterials under extreme loading conditions. The use of atomistic simulation may be a potential solution in the long run. However, it is well known that the capability of this approach is much limited by its need of prohibitive computing time and an astronomical amount of data

generated in the calculations. Wave propagation analysis using continuum models, especially using non-local elasticity models can be used to address the above problems.

Wave propagation studies mainly include the estimation of wavenumber and wave speeds such as phase and group speeds. The concept of group velocity may be useful in understanding the dynamics of carbon nanotubes, since it is related to the energy transportation of wave propagation. The primary objective of this book is to study the wave propagation in nanostructures, so as to examine the effect of length scales on the wave dispersion from the viewpoint of group velocity or energy transportation. To describe the effect of microstructures of a nanostructure on its mechanical properties, it is assumed that the model of the nanostructure is made of a kind of non-local elastic material, where the stress state at a given reference location depends not only on the strain of this location but also on the higher order gradient of strain, so as to take the influence of the microstructures into account. It is reported that both local elastic models (where effects of nano scale is not considered) and non-local elastic models (where the effect of scale is considered) can offer the correct prediction when the wavenumber is lower. However, the results of the elastic model remarkably deviate from those given by the non-local elastic model with an increase in the wavenumber. As a result, the microstructures play an important role in the dispersion of waves in nanoscale structures. Since terahertz physics of nanoscale materials and devices are the main concerns in wave characteristics of CNTs, the small-scale effect must be of significance in achieving accurate dispersion relations as the wavelength in the frequency domain is in the order of nanometers.

In addition, recent progress in nanomaterials science has made it possible to produce nanofibers of dielectric, ferroelectric, and other smart polymeric materials, which are potential candidates for nanosensors and transducers and also can be directly integrated into polymeric matrix to form smart nanocomposites. In the case of dynamic characterization and device design based on these functional nanofilamentary materials, studies reported in the literature were mainly focused on their linearly elastic behavior. However, in many cases, wave phenomena may happen in materials with large prestretch. Without a doubt, examination of wave phenomena in polymer nanofibers is a topic of interest in exploring their promising industrial applications. It is expected that the dynamic response of polymer nanofibers may exhibit some unique characteristics owing to their nanoscale geometries.

Since controlled experiments at the nanoscale are difficult, and with atomistic simulation being computationally expensive, continuum modeling can prove to be very valuable in the advancement of nanoscale structures but it needs further improvement and development. Continuum elastic beam models have been effectively used to study vibrations and wave propagation in nanostructures. In view of growing interest in terahertz vibrations and waves of nanoscale materials and devices, it is relevant to systematically study terahertz wave propagation in individual nanostructures. Since terahertz physics of nanoscale materials and devices are major concerns for nanostructure's wave characteristics, small-scale effect needs to be considered in the mathematical models (especially the continuum models) as the wavelength is normally of the order of nanometer. The main scope of this book is to apply nonlocal continuum modelling to study wave characteristics of all type of nanostructures.

1.4 Outline and Scope of the Book

The entire book is organized into 10 chapters. In Chap. 2, we first present a brief introduction to concepts of wave propagation in structures and all the necessary tools required for wave propagation studies. In particular, the spectral analysis, determination of general spectrum and dispersion relations are addressed for some important waveguides. The available approaches to obtain the wavenumber and the wave amplitudes are also presented in this chapter. In Chap. 3, the basic concepts of the nonlocal elasticity theory are discussed. Various types of nonlocalness, properties of nonlocal kernels and the constitutive relations in various coordinate systems are also briefly outlined. In Chap. 4, an introduction to Molecular Dynamics (MD) simulations and the application of MD simulations in studying the wave propagation characteristic of nanostructures are presented. Chapter 5 addresses a self-consistent method of estimation of nonlocal scale parameter for armchair, zigzag and chiral type nanotubes based on molecular structural mechanics and wave propagation methods. Nonlocal scale effects on length dependent in-plane stiffness of nanotubes with various end conditions are also given in this chapter. In Chap. 6, axial/longitudinal and torsional wave propagation in nanorods is presented. Various nonlocal models are used for formulating the governing equations for nanorods. Extraction of second and fourth order strain gradient models from nonlocal stress gradient model is also presented. Nonlocal spectral finite element formulation for studying the axial and torsional wave propagation in nanoscale rods is also given in this chapter. Wave propagation in nanobeams is discussed in Chap. 7. Nonlocal governing equations for Bernoulli-Euler and Timoshenko beam models are also obtained. Generally encountered problems in nanoscience community, like rotating nanotubes, fluid carrying nanotubes, magnetic field effects and surface effects on wave propagation are also presented in detail. In Chap. 8, nonlocal scale and van-der-Waals effects on wave propagation in multi-walled carbon nanotubes are presented with examples of single-, double-, and triple-walled CNTs. In Chap. 9, wave dispersion characteristics of coupled one-dimensional nanosystems are discussed. These coupled systems are formulated based on basic axial rod model, Euler-Bernoulli and Timoshenko beam models. Chapter 10 addresses the two-dimensional wave propagation in nanoscale plate like structures such as graphene is presented. Problems involving substrate effects, temperature effects and surface effects are also formulated based on nonlocal elasticity theory and discussed in detail. Three dimensional wave propagation in empty and fluid filled nanoshells is presented in Chap. 11. The coupling among axial, flexural, shear and contraction wave modes is also formulated and discussed.

1.5 Summary

In this chapter, the basic structure of CNT and the types of CNTs are discussed briefly. The properties of CNTs along with their applications are discussed in this chapter. The different hybridization of the carbon nanostructures is discussed next

followed by a section on the need for wave propagation analysis. The chapter ends with an outline and scope of this textbook

References

1. R.P. Feynman, There's plenty of room at the bottom. *Eng. Sc.* **23**, 22–36 (1960)
2. www.uspto.gov
3. S. Iijima, Helical microtubes of graphitic carbon. *Nature* **354**, 56–58 (1991)
4. M. Monthieux, V. Kuznetsov, Who should be given the credit for the discovery of carbon nanotubes? *Carbon* **44**(9), 1621–1623 (2006)
5. J.W. Mintmire, B.L. Dunlap, C.T. White, Are fullerene tubules metallic? *Phys. Rev. Lett.* **68**(5), 631–636 (1992)
6. D.S. Bethune, C.H. Klang, M.S. De Vries, G. Gorman, R. Savoy, J. Vazquez, R. Beyers, Cobalt-catalyzed growth of carbon nanotubes with single-atomic-layer walls. *Nature* **363**, 605607 (1993)
7. S. Iijima, T. Ichihashi, Single-shell carbon nanotubes of 1-nm diameter. *Nature* **363**, 603605 (1993)
8. T.L.L. Brown, B.E. Bursten, H.E. Lemay, *Chemistry: The Central Science*, 8th edn. (Prentice-Hall, London, 1999)
9. N. Hamada, S. Savada, A. Oshiyama, New one-dimensional conductors: graphitic microtubes. *Phys. Rev. B* **68**, 1579 (1992)
10. M. Meo, M. Rossi, A molecular-mechanics based finite element model for strength prediction of single wall carbon nanotubes. *Mater. Sci. Eng. A* **454**, 170–177 (2007)
11. B.I. Yakobson, J. Brabec Bernholc, Mechanical properties of carbon nanotubes, in *Nanomechanics, Carbon nanotubes: Synthesis, Structure, Properties and Applications*, ed. by M.S. Dresselhaus, G. Dresselhaus (Springer, New York, 1996)
12. C. Li, T.W. Chou, A structural mechanics approach for analysis of carbon nanotubes. *Int. J. Solids Struct.* **40**, 2487–2499 (2003)
13. M.S. Dresselhaus, G. Dresselhaus, R. Saito, Physics of carbon nanotubes. *Carbon* **33**(7), 883–891 (1995)
14. S. Saito, D. Dresselhaus, M.S. Dresselhaus, *Physical Properties of Carbon Nanotubes* (Imperial College Press, London, 1998)
15. M.J. O'Connell, *Carbon Nanotubes: Properties and Applications* (CRC Press Taylor & Francis Group, Boca Raton, 2006)
16. M. Endo, S. Iijima, *Carbon Nanotubes* (Elsevier Science Ltd, The Boulevard, Langford Lane, 1996)
17. L. Vaccarini, C. Goze, L. Henrard, E. Hernandez, P. Bernier, A. Rubio, Mechanical and electronics properties of carbon and boron-nitride nanotubes. *Carbon* **38**, 1681–1690 (2000)
18. C.M. Hernandez, T.W. Murray, S. Krishnaswamy, Photoacoustic characterization of the mechanical properties of thin films. *Appl. Phys. Lett.* **80**(4), 691–693 (2002)
19. J. Philip, P. Hess, T. Feygelson, J.E. Butler, S. Chattopadhyay, K.H. Chen, L.C. Chen, Elastic mechanical and thermal properties of nanocrystalline diamond films. *J. Appl. Phys.* **93**(4), 2164–2171 (2003)
20. R. Ramprasad, N. Shi, Scalability of phononic crystal heterostructures. *Appl. Phys. Lett.* **87**, 111101 (2005)
21. A. Sampathkumar, T.W. Murray, K.L. Ekinci, Photothermal operation of high frequency nanoelectromechanical systems. *Appl. Phys. Lett.* **88**, 223104 (2006)
22. D. Schneider, T. Witke, T. Schwarz, B. Schoneich, B. Schultrich, Testing ultra-thin films by laser-acoustics. *Surf. Coat. Technol.* **126**, 136–141 (2000)

23. C. Sirtori, Bridge for the terahertz gap. *Nature* **417**, 132–133 (2002)
24. T. Jeon, K. Kim, Terahertz conductivity of anisotropic single walled carbon nanotube films. *Appl. Phys. Lett.* **80**, 34033405 (2002)
25. G.A. Antonelli, H.J. Maris, Picosecond ultrasonics study of the vibrational modes of a nanostructure. *J. Appl. Phys.* **91**, 32613267 (2002)

Chapter 2

Introductory Concepts of Wave Propagation Analysis in Structures

Wave propagation is a transient dynamic phenomenon resulting from short duration loading. Such transient loadings have high frequency content. The main difference between the structural dynamics and wave propagation in structures arises due to high frequency excitations in the later case. Structures very often experience such loadings in the forms of impact and blast loadings like gust, bird hit, tool drops etc. Apart from these, the wave propagation studies are also important to understand the dynamic characteristics of a structure at higher frequencies due to their various real-world applications. Structural health monitoring or detection of damage is one such important application. As wave propagation deals with higher frequencies, diagnostic waves can be used to predict the presence of even minute defects, which occur at initiation of damage and propagate them till the failure of the structure. In many aircraft structures, the undesired vibration and noise transmit from the source to the other parts in form of wave propagation and this requires control or reduction, which is again an important application of wave propagation studies.

A structure, when subjected to dynamic loads, will experience stresses of varying degree of severity depending upon the load magnitude and its duration. If the temporal variation of load is of large duration (of the order of seconds), the intensity of the load felt by the structure will usually be of lower severity and such problems fall under the category of structural dynamics. For such problems, there are two parameters which are of paramount importance in the determination of its response, namely the *natural frequency* of the system and its *normal modes* (mode shapes). The total response of structure is obtained by the superposition of first few normal modes. Large duration of the load makes it low on the frequency content, and hence the load will make only the first few modes to get excited. Hence, the structure could be idealized with fewer unknowns (which we call as degrees of freedom). However, when the duration of load is small (of the order of microseconds), the stress waves are set up, which starts propagating in the medium with certain velocity. Hence, the response is necessarily transient in nature and in the process, many normal modes will get excited. Hence, the model sizes will be many orders bigger than what is required for the structural dynamics problem. Such problems come under the category of wave propagation.

In Sect. 1.3, the need to study wave propagation in structures was highlighted. It is quite well-known that nanostructures can propagate waves of the order of terahertz. Propagation of waves in such structures can be studied using various modeling techniques highlighted in Chap. 3. For example, modeling technique such as ab initio atomistic modeling or molecular dynamics methods can be employed to study wave propagation in such nanostructures. However, the main limitation of these methods is the computational time that these methods will take. Some researchers have used finite element method coupled with molecular mechanics model to solve such problems. However, if the frequency content of the problem is of the terahertz level, then for FE modeling, one needs a FE mesh compatible with its wavelength, which is extremal small at the terahertz frequency. These limitations can be overcome to some extent by using Spectral Finite Element Method (SFEM), which is the FE method in the frequency domain. It uses the spectral analysis to understand the physics of wave propagation, whose results will be directly used in the SFEM formulation. This chapter mainly deals with the spectral analysis of motion, which will tell about the nature of waves that is propagating in the medium and the speed with which the waves are propagating.

2.1 Introduction to Wave Propagation

The key factor in the wave propagation is the propagating velocity, level of attenuation of the response and its wavelengths. Hence, phase information of the response is one of the important parameters, which is of no concern in the structural dynamic problems [1].

The wave propagation is a multi-modal phenomenon, and hence the analysis becomes quite complex when the problem is solved in the time domain. This is because, the problem by its nature is a high frequency content problem. Hence, the analysis methods based on the frequency domain is normally preferred for wave propagation problems. That is, all the governing equations, boundary conditions, and the variables are transformed into the frequency domain using any of the integral transforms available. The most common transformation for transforming the problem to the frequency domain is the Fourier Transforms. This transform has the discrete representation and hence amenable for numerical implementation, which makes it very attractive for its usage in the wave propagation problems. By transforming the problem into frequency domain, the complexity of the governing partial differential equation is reduced by removing the time variable out of picture, making the solution simpler than the original equation. In wave propagation problems, we are concerned about two parameters, namely the wavenumber and the speeds of the propagation (normally referred to as group speeds).

There are many types of waves that can be generated in structure. Wavenumber reveals the type of waves that are generated. Hence, in wave propagation problems, two important relations are very important, namely the spectrum relations, which is plot of the wavenumber with the frequency and the dispersion relations, which is a

plot of wave velocity with the frequency. These relations reveal the characteristics of different waves that are generated in a given structure.

2.2 Spectral Analysis

Spectral analysis determines the local wave behavior for different waveguides and hence the wave characteristics, namely the *spectrum* and the *dispersion* relation. These local characteristics are synthesized over large number of frequencies to get the global wave behavior. Spectral analysis uses discrete Fourier transform to represent a field variable (say displacement) as a finite series involving a set of coefficients, which requires to be determined based on the boundary conditions of the problem [1–3].

Spectral analysis enables the determination of two important wave parameters, namely the wavenumbers and the group speeds (discussed in next section). These parameters are not only required for spectral element formulation [1], but also to understand the wave mechanics in a given waveguide. These parameters enable us to know whether the wave mode is a propagating mode or a damping mode or a combination of these two (propagation as well as wave amplitude attenuation). If the wave is propagating, the wavenumber expression will let us know whether it is nondispersive (that is, the wave retains its shape as it propagates) or dispersive (when the wave changes its shape as it propagates). More details on spectral analysis and applications to several problems can be found in Refs. [1, 4, 5]. In the next subsection, we will define some of the commonly used wave propagation terminologies.

2.3 Wave Propagation Terminologies

1. Waveguide

Any structural element is called a waveguide as it guides the wave in a particular manner. For example, a bulk or a nano rod essentially supports only the axial motion and hence it is called axial or longitudinal waveguide. In the case of a beam, only bending motion is possible and hence the beam is called the flexural waveguide. In the case of shafts, the only possible motion is the twist and hence they are called torsional waveguide. In case of laminated composite beam, due to stiffness coupling both axial and flexural motions are possible. In general, if there are n highly coupled governing partial differential equations, then such a waveguide can support n different motions.

2. Wavenumber

This is a frequency-dependent parameter that determines the following:

- Whether the wave is propagating or nonpropagating or will propagate after certain frequency.

- It also determines the type of wave, namely dispersive or nondispersive wave.

Nondispersive waves are those that retain its shape as it propagates, while the dispersive waves are those that completely change its shape as it propagates. That is if the wavenumber (k) is expressed as a linear function of frequency (ω) as $k = c_1\omega$, (c_1 is a constant) then the waves will be nondispersive in nature. Wavenumber in rods and in general for most second-order system, will be of this form and hence the waves will be nondispersive in nature. However, if the wave number is of the form $k = c_2\omega^n$, (c_2 is a constant) the waves will essentially be dispersive. Such a behavior can be seen in higher order systems such as beams and plates. In such cases, the wave speeds will change with the frequencies. The plot of wavenumber with the frequency is usually referred to as spectrum relations.

3. Phase speed

These are the speeds of the individual particles that propagate in the structure. They are related to the wavenumber through the relation

$$C_p = \frac{\omega}{\text{Real}(k)} \quad (2.1)$$

If the waves are nondispersive in nature (that is $k = a\omega$), then the phase speeds are constant and independent of frequency. Conversely, if the phase speeds are constant, then such a system is nondispersive system. Phase speed is not associated with transfer of any physical quantity (e.g., mass, momentum or energy) in a waveguide.

4. Group speed

Group velocity is associated with the propagation of a group of waves of similar frequency. During the propagation of waves, groups of particles, travel in bundles. The speeds of each of these bundle are called the group speed of the wave. They are mathematically expressed as

$$C_g = \frac{\partial\omega}{\partial k} \quad (2.2)$$

Again here, for nondispersive system, the group speeds are constant and independent of frequency. Hence, the time of arrival of all waves will be based on this frequency. The plot of phase/group speeds with the frequency is called the dispersion relations. This is a velocity of the energy transportation and it must be bounded. Monograph [1] derives the expression for the wavenumbers and group speeds for some commonly used metallic and composite waveguides in engineering.

5. Relation between group and phase speeds

Since from Eq. (2.1) we have

$$k = \frac{\omega}{C_p} \quad (2.3)$$

Substituting Eq. (2.1) into Eq. (2.2) gives

$$C_g = d\omega \left[d \left(\frac{\omega}{C_p} \right) \right]^{-1} = d\omega \left[\frac{d\omega}{C_p} - \omega \frac{dC_p}{C_p^2} \right]^{-1} = C_p^2 \left[C_p - \omega \frac{dC_p}{d\omega} \right]^{-1} \quad (2.4)$$

Using $\omega = 2\pi f$,

$$C_g = C_p^2 \left[C_p - (ft) \frac{dC_p}{d(ft)} \right]^{-1} \quad (2.5)$$

where ft denotes the frequency times thickness.

- When the derivative of C_p with respect to ft becomes zero, $C_g = C_p$.
- As the derivative of C_p with respect to ft approaches infinity (that is, cut-off frequency), C_g approaches zero.

6. Cut-off Frequency

In some waveguides, some waves will start propagating only after certain frequency called the cut-off frequency. The wavenumber and group speeds before this frequency will be imaginary and zero, respectively. In the next section, we will outline a procedure to compute the cut-off frequency for the second- and fourth-order systems.

2.4 Spectrum and Dispersion Relations

Here, two important frequency-dependent wave characteristics, namely, spectrum and dispersion relations, are obtained for a generalized system defined by the second- and fourth-order partial differential equations (PDE). These relations are the frequency variation of the wave parameters termed as wavenumbers and wave speeds, respectively. These parameters are essential to understand the wave mechanics in a given waveguide and are also required for SFEM formulation. These parameters provide information like whether the wave mode is a propagating mode or a damping mode or a combination of these two (propagation as well as wave amplitude attenuation). Next, for a propagating mode, the nature of frequency variation of wavenumbers gives information whether the mode is nondispersive, i.e., the wave retains its shape as it propagates or dispersive where the shape changes with propagation. In this section, these parameters are explained using the example of a generalized one-dimensional second- and fourth-order systems.

2.4.1 Second-Order PDE

The spectral analysis starts with the partial differential equation governing the waveguide. Considering a generalized second-order partial differential equation given by

$$p \frac{\partial^2 u}{\partial x^2} + q \frac{\partial u}{\partial x} = r \frac{\partial^2 u}{\partial t^2} \quad (2.6)$$

where p , q , and r are known constants depending on the material properties and geometry of the waveguide. $u(x, t)$ is the field variable to be solved for with x being the spatial dimension and t the temporal dimension. First, $u(x, t)$ is transformed to frequency domain using discrete Fourier transform (DFT) as

$$u(x, t) = \sum_{n=1}^{N-1} \hat{u}_n(x, \omega_n) e^{j\omega_n t} \quad (2.7)$$

where ω_n is the discrete circular frequency in rad/sec and N is the total number of frequency points used in the transformation. The ω_n is related to the time window by

$$\omega_n = n\Delta\omega = \frac{n\omega_f}{N} = \frac{n}{N\Delta t} = \frac{n}{T} \quad (2.8)$$

where Δt is the time sampling rate and ω_f is the highest frequency captured by Δt . The frequency content of the load decides N and consideration of the wrap around and aliasing problem decides $\Delta\omega$. More details and associated problems are given in Ref. [1].

Here, \hat{u}_n is the n th DFT coefficient and can also be referred to as the coefficient at frequency ω_n . \hat{u}_n varies only with x . Substituting Eq. (2.7) into Eq. (2.6), we get

$$p \frac{d^2 \hat{u}_n}{dx^2} + q \frac{d\hat{u}_n}{dx} + r\omega_n^2 \hat{u}_n = 0, \quad n = 0, 1, \dots, N-1 \quad (2.9)$$

Thus, through DFT, the governing PDE given by Eq. (2.6) is reduced to N ODE. Equation (2.9) being constant coefficient ODEs, have a solution of the form $\hat{u}_n(x) = A_n e^{jk_n x}$, where A_n are the unknown constants, which will be computed from the boundary values and k_n is called the wavenumbers corresponding to the frequency ω_n . Substituting the above solution into Eq. (2.9), we get the following characteristic equation to determine k_n ,

$$\left(-pk_n^2 + jqk_n + r\omega_n^2\right) A_n = 0 \quad (2.10)$$

The subscript n is dropped hereafter for simplified notations. The above equation is quadratic in k and has two roots corresponding to the incident and reflected waves. If the wavenumbers are real, then the wave is called propagating mode. On the

other hand, if the wavenumbers are purely imaginary, then the wave damps out as it propagates and hence is called evanescent mode. If wavenumbers are complex having both the real and imaginary parts, then the wave with such a wavenumber will attenuate as they propagate. These waves are normally referred to as inhomogeneous waves. The set of the wavenumbers obtained by solving the characteristic Eq. (2.10) is given as

$$\begin{aligned} k_1 &= j \frac{q}{2p} + \sqrt{-\frac{q^2}{4p^2} + \frac{r\omega^2}{p}} \\ k_2 &= j \frac{q}{2p} - \sqrt{-\frac{q^2}{4p^2} + \frac{r\omega^2}{p}} \end{aligned} \quad (2.11)$$

Equation (2.11) is the generalized expression for the determination of the wavenumbers. Different wave behaviors are possible depending upon the values of the radical $\frac{r\omega^2}{p} - \frac{q^2}{4p^2}$. As an example, for a case with $q = 0$, the wavenumbers are given as

$$\begin{aligned} k_1 &= \omega \sqrt{\frac{r}{p}} \\ k_2 &= -\omega \sqrt{\frac{r}{p}} \end{aligned} \quad (2.12)$$

For such a case, the wavenumbers are real and hence the corresponding waves are propagating. When $r\omega^2/p < q^2/4p^2$, then the wavenumber is purely imaginary and the system will not allow any way to propagate. However, when $r\omega^2/p > q^2/4p^2$, the wavenumber will be complex and in this case, the waves will attenuate as they propagate.

Next, two other important wave parameters, namely, phase speed (C_p) and group speed (C_g), are briefly explained.

Let us consider the previous example where wavenumbers vary linearly with frequency as given by Eq. (2.12). Correspondingly, the wave speeds are obtained as follows:

$$\begin{aligned} C_p &= \frac{\omega}{k} = \sqrt{\frac{p}{r}} \\ C_g &= \frac{d\omega}{dk} = \sqrt{\frac{p}{r}} \end{aligned} \quad (2.13)$$

We find that both group and phase speeds are constant and equal. Hence, when wavenumbers vary linearly with frequency ω , the wave retains its shape as it propagates. Such waves are called nondispersive waves. When wavenumbers have a nonlinear variation with frequency, the phase and group speeds will not be constant but will be function of frequency. As a result, each frequency component will travel

with different speeds and the wave shape will not be preserved with wave propagation. Such waves are called dispersive waves. For nonzero values of p , q and r , the expression for phase and group speeds become

$$\begin{aligned} C_p &= \operatorname{Re} \left(\frac{\omega}{\sqrt{\frac{r\omega^2}{p} - \frac{q^2}{4p^2}}} \right) \\ C_g &= \operatorname{Re} \left(\frac{p\sqrt{\frac{r\omega^2}{p} - \frac{q^2}{4p^2}}}{r\omega} \right) \end{aligned} \quad (2.14)$$

Here “Re” represents *real* part of the expression. Thus, it can be seen that the wave speeds C_p and C_g are not the same and hence the waves are dispersive in nature. The value of the radical, however, depends on frequency and there can be a frequency after which the wavenumbers transit from being purely imaginary to complex or real wavenumbers resulting in propagation of the wave mode. This transition frequency is called the *cut-off frequency* (ω_c) and can be derived by equating the radical to zero. The expression for the cut-off frequency for this second-order system is given as

$$\omega_c = \frac{q}{2\sqrt{pr}} \quad (2.15)$$

Once the wavenumbers are determined the solution of the transformed ODEs given by Eq. (2.9) can be written as

$$\hat{u}(x, \omega) = A_1 e^{-jk_1 x} + A_2 e^{-jk_2 x} \quad (2.16)$$

The unknown constants A_1 and A_2 can be evaluated in terms of the physical boundary conditions of the one-dimensional waveguide. This can be done in a formal manner using the spectral finite element technique which will be explained in details later. For $q = 0$ the above equation is of the form,

$$\hat{u}(x, \omega) = A_1 e^{-jkx} + A_2 e^{jkx}, \quad k = \omega \sqrt{\frac{r}{p}} \quad (2.17)$$

where A_1 represent the incident wave coefficient while A_2 stands for the reflected wave coefficient.

2.4.2 Fourth Order PDE

Next, let us consider a fourth-order system and study its wave behavior. Consider the following governing PDE

$$p \frac{\partial^4 w}{\partial x^4} + qw + r \frac{\partial^2 w}{\partial t^2} = 0 \quad (2.18)$$

where $w(x, t)$ is the field variable and p , q , and r are arbitrary known constants depending on the material and geometric properties of the waveguide as in the case of the second-order system. The above equation is similar to the equation of motion of a Euler–Bernoulli beam on elastic foundation. The DFT of $w(x, t)$ can be written in a similar form as Eq. (2.7),

$$w(x, t) = \sum_{n=1}^{N-1} \hat{w}_n(x, \omega_n) e^{j\omega_n t} \quad (2.19)$$

Substituting Eq. (2.19) into the governing PDE given by Eq. (2.18) we get the reduced ODEs as

$$p \frac{d^4 \hat{w}_n}{dx^4} + (q - r\omega_n^2) \hat{w}_n = 0 \quad (2.20)$$

The above ODEs have constant coefficients and hence the solution will be of the form $\hat{w}_n(x) = A_n e^{jk_n x}$. Substituting this solution into Eq. (2.20) we get the characteristic equation for solution of the wavenumbers. Again the subscript n is dropped hereafter for simplified notations and all the following equations have to be derived for n varying from 0 to $N-1$. The characteristic equation is of the form

$$pk^4 + q - r\omega^2 = 0 \quad \text{or} \quad k^4 - \left(\frac{r}{p} \omega^2 - \frac{q}{p} \right) = 0 \quad (2.21)$$

This is a fourth-order equation and will give two sets of wavenumbers. The type of wave is dependent upon the numerical value of $\frac{r}{p} \omega^2 - \frac{q}{p}$. For $\frac{r}{p} \omega^2 > \frac{q}{p}$, the solution of Eq. (2.21) will give the following wavenumbers,

$$\begin{aligned} k_1 &= +\alpha, & k_2 &= -\alpha \\ k_3 &= +j\alpha, & k_4 &= -j\alpha \end{aligned} \quad (2.22)$$

where $\alpha = \left(\frac{r}{p} \omega^2 - \frac{q}{p} \right)^{1/4}$. In the above equation, k_1 and k_2 represent the propagating wave modes while k_3 and k_4 are the damping or evanescent modes. From the above equations, we find that the wavenumbers are nonlinear functions of the frequency, and hence the corresponding waves are expected to be highly dispersive in nature. Also, using the above expression we can find the phase and group speeds for the propagating mode from Eq. (2.13).

Next, consider the case when $\frac{r}{p} \omega^2 < \frac{q}{p}$. For such conditions, the wavenumbers are given by

$$\begin{aligned}
k_1 &= +\frac{1+j}{\sqrt{2}}\alpha, & k_2 &= -\frac{1+j}{\sqrt{2}}\alpha \\
k_3 &= +\frac{-1+j}{\sqrt{2}}\alpha, & k_4 &= -\frac{-1+j}{\sqrt{2}}\alpha
\end{aligned} \tag{2.23}$$

From the above equation, we see that the change of sign of $\frac{r}{p}\omega^2 - \frac{q}{p}$ has completely changed the wave behavior. Now, all the wavenumbers have both real and imaginary parts. Hence, all the wave modes are propagating as well as attenuating. The initial evanescent mode also becomes a propagating mode after the cut-off frequency ω_c .

The expression for the cut-off frequency obtained by equating $\frac{r}{p}\omega^2 - \frac{q}{p}$ to zero is

$$\omega_c = \frac{q}{r} \tag{2.24}$$

Again, if $q = 0$, the cut-off frequency vanishes and the wave behavior is similar to the first case, i.e., it will have propagating and damping modes. In all cases, however, the waves will be highly dispersive in nature.

The solution of the fourth-order governing Eq. (2.20) can be written as

$$\hat{w}(x, \omega) = A_1 e^{-j\alpha x} + B_1 e^{-\alpha x} + A_2 e^{j\alpha x} + B_2 e^{\alpha x} \tag{2.25}$$

As in the previous case, A_1, B_1 are the incident wave coefficients and A_2, B_2 are the reflected wave coefficients. These unknown constants can be determined in terms of the physical boundary conditions of the beam.

From the above discussion, we see that the spectral analysis gives an insight into the wave mechanics of a system defined by its governing differential equation. Though spectral analysis can be done similarly using wavelet transform, it is not as straightforward as Fourier transform-based analysis. This is because the wavelet basis functions are bounded both in time and frequency unlike the basis for Fourier transform which is unbounded in time. This has been explained in greater detail with application to nanostructures in the other chapters.

In the last section, the parameters, wavenumber, and wave speed were explained with the examples of generalized second- and fourth-order partial differential wave equations. The wavenumbers k were obtained as a function of frequency by solving second- and fourth-order polynomial equations, respectively. The computation of wavenumbers is, however, not so straightforward for structures with higher complexities (especially for the cases when the characteristic equation for solution of wavenumbers is of the order greater than 3). For one-dimensional structures such cases arise when the governing equation is a set of coupled PDEs and a couple of such examples are Timoshenko beam and other higher order beams. In a Timoshenko beam, the governing equations consist of two coupled PDEs with transverse and shear displacements as the variables. Another common example of structure having a set of coupled PDEs is the governing equations for a composite beam with asymmetric ply lay-up resulting in elastic coupling. In addition to the different one-dimensional structures, computation of wavenumbers for two-dimensional structures is also dif-

ficult primarily, because the wavenumbers here are a function of both frequency and wavenumber in the other direction.

In order to handle such problems, generalized and computationally implementable methods have been proposed to calculate the wavenumbers and associated wave amplitude. The two different approaches to solve the problem are based on singular value decomposition (SVD) and polynomial eigenvalue problem (PEP) methods. The methods are described briefly in refs. [1, 4, 5].

2.5 Summary

In this chapter, a brief introduction to wave propagation is given. First, the different terminologies used in wave propagation are defined. This is followed by a brief description of wave characteristics for systems defined by second- and fourth-order PDEs. The wave behavior is described based on wavenumbers and group speeds. Existence of cut-off frequencies in these two systems is also highlighted.

The PDEs that govern the nano waveguides described by nonlocal elasticity (which is the focus of this book) are normally defined by either second- or fourth-order PDEs. However, their form is entirely different than what is described in this chapter. The concepts outlined in this chapter will be very important and necessary for the reader to understand the wave propagation in different nano waveguides that are outlined in the later chapters of the book.

References

1. S. Gopalakrishnan, A. Chakraborty, D. Roy Mahapatra, *Spectral Finite Element Method* (Springer, London, 2008)
2. J.F. Doyle, *Wave propagation in structures* (Springer, New York, 1997)
3. A. Graff, *Wave Motion in Elastic Solids* (Dover Publications, New York, 1995)
4. S. Gopalakrishnan, M. Mitra, *Wavelet Methods for Dynamical Problems* (Taylor and Francis Group, LLC, Boca Raton, FL, 2010)
5. U. Lee, *Spectral Finite Element Method*, (Cambridge University Press, Cambridge, 2009)

Chapter 3

Various Modeling Techniques for Nanostructures

Mathematical modeling of structures at the micro and macroscales are quite well known and the methods have been well established. The laws of physics, which is fundamental to any modeling, is pretty well understood at these scales. At the nanometer levels, we need to deal with atoms, molecules, and their interactions. The laws of physics, at these scales, are not that well understood. The main difference lies in representing the models in different scales. That is, the philosophy of modeling at different scales are different. At the nanoscales, forces have no meaning, while at the micro and macroscales, they are the main drivers. At the nanoscales, it is the *interatomic potentials* [1], that plays an important part in understanding the behavior of the nanostructures. A number of different interatomic potentials have been propounded by many scientists for different conditions and the Ref. [1] gives a good overview of these potentials. As mentioned earlier, one can modify the bulk properties of the material by manipulating the atoms and molecules at the nanoscales. That is, using the interatomic potentials and the laws of physics at the nanoscales, one has to predict the bulk properties such as phase information, structural property information, etc., as illustrated in Fig. 3.1.

The most common approach to materials modeling is based on the *divide and conquer* strategy wherein methods appropriate to particular lengths and timescales are used to address aspects of materials phenomena that operate only over those scales. This has led to several independent methodological streams, which can be broadly categorized as ab initio density functional theory, molecular dynamics, statistical methods based on Monte Carlo algorithms and continuum mechanics as shown in Fig. 3.2. Each of these methods is computationally intensive in its own right, and hence most of the initial efforts was directed in optimizing algorithms, potentials, and parameters for each method individually, rather than generating information for input into other methods. The Fig. 3.2 clearly show the length and timescales over which these methods are valid. However, the expanding capabilities of computational methods due to the increasing power of computers and continuing development of efficient algorithms, together with advances in the synthesis, analysis, and visualization of materials at increasingly finer spatial and temporal resolutions, has spawned a

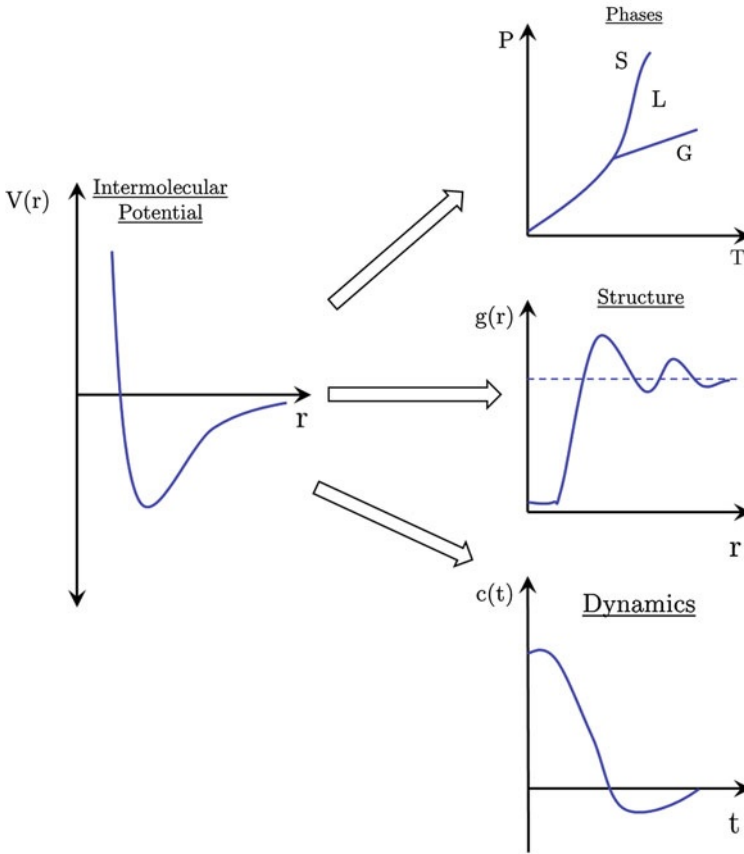


Fig. 3.1 Simulations as a bridge between microscopic and macroscopic

huge effort in the multiscale descriptions of materials phenomena. In this section, we describe the building blocks of these methods. The following section will describe how these are combined within multiscale modeling strategies.

3.1 First-Principles Methods (Atomistic Simulations)

With respect to theoretical tools of computational materials science, one can broadly divide them into two groups; empirical methods and *ab initio* (first principles) methods. In empirical methods, one employs classical (such as pair potentials) or quantum mechanical modeling (such as tight-binding) using various functional forms with adjustable parameters fitted to experimental observations or accurate calculations. Calculations based on empirical methods are generally quite fast from a computa-

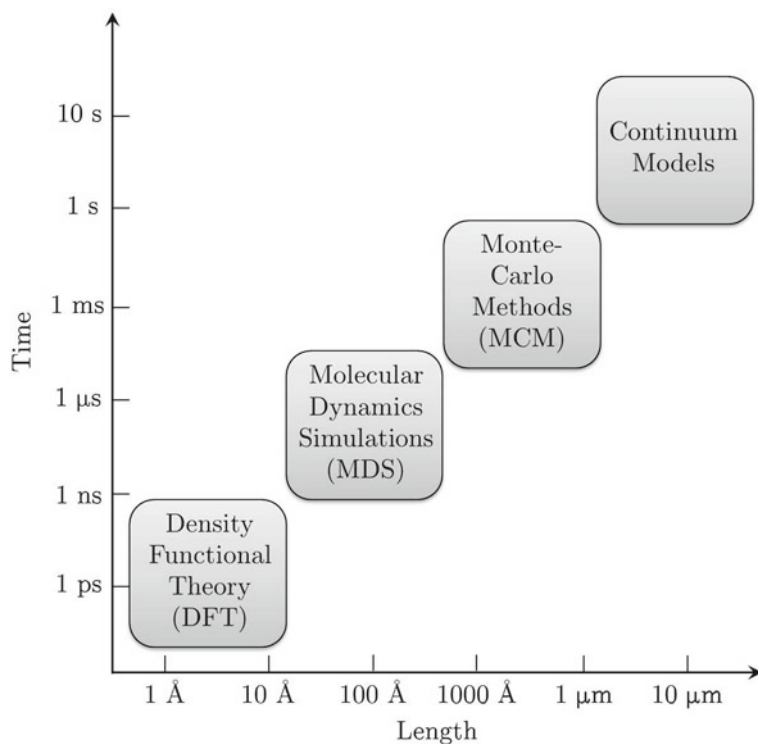


Fig. 3.2 The hierarchy of modeling methods for the range of length and timescales over which they typically used

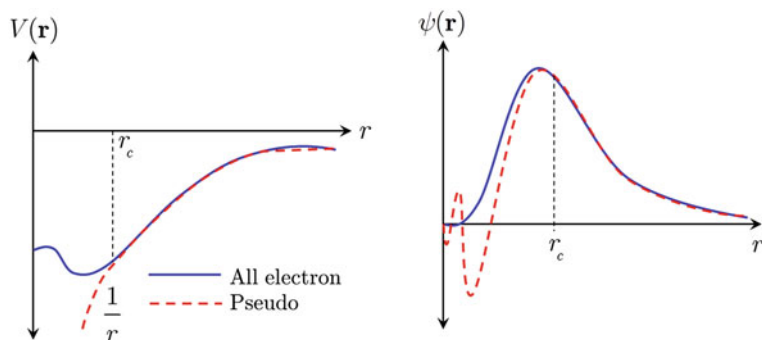


Fig. 3.3 Schematic representation of a pseudopotential (left, smooth curve) and a pseudowavefunction (right, smooth curve) along with the all-electron potential (with the $1/r$ tail) and wavefunction (dotted curves). Notice that the all-electron and pseudofunctions are identical beyond the radial cut-off r_c and the pseudofunctions are smooth inside the core region

tional point of view, but they may often lack the degree of accuracy and reliability needed to examine individual microscopic material properties. In *ab initio* methods, on the other hand, one uses quantum mechanical modeling with no adjustable parameters and few well-justified and tested approximations, and the atomic numbers of the constituent atoms are the only input to the calculations. These methods offer a level of accuracy one needs to understand most physical properties in a wide range of materials. However, compared to empirical methods, the high degree of accuracy and reliability of *ab initio* calculations is compensated by the large computational demand that they impose. One important class of such methods that have been very extensively used in the past two decades are the *ab initio* density functional methods.

The observable properties of solids are governed by quantum mechanics, as expressed by solutions of a Schrödinger equation for the motion of the electrons and the nuclei. However, because of the inherent difficulty of obtaining even grossly approximate solutions of the full many-body Schrödinger equation, one typically focuses on reduced descriptions that are believed to capture the essential energetics of the problem of interest. Hohenberg, and Kohn [2], formulated a theory based on the electron density, in terms of which the solution of the Schrödinger equation could be given a sound mathematical basis. This method is based on two hypotheses, which can be stated as:

1. The total energy of an electron system in an external potential is a unique functional of the total electron density; and
2. The density that minimizes the energy is the ground-state density, and this minimum energy is the ground-state energy of the system.

3.1.1 Density Functional Theory

Density functional theory (DFT) provides a tractable way of solving the quantum equations of motions for a system of interacting electrons under an external potential, such as the electron-ion interaction potential v_{ion} in a solid. In 1964, Hohenberg and Kohn [2] proved a famous theorem, which states that the ground-state energy of an electron gas with a nondegenerate ground state under an external potential is a unique functional of the electron charge density $\rho(\mathbf{r})$ and that this energy functional assumes its minimum value (ground state energy) for the correct (ground state) $\rho(\mathbf{r})$. A year later, Kohn and Sham [3] expressed this charge density in terms of ortho-normal single particle wave functions $\{\psi_n(\mathbf{r})\}$ as

$$\rho(\mathbf{r}) = \sum_{n,\text{occ.}} |\psi_n(\mathbf{r})|^2 \quad (3.1)$$

where the sum is over occupied single particle orbitals. This allowed them to write the ground-state energy of the electron gas as

$$E[\rho(\mathbf{r})] = -\frac{1}{2} \sum_n \int \psi_n^*(\mathbf{r}) \nabla^2 \psi_n(\mathbf{r}) + \int \rho(\mathbf{r}) v_{\text{ion}}(\mathbf{r}) d\mathbf{r} + \frac{1}{2} \int \int \frac{\rho(\mathbf{r})\rho(\mathbf{r}')}{|\mathbf{r} - \mathbf{r}'|} d\mathbf{r} d\mathbf{r}' + E_{\text{xc}}[\rho(\mathbf{r})] \quad (3.2)$$

In this expression, the first term is the kinetic energy of a noninteracting electron gas at the same density, the second term is the potential energy due to the electron-ion interaction. The third term is the classical Hartree energy, and the last term is the so-called exchange-correlation energy. Treating $\psi_n(\mathbf{r})$ and ψ_n^* as the variational parameters, one arrives at a single particle Schrödinger equation, given as

$$\left(-\frac{1}{2} \nabla^2 + v_{\text{eff}}[\mathbf{r}, \rho(\mathbf{r})] \right) \psi_n(\mathbf{r}) = \epsilon_n \psi_n(\mathbf{r}) \quad (3.3)$$

where the effective potential $v_{\text{eff}}[\mathbf{r}, \rho(\mathbf{r})]$ is given as

$$v_{\text{eff}}[\mathbf{r}, \rho(\mathbf{r})] = v_{\text{ion}}(\mathbf{r}) + \int \frac{\rho(\mathbf{r}')}{|\mathbf{r} - \mathbf{r}'|} d\mathbf{r}' + v_{\text{xc}}[\rho(\mathbf{r})] \quad (3.4)$$

where

$$v_{\text{xc}}[\rho(\mathbf{r})] = \frac{\delta E_{\text{xc}}}{\delta \rho(\mathbf{r})} \quad (3.5)$$

is the exchange-correlation potential. Due to the dependence of v_{eff} on $\rho(\mathbf{r})$, which depends on the solutions $\psi_n(\mathbf{r})$ of the Schrödinger equation, Eqs. (3.1), (3.3), and (3.4), known as the Kohn-Sham (KS) equations, have to be solved self-consistently.

In actual implementation of DFT for investigating material properties, there is a large number of different approaches with respect to algorithms, basis functions, representation of the electron-ion interaction, computational space, and approximation to the exchange-correlation potential. Of all the different DFT methods, the ab initio pseudopotential total energy method is perhaps the most widely used state-of-the-art method of choice [4]. This method, which can be implemented in both momentum and real space, has a very good track record for investigating structural, electronic, and optical properties of a large variety of materials. In fact, an examination of major breakthroughs in ab initio materials modeling over the past two decades shows that pseudopotentials have played an invaluable role in this respect.

3.1.2 *Ab initio Pseudopotentials*

The pseudopotential method relies on the separation (in both energy and space) of electrons into core and valence electrons and that most physical and chemical properties of materials are determined by valence electrons in the interstitial region. One can therefore combine the full ionic potential with that of the core electrons' to give an

effective potential (called the pseudopotential), which acts on the valence electrons only. On top of this, one can also remove the rapid oscillations of the valence wavefunctions inside the core region such that the resulting wavefunction and potential are smooth. Figure 3.3 shows a schematic representation of a pseudopotential and a pseudowavefunction along with the corresponding all-electron counterparts. Beyond a chosen cut-off radius r_c , the all-electron and pseudofunctions (potential and wavefunction) are identical, while inside the core region both the pseudopotential and pseudowavefunction are smoothly varying. After the construction of these pseudofunctions for a single atom and ensuring that their scattering properties are almost identical to those of the all-electron functions, they can be used in any chemical environment without any significant loss of transferability [5].

3.2 Molecular Dynamics

An introduction to classical molecular dynamics simulations especially for wave propagation analysis in nanostructures is presented in this section. Quantum molecular dynamics simulations are limited to system sizes of a few hundred atoms and to elapsed real times of a few picoseconds. Accordingly, the first step in the coarse graining of the full quantum mechanical description of a dynamical process is to remove the electronic degrees of freedom from the problem. This is accomplished by first using the BornOppenheimer approximation to separate the electronic and nuclear coordinates. The total energy is then calculated for each set of N nuclear positions R_i , for $i = 1, 2, \dots, N$; from this the forces exerted on each atom by all other atoms can be determined. Interpolation between these points yields a potential energy surface $U(\{\mathbf{R}_i\})$. Regarding the atoms as classical particles moving on this surface, the quantum mechanical motion governed by the Schrödinger equation is replaced by Newton's equation of classical mechanics:

$$\mathbf{F}_i = m_i \frac{d^2 \mathbf{R}_i}{dt^2} \quad (3.6)$$

where m_i is the mass of the i th atom and the force \mathbf{F}_i acting on this atom is calculated from the interatomic potential energy according to

$$\mathbf{F}_i = -\nabla_i U \quad (3.7)$$

Thus, the classical Hamiltonian \mathcal{H} of the system is

$$\mathcal{H}_{\text{MD}} = \frac{1}{2} \sum_i m_i \mathbf{V}_i^2 + U \quad (3.8)$$

where \mathbf{V}_i is the velocity of the i th atom. These are the equations of the molecular dynamics method [6, 7].

There are two primary aspects to the practical implementation of molecular dynamics: (i) the numerical integration of the equations of motion together with the boundary conditions and any constraints on the system; and (ii) the choice of the potential. For a system of N particles, Eq. (3.6) represents a system of $3N$ second-order differential equations. This system can be expressed as $6N$ first-order differential equations by introducing the velocity as a separate variable:

$$\frac{d\mathbf{R}_i}{dt} = \mathbf{V}_i, \quad \frac{d\mathbf{V}_i}{dt} = \frac{d\mathbf{F}_i}{m_i} \quad (3.9)$$

The systems of Eqs. (3.6) or (3.9) are solved numerically with finite difference methods to obtain the trajectories of the atoms on the potential energy surface. The most common integrators are based on the Verlet algorithm [8, 9] and its descendents, and predictor corrector methods [10]. When applied to the system in Eq. (3.9), these algorithms are used to iteratively update the forces, the velocities, and the positions over the timescale of the simulation. Parallel computing with spatial decomposition [11] has extended the system sizes that can be studied with molecular dynamics to $N \sim 10^6 - 10^9$ [12].

3.2.1 Potential Functions

A good account of various inter atomic potentials is given in ref. [1]. The choice of potential for a molecular dynamics simulation is determined by factors such as the bond type, the desired accuracy, transferability, and the available computational resources. Potentials can be categorized broadly as

1. Pair potentials,
2. Empirical many-body potentials and
3. Quantum mechanical potentials.

Two-body, or pair, potentials, such as the Lennard-Jones [13] and Morse [14] potentials, are used for large-scale simulations where computational efficiency is paramount, and in addition, a generic description is sufficient, rather than detailed comparisons with a particular materials system. For systems where multibody interactions are important, the Stillinger–Weber [15], Tersoff [16], and Brenner [17] potentials are often used for covalent materials, and embedded-atom [18], effective medium [19] and Finnis–Sinclair potentials [20] are common choices for metals. Such potentials are empirical in that they are parametrized by fitting either to a set of experimental measurements or to quantum mechanical calculations of representative atomic configurations. Typical properties used for such parametrizations are the lattice constant, binding energy, elastic constants, and vacancy formation energies. The basic assumption of this approach is that the fitting captures the essential features of

the interatomic potential for the phenomenon of interest. However, large local departures from the coordination or bonding used for the parametrization can take such potentials outside their domain of validity and lead to unreliable results. This has fostered efforts at deriving interatomic potentials directly from quantum mechanical principles. Foremost among these are potentials based on [21] and derived from [22] tight binding theory and those based on the Kohn-Sham equations using generalized pseudopotential theory [23].

The basic limitation of the molecular dynamics method is that the processes such as atomic diffusion are inherently multiscale phenomena. The integration time step must be small enough to capture the dynamics of the vibration modes of the system, with frequencies of the order of 10^{13} s^{-1} . This requires time steps in the *femtosecond* range. However, the residence time of an atom between hops is of the order of *microseconds*, and the interactions responsible for aggregation phenomena occur over a timescale of *milliseconds* to *minutes*. This ‘time gap’ is evident from the trajectories of atoms, which have their complex orbitals localized around their initial sites with only rare excursions to neighbouring sites [24]. Several methods have been developed for accelerating molecular dynamics process with such rare events based on stimulating the transitions to occur faster than in an ordinary simulation [25]. In favorable circumstances, molecular dynamics simulations can be extended to microseconds.

3.3 Molecular Dynamics for Wave Propagation in CNT

First we will review some of the relevant literature pertaining to molecular dynamics applied to CNTs. In addition to continuum mechanics models, atomistic simulations have been carried out to explore the vibration characteristics of CNTs. Li and Chou [26] employed the molecular structural mechanics method and modeled the SWCNT as an equivalent space frame-like structure to examine the feasibility of using SWCNT as a nanoresonator. The predicted fundamental frequencies of clamped-free or clamped SWCNTs were sensitive to dimensions such as length, diameter as well as boundary conditions, but the frequencies are relatively insensitive to chirality of the tubes. Later, Li and Chou [27] extended their work to assess the vibration behavior of MWCNTsCarbon nanotube!Multi-Wall by considering the van-der-Waals interaction between the adjacent tubes. They observed that the frequencies of SWCNTs and DWCNTs were not sensitive to vibration modes, which are in contradiction with the results reported by Cao et al. [28]. By using the same model, Li and Chou [29] assessed the SWCNTs as nanomechanical resonators in the presence of the axial strain or pressure. It was reported that the fundamental frequencies of the SWCNTs decreases with increasing tensile strain, a trend that is in conflict with experimental results of Sazonova et al. [30]. The contradictory results presented by Li and Chou [27, 29] may be due to the simplified molecular structural mechanics model in which only the deformed positions of carbon atoms are computed while neglecting the more important stretching energy term which

accounts for the effects such as bond length and angle changes caused by the surrounding atoms [28, 31]. A comprehensive molecular dynamics study based on the COMPASS (Condensed phased Optimized Molecular Potential for Atomistic Simulation Studies) force field and continuum analysis was carried out by Cao et al. [31] to investigate the fundamental frequency shift of deformed clamped-clamped SWCNTs under axial loadings, bending and torsion. The results given by the beam model or the cylindrical shell model are in good agreement with those obtained from MD simulations, provided that the Young's modulus and wall thickness are carefully selected. Yao and Lordi [32] performed MD simulations using the universal force field (UFF) to determine the Young's modulus of various clamped-free SWCNTs from their thermal vibration frequencies by using the frequency equations based on the Euler beam theory. The atomistic studies performed on the vibration behaviors of CNTs so far are limited. Most of the available continuum beam models for the free transverse vibration of CNTs provide analytical natural frequencies of CNTs under various boundary conditions but the accuracy of the results is questionable. More experimental or atomistic simulations works are required to validate the applicability of the continuum models. Zhang et. al. [33] provided the complete characteristics of vibrating CNTs by performing MD simulations based on the well-known reactive empirical bond-order (REBO) potential [34].

As mentioned earlier, molecular dynamics simulation is indeed a powerful tool for the analysis of nanoscale systems. The basic concept of MD simulations is to simulate the time evolution of a system of atoms. The atoms in the system are treated as point-like masses that interact with one another according to an assumed potential energy. The second-generation REBO potential [34] is adopted to simulate SWCNTs by Zhang et. al. [33]. This potential can reproduce more accurately the realistic chemical bond properties of hydrocarbon molecules. The second-generation REBO potential relative to its earlier version [35] contains improved analytical functions and an expanded database, which leads to a significantly better description of chemical and mechanical properties for hydrocarbon molecules and diamond [36] that compare reasonably well to first principles prediction.

The REBO potential is given by the sum of energy over the bonds, i.e.,

$$E_B = \sum_i \sum_{j>i} [V_R(r_{ij}) - \bar{b}_{ij} V_A(r_{ij})] \quad (3.10)$$

where V_R denotes the inter-atomic repulsion (core-core, etc), V_A the attraction from the valence electrons, r_{ij} is the distance between pairs of nearest-neighboring atoms i and j , and \bar{b}_{ij} is the reactive empirical bond order depending on local bonding environment. In the simulations, the bonding atomistic interaction in SWCNTs is described by the REBO potential while the nonbonding interaction is neglected to enhance the computational efficiency since it has been proven to have minimal contribution to the total strain energy.

The successful application of continuum models into CNTs depends strongly on the selected Young's modulus E and effective thickness h . In order to determine the

Young's modulus, one needs to estimate the thickness first. However, the thickness of SWCNTs with a single layer of atoms is ambiguous. Conventionally, the inter-layer spacing of graphite $h = 0.34$ nm is taken as the CNT thickness. On the other hand, considerable atomistic simulations in the literature have presented scattered thicknesses for SWCNTs in the range of $0.066 - 0.34$ nm. Huang et al. [37] bypassed atomistic simulations and developed an analytical approach to explain the ambiguity. It is found that the thickness, and therefore elastic moduli, depends on loading type, interatomic potential, nanotube radius and chirality. This dependence explains why the thickness obtained from prior atomistic simulations are scattered. Huane et al. [37] obtained the longitudinal wave velocity in nanotube as 1.91×10^3 m/s. Similar value was also obtained by Zhang et al. [33] from the REBO potential. They also presented results of molecular dynamics on vibration characteristics of nanotubes.

The MD simulation technique (using NanoHive-1 software [38]) is used to simulate torsional wave propagation on (6,6) and (10,10) armchair nanotubes by Khademolhosseini et al. [39]. The simulations are based on the Adaptive Intermolecular Reactive Empirical Bond Order (AIREBO) potential [40] which is widely used for simulating CNTs. They estimated the wave group and phase speeds in (6,6) and (10,10) CNTs using MD simulation and the results are compared with the nonlocal continuum shell (nonlocal elasticity models are explained in Sect. 3.9 and in Chap. 4 in detail) results to estimate the nonlocal scale parameter. Their results are used in the later chapters for comparison with the other nonlocal elasticity models. Taking into account that the group velocity governs the flow of energy in a system, this error could be a significant factor in the design of devices such as torsional oscillators or electro-mechanical delay elements based on CNT torsion, and has to be accounted for. The superiority of the nonlocal model over the classical model in predicting the real dispersion behavior of torsional waves in CNTs is also established in the later chapters.

Chen et al. [41] investigated the mechanical wave propagation in single-walled carbon nanotubes induced by two oscillating tips, using molecular dynamics simulations. They found a mandatory correlation condition between the tip oscillation frequency and magnitude in order to generate a quasi-steady-state standing wave with a characteristic wavelength and frequency changing with the tube radius, but independent of tip conditions. Their findings suggest the possibility of using SWCNTs as nanopumping systems for potential applications of fluid transport and drug delivery.

Hu et al. [42] have shown that the molecular dynamics simulations for wave dispersion prediction by the nonlocal elastic cylindrical shell theory are in good agreement with that of the MD simulations in a wide frequency range upto the terahertz region. The nonlocal elastic shell theory provides a better prediction of the dispersion relationships than the classical shell theory when the wavenumber is large enough for the carbon nanotube microstructure to have a significant influence on the wave dispersion. The value of parameter e_0 is estimated based on the MD result to predict the dispersion of transverse wave in CNTs through the usage of nonlocal shell models. The results of their study indicate that the nonlocal elastic cylindrical shell

model is able to offer a better prediction for transverse and torsional wave dispersion in CNTs than the local elastic shell model when the wavenumber is large enough.

Lin et al. [43] pursued the MD simulation to study the propagation and scattering of longitudinal sinusoidal and humped waves in SWCNTs. Their research results are summarized here. For SWCNTs with a smooth bend, the wave experiences no barrier in propagation when the wave length is comparable or smaller than the radius of the bending curvature. A different situation is encountered for buckled SWCNTs. Reflection is observed for all bending angles.

3.4 Molecular Dynamics Simulation for Wave Propagation in Graphene

Very few studies are available for wave propagation in graphene based on MD simulations. Recently, Wang et al. [44] developed a nonlocal elastic plate model that accounts for the scale effects for wave propagations in graphene sheets. Moreover, a finite element model developed from the weak-form of the elastic plate model is reported to fulfill a comprehensive wave study in the sheets and realize an application of the sheets as gas sensors. The applicability of the finite element model is verified by molecular dynamics simulations.

The studies show that the nonlocal finite element plate model is indispensable in predicting graphene phonon dispersion relations, especially at wavelengths < 1 nm, when the small-scale effect becomes dominant. Moreover, the nonlocal parameter $e_0 a$, a key parameter in the nonlocal model, is calibrated through the verification process. The dependence of the small-scale effect and the width of sheets on the dispersion relation is also investigated, and simulation results show that the phase velocity decreases to an asymptotic value with the width of sheets reaches a sufficiently large size. These results are also verified with the nonlocal models presented by the authors in the later chapters.

Conducting experiments are appropriate ways to analyze the behavior of the nanostructures. However, it suffers from the drawback that controlling every parameter in nanoscale is a difficult task. Further, employing the MD simulations requires large time and high computational resources. Because of the above-mentioned limitations in the mechanical analyses of nanostructures, theoretical and mathematical modeling becomes an important issue concerning its nanoengineering applications. Continuum models of nanostructures have thus received more attention and few studies are available for wave propagation in graphene based on MD simulations. Recently, Wang et al. [44] developed a nonlocal elastic plate model that accounts for the scale effects for wave propagations in graphene sheets. Moreover, a finite element model developed from the weak-form of the elastic plate model is reported to fulfill a comprehensive wave study in the sheets and realize an application of the sheets as gas sensors. The applicability of the finite element model is verified by molecular dynamics simulations.

3.5 Monte Carlo Methods

The next step for coarse graining is to address the ‘time gap’ problem of molecular dynamics. The basis of Monte Carlo methods [45] is that the deterministic Eq. (3.6) of the molecular dynamics method are replaced by stochastic transitions for the slow processes in the system. The name ‘Monte Carlo’ was coined by John von Neumann [46] and refers to the random sampling of numbers, in analogy to gambling in Monte Carlo, Monaco, a city renowned for its casinos. In their most general form, Monte Carlo methods are stochastic algorithms for exploring phase space, but their implementation for equilibrium and nonequilibrium calculations is somewhat different. We first review the Metropolis algorithm, which is the basis of applications to equilibrium systems.

3.5.1 The Metropolis Algorithms

Consider the thermodynamic average $\langle y \rangle$ of a variable with values y_i in state i that has energy E_i ,

$$\langle y \rangle = \frac{\sum_i y_i p_i}{\sum_i p_i} \quad (3.11)$$

in which the probabilities is given by $p_i = e^{-E_i/k_B T}$, where k_B is Boltzmann’s constant and T is the absolute temperature. If the system is initially in a state i , detailed balance requires that the rate of transitions T_{ij} from state i to state j satisfies the equation

$$\frac{T_{ij}}{T_{ji}} = \frac{p_j}{p_i} = e^{-(E_j - E_i)/k_B T} \quad (3.12)$$

The right-hand side of this equation is known, and hence to generate a set of states with the distribution p_i , the T_{ij} are chosen as

1. if $p_j > p_i$ ($E_j < E_i$): $T_{ij} = 1$
2. if $p_j \leq p_i$ ($E_j \geq E_i$): $T_{ij} = e^{-(E_j - E_i)/k_B T}$

A random number $r \in (0, 1)$ is then selected and the system is moved to state j only if $r < e^{-(E_j - E_i)/k_B T}$. This is the Metropolis algorithm [47].

3.5.2 Kinetic Monte Carlo Simulations

Suppose that the probability of finding a system in state σ at time t is $P(\sigma, t)$ and that the rate of transitions per unit time from σ to σ' is $W(\sigma, \sigma')$. The equation of motion for P is the master equation [48]:

$$\frac{\partial P}{\partial t} = \sum_{\sigma'} P(\sigma', t) W(\sigma', \sigma) - \sum_{\sigma'} P(\sigma, t) W(\sigma, \sigma') \quad (3.13)$$

Kinetic Monte Carlo (KMC) methods are algorithms that solve the master equation by accepting and rejecting transitions with probabilities that yield the correct evolution of a nonequilibrium system.

The KMC method represents an additional level of abstraction beyond the molecular dynamics method. The effect of fast dynamical events is taken into account by using stochastic transition rates for slower events. These transition rates are often represented as the product of an attempt rate and the probability of success per attempt, which is taken as an exponential involving the energy barrier to the process. Every event i is assigned a rate r_i :

$$r_i = \nu_i e^{-E_i/k_B T} \quad (3.14)$$

where ν_i is a frequency prefactor, typically of the order of a vibrational frequency (10^{13} s^{-1}) for surface processes [49], E_i is the free energy barrier for the process and T is the absolute temperature. Although the details of the underlying mechanism for kinetic processes are lost, the explicit calculation of atomic trajectories is avoided. Hence, KMC simulations can be performed over real times, running into seconds, hours, or days, as required. In essence, the factor ν_i in Eq. (3.14) represents the timescale of the fastest process, which is computed explicitly in the molecular dynamics method, but the exponential factor increases this timescale in the KMC method to that of the actual transitions. The KMC method thereby offers considerable advantages over the molecular dynamics method, both in terms of the real time over which the simulation evolves, and the number of atoms included in the simulation, because much of the computational overhead in molecular dynamics is used to evolve the system between rare events.

The construction of a model for a KMC simulation can often benefit from a related classical or quantum molecular dynamics simulation to identify the important physical process and estimate the prefactors and kinetic barriers. The transition rates are particular to the processes of interest and must be determined either by direct calculation, from a first-principles calculation or a molecular dynamics simulation, or inferred from experiment. The feasibility of performing detailed simulations over experimental timescales allows various parametrizations to be tested and models of kinetic phenomena to be validated. Such simulations play a key role in several multiscale modeling strategies.

3.6 Continuum Modeling

Continuum equations, typically in the form of deterministic or stochastic partial differential equations, are at the pinnacle of the coarse-graining hierarchy. The underlying atomic structure of matter is neglected altogether and is replaced with a con-

tinuous and differentiable mass density. Analogous replacements are made for other physical quantities such as energy and momentum. Differential equations are then formulated either from basic physical principles, such as the conservation of energy or momentum, or by invoking approximations within a particular regime. For example, the standard equations of fluid mechanics are derived from conservation laws, but are asymptotically valid only in the limit where the timescales of molecular motion are much shorter than those of the fluid flow [50]. This can be justified for simple fluids, but not for fluids composed of complex molecules such as polymers. The rheology of complex fluids is modeled with constitutive relations that account for the deformation history of the fluid and acknowledge the molecular origins of deformation and flow.

There are many benefits of a continuum representation of materials phenomena. Foremost among these is the ability to examine macroscopic regions in a space over extended periods of time. This is facilitated by extensive libraries of numerical methods for integrating deterministic and stochastic differential equations. The best known of these is the finite element method [51]. This is a general method for solving differential equations whereby the region of interest is tessellated with a uniform or nonuniform mesh determined by contiguous components called ‘elements’. The solution of the differential equation is discretized on the mesh points, called nodes, and interpolated within the elements. A partial differential equation is thereby replaced by a set of coupled ordinary (algebraic) equations and solved numerically for the values of the solution at the nodal points. The main advantage of the finite element method is the flexibility in modeling geometric complexity, material inhomogeneities, and anisotropies, all within a computationally efficient framework.

We will now briefly describe the finite element process. This is a well-established numerical method and there are many classic texts that are available on the subject. The main aim here is to provide a bird’s eye view of the method so that the reader can understand as to where the finite element method stands as regards the modeling of nanostructures. Consider the deformation of a material from a reference state \mathbf{r}_0 to a deformed state \mathbf{r} , which may vary with time. The displacement vector field $\mathbf{u}(\mathbf{r}, t)$ is defined in terms of these states as

$$\mathbf{u}(\mathbf{r}, t) = \mathbf{r}(t) - \mathbf{r}_0 \quad (3.15)$$

Within the framework of linear elasticity, the components ε_{ij} of the strain tensor are given in terms of the components (u_1, u_2, u_3) of \mathbf{u} by

$$\varepsilon_{ij} = 0.5(\partial_j u_i + \partial_i u_j) \quad (3.16)$$

where

$$\partial_k = \frac{\partial}{\partial r_k} \quad (3.17)$$

and (r_1, r_2, r_3) are the components of \mathbf{r} . The Hamiltonian \mathcal{H} is expressed as the sum of kinetic and potential energy contributions as

$$\mathcal{H} = \frac{1}{2} \int \rho \dot{\mathbf{u}}^2 d\mathbf{r} + \frac{1}{2} \int \varepsilon_{ij} C_{ijkl} \varepsilon_{kl} d\mathbf{r} \quad (3.18)$$

where ρ is the mass density of the material, C_{ijkl} are the components of the elasticity tensor and summation is implied over repeated indices.

The finite element representation of the displacement field is defined at the nodes of the elements, and shape functions (sometimes called interpolation functions or basis functions) are used to extend this field throughout each element. Denoting by $\phi_i(\mathbf{r})$ the shape function for the i th node, the displacement field is

$$\mathbf{u}(\mathbf{r}, t) = \sum_{i=1}^{N_q} \phi_i(\mathbf{r}) \mathbf{u}_i(t) \quad (3.19)$$

in which N_q is the number of nodes and $\mathbf{u}_i(t)$ is the displacement at the i th node. This relation implies two important properties of shape functions [51]: (i) a shape function takes the value 0 or 1 at a nodal point \mathbf{r}_j : $\phi_i(\mathbf{r}_j) = \delta_{ij}$, where δ_{ij} is the Kronecker delta; and (ii) the sum of all shape functions at any point \mathbf{r} is unity: $\sum_i \phi_i(\mathbf{r}) = 1$.

A common choice for the shape function is linear interpolation, whereby the basis function has the value unity at a given node and decreases to zero linearly at the nearest neighbor nodes, and is zero elsewhere. This is also a convenient choice for coupling to methods with atomic resolution because it permits a one-to-one correspondence between nodes and atoms. Upon substitution of Eq. (3.19) into (3.18), we obtain the finite element approximation to the elastic Hamiltonian:

$$\mathcal{H}_{\text{FE}} = \frac{1}{2} \sum_{i,j=1}^{N_q} \sum_{\ell=1}^{N_e} \left(\dot{\mathbf{u}}_i^\ell \mathbf{M}_{ij}^\ell \dot{\mathbf{u}}_j^\ell + \mathbf{u}_i^\ell \mathbf{K}_{ij}^\ell \mathbf{u}_j^\ell \right) \quad (3.20)$$

where N_e is the number of elements and M and K are the finite element mass and stiffness matrices, respectively. For atomic-size elements, the mass can be collapsed onto the nodes rather than being uniformly distributed, in which case the mass matrix becomes diagonal: $M_{ij} = m_i \delta_{ij}$. Equations of motion for the displacement at the nodes, in the form of a set of coupled ordinary differential equations, can now be obtained from the finite element Hamiltonian in terms of the forces from the surrounding nodes. Complementing the numerical solution of partial differential equations is the vast analytic methodology for identifying asymptotic scaling regimes and performing stability analyses.

Additionally, if a continuum equation can be systematically derived from atomistic principles, there is the possibility of discriminating between inherently atomistic effects and those that find a natural expression in a coarse-grained framework. Continuum equations also provide the opportunity for examining the effect of apparently

minor modifications to the description of atomistic processes on the coarse-grained evolution of a system which, in turn, facilitates the systematic reduction of full models to their essential components.

3.7 Methods of Multiscale Modeling

Each of the methods described in the preceding section is best suited to a particular level of accuracy, as dictated by the successive elimination of the original degrees of freedom. Density function methods provide a quantum mechanical description of electrons and nuclei, which is appropriate for processes such as crack formation, chemical reactions, and surface kinetics. In these cases, the chemical bonds deviate appreciably from their equilibrium configurations and, especially in extreme cases, such as fracture, break. Where deviations from equilibrium are small but atomistic resolution is still necessary, molecular dynamics offers many computational advantages over a full density functional calculation. Monte Carlo methods are especially useful for obtaining statistical information about a system from the transition rates between configurations, whether in equilibrium or driven away from equilibrium. Finally, continuum equations provide a reduced description in terms of continuous fields for the coarse-grained evolution of the system.

The fundamental tenet of multiscale modeling is that the information at each scale is systematically incorporated in a manner that transcends the single-scale description. There are two basic strategies for accomplishing this: sequential and concurrent. In the sequential approach, the information from a calculation over particular length and timescales is used as input into a more coarse-grained method. This approach presumes that the phenomenon of interest can be separated into processes that operate at distinct length and timescales. In concurrent multiscale modeling, these disparate scales are combined within a single hybrid scheme, typically involving atomistic and continuum calculations. The main theoretical challenge is to merge the two descriptions in a manner that avoids any spurious effects due to this heterogeneity. This approach is well suited to the simulation of fracture, where the complex feedback between the atomic-scale interactions and the macroscopic stresses preempts a clear-cut separation of scales.

Several methodologies have been implemented within the sequential and concurrent frameworks. In the next few sections, we will review the main approaches and provide examples of each methodology. Methods of sequential multiscale modeling include sequential parametrization, interface propagation, and systematic coarse graining. Concurrent strategies typically combine an atomistic method, such as an *ab initio* density functional calculation or molecular dynamics simulation, with continuum equations that are solved with a finite element method or some other discretization. An introduction to several multiscale methods may be found in the reference [52].

3.8 Overview on Length Scales

Single-scale methods such as ab initio quantum mechanical methods or molecular dynamics (MD) will have difficulty in analyzing such hybrid structures due to the limitations in terms of the time and length scales that each method is confined to. Because of the availability of accurate interatomic potentials for a wide range of materials, classical MD simulations have become prominent as a tool for elucidating complex physical phenomena. However, the length and timescales that can be probed using MD are still fairly limited.

For the study of nanoscale mechanics and materials, we must model up to a scale of several microns, consisting of billions of atoms, which is too large for MD simulations. Therefore, the need arises to couple atomistic methods with approaches that operate at larger length scales and longer timescales.

Continuum methods have in contrast had much success in the macroscale modeling and simulation of structures. Finite element (FE) methods are now the standard numerical analysis tool to study such diverse problems as the modeling of crash-worthiness in automobiles, the fluid-structure interaction of submarines, plasticity in manufacturing processes, and blast and impact simulations. Therefore, the logical approach taken by many researchers in the desire to create truly multiple scale simulations that exist at disparate length and timescales has been to couple MD and FE in some manner.

The major problem in multiscale simulations is that of pathological wave reflection, which occurs at the interface between the MD and FE regions. The issue is that wavelengths emitted by the MD region are considerably smaller than that which can be captured by the continuum FE region. Because of this and the fact that an energy conserving formulation is typically used, the wave must go somewhere and is thus reflected back into the MD domain. This leads to spurious reflections from the FE-MD interface and spurious heat generation in the MD region, and a contamination of the simulation. The retention of heat within the MD region can have extremely deleterious effects, particularly in instances of plasticity where heat generated within the MD region is trapped; in such an extreme situation, melting of the MD region may eventually occur.

A separate, but related issue to effective multiscale modeling is that of extending the timescale available to MD simulations. This issue still remains despite the efforts of the current multiscale methods to limit the MD region to a small portion of the computational domain. Despite the reduction in the MD system size, limits still exist on the duration of time that the MD system can be simulated. Research has been on-going in the physics community to prolong the MD simulation time, particularly for infrequent events such as surface diffusion. Two excellent examples of the types of methods currently under investigation can be found in the works of Voter et al. [53, 54].

This size limit of computation is far short to reach the macroscale such that molecular dynamics alone cannot predict the properties and response of macroscopic materials directly from their nano- and microstructures. Other atomistic methods also

have difficulties for large systems. For example, the widely used conjugate gradient method in molecular mechanics, the computational effort is of the order $-N^2$, where N is the system size. It is therefore not suitable for large systems, nor for the rapid simulation of nanoscale components that are up to a few hundred nanometers in size.

On the other hand, the conventional continuum methods such as the finite element method (FEM) are not applicable to nanoscale components because they are developed for macroscale problems. The macroscale material behaviors are incorporated in the conventional continuum FEM via the constitutive models of solids, which are usually empirical and are determined from macroscale experiments such as simple tension tests. These constitutive models represent the collective behavior of many atoms, and cannot accurately predict the response of discrete atoms. For example, for a uniform deformation on the macroscale (as in a simple tension test), the atomic motion may not be uniform at the atomic scale even for a perfect atomic structure without defects [55]. Furthermore, most atomistic interactions are multi-body in nature, i.e., the energy in an atomic bond between a pair of atoms depends on the positions of atoms both in and outside the pair (e.g., [56]). This ‘*nonlocal*’ dependence of energy is inconsistent with the macroscopic, local constitutive model in the conventional FEM.

Since the atomistic simulations and continuum FEM have difficulties to *scale up* and *scale down*, respectively, multiscale computation methods have emerged as a viable means to study materials and systems across different length scales (e.g., [57–60]). The basic idea is to combine the atomistic simulation methods which capture the nanoscale physics laws with the continuum FEM, which represents the collective behavior of atoms but significantly reduces the degrees of freedom. One approach is to use the atomistic simulation methods for domains in which the discrete motion of atoms is important and must be accounted for, and use the continuum FEM for the rest where the response of materials and systems can be represented by the continuum models. Such an approach involves artificially introduced interfaces between domains of atomistic and continuum simulation methods. It requires the interface conditions, which add significant computational efforts, and may lead to computation errors. Another approach in the atomistic continuum linkage is quasicontinuum method [61–63]. The interatomic potential is directly incorporated into the continuum FEM method via the Cauchy Born rule (e.g., [5]) to obtain the continuum strain energy density from the energy stored in atomic bonds. The quasicontinuum method involves both discrete atoms and continuum solids, and the method can also account for the *nonlocal effect* [63], i.e., the multibody atomistic interactions. However, the spurious or *ghost force* appears at the interface between the domains of (local) continuum and (nonlocal) atomistic simulations in the quasicontinuum method [61]. The quasicontinuum analysis uses the conjugate gradient method [62], which is an order $-N^2$ method and is not suitable for large problems. Recently, Wagner and Liu [60] coupled the atomistic and continuum simulations using a bridging scale decomposition.

3.9 Nonlocal Theories in Continuum Mechanics

In standard continuum mechanics, a solid body is decomposed into a set of idealized, infinitesimal material volumes, each of which can be described independently as far as the constitutive behavior is concerned. Of course, this does not mean that the individual material points are completely isolated, but their interaction can take place only on the level of balance equations, through the exchange of mass, momentum, energy, and entropy.

Constructing a material model, one must select a certain resolution level below which the microstructural details are not explicitly ‘visible’ to the model and need to be taken into account approximately and indirectly, by an appropriate definition of effective material properties. Also, one should specify the characteristic wavelength of the imposed deformation fields that can be expected for the given type of geometry and loading. Here, the notion of characteristic wavelength has to be understood in a broad sense, not only as the spatial period of a dynamic phenomenon but also as the length on which the value of strain changes substantially in static problems. If the characteristic wavelength of the deformation field remains above the resolution level of the material model, a conventional continuum description can be adequate. On the other hand, if the deformation field is expected to have important components with wavelengths below the resolution level, the model needs to be enriched so as to capture the real processes more adequately. Instead of refining the explicit resolution level, it is often more effective to use various forms of the so-called *enriched* or *generalized continuum* formulations.

The enrichments are in general referred to as nonlocal, but this adjective must be understood in the broad sense, covering both strongly nonlocal and weakly nonlocal formulations. Precise mathematical definitions of strong and weak nonlocality were given by Rogula [64] and are also explained in Bazant and Jirasek [65]. Here, we only note that strongly nonlocal theories are exemplified by integral-type formulations with weighted spatial averaging or by implicit gradient models, while weakly nonlocal theories include for instance explicit gradient models. Entire concept of this book is based on nonlocal elasticity, that is, we bring in the scale information in continuum formulation. The Chap. 3 deals with the formulations concerning nonlocal elasticity equations.

Let us now explain how the nonlocal theory is different from the local or standard continuum theory. In standard continuum elasticity it is assumed that the density of elastic energy stored per unit volume, w , depends only on the strain tensor, which is directly related to the deformation gradient, i.e., to the first gradient of the displacement field. The elastic energy stored by the entire body, W , is then evaluated as the spatial integral of the elastic energy density. In the one-dimensional setting, one can write

$$W = \int_L w(u'(x)) dx \quad (3.21)$$

where $u' = du/dx$ is the strain, further denoted as ε , and L is the interval representing geometrically the one-dimensional body. In linear elasticity, the elastic energy density is given by

$$w(\varepsilon) = \frac{1}{2}E\varepsilon^2 \quad (3.22)$$

is a quadratic function of strain.

In the standard continuum theory, propagation of waves in a homogeneous one-dimensional linear elastic medium is described by the hyperbolic partial differential equation

$$\rho\ddot{u} - Eu'' = 0 \quad (3.23)$$

where ρ is the mass density, E is the elastic modulus, $u(x, t)$ is the displacement and, as usual, over dots stand for derivatives with respect to time t and primes for derivatives with respect to the spatial coordinate x . Since ρ and E are constant coefficients, Eq. (3.23) admits solutions of the form

$$u(x, t) = e^{i(kx - \omega t)} \quad (3.24)$$

where i is the imaginary unit, ω is the circular frequency, k is the wavenumber, and $c = \omega/k$ is the wave velocity. In the next few subsections, we will discuss how enrichments can be introduced to bring in certain scale parameter in the continuum equations.

3.9.1 Strain-Gradient Elasticity

One class of enrichments is based on the incorporation of higher gradients (or derivatives) of the displacement field. In general, the elastic energy density can be assumed to depend on higher derivatives of displacements such as u'' , u''' , u^{iv} , etc. The simplest strain-gradient theory of elasticity uses enrichment by the second displacement gradient, u'' , which is equal to the strain gradient, ε' , further denoted as η . If we consider one single material point only, the strain gradient is locally independent of the strain value. In the linear case, the enriched elastic energy density potential is written as

$$w(\varepsilon, \eta) = \frac{1}{2}E\varepsilon^2 + \frac{1}{2}C\eta^2 \quad (3.25)$$

where C is a higher order elastic modulus. The variation of elastic energy density is given by

$$\delta w = \frac{\partial w}{\partial \varepsilon} \delta \varepsilon + \frac{\partial w}{\partial \eta} \delta \eta = \sigma \delta \varepsilon + \chi \delta \eta \quad (3.26)$$

where $\sigma = \frac{\partial w}{\partial \varepsilon} = E\varepsilon$ is the (Cauchy) stress and $\chi = \frac{\partial w}{\partial \eta} = C\eta$ is the so-called double stress. Based on the extended form of the principle of virtual work, it is possible to derive the static equilibrium equation

$$(\sigma - \chi')' + b = 0 \quad (3.27)$$

where b is the body force density. In dynamics, b is replaced by the inertial force density, $-\rho\ddot{u}$. Combining this with the constitutive equations $\sigma = E\varepsilon$ and $\chi = C\eta$ and with the kinematic equations $\varepsilon = u'$ and $\eta = u''$, we obtain the wave equation of strain-gradient elasticity

$$\rho\ddot{u} - Eu'' + Cu^{iv} = 0 \quad (3.28)$$

which differs from the standard wave Eq. (3.23) by the presence of a term with the fourth spatial derivative of displacement.

When $C = 0$, the model reduces to standard elasticity. In strain-gradient elasticity it is usually assumed that the higher order modulus C is positive. This assumption leads to a convex energy potential and permits to generalize certain uniqueness theorems known from standard elasticity. However, for $C > 0$, the phase velocity increases with increasing wavenumber. We know that the discrete mass-spring model exhibits the opposite trend, and this is also confirmed by measurements of dispersion curves in real crystals. Even for heterogeneous continua, the dispersion curves (determined experimentally or by analytical solution of some simple cases) typically have negative curvature. So the strain-gradient theory gives a reasonable approximation of the dispersion effect only if the higher order modulus C is negative. Convexity of the elastic potential is then lost and uniqueness cannot be guaranteed.

Indeed, if $C = -E\ell^2$, where ℓ is a model parameter with the dimension of length, the phase velocity of a harmonic wave with wavenumber $k_{\text{crit}} = 1/\ell$ vanishes. This means that the equation of motion (3.28) is satisfied by a stationary wave of wavelength $2\pi/k_{\text{crit}} = 2\pi\ell$. A similar result was found for the discrete mass-spring model, but in that case the stationary wave in reality represented a uniform translation, because the values of the displacements had physical meaning only at discrete points with spacing equal to the critical wavelength. In contrast to that, a stationary wave in a continuous elastic medium is physically inadmissible [66].

3.9.2 Models with Mixed Spatial-Temporal Derivatives

Due to the unstable behavior of short waves, Eq. (3.28) is sometimes called the *bad Boussinesq problem*. This equation can describe dispersion of waves with moderate wavenumbers but leads to instabilities if waves shorter than the critical wavelength $2\pi\ell$ are involved. If the body of interest is discretized by finite elements, the minimum wavelength that can be captured by the numerical approximation is proportional to

the element size. Therefore, for meshes that are sufficiently coarse with respect to the material length parameter ℓ , the numerical solution leads to reasonable results. However, upon mesh refinement, the solution becomes polluted by unstable modes rapidly oscillating in space.

Several modifications of the bad Boussinesq problem were proposed in the literature. Fish et al. [67] replaced the term with the fourth spatial derivative, u^{iv} , by a term with a mixed derivative, \ddot{u}'' . Their arguments can be rephrased and expanded as follows: For small wavenumbers, the fourth-order term in Eq. (3.28) is negligible with respect to the second-order terms, so we can write $Eu'' \approx \rho\ddot{u}$. Differentiating this twice with respect to x , we obtain $Eu^{iv} \approx \rho\ddot{u}''$. Finally, replacing in Eq. (3.28) u^{iv} by $(\rho/E)\ddot{u}''$ and C by $-E\ell^2$ yields a modified wave equation

$$\rho\ddot{u} - Eu'' - \rho\ell^2\ddot{u}'' = 0 \quad (3.29)$$

which was called by Fish et al. [67] as the *good Boussinesq problem*. This problem can be expected to have similar solutions to the original bad Boussinesq problem at low wavenumbers, however, we can expect a different asymptotic behavior for high wavenumbers.

With a proper choice of parameters, the model can reasonably approximate dispersion and it does not suffer any unstable behavior at shorter wavelengths. Its disadvantage is that the presence of the fourth derivative u^{iv} requires either a C^1 -continuous finite element approximation (which is hard to construct on general meshes in multiple dimensions) or a mixed approach with independent approximations of several fields (e.g., the displacement field, stress field, the strain field, etc.). Also, nonstandard higher order boundary conditions are needed on the physical boundary of the investigated body.

3.9.3 Integral-Type Nonlocal Elasticity

Another class of enrichments is based on weighted spatial averaging. The simplest model of this kind can be derived from the elastic potential

$$W = \frac{1}{2} \int_L \int_L E(x, \xi) \varepsilon(x) \varepsilon(\xi) dx d\xi \quad (3.30)$$

where $E(x, \xi)$ is a function describing the generalized elastic modulus. The variation of elastic energy is evaluated as

$$\delta W = \frac{1}{2} \int_L \int_L E(x, \xi) \delta\varepsilon(x) \varepsilon(\xi) dx d\xi + \frac{1}{2} \int_L \int_L E(x, \xi) \varepsilon(x) \delta\varepsilon(\xi) dx d\xi \quad (3.31)$$

This implies

$$\delta W = \frac{1}{2} \int_L \int_L [E(x, \xi) + E(\xi, x)] \varepsilon(\xi) d\xi \delta \varepsilon(x) dx \quad (3.32)$$

This can be written in the usual form $\delta W = \int_L \sigma(x) \delta \varepsilon(x) dx$ if the stress is defined as

$$\sigma(x) = \int_L E_s(x, \xi) \varepsilon(\xi) d\xi \quad (3.33)$$

where

$$E_s(x, \xi) = \frac{1}{2} [E(x, \xi) + E(\xi, x)] \quad (3.34)$$

is the elastic modulus function symmetrized with respect to its arguments. The corresponding equilibrium equations derived from the principle of virtual work by keeping this in their standard form, $\sigma' + b = 0$. Consequently, the wave equation for this model reads

$$\rho \frac{\partial^2 u(x, t)}{\partial t^2} - \frac{\partial}{\partial x} \int_L E_s(x, \xi) \frac{\partial u(\xi, t)}{\partial \xi} d\xi = 0 \quad (3.35)$$

Since function $E_s(x, \xi)$ reflects the strength of long-distance interaction between points x and ξ , its value can be expected to be negligible if the distance between x and ξ is large compared to the internal length of the material (which corresponds to the characteristic size and spacing of major heterogeneities). For functions E_s with a sufficiently fast decay, the integrals in Eqs. (3.33) and (3.35) make sense even if the integration domain L is considered as the entire real axis. If the body is infinite and macroscopically homogeneous, function $E_s(x, \xi)$ should depend only on the distance between x and ξ . Bearing in mind these restrictive assumptions, we present the modulus function in the form

$$E_s(x, \xi) = E_0 \alpha_0(x - \xi) \quad (3.36)$$

where E_0 is a reference value of the elastic modulus and α_0 is a dimensionless even function, further called the *nonlocal weight function*.

Substituting the assumed harmonic form of an elastic wave into the transformed wave equation

$$\rho \frac{\partial^2 u(x, t)}{\partial t^2} - E_0 \int_{-\infty}^{+\infty} \alpha_0(x - \xi) \frac{\partial^2 u(\xi, t)}{\partial \xi^2} d\xi = 0 \quad (3.37)$$

we obtain the dispersion equation

$$-\rho \omega^2 + E_0 k^2 \alpha_0^*(k) = 0 \quad (3.38)$$

in which

$$\alpha_0^*(k) = \int_{-\infty}^{+\infty} \alpha_0(r) e^{-ikr} dr \quad (3.39)$$

is the Fourier image of the nonlocal weight function $\alpha_0(r)$. Relation (3.38) shows that there is a unique correspondence between the dispersion law and the Fourier image of the nonlocal weight function.

The transformation of the model of Fish et al. [67] into a integral-type nonlocal model can also be performed directly. At a fixed time instant, Eq. (3.29) can be written as

$$\ddot{u} - \ell^2 \ddot{u}'' = \frac{E}{\rho} u'' \quad (3.40)$$

and interpreted as an ordinary differential equation for the unknown acceleration \ddot{u} , with the current displacement u considered as known. Equation (3.40) has the form of the so-called Helmholtz equation, and its solution satisfying conditions of boundedness (which play the role of boundary conditions at plus and minus infinity) can be expressed as

$$\ddot{u}(x, \xi) = \frac{E}{\rho} \int_{-\infty}^{+\infty} G(x, \xi) u''(\xi, \ell) d\xi \quad (3.41)$$

where $G(x, \xi)$ is the Green function of the Helmholtz equation, formally obtained as the solution of this equation with the Dirac distribution $\delta(\xi)$ on the right-hand side. It turns out that the Green function in this case given by

$$G(x, \xi) = \frac{1}{2\ell} e^{-\frac{|x-\xi|}{\ell}} \quad (3.42)$$

and so Eq. (3.41) is in fact equivalent with Eq. (3.37) if the nonlocal weight function α_0 is selected according to formula $\alpha_0(r) = \frac{1}{2\ell} e^{-\frac{|r|}{\ell}}$.

The common denominator of all examples presented in the preceding sections is that the characteristic wavelength of the deformation field becomes comparable to the characteristic size of the internal material structure. Here, the notion of characteristic wavelength has to be understood in a broad sense, not only as the spatial period of a dynamic phenomenon, but also as the length on which the value of strain changes substantially in static problems. Such a more general definition could be based, e.g., on a suitably normalized ratio between the maximum strain and the maximum strain gradient (both in absolute values). Thus the characteristic wavelength is necessarily close to the internal material length if the size of the specimen is not much larger than the size and spacing of major heterogeneities, or if strain localizes due to softening.

The enrichment terms introduced by various generalized continuum theories have a differential or integral character, but all of them can be considered as nonlocal, at least in the weak sense. They always introduce a model parameter with the dimension of length, which reflects the internal length scale of the material.

The nonlocal enrichments can be useful in a wide range of mechanical problems. Unfortunately, so far there is no general and universally accepted theory covering this entire range within one unified framework. Although the first nonlocal theories were pioneered in the 1960s, there are many problems that still remains open and many issues unresolved. Some of the most challenging questions include the correct

formulation of boundary conditions, micro–mechanical justification of models with nonlocal internal variables, or identification techniques for the internal length parameter and its possible evolution.

The limitation of the applicability of the classical or local continuum modeling, such as beam and shell models, is partly due to the fact that the classical modeling does not admit intrinsic size dependence in elastic solutions of inclusions and inhomogeneities. It is thus concluded that the applicability of classical continuum modeling to revealing small scales is questionable, since the material microstructure at small size, such as the lattice spacing between individual atoms, becomes increasingly important and the discrete structure of the material can no longer be homogenized into a continuum. Therefore, newly proposed continuum modeling rather than the classical continuum modeling is expected to take into account the scale effect while handling large-scale nanomaterial analysis. At nanometer scales, size effects often become prominent, the cause of which needs to be explicitly addressed with an increasing interest in the general area of nanotechnology. The modeling of such a size-dependent phenomenon has become an interesting subject nowadays.

The scale effect was accounted for in elasticity theory by assuming the stress at a reference point to be a functional of the strain field at every point in the body by the nonlocal elasticity theory (it will be discussed in detail in the preceding chapters). In this way, the scale effect could be considered in the constitutive equations simply as a material parameter, while the classical elasticity theory cannot account for the scale effect, since the stress state is dependent uniquely on the strain state at the same point. Askes and Aifantis [68] present their discussion on the controversy regarding dynamic nonlocal elasticity and static nonlocal elasticity.

Chapter 4 details the nonlocal elasticity theory in greater depth. A lot of emphasis is given to this theory in this book since the focus of this book is to bring in the role played by the scale parameter in the wave propagation in CNTs and Graphene structures.

3.10 Summary

This chapter gives a brief outline of all the available mathematical modeling methods for nanostructures. The major part of the chapter deals with explanation of different modeling schemes for nanostructures, where the atomistic, molecular dynamics, continuum modeling, and multiscale modeling schemes are described in detail. Among the atomistic models, ab initio models and the models based on density functional theory are reviewed in detail. Next, the molecular dynamics modeling procedure is given. In particular, molecular dynamics models for wave propagation in CNTs and Graphene are reviewed in detail. This is followed by a brief review of Monte Carlo methods. Among the continuum modeling schemes, the nonlocal elasticity models, which is primary focus of this book, is dealt in detail. Here, different enrichment schemes, each of which introduces a scale parameter, are discussed in great detail in this chapter

References

1. S. Yip (ed.), *Handbook of Materials Modeling* (Springer, Netherlands, 2005)
2. P. Hohenberg, W. Kohn, Inhomogeneous electron gas. *Phys. Rev. B* **136**, 864–871 (1963)
3. W. Kohn, L.J. Sham, Self-consistent equations including exchange and correlation effects. *Phys. Rev. B* **140**, 1133–1138 (1965)
4. M.C. Payne, M.P. Teter, D.C. Allan, T. Arias, J.D. Joannopoulos, Iterative minimization techniques for abinitio total-energy calculations: molecular dynamics and conjugate gradients. *Rev. Mod. Phys.* **64**, 1045–1097 (1992)
5. M.T. Yin, M.L. Cohen, Theory of Ab initio pseudopotential calculations. *Phys. Rev. B* **25**, 7403–7412 (1982)
6. J.M. Haile, *Molecular Dynamics Simulation* (John Wiley, New York, 1992)
7. D.C. Rapaport, *The Art of Molecular Dynamics Simulation* (Cambridge University Press, Cambridge, 1992)
8. L. Verlet, Computer experiments on classical fluids: I. Thermodynamical properties of Lennard-Jones molecules. *Phys. Rev. B* **159**, 98–103 (1967)
9. L. Verlet, Computer experiments on classical fluids: II. Equilibrium correlation functions. *Phys. Rev. B* **165**, 201–214 (1968)
10. C.W. Gear, *Numerical Initial Value Problems in Ordinary Differential Equations* (Prentice-Hall, Englewood Cliffs, 1971)
11. S. Plimpton, Fast parallel algorithms for short-range molecular dynamics. *J. Comput. Phys.* **117**, 1–19 (1995)
12. S. Ogata, T.J. Campbell, R.K. Kalia, A. Nakano, P. Vashishta, S. Vemparala, Scalable and portable implementation of the fast multipole method on parallel computers. *Comput. Phys. Commun.* **153**, 445–461 (2003)
13. J.E. Jones, On the determination of molecular fields: II. From the equation of state of a gas. *Proc. R. Soc. A* **106**, 463–477 (1924)
14. P.M. Morse, Diatomic molecules according to the wave mechanics: II. Vibrational levels. *Phys. Rev. B* **34**, 57–64 (1929)
15. F.H. Stillinger, T.A. Weber, Computer simulation of local order in condensed phases of silicon. *Phys. Rev. B* **31**, 5262–5271 (1985)
16. J. Tersoff, New empirical model for the structural properties of silicon. *Phys. Rev. Lett.* **56**, 632–635 (1986)
17. D.W. Brenner, Empirical potential for hydrocarbons for use in simulating the chemical vapor deposition of diamond films. *Phys. Rev. B* **42**, 9458–9471 (1990)
18. M.S. Daw, M.I. Baskes, Semiempirical, quantum mechanical calculation of hydrogen embrittlement in metals. *Phys. Rev. Lett.* **50**, 1285–1288 (1983)
19. K.W. Jacobsen, J.K. Nørskov, M.J. Puska, Interatomic interactions in the effective-medium theory. *Phys. Rev. B* **35**, 7423–7442 (1987)
20. M.W. Finnis, J.E. Sinclair, A simple empirical N-body potential for transition metals. *Philos. Mag. A* **50**, 45–55 (1984)
21. R.E. Cohen, M.J. Mehl, D.A. Papaconstantopoulos, Tight-binding total-energy method for transition and noble metals. *Phys. Rev. B* **50**, 14694–14697 (1994)
22. D.G. Pettifor, New many-body potential for the bond order. *Phys. Rev. Lett.* **63**, 2480–2483 (1989)
23. J.A. Moriarty, Density-functional formulation of the generalized pseudopotential theory: III. Transitionmetal interatomic potentials. *Phys. Rev. B* **38**, 3199–3231 (1988)
24. M. Schneider, A. Rahman, I.K. Schuller, Role of relaxation in epitaxial growth—a molecular dynamics study. *Phys. Rev. Lett.* **55**, 604–606 (1985)
25. A.F. Voter, F. Montalenti, T.C. Germann, Extending the time scales in atomistic simulation of materials. *Ann. Rev. Mater. Res.* **32**, 321–346 (2002)
26. C.Y. Li, T.W. Chou, Single-walled carbon nanotubes as ultrahigh frequency nanomechanical resonators. *Phys. Rev. B* **68**, 073405 (2003)

27. C.Y. Li, T.W. Chou, Vibrational behaviors of multiwalled-carbon-nanotube-based nanomechanical resonators. *Appl. Phys. Lett.* **84**, 121–123 (2003)
28. G.X. Cao, X. Chen, J.W. Kysar, Thermal vibration and apparent thermal contraction of single-walled carbon nanotubes. *J. Mech. Phys. Solids* **54**, 1206–1236 (2006)
29. C.Y. Li, T.W. Chou, Strain and pressure sensing using single-walled carbon nanotubes. *Nanotechnology* **15**, 1493–1496 (2004)
30. V. Sazonova, Y. Yaish, H. Ustunel, D. Roundy, T.A. Arias, P.L. McEuen, A tunable carbon nanotube electromechanical oscillator. *Nature* **431**, 284 (2004)
31. G.X. Cao, X. Chen, J.W. Kysar, Strain sensing of carbon nanotubes: numerical analysis of the vibrational frequency of deformed sing-wall carbon nanotubes. *Phys. Rev. B* **72**, 195412 (2005)
32. Q. Zhao, Z.H. Gan, O.K. Zhuang, Electrochemical sensors based on carbon nanotubes. *Electroanalysis* **14**, 1609–1613 (2002)
33. Y.Y. Zhang, C.M. Wang, V.B.C. Tan, Assessment of Timoshenko beam models for vibrational behavior of single-walled carbon nanotubes using molecular dynamics. *Adv. Appl. Math. Mech.* **1**(1), 89–106 (2009)
34. D.W. Brenner, O.A. Shenderova, J.A. Harrison, S.J. Stuart, B. Ni, S.B. Sinnott, A second-generation reactive empirical bond order (REBO) potential energy expression for hydrocarbons. *J. Phys.: Condens. Matter* **14**, 783–802 (2002)
35. D.W. Brenner, Empirical potential for hydrocarbons for use in simulation the chemical vapor deposition of diamond films. *Phys. Rev. B* **42**, 9458 (1990)
36. O.A. Shenderova, D.W. Brenner, A. Omeltchenko, X. Su, L.H. Yang, Atomistic modeling of the fracture of polycrystalline diamond. *Phys. Rev. B* **61**, 3877 (2000)
37. Y. Huang, J. Wu, K.C. Hwang, Thickness of graphene and single-wall carbon nanotubes. *Phys. Rev. B* **74**, 245413 (2006)
38. NanoHive-1, v. 1.2.0-b1., Nanorex Inc., <http://www.nanorex.com> (2005)
39. F. Khademolhosseini, A.S. Phani, A. Nojeh, R.K.N.D. Rajapakse, Nonlocal continuum modeling and molecular dynamics simulation of torsional vibration of carbon nanotubes. *IEEE Trans. Nanotechnol.* **11**(2), 34–43 (2011)
40. S.J. Stuart, A.B. Tutein, J.A. Harrison, A reactive potential for hydrocarbons with intermolecular interactions. *J. Chem. Phys.* **112**, 6472–6486 (2000)
41. M. Chen, J. Zang, D. Xiao, F. Liu, Mechanical wave propagation in carbon nanotubes driven by an oscillating tip actuator. *J. Appl. Phys.* **105**, 026102 (2009)
42. Y.G. Hu, K.M. Liew, Q. Wang, X.Q. He, B.I. Yakobson, Nonlocal shell model for elastic wave propagation in single-and double-walled carbon nanotubes. *J. Mech. Phys. Solids* **56**, 3475–3485 (2008)
43. C. Lin, H. Wang, W. Yang, Wave propagation and scattering in deformed single-wall carbon nanotubes. *J. Comput. Theor. Nanosci.* **8**(10), 2019–2024 (2011)
44. B. Arash, Q. Wang, K.M. Liew, Wave propagation in graphene sheets with nonlocal elastic theory via finite element formulation. *Comput. Methods Appl. Mech. Eng.* **223–224**, 1–9 (2012)
45. D. Landau, K. Binder, *A Guide to Monte Carlo Simulations in Statistical Physics* (Cambridge University Press, Cambridge, 2000)
46. D.D. Mc Cracken, The Monte Carlo method. *Sci. Am.* **192**, 90–95 (1955)
47. N. Metropolis, A.W. Rosenbluth, M.N. Rosenbluth, A.H. Teller, E. Teller, Equation of state calculations by fast computing machines. *J. Chem. Phys.* **21**, 1087–1092 (1953)
48. N.G. Van Kampen, *Stochastic Processes in Physics and Chemistry* (North-Holland, Amsterdam, 1981)
49. Z. Wang, E.G. Seebauer, Estimating pre-exponential factors for desorption from semiconductors: consequences for a priori process modelling. *Appl. Surf. Sci.* **181**, 111–120 (2001)
50. G.K. Batchelor, *An Introduction to Fluid Dynamics* (Cambridge University Press, Cambridge, 1967)
51. J.N. Reddy, *An Introduction to the Finite Element Method* (McGraw-Hill, New York, 1993)
52. H.S. Park, W.K. Liu, An introduction and tutorial on multiple-scale analysis in solids. *Comput. Methods Appl. Mech. Eng.* **193**, 1733–1772 (2004)

53. A.F. Voter, Hyperdynamics: accelerated molecular dynamics of infrequent events. *Phys. Rev. Lett.* **78**(20), 3908–3911 (1997)
54. A.F. Voter, F. Montalenti, T.C. Germann, Extending the time scale in atomistic simulation of materials. *Annu. Rev. Mater. Res.* **32**, 321–346 (2002)
55. P. Zhang, Y. Huang, P.H. Geubelle, P.A. Klein, K.C. Hwang, The elastic modulus of single-wall carbon nanotubes: a continuum analysis incorporating interatomic potentials. *Int. J. Solids Struct.* **39**, 3893–3906 (2002)
56. D.W. Brenner, O.A. Shenderova, J.A. Harrison, S.J. Stuart, B. Ni, S.B. Sinnott, A second-generation reactive empirical bond order (REBO) potential energy expression for hydrocarbons. *J. Phys.: Condens. Matter* **14**(4), 783–802 (2002)
57. W.A. Curtin, R.E. Miller, Atomistic/continuum coupling in computational materials science. *Modell. Simul. Mater. Sci. Eng.* **11**(3), R33–R68 (2003)
58. M. Arroyo, T. Belytschko, An atomistic-based finite deformation membrane for single layer crystalline films. *J. Mech. Phys. Solids* **50**(9), 1941–1977 (2002)
59. W.E.Z. Huang, Matching conditions in atomistic/continuum modeling of materials. *Phys. Rev. Lett.* **87**, 135501 (2001)
60. G.J. Wagner, W.K. Liu, Coupling of atomistic and continuum simulations using bridging scale decomposition. *J. Comput. Phys.* **190**, 249–274 (2003)
61. V.B. Shenoy, R. Miller, E.B. Tadmor, D. Rodney, R. Phillips, M. Ortiz, An adaptive finite element approach to atomic-scale mechanics the quasicontinuum method. *J. Mech. Phys. Solids* **47**(3), 611–642 (1999)
62. L.E. Shilkrot, W.A. Curtin, R.E. Miller, A coupled atomistic/continuum model of defects in solids. *J. Mech. Phys. Solids* **50**(10), 2085–2106 (2002)
63. E.B. Tadmor, M. Ortiz, R. Phillips, Quasicontinuum analysis of defects in solids. *Philos. Mag. A* **73**(6), 1529–1563 (1996)
64. D. Rogula, Introduction to nonlocal theory of material media, in *Nonlocal Theory of Material Media*, ed. by D. Rogula, CISM Courses and Lectures, vol 268 (Springer, New York, 1982) pp. 125–222
65. Z.P. Bazant, M. Jirasek, Nonlocal Integral formulations of plasticity and damage: survey of progress. *J. Eng. Mech.* **128**, 1119–1149 (2002)
66. M. Jirasek, Nonlocal theories in continuum mechanics. *Acta Polytech.* **44**, 5–6 (2004)
67. J. Fish, W. Chen, G. Nagai, onlocal dispersive model for wave propagation in heterogeneous media, Part I: one-dimensional case. *Int. J. Numer. Methods Eng.* **54**, 331–346 (2002)
68. H. Askes, E. Aifantis, Gradient elasticity theories in statics and dynamics a unification of approaches. *Int. J. Fract.* **139**, 297–304 (2006)

Chapter 4

Theory of Nonlocal Elasticity

Continuum theories describe a system in terms of a few variables such as mass, temperature, voltage, and stress, which are highly suited for direct measurements of these variables. Their successes, expediency, and practicality, have been demonstrated and tested throughout the history of science through explaining and predicting diverse physical phenomena.

The physical world is composed of atoms moving under the influence of their mutual interaction forces. These interactions at microscopic scale are the physical origin of many macroscopic phenomena. Atomistic investigation helps to identify macroscopic quantities and their correlations, and enhance our understanding of various physical theories. To explain the fundamental departure of microcontinuum theories from the classical continuum theories, the former is a continuum model embedded with microstructures to describe the microscopic motion, or a nonlocal model to describe the long-range material interaction. This extends the application of the continuum model to microscopic space and short-time scales. Micromorphic theory [1, 2] treats a material body as a continuous collection of a large number of deformable particles, with each particle possessing finite size and inner structure. Using assumptions such as infinitesimal deformation and slow motion, micromorphic theory can be reduced to Mindlin's microstructure theory [3]. When the microstructure of the material is considered rigid, it becomes the micropolar theory [1]. Assuming a constant microinertia, micropolar theory is identical to the cosserat theory [4]. Eliminating the distinction of macromotion of the particle and the micromotion of its inner structure, it becomes couple stress theory [5, 6]. When the particle reduces to the mass point, all the theories reduce to the classical or ordinary continuum mechanics.

4.1 Need for Nonlocal Elasticity for Nanostructures

The nanostructures length scales are often sufficiently small, and hence for the applicability of classical continuum models, we need to consider the small length scales such as lattice spacing between individual atoms, grain size, etc. Although

solution through molecular dynamics (MD) simulation is a possibility for such problems, its large computational cost prohibits its use for a general analysis. The conventional continuum models cannot handle scale effects. Hence the best alternative is to use those methods which provide the simplicity of continuum models and at the same time incorporate the effects of scale in such chosen continuum models.

The length scales associated with nanostructures like carbon nanotubes are such that to apply any classical continuum techniques, we need to consider the small length scales such as lattice spacing between individual atoms, grain size, etc. This makes a consistent classical continuum model formulation very challenging. Hence, the Eringen's nonlocal elasticity theory [7–10] is useful tool in treating phenomena whose origins lie in the regimes smaller than the classical continuum models. This theory takes account of remote action forces between atoms. This causes the stresses to depend on the strains not only at an individual point under consideration, but at all points of the body. In this theory, the internal size or scale could be represented in the constitutive equations simply as material parameters. Such a nonlocal continuum mechanics has been widely accepted and has been applied to many problems including wave propagation, dislocation, crack problems, etc. [11]. Recently, there has been great interest in the application of nonlocal continuum mechanics for modeling and analysis of nanostructures such as CNTs and graphene sheets. Application of nonlocal continuum theory to nanotechnology problems was initially addressed by Peddison et al. [11], in which the static deformation of a beam structures based on a simplified nonlocal model was analyzed.

4.2 Introduction to Nonlocal Elasticity

Eringen's nonlocal theory of elasticity accommodates an equivalent effect due to nearest neighbor interaction and beyond the single lattice in the sense of lattice average stress and strain. This theory assumes that the stress state at a reference point $\mathbf{x} = (x_1, x_2, x_3)$ in the body is regarded to be dependent not only on the strain state at \mathbf{x} but also on the strain states at all other points \mathbf{x}' of the body. This is in accordance with atomic theory of lattice dynamics and experimental observations on phonon dispersion. The most general form of the constitutive relation in the nonlocal elasticity type representation involves an integral over the entire region of interest. The integral contains a nonlocal kernel function, which describes the relative influences of the strains at various locations on the stress at a given location. The constitutive equations of linear, homogeneous, isotropic, and nonlocal elastic solid with zero body forces are given by [8]

$$\sigma_{kl,k} + \rho(f_l - \ddot{u}_l) = 0 \quad (4.1)$$

$$\sigma_{kl}(\mathbf{x}) = \int_{\Omega} \alpha(|\mathbf{x} - \mathbf{x}'|, \xi) \sigma_{kl}^c(\mathbf{x}') d\Omega(\mathbf{x}') \quad (4.2)$$

$$\sigma_{kl}^c(\mathbf{x}') = \lambda e_{rr}(\mathbf{x}')\delta_{kl} + 2\mu e_{kl}(\mathbf{x}') \quad (4.3)$$

$$e_{kl}(\mathbf{x}') = \frac{1}{2} \left(\frac{\partial u_k(\mathbf{x}')}{\partial x'_l} + \frac{\partial u_l(\mathbf{x}')}{\partial x'_k} \right) \quad (4.4)$$

Equation (4.1) is the equilibrium equation, where σ_{kl} , ρ , f_l , and u_l are the stress tensor, mass density, body force density, and displacement vector at a reference point \mathbf{x} in the body, respectively, at time t . Equation (4.3) is the classical constitutive relation where $\sigma_{kl}^c(\mathbf{x}')$ is the classical stress tensor at any point \mathbf{x}' in the body, which is related to the linear strain tensor $e_{kl}(\mathbf{x}')$ at the same point through the lame constants λ and μ . Equation (4.4) is the classical strain–displacement relationship. The only difference between Eqs. (4.1)–(4.4) and the corresponding equations of classical elasticity is the introduction of Eq. (4.2), which relates the global (or nonlocal) stress tensor σ_{kl} to the classical stress tensor $\sigma_{kl}^c(\mathbf{x}')$ using the modulus of nonlocalness. The modulus of nonlocalness or the nonlocal modulus $\alpha(|\mathbf{x} - \mathbf{x}'|, \xi)$ is the kernel of the integral equation (4.2) and contain parameters which correspond to the nonlocalness [12]. A dimensional analysis of Eq. (4.2) clearly shows that the nonlocal modulus has dimensions of $(\text{length})^{-3}$ and so it depends on a characteristic length ratio a/ℓ where a is an internal characteristic length (lattice parameter, size of grain, or granular distance) and ℓ is an external characteristic length of the system (wavelength, crack length, size, or dimensions of sample) [10], Ω is the region occupied by the body. Therefore the nonlocal modulus can be written in the following form:

$$\alpha = \alpha(|\mathbf{x} - \mathbf{x}'|, \xi), \quad \xi = \frac{e_0 a}{\ell} \quad (4.5)$$

where e_0 is a constant appropriate to the material and has to be determined for each material independently [10].

Making certain assumptions [10], the integro-partial differential equations of nonlocal elasticity can be simplified to partial differential equations. For example, Eq. (4.2) takes the following simple form:

$$(1 - \xi^2 \ell^2 \nabla^2) \sigma_{kl}(\mathbf{x}) = \sigma_{kl}^c(\mathbf{x}) = C_{klmn} \varepsilon_{mn}(\mathbf{x}) \quad (4.6)$$

where C_{ijkl} is the elastic modulus tensor of classical isotropic elasticity and ε_{ij} is the strain tensor. Where ∇^2 denotes the second order spatial gradient applied on the stress tensor $\sigma_{kl,k}$ and $\xi = e_0 a/\ell$. The validity of Eq. (4.6) has been justified by comparing the expressions for frequency of waves from the nonlocal model above with those of the Born-Karman model of lattice dynamics [10]. Eringen reports a maximum difference of 6%, and a perfect match for nonlocal constant value of $e_0 = 0.39$ [10]. To the best of authors knowledge, no experiments have been conducted on CNT to determine the value of e_0 , which has been assumed as a constant appropriate to each material in the published literature. In the upcoming sections, a summary of the works done so far to estimate the nonlocal scale parameter is presented.

Generally used kernel function $\alpha(|\mathbf{x} - \mathbf{x}'|, \xi)$ is given in [9] is of the form

$$\alpha(|\mathbf{x}|, \xi) = \frac{1}{2\pi\xi^2\ell^2} K_0\left(\frac{\sqrt{\mathbf{x} \cdot \mathbf{x}}}{\xi\ell}\right) \quad (4.7)$$

where K_0 is the modified Bessel's function.

As $\xi \rightarrow 0$, α must revert to the Dirac delta measure so that classical elasticity limit is included in the limit of vanishing internal characteristic length, that is,

$$\lim_{\xi \rightarrow 0} \alpha(|\mathbf{x} - \mathbf{x}'|, \xi) = \delta(|\mathbf{x} - \mathbf{x}'|) \quad (4.8)$$

We therefore expect that α is a *delta sequence*.

In the theory of nonlocal elasticity, the stress at a reference point \mathbf{x} is considered to be a functional of the strain field at every point \mathbf{x}' in the body. For homogeneous isotropic bodies, the linear theory leads to a set of integro-partial differential equations for the displacement field, which are generally difficult to solve. For a special class of kernels, these equations are reducible to a set of singular partial differential equations for which the literature is extensive.

The selection of the appropriate class of kernels is not ad hoc but fairly general, based on mathematical conditions of admissibility and physical conditions of verifiability. For example, the dispersion curves available from lattice dynamics and phonon dispersion experiments provide excellent testing on the success of these kernels. Ultimately, these kernels should be expressed in terms of interatomic force potentials or correlation functions. Presently, several solutions obtained for various problems support the theory advanced here. For example, the dispersion curve, obtained for plane waves are in excellent agreement with those of the Born-Karman theory of lattice dynamics. The dislocation core and cohesive (theoretical) stress predicted by nonlocal theory are close to those known in the physics of solids. Moreover, nonlocal theory reduces to classical (local theory) in the long wavelength limit and to atomic lattice dynamics in the short wavelength limit. These and several other considerations lead us to the exciting prospect that by means of nonlocal elasticity, excellent approximation may be provided for a large class of physical phenomena with characteristic lengths ranging from microscopic to macroscopic scales. This situation becomes specially promising in dealing with imperfect solids, dislocations, and fracture, since in these cases, the internal (atomic) state of the body is difficult to characterize.

The solution of nonlocal elasticity problems are however difficult mathematically, since little is known on the treatment of integro-partial differential equations, especially for mixed boundary value problems. Therefore, the treatment of these problems by means of singular differential equations is promising. This is born out, at least, with the treatment of two problems here, namely the screw dislocation and Rayleigh surface waves. Results for both problems are gratifying in that they are supported by atomic lattice dynamics and experiments.

For nonlocal elasticity, there exists a differential form for the stress-strain relation [8],

$$(1 - \xi^2 \ell^2 \nabla^2) \sigma_{ij} = C_{ijkl} \varepsilon_{kl} \quad (4.9)$$

where the operator ∇^2 is the Laplacian operator. Notice that in the nonlocal elasticity, the effect of small length scale is considered by incorporating the internal parameter length into the constitutive equation. One may also see that when the internal characteristic length a is neglected, i.e., the particles of a medium are considered to be continuously distributed, then $\xi = 0$, and Eq.(4.9) reduces to the constitutive equation of classical elasticity.

4.3 Types of Nonlocality

The local dependence of a physical quantity (the effect r) at a point \mathbf{x} of space at time $\tau(r(x, y, z, \tau))$ on another physical quantity (the cause p) at the same point \mathbf{x} and at the same time $\tau(p(x, y, z, \tau))$ has the general form

$$r(x, y, z, \tau) = r(p(x, y, z, \tau)) \quad (4.10)$$

1. Spatial nonlocality

It means that the effect R at the point \mathbf{x} at time τ depends on the causes at all points \mathbf{x}' at the same instant of time:

$$R(x, y, z, \tau) = \int_V \alpha(|\mathbf{x} - \mathbf{x}'|, \xi) r(p(x', y', z', \tau)) dx' dy' dz' \quad (4.11)$$

2. Temporal nonlocality (materials with memory)

The effect R at the point \mathbf{x} at time τ depends on the history of causes at the point \mathbf{x} over all preceding time and at the present instant:

$$R(x, y, z, \tau) = \int_{-\infty}^{\tau} \beta(\tau - \tau', \zeta) r(p(x, y, z, \tau')) d\tau' \quad (4.12)$$

3. Mixed nonlocality

It is the simultaneous effects of memory and spatial nonlocalness. For this case we have an effect R at the point \mathbf{x} at time τ that depends on the causes at all spatial points \mathbf{x}' and at all times $\tau' \leq \tau$:

$$R(x, y, z, \tau) = \int_{-\infty}^{\tau} \int_V \gamma(|\mathbf{x} - \mathbf{x}'|, \tau - \tau', \xi, \zeta) r(p(x', y', z', \tau')) dx' dy' dz' d\tau' \quad (4.13)$$

Here V is the volume occupied by the body.

The moduli of nonlocalness $\alpha(|\mathbf{x} - \mathbf{x}'|, \xi)$, $\beta(\tau - \tau', \zeta)$, $\gamma(|\mathbf{x} - \mathbf{x}'|, \tau - \tau', \zeta, \xi)$, the kernels of the integral relations Eqs.(4.11)–(4.13), contain parameters that correspond to the nonlocalness:

$$\xi = \frac{L_{\text{int}}}{L_{\text{ext}}} \quad (4.14)$$

$$\zeta = \frac{T_{\text{int}}}{T_{\text{ext}}} \quad (4.15)$$

where L_{int} is the internal characteristic length (the lattice parameter, or size of grain), L_{ext} is the external characteristic length (wavelength, or size of the sample); T_{int} is the internal characteristic time (relaxation time, time for a signal to travel between molecules), T_{ext} is the external characteristic time (the time of application of the external action, period of vibration and so forth) [13].

If we consider the stress–strain state of a rigid body, the cause is the strain ε , and the effect is the stress σ . The corresponding local and different types of nonlocal linear equations of state have the following form:

- Local or Classical constitutive relation:

$$\sigma_{ij}(x, y, z, \tau) = C_{ijkl}\varepsilon_{km}(x, y, z, \tau), \quad (4.16)$$

- Spatial nonlocalness:

$$\sigma_{ij}(x, y, z, \tau) = \int_V \alpha_{ijkl}(|\mathbf{x} - \mathbf{x}'|, \xi) \varepsilon_{km}(x', y', z', \tau) dx' dy' dz', \quad (4.17)$$

- Temporal nonlocalness:

$$\sigma_{ij}(x, y, z, \tau) = \int_{-\infty}^{\tau} \beta_{ijkl}(\tau - \tau', \zeta) \varepsilon_{km}(x, y, z, \tau') d\tau', \quad (4.18)$$

- Mixed nonlocalness (both spatial and temporal):

$$\sigma_{ij}(x, y, z, \tau) = \int_{-\infty}^{\tau} \int_V \gamma_{ijkl}(|\mathbf{x} - \mathbf{x}'|, \tau - \tau', \xi, \zeta) \varepsilon_{km}(x', y', z', \tau') dx' dy' dz' d\tau'. \quad (4.19)$$

It is obvious that the local elastic body is obtained from Eq. (4.17) by passing to the limit as $\xi \rightarrow 0$, since

$$\lim_{\xi \rightarrow 0} \alpha_{ijkl}(|\mathbf{x} - \mathbf{x}'|, \xi) = C_{ijkl} \delta(|\mathbf{x} - \mathbf{x}'|) \quad (4.20)$$

Hence in the long-wave limit the nonlocal theory of elasticity reduces to the classical theory of elasticity, and in the short-wave limit it agrees with the theory of the atomic lattice.

4.3.1 Properties of the Kernels

We may express α in a more appropriate form as

$$\alpha = \alpha(|\mathbf{x} - \mathbf{x}'|, \xi), \quad \xi = \frac{e_0 a}{\ell}$$

where e_0 is a constant appropriate to the material.

The nonlocal modulus has the following interesting properties.

1. It acquires its maximum at $\mathbf{x}' = \mathbf{x}$ attenuating with $|\mathbf{x} - \mathbf{x}'|$
2. When $\xi \rightarrow 0$, α must revert to the Dirac delta measure so that classical elasticity limit is included in the limit of vanishing internal characteristic length

$$\lim_{\xi \rightarrow 0} \alpha(|\mathbf{x} - \mathbf{x}'|, \xi) = \delta(|\mathbf{x} - \mathbf{x}'|) \quad (4.21)$$

We therefore expect that α is a delta sequence. That is, nonlocal dependence becomes local in passage to the limit,

3. For small internal characteristic lengths, i.e., when $\xi \rightarrow 1$, nonlocal theory should approximate atomic lattice dynamics
4. By matching the dispersion curves of plane waves with those of atomic lattice dynamics (or experiments), we can determine α for a given material. Several different forms have been found (some of the most important forms are also given in this section)
5. We observe that all nonlocal moduli given above are normalized so that their integrals over the domain of integration (line, surface, or volume) give unity. Moreover, they are all δ sequence, i.e., when $\xi \rightarrow 0$ we obtain the Dirac delta function, Because of this property, nonlocal elasticity in the limit $\xi \rightarrow 0$ reverts to classical elasticity as can be seen by letting $\xi \rightarrow 0$ in Eq.(4.2), to obtain Hooke's law of classical elasticity.
6. We now exploit the above observation further by assuming the following: When α takes on a Greens function of a linear differential operator \mathcal{L} , i.e.,

$$\mathcal{L}\alpha(|\mathbf{x} - \mathbf{x}'|) = \delta(|\mathbf{x} - \mathbf{x}'|) \quad (4.22)$$

the nonlocal constitutive relation Eq.(4.2) is reduced to the differential equation

$$\mathcal{L}\sigma_{ij} = \sigma_{ij}^c \quad (4.23)$$

and the integro-partial differential equation (4.1) is correspondingly reduced to the partial differential equation

$$\sigma_{ij} + \mathcal{L}(f_i - \rho \ddot{u}_i) = 0 \quad (4.24)$$

By matching the dispersion curves with lattice models, Eringen [8, 9] proposed a nonlocal model with the linear differential operator \mathcal{L} defined by

$$\mathcal{L} = 1 - (e_0 a)^2 \nabla^2 \quad (4.25)$$

where a is an internal characteristic length (lattice parameter, granular size or molecular diameters) and e_0 is a constant appropriate to each material for adjusting the model to match some reliable results by experiments or other theories. Therefore, according to Eqs. (4.2), (4.3), (4.4), and (4.9), the constitutive relations may be simplified to

$$\left(1 - (e_0 a)^2 \nabla^2\right) \sigma_{ij} = \sigma_{ij}^c = C_{ijkl} \varepsilon_{kl} \quad (4.26)$$

For simplicity and to avoid solving integro-partial differential equations, the nonlocal elasticity model, defined by the relations given by Eqs. (4.23)–(4.26), has been widely adopted for tackling various problems of linear elasticity and micro-/nanostructural mechanics.

Eringen [9] has studied the properties of the functions $\alpha(|\mathbf{x} - \mathbf{x}'|, \xi)$ and proposed some specific expressions for these kernels, which are in good agreement with the results of the theory of crystal lattice. For example, the following are some examples which have found applications:

One-Dimensional Moduli:

$$\begin{aligned} \alpha(|\mathbf{x} - \mathbf{x}'|, \xi) &= \frac{1}{\ell \xi} \left(1 - \frac{|\mathbf{x} - \mathbf{x}'|}{\ell \xi}\right), \quad |\mathbf{x} - \mathbf{x}'| < \ell \xi \\ &= 0, \quad |\mathbf{x} - \mathbf{x}'| \geq \ell \xi \end{aligned} \quad (4.27)$$

$$\alpha(|\mathbf{x} - \mathbf{x}'|, \xi) = \frac{1}{2\ell \xi} \exp\left(-\frac{|\mathbf{x} - \mathbf{x}'|}{\xi}\right) \quad (4.28)$$

$$\alpha(|\mathbf{x} - \mathbf{x}'|, \xi) = \frac{1}{\ell \sqrt{\pi \xi}} \exp\left(-\frac{|\mathbf{x} - \mathbf{x}'|^2}{\ell^2 \xi}\right) \quad (4.29)$$

Two-Dimensional Moduli:

$$\alpha(|\mathbf{x} - \mathbf{x}'|, \xi) = \frac{1}{2\pi \ell^2 \xi^2} K_0\left(\frac{\sqrt{|\mathbf{x} - \mathbf{x}'|}}{\ell \xi}\right) \quad (4.30)$$

where K_0 is the modified Bessel's function.

$$\alpha(|\mathbf{x} - \mathbf{x}'|, \xi) = \frac{1}{\pi \ell^2 \xi} \exp\left(-\frac{|\mathbf{x} - \mathbf{x}'|^2}{\ell^2 \xi}\right) \quad (4.31)$$

Three-Dimensional Moduli:

$$\alpha(|\mathbf{x} - \mathbf{x}'|, \xi) = \frac{1}{4\pi\ell^2\xi^2} \exp\left(-\frac{\sqrt{|\mathbf{x} - \mathbf{x}'|}}{\ell\xi}\right) \quad (4.32)$$

$$\alpha(|\mathbf{x} - \mathbf{x}'|, \xi) = \frac{1}{8(\pi\eta)^{3/2}} \exp\left(-\frac{|\mathbf{x} - \mathbf{x}'|^2}{4\eta}\right) \quad (4.33)$$

where $\eta = a_l^2/(4C^2)$; a_l is the lattice parameter; C is the corresponding constant, which can be determined either by experiment or by applying the results of the theory of the atomic lattice.

4.4 Nonlocal Constitutive Relations

In this section, we will give the nonlocal constitutive relations for 1D, 2D, 3D, and axisymmetric problems, which will be extensively used in the later chapters for deriving the dispersion relations for different nano waveguides.

4.4.1 Nonlocal Constitutive Relation for 1D Problems

According to nonlocal elasticity, the constitutive relation of nonlocal elasticity for 1D problems is expressed as

$$\sigma_{xx} - (e_0a)^2 \frac{d^2\sigma_{xx}}{dx^2} = E\varepsilon_{xx} \quad (4.34)$$

4.4.2 Nonlocal Constitutive Relations for 2D Problems

According to nonlocal elasticity, the constitutive relations of nonlocal elasticity for 2D problems are expressed as

$$\sigma_{xx} - (e_0a)^2 \left[\frac{\partial^2\sigma_{xx}}{\partial x^2} + \frac{\partial^2\sigma_{xx}}{\partial y^2} \right] = \frac{E}{1-\nu^2} (\varepsilon_{xx} + \nu\varepsilon_{yy}) \quad (4.35)$$

$$\sigma_{yy} - (e_0a)^2 \left[\frac{\partial^2\sigma_{yy}}{\partial x^2} + \frac{\partial^2\sigma_{yy}}{\partial y^2} \right] = \frac{E}{1-\nu^2} (\varepsilon_{yy} + \nu\varepsilon_{xx}) \quad (4.36)$$

$$\tau_{xy} - (e_0a)^2 \left[\frac{\partial^2 \tau_{xy}}{\partial x^2} + \frac{\partial^2 \tau_{xy}}{\partial y^2} \right] = \frac{E}{2(1+\nu)} \gamma_{xy} \quad (4.37)$$

4.4.3 Nonlocal Constitutive Relations for 3D Problems

According to nonlocal elasticity, the constitutive relations of nonlocal elasticity for 3D problems are expressed as

$$\sigma_{xx} - (e_0a)^2 \left[\frac{\partial^2 \sigma_{xx}}{\partial x^2} + \frac{\partial^2 \sigma_{xx}}{\partial y^2} + \frac{\partial^2 \sigma_{xx}}{\partial z^2} \right] = \frac{E}{1-\nu^2} (\varepsilon_{xx} + \nu \varepsilon_{yy} + \nu \varepsilon_{zz}) \quad (4.38)$$

$$\sigma_{yy} - (e_0a)^2 \left[\frac{\partial^2 \sigma_{yy}}{\partial x^2} + \frac{\partial^2 \sigma_{yy}}{\partial y^2} + \frac{\partial^2 \sigma_{yy}}{\partial z^2} \right] = \frac{E}{1-\nu^2} (\varepsilon_{yy} + \nu \varepsilon_{xx} + \nu \varepsilon_{zz}) \quad (4.39)$$

$$\sigma_{zz} - (e_0a)^2 \left[\frac{\partial^2 \sigma_{zz}}{\partial x^2} + \frac{\partial^2 \sigma_{zz}}{\partial y^2} + \frac{\partial^2 \sigma_{zz}}{\partial z^2} \right] = \frac{E}{1-\nu^2} (\varepsilon_{zz} + \nu \varepsilon_{yy} + \nu \varepsilon_{xx}) \quad (4.40)$$

$$\tau_{xy} - (e_0a)^2 \left[\frac{\partial^2 \tau_{xy}}{\partial x^2} + \frac{\partial^2 \tau_{xy}}{\partial y^2} + \frac{\partial^2 \tau_{xy}}{\partial z^2} \right] = \frac{E}{2(1+\nu)} \gamma_{xy} \quad (4.41)$$

$$\tau_{yz} - (e_0a)^2 \left[\frac{\partial^2 \tau_{yz}}{\partial x^2} + \frac{\partial^2 \tau_{yz}}{\partial y^2} + \frac{\partial^2 \tau_{yz}}{\partial z^2} \right] = \frac{E}{2(1+\nu)} \gamma_{yz} \quad (4.42)$$

$$\tau_{zx} - (e_0a)^2 \left[\frac{\partial^2 \tau_{zx}}{\partial x^2} + \frac{\partial^2 \tau_{zx}}{\partial y^2} + \frac{\partial^2 \tau_{zx}}{\partial z^2} \right] = \frac{E}{2(1+\nu)} \gamma_{zx} \quad (4.43)$$

where σ_{xx} , σ_{yy} , σ_{zz} are the normal stresses, τ_{xy} , τ_{yz} , τ_{zx} are the shear stresses, ε_{xx} , ε_{yy} , ε_{zz} are the normal strains, γ_{xy} , γ_{yz} , γ_{zx} are the shear strains. E is the Young's modulus of the material, ν is the Poisson ratio, and the parameter e_0a is the scale coefficient that captures the small scale effect on the response of structures in nano-size.

4.4.4 Nonlocal Constitutive Relations for Cylindrical Shell Problems

Carbon nanotubes may be modeled by nonlocal cylindrical shells. Hence, for the case of cylindrical shells, the nonlocal constitutive relations in polar coordinate system (R, θ) are given by

$$\sigma_{xx} - (e_0a)^2 \left[\frac{\partial^2 \sigma_{xx}}{\partial x^2} + \frac{1}{R^2} \frac{\partial^2 \sigma_{xx}}{\partial \theta^2} \right] = \frac{E}{1-\nu^2} (\varepsilon_{xx} + \nu \varepsilon_{\theta\theta}) \quad (4.44)$$

$$\sigma_{\theta\theta} - (e_0 a)^2 \left[\frac{\partial^2 \sigma_{\theta\theta}}{\partial x^2} + \frac{1}{R^2} \frac{\partial^2 \sigma_{\theta\theta}}{\partial \theta^2} \right] = \frac{E}{1 - \nu^2} (\varepsilon_{\theta\theta} + \nu \varepsilon_{xx}) \quad (4.45)$$

$$\tau_{x\theta} - (e_0 a)^2 \left[\frac{\partial^2 \tau_{x\theta}}{\partial x^2} + \frac{1}{R^2} \frac{\partial^2 \tau_{x\theta}}{\partial \theta^2} \right] = \frac{E}{2(1 + \nu)} \gamma_{x\theta} \quad (4.46)$$

where R is the radius of the shell.

4.5 Summary

A brief introduction and the concepts of the nonlocal elasticity are presented in this chapter. The fundamental governing equations of nonlocal elasticity are also presented and the properties of the kernel functions are also discussed. The major properties of the kernel are the following:

- $\alpha(|\mathbf{x} - \mathbf{x}'|, \xi)$ has a maximum at $|\mathbf{x} - \mathbf{x}'|$,
- $\alpha(|\mathbf{x} - \mathbf{x}'|, \xi)$ tends rapidly to zero as $|\mathbf{x} - \mathbf{x}'|$ increases,
- $\alpha(|\mathbf{x} - \mathbf{x}'|, \xi)$ is a continuous function of $|\mathbf{x} - \mathbf{x}'|$,
- $\alpha(|\mathbf{x} - \mathbf{x}'|, \xi)$ is a delta sequence, tending to the Dirac delta function (δ) as $\xi \rightarrow 0$:
- $\int_V \alpha(|\mathbf{x} - \mathbf{x}'|, \xi) dV(\mathbf{x}') = 1$.

Finally, the simplified nonlocal constitutive relation is given in cartesian and cylindrical coordinate systems, which are useful for formulating the governing equations of nanostructures. The nonlocal theory and the equations presented in this chapter forms the basis for the study of wave propagation in nano waveguides, which are presented in the following chapters of the book.

References

1. A.C. Eringen, E.S. Suhubi, Nonlinear theory of simple micro-elastic solids I. Int. J. Eng. Sci. **2**, 189203 (1964)
2. A.C. Eringen, *Microcontinuum Field Theories I: Foundations and Solids* (Springer, New York, 1999)
3. R.D. Mindlin, Microstructure in linear elasticity. Arch. Ration. Mech. Anal. **16**, 5178 (1964)
4. E.F. Cosserat, *Theorie des Corps Deformable* (Hermann, Paris, 1909)
5. R.D. Mindlin, H.F. Tiersten, Effects of couple stresses in linear elasticity. Arch. Ration. Mech. Anal. **11**, 415448 (1962)
6. R.A. Toupin, Elastic materials with couple-stresses. Arch. Ration. Mech. Anal. **11**, 385414 (1962)
7. A.C. Eringen, D.G.B. Edelen, On non-local elasticity. Int. J. Eng. Sci. **10**, 233–243 (1972)
8. A.C. Eringen, On differential equations of nonlocal elasticity and solutions of screw dislocation and surface waves. J. Appl. Phys. **54**, 4703 (1983)
9. A.C. Eringen, *Non-local Polar Field Models* (Academic Press, New York, 1996)
10. A.C. Eringen, Linear theory of non-local elasticity and dispersion of plane waves. Int. J. Eng. Sci. **10**, 425–435 (1972)

11. J. Peddieson, G.R. Buchanan, R.P. McNitt, Application of nonlocal continuum models to nanotechnology. *Int. J. Eng. Sci.* **41**, 3053-12 (2003)
12. Y.Z. Povstenko, The nonlocal theory of elasticity and its applications to the description of defects in solid bodies. *J. Math. Sci.* **97**(1), 3840–3845 (1999)
13. A.C. Eringen, Vistas of nonlocal continuum physics. *Int. J. Eng. Sci.* **30**(10), 1551–1565 (1992)

Chapter 5

Material Property and Nonlocal Scale Parameter Estimation for Carbon Nanotubes

The estimation of mechanical material properties such as Young's modulus, shear modulus, and Poisson's ratio for CNTs has always been difficult to measure due to their small sizes. Researchers have always used mathematical models to roughly estimate these properties. In addition, the value of nonlocal parameters which introduces the scale effects in continuum models, has been extensively reported in the literature with different researchers reporting values of this parameter and they are found to have a large scatter. In this chapter, we will outline a few modeling procedures to determine the in-plane stiffness (Young's modulus) and the nonlocal scale parameter.

Material properties of carbon nanotubes, such as the in-plane stiffness, shear modulus, and bending rigidity, have been explored experimentally and numerically. Krishnan et al. [1] estimated the Young's modulus of SWCNTs to be $0.9 \sim 1.7$ TPa by observing their freestanding room temperature vibrations in a transmission electron microscope. Salvetat et al. [2] used an atomic force microscope and a special substrate to estimate the elastic and shear moduli of an SWCNT to be of the order of 1 TPa and 1 GPa, respectively. The length-dependent in-plane stiffness and shear modulus of chiral and achiral SWCNTs subjected to axial compression and torsion were discovered via molecular simulations [3]. It is expected that nonlocal elasticity can be applied to reveal the scale effect on the material properties of CNTs. Wang et al. [4], estimated the length-dependent stiffness from the nonlocal elasticity and verified through molecular simulation results and recommended that the nonlocal parameter is about 0.7 nm for the application of the nonlocal theory in analysis of carbon nanotubes. However, there is currently no consensus on the value of the nonlocal parameter that should be used to model CNTs and this could be the subject of further research.

This chapter presents the estimation of material property, length-dependent in-plane stiffness, and the nonlocal scale parameter for armchair, zigzag, and chiral nanotubes.

5.1 Length-Dependent In-plane Stiffness of Carbon Nanotubes

In this section, the length-dependent in-plane stiffness of SWCNTs is investigated via Eringen's theory of nonlocal elasticity. The SWCNT is modeled as an Euler-Bernoulli beam subjected to axial compression. From the derived nonlocal governing equation, a closed-form solution for the material property of SWCNT is obtained for various boundary conditions.

5.1.1 Governing Equations for SWCNT

Consider a CNT shown in Fig. 5.1a and the corresponding hollow circular beam idealization shown in Fig. 5.1b.

For the present analysis the CNT is modeled as a Euler-Bernoulli beam. Based on the Euler-Bernoulli beam theory the displacement field is given as

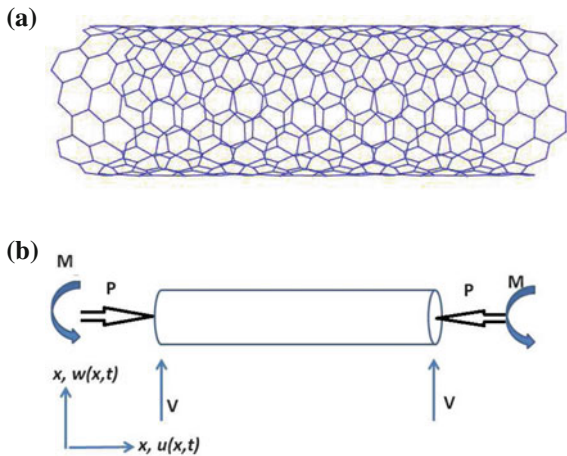
$$u = -z \frac{\partial w}{\partial x}, \quad v = 0, \quad w = w(x) \quad (5.1)$$

where w is transverse displacements of the point $(x, 0)$ on the middle plane (i.e., $z = 0$) of beam. The only nonzero strain of this beam theory is

$$\varepsilon_{xx} = -z \frac{\partial^2 w}{\partial x^2} \quad (5.2)$$

This is also called as bending strain. The equations of motion of the Euler-Bernoulli beam theory are given by

Fig. 5.1 **a** A typical CNT
b Hollow circular beam idealization of CNT subjected to axial compression



$$\frac{\partial Q}{\partial x} = 0 \quad (5.3)$$

$$\frac{\partial^2 M}{\partial x^2} - \frac{\partial}{\partial x} \left(P \frac{\partial w}{\partial x} \right) = 0 \quad (5.4)$$

where

$$Q = \int_A \sigma_{xx} dA, \quad M = \int_A z \sigma_{xx} dA \quad (5.5)$$

Here, Q , M , and P are the axial force, bending moment, and the axial compressive load, respectively, and σ_{xx} is the axial stress on the yz -section in the direction of x .

Using the nonlocal constitutive relation, one can express stress resultants in terms of strains. As opposed to the linear algebraic equations between the stress resultants and strains in a local theory, the nonlocal constitutive relations lead to differential relations involving the stress resultants and the strains. In the following, we present these relations for homogeneous isotropic beams. The nonlocal constitutive relation takes the following special form for one-dimensional case:

$$\sigma_{xx} - (e_0 a)^2 \frac{\partial^2 \sigma_{xx}}{\partial x^2} = E \varepsilon_{xx} \quad (5.6)$$

where E is the Young's modulus of the beam. Using Eqs. (5.5) and (5.6), we have

$$Q - (e_0 a)^2 \frac{\partial^2 Q}{\partial x^2} = EA \frac{\partial u}{\partial x} \quad (5.7)$$

$$M - (e_0 a)^2 \frac{\partial^2 M}{\partial x^2} = EI \kappa_e \quad (5.8)$$

where $I = \int_A z^2 dA$ is moment of inertia of beam cross section and $\kappa_e = -\frac{\partial^2 w}{\partial x^2}$ is bending strain of the beam.

With the help of nonlocal constitutive relation and equations of motion, the bending moment can be expressed in terms of the generalized displacements. By substituting Eq. (5.8) into Eq. (5.4), we get

$$M = -EI \frac{\partial^2 w}{\partial x^2} + (e_0 a)^2 \frac{\partial}{\partial x} \left(P \frac{\partial w}{\partial x} \right) \quad (5.9)$$

Substituting M from Eq. (5.9) into Eq. (5.4), we obtain the governing partial differential equation of motion of Euler-Bernoulli beam under axial compressive load (P) as

$$-EI \frac{\partial^4 w}{\partial x^4} + (e_0 a)^2 \frac{\partial^2}{\partial x^2} \left[\frac{\partial}{\partial x} \left(P \frac{\partial w}{\partial x} \right) \right] - \frac{\partial}{\partial x} \left(P \frac{\partial w}{\partial x} \right) = 0 \quad (5.10)$$

Assuming axial compressive load $P = \widehat{P} = \text{constant}$ and also constant material and geometric properties, the governing equation can be rewritten as

$$-EI \frac{\partial^4 w}{\partial x^4} + (e_0 a)^2 \widehat{P} \frac{\partial^4 w}{\partial x^4} - \widehat{P} \frac{\partial^2 w}{\partial x^2} = 0 \quad (5.11)$$

If we assume $e_0 a = 0$, the classical Euler-Bernoulli beam equation can be recovered.

5.1.2 Solution of Governing Equations

By integrating Eq. (5.11) twice with respect to x , one can obtain

$$-EI \frac{d^2 w}{dx^2} + (e_0 a)^2 \widehat{P} \frac{d^2 w}{dx^2} - \widehat{P} w = T_1 x + T_2 \quad (5.12)$$

where T_1 and T_2 are constants of integration, determined from the boundary conditions. The solution of this second-order ordinary differential equation consists of a homogeneous solution and a particular solution. The homogeneous solution is obtained from

$$\frac{d^2 w}{dx^2} + \lambda^2 w = 0 \quad (5.13)$$

where

$$\lambda^2 = \frac{\widehat{P}}{EI - (e_0 a)^2 \widehat{P}} \quad (5.14)$$

The complete solution is

$$w(x) = S_1 \sin \lambda x + S_2 \cos \lambda x + \frac{1}{\lambda^2} (T_1 x + T_2) \quad (5.15)$$

or

$$\frac{dw(x)}{dx} = S_1 \lambda \cos \lambda x - S_2 \lambda \sin \lambda x + \frac{1}{\lambda^2} T_1 \quad (5.16)$$

The four constants S_1 , S_2 , T_1 and T_2 are determined using the four boundary conditions of the problem. For the present problem, once λ is known, the buckling load can be determined using Eq. (5.14). Using the buckling load expression one can easily obtain the length-dependent in-plane stiffness. Now we will solve the problem for three different boundary configurations of CNT as shown below.

5.1.3 In-plane Stiffness Ratio Estimation

In this section, the procedure to determine the in-plane stiffness of different SWCNTs is outlined. The procedure will be based on the solution to nonlocal elasticity beam equations with in-plane axial loads. The procedure is outlined for beams with three different boundary conditions, namely simply supported, clamped-clamped, and clamped-free boundary conditions.

5.1.3.1 Simply Supported SWCNT

The boundary conditions for the simply supported problem are

$$\begin{aligned} w(x)|_{x=0} = 0, \quad M(x) &\equiv \left(-EI \frac{d^2 w(x)}{dx^2} + (e_0 a)^2 P \frac{d^2 w(x)}{dx^2} \right) \Big|_{x=0} = 0, \\ w(x)|_{x=L} = 0, \quad M(x) &\equiv \left(-EI \frac{d^2 w(x)}{dx^2} + (e_0 a)^2 P \frac{d^2 w(x)}{dx^2} \right) \Big|_{x=L} = 0 \end{aligned} \quad (5.17)$$

Substitution of Eq. (5.15) in the above boundary conditions leads to

$$S_1 \sin \lambda L = 0, \quad S_2 = 0, \quad T_1 = 0, \quad T_2 = 0 \quad (5.18)$$

For nonzero deflection ($w \neq 0$), we must have

$$S_1 \neq 0, \quad \sin \lambda L = 0 \quad (5.19)$$

which implies $\lambda = \frac{n\pi}{L}$. Using Eq. (5.14), the buckling load for the simply supported case is obtained as

$$\widehat{P} = \frac{EI \left(\frac{n\pi}{L} \right)^2}{1 + (e_0 a)^2 \left(\frac{n\pi}{L} \right)^2} \quad (5.20)$$

The critical buckling load, i.e., the smallest value of \widehat{P} at which the beam buckling occurs is $n = 1$. Now the critical buckling load is obtained as

$$\widehat{P}_{\text{cr}} = \frac{EI}{L^2} \left[\frac{\pi^2}{1 + \left(\frac{e_0 a}{L} \right)^2 \pi^2} \right] \quad (5.21)$$

which shows the equivalent size-dependent Young's modulus in the form of

$$E' = \frac{E}{1 + \left[\frac{e_0 a}{L} \right]^2 \pi^2} \quad (5.22)$$

This stiffness ratio (E'/E) is purely a function of nonlocal scaling parameter and the length of CNT.

5.1.3.2 Clamped–Clamped SWCNT

Assume the case where both the ends of the beam are clamped and are subjected to axial compressive load. The boundary conditions for this case are given as

$$\begin{aligned} w(x)|_{x=0} = 0, \quad \left. \frac{dw(x)}{dx} \right|_{x=0} &= 0, \\ w(x)|_{x=L} = 0, \quad \left. \frac{dw(x)}{dx} \right|_{x=L} &= 0 \end{aligned} \quad (5.23)$$

Substitution of Eq. (5.15) in the above boundary conditions leads to the following transcendental equation:

$$2(\cos \lambda L - 1) + \lambda L \sin \lambda L = 0 \quad (5.24)$$

which can be solved by an iterative method (such as Newton's method) for various roots of the equation. The smallest root of this equation is $\lambda = 2\pi$, and the critical buckling load becomes

$$\hat{P}_{cr} = \frac{EI}{L^2} \left[\frac{4\pi^2}{1 + 4 \left(\frac{e_0 a}{L^2} \right)^2 \pi^2} \right] \quad (5.25)$$

which shows the equivalent size-dependent Young's modulus in the form of

$$E' = \frac{E}{1 + 4 \left[\frac{(e_0 a)^2}{L^2} \right] \pi^2} \quad (5.26)$$

The stiffness ratio obtained for the clamped case is also a function of nonlocal scaling parameter and the length of the CNT.

5.1.3.3 Cantilever SWCNT

The boundary conditions for this case are given as

$$\begin{aligned} w(x)|_{x=0} = 0, \quad \left. \frac{dw(x)}{dx} \right|_{x=0} &= 0, \\ Q(x)|_{x=L} = 0, \quad M(x)|_{x=L} &= 0 \end{aligned} \quad (5.27)$$

Substituting Eq. (5.15) in the above four boundary conditions, we get

$$S_1 = 0, \quad S_2 \cos \lambda L = 0, \quad T_1 = 0, \quad T_2 + S_2 \lambda^2 = 0 \quad (5.28)$$

For nonzero solution of $w(x)$, we have

$$\cos \lambda L = 0 \quad (5.29)$$

which gives

$$\lambda = \frac{(2n - 1)\pi}{2L} \quad (5.30)$$

and the critical buckling load becomes

$$\widehat{P}_{\text{cr}} = \frac{EI}{L^2} \left[\frac{\pi^2}{4 + \left(\frac{e_0 a}{L}\right)^2 \pi^2} \right] \quad (5.31)$$

which shows the equivalent size-dependent Young's modulus in the form of

$$E' = \frac{E}{1 + \left[\frac{e_0 a}{L}\right]^2 \frac{\pi^2}{4}} \quad (5.32)$$

It can be seen from the above formulations that the stiffness ratio is purely a function of the nonlocal scaling parameter and the length of the CNT.

5.1.4 Numerical Results and Discussion

In this section, the dependence of the in-plane stiffness ratio (E'/E) on the length of SWCNT for various nonlocal scaling parameters is analyzed. For the present analysis the nonlocal scaling parameter values are assumed as 0.5, 1.0, 1.5 and 2.0 nm. Various carbon nanotubes having lengths ranging from 2 to 20 nm are considered for the analysis.

The length-dependent in-plane stiffness variation of simply supported SWCNT is shown in Fig. 5.2. The figure shows that the stiffness ratio decreases as $e_0 a$ increases. It can also be seen that the stiffness ratio difference for different nonlocal scaling parameters dips as the length of CNT increases. For very long CNTs the stiffness ratio is almost equal to unity, so that the stiffness ratio will not vary with $e_0 a$ for very long CNTs. In other words, the impact of the nonlocal effect on the stiffness ratio is negligible for CNTs of micrometer scale length. But when the length of CNTs reaches the nanoscale, the nonlocal effect becomes important, especially for the shorter CNTs.

Stiffness ratio variation of clamped-clamped SWCNT is shown in Fig. 5.3. As in the case of simply supported SWCNT, the stiffness ratio is very high for $e_0 a = 0.5$ nm and is small for $e_0 a = 2.0$ nm. The stiffness ratio difference for various nonlocal scaling parameters is very high for short CNTs and very small for long CNTs (See Fig. 5.3). Even for very long CNTs the stiffness ratio is not converging to unity for

Fig. 5.2 In-plane stiffness ratio of simply supported single-walled carbon nanotubes with various lengths

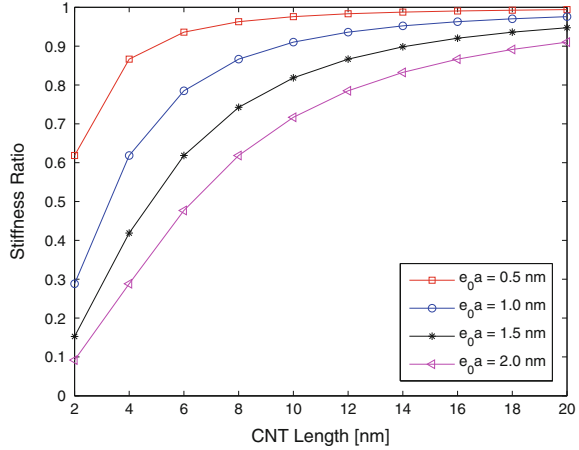
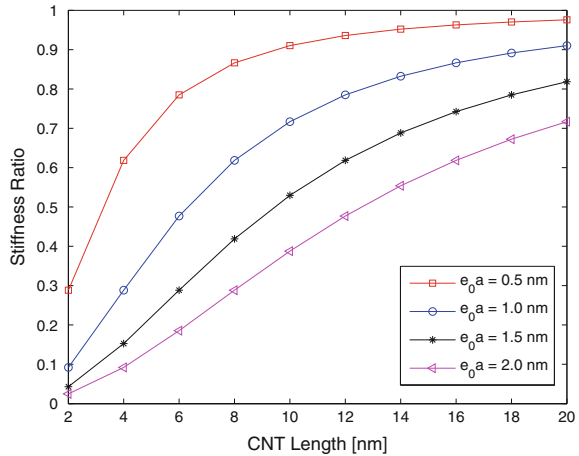


Fig. 5.3 In-plane stiffness ratio of clamped clamped single-walled carbon nanotubes with various lengths



this case. As e_0a increases the variation of the stiffness ratio with length of the CNT is almost linear.

For cantilever SWCNT the stiffness variation with length of the CNT is different from simply supported and clamped cases. Figure 5.4 shows that the stiffness ratio difference for various e_0a values is very small for long CNTs. As the length of the CNT increases the stiffness ratio tends to unity and is independent of the nonlocal scaling parameter.

A comparison of the in-plane stiffness ratio of SWCNTs with various boundary conditions is shown in Fig. 5.5. This figure shows that, for a given e_0a , the stiffness ratio of the cantilever SWCNT is very high compared to the simply supported and clamped SWCNTs. The clamped SWCNT has very low stiffness ratio compared to the simply supported and cantilever cases. The variation of the ratio is observed again from the figure, indicating the lower stiffness for shorter SWCNTs and an asymptotic stiffness for longer CNTs. These results are also presented in [5].

Fig. 5.4 In-plane stiffness ratio of cantilever single-walled carbon nanotubes with various lengths

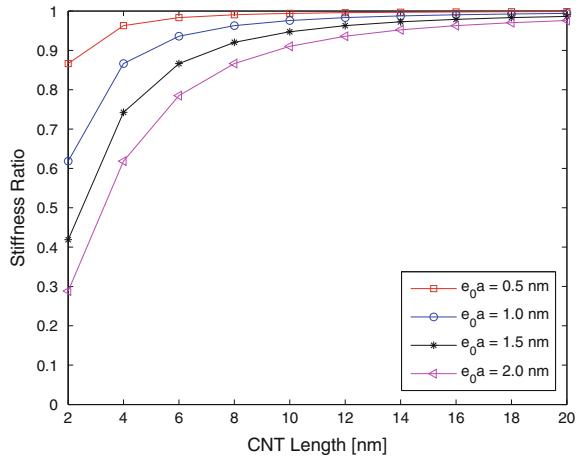
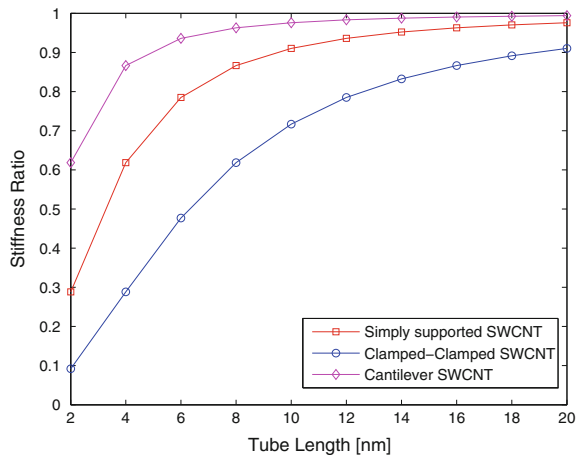


Fig. 5.5 A Comparison of in-plane stiffness ratio of simply supported, clamped-clamped, and cantilever type of single-walled carbon nanotubes with various lengths for nonlocal scaling parameter $e_0 a = 1.0$ nm

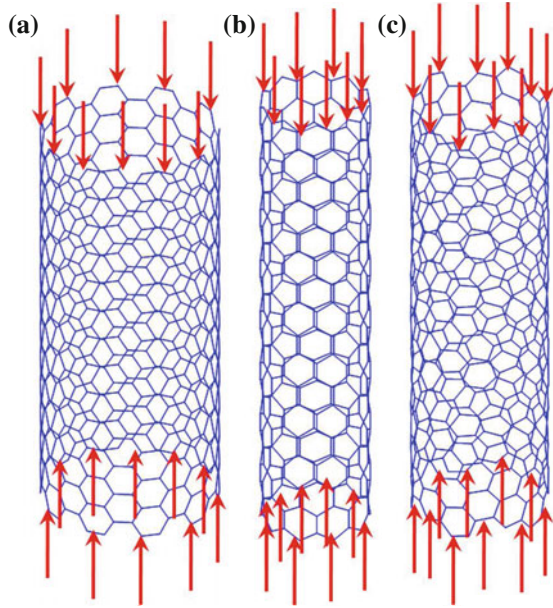


In the following section, these results are utilized to estimate the nonlocal scale parameter for the analysis of carbon nanotubes.

5.2 Material Property Estimation: A Comparison with Nonlocal Rod Model

Typical single-walled carbon nanotube structures are shown in Fig. 5.6. A major feature of the structure is the hexagon pattern that repeats itself periodically in space. As a result of the periodicity, each atom is bonded to three neighboring atoms. Such structure is mainly due to the process of sp^2 hybridization [6] (which is explained in

Fig. 5.6 Single-walled carbon nanotubes under compression: **a** armchair, **b** zigzag and **c** chiral



Chap. 1) during which one s -orbital and two p -orbitals combine to form three hybrid sp^2 -orbitals at 120° to each other within a plane. Based on the chirality [7], SWCNTs can have three different configurations. They are armchair (see Fig. 5.6a), zigzag (see Fig. 5.6b), and chiral (see Fig. 5.6c) configurations; denoted as (n, n) , $(n, 0)$ and (n, m) , respectively [7]. Armchair and zigzag CNTs are generally named as *chiral* since they exhibit a mirror symmetry plane, perpendicular to the tube axis [8].

In the classical (local) elastic model, the stress state at a given point is regarded as being determined uniquely by the strain state at that same point. In the nonlocal model, on the other hand, the stress state at a given point is regarded as being determined by the strain states of all points in the body. This recognizes the finite range of interatomic and intermolecular forces. While the constitutive equation of classical elasticity is an algebraic relationship between the stress and strain tensors, that of nonlocal elasticity involves spatial integrals which represent weighted averages of the contributions of the strain tensors of all points in the body to the stress tensor at the given point. Under certain conditions, these integral constitutive equations can be converted into equivalent differential constitutive equations.

Material properties of CNTs, such as the in-plane stiffness, shear modulus, and bending rigidity, have been explored experimentally and numerically [1–3]. It is expected that nonlocal elasticity can be applied to reveal the scale effect on the material properties of CNTs. Recently, Wang et al. [4] estimated the length-dependent stiffness of carbon nanotubes based on the nonlocal rod theory and verified through molecular simulation results and recommended the nonlocal parameter as 0.7 nm for the application of the nonlocal theory in analysis of carbon nanotubes. However,

there is currently no consensus on the value of the nonlocal parameter that should be used to model CNTs and this could be the subject of further research. In the last section, the length-dependent in-plane stiffness of SWCNTs was investigated based on nonlocal Bernoulli-Euler beam theory. The value of nonlocal scale parameter recommended by Wang et al. [4] will be applicable only for axial deformation of nanostructures. Their model did not consider the transverse deformation due to axial compression. Such effect is considered in the present problem to obtain the nonlocal scale parameter by estimating the length-dependent in-plane stiffness. From the present analysis, the value of the scale coefficient is recommended to be about 0.11 nm for the application of the nonlocal theory in analysis of carbon nanotubes. Wang's work is applicable only where the axial displacement of the nanostructures is the main concern. It is not applicable to the structures undergoing flexural/lateral deformation. In this section, the nonlocal parameter is estimated for the case of the flexural deformation of nanotubes. Most of the modeling and analysis problems of nanostructures, such as bending, buckling, vibration, etc., are based on the flexural deflection of the nanotubes. For all modeling and analyses based on flexural displacement, an accurate estimate of nonlocal scaling parameter is required. Such an attempt is made in this work. Hence, the nonlocal parameter obtained in this work is directly useful in the analysis and design of next-generation nanostructures.

Usually, the magnitude of the nonlocal parameter e_0a (where a is carbon-carbon bond length), determines the nonlocal effect in the analysis. The modeling and analyses of nanostructures based on flexural displacement require an accurate estimate of nonlocal scaling parameter. Such attempt is made in the present section.

In the previous section, the SWCNT is modeled as an elastic continuum beam model incorporating the nonlocal effects to determine the in-plane stiffness properties. The governing equation for this CNT in nonlocal continuum is presented in Eq. (5.10). In the previous section, for clamped-clamped SWCNT, the equivalent size-dependent Young's modulus has been shown in the form of

$$E' = \frac{E}{1 + 4 \left[\frac{(e_0a)^2}{L^2} \right] \pi^2} \quad (5.33)$$

In the following section, this size-dependent Young's modulus derived from the nonlocal elastic beam theory will be verified from the molecular simulation results given in [3], and an estimate of the scale coefficient is proposed for the application of nonlocal elasticity for analysis of CNTs based on the verification.

5.2.1 Numerical Results and Discussions

In this section, the in-plane stiffness ratio (E'/E) (see Eq. (5.33)) obtained from the nonlocal elasticity theory is compared with molecular dynamic simulation results [3], to obtain the nonlocal scaling parameter (e_0a) for the analysis of nanotubes. Wang

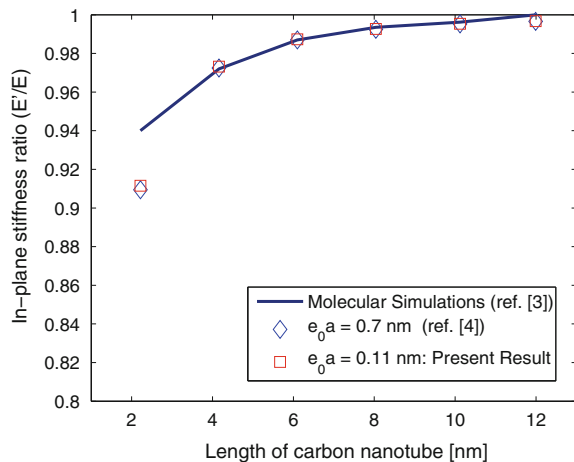
[3] conducted the molecular mechanics simulations via the commercial software *Materials Studio* to study the in-plane stiffness of (8, 0), (8, 8), and (8, 4) SWCNTs with various lengths, subjected to compression (see Fig. 5.6a, b and c, respectively, for zigzag, armchair, and chiral SWCNTs under compression). The simulations were carried out at a temperature of 1 °K to avoid the thermal effect. In view of the current debate on the thickness of CNTs, the derivation of the in-plane stiffness, $E \times h$, rather than the modulus E , would avoid arguments on the values of the effective thickness of CNTs [4]. In the simulations [3], the two ends of three SWCNTs of various lengths were clamped through prohibiting any motions on all atoms on the two edges. In compression motion of CNTs, the incremental displacement step was chosen as 0.1 Å. The present simulations investigate the ratio of the length-dependent in-plane stiffness obtained from the nonlocal elastic beam theory, which depend on the length of CNT. In the simulations, the lengths of CNT are chosen as follows:

- Zigzag (8,0) SWCNT: $L = 2.218, 4.159, 6.099, 8.041, 10.121, 11.993$ nm
- Armchair (8,8) SWCNT: $L = 2.656, 4.349, 6.283, 8.692, 11.574$ nm
- Chiral (8,4) SWCNT: $L = 2.204, 4.419, 6.628, 8.837, 10.109, 12.151$ nm

The in-plane stiffness ratio of the zigzag (8,0) CNTs obtained from molecular simulations is shown in Fig. 5.7 by the solid line. It was determined that the stiffness increases from $Eh = 354.001$ J/m² to $Eh = 375.181$ J/m² from the shorter size, $L = 2.218$ nm, to the larger size $L = 11.993$ nm. The asymptotic value is independent of the size of the CNTs, and hence can be viewed as the in-plane stiffness of the structure based on local/classical elastic beam theory. Therefore, the stiffness ratio is calculated by the ratio of the in-plane stiffness of CNTs at every specific length to the asymptotic value. Obvious scale effect on the in-plane stiffness is secured for tubes shorter than 10 nm.

The stiffness ratio versus the length of zigzag CNTs is plotted in Fig. 5.7. It has been shown that the values of in-plane stiffness of zigzag CNTs obtained from

Fig. 5.7 A comparison of in-plane stiffness ratio of zigzag (8, 0) single-walled carbon nanotubes for various lengths based on nonlocal rod and beam theories with the molecular dynamics simulations



molecular mechanics simulations match with the nonlocal beam theory results at nonlocal scale coefficient of $e_0a = 0.11$ nm. The simulations are again compared with the results obtained by Wang et al. [4]. They suggest that the scale coefficient in the nonlocal theory is about 0.7 nm for the application of the nonlocal theory in analysis of carbon nanotubes based on nonlocal rod theory. The in-plane stiffness ratio results obtained from the present nonlocal beam theory (for $e_0a = 0.11$ nm) match exactly with the results obtained from nonlocal rod theory (for $e_0a = 0.7$ nm) and also with that of the molecular mechanics simulations. Hence, it is recommended that the value of e_0a should be 0.11 nm for the application of the nonlocal theory in analysis of CNTs, where CNT is modeled as an elastic beam.

The variation of the in-plane stiffness ratio is clearly observed from the dotted markers, and is qualitatively in agreement with the molecular simulation results. It is shown that the ratio is less than a unit for shorter CNTs, but approaches to a unit at larger sizes, showing a low stiffness of the material for shorter sizes. Overall, the comparison of the ratio between the nonlocal theory and the molecular simulation results first verifies the applicability of the nonlocal elastic beam theory in the estimation of the length-dependent stiffness. Furthermore, the comparison results provide a good estimate of the scale coefficient, in particular for the evaluation of stiffness of CNTs. So far, there is no rigorous study made on estimating the scale coefficient. It is concluded that the scale coefficient should be different for different physical applications. The estimate of the value $e_0a = 0.11$ nm in this section is only recommended for the estimation of the stiffness of CNTs subjected to axial loading, where CNTs are modeled as Bernoulli-Euler type of beam.

The stiffness ratio versus the length of armchair CNTs is plotted in Fig. 5.8. Similarly, the stiffness ratio is calculated by the ratio of the in-plane stiffness of CNTs at every specific length to the asymptotic value. The variation of the ratio is observed again from Fig. 5.8, indicating the lower stiffness for shorter SWCNTs and an asymptotic stiffness for longer CNTs. Again here, the values of in-plane stiffness

Fig. 5.8 A comparison of in-plane stiffness ratio of armchair (8, 8) single-walled carbon nanotubes for various lengths based on nonlocal rod and beam theories with the molecular dynamics simulations

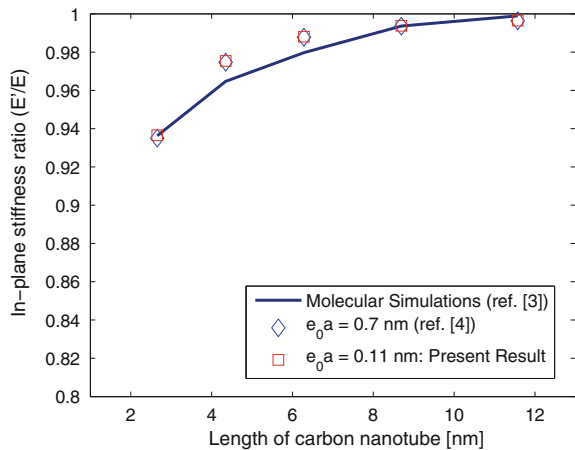
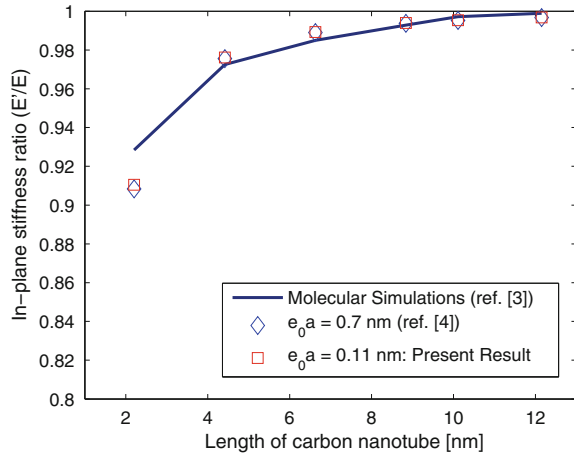


Fig. 5.9 A comparison of in-plane stiffness ratio of chiral (8, 4) single-walled carbon nanotubes for various lengths based on nonlocal rod and beam theories with the molecular dynamics simulations



of armchair CNTs obtained from molecular mechanics simulations match with the nonlocal beam theory results at nonlocal scale coefficient of $e_0a = 0.11$ nm.

The stiffness ratio versus the length of achiral CNTs is plotted in Fig. 5.9. The length measurements of the chiral CNTs are more tedious than those of achiral CNTs since the repeated units display themselves in a helical direction, and not a straight longitudinal direction in achiral tubes. Therefore, the solid line represents the molecular simulations result and is not as smooth as those for achiral tubes because of the coarse length measurement for the chiral CNTs. From the comparison of the stiffness ratio via the nonlocal elasticity and the molecular simulations, the length-dependent stiffness for shorter CNTs is again examined. It has been shown that the values of in-plane stiffness of achiral CNTs obtained from molecular mechanics simulations match with the nonlocal beam theory results at nonlocal scale coefficient of $e_0a = 0.11$ nm. The simulations are again compared with the results obtained by Wang et al. [4]. Hence, it can again be emphasized that the value of e_0a should be 0.11 nm for the application of the nonlocal theory in analysis of achiral CNTs. The present model can also be used for longer length nanotubes.

5.3 Prediction of Nonlocal Scale Parameter: A Molecular Structural Mechanics and Nonlocal Elasticity Model

In this section, Eringen's nonlocal elasticity theory's [9] small-scale parameter is obtained analytically. This theory assumes the stress at a reference point to be a function of the strain field at every point in the body. It allows one to account for the small-scale effect that becomes significant when dealing with micro and nanostructures, especially those effects due to atomic orbital interaction, quantum-mechanical

tunneling, and electron-phonon interaction. Also, a method of identifying the small scaling parameter e_0 in the nonlocal theory is not yet known. Eringen proposed $e_0 = 0.39$ by matching the dispersion curves via nonlocal theory for plane wave and Born-Karman model of lattice dynamics applied at the Brillouin zone boundary ($k = \frac{\pi}{a}$), where a is the distance between atoms and k is the wavenumber in the phonon analysis [10]. On the other hand, Eringen proposed $e_0 = 0.31$ in his study [11] for Rayleigh surface wave via nonlocal continuum mechanics and lattice dynamics. Sudak [12] proposed that $e_0 = 112.7$. Also, no experiments have been conducted to determine the value of e_0 for CNT. Wang and Hu [13] proposed that $e_0 = \frac{1}{\sqrt{12}}$ and used this value in a nonlocal beam model of SWCNT. Zhang et al. [14] estimated that $e_0 \approx 0.82$ by matching the theoretical buckling strain obtained by the nonlocal thin shell model of CNT obtained by Zhang et al. [15] to those from the molecular mechanics simulations given by Sears and Batra [16]. Wang [17] estimated that $e_0 a < 2.0$ nm (which give $e_0 = 14.08$) for an SWCNT wave propagation at frequencies greater than 10 THz.

A review of the above studies naturally force us to assume that the scale parameter (e_0) is actually a function of atomic structure, chirality, and frequency. This problem of identification of the functional relation is what the present section will focus on.

In this section, we present a simple analytical molecular structural mechanics model incorporating the modified Morse potential function [18] to estimate elastic constants and stress–strain relationships of nanotubes under tensile and torsion loadings. The analytical model originated from [19] and was extended to model the torsion behavior of carbon nanotubes. By incorporating the modified Morse potential, it is possible to predict the the stress–strain relationships, hence, the strength and strain to failure of nanotubes. Detailed derivations are presented and the predicted results are demonstrated and discussed with a few computational examples. This study shows that it is possible to develop analytical methodologies based on molecular mechanics and nonlocal elasticity theory to quantify mechanical behavior of a nanotube.

For obtaining these nonlocal constitutive relations according to our formulation, we elaborate them as

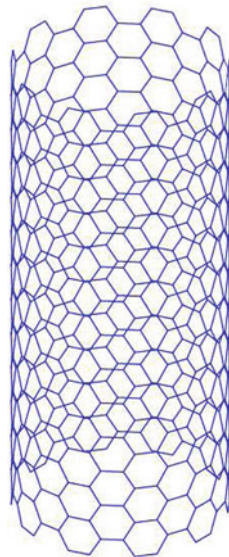
$$\sigma_{xx} - (e_0^{xx} a)^2 \nabla^2 \sigma_{xx} = C_{11} (\varepsilon_{xx} + \nu \varepsilon_{\theta\theta}) \quad (5.34)$$

$$\sigma_{\theta\theta} - (e_0^{\theta\theta} a)^2 \nabla^2 \sigma_{\theta\theta} = C_{11} (\varepsilon_{\theta\theta} + \nu \varepsilon_{xx}) \quad (5.35)$$

$$\tau_{x\theta} - (e_0^{x\theta} a)^2 \nabla^2 \tau_{x\theta} = C_{66} \gamma_{x\theta} \quad (5.36)$$

where $\nabla^2 = \frac{\partial^2}{\partial x^2} + \frac{1}{R^2} \frac{\partial^2}{\partial \theta^2}$, R is the radius of carbon nanotube, $C_{11} = E/(1 - \nu^2)$, $C_{66} = E/(2(1 + \nu))$. Here, we assume different values of nonlocal scale parameters for different directions of the single-walled carbon nanotube. If we want to solve for e_0 using the above three equations, then we need to approximate the gradient term (∇^2). The stress field depends on the displacement field, so that for a harmonic wave field in an SWCNT, the displacement field can be written in complex form as [20]:

Fig. 5.10 A (10, 10) arm-chair type of single-walled carbon nanotubes of length 34.6717 nm, consists of 580 carbon atoms arranged in hexagonal array fashion



$$\mathbf{u}(x, t) = \hat{\mathbf{u}} e^{-jk_1x} e^{-jk_2\theta} e^{-j\omega t} \quad (5.37)$$

Here $\hat{\mathbf{u}}$ is the frequency amplitude of displacement field of SWCNT. k_1 and k_2 are the wavenumbers in axial and circumferential directions, respectively, ω is the angular frequency of the wave motion, and $j = \sqrt{-1}$.

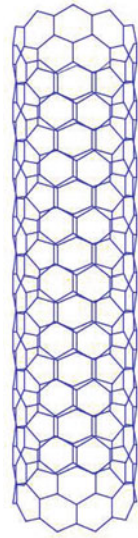
The gradient term with the nonlocal scaling parameter e_0 in nonlocal constitutive relation with $\tau = e_0 a / \ell$ is supposed to capture the small-scale effect on the dynamic mechanical response of the nanotube. In our study we consider $a = 1.42 \text{ \AA}$, and the scaling parameter (e_0) is derived using molecular mechanics and geometry of CNT. In this section, the estimation of e_0 is presented only for armchair (see Fig. 5.10) and zigzag (see Fig. 5.11) type of SWCNTs. However, the procedure is general and can be extended for all types of CNTs.

5.3.1 Armchair SWCNTs

The total potential energy (E_t) of an SWCNT subjected to small strains can be expressed as the sum of energies (U_ρ) and (U_θ) associated with the variation of bond length and bond angle, respectively [21] given by

$$E_t = U_\rho + U_\theta = \sum_i \frac{1}{2} K_\rho (\Delta r_i)^2 + \sum_j \frac{1}{2} K_\theta (\Delta \theta_j)^2 \quad (5.38)$$

Fig. 5.11 A (10, 0) zigzag type of single-walled carbon nanotube of length 34.47 nm, consists of 340 carbon atoms arranged in hexagonal array fashion



where Δr_i is the elongation of i th bond and $\Delta\theta_j$ is the variation of j th bond angle and K_ρ and K_θ are the related force constants respectively.

We consider the *stick-spiral* model [19] and analyze the equilibrium of the local structure of the SWCNT. In this model, an elastic stick with an axial stiffness of K_ρ and an infinite bending stiffness is used to model the force-stretch relationship of the C–C bond, and a spiral spring with a stiffness of K_θ is used to model the twisting moment resulting from an angular distortion of the bond angle [21].

Observe that the total potential energy of SWCNT in Eq. (5.38) is a function of the change in the bond lengths and the bond angles. So we need to express these in terms of strains (axial, circumferential, and shear strain) and then differentiate the total potential energy expression with respect to these strains to get the respective stresses. The stress relations obtained in this way can then be substituted in the assumed nonlocal constitutive relations, which contains the nonlocal scaling parameter (e_0). With this, it would then be possible to determine e_0 , which is the main idea in this section.

An armchair nanotube (n, n) subjected to a longitudinal tensile stress is studied first. Figure 5.12a and b shows an equilibrium configuration of the tube and the associated forces and moments in three chemical bonds a, b, b , and three bond angles α, β, β resulting from a bond elongation Δa and two bond angle variances $\Delta\alpha$ and $\Delta\beta$. The relationship between stress and the bond stretch and bond angle variation can be determined through equilibrium and geometry of the tube structure. Similar to the idea of modeling the molecular structure as an effective *stick-spiral* system by Chang and Gao [19], we use a stick with

$$F(\Delta r) = 2\beta D_e(1 - e^{-\beta\Delta r})e^{-\beta\Delta r} \quad (5.39)$$

Fig. 5.12 Schematic illustration of an armchair carbon nanotube **a** analytical model for tension (F) and **b** analytical model for shear (τ), α and β are the bond angles, a , b and c are the C–C bond lengths

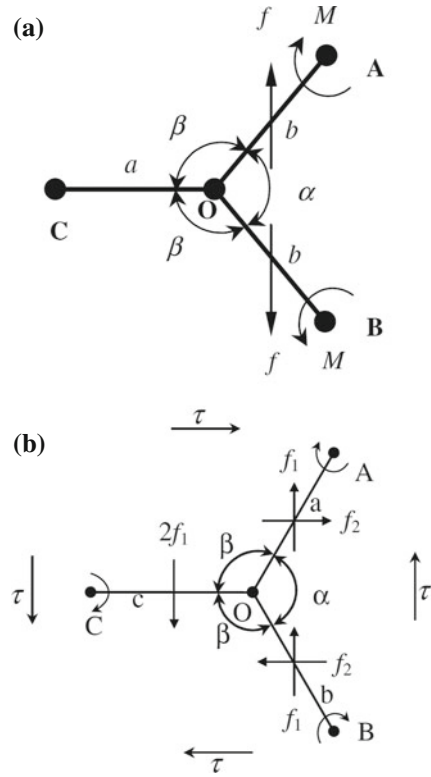


Table 5.1 Parameters of Brenner potential

Parameter	Value	Units
D_e	0.6031	nN-nm
β	26.25	nm ⁻¹
K_θ	1.42	nN-nm/rad ²
K_ρ	0.754	rad ⁴

to model the force-stretch relationship of the CC bond and a spiral spring with

$$M(\Delta\theta) = K_\theta \Delta\theta \left[1 + 3K_\rho (\Delta\theta)^4 \right] \tag{5.40}$$

to model the angle bending moment resulting from an angular variation of bond angle. The stick is assumed to have an infinite bending stiffness. The parameters calibrated by Belytschko et al. [18] with the Brenner potential are given in Table 5.1.

The axial strain (ϵ_{xx}), circumferential strain ($\epsilon_{\theta\theta}$), and shear strain ($\gamma_{x\theta}$) of armchair carbon nanotube can be calculated as [18, 19, 22]:

$$\varepsilon_{xx} = \frac{\Delta b \sin\left(\frac{\alpha}{2}\right) + \frac{b}{2} \cos\left(\frac{\alpha}{2}\right) \Delta\alpha}{b \sin\left(\frac{\alpha}{2}\right)} \quad (5.41)$$

$$\varepsilon_{\theta\theta} = \frac{\Delta b \cos\left(\frac{\alpha}{2}\right) - \frac{b}{2} \sin\left(\frac{\alpha}{2}\right) \Delta\alpha}{a + b \cos\left(\frac{\alpha}{2}\right)} \quad (5.42)$$

$$\gamma_{x\theta} = \frac{a\Delta\beta + \Delta b \sin\left(\frac{\alpha}{2}\right)}{b(1 + \cos\left(\frac{\alpha}{2}\right))} + \frac{2\Delta b \cos\left(\frac{\alpha}{2}\right)}{2b \sin\left(\frac{\alpha}{2}\right)} \quad (5.43)$$

Solving for $\Delta\alpha$ and Δb from Eqs. (5.41) and (5.42) and $\Delta\beta$ from Eq. (5.43) as

$$\Delta b = b \sin^2\left(\frac{\alpha}{2}\right) \varepsilon_{xx} + \left[a + b \cos\left(\frac{\alpha}{2}\right)\right] \cos\left(\frac{\alpha}{2}\right) \varepsilon_{\theta\theta} \quad (5.44)$$

$$\Delta\alpha = 2 \cos\left(\frac{\alpha}{2}\right) \sin\left(\frac{\alpha}{2}\right) \varepsilon_{xx} - \frac{2}{b} \left[a + b \cos\left(\frac{\alpha}{2}\right)\right] \sin\left(\frac{\alpha}{2}\right) \varepsilon_{\theta\theta} \quad (5.45)$$

$$\Delta\beta = \frac{b}{a} \left[1 + \cos\left(\frac{\alpha}{2}\right)\right] \gamma_{x\theta} - 2 \left\{ \frac{b}{a} \sin\left(\frac{\alpha}{2}\right) \varepsilon_{xx} + \frac{\cos\left(\frac{\alpha}{2}\right)}{a \sin\left(\frac{\alpha}{2}\right)} \left[a + b \cos\left(\frac{\alpha}{2}\right)\right] \varepsilon_{\theta\theta} \right\} \quad (5.46)$$

The armchair single-walled carbon nanotube are subjected to tension (see Fig. 5.12a) and torsion (see Fig. 5.12b) loadings, only bond stretching and angle variation terms are significant in the total system potential energy.

For an armchair carbon nanotube, the number of the hexagonal carbon ring units along the circumferential direction is $2n$. Assuming that the number of the hexagonal carbon ring units along the axial direction is N , thus there are $2Nn$ hexagonal carbon ring units, and $4Nn$ bonds b in an armchair carbon nanotube. In addition, there are $4Nn$ angles α and $8Nn$ angles β in an armchair carbon nanotube for a hexagonal carbon ring unit composed of two angles α and four angles β . Based on the above hypotheses, we can find that the length of a (n, n) carbon nanotube is, $L = \sqrt{3}Na$. Hence the total molecular potential energy of an armchair carbon nanotube is

$$U_{TPE} = U_b + U_\alpha + U_\beta \quad (5.47)$$

where

$$U_b = 4Nn \left[\frac{1}{2} K_\rho (\Delta b)^2 \right] \quad (5.48)$$

$$U_\alpha = 4Nn \left[\frac{1}{2} K_\theta (\Delta\alpha)^2 \right] \quad (5.49)$$

$$U_\beta = 8Nn \left[\frac{1}{2} K_\theta (\Delta\beta)^2 \right] \quad (5.50)$$

This implies

$$U_{TPE} = 2NnK_\rho(\Delta b)^2 + 2NnK_\theta(\Delta\alpha)^2 + 4NnK_\theta(\Delta\beta)^2 \quad (5.51)$$

The axial, circumferential, and shear stresses are obtained by differentiating the above total molecular structural potential energy with respect to the corresponding stresses as

$$\sigma_{xx} = 4NnK_\rho\Delta b \left(\frac{\partial \Delta b}{\partial \varepsilon_{xx}} \right) + 4NnK_\theta\Delta\alpha \left(\frac{\partial \Delta\alpha}{\partial \varepsilon_{xx}} \right) + 8NnK_\theta\Delta\beta \left(\frac{\partial \Delta\beta}{\partial \varepsilon_{xx}} \right) \quad (5.52)$$

$$\sigma_{\theta\theta} = 4NnK_\rho\Delta b \left(\frac{\partial \Delta b}{\partial \varepsilon_{\theta\theta}} \right) + 4NnK_\theta\Delta\alpha \left(\frac{\partial \Delta\alpha}{\partial \varepsilon_{\theta\theta}} \right) + 8NnK_\theta\Delta\beta \left(\frac{\partial \Delta\beta}{\partial \varepsilon_{\theta\theta}} \right) \quad (5.53)$$

$$\tau_{x\theta} = 4NnK_\rho\Delta b \left(\frac{\partial \Delta b}{\partial \gamma_{x\theta}} \right) + 4NnK_\theta\Delta\alpha \left(\frac{\partial \Delta\alpha}{\partial \gamma_{x\theta}} \right) + 8NnK_\theta\Delta\beta \left(\frac{\partial \Delta\beta}{\partial \gamma_{x\theta}} \right) \quad (5.54)$$

Simplifying the above-mentioned stresses and writing in matrix form as

$$\{\sigma\} = [U_{am}]\{\varepsilon\} \quad (5.55)$$

Here the size of the matrices $\{\sigma\}$, $[U_{am}]$ and $\{\varepsilon\}$ are 3×1 , 3×3 and 3×1 , respectively. The elements of the matrix $[U_{am}]$ are $(U_{am}^{(ij)})$, $i, j = 1, 2, 3$

$$U_{am}^{(11)} = 4nN \left[K_\rho b^2 \sin^4 \left(\frac{\alpha}{2} \right) + 4K_\theta \cos^2 \left(\frac{\alpha}{2} \right) \sin^2 \left(\frac{\alpha}{2} \right) + 8K_\theta \left(\frac{b}{a} \right)^2 \sin^2 \left(\frac{\alpha}{2} \right) \right] \quad (5.56)$$

$$U_{am}^{(12)} = U_{am}^{(21)} = 4nN \left(a + b \cos \left(\frac{\alpha}{2} \right) \right) \left[K_\rho b \cos \left(\frac{\alpha}{2} \right) \sin^2 \left(\frac{\alpha}{2} \right) - \frac{4}{b} K_\theta \cos \left(\frac{\alpha}{2} \right) \sin^2 \left(\frac{\alpha}{2} \right) + 8K_\theta \frac{b}{a^2} \right] \quad (5.57)$$

$$U_{am}^{(13)} = U_{am}^{(31)} = 4nN \left[4K_\theta \left(\frac{b}{a} \right)^2 \left(1 + \cos \left(\frac{\alpha}{2} \right) \right) \sin \left(\frac{\alpha}{2} \right) \right] \quad (5.58)$$

$$U_{am}^{(22)} = 4nN \left(a + b \cos \left(\frac{\alpha}{2} \right) \right)^2 \left[K_\rho \cos^2 \left(\frac{\alpha}{2} \right) + \frac{4}{b^2} K_\theta \sin^2 \left(\frac{\alpha}{2} \right) + 8K_\theta \frac{b}{a^2} \cos \left(\frac{\alpha}{2} \right) \right] \quad (5.59)$$

$$U_{am}^{(23)} = U_{am}^{(32)} = 4nN \left[4K_\theta \frac{b \cos \left(\frac{\alpha}{2} \right)}{a^2 \sin \left(\frac{\alpha}{2} \right)} \left(1 + \cos \left(\frac{\alpha}{2} \right) \right) \left(a + b \cos \left(\frac{\alpha}{2} \right) \right) \right] \quad (5.60)$$

$$U_{am}^{(33)} = 4nN \left[2K_\theta \left(\frac{b}{a} \right)^2 \left(1 + \cos \left(\frac{\alpha}{2} \right) \right)^2 \right] \quad (5.61)$$

It should be noted that the angle α and β of armchair nanotubes have been found from *ab initio* calculations [23] where $\alpha \approx 2\pi/3$ and $\beta = \pi - \cos^{-1} \left[0.5 \cos \left(\frac{\pi}{2n} \right) \right]$. Based on the assumption of the displacement field (Eq. (5.37)), the nonlocal constitutive relations (Eqs. (5.34)–(5.36)) become

$$\left[1 + (e_0^{xx} a)^2 \left(k_1^2 + \frac{k_2^2}{R^2} \right) \right] \sigma_{xx} = C_{11} (\varepsilon_{xx} + \nu \varepsilon_{\theta\theta}) \quad (5.62)$$

$$\left[1 + (e_0^{\theta\theta} a)^2 \left(k_1^2 + \frac{k_2^2}{R^2} \right) \right] \sigma_{\theta\theta} = C_{11} (\varepsilon_{\theta\theta} + \nu \varepsilon_{xx}) \quad (5.63)$$

$$\left[1 + (e_0^{x\theta} a)^2 \left(k_1^2 + \frac{k_2^2}{R^2} \right) \right] \tau_{x\theta} = C_{66} \gamma_{x\theta} \quad (5.64)$$

Assuming that $k_1 = 2\pi\xi/a$ and $k_2 = 2\pi\eta/a$ (ξ, η are integers) are wavenumbers in axial and circumferential direction, R is the radius of the CNT and a is the C–C bond-length (1.42 Å). Rewriting Eqs. (5.62)–(5.64) in matrix form as

$$[E_0]\{\sigma\} = [\bar{C}]\{\varepsilon\} \quad (5.65)$$

where

$$[E_0] = [I] + \left(k_1^2 + \frac{k_2^2}{R^2} \right) \text{diag} \left[(e_0^{xx} a)^2, (e_0^{\theta\theta} a)^2, (e_0^{x\theta} a)^2 \right] \quad (5.66)$$

$$[\bar{C}] = \begin{bmatrix} C_{11} & \nu C_{11} & 0 \\ \nu C_{11} & C_{11} & 0 \\ 0 & 0 & C_{66} \end{bmatrix} \quad (5.67)$$

where $[I]$ is a 3×3 identity matrix and diag represents diagonal matrix.

Substituting Eq. (5.55) into Eq. (5.65) leads to

$$[E_0][U_{am}]\{\varepsilon\} = [\bar{C}]\{\varepsilon\} \quad (5.68)$$

This is an eigenvalue problem. We need to solve for the nonlocal scaling parameters which are the eigenvalues of the system given by Eq. (5.68). Let us assume $\lambda = e_0 a$, and solving the eigenvalue problem (Eq. (5.68)) as

$$|[\bar{C}] - [E_0][U_{am}]| = |[F_5] - \lambda^2[F_6]| = 0 \quad (5.69)$$

where

$$[F_5] = ([\bar{C}] - [U_{am}]) \quad (5.70)$$

$$[F_6] = \left(k_1^2 + \frac{k_2^2}{R^2} \right) [U_{am}] \quad (5.71)$$

One can get three expressions for λ (eige values), which are e_0^{xx} , $e_0^{\theta\theta}$ and $e_0^{x\theta}$ and are obtained as:

$$e_0^{xx} = \frac{1}{3aS_1} \left(\frac{S_0^{1/3}}{2} - \frac{6S_1S_3 - 2S_2^2}{S_0^{1/3}} - S_2 \right) \quad (5.72)$$

$$e_0^{\theta\theta} = \frac{1}{3aS_1} \left(-\frac{S_0^{1/3}}{4} + \frac{3S_1S_3 - S_2^2}{S_0^{1/3}} - S_2 + \frac{j\sqrt{3}}{2} \left[\frac{S_0^{1/3}}{2} + \frac{6S_1S_3 - 2S_2^2}{S_0^{1/3}} \right] \right) \quad (5.73)$$

$$e_0^{x\theta} = \frac{1}{3aS_1} \left(-\frac{S_0^{1/3}}{4} + \frac{3S_1S_3 - S_2^2}{S_0^{1/3}} - S_2 - \frac{j\sqrt{3}}{2} \left[\frac{S_0^{1/3}}{2} + \frac{6S_1S_3 - 2S_2^2}{S_0^{1/3}} \right] \right) \quad (5.74)$$

where the parameters S_0 , S_1 , S_2 and S_3 are given below.

$$S_0 = 36S_1S_2S_3 - 108S_1^2S_4 - 8S_2^3 + 12\sqrt{3}S_1 \left(4S_1S_3^3 - S_2^2S_3^2 - 18S_1S_2S_3S_4 + 27S_1^2S_4^2 + 4S_2^3S_4 \right)^{1/2} \quad (5.75)$$

$$S_1 = -F_6^{11}F_6^{22}F_6^{33} + F_6^{11}F_6^{23}F_6^{32} + F_6^{21}F_6^{21}F_6^{33} - F_6^{21}F_6^{13}F_6^{32} - F_6^{12}F_6^{23}F_6^{31} + F_6^{13}F_6^{22}F_6^{31} \quad (5.76)$$

$$S_2 = F_5^{22}F_6^{11}F_6^{33} + F_5^{33}F_6^{11}F_6^{22} - F_5^{23}F_6^{11}F_6^{32} - F_5^{32}F_6^{11}F_6^{23} + F_5^{11}F_6^{22}F_6^{33} - F_5^{11}F_6^{23}F_6^{32} - F_5^{12}F_6^{21}F_6^{33} - F_6^{12}F_6^{21}F_6^{33} - F_5^{13}F_6^{21}F_6^{31} + F_5^{32}F_6^{13}F_6^{21} - F_5^{21}F_6^{12}F_6^{33} - F_5^{21}F_6^{32}F_6^{13} + F_5^{12}F_6^{23}F_6^{31} + F_6^{21}F_6^{23}F_6^{31} - F_5^{13}F_6^{22}F_6^{31} - F_5^{22}F_6^{13}F_6^{31} + F_5^{31}F_6^{23}F_6^{31} - F_6^{31}F_6^{13}F_6^{22} \quad (5.77)$$

$$\begin{aligned}
S_3 = & -F_5^{22}F_5^{33}F_6^{11} + F_5^{23}F_5^{32}F_6^{11} - F_5^{11}F_5^{22}F_6^{33} - F_5^{11}F_5^{33}F_6^{22} + F_5^{11}F_5^{23}F_6^{32} \\
& + F_5^{11}F_5^{32}F_6^{23} + F_5^{12}F_5^{33}F_6^{12} - F_5^{12}F_5^{21}F_6^{33} + F_5^{21}F_5^{33}F_6^{12} - F_5^{21}F_5^{33}F_6^{12} \\
& - F_5^{13}F_5^{21}F_6^{32} - F_5^{21}F_5^{32}F_6^{13} - F_5^{12}F_5^{23}F_6^{31} + F_5^{13}F_5^{22}F_5^{31} - F_5^{12}F_5^{31}F_5^{23} \\
& - F_5^{23}F_5^{31}F_6^{12} + F_5^{13}F_5^{31}F_6^{22} + F_5^{22}F_5^{31}F_6^{14}
\end{aligned} \tag{5.78}$$

$$\begin{aligned}
S_4 = & F_5^{12}F_5^{23}F_5^{31} - F_5^{13}F_5^{22}F_5^{31} + F_5^{13}F_5^{21}F_5^{32} + F_5^{11}F_5^{22}F_5^{33} - F_5^{11}F_5^{23}F_5^{32} \\
& - F_5^{12}F_5^{21}F_5^{33}
\end{aligned} \tag{5.79}$$

$$\begin{aligned}
F_5^{11} &= C_{11} - U_{am}^{(11)}, F_5^{12} = \nu C_{11} - U_{am}^{(21)}, F_5^{13} = -U_{am}^{(31)}, \\
F_5^{21} &= \nu C_{11} - U_{am}^{(12)}, F_5^{22} = C_{11} - U_{am}^{(22)}, F_5^{23} = -U_{am}^{(32)}, \\
F_5^{31} &= -U_{am}^{(13)}, F_5^{32} = -U_{am}^{(23)}, F_5^{33} = C_{66} - U_{am}^{(33)}.
\end{aligned} \tag{5.80}$$

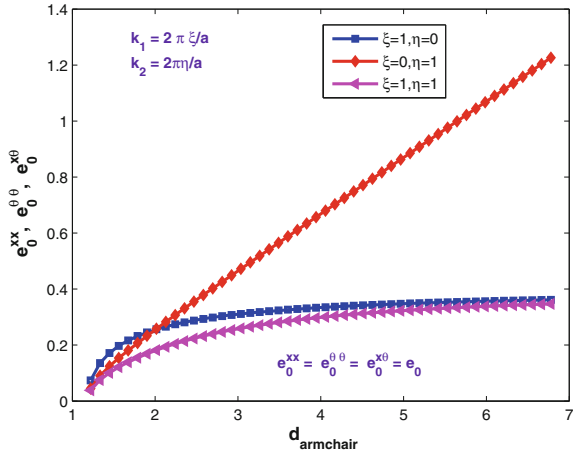
$$\begin{aligned}
F_6^{11} &= \left(k_1^2 + \frac{k_2^2}{R^2}\right)U_{am}^{(11)}, F_6^{12} = \left(k_1^2 + \frac{k_2^2}{R^2}\right)U_{am}^{(12)}, F_6^{13} = \left(k_1^2 + \frac{k_2^2}{R^2}\right)U_{am}^{(13)}, \\
F_6^{21} &= \left(k_1^2 + \frac{k_2^2}{R^2}\right)U_{am}^{(21)}, F_6^{22} = \left(k_1^2 + \frac{k_2^2}{R^2}\right)U_{am}^{(22)}, F_6^{23} = \left(k_1^2 + \frac{k_2^2}{R^2}\right)U_{am}^{(23)}, \\
F_6^{31} &= \left(k_1^2 + \frac{k_2^2}{R^2}\right)U_{am}^{(31)}, F_6^{32} = \left(k_1^2 + \frac{k_2^2}{R^2}\right)U_{am}^{(32)}, F_6^{33} = \left(k_1^2 + \frac{k_2^2}{R^2}\right)U_{am}^{(33)}.
\end{aligned} \tag{5.81}$$

Here S_0 , S_1 , S_2 and S_3 are functions of chirality (n, m) of SWCNT and axial and circumferential wavenumbers $k_1 = 2\pi\xi/a$ and $k_2 = 2\pi\eta/a$, respectively. The variation of the nonlocal scaling parameters for armchair SWCNT are plotted in Fig. 5.13, for various modes of wave propagation.

Let us now discuss the variation of e_0 for an armchair CNT. The variation of the nonlocal scaling parameter with respect to SWCNT diameter (or chirality) for armchair type of SWCNTs is shown in Fig. 5.13, for various modes of wave propagation. For $(\xi = 1, \eta = 0)$ —first axial mode, $(\xi = 0, \eta = 1)$ —first torsional mode, and $(\xi = 1, \eta = 1)$ —first coupled axial—torsional mode. This figure shows that for a given wave branch, the variations in the nonlocal scaling parameters over the CNT diameter are identical (see Fig. 5.13). This implies that $e_0^{xx} = e_0^{\theta\theta} = e_0^{x\theta} = e_0$. From Fig. 5.13, one can observe the following phenomena for armchair type of CNTs.

(i) The value of e_0 is almost constant for $\xi = 1, \eta = 0$, which means that there is only axial mode of wave propagation in SWCNT. The value of e_0 starts from a very small value for smaller diameters of CNT and the value saturates at ≈ 0.3617 .

Fig. 5.13 Nonlocal scaling parameter variation with CNT diameter for armchair carbon nanotube for the case of longitudinal ($\xi = 1, \eta = 0$), torsional ($\xi = 0, \eta = 1$) and coupled ($\xi = 1, \eta = 1$) modes of wave propagation, k_x and k_θ are the axial and circumferential wavenumbers



(ii) The variation in e_0 is linear with the SWCNT diameter for $\xi = 0, \eta = 1$, i.e., when there is only torsional type wave propagation in SWCNT.

(iii) Finally, when there is a coupled axial–torsional mode of wave propagation in the SWCNT, i.e., ($\xi = 1, \eta = 1$), then the value of e_0 approaches to the value of e_0 obtained in the case of purely axial mode of wave propagation for large diameters and purely torsional mode of wave propagation for small diameters of the SWCNT. This value saturates at ≈ 0.3458 .

5.3.2 Zigzag SWCNTs

Consider a zigzag SWCNT ($n, 0$) with the stick-spiral model as shown in Fig. 5.14a and b, subjected to tensile loading and torsional loading, respectively. Now, the axial strain (ε_{xx}), circumferential strain ($\varepsilon_{\theta\theta}$) and shear strain ($\gamma_{x\theta}$) of zigzag CNT can be obtained from the geometrical deformation of the stick-spiral model as [18, 19, 22]:

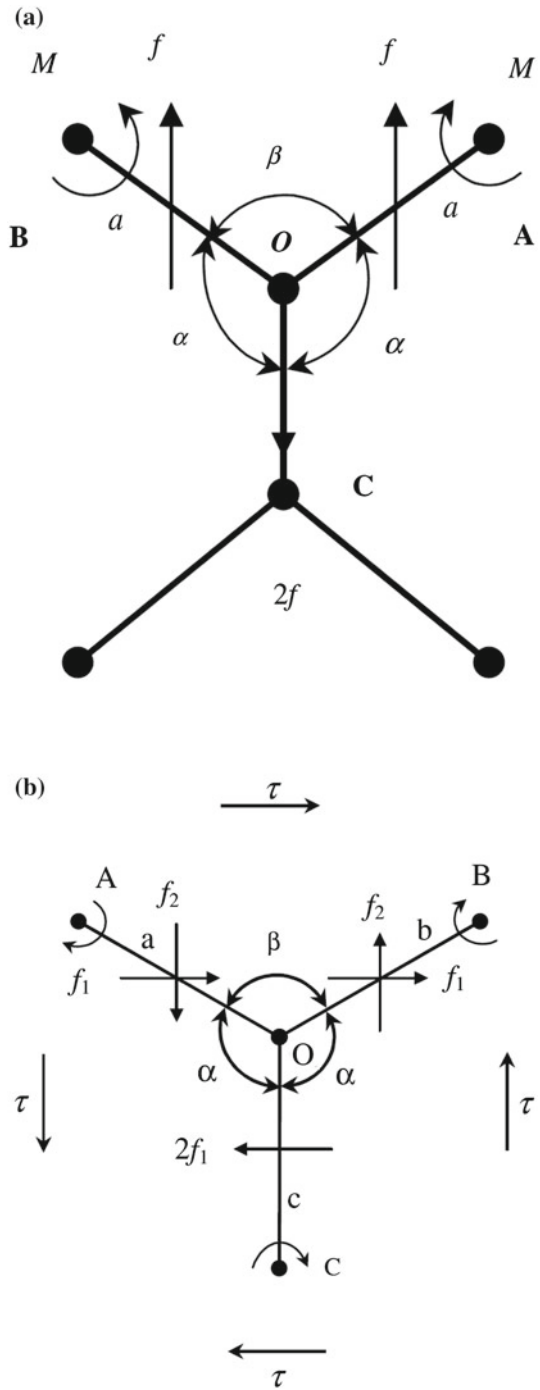
$$\varepsilon_{xx} = \frac{\Delta b + \Delta a \cos(\pi - \alpha) + a \sin(\pi - \alpha) \Delta \alpha}{b + a \cos(\pi - \alpha)} \quad (5.82)$$

$$\varepsilon_{\theta\theta} = \frac{\Delta a \sin(\pi - \alpha) - a \cos(\pi - \alpha) \Delta \alpha}{a \sin(\pi - \alpha)} \quad (5.83)$$

$$\gamma_{x\theta} = \frac{b \Delta \alpha + \Delta a \sin(\pi - \alpha)}{a(1 + \cos(\pi - \alpha))} + \frac{2 \Delta a \cos(\pi - \alpha)}{2a \sin(\pi - \alpha)} \quad (5.84)$$

Solving Eqs. (5.82)–(5.84) for Δa , Δb and $\Delta \alpha$ as

Fig. 5.14 Schematic illustration of a zigzag carbon nanotube **a** analytical model for tension (F) and **b** analytical model for shear (τ), α and β are the bond angles, a , b , and c are the C-C bond lengths



$$\{\Delta\} = [U_{zz1}]\{\varepsilon\} \quad (5.85)$$

where

$$\{\Delta\} = \{\Delta a \quad \Delta b \quad \Delta\alpha\}^T \quad (5.86)$$

$$\{\varepsilon\} = \{\varepsilon_{xx} \quad \varepsilon_{\theta\theta} \quad \gamma_{x\theta}\}^T \quad (5.87)$$

$$U_{zz1}^{(12)} = \frac{ab \sin^2(\pi - \alpha)}{(b + a \cos(\pi - \alpha)) \sin^2(\pi - \alpha) + a(1 + \cos(\pi - \alpha)) \cos^2(\pi - \alpha)} \quad (5.88)$$

$$U_{zz1}^{(13)} = \frac{a^2(1 + \cos(\pi - \alpha)) \cos(\pi - \alpha) \sin(\pi - \alpha)}{(b + a \cos(\pi - \alpha)) \sin^2(\pi - \alpha) + a(1 + \cos(\pi - \alpha)) \cos^2(\pi - \alpha)} \quad (5.89)$$

$$U_{zz1}^{(22)} = \frac{a \sin^2(\pi - \alpha) (a + (a - b) \cos(\pi - \alpha))}{(b + a \cos(\pi - \alpha)) \sin^2(\pi - \alpha) + a(1 + \cos(\pi - \alpha)) \cos^2(\pi - \alpha)} \quad (5.90)$$

$$U_{zz1}^{(23)} = -\frac{a^2 \sin(\pi - \alpha)(1 + \cos(\pi - \alpha))}{(b + a \cos(\pi - \alpha)) \sin^2(\pi - \alpha) + a(1 + \cos(\pi - \alpha)) \cos^2(\pi - \alpha)} \quad (5.91)$$

$$U_{zz1}^{(32)} = -\frac{a(1 + \cos(\pi - \alpha)) \sin(\pi - \alpha)}{(b + a \cos(\pi - \alpha)) \sin^2(\pi - \alpha) + a(1 + \cos(\pi - \alpha)) \cos^2(\pi - \alpha)} \quad (5.92)$$

$$U_{zz1}^{(33)} = \frac{a(1 + \cos(\pi - \alpha)) \sin^2(\pi - \alpha)}{(b + a \cos(\pi - \alpha)) \sin^2(\pi - \alpha) + a(1 + \cos(\pi - \alpha)) \cos^2(\pi - \alpha)} \quad (5.93)$$

$$U_{zz1}^{(21)} = b + a \cos(\pi - \alpha) \quad (5.94)$$

$$U_{zz1}^{(11)} = U_{zz1}^{(31)} = 0 \quad (5.95)$$

The relationship between the bond angles α and β is

$$\Delta\beta = \frac{2 \cos \alpha}{\cos\left(\frac{\beta}{2}\right)} \cos\left(\frac{\pi}{n}\right) \Delta\alpha \quad (5.96)$$

For simplicity we express Eq.(5.96) as

$$\Delta\beta = \Gamma \Delta\alpha \quad (5.97)$$

where

$$\Gamma = \frac{2 \cos \alpha}{\cos\left(\frac{\beta}{2}\right)} \cos\left(\frac{\pi}{n}\right) \quad (5.98)$$

For a zigzag carbon nanotube, the number of the hexagonal carbon ring units along the circumferential direction is n . Assuming that the number of the hexagonal carbon ring units along the axial direction is N , there are Nn hexagonal carbon ring units, and $2Nn$ bonds b in a zigzag carbon nanotube. And there are $2Nn$ angles α and $4Nn$ angles β in a zigzag carbon nanotube for a hexagonal carbon ring unit composed of two angles α and four angles β . Hence, the total molecular potential energy of a zigzag carbon nanotube is

$$U_{TPE} = U_a + U_b + U_\alpha + U_\beta \quad (5.99)$$

where

$$U_a = 2Nn \left[\frac{1}{2} K_\rho (\Delta a)^2 \right] \quad (5.100)$$

$$U_b = 2Nn \left[\frac{1}{2} K_\rho (\Delta b)^2 \right] \quad (5.101)$$

$$U_\alpha = 2Nn \left[\frac{1}{2} K_\theta (\Delta\alpha)^2 \right] \quad (5.102)$$

$$U_\beta = 4Nn \left[\frac{1}{2} K_\theta (\Delta\beta)^2 \right] \quad (5.103)$$

This implies that

$$U_{TPE} = NnK_\rho(\Delta a)^2 + NnK_\rho(\Delta b)^2 + NnK_\theta(\Delta\alpha)^2 + 2NnK_\theta(\Delta\beta)^2 \quad (5.104)$$

Simplifying the above equation as

$$U_{TPE} = NnK_\rho \left[(\Delta a)^2 + (\Delta b)^2 \right] + NnK_\theta \left[1 + 2\Gamma^2 \right] (\Delta\alpha)^2 \quad (5.105)$$

The axial, circumferential, and shear stresses are obtained by differentiating the above total molecular structural potential energy with respect to the corresponding stresses as

$$\sigma_{xx} = \frac{\partial U_{TPE}}{\partial \varepsilon_{xx}} = 2nNK_\rho \left[\Delta a \frac{\partial \Delta a}{\partial \varepsilon_{xx}} + \Delta b \frac{\partial \Delta b}{\partial \varepsilon_{xx}} \right] + 2nNK_\theta (1 + 2\Gamma^2) \Delta \alpha \frac{\partial \Delta \alpha}{\partial \varepsilon_{xx}} \quad (5.106)$$

$$\sigma_{\theta\theta} = \frac{\partial U_{TPE}}{\partial \varepsilon_{\theta\theta}} = 2nNK_\rho \left[\Delta a \frac{\partial \Delta a}{\partial \varepsilon_{\theta\theta}} + \Delta b \frac{\partial \Delta b}{\partial \varepsilon_{\theta\theta}} \right] + 2nNK_\theta (1 + 2\Gamma^2) \Delta \alpha \frac{\partial \Delta \alpha}{\partial \varepsilon_{\theta\theta}} \quad (5.107)$$

$$\tau_{x\theta} = \frac{\partial U_{TPE}}{\partial \gamma_{x\theta}} = 2nNK_\rho \left[\Delta a \frac{\partial \Delta a}{\partial \gamma_{x\theta}} + \Delta b \frac{\partial \Delta b}{\partial \gamma_{x\theta}} \right] + 2nNK_\theta (1 + 2\Gamma^2) \Delta \alpha \frac{\partial \Delta \alpha}{\partial \gamma_{x\theta}} \quad (5.108)$$

Simplifying the above three equations and writing in matrix form as

$$\{\sigma\} = [U_{zz2}]\{\varepsilon\} \quad (5.109)$$

where the elements of the matrix $[U_{zz2}]$ are $(U_{zz2}^{(ij)})$, $i, j = 1, 2, 3$

$$U_{zz2}^{(11)} = 2nNK_\rho (U_{zz1}^{(21)})^2 \quad (5.110)$$

$$U_{zz2}^{(12)} = U_{zz2}^{(21)} = 2nNK_\rho U_{zz1}^{(21)} U_{zz1}^{(22)} \quad (5.111)$$

$$U_{zz2}^{(13)} = U_{zz2}^{(31)} = -2nNK_\rho U_{zz1}^{(21)} U_{zz1}^{(23)} \quad (5.112)$$

$$U_{zz2}^{(22)} = 2nN \left[K_\rho (U_{zz1}^{(11)})^2 + K_\rho (U_{zz1}^{(22)})^2 + K_\theta (1 + 2\Gamma^2) (U_{zz1}^{(31)})^2 \right] \quad (5.113)$$

$$U_{zz2}^{(23)} = U_{zz2}^{(32)} = 2nN \left[K_\rho U_{zz1}^{(11)} U_{zz1}^{(12)} - K_\rho U_{zz1}^{(22)} U_{zz1}^{(23)} + K_\theta (1 + 2\Gamma^2) U_{zz1}^{(31)} U_{zz1}^{(32)} \right] \quad (5.114)$$

$$U_{zz2}^{(33)} = 2nN \left[K_\rho (U_{zz1}^{(12)})^2 + K_\rho (U_{zz1}^{(23)})^2 + K_\theta (1 + 2\Gamma^2) (U_{zz1}^{(32)})^2 \right] \quad (5.115)$$

Substituting Eq. (5.109) into Eq. (5.65) gives

$$[E_0][U_{zz2}]\{\varepsilon\} = [\bar{C}]\{\varepsilon\} \quad (5.116)$$

This is an eigenvalue problem. We need to solve for the nonlocal scaling parameters which are the eigenvalues of the system given by Eq. (5.116). Assuming $\lambda = e_0 a$, and solving the eigenvalue problem (Eq. (5.116)) as

$$|[\bar{C}] - [E_0][U_{zz2}]| = |[F_7] - \lambda^2[F_8]| = 0 \quad (5.117)$$

where

$$[F_7] = ([\bar{C}] - [U_{zz2}]) \quad (5.118)$$

$$[F_8] = \left(k_1^2 + \frac{k_2^2}{R^2} \right) [U_{zz2}] \quad (5.119)$$

One can get three expressions for λ (eigenvalues), corresponding to e_0^{xx} , $e_0^{\theta\theta}$ and $e_0^{x\theta}$ and are obtained as:

$$e_0^{xx} = \frac{1}{3aX_1} \left(\frac{X_0^{1/3}}{2} - \frac{6X_1X_3 - 2X_2^2}{X_0^{1/3}} - X_2 \right) \quad (5.120)$$

$$e_0^{\theta\theta} = \frac{1}{3aX_1} \left(-\frac{X_0^{1/3}}{4} + \frac{3X_1X_3 - X_2^2}{X_0^{1/3}} - X_2 + \frac{j\sqrt{3}}{2} \left[\frac{X_0^{1/3}}{2} + \frac{6X_1X_3 - 2X_2^2}{X_0^{1/3}} \right] \right) \quad (5.121)$$

$$e_0^{x\theta} = \frac{1}{3aX_1} \left(-\frac{X_0^{1/3}}{4} + \frac{3X_1X_3 - X_2^2}{X_0^{1/3}} - X_2 - \frac{j\sqrt{3}}{2} \left[\frac{X_0^{1/3}}{2} + \frac{6X_1X_3 - 2X_2^2}{X_0^{1/3}} \right] \right) \quad (5.122)$$

where the parameters X_0 , X_1 , X_2 and X_3 are given below.

$$X_0 = 36X_1X_2X_3 - 108X_1^2X_4 - 8X_2^3 + 12\sqrt{3}X_1 \left(4X_1X_3^3 - X_2^2X_3^2 - 18X_1X_2X_3X_4 + 27X_1^2X_4^2 + 4X_2^3X_4 \right)^{1/2} \quad (5.123)$$

$$X_1 = -F_8^{11}F_8^{22}F_8^{33} + F_8^{11}F_8^{23}F_8^{32} + F_8^{21}F_8^{21}F_8^{33} - F_8^{21}F_8^{13}F_8^{32} - F_8^{12}F_8^{23}F_8^{31} + F_8^{13}F_8^{22}F_8^{31} \quad (5.124)$$

$$X_2 = F_7^{22}F_8^{11}F_8^{33} + F_7^{33}F_8^{11}F_8^{22} - F_7^{23}F_8^{11}F_8^{32} - F_7^{32}F_8^{11}F_8^{23} + F_7^{11}F_8^{22}F_8^{33} - F_7^{11}F_8^{23}F_8^{32} - F_7^{12}F_8^{21}F_8^{33} - F_8^{12}F_8^{21}F_8^{33} - F_7^{13}F_8^{21}F_8^{31} + F_7^{32}F_8^{13}F_8^{21} - F_7^{21}F_8^{12}F_8^{33} - F_7^{21}F_8^{32}F_8^{13} + F_7^{12}F_8^{23}F_8^{31} + F_8^{21}F_8^{23}F_8^{31} - F_7^{13}F_8^{22}F_8^{31} - F_7^{22}F_8^{13}F_8^{31} + F_7^{31}F_8^{23}F_8^{31} - F_8^{31}F_8^{13}F_8^{22} \quad (5.125)$$

$$X_3 = -F_7^{22}F_7^{33}F_8^{11} + F_7^{23}F_7^{32}F_8^{11} - F_7^{11}F_7^{22}F_8^{33} - F_7^{11}F_7^{33}F_8^{22} + F_7^{11}F_7^{23}F_8^{32} + F_7^{11}F_7^{32}F_8^{23} + F_7^{12}F_7^{33}F_8^{12} - F_7^{12}F_7^{21}F_8^{33} + F_7^{21}F_7^{33}F_8^{12} - F_7^{21}F_7^{33}F_8^{12} - F_7^{13}F_7^{21}F_8^{32} - F_7^{21}F_7^{32}F_8^{13} - F_7^{12}F_7^{23}F_8^{31} + F_7^{13}F_7^{22}F_7^{31} - F_7^{12}F_7^{31}F_7^{23} - F_7^{23}F_7^{31}F_8^{12} + F_7^{13}F_7^{31}F_8^{22} + F_7^{22}F_7^{31}F_8^{14} \quad (5.126)$$

$$X_4 = F_7^{12} F_7^{23} F_7^{31} - F_7^{13} F_7^{22} F_7^{31} + F_7^{13} F_7^{21} F_7^{32} + F_7^{11} F_7^{22} F_7^{33} - F_7^{11} F_7^{23} F_7^{32} - F_7^{12} F_7^{21} F_7^{33} \quad (5.127)$$

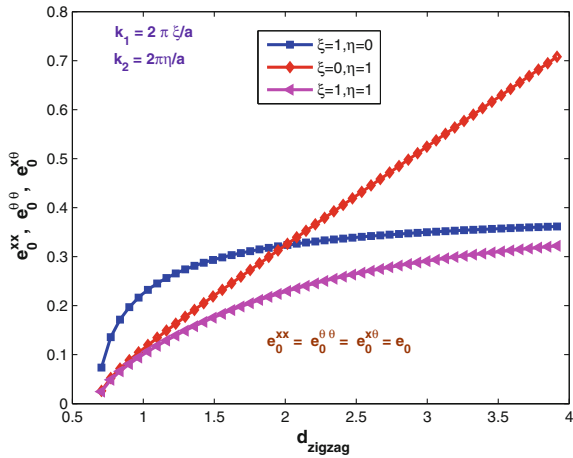
$$\begin{aligned} F_7^{11} &= C_{11} - U_{zz2}^{(11)}, & F_7^{12} &= \nu C_{11} - U_{zz2}^{(21)}, & F_7^{13} &= -U_{zz2}^{(31)}, \\ F_7^{21} &= \nu C_{11} - U_{zz2}^{(12)}, & F_7^{22} &= C_{11} - U_{zz2}^{(22)}, & F_7^{23} &= -U_{zz2}^{(32)}, \\ F_7^{31} &= -U_{zz2}^{(13)}, & F_7^{32} &= -U_{zz2}^{(23)}, & F_7^{33} &= C_{66} - U_{zz2}^{(33)}. \end{aligned} \quad (5.128)$$

$$\begin{aligned} F_8^{11} &= \left(k_1^2 + \frac{k_2^2}{R^2}\right) U_{zz2}^{(11)}, & F_8^{12} &= \left(k_1^2 + \frac{k_2^2}{R^2}\right) U_{zz2}^{(12)}, & F_8^{13} &= \left(k_1^2 + \frac{k_2^2}{R^2}\right) U_{zz2}^{(13)}, \\ F_8^{21} &= \left(k_1^2 + \frac{k_2^2}{R^2}\right) U_{zz2}^{(21)}, & F_8^{22} &= \left(k_1^2 + \frac{k_2^2}{R^2}\right) U_{zz2}^{(22)}, & F_8^{23} &= \left(k_1^2 + \frac{k_2^2}{R^2}\right) U_{zz2}^{(23)}, \\ F_8^{31} &= \left(k_1^2 + \frac{k_2^2}{R^2}\right) U_{zz2}^{(31)}, & F_8^{32} &= \left(k_1^2 + \frac{k_2^2}{R^2}\right) U_{zz2}^{(32)}, & F_8^{33} &= \left(k_1^2 + \frac{k_2^2}{R^2}\right) U_{zz2}^{(33)}. \end{aligned} \quad (5.129)$$

Here, X_0 , X_1 , X_2 and X_3 are functions of chirality (n, m) of SWCNT and axial and circumferential wavenumbers $k_1 = 2\pi\xi/a$ and $k_2 = 2\pi\eta/a$, respectively. The variation of the nonlocal scaling parameters for armchair CNT is plotted in Fig. 5.15, for various modes of wave propagation.

Let us next discuss the variation of e_0 for zigzag CNTs. The variation of the nonlocal scaling parameter with respect to SWCNT diameter (or chirality) for zigzag type of SWCNTs is shown in Fig. 5.15, for various modes of wave propagation. For

Fig. 5.15 Nonlocal scaling parameter variation with CNT diameter for zigzag carbon nanotube for the case of longitudinal ($\xi = 1, \eta = 0$), torsional ($\xi = 0, \eta = 1$), and coupled ($\xi = 1, \eta = 1$) modes of wave propagation, k_1 and k_2 are the axial and circumferential wavenumbers



($\xi = 1, \eta = 0$)—first axial mode, ($\xi = 0, \eta = 1$)—first torsional mode, and ($\xi = 1, \eta = 1$)—first coupled axial—torsional mode. This figure shows that for a given wave branch, the variations in the nonlocal scaling parameters over the CNT diameter are identical (see Fig. 5.15). This implies that $e_0^{xx} = e_0^{\theta\theta} = e_0^{x\theta} = e_0$.

From Fig. 5.15, one can observe the following phenomena for zigzag type of CNTs.

(i) The value of e_0 is almost constant for $\xi = 1, \eta = 0$, which means that there is only axial mode of wave propagation in SWCNT. The value of e_0 starts from a very small value for smaller diameters of CNT and the value saturates at ≈ 0.3617 .

(ii) The variation in e_0 is linear with the SWCNT diameter for $\xi = 0, \eta = 1$, i.e., when there is only torsional type wave propagation in SWCNT.

(iii) Finally, when there is a coupled axial—torsional mode of wave propagation in the SWCNT, i.e., ($\xi = 1, \eta = 1$), then the value of e_0 approaches to the value of e_0 obtained in the case of purely axial mode of wave propagation for large diameters and purely torsional mode of wave propagation for small diameters of the SWCNT. This value saturates at ≈ 0.3221 .

The study performed in this and in the previous section helps one to use these obtained values of e_0 based on the CNT diameter (or chirality), to analyze the wave dispersion behavior in CNTs via nonlocal continuum mechanics.

5.3.3 Chiral SWCNTs

The previous sections dealt with the estimation of nonlocal scale parameter for different types of nanotubes separately. In this section, we formulate a generalized model to estimate the nonlocal scale parameter for all types of nanotubes just by changing the indices m and n . The present model results are also compared with the previous sections' results.

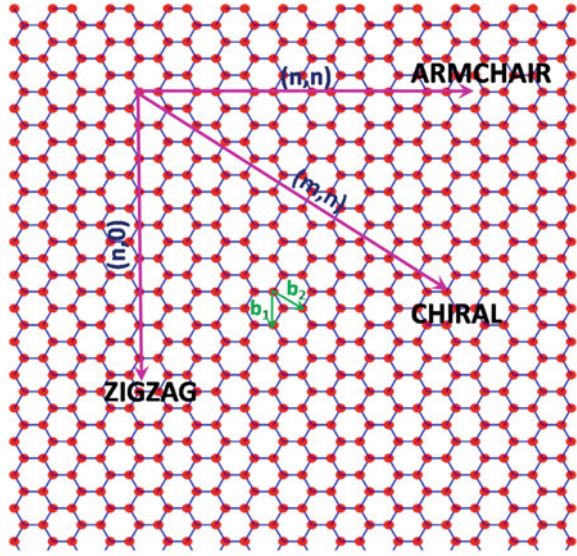
An SWCNT can be viewed as a hexagonal graphene sheet (see Fig. 5.16) rolled into a seamless tube. The graphene sheet can be rolled up with various different angles, which is quantified as a chiral angle. The CNTs obtained from graphene sheet are one atom thick. The fundamental structure of SWCNTs can be classified into three categories as zigzag, armchair, and chiral (see Figs. 5.16 and 5.17) in terms of the chiral vector \mathbf{C} and chiral angle ϕ . The chiral vector is defined as

$$\mathbf{C} = n\mathbf{b}_1 + m\mathbf{b}_2. \quad (5.130)$$

where \mathbf{b}_1 and \mathbf{b}_2 are unit vectors, the integer pairs (n, m) are the chiral parameters, which describe the structure of the CNTs. The chiral angle is given by

$$\phi = \cos^{-1} \left(\frac{2n + m}{2\sqrt{n^2 + nm + n^2}} \right). \quad (5.131)$$

Fig. 5.16 Schematic diagram of graphene sheet of $40 \text{ \AA} \times 40 \text{ \AA}$, consisting of 390 carbon atoms arranged in hexagonal array showing base vectors (\mathbf{b}_1 , \mathbf{b}_2). The schematic figure also shows the three possible types of chirality to form the respective single-walled carbon nanotubes



The symmetry groups of CNTs are denoted as zigzag CNT $(n, 0)$ ($\phi = 0$) and the armchair CNT (n, n) ($\phi = \pi/6$). If $n \neq m$, the CNT is called chiral CNT (n, m) ($0 < \phi < \pi/6$). The modulus of the chiral vector represents the circumference of the tube from which the tube diameter is obtained as

$$d_{nt} = \frac{\sqrt{3}a}{\pi} \sqrt{n^2 + nm + m^2}, \quad (5.132)$$

where a is the C–C bond length (for SWCNT, $a \approx 0.142 \text{ nm}$). The modulus of the translation vector (\mathbf{T}) represents the length of the tube (see Fig. 5.17).

The total potential energy (E_t) of a single-walled carbon nanotube (SWCNT), see Fig. 5.18, subjected to small strains can be expressed as the sum of energies (U_ρ) and (U_θ) associated with the variation of bond length and bond angle, respectively (see Chang et al. [21]). In this discussion we will consider the SWCNT subjected to axial force only, so that the other energies associated with inversion, torsion, van der Waals, electrostatic interactions etc., are negligible. Now, the total potential energy can be written as

$$E_t = U_\rho + U_\theta = \sum_i \frac{1}{2} K_\rho (\Delta r_i)^2 + \sum_j \frac{1}{2} K_\theta (\Delta \theta_j)^2 \quad (5.133)$$

where Δr_i is the elongation of i th bond and $\Delta \theta_j$ is the variation of j th bond angle and K_ρ and K_θ are the related force constants respectively.

As before, we consider the 'stick-spiral' model proposed by Chang and Gao [19] and analyze the equilibrium situation of the local structure of the SWCNT. The

Fig. 5.17 Schematic diagram of graphene sheet ($30 \text{ \AA} \times 30 \text{ \AA}$) consisting of 390 carbon atoms (generated in MatLab), showing chiral vector (**C**), chiral angle (ϕ), translation vector (**T**) and base vectors $\mathbf{b}_1 = \mathbf{a}$, $\mathbf{b}_2 = \mathbf{b}$ to define an SWCNT and n, m are the chiral parameters

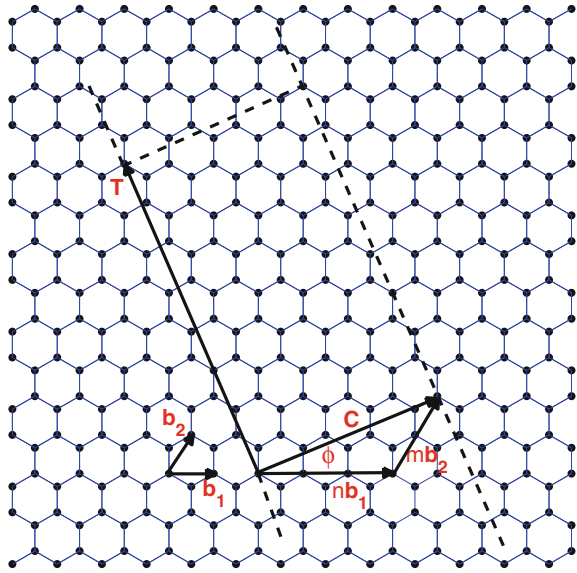
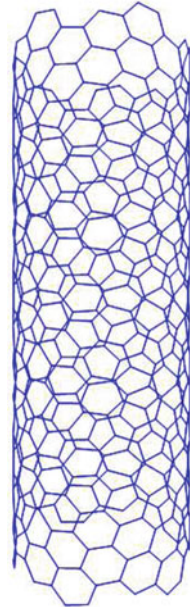


Fig. 5.18 A schematic of (10,5) chiral type of single-walled carbon nanotube of length 34.563 nm, consists of 450 carbon atoms arranged in hexagonal fashion



procedure to determine the nonlocal parameter is similar to what was presented in the previous section.

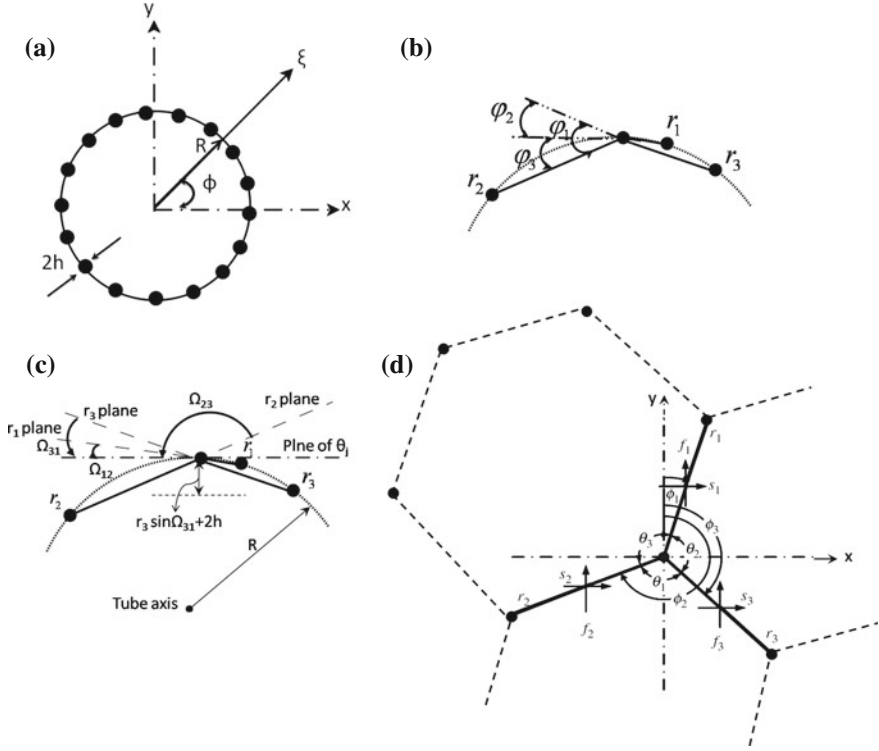


Fig. 5.19 **a** Thickness coordinate and cross section of the single-walled carbon nanotube, **b** top view of the local structure shows the torsion angles, **c** out-of plane rotations in the top view of the local structure, and **d** schematic diagram show the nearest neighbor interaction (side view)

Let us consider an SWCNT with chirality (n, m) subjected to an axial force F , an internal pressure P_0 , and an axial torque M_T . First, we express the strains in terms of the change in the bond lengths (Δr_i) and the bond angles $\Delta\theta_j$ and chirality (n, m) of the SWCNT. These equations are solved for the (Δr_i) as a function of the three in-plane strains. These axial, circumferential, and shear strains are calculated by Chang et al. [21] with the geometric description of the lattice structure in the SWCNT (see Fig. 5.19) as follows:

$$\varepsilon_{xx} = \alpha \Delta [(2n + m)r_1 \cos \phi_1 - (n - m)r_2 \cos \phi_2 - (2m + n)r_3 \cos \phi_3] \quad (5.134)$$

$$\varepsilon_{\theta\theta} = \beta \Delta [mr_1 \sin \phi_1 - (n + m)r_2 \sin \phi_2 + nr_3 \sin \phi_3] \quad (5.135)$$

$$\gamma_{x\theta} = \alpha \Delta [(2n + m)r_1 \sin \phi_1 - (n - m)r_2 \sin \phi_2 - (2m + n)r_3 \sin \phi_3] \quad (5.136)$$

$$\nu = -\varepsilon_{\theta\theta} / \varepsilon_{xx} \quad (5.137)$$

where (n, m) is the chirality of SWCNT and ϕ_1, ϕ_2, ϕ_3 are the chiral angles defined in Fig. 5.19d and ν is the Poisson's ratio, and

$$\alpha = \frac{1}{3a\sqrt{n^2 + nm + m^2}}, \quad (5.138)$$

$$\beta = \frac{1}{\sqrt{3}a\sqrt{n^2 + nm + m^2}} \quad (5.139)$$

The chiral angles (ϕ_i) for an undeformed (n, m) SWCNT are given as

$$\phi_1 = \cos^{-1} \left(\frac{2n + m}{2\sqrt{n^2 + nm + m^2}} \right) \quad (5.140)$$

$$\phi_2 = \frac{4\pi}{3} + \phi_1 \quad (5.141)$$

$$\phi_3 = \frac{2\pi}{3} + \phi_1 \quad (5.142)$$

Equations (5.134)–(5.136) are rewritten in matrix form as

$$\{\varepsilon\} = [T_1]\{\Delta\phi\} + [T_2]\{\Delta r\} \quad (5.143)$$

where

$$\{\varepsilon\} = \{\varepsilon_{xx} \ \varepsilon_{\theta\theta} \ \gamma_{x\theta}\}^T \quad (5.144)$$

$$\{\Delta\phi\} = \{\Delta\phi_1 \ \Delta\phi_2 \ \Delta\phi_3\}^T \quad (5.145)$$

$$\{\Delta r\} = \{\Delta r_1 \ \Delta r_2 \ \Delta r_3\}^T \quad (5.146)$$

$$[T_1] = \begin{bmatrix} -\alpha(2n + m)r_1 \sin \phi_1 & \alpha(n - m)r_2 \sin \phi_2 & \alpha(2m + n)r_3 \sin \phi_3 \\ \beta m r_1 \cos \phi_1 & -\beta(n + m)r_2 \cos \phi_2 & \beta n r_3 \cos \phi_3 \\ \alpha(2n + m)r_1 \cos \phi_1 & -\alpha(n - m)r_2 \cos \phi_2 & -\alpha(2m + n)r_3 \cos \phi_3 \end{bmatrix} \quad (5.147)$$

$$[T_2] = \begin{bmatrix} \alpha(2n + m) \cos \phi_1 & -\alpha(n - m) \cos \phi_2 & -\alpha(2m + n) \cos \phi_3 \\ \beta m \sin \phi_1 & -\beta(n + m) \sin \phi_2 & \beta n \sin \phi_3 \\ \alpha(2n + m) \sin \phi_1 & -\alpha(n - m) \sin \phi_2 & -\alpha(2m + n) \sin \phi_3 \end{bmatrix} \quad (5.148)$$

It should be noted that $\Delta\phi_i$ is dependent on Δr_i geometrically. This geometrical relationship is determined by using the equilibrium of lattice due to the force field as expressed below.

We considered the (n, m) SWCNT as subjected to an axial force F , an internal pressure P_0 , and an axial torque M_T . The relationship between the external and internal forces is

$$F = (n + m)f_1 + mf_2 \quad (5.149)$$

$$P_0 = -\frac{1}{TR}[(n - m)s_1 + (2n + m)s_2] \quad (5.150)$$

$$M_T = [(n + m)s_1 + ms_2] \times R \quad (5.151)$$

where R is tube radius, T is the magnitude of the translation vector \mathbf{T} and f_i , and s_i are forces on the C–C bonds along axial and circumferential directions (see Fig. 5.19), respectively. Now the equilibrium of the local structure of the SWCNT needs

$$f_1 + f_2 + f_3 = 0 \quad (5.152)$$

$$s_1 + s_2 + s_3 = 0 \quad (5.153)$$

The force equilibrium and the moment equilibrium of the three C–C bonds can be obtained as, respectively,

$$f_i \cos \phi_i + s_i \sin \phi_i = K_\rho \Delta r_i, \quad i = 1, 2, 3 \quad (5.154)$$

$$\frac{r_i}{2} (f_i \sin \phi_i - s_i \cos \phi_i) = K_\theta (\Delta \theta_j \cos \Omega_{ij} + \Delta \theta_k \cos \Omega_{ik}), \quad (5.155)$$

$$i, j, k = 1, 2, 3; i \neq j \neq k$$

where Ω_{ij} (can be seen clearly from the top view of the CNT) is the twist angle between the plane through r_i and parallel to the nanotube axis and the plane of θ_j (tangential to the tube) as shown in Fig. 5.19d. This twist angle Ω_{ij} (Fig. 5.19c) is obtained as

$$\cos \Omega_{ij} = (\cos \phi_i \sin \phi_k \cos \phi_j - \sin \phi_i \cos \phi_k) / \sin \theta_j, \quad i, j, k = 1, 2, 3; i \neq j \neq k \quad (5.156)$$

The chiral angles ϕ_i , the out-of plane torsion angles φ_i (see Fig. 5.19b), and the bond angles θ_i are defined in Fig. 5.19d. The geometry of the lattice of an SWCNT satisfies the following relation:

$$\cos \theta_i = \sin \phi_j \sin \phi_k \cos \varphi_i + \cos \phi_j \cos \phi_k, \quad i, j, k = 1, 2, 3; i \neq j \neq k \quad (5.157)$$

From Eqs. (5.156) and (5.157), the change in bond angle ($\Delta \theta_i$) is obtained as

$$\Delta \theta_i = -(\Delta \phi_j \cos \Omega_{ji} + \Delta \phi_k \cos \Omega_{ki}), \quad i, j, k = 1, 2, 3; i \neq j \neq k \quad (5.158)$$

Substituting Eq. (5.158) into Eq. (5.155), the moment equilibrium equation becomes

$$\frac{r_i}{2K_\theta} (f_i \sin \phi_i - s_i \cos \phi_i) = A_{ii} \Delta \phi_i + A_{ij} \Delta \phi_j + A_{ik} \Delta \phi_k, \quad (5.159)$$

$$i, j, k = 1, 2, 3; i \neq j \neq k$$

where

$$A_{ii} = -(\cos^2 \Omega_{ij} + \cos^2 \Omega_{ik}) \quad (5.160)$$

$$A_{ij} = -\cos \Omega_{ik} \cos \Omega_{jk} \quad (5.161)$$

$$A_{ik} = -\cos \Omega_{ij} \cos \Omega_{kj} \quad (5.162)$$

The cylindrical structure of an SWCNT is characterized by its chiral vector, the dislocation between the head and the tail of the chiral vector, which should be zero under stress-free condition. This feature actually gives compatible equations for a stress-free SWCNT as follows:

$$\Delta[mr_1 \cos \phi_1 - (n + m)r_2 \cos \phi_2 + nr_3 \cos \phi_3] = 0 \quad (5.163)$$

Now, we introduce two series of internal forces p_i and q_i through Eqs. (5.154) and (5.155), which are expressed as

$$f_i \cos \phi_i + s_i \sin \phi_i = K_\rho \Delta r_i \equiv p_i, \quad i = 1, 2, 3 \quad (5.164)$$

$$\frac{r_i}{2K_\theta} (f_i \sin \phi_i - s_i \cos \phi_i) = A_{ii} \Delta \phi_i + A_{ij} \Delta \phi_j + A_{ik} \Delta \phi_k \equiv \frac{r_i q_i}{2K_\theta},$$

$$i, j, k = 1, 2, 3; \quad i \neq j \neq k \quad (5.165)$$

This implies that the internal bond forces f_i and s_i are given as

$$f_i = p_i \cos \phi_i + q_i \sin \phi_i, \quad i = 1, 2, 3 \quad (5.166)$$

$$s_i = p_i \sin \phi_i - q_i \cos \phi_i, \quad i = 1, 2, 3 \quad (5.167)$$

Substituting Eqs. (5.166) and (5.167) into Eqs. (5.149)–(5.153), we get

$$F = (n + m)(p_1 \cos \phi_1 + q_1 \sin \phi_1) + m(p_2 \cos \phi_2 + q_2 \sin \phi_2) \quad (5.168)$$

$$P_0 = -\frac{1}{TR} [(n - m)(p_1 \sin \phi_1 - q_1 \cos \phi_1) + (2n + m)(p_2 \sin \phi_2 - q_2 \cos \phi_2)] \quad (5.169)$$

$$M_T = R[(n + m)(p_1 \sin \phi_1 - q_1 \cos \phi_1) + m(p_2 \sin \phi_2 - q_2 \cos \phi_2)] \quad (5.170)$$

$$(p_1 \sin \phi_1 + p_2 \sin \phi_2 + p_3 \sin \phi_3) + (q_1 \cos \phi_1 + q_2 \cos \phi_2 + q_3 \cos \phi_3) = 0 \quad (5.171)$$

$$(p_1 \cos \phi_1 + p_2 \cos \phi_2 + p_3 \cos \phi_3) - (q_1 \sin \phi_1 + q_2 \sin \phi_2 + q_3 \sin \phi_3) = 0 \quad (5.172)$$

Once two of the external forces (P_0 and M_T) are known, p_i can be expressed as a function of q_i . We assume that the SWCNT is subjected only to an axial force F , thus we have internal pressure $P_0 = 0$ and axial torque $M_T = 0$. Using this information in Eqs. (6.27), (5.170) and (5.172) and rearranging in p_i and q_i , one has

$$\begin{Bmatrix} p_1 \\ p_2 \\ p_3 \end{Bmatrix} = \begin{bmatrix} \cot \phi_1 & 0 & 0 \\ 0 & \cot \phi_2 & 0 \\ 0 & 0 & \cot \phi_3 \end{bmatrix} \begin{Bmatrix} q_1 \\ q_2 \\ q_3 \end{Bmatrix} = [M]\{q\} \quad (5.173)$$

Combining Eqs. (5.163), (5.165)–(5.167) and (5.171) and eliminating f_i , s_i , and p_i , we get

$$B_1 \Delta \phi_1 + B_2 \Delta \phi_2 + B_3 \Delta \phi_3 + C_1 \mu a \frac{q_1}{2K_\theta} + C_2 \mu a \frac{q_2}{2K_\theta} + C_3 \mu a \frac{q_3}{2K_\theta} = 0 \quad (5.174)$$

$$D_1 q_1 + D_2 q_2 + D_3 q_3 = 0 \quad (5.175)$$

where

$$\{B_1, B_2, B_3\} = \{m \sin \phi_1, -(n+m) \sin \phi_2, n \sin \phi_3\} \quad (5.176)$$

$$\{C_1, C_2, C_3\} = -2 \{m \cos \phi_1, -(n+m) \cos \phi_2, n \cos \phi_3\} [M] \quad (5.177)$$

$$\{D_1, D_2, D_3\} = \{\cos \phi_1, \cos \phi_2, \cos \phi_3\} [M] + \{\sin \phi_1, \sin \phi_2, \sin \phi_3\} \quad (5.178)$$

Using Eq. (5.164), we have

$$K_\rho \{\Delta r\} = \{p\} \quad (5.179)$$

Substituting Eq. (5.173) into Eq. (5.179) we get

$$K_\rho \{\Delta r\} = [M]\{q\} \quad (5.180)$$

For undeformed SWCNT, $r_1 = r_2 = r_3 = a$ and from Eqs. (5.164), (5.174) and (5.175), we obtain the following relations:

$$\Delta \phi_i = \psi_i \Delta \phi_3 \quad (5.181)$$

$$q_i = 2\mu K_\rho a Q_i \Delta \phi_3 \quad (5.182)$$

where

$$\psi_i = \frac{x_i + y_i \mu}{x_3 + y_3 \mu} \quad (5.183)$$

$$Q_i = \frac{z_i}{x_3 + y_3 \mu} \quad (5.184)$$

$$\mu = \frac{K_\theta}{K_\rho a^2} \quad (5.185)$$

$$x_i = (A_{ik} D_i + A_{jk} D_j + A_{kk} D_k) B_j - (A_{ij} D_i + A_{jj} D_j + A_{kj} D_k) B_k \quad (5.186)$$

$$y_i = (A_{ik} D_i + A_{jk} D_j + A_{kk} D_k) (A_{ij} C_i + A_{jj} C_j + A_{kj} C_k) - (A_{ij} D_i + A_{jj} D_j + A_{kj} D_k) (A_{ik} C_i + A_{jk} C_j + A_{kk} C_k) \quad (5.187)$$

$$z_i = [A_{ik} (A_{kj} D_k + A_{jj} D_j) - A_{ij} (A_{kk} D_k + A_{jk} D_j)] B_i + [A_{ii} (A_{kk} D_k + A_{jk} D_j) - A_{ik} (A_{ki} D_k + A_{ji} D_j)] B_j + [A_{ij} (A_{ki} D_k + A_{ji} D_j) - A_{ii} (A_{kj} D_k + A_{jj} D_j)] B_k \quad (5.188)$$

with i, j, k are counted in clockwise direction. Using Eq. (5.182) in Eq. (5.180), we get

$$\{\Delta r\} = 2\mu a [M] \{Q\} \Delta \phi_3 \quad (5.189)$$

where

$$\{Q\} = \{Q_1 \ Q_2 \ Q_3\}^T \quad (5.190)$$

and the parameters Q_i and μ are defined in Eq. (5.184) and Eq. (5.185), respectively. From Eq. (5.189), one can have three expressions for $\Delta \phi_3$ as given below:

$$\Delta \phi_3 = \frac{\Delta r_1}{2\mu a Q_1 \cot \phi_1} \quad (5.191)$$

$$\Delta \phi_3 = \frac{\Delta r_2}{2\mu a Q_2 \cot \phi_2} \quad (5.192)$$

$$\Delta \phi_3 = \frac{\Delta r_3}{2\mu a Q_3 \cot \phi_3} \quad (5.193)$$

Combining Eqs. (5.181), (5.182), and Eqs. (5.191)–(5.193) we obtain the nontrivial solution in $\Delta \phi_j$ as

$$\Delta \phi_1 = \psi_1 \Delta \phi_3 = \psi_1 \frac{\Delta r_1}{2\mu a Q_1 \cot \phi_1} \quad (5.194)$$

$$\Delta \phi_2 = \psi_2 \Delta \phi_3 = \psi_2 \frac{\Delta r_2}{2\mu a Q_2 \cot \phi_2} \quad (5.195)$$

Substituting Eqs. (5.194) and (5.195) into Eq. (5.145), we get

$$\{\Delta\phi\} = \begin{bmatrix} \frac{\Delta\psi_1}{2\mu a Q_1 \cot\phi_1} & 0 & 0 \\ 0 & \frac{\Delta\psi_2}{2\mu a Q_2 \cot\phi_2} & 0 \\ 0 & 0 & \frac{\Delta\psi_3}{2\mu a Q_3 \cot\phi_3} \end{bmatrix} \begin{Bmatrix} \Delta r_1 \\ \Delta r_2 \\ \Delta r_3 \end{Bmatrix} = [\bar{\Psi}]\{\Delta r\} \quad (5.196)$$

Eliminating $\Delta\phi$ in Eq. (5.143) with the use of Eq. (5.196) and solving for $\{\Delta r\}$ as

$$\{\Delta r\} = ([T_1][\bar{\Psi}] + [T_2])^{-1} \{\varepsilon\} = [J_1]\{\varepsilon\} \quad (5.197)$$

Having determined the relationship between the bond elongation $\{\Delta r\}$ and continuum strain $\{\varepsilon\}$ from the original Eq. (5.143), the other variables $\Delta\theta_j$ are expressed also in terms of $\{\varepsilon\}$ as follows. The expression for the change in bond angles $\Delta\theta_j$ is given in Eq. (5.158) and is written in matrix form as

$$\{\Delta\theta\} = \begin{bmatrix} 0 & -\cos\Omega_{21} & -\cos\Omega_{31} \\ -\cos\Omega_{12} & 0 & -\cos\Omega_{32} \\ -\cos\Omega_{13} & -\cos\Omega_{23} & 0 \end{bmatrix} \{\Delta\phi\} = [T_3]\{\Delta\phi\} \quad (5.198)$$

Substituting Eqs. (5.196) and (5.197) into Eq. (5.198), we finally get

$$\{\Delta\theta\} = [T_3][\bar{\Psi}]\{\Delta r\} = [T_3][\bar{\Psi}]([T_1][\bar{\Psi}] + [T_2])^{-1} \{\varepsilon\} = [J_2]\{\varepsilon\} \quad (5.199)$$

To this end, Eqs. (5.197) and (5.199) map the atomistic variables ($\{\Delta r\}$ and $\{\Delta\theta\}$) into continuum variable $\{\varepsilon\}$.

From Eqs. (5.197) and (5.199), we have closed-form expressions for the change in bond lengths and the change in bond angles as functions of the three in-plane strains. Notice that these expressions are given for the assumed model of lattice structure as shown in Fig. 5.19d. Substituting these two expressions for strain in the atomic potential energy (see Eq. (5.133)) and differentiating with respect to the three in-plane strains, we get the respective stresses (axial, circumferential, and shear) as

$$\sigma_{xx} = \frac{1}{V} \int_{\mathcal{E}} \frac{\partial E_t}{\partial \varepsilon_{xx}} \equiv \sum_i K_\rho \Delta r_i \frac{\partial \Delta r_i}{\partial \varepsilon_{xx}} + \sum_j K_\theta \Delta \theta_j \frac{\partial \Delta \theta_j}{\partial \varepsilon_{xx}} \quad (5.200)$$

$$\sigma_{\theta\theta} = \frac{1}{V} \int_{\mathcal{E}} \frac{\partial E_t}{\partial \varepsilon_{\theta\theta}} \equiv \sum_i K_\rho \Delta r_i \frac{\partial \Delta r_i}{\partial \varepsilon_{\theta\theta}} + \sum_j K_\theta \Delta \theta_j \frac{\partial \Delta \theta_j}{\partial \varepsilon_{\theta\theta}} \quad (5.201)$$

$$\tau_{x\theta} = \frac{1}{V} \int_{\mathcal{E}} \frac{\partial E_t}{\partial \gamma_{x\theta}} \equiv \sum_i K_\rho \Delta r_i \frac{\partial \Delta r_i}{\partial \gamma_{x\theta}} + \sum_j K_\theta \Delta \theta_j \frac{\partial \Delta \theta_j}{\partial \gamma_{x\theta}} \quad (5.202)$$

where $i, j = 1, 2, 3$; \mathcal{E} is the domain of interest, V is the volume occupied by the 3-atom system, which can be obtained as $V = A(r_3 \sin\Omega_{31} + 2h)$, where A is the area of the three atom system, $2h$ is the thickness of the SWCNT sheet (approximately the s-orbital diameter of carbon atom), r_3 is the bond length of the third atom, and Ω_{31} is the twist angle as shown in Fig. 5.19c. The area of the three atom system is

obtained as

$$A = \frac{1}{2} \begin{vmatrix} r_1 \sin \phi_1 & -r_2 \sin \phi_2 & r_3 \sin \phi_3 \\ r_1 \cos \phi_1 & r_2 \cos \phi_2 & -r_3 \cos \phi_3 \\ 1 & 1 & 1 \end{vmatrix} \quad (5.203)$$

Equations (5.200)–(5.202) can be rewritten as

$$\sigma_{xx} = K_\rho \{\Delta r\}^T \frac{\partial}{\partial \varepsilon_{xx}} \{\Delta r\} + K_\theta \{\Delta \theta\}^T \frac{\partial}{\partial \varepsilon_{xx}} \{\Delta \theta\} \quad (5.204)$$

$$\sigma_{\theta\theta} = K_\rho \{\Delta r\}^T \frac{\partial}{\partial \varepsilon_{\theta\theta}} \{\Delta r\} + K_\theta \{\Delta \theta\}^T \frac{\partial}{\partial \varepsilon_{\theta\theta}} \{\Delta \theta\} \quad (5.205)$$

$$\tau_{x\theta} = K_\rho \{\Delta r\}^T \frac{\partial}{\partial \gamma_{x\theta}} \{\Delta r\} + K_\theta \{\Delta \theta\}^T \frac{\partial}{\partial \gamma_{x\theta}} \{\Delta \theta\} \quad (5.206)$$

Substituting Eqs. (5.197) and (5.199) into Eqs. (5.204)–(5.206), we get

$$\sigma_{xx} = K_\rho \{\varepsilon\}^T [J_1]^T [J_1] \frac{\partial \{\varepsilon\}}{\partial \varepsilon_{xx}} + K_\theta \{\varepsilon\}^T [J_2]^T [J_2] \frac{\partial \{\varepsilon\}}{\partial \varepsilon_{xx}} \quad (5.207)$$

$$\sigma_{\theta\theta} = K_\rho \{\varepsilon\}^T [J_1]^T [J_1] \frac{\partial \{\varepsilon\}}{\partial \varepsilon_{\theta\theta}} + K_\theta \{\varepsilon\}^T [J_2]^T [J_2] \frac{\partial \{\varepsilon\}}{\partial \varepsilon_{\theta\theta}} \quad (5.208)$$

$$\tau_{x\theta} = K_\rho \{\varepsilon\}^T [J_1]^T [J_1] \frac{\partial \{\varepsilon\}}{\partial \varepsilon_{x\theta}} + K_\theta \{\varepsilon\}^T [J_2]^T [J_2] \frac{\partial \{\varepsilon\}}{\partial \varepsilon_{x\theta}} \quad (5.209)$$

Introducing $[F_1] = [J_1]^T [J_1]$ and $[F_2] = [J_2]^T [J_2]$, and then simplifying Eqs. (5.207)–(5.209), we get the continuum equivalent constitutive relation for the lattice as

$$\{\sigma\} = [J_3] \{\varepsilon\} \quad (5.210)$$

where

$$\{\sigma\} = \{\sigma_{xx} \ \sigma_{\theta\theta} \ \sigma_{x\theta}\}^T \quad (5.211)$$

$$[J_3] = \begin{bmatrix} K_\rho F_1^{11} + K_\theta F_2^{11} & K_\rho F_1^{21} + K_\theta F_2^{21} & K_\rho F_1^{31} + K_\theta F_2^{31} \\ K_\rho F_1^{12} + K_\theta F_2^{12} & K_\rho F_1^{22} + K_\theta F_2^{22} & K_\rho F_1^{32} + K_\theta F_2^{32} \\ K_\rho F_1^{13} + K_\theta F_2^{13} & K_\rho F_1^{23} + K_\theta F_2^{23} & K_\rho F_1^{33} + K_\theta F_2^{33} \end{bmatrix} \quad (5.212)$$

Equation (5.210) is the stress–strain relation obtained from the molecular mechanics model of an (n, m) chiral SWCNT. Our next step is to find the nonlocal scaling parameter (e_0) which appears in the nonlocal constitutive equations. This nonlocal model corresponds to the entire SWCNT as one-dimensional tubular structure. For obtaining these nonlocal constitutive relations according to our formulation, we elaborate nonlocal constitutive relations as

$$\sigma_{xx} - (e_0^{xx} a)^2 \nabla^2 \sigma_{xx} = C_{11}(\varepsilon_{xx} + \nu \varepsilon_{\theta\theta}) \quad (5.213)$$

$$\sigma_{\theta\theta} - (e_0^{\theta\theta} a)^2 \nabla^2 \sigma_{\theta\theta} = C_{11}(\varepsilon_{\theta\theta} + \nu \varepsilon_{xx}) \quad (5.214)$$

$$\tau_{x\theta} - (e_0^{x\theta} a)^2 \nabla^2 \tau_{x\theta} = C_{66} \gamma_{x\theta} \quad (5.215)$$

where $\nabla^2 = \frac{\partial^2}{\partial x^2} + \frac{1}{R^2} \frac{\partial^2}{\partial \theta^2}$ (R = radius of the CNT), $C_{11} = \frac{E}{(1-\nu^2)}$, $C_{66} = \frac{E}{2(1+\nu)}$. If we want to solve for e_0 using the above three equations, we need to approximate the gradient term (∇^2). For a harmonic wave field in an SWCNT, the displacement field can be written in complex form as (because stress field depends on the displacement field), see Gopalakrishnan et al. [20]:

$$\mathbf{u}(x, t) = \hat{\mathbf{u}} e^{-jk_x x} e^{-jk_\theta \theta} e^{-j\omega t} \quad (5.216)$$

where $\hat{\mathbf{u}}$ is the frequency amplitudes displacement of SWCNT, k_x and k_θ are the wavenumbers in axial and circumferential directions, respectively, ω is the angular frequency of the wave motion, and $j = \sqrt{-1}$.

By substituting the displacement field (Eq. (5.216)) in the nonlocal constitutive relations (Eqs. (5.213)–(5.215)), we get

$$\left[1 + (e_0^{xx} a)^2 \left(k_x^2 + \frac{k_\theta^2}{R^2} \right) \right] \sigma_{xx} = C_{11}(\varepsilon_{xx} + \nu \varepsilon_{\theta\theta}) \quad (5.217)$$

$$\left[1 + (e_0^{\theta\theta} a)^2 \left(k_x^2 + \frac{k_\theta^2}{R^2} \right) \right] \sigma_{\theta\theta} = C_{11}(\varepsilon_{\theta\theta} + \nu \varepsilon_{xx}) \quad (5.218)$$

$$\left[1 + (e_0^{x\theta} a)^2 \left(k_x^2 + \frac{k_\theta^2}{R^2} \right) \right] \tau_{x\theta} = C_{66} \gamma_{x\theta} \quad (5.219)$$

where $k_x = \frac{2\pi\xi}{a}$ and $k_\theta = \frac{2\pi\eta}{a}$ (here ξ and η are integers) are wavenumbers in axial and circumferential directions, respectively, R is the radius of the CNT, and a is the carbon–carbon bond-length (~ 1.42 Å) in SWCNT. Equations (5.217)–(5.219) are rewritten in matrix form as

$$[E_0]\{\sigma\} = [\bar{C}]\{\varepsilon\} \quad (5.220)$$

where

$$[E_0] = [I] + \left(k_x^2 + \frac{k_\theta^2}{R^2} \right) \begin{bmatrix} (e_0^{xx} a)^2 & 0 & 0 \\ 0 & (e_0^{\theta\theta} a)^2 & 0 \\ 0 & 0 & (e_0^{x\theta} a)^2 \end{bmatrix} \quad (5.221)$$

$$[\bar{C}] = \begin{bmatrix} C_{11} & \nu C_{11} & 0 \\ \nu C_{11} & C_{11} & 0 \\ 0 & 0 & C_{66} \end{bmatrix} \quad (5.222)$$

where $[I]$ is a 3×3 identity matrix. Equation (5.220) describes the assumed nonlocal constitutive relations. Substitution of Eq. (5.210) into Eq. (5.220) leads to

$$[E_0][J_3]\{\varepsilon\} = [\bar{C}]\{\varepsilon\} \quad (5.223)$$

This is an eigenvalue problem. We need to solve for the nonlocal scaling parameters which are the eigenvalues of the system in Eq. (5.223). Introducing $\lambda = (e_0 a)^2$ in (Eq. (5.223)), one has

$$Det \left[[\bar{C}] - [E_0][J_3] \right] = Det \left[[F_3] - \lambda[F_4] \right] = 0 \quad (5.224)$$

where

$$[F_3] = [\bar{C}] - [J_3] \quad (5.225)$$

$$[F_4] = \left(k_x^2 + \frac{k_\theta^2}{R^2} \right) [J_3] \quad (5.226)$$

There are three eigenvalues for the system in Eq. (5.223), which can be written as

$$\sqrt{\lambda_1} = e_0^{xx} = \pm \frac{1}{3aL_1} \left(\frac{L_0^{1/3}}{2} - \frac{6L_1L_3 - 2L_2^2}{L_0^{1/3}} - L_2 \right) \quad (5.227)$$

$$\sqrt{\lambda_2} = e_0^{\theta\theta} = \pm \frac{1}{3aL_1} \left(-\frac{L_0^{1/3}}{4} + \frac{3L_1L_3 - L_2^2}{L_0^{1/3}} - L_2 + \frac{j\sqrt{3}}{2} \left[\frac{L_0^{1/3}}{2} + \frac{6L_1L_3 - 2L_2^2}{L_0^{1/3}} \right] \right) \quad (5.228)$$

$$\sqrt{\lambda_3} = e_0^{x\theta} = \pm \frac{1}{3aL_1} \left(-\frac{L_0^{1/3}}{4} + \frac{3L_1L_3 - L_2^2}{L_0^{1/3}} - L_2 - \frac{j\sqrt{3}}{2} \left[\frac{L_0^{1/3}}{2} + \frac{6L_1L_3 - 2L_2^2}{L_0^{1/3}} \right] \right) \quad (5.229)$$

where the parameters L_0 , L_1 , L_2 and L_3 are given below.

$$L_0 = 36L_1L_2L_3 - 108L_1^2L_4 - 8L_2^3 + 12\sqrt{3}L_1 \left(4L_1L_3^3 - L_2^2L_3^2 - 18L_1L_2L_3L_4 + 27L_1^2L_4^2 + 4L_2^3L_4 \right)^{1/2} \quad (5.230)$$

$$L_1 = -F_4^{11}F_4^{22}F_4^{33} + F_4^{11}F_4^{23}F_4^{32} + F_4^{21}F_4^{21}F_4^{33} - F_4^{21}F_4^{13}F_4^{32} - F_4^{12}F_4^{23}F_4^{31} + F_4^{13}F_4^{22}F_4^{31} \quad (5.231)$$

$$\begin{aligned}
L_2 = & F_3^{22} F_4^{11} F_4^{33} + F_3^{33} F_4^{11} F_4^{22} - F_3^{23} F_4^{11} F_4^{32} - F_3^{32} F_4^{11} F_4^{23} + F_3^{11} F_4^{22} F_4^{33} \\
& - F_3^{11} F_4^{23} F_4^{32} - F_3^{12} F_4^{21} F_4^{33} - F_4^{12} F_4^{21} F_4^{33} - F_3^{13} F_4^{21} F_4^{31} + F_3^{32} F_4^{13} F_4^{21} \\
& - F_3^{21} F_4^{12} F_4^{33} - F_3^{21} F_4^{32} F_4^{13} + F_3^{12} F_4^{23} F_4^{31} + F_4^{21} F_4^{23} F_4^{31} - F_3^{13} F_4^{22} F_4^{31} \\
& - F_3^{22} F_4^{13} F_4^{31} + F_3^{31} F_4^{23} F_4^{31} - F_4^{31} F_4^{13} F_4^{22}
\end{aligned} \tag{5.232}$$

$$\begin{aligned}
L_3 = & -F_3^{22} F_3^{33} F_4^{11} + F_3^{23} F_3^{32} F_4^{11} - F_3^{11} F_3^{22} F_4^{33} - F_3^{11} F_3^{33} F_4^{22} + F_3^{11} F_3^{23} F_4^{32} \\
& + F_3^{11} F_3^{32} F_4^{23} + F_3^{12} F_3^{33} F_4^{12} - F_3^{12} F_3^{21} F_4^{33} + F_3^{21} F_3^{33} F_4^{12} - F_3^{21} F_3^{33} F_4^{12} \\
& - F_3^{13} F_3^{21} F_4^{32} - F_3^{21} F_3^{32} F_4^{13} - F_3^{12} F_3^{23} F_4^{31} + F_3^{13} F_3^{22} F_3^{31} - F_3^{12} F_3^{31} F_3^{23} \\
& - F_3^{23} F_3^{31} F_4^{12} + F_3^{13} F_3^{31} F_4^{22} + F_3^{22} F_3^{31} F_4^{14}
\end{aligned} \tag{5.233}$$

$$\begin{aligned}
L_4 = & F_3^{12} F_3^{23} F_3^{31} - F_3^{13} F_3^{22} F_3^{31} + F_3^{13} F_3^{21} F_3^{32} + F_3^{11} F_3^{22} F_3^{33} - F_3^{11} F_3^{23} F_3^{32} \\
& - F_3^{12} F_3^{21} F_3^{33}
\end{aligned} \tag{5.234}$$

$$\begin{aligned}
F_3^{11} = & C_{11} - K_\rho F_1^{11} - K_\theta F_2^{11}, \quad F_3^{12} = \nu C_{11} - K_\rho F_1^{21} - K_\theta F_2^{21}, \\
F_3^{13} = & -K_\rho F_1^{31} - K_\theta F_2^{31}, \quad F_3^{21} = \nu C_{11} - K_\rho F_1^{12} - K_\theta F_2^{12}, \\
F_3^{22} = & C_{11} - K_\rho F_1^{22} - K_\theta F_2^{22}, \quad F_3^{23} = -K_\rho F_1^{32} - K_\theta F_2^{32}, \\
F_3^{31} = & -K_\rho F_1^{13} - K_\theta F_2^{13}, \quad F_3^{32} = -K_\rho F_1^{23} - K_\theta F_2^{23}, \\
F_3^{33} = & C_{66} - K_\rho F_1^{33} - K_\theta F_2^{33}.
\end{aligned} \tag{5.235}$$

$$\begin{aligned}
F_4^{11} = & \left(k_x^2 + \frac{k_\theta^2}{R^2} \right) J_3^{11}, \quad F_4^{12} = \left(k_x^2 + \frac{k_\theta^2}{R^2} \right) J_3^{12}, \quad F_4^{13} = \left(k_x^2 + \frac{k_\theta^2}{R^2} \right) J_3^{13}, \\
F_4^{21} = & \left(k_x^2 + \frac{k_\theta^2}{R^2} \right) J_3^{21}, \quad F_4^{22} = \left(k_x^2 + \frac{k_\theta^2}{R^2} \right) J_3^{22}, \quad F_4^{23} = \left(k_x^2 + \frac{k_\theta^2}{R^2} \right) J_3^{23}, \\
F_4^{31} = & \left(k_x^2 + \frac{k_\theta^2}{R^2} \right) J_3^{31}, \quad F_4^{32} = \left(k_x^2 + \frac{k_\theta^2}{R^2} \right) J_3^{32}, \quad F_4^{33} = \left(k_x^2 + \frac{k_\theta^2}{R^2} \right) J_3^{33}.
\end{aligned} \tag{5.236}$$

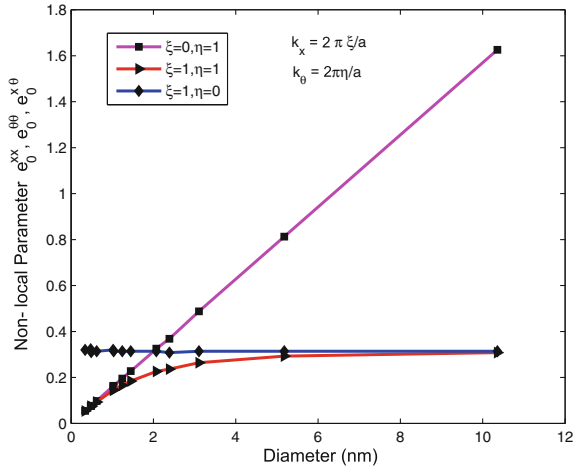
Here L_0 , L_1 , L_2 and L_3 are functions of chirality (n, m) of SWCNT, and the axial and circumferential wavenumbers are $k_x = 2\pi\xi/a$ and $k_\theta = 2\pi\eta/a$, respectively.

The values used for the constants of SWCNTs are given in Table 5.2. The variation of the nonlocal scaling parameters for chiral types of SWCNTs are shown in Fig. 5.20, for various modes of wave propagation. For $(\xi = 1, \eta = 0)$ —first axial mode, $(\xi = 0, \eta = 1)$ —first torsional mode, and $(\xi = 1, \eta = 1)$ —first coupled axial—

Table 5.2 Properties of SWCNTs used for the analysis

Property	Value	Units
Young's modulus (E)	1.05	TPa
Density (ρ)	2700	kg/m ³
Thickness (t)	0.34	nm
Axial stiffness of bond (K_ρ)	742	nN/nm
Angular stiffness of bond (K_θ)	1.42	nN nm

Fig. 5.20 Nonlocal parameter variation for chiral type of SWCNTs ($n \neq m$) for the case of longitudinal ($\xi = 1, \eta = 0$), torsional ($\xi = 0, \eta = 1$), and coupled ($\xi = 1, \eta = 1$) modes of wave propagation, k_x and k_θ are the axial and circumferential wavenumbers respectively. The result also shows that the nonlocal scale parameters are all equal, i.e., $e_0^{xx} = e_0^{x\theta} = e_0^{\theta\theta} = e_0$



torsional mode. The figure shows that for a given wave branch, the variation in the nonlocal scaling parameters over tube diameter are identical (see Fig. 5.20). This implies that $e_0^{xx} = e_0^{\theta\theta} = e_0^{x\theta} = e_0$.

From Fig. 5.20, one can observe the following phenomena for chiral type of SWCNTs.

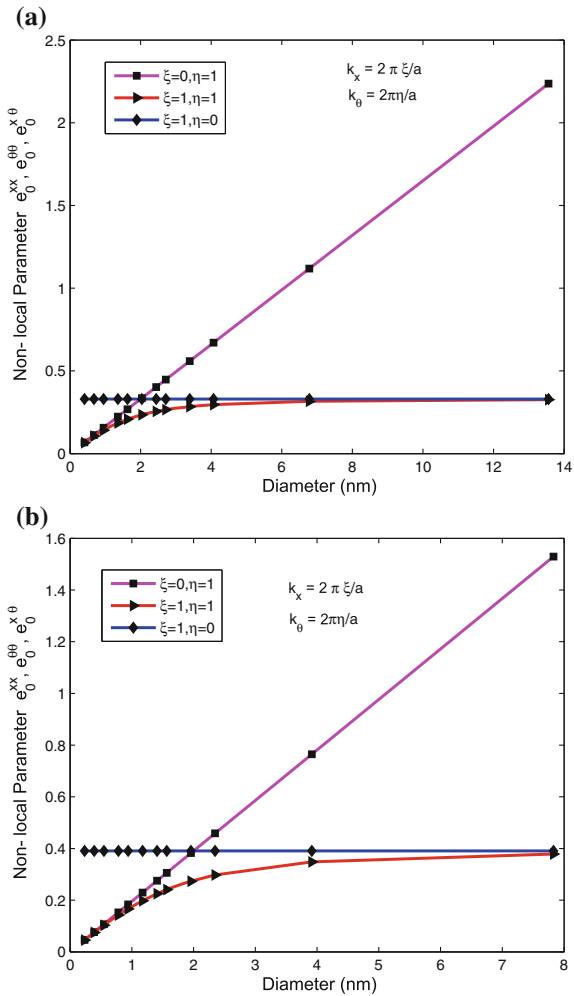
(i) The value of e_0 is almost constant for $\xi = 1, \eta = 0$, which means that there is only axial mode of wave propagation in SWCNT. The value of $e_0 = e_0^{xx} = e_0^{\theta\theta} = e_0^{x\theta} \approx 0.314 - 0.318$ for chiral type of SWCNTs.

(ii) The variation in e_0 is linear with the SWCNT diameter for $\xi = 0, \eta = 1$, i.e., when there is only torsional type wave propagation in SWCNT.

(iii) Finally, when there is a coupled axial-torsional mode of wave propagation in the SWCNT, i.e., ($\xi = 1, \eta = 1$), then the value of e_0 approaches to the value of e_0 obtained in the case of purely axial mode of wave propagation for large diameters and purely torsional mode of wave propagation for small diameters of the SWCNT.

These observations are similar to those observed for the armchair and zigzag type of SWCNTs given in the previous section and these results are also given in [24].

Fig. 5.21 Nonlocal parameter variation for **a** armchair and **b** Zigzag type of SWCNTs for the case of longitudinal or axial ($\xi = 1, \eta = 0$), torsional ($\xi = 0, \eta = 1$) and coupled ($\xi = 1, \eta = 1$) modes of wave propagation, k_x and k_θ are the axial and circumferential wavenumbers respectively. The result also shows that the nonlocal scale parameters are all equal, i.e., $e_0^{xx} = e_0^{x\theta} = e_0^{\theta\theta} = e_0$



Next, if we use $n = m$ and $m = 0$ in the present formulation, the variation e_0 can be obtained for armchair and zigzag type of SWCNTs, respectively. The variation of the nonlocal scaling parameter with respect to SWCNT diameter (or chirality) for armchair and zigzag type of SWCNTs are shown in Fig. 5.21a and b, respectively, for various modes of wave propagation. The value of e_0 is almost constant for $\xi = 1, \eta = 0$, which means that there is only axial mode of wave propagation in SWCNT. The value of $e_0 = e_0^{xx} = e_0^{\theta\theta} = e_0^{x\theta} \approx 0.3298$ for armchair, 0.3906 for zigzag type of SWCNTs. The other observations are similar to that of chiral type of SWCNTs.

The values of e_0 for armchair and zigzag type of SWCNTs obtained from the present formulation exactly match with those obtained by Narendar et al. [24]. Hence,

the present formulation is a generalized one and can be easily applicable for all the three types of SWCNTs.

5.4 Summary

This chapter investigated the application of nonlocal elastic beam theory in estimation of length-dependent stiffness of SWCNTs. The results from the nonlocal elasticity demonstrate that the length-dependent stiffness is small for shorter SWCNTs and is large (maximum unity) for longer SWCNTs. It has been found that the clamped SWCNT has very low stiffness and that of the cantilever SWCNT has very high stiffness for a given nonlocal scaling parameter.

An approximate estimation of nonlocal scale parameter is also presented in this chapter. The length-dependent stiffness is revealed from the nonlocal elasticity and verified through molecular simulation results. From the analysis, the value of the scale coefficient (e_0a) in the nonlocal theory was recommended to be about 0.11 nm for the application of the nonlocal elasticity theory in the analysis of single-walled carbon nanotubes, where CNTs are modeled as beam. The modeling and analyses of nanostructures, based on flexural displacement, require an accurate estimate of nonlocal scaling parameter. Such attempt was made in this chapter. The presented value of e_0a can provide useful guidance for the study and design of the next generation of nano devices that make use of the properties of single-walled carbon nanotubes.

Next, an expression for the nonlocal scaling parameter are derived as a function of the geometric properties of the SWCNTs. Following that a self-consistent method is developed for the linearization of the ultrasonic wave propagation in SWCNTs. The obtained nonlocal parameters show that the general three-dimensional elastic problem leads to a single nonlocal scaling parameter (e_0). This value of e_0 is almost constant irrespective of the chirality of the CNT for an axial mode of wave propagation and shows a linear variation with the chirality for torsional mode of wave propagation. When there is a coupled axial–torsional mode of wave propagation the value of e_0 approaches to the value of e_0 obtained in the case of purely axial mode of wave propagation for large diameters, and a purely torsional mode of wave propagation for small diameter of the SWCNTs.

At the end, an expression for the nonlocal scaling parameter was derived as a function of the geometric properties of the chiral type ($n \neq m$) of SWCNTs. Even in this case, the obtained nonlocal parameters show that the general three-dimensional elastic problem again leads to a single nonlocal scaling parameter (e_0). This value of e_0 is almost constant irrespective of the chirality of the CNT for an axial mode of wave propagation and shows a linear variation with the chirality for torsional mode of wave propagation. When there is a coupled axial–torsional mode of wave propagation, the value of e_0 approaches to the value of e_0 obtained in the case of purely axial mode of wave propagation for large diameters, and a purely torsional mode of wave propagation for small diameter of the SWCNTs. The values of e_0 for armchair and zigzag type of SWCNTs obtained from the present formulation exactly

match with those available in the literature. This formulation was a generalized one and can be easily applicable for all the three types of SWCNTs to calculate the nonlocal scale parameter.

Because of the future promising exploration in nanotechnology, focus is being put in the miniaturization of mechanical and electromechanical devices. Attention is sought toward the development of nanodevices and nanomachines. The length scales associated with such nanostructures are that to apply any classical continuum techniques, we need to consider small length scales such as the lattice spacing between individual atoms, surface properties, grain size, etc. This makes a physically consistent classical continuum model formulation very challenging. So, the next chapter presents the application of nonlocal elasticity theories such as stress gradient, second- and fourth-order strain gradient theories to analyze the wave dispersion behavior of one-dimensional nanostructures such as nanorods. Here, the subject of interest is only the dispersion of the axial and torsional waves in nanorods. Next, the spectral finite element (SFE) formulation of nanorods is also presented. The exact frequency-dependent shape functions and the dynamic stiffness matrix for the nanorod are obtained as functions of non-classical scale parameter.

References

1. A. Krishnan, E. Dujardin, T. Ebbesen, P.N. Yianilos, M.M.J. Treacy, Young's modulus of single-walled nanotubes. *Phys. Rev. B* **58**, 14043 (1998)
2. J.P. Salvetat, G.A. Briggs, J.M. Bonard, R.R. Basca, A.J. Kulik, T. Stockli, N.A. Burnham, L. Forro, Elastic and shear moduli of single-walled carbon nanotube ropes. *Phys. Rev. Lett.* **82**, 944 (1999)
3. Q. Wang, Length dependent mechanical properties of carbon nanotubes. *J. Comput. Theor. Nanosci.* **5**, 1454–1457 (2008)
4. Q. Wang, Q.K. Han, B.C. Wen, Estimate of material property of carbon nanotubes via nonlocal elasticity. *Adv. Theor. Appl. Mech.* **1**, 1–10 (2008)
5. S. Narendar, S. Gopalakrishnan, Theoretical estimation of length dependent in-plane stiffness of single walled carbon nanotubes using the nonlocal elasticity theory. *J. Comput. Theor. Nanosci.* **7**(11), 2349–2354 (2010)
6. T.L.L. Brown, B.E. Bursten, H.E. Lemay, *Chemistry: The Central Science*, 8th edn. (Prentice-Hall, Upper Saddle River, 1999)
7. N. Hamada, S. Savada, A. Oshiyama, New one-dimensional conductors: graphitic microtubes. *Phys. Rev. B* **68**, 1579 (1992)
8. M. Meo, M. Rossi, A molecular-mechanics based finite element model for strength prediction of single wall carbon nanotubes. *Mater. Sci. Eng. A* **454–455**, 170–177 (2007)
9. A.C. Eringen, Non-local polar elastic continua. *Int. J. Eng. Sci.* **10**, 1–10 (1972)
10. A.C. Eringen, Linear theory of non-local elasticity and dispersion of plane waves. *Int. J. Eng. Sci.* **10**, 425–435 (1972)
11. A.C. Eringen, On differential equations of nonlocal elasticity and solutions of screw dislocation and surface waves. *J. Appl. Phys.* **54**, 4703 (1983)
12. L.J. Sudak, Column buckling of multiwalled carbon nanotubes using nonlocal continuum mechanics. *J. Appl. Phys.* **94**(11), 7281 (2003)
13. L.F. Wang, H.Y. Hu, Flexural wave propagation in single-walled carbon nanotubes. *Phys. Rev. Lett.* **71**, 195412 (2005)

14. Y.Q. Zhang, G.R. Liu, X.Y. Xie, Free transverse vibration of double-walled carbon nanotubes using a theory of nonlocal elasticity. *Physical Review B* **71**, 195404 (2005)
15. Y.Q. Zhang, G.R. Liu, J.S. Wang, Small-scale effects on buckling of multiwalled carbon nanotubes under axial compression. *Phys. Rev. Lett.* **70**, 205430 (2004)
16. A. Sears, R.C. Batra, Macroscopic properties of carbon nanotubes from molecular mechanics simulations. *Phys. Rev. B* **69**, 235406 (2004)
17. Q. Wang, Wave propagation in carbon nanotubes via nonlocal continuum mechanics. *J. Appl. Phys.* **98**, 124301 (2005)
18. T. Belytschko, S.P. Xiao, Coupling methods for continuum model with molecular model. *Int. J. Multiscale Comput. Eng.* **1**, 115–126 (2000)
19. T. Chang, H. Gao, Size-dependent elastic properties of a single-walled carbon nanotube via a molecular mechanics model. *J. Mech. Phys. Solids* **51**, 1059–1074 (2003)
20. S. Gopalakrishnan, A. Chakraborty, D. Roy Mahapatra, *Spectral Finite Element Method*. (Springer-Verlag, London, 2008)
21. T. Chang, J. Geng, X. Guo, Prediction of chirality- and size-dependent elastic properties of single-walled carbon nanotubes via a molecular mechanics model. *Proc. R. Soc. A* **462**, 2523–2540 (2006)
22. Y. Wu, X. Zhang, A.Y.T. Leung, W. Zhong, An energy equivalent model on studying the mechanical properties of single-walled carbon nanotubes. *Thin Walled Str.* **44**, 667–676 (2006)
23. J.R. Xiao, B.A. Gama, J.W. Gillespie Jr, An analytical molecular structural mechanics model for the mechanical properties of carbon nanotubes. *International Journal of Solids and Structures* **42**, 3075–3092 (2005)
24. S. Narendar, D. Roy Mahapatra, S. Gopalakrishnan, Prediction of nonlocal scaling parameter for armchair and zigzag single-walled carbon nanotubes based on molecular structural mechanics, nonlocal elasticity and wave propagation. *Int. J. Eng. Sci.* **49**, 509–522 (2011)

Chapter 6

Wave Propagation in 1D-Nanostructures: Nanorods

A nanostructure is defined as a material system or object where at least one of the dimensions lies below 100 nm. Nanostructures can be classified into three different categories: zero-dimensional (0D); one-dimensional (1D); two-dimensional (2D). 0D nanostructures are materials in which all three dimensions are at the nanoscale. A good example of these materials is buckminsterfullerenes [1] and quantum dots [2]. 1D nanostructures are materials that have two physical dimensions in the nanometer range while the third dimension can be large, such as in the carbon nanotube [3]. 2D nanostructures, or thin films, have one of their dimension in the nanometer range and are used readily in the processing of complimentary metal-oxide semiconductor transistors [4] and micro-electro-mechanical systems (MEMS) [5]. The focus of this chapter is on one-dimensional nanostructures. 1D nanostructures (here we call them nanorods or nanoshafes) have stimulated a great deal of interest due to their importance in fundamental scientific research and potential technological applications in nanoelectronic, nanooptoelectronic and nanoelectro-mechanical systems. Rod-shaped viruses, such as tobacco mosaic viruses and M13 bacteriophage, have been utilized as biological templates in the synthesis of semiconductor and metallic nanowires [6]. They were also proposed as elements in the biologically inspired nanoelectronic circuits. Vibrational and wave modes will affect the properties of the inorganic-organic interface [6].

The length scales associated with nanostructures like carbon nanotubes, nanofibers, nanowires, nanorods, graphene sheets are such that to apply any classical continuum techniques, we need to consider the small length scales such as lattice spacing between individual atoms, surface properties, and grain size. This makes a physically consistent classical continuum model formulation very challenging. The Eringen's nonlocal elasticity theory [7] discussed in Chap. 4, is a useful tool in treating phenomena whose origins lie in the regimes smaller than the classical continuum models. In this theory, the internal size or scale could be represented in the constitutive equations simply as material parameters. Such a nonlocal continuum mechanics has been widely accepted and has been applied to many problems including wave propagation, dislocation, crack problems, etc [8]. Recently, there has been

great interest in the application of nonlocal continuum mechanics for modeling and analysis of nanostructures.

In this chapter, the nonlocal elasticity theory has been incorporated into classical rod/bar model to capture unique features of the nanorods under the umbrella of continuum mechanics theory. The nonlocal behavior will be brought out through nonlocal stress and strain gradient models. We will call these models as NLSGM for NonLocal Stress Gradient Models and NLStGM for NonLocal Strain Gradient Models. Two variants of NLStGM will be discussed, one based on second-order gradient models and the second one will be based on fourth-order gradient models. Some of the stability issues of the second-order gradient models will be discussed in depth. The effect of lateral inertia on the strain gradient models and their stabilizing effect is discussed in this chapter. The analysis will then be extended to study torsional wave propagation in nanoshafes. The chapter ends with a brief introduction to spectral finite element(SFE) and its application to nanorods.

6.1 Axial Wave Propagation in NLSGM Nanorod

In Chap. 3 and Sect. 3.9.1, we had introduced both the stress and strain gradient nonlocal models. In this chapter, we dwell on these models in more detail. In this section, we will study the axial wave propagation behavior in a nanorod, which is modeled using nonlocal stress gradient models.

6.1.1 Governing Equations for NLSGM Nanorods

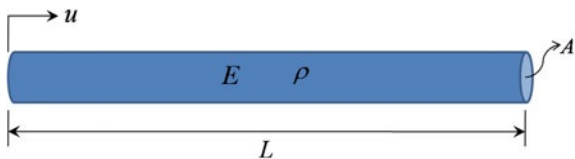
For one-dimensional nonlocal elasticity, there exists a differential form for the stress-strain relation as

$$(1 - \xi^2 \ell^2 \nabla^2) \sigma_{ij} = C_{ijkl} \varepsilon_{kl} \quad (6.1)$$

where the operator ∇^2 is the Laplacian operator. Notice that in the nonlocal elasticity, the effect of small length scale is considered by incorporating the internal parameter length into the constitutive equation. One may also see that when the internal characteristic length a is neglected, i.e., the particles of a medium are considered to be continuously distributed, then $\xi = e_0 a / \ell = 0$, and Eq. (6.1) reduces to the constitutive equation of classical elasticity.

Figure 6.1 schematically describes a nanorod under discussion and serves to introduce the axial coordinate x , the axial displacement $u = u(x, t)$, the length L , the Young's modulus E , and the density ρ . The displacement field and strain for this nanorod are given by

Fig. 6.1 A Nanorod, showing length L , Young's modulus E , density ρ , cross-sectional area A and longitudinal displacement u



$$u = u(x, t) \quad (6.2)$$

$$\varepsilon_{xx} = \frac{\partial u}{\partial x} \quad (6.3)$$

For thin rods Eq. (6.1) can be written in the following one dimensional form

$$\sigma_{xx} - (e_0a)^2 \frac{\partial^2 \sigma_{xx}}{\partial x^2} = E \varepsilon_{xx} = E \frac{\partial u}{\partial x} \quad (6.4)$$

where E is the modulus of elasticity, σ_{xx} and ε_{xx} are the local stress and strain components in the x direction, respectively. The equation of motion for an axial rod can be obtained as

$$\frac{\partial N}{\partial x} = \rho A \frac{\partial^2 u}{\partial t^2} \quad (6.5)$$

where N is the axial force per unit length for local or classical elasticity and is defined by

$$N = \int_A \sigma_{xx} dA \quad (6.6)$$

Using Eqs. (6.4 and 6.6), we have

$$N - (e_0a)^2 \frac{\partial^2 N}{\partial x^2} = EA \frac{\partial u}{\partial x} \quad (6.7)$$

Substitution of the first derivative of N from Eq. (6.5) into Eq. (6.7), we obtain

$$N = EA \frac{\partial u}{\partial x} + (e_0a)^2 \rho A \frac{\partial^3 u}{\partial x \partial t^2} \quad (6.8)$$

Substituting N from Eq. (6.8) into the equation of motion (6.5), we obtain

$$EA \frac{\partial^2 u}{\partial x^2} + (e_0a)^2 \rho A \frac{\partial^4 u}{\partial x^2 \partial t^2} = \rho A \frac{\partial^2 u}{\partial t^2} \quad (6.9)$$

Equation (6.9) is the consistent fundamental governing equation of motion for non-local rod model. When $e_0a = 0$, it is reduced to the equation of classical rod model.

6.1.2 Wave Characteristics in NLSGM Nanorods

In this section, using the wave propagation concepts highlighted in Chap. 2, we will determine two important wave parameters, namely the wavenumber and the two different wave speeds (phase speeds and group speeds). We will also study the special features that nonlocal scale parameter will introduce in these variables and their implications in the wave propagation.

The axial wavenumber in a nanorod is computed as follows. For analyzing the ultrasonic wave dispersion characteristics in nanorods, we assume that a harmonic type of wave solution for the displacement field $u(x, t)$ and it can be expressed in complex form as [9, 10]

$$u(x, t) = \sum_{p=0}^{P-1} \sum_{q=0}^{Q-1} \hat{u}(x, \omega_q) e^{-j(k_p x - \omega_q t)} \quad (6.10)$$

where P and Q are the number of time sampling points and number spatial sampling points respectively. ω_q is the circular frequency at the q^{th} time sample. Similarly, k_p is the axial wavenumber at the p th spatial sample point. Substituting Eq. (6.10) into the governing partial differential equation Eq. (6.9), we get the dispersion relation as follows. Hereafter the subscripts p and q in Eq. (6.10) are dropped for simplified notations. Here $j = \sqrt{-1}$.

$$-k^2 + (e_0 a)^2 \eta^2 \omega^2 k^2 + \eta^2 \omega^2 = 0 \quad (6.11)$$

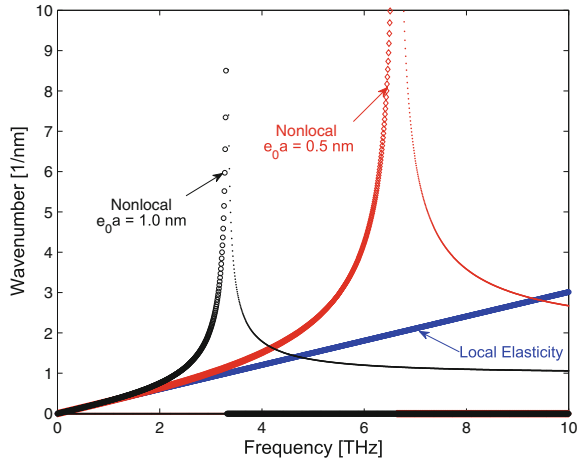
where $\eta = \sqrt{\frac{\rho}{E}}$. This dispersion relation is solved for the wavenumbers as

$$k_{1,2} = \pm \sqrt{\frac{\eta^2 \omega^2}{1 - (e_0 a)^2 \eta^2 \omega^2}} \quad (6.12)$$

The wave frequency is a function of wavenumber k , the nonlocal scaling parameter $e_0 a$, and the material properties (E & ρ) of the nanorod. If $e_0 a = 0$, the wavenumber is directly proportional to wave frequency, which will give a nondispersive wave behavior (for more details refer to Chap. 2). The cut-off frequency of this nanorod is obtained by setting $k = 0$ in the dispersion relation Eq. (6.11). For the present case, the cut-off frequency is zero, that is, the axial wave starts propagating from zero frequency.

The spectrum relation plot as a function of nonlocal scale parameter $e_0 a$ is shown in Fig. 6.2. From this figure, one can observe that at certain frequencies, the wavenumber is tending to infinity and value of this frequency, which is called the escape frequency, decreases with increase in the scale parameter. Its value can be analytically determined by looking at the wavenumber expression Eq. (6.12) and setting $k \rightarrow \infty$. Which is given as

Fig. 6.2 A comparison of the wavenumber (*thick lines*-real; *thin lines*-imaginary) dispersion in a nanorod obtained from local ($e_0a = 0$ nm) and nonlocal ($e_0a = 0.5$ nm and $e_0a = 1.0$ nm) elasticity theories

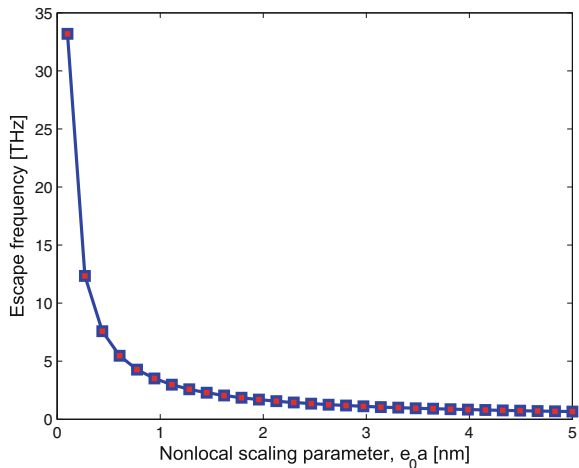


$$\omega_{escape} = \frac{1}{(e_0a)\eta} = \frac{1}{e_0a} \sqrt{\frac{E}{\rho}} \tag{6.13}$$

The escape frequency is inversely proportional to the nonlocal scaling parameter and is independent of the diameter of the nanorod. The variation of the escape frequency with nonlocal scaling parameter is shown in Fig. 6.3.

Next, we will compute the two different wave speeds, namely the phase speeds and the group speeds, whose expressions are given by

Fig. 6.3 Escape frequency variation of the axial wave in a nanorod with nonlocal scaling parameter



$$C_{phase} = \frac{\omega}{k} = \frac{1}{\eta} \left[1 - (e_0 a)^2 \eta^2 \omega^2 \right]^{1/2} \quad (6.14)$$

$$C_{group} = \frac{\partial \omega}{\partial k} = \frac{1}{\eta} \left[1 - (e_0 a)^2 \eta^2 \omega^2 \right]^{3/2} \quad (6.15)$$

These wave speeds also depend on the nonlocal scaling parameter. When $e_0 a = 0$, both the wave speeds are equal (i.e., $C_{phase} = C_{group} = 1/\eta = \sqrt{E/\rho}$), which is already proved for local or classical bars/rods [10]. The phase speed and group speed dispersion curves with wave frequency are shown in Figs. 6.4 and 6.5 respectively.

Next, based on the equations derived above, we will generate wavenumber and dispersion plots as a function of scale parameter e_0 for NLSGM model. For the present analysis, a SWCNT is assumed as a nanorod. The values of the radius, thickness, Young's modulus, and density are assumed as 3.5 nm, 0.35 nm, 1.03 TPa, and 2300 kg/m³, respectively.

Figure 6.2 shows the real and imaginary parts of the axial wavenumber of a nanorod. The thick lines represent the real part and the thin lines show the imaginary part of the wavenumbers. From Fig. 6.2, for a nanorod, it can be seen that there is only one mode of wave propagation, i.e., axial or longitudinal. For local or classical model, the wavenumbers for the axial mode have a linear variation with the frequency which is in the THz range. The linear variation of the wavenumbers denotes that the waves will propagate nondispersively, i.e., the waves do not change their shapes as they propagate. On the other hand, the wavenumbers obtained from nonlocal elasticity have a nonlinear variation with the frequency, which indicates that the waves are dispersive in nature. However, the wavenumbers of this wave mode have a substantial real part starting from the zero frequency. This implies that the mode starts propagating at any excitation frequency and does not have a cut-off frequency. At the escape frequency, which was defined earlier, the wavenumbers tend to infinity as shown in Fig. 6.2. Hence, the nonlocal elasticity model shows that the wave will propagate only up to certain frequencies and after that the wave will not propagate.

The escape frequencies are purely a function of the nonlocal scaling parameter. The variation of the escape frequency with nonlocal parameter is shown in Fig. 6.3. It shows that, as $e_0 a$ increases the escape frequency decreases, such variation can also be observed from Fig. 6.2. For very small values of $e_0 a$, the escape frequencies are very large, and at higher values of $e_0 a$ the escape frequencies are very small and approach to a constant value.

Figures 6.4 and 6.5, plot the wave speeds for the nanorod obtained from both local and nonlocal models. Because of the linear variation of wavenumber with wave frequency from local elasticity, the phase speed ($C_p = Real\left(\frac{\omega}{k}\right)$) and group speed ($C_g = Real\left(\frac{d\omega}{dk}\right)$) for the axial mode has a constant value for all the frequencies, and hence the wave does not change its shape as it propagate. It can also be observed that the axial wave speed is similar for local and nonlocal cases at zero frequency. In nonlocal elasticity, at escape frequency, the wavenumber tends to infinity, and

Fig. 6.4 A comparison of the phase speed dispersion in a nanorod obtained from local ($e_0a = 0$ nm) and nonlocal ($e_0a = 0.5$ nm and $e_0a = 1.0$ nm) elasticity theories

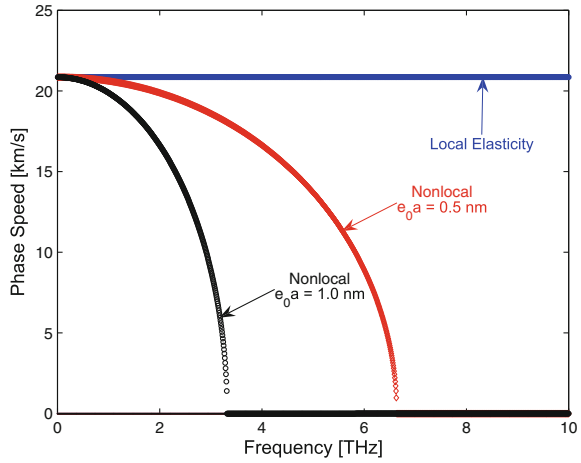
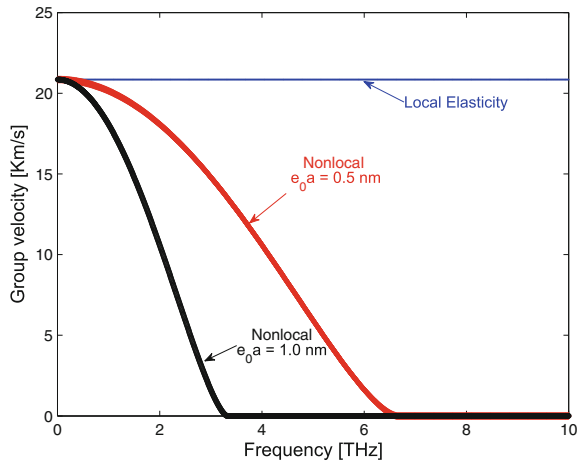


Fig. 6.5 A comparison of the group speed dispersion in a nanorod obtained from local ($e_0a = 0$ nm) and nonlocal ($e_0a = 0.5$ nm and $e_0a = 1.0$ nm) elasticity theories



hence the phase and group speeds tend to zero, indicating localization and stationary behavior.

It can be concluded that the wave dispersion characteristics in a nanorod is drastically different for local and nonlocal models. The local model predicts that the wave will propagate at all frequencies, while the nonlocal model shows that the wave will propagate up to certain frequencies only depending on the nonlocal scaling parameter [11]. The results presented in this section can provide useful guidance for the study and design of the next generation of nanodevices that make use of the wave propagation properties of carbon nanotubes.

6.2 Axial Wave Propagation NLStGM Nanorods

Strain-gradient elasticity is widely used as a suitable alternative to size-independent classical continuum elasticity to, at least partially, capture elastic size effects at the nanoscale. The strain-gradient elasticity may be of practical importance for materials possessing a nonhomogeneous microstructure like amorphous silica and polymers. In other words, it is believed that nonlocal, and in particular, strain-gradient elasticity is largely irrelevant for most material systems except at impossibly small sizes. As evident, polymers and amorphous materials appear to be the exceptions. Covalent semiconductors like Silicon, however, possess higher nonlocal length scales compared to metals which may be attributed to the short-ranged nature of inter-atomic forces in metal.

Although the strain-gradient elasticity is irrelevant for most crystalline metals and ceramics, we wish to point out that under certain circumstances, strain-gradient elasticity is quite useful even in materials exhibiting small nonlocal characteristic length scales such as, in analysis of defects. In this regard, the reader is advised to see the recent work of Zhang et al. [12] who have shown the utility of using nonlocal elasticity for the analysis of defects in graphene. In addition, materials with a microstructure such as foams or composites may be fruitfully modeled using strain-gradient elasticity.

Classical continuum theories assume that the stresses in a material point depend only on the first-order derivative of the displacements, that is on the strains, and not on higher order displacement derivatives. As a consequence of this limitation on the kinematic field, a classical continuum is not always capable of adequately describing heterogeneous phenomena. For instance, unrealistic singularities in the stress and/or strain field may occur nearby imperfections. Furthermore, severe problems in the simulation of localization phenomena with classical continua have been encountered, such as loss of well posedness in the mathematical description. To avoid these types of deficiencies, it has been proposed to include higher order strain gradients into the constitutive equations, so that the defects of the classical continuum may be successfully overcome [13, 14]. The second-order strain gradients that are normally used for these purposes, introduce accessory material parameters that reflect the microstructural properties of the material. These were earlier discussed in Sect. 3.9.1.

The higher order gradients can improve the performance of the classical continuum in the sense that the dispersive behavior of the discrete model is reproduced with a higher accuracy, [15–17]. This is a direct consequence of the procedure that is commonly used to enhance the classical continuum with higher order gradients. Homogenization of the discrete medium may lead to higher order gradients in a direct and straightforward manner. If regularization of singularities or discontinuities is required, higher order gradients are used for smoothing the nonuniformity or singularities in the strain field. On the other hand, if a more accurate representation of the discrete microstructure is desired, the higher order gradients are used to introduce a nonuniformity in the strain field.

Expansion of the general integral constitutive equation of nonlocal elasticity (see [7]) for $e_0a/L \ll 1$, retention of only the first two terms, and simplification to the case of uniaxial stress produces

$$\sigma(x) = E \left(\varepsilon(x) + (e_0a)^2 \frac{d^2\varepsilon(x)}{dx^2} \right) \quad (6.16)$$

This is a second-order strain gradient model with nonlocal scale effects.

In the same way, retention of only the first three terms, and simplification to the case of uniaxial stress produces

$$\sigma(x) = E \left(\varepsilon(x) + (e_0a)^2 \frac{d^2\varepsilon(x)}{dx^2} + (e_0a)^4 \frac{d^4\varepsilon(x)}{dx^4} \right) \quad (6.17)$$

This is a fourth-order strain gradient model with nonlocal scale effects. Next, we will derive the governing equation of motion for nanorod based on the above mentioned two constitutive relations Eqs. (6.16 and 6.17).

6.2.1 Governing Equations for Second and Fourth-Order NLStGM Nanorods

We will first derive the governing differential equation for second-order NLStGM nanorod. Figure 6.1 schematically describes a nanorod under discussion and serves to introduce the axial coordinate x , the axial displacement $u = u(x, t)$, the rod length L , the rod Young's modulus E , and the density ρ . The displacement field and strain for this nanorod are given by

$$u = u(x, t) \quad (6.18)$$

$$\varepsilon = \frac{\partial u}{\partial x} \quad (6.19)$$

First, we derive the governing differential equations for the nanorod using second-order strain gradient model (see Eq. (6.16)). The potential (Π) and kinetic (Γ) energies of the nanorod are

$$\Pi^s = \frac{1}{2} \int_V \sigma(x) \varepsilon(x) dV = \frac{1}{2} \int_V \left(\varepsilon(x) + (e_0a)^2 \frac{\partial^2 \varepsilon(x)}{\partial x^2} \right) \varepsilon(x) dV \quad (6.20)$$

$$\Gamma^s = \frac{1}{2} \int_V \rho \left(\frac{\partial u(x, t)}{\partial t} \right)^2 dV \quad (6.21)$$

Here superscript s represents for the second-order strain gradient model. Assuming a uniform nanorod, Eqs. (6.20 and 6.21) rewritten as

$$\Pi^s = \frac{1}{2}A \int_0^L \left(\varepsilon(x) + (e_0a)^2 \frac{\partial^2 \varepsilon(x)}{\partial x^2} \right) \varepsilon(x) dx \quad (6.22)$$

$$\Gamma^s = \frac{1}{2}\rho A \int_0^L \left(\frac{\partial u(x, t)}{\partial t} \right)^2 dx \quad (6.23)$$

Applying Hamilton's principle

$$\delta \int_{t_1}^{t_2} L^s dt = \delta \int_{t_1}^{t_2} (\Gamma^s - \Pi^s) dt = 0 \quad (6.24)$$

Expanding this, and integrating by parts, we obtain the nonlocal governing partial differential equation for the nanorod obtained from the second-order strain gradient model as

$$EA(e_0a)^2 \frac{\partial^4 u(x, t)}{\partial x^4} + EA \frac{\partial^2 u(x, t)}{\partial x^2} - \rho A \frac{\partial^2 u(x, t)}{\partial t^2} = 0 \quad (6.25)$$

This is a fourth-order governing differential equation for nanorod based on nonlocal second-order strain gradient model. One can substitute $e_0a = 0$ in Eq. (6.25), to recover the local or classical rod equation, which is a second-order differential equation.

Next, we will derive the governing differential equation for fourth-order NLStGM nanorods. Now assuming the same displacement field and strain-displacement relations (given in Eqs. (6.18 and 6.50)) and using the fourth-order strain gradient model (see Eq. (6.17)), the kinetic and potential energies can be expressed as

$$\Pi^f = \frac{1}{2} \int_V \sigma(x) \varepsilon(x) dV = \frac{1}{2} \int_V \left(\varepsilon(x) + (e_0a)^2 \frac{d^2 \varepsilon(x)}{dx^2} + (e_0a)^4 \frac{d^4 \varepsilon(x)}{dx^4} \right) \varepsilon(x) dV \quad (6.26)$$

$$\Gamma^f = \frac{1}{2} \int_V \rho \left(\frac{\partial u(x, t)}{\partial t} \right)^2 dV \quad (6.27)$$

Here superscript f represents the fourth-order strain gradient model. For a uniform nanorod, Eqs. (6.26, 6.27) rewritten as

$$\Pi^f = \frac{1}{2}A \int_0^L \left(\varepsilon(x) + (e_0a)^2 \frac{d^2 \varepsilon(x)}{dx^2} + (e_0a)^4 \frac{d^4 \varepsilon(x)}{dx^4} \right) \varepsilon(x) dx \quad (6.28)$$

$$\Gamma^f = \frac{1}{2}\rho A \int_0^L \left(\frac{\partial u(x, t)}{\partial t} \right)^2 dx \quad (6.29)$$

Applying the Hamilton's principle,

$$\delta \int_{t_1}^{t_2} L^f dt = \delta \int_{t_1}^{t_2} (\Gamma^f - \Pi^f) dt = 0 \quad (6.30)$$

and integrating by parts, the nonlocal governing differential equation for the nanorod from fourth-order strain gradient model is derived as

$$EA(e_0a)^4 \frac{\partial^6 u(x, t)}{\partial x^6} + EA(e_0a)^2 \frac{\partial^4 u(x, t)}{\partial x^4} + EA \frac{\partial^2 u(x, t)}{\partial x^2} - \rho A \frac{\partial^2 u(x, t)}{\partial t^2} = 0 \quad (6.31)$$

This is a sixth-order governing differential equation for nanorod based on fourth-order strain gradient model, and again we observe that when $e_0a = 0$, local/classical rod equation can be recovered.

6.2.2 Uniqueness and Stability of Second-Order NLStGM Nanorods

Strain gradients can be used to introduce heterogeneity into the continuum. As a result, the dispersive character of waves observed in experiments, and hence the discrete material models can be simulated with a higher accuracy [17, 18]. By homogenizing a discrete medium, a second-gradient model of the type given in Eq. (6.16) can be derived. To derive the uniqueness of the model, we need to first establish the analytical solution of second-order constitutive strain gradient model given by Eq. (6.16). This is done by combining the constitutive equation with the uniaxial equilibrium equation $\frac{\partial \sigma}{\partial x} = 0$ (no body forces are considered) and the kinematic relation Eq. (6.3). The use of Eq. (6.16) leads to an analytical solution for u of the form

$$u = C_1 + C_2 x + C_3 \sin\left(\frac{x}{e_0a}\right) + C_4 \cos\left(\frac{x}{e_0a}\right) \quad (6.32)$$

where C_i are constants that have to be determined according to the boundary conditions. The response of the classical continuum is given by the constants C_1 and C_2 only.

We will next examine the uniqueness of the obtained analytical solution following [19], the uniqueness of the static analytical solution is investigated next. To this end, it is assumed that two different solutions u_1 and u_2 exist that satisfy the equilibrium equation and the nonhomogeneous boundary conditions. For a proof of uniqueness, the difference between these two solutions $\Delta u = u_1 - u_2$ should vanish. This difference solution should then satisfy the equilibrium equation and the homogeneous boundary conditions. A specimen of length L is considered, and the boundary conditions for the difference solution are taken as $\Delta u = 0$ and $\frac{\partial \Delta u}{\partial x} = 0$ both at $x = 0$ and at $x = L$. The four boundary conditions lead to the following system of equations:

$$\begin{bmatrix} 1 & 0 & 0 & 1 \\ 1 & L & \sin\left(\frac{L}{e_0a}\right) & \cos\left(\frac{L}{e_0a}\right) \\ 0 & 1 & \frac{1}{L} & 0 \\ 0 & 1 & \frac{1}{L} \cos\left(\frac{L}{e_0a}\right) & -\frac{1}{L} \sin\left(\frac{L}{e_0a}\right) \end{bmatrix} \begin{bmatrix} C_1 \\ C_2 \\ C_3 \\ C_4 \end{bmatrix} = \begin{bmatrix} 0 \\ 0 \\ 0 \\ 0 \end{bmatrix} \quad (6.33)$$

By eliminating C_1 and C_2 , a reduced coefficient matrix for C_3 and C_4 according to Eq. (6.16) can be determined. For finding a nontrivial solution for Δu (which corresponds to nonuniqueness) the determinant of this reduced coefficient matrix should vanish, i.e.,

$$\begin{vmatrix} \sin\left(\frac{L}{e_0a}\right) - \frac{L}{e_0a} \cos\left(\frac{L}{e_0a}\right) - 1 \\ \cos\left(\frac{L}{e_0a}\right) - 1 & -\sin\left(\frac{L}{e_0a}\right) \end{vmatrix} = 0 \quad (6.34)$$

that implies

$$\frac{L}{e_0a} \sin\left(\frac{L}{e_0a}\right) + 2 \cos\left(\frac{L}{e_0a}\right) - 2 = 0 \quad (6.35)$$

which is satisfied when $\frac{L}{e_0a} = 2\pi\alpha$ with α an arbitrary integer. Thus, uniqueness cannot be guaranteed for the model of Eq. (6.16) in the case $\frac{L}{e_0a} = 2\pi\alpha$.

In the above procedure, the higher order boundary conditions are taken as prescribed values for the first derivative of the displacement. The use of different higher order boundary conditions leads to different considerations with respect to uniqueness. Taking prescribed second-order derivatives of the displacement can also lead to nonunique solutions with the model of Eq. (6.32). Although not shown here, in this case, the values of $\frac{L}{e_0a}$ for which nonunique solutions are obtained coincide with those obtained via Eq. (6.35).

Next, we have to establish the stability of the second-order NLStGM. The stability of the second-order strain gradient model of Eq. (6.16) is studied by means of the potential energy density \mathfrak{H} , given by

$$\mathfrak{H} = \int_{\varepsilon} \sigma d\varepsilon \quad (6.36)$$

Substitution of the constitutive equation Eq. (6.16), integrating the higher order terms by parts, and carrying out the integration results in the following equation.

$$\mathfrak{H} = \frac{1}{2} E \left[\varepsilon^2 - (e_0a)^2 \left(\frac{\partial \varepsilon}{\partial x} \right)^2 \right] \quad (6.37)$$

In the derivation procedure above, the boundary integrals are assumed to vanish. This has severe implications for the stability of the model: positive terms have a stabilizing

effect on the overall response, while negative terms are destabilizing. Thus, the model according to Eq. (6.16) may become unstable.

In summary, the second-order strain gradient model can become unstable and uniqueness is not guaranteed. This model bears the closest relation with the discrete model (a positive sign in front of the higher order term). However, the use of this model in engineering practice is limited due to the possible emergence of nonuniqueness and instability, which may have a devastating effect on its response [20].

6.2.3 Wave Characteristics of Second-Order NLStGM Nanorods

For analyzing the ultrasonic wave dispersion characteristics in nanorods, we assume that a harmonic type of wave solution for the displacement field $u(x, t)$ and it can be expressed in complex form as [9, 10]:

$$u(x, t) = \hat{u}(x, \omega) e^{-j(kx - \omega t)} \quad (6.38)$$

where $\hat{u}(x, \omega)$ is the frequency domain amplitude of the longitudinal displacement, k is the wavenumber and ω is the angular frequency of the wave motion and $j = \sqrt{-1}$. Substituting Eq. (6.38) in the nonlocal governing equation of nanorod obtained from the second-order strain gradient model Eq. (6.25) gives the following dispersion relation,

$$(e_0a)^2 k^4 - k^2 + \eta^2 \omega^2 = 0 \quad (6.39)$$

where $\eta = \sqrt{\frac{\rho}{E}}$. This dispersion relation is solved for the wave frequency as

$$\omega^s = \frac{k}{\eta} \sqrt{1 - (e_0a)^2 k^2} \quad (6.40)$$

The wave frequency is a function of wavenumber k , the nonlocal scaling parameter e_0a and the material properties (E & ρ) of the nanorod. For the present analysis, we are considering both wave speeds (phase and group speeds) of the wave and are given by

$$C_p^s = \frac{\omega^s}{k} = \frac{1}{\eta} \sqrt{1 - (e_0a)^2 k^2} \quad (6.41)$$

$$C_g^s = \frac{\partial \omega^s}{\partial k} = \frac{1 - 2(e_0a)^2 k^2}{\eta [1 - (e_0a)^2 k^2]} \quad (6.42)$$

These wave speeds also depend on the nonlocal scaling parameter. When $e_0a = 0$, both the wave speeds are equal (i.e., $C_p^s = C_g^s = 1/\eta = \sqrt{E/\rho}$), which is already proved for local or classical bars/rods [10].

We will next compute some of the important features of second-order NLStGM. First, we will compute the critical wavenumber. We call *critical wavenumber* as a wavenumber at zero frequency. From the dispersion relation Eq. (6.39), by setting the wave frequency (ω) to zero, gives the critical wavenumber as

$$k_{cr} = \pm \frac{1}{\sqrt{e_0 a}} \quad (6.43)$$

The critical wavenumber is purely a function of internal length scale only.

Next, we can compute the number of waves along the nanorod. The number of wavelengths (N) along the nanorod is defined as $N = L/\lambda$, where L is the length of the nanorod and λ is the wavelength. The wavelength is related to wavenumber as $\lambda = 2\pi/k$, here the wavenumber is critical Eq. (6.43). Thus the number of wavelengths along the nanorod is given by

$$N = \frac{L}{2\pi \sqrt{e_0 a}} \quad (6.44)$$

6.2.4 Wave Characteristics of Fourth-Order NLStGM Nanorods

As in the case of second-order models, we will compute the wavenumber, phase speed and group speeds for this case. Substituting Eq. (6.38) in the nonlocal governing partial differential equation of nanorod obtained from the fourth-order strain gradient model Eq. (6.31) gives the following dispersion relation,

$$-(e_0 a)^4 k^6 + (e_0 a)^2 k^4 - k^2 + \eta^2 \omega^2 = 0 \quad (6.45)$$

Solving this dispersion relation for wave frequency as

$$\omega^f = \frac{k}{\eta} \sqrt{1 - (e_0 a)^2 k^2 + (e_0 a)^4 k^4} \quad (6.46)$$

The phase and the group speeds of an ultrasonic wave in nanorod are given as

$$C_p^f = \frac{\omega^f}{k} = \frac{1}{\eta} \sqrt{1 - (e_0 a)^2 k^2 + (e_0 a)^4 k^4} \quad (6.47)$$

$$C_g^f = \frac{\partial \omega^f}{\partial k} = \frac{1 - 2(e_0 a)^2 k^2 [1 - (e_0 a)^2 k^2]}{\eta \{1 - (e_0 a)^2 k^2 [1 - (e_0 a)^2 k^2]\}} \quad (6.48)$$

On substitution of $e_0 a = 0$ in Eqs. (6.47 and 6.48), gives $C_p^f = C_g^f = 1/\eta = \sqrt{E/\rho}$.

6.2.5 Numerical Results and Discussion

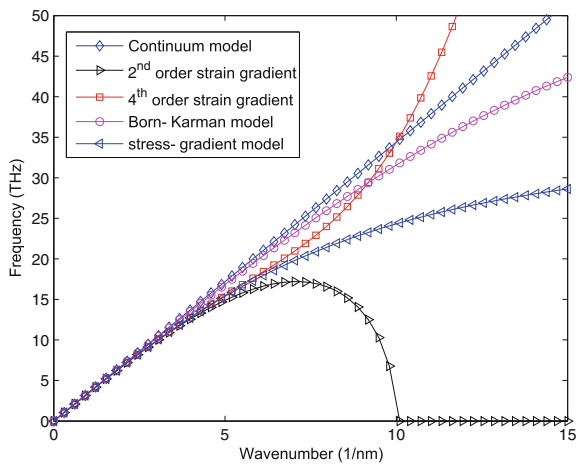
For the present analysis, a SWCNT is assumed as a nanorod. The values of the diameter (d), Young’s modulus (E) and density (ρ) are assumed as 5 nm, 1.06 TPa, and 2270 kg/m³, respectively.

The spectrum and dispersion curves for nanorod obtained from both strain gradient models (assuming $e_0a = 0.02$ nm. as length increases $e_0a/L \ll 1$) are shown in Fig. 6.6. The results obtained from classical continuum model are also shown in those figures for comparison.

The spectrum and dispersion relations obtained from the classical continuum model show that the waves in nanorod are nondispersive, i.e., the wavenumber has a linear relation with the wave frequency or the phase or group speeds are constant (see Figs. 6.6–6.9). Both the strain gradient models show that the waves in nanorod are dispersive in nature. It can also be seen that the fourth-order strain gradient model give improved approximation over the second-order strain gradient model, as compared to the classical continuum model. And also the results are compared with the Born–Karman model [21], and the stress gradient model [22].

The instability of the second-order strain gradient model can be seen developing in Fig. 6.6 for wavenumbers larger than $\frac{1}{\sqrt{e_0a}}$, where the angular frequency and the phase velocity become imaginary. This means that waves with larger wavenumbers (or, equivalently, with smaller wavelengths) cannot propagate through this medium. Instead, the imaginary frequency and velocity imply that the response occurs everywhere in the medium instantaneously. This is physically unrealistic. Therefore, these smaller wavelengths should not be considered. Filtering shorter waves occurs automatically in a discrete medium, where wavelengths smaller than two times the particle size cannot be monitored. However, in a continuous medium, all wavelengths can in principle be present. Especially when shock waves are investigated, waves with

Fig. 6.6 Wavenumber dispersion with wave frequency obtained from classical continuum model, second and fourth-order strain gradient models



all wavelengths are triggered by the loading. The imaginary angular frequency (or phase velocity) of these high-frequency waves prohibits a proper wave propagation simulation with this model. The cut-off value for the wavenumber occurs at $k = \frac{1}{\sqrt{e_0 a}}$ (see Fig. 6.6). In the response of the fourth-order strain gradient model, the effect of these high frequency waves is of minor importance. In summary, the wave behavior in second and fourth-order NLStGM is quite different and in addition, instability in the second-order model can be clearly seen.

The effect of $e_0 a$ on the wave behavior in nanorods is shown in Figs. 6.7–6.9. Figure 6.7 shows the effect of $e_0 a$ on wavenumber dispersion in nanorod obtained from different models. As $e_0 a$ increase, the wavenumbers obtained from both strain gradient models will decrease with wave frequency. And the corresponding wave speeds will decrease (as $e_0 a$ increases) as shown in Figs. 6.8 and 6.9. The phase speeds obtained from the second-order strain gradient model are zero at a particular wave frequency (i.e., at critical wavenumber) and this critical wavenumber is also decreases with increase in $e_0 a$ (see Fig. 6.8). A similar type of phenomena is also observed for group speed variation as shown in Fig. 6.9.

As shown in Fig. 6.6, for the case of the second-order strain gradient model, the wave frequency is zero at zero wavenumber and also at the value of 2.02 nm^{-1} . The wavenumber at which the wave frequency is zero is called as critical wavenumber k_{cr} (see Eq. (6.43)). This critical wavenumber is purely a function of the nonlocal scaling parameter ($e_0 a$). As $e_0 a$ increases, the critical wavenumber decreases as shown in Fig. 6.10. It is found that, for second-order strain gradient model, for wavenumbers higher than k_{cr} , the waves cannot propagate through this medium.

The effect of the nonlocal scaling parameter on the number of waves (N) along the nanorod is shown in Fig. 6.11, for rod lengths of 10, 50 and 100 nm. A relation among the number of wave N , nonlocal scaling parameter $e_0 a$, and the length of the rod L is shown in Eq. (6.44). This relation is obtained from the second-order strain gradient

Fig. 6.7 Effect of nonlocal scaling parameter ($e_0 a$) on wavenumber dispersion in nanorod

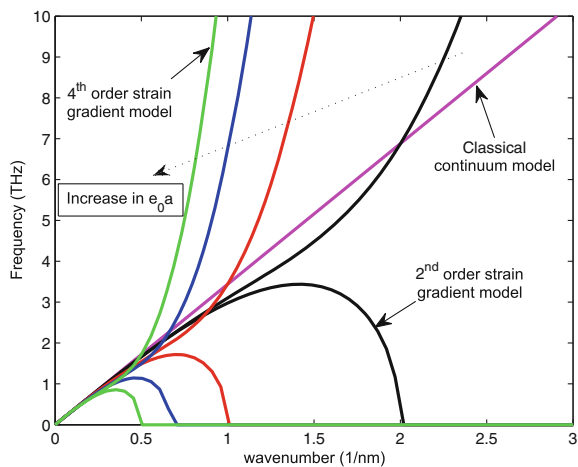


Fig. 6.8 Effect of nonlocal scaling parameter (e_0a) on phase speed dispersion in nanorod

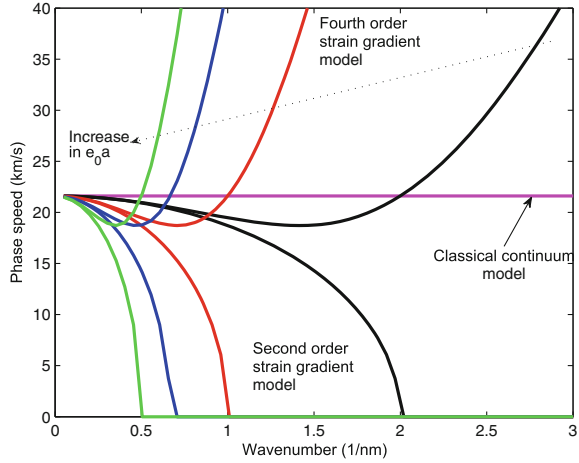
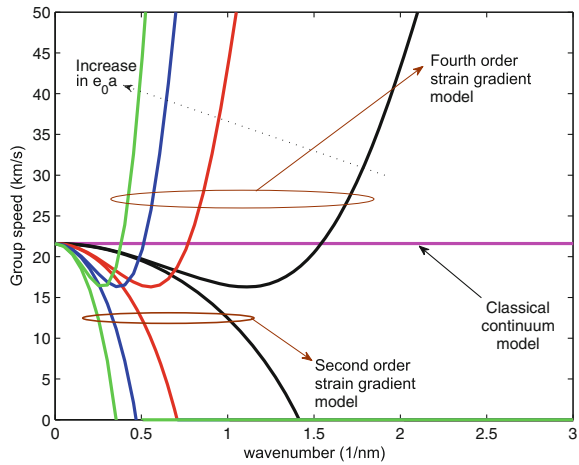


Fig. 6.9 Effect of nonlocal scaling parameter (e_0a) on Group dispersion in nanorod



model only. For number of waves along the nanorod are directly proportional to the length of the nanorod. The number of waves along the nanorod will decrease as e_0a increases (see Fig. 6.11). For very small values of e_0a , the number of waves along the nanorod are very high, for long length nanorods. For $e_0a > 0.1$ nm, the number of waves along the rod is almost constant and this constant number is different for different lengths of nanorod.

Finally, the wave dispersion behavior of nanorods, incorporating a constitutive law that includes a length scale, can be analyzed using a direct Newtonian approach (stress gradient model) and a variational approach (strain gradient model). The latter approach provides the governing field equations and the variationally consistent sets of boundary conditions. Incorporation of small length scale effects is found to significantly affect the wave dispersion behavior in nanorods. Strain-gradient elasticity is

Fig. 6.10 Critical wavenumber (obtained from second-order strain gradient model) variation with nonlocal scaling parameter

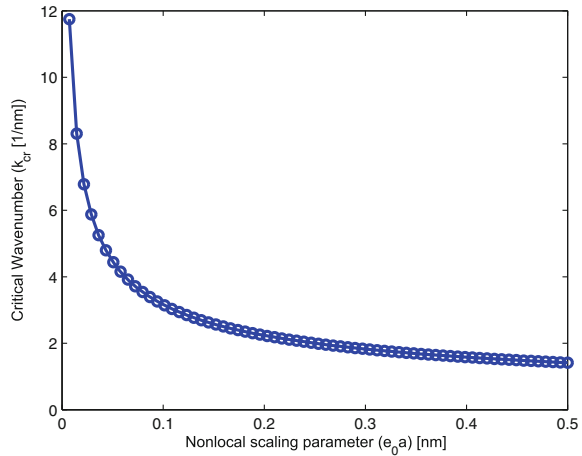
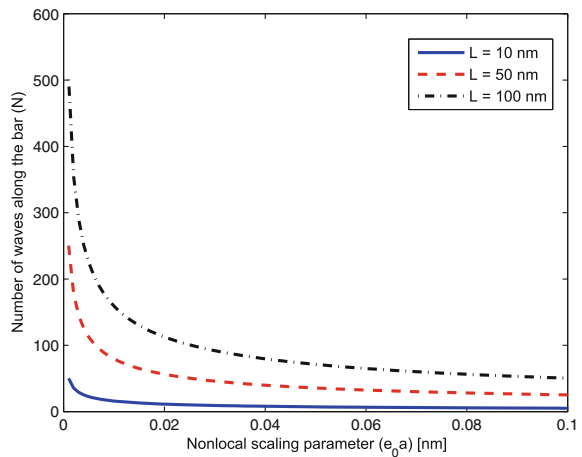


Fig. 6.11 Relation between the number of waves along the nanorod and the nonlocal scaling parameter obtained from second-order strain gradient model, L is the length of the nanorod



quite useful even in materials exhibiting small nonlocal characteristic length scales. More details on these concepts can also be found in [23].

Noting the significant computational costs of MD simulations, other approaches such as the present one have emerged for the modeling of CNTs. The present model's computational costs is negligible compared to the MD calculations and provide for efficient parametric studies. The presented nanorod wave propagation solutions based on nonlocal stress model should be useful to engineers who are designing micro- and nanoelectromechanical devices. Moreover, the higher order strain gradient solutions serve as benchmarks for reference, convergence, and accuracy of numerical solutions for static and dynamic analysis of nanostructures obtained from other mathematical and computational approaches such as molecular dynamics simulations.

6.3 Axial Wave Propagation in Nanorods with Lateral Inertia

The dynamic testing of materials and components often involves predicting the propagation of stress waves in slender rods. Time-domain analysis of wave propagation in nanorods has received less attention. However, the nonlocal scale effect has been incorporated in the one-dimensional wave equation, which is valid within a certain frequency range. For elastic bars, the effect of lateral inertia was predicted by Love [24] a century ago. Love defined the kinetic and strain energy in an elastic rod and derived an equation that incorporated the effect of lateral motion on axial waves using the calculus of variations (see [24, 25]). It is not possible to repeat this analysis for a nonlocal nanomaterial as the necessary expressions for strain energy are not derivable. An alternative derivation is presented here. Due to the Poisson's ratio effect, there is kinetic energy in lateral as well as in the axial direction. This kinetic energy is used to define a new concept called the *effective density*, which is related to the density via a differential operator. Thereafter, expressing Newton's second law in terms of the *effective density* results in a fifth-order partial differential equation (PDE), which represents longitudinal waves in a nonlocal bar.

6.3.1 NLSGM-Based Governing Equations for Nanorods with Lateral Inertia

Figure 6.12 schematically describes a nanorod under, which has a axial coordinate x , lateral coordinate y , the axial displacement $u = u(x, t)$, the Young's modulus E , the density ρ , the Poisson's ratio ν , and cross sectional area A . The displacement field (X -direction), strain, strain rate, and particle velocity associated with the displacement field in X -direction for this nanorod are given by

$$u = u(x, t) \quad (6.49)$$

$$\varepsilon_{xx} = \frac{\partial u}{\partial x} \quad (6.50)$$

$$\dot{\varepsilon}_{xx} = \frac{\partial \varepsilon_{xx}}{\partial t} = \frac{\partial^2 u}{\partial x \partial t} \quad (6.51)$$

$$V = \dot{u} = \frac{\partial u}{\partial t} \quad (6.52)$$

Due to Poisson's ratio ν , there are displacement fields v and w in Y - and Z -directions, respectively. For example, the strain and the derivative of the displacement with time in the Y -direction are, respectively,

$$\varepsilon_{yy} = -\nu \varepsilon_{xx} \quad (6.53)$$

$$\dot{v} = -\nu y \dot{\varepsilon}_{xx} \quad (6.54)$$

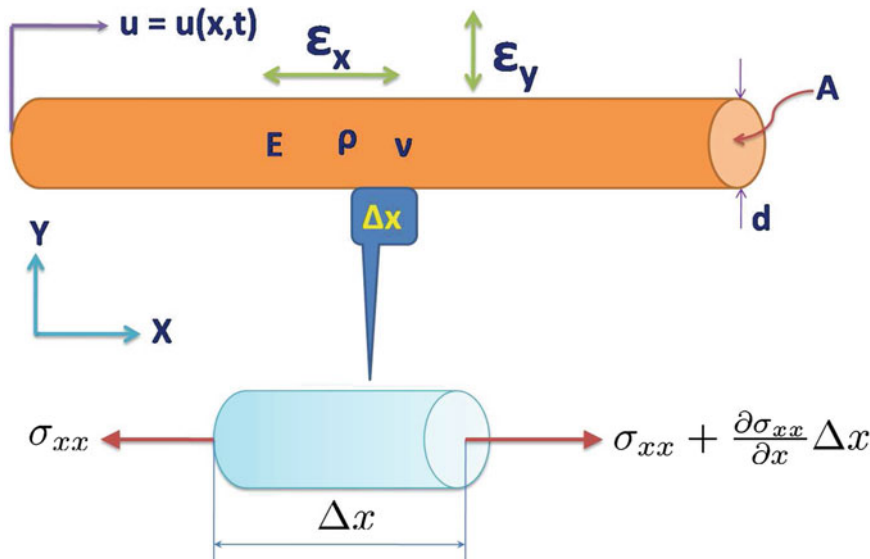


Fig. 6.12 A nanorod, showing Young’s modulus E , density ρ , Poisson’s ratio ν , diameter d , cross-sectional area A , longitudinal displacement $u = u(x, t)$, strain along X - direction ϵ_x and strain along Y - direction ϵ_y

The kinetic energy of the infinitesimal length Δx of the rod (see Fig. 6.12) is

$$\Delta \Pi^e = \frac{1}{2} \rho A \Delta x \left(V^2 + \nu^2 \zeta^2 \dot{\epsilon}_{xx}^2 \right) \tag{6.55}$$

where ρ is the density, A is the cross-sectional area and ζ is the radius of gyration of the solid circular cross-section. Lagrange’s equation of the second kind is used here to derive an equation of motion of the system. The behavior of the system is analogous to that of a completely plastic in-line collision of two unequal masses, that is, the rigid falling mass and the *effective mass* of the two plates. The effective mass of the plates consists of two terms. These two terms represent the longitudinal and transverse inertia of the actual specimen. Here, an *effective density* is used to incorporate the effect of lateral inertia in a one-dimensional wave equation. The mathematical rigor of the derivation of the effective mass in [26] is not attempted. Rather, it is postulated that the effect of lateral inertia effect can be incorporated in a wave model using the concept of *effective density*. The validity of the approach is supported by comparison with two other wave theories. It is then shown that the new wave equation is equivalent to Love’s equation for stress waves in elastic bars when rate dependency is removed from the material model.

Hence, an effective density is used to incorporate the effect of lateral inertia in a one-dimensional nonlocal wave equation. An effective density ρ_{eff} is now introduced such that the kinetic energy of the element Δx is $\Delta \Pi_{eff}^e$, where

$$\Delta \Pi_{eff}^e = \frac{1}{2} \rho_{eff} A \Delta x V^2 \quad (6.56)$$

Using Newton's second law, the net longitudinal force acting on the element Δx (see Fig. 6.12) is

$$\Delta \sigma_{xx} \times A = \rho_{eff} A \frac{\partial^2 u}{\partial t^2} \times \Delta x \quad (6.57)$$

In the limiting case as $\Delta x \rightarrow 0$, Eq. (6.57) can be written as

$$\frac{\partial \sigma_{xx}}{\partial x} = \rho_{eff} \frac{\partial^2 u}{\partial t^2} \quad (6.58)$$

To find the relationship between ρ_{eff} and ρ , a functional \mathcal{U}_e is defined as the kinetic energy error when using the effective density, i.e.,

$$\begin{aligned} \mathcal{U}_e &= \int \int [\Delta \Pi^e - \Delta \Pi_{eff}^e] dx dt \\ &= \int \int \left[\frac{1}{2} \rho A (V^2 + v^2 \zeta^2 \dot{\epsilon}_{xx}^2) - \left(\frac{1}{2} \rho_{eff} A V^2 \right) \right] dx dt \end{aligned} \quad (6.59)$$

substituting for strain rate and particle velocity in Eq. (6.59), the minimization of \mathcal{U}_e requires minimization of the following functional:

$$\mathcal{N}_e = \int \int \left\{ \left[\rho V^2 + \rho v^2 \zeta^2 \left(\frac{\partial V}{\partial x} \right)^2 - \rho_{eff} V^2 \right] \right\} dx dt \quad (6.60)$$

The functional in Eq. (6.60) can be written in terms of the displacement u as

$$\mathcal{N}_e = \int \int \left\{ (\rho - \rho_{eff}) \left[\frac{\partial u}{\partial t} \right]^2 + \rho v^2 \zeta^2 \left[\frac{\partial^2 u}{\partial x \partial t} \right]^2 \right\} dx dt \quad (6.61)$$

The integrand of the functional \mathcal{N}_e is

$$f \left(\frac{\partial u}{\partial t}, \frac{\partial^2 u}{\partial x \partial t} \right) = (\rho - \rho_{eff}) \left[\frac{\partial u}{\partial t} \right]^2 + \rho v^2 \zeta^2 \left[\frac{\partial^2 u}{\partial x \partial t} \right]^2 \quad (6.62)$$

In order to minimize \mathcal{N}_e in Eq. (6.61), the integrand $f \left(\frac{\partial u}{\partial t}, \frac{\partial^2 u}{\partial x \partial t} \right)$ should satisfy the following equation:

$$\frac{\partial^2}{\partial x \partial t} \left[\frac{\partial f \left(\frac{\partial u}{\partial t}, \frac{\partial^2 u}{\partial x \partial t} \right)}{\partial \frac{\partial^2 u}{\partial x \partial t}} \right] - \frac{\partial}{\partial t} \left[\frac{\partial f \left(\frac{\partial u}{\partial t}, \frac{\partial^2 u}{\partial x \partial t} \right)}{\partial \frac{\partial u}{\partial t}} \right] = 0 \quad (6.63)$$

Therefore, Eq. (6.63) is identical to the following partial differential equation:

$$\rho_{eff} \frac{\partial^2 u}{\partial t^2} = \rho \frac{\partial^2 u}{\partial t^2} - \rho v^2 \zeta^2 \frac{\partial^4 u}{\partial x^2 \partial t^2} \quad (6.64)$$

Equation (6.64) gives the relationship between the effective density and the density that minimizes the effective density error, \bigcup_e , defined in Eq. (6.59), over the length of the nanorod and the time of motion. Substituting this expression in Eq. (6.58) gives

$$\frac{\partial \sigma_{xx}}{\partial x} = \rho \frac{\partial^2 u}{\partial t^2} - \rho v^2 \zeta^2 \frac{\partial^4 u}{\partial x^2 \partial t^2} \quad (6.65)$$

The constitutive model employed here is that obtained from the theory of nonlocal/nonclassical continuum mechanics. For thin rods Eq. (6.1) can be written in the following one-dimensional form

$$\sigma_{xx} - \alpha^2 \frac{\partial^2 \sigma_{xx}}{\partial x^2} = E \varepsilon_{xx} = E \frac{\partial u}{\partial x} \quad (6.66)$$

where E is the modulus of elasticity, σ_{xx} and ε_{xx} are the local stress and strain components in the x direction, respectively and $\alpha = e_0 a$, nonlocal scaling parameter. Differentiating the Eq. (6.66) with respect to x on both sides, gives

$$\frac{\partial \sigma_{xx}}{\partial x} - (e_0 a)^2 \frac{\partial^3 \sigma_{xx}}{\partial x^3} = E \frac{\partial \varepsilon_{xx}}{\partial x} = E \frac{\partial^2 u}{\partial x^2} \quad (6.67)$$

Substituting Eq. (6.65) in Eq. (6.67) leads to

$$E \frac{\partial^2 u}{\partial x^2} = \rho \frac{\partial^2 u}{\partial t^2} - \rho v^2 \zeta^2 \frac{\partial^4 u}{\partial x^2 \partial t^2} - \alpha^2 \rho \frac{\partial^4 u}{\partial x^2 \partial t^2} + \alpha^2 \rho v^2 \zeta^2 \frac{\partial^6 u}{\partial x^4 \partial t^2} \quad (6.68)$$

Equation (6.68) is the consistent fundamental governing equation of motion for non-local rod model including the effect of lateral inertia/Poisson's ratio effect [27]. When $\alpha = e_0 a = 0$ and $v = 0$, it is reduced to the equation of local or classical rod model.

6.3.2 Wave Characteristics of Nanorods with Lateral Inertia

For analyzing the ultrasonic/terahertz wave dispersion characteristics in nanorods, we assume that a harmonic type of wave solution for the displacement field $u(x, t)$ and it can be expressed in complex form as:

$$u(x, t) = \sum_{p=0}^{P-1} \sum_{q=0}^{Q-1} \hat{u}(x, \omega_q) e^{-j(k_p x - \omega_q t)} \quad (6.69)$$

where P and Q are the number of time sampling points and number spatial sampling points respectively and $j = \sqrt{-1}$. ω_q is the circular frequency at the q^{th} time sample. Similarly, k_p is the axial wavenumber at the p th spatial sample point. Substituting Eq. (6.69) into the governing partial differential equation Eq. (6.68), we get the characteristic equation (dispersion relation).

$$-k^2 + \eta^2 \alpha^2 \omega^2 k^2 + \eta^2 \omega^2 + \eta^2 \nu^2 \zeta^2 \alpha^2 \omega^2 k^4 + \eta^2 \nu^2 \zeta^2 \omega^2 k^2 = 0 \quad (6.70)$$

where $\eta = \sqrt{\frac{\rho}{E}}$. The dispersion relation is solved for the wavenumbers or wave frequencies as

$$k_{1,2,3,4} = \pm \sqrt{\frac{-T_2 \pm \sqrt{T_2^2 - 4T_4 T_0}}{2T_4}} \quad (6.71)$$

where $T_4 = \eta^2 \nu^2 \zeta^2 \alpha^2 \omega^2$, $T_2 = \eta^2 \alpha^2 \omega^2 + \eta^2 \nu^2 \zeta^2 \omega^2 - 1$ and $T_0 = \eta^2 \omega^2$. The wave frequency is a function of wavenumber k , the nonlocal scaling parameter $\alpha = e_0 a$ and the material properties (E , ν & ρ) of the nanorod. This shows a nonlinear relation between wavenumber and wave frequency, i.e., the obtained axial waves in nanorod are dispersive in nature. The present results are compared with the results obtained from classical continuum model, second & fourth-order strain gradient models, stress gradient model and Born–Karman model. If $\alpha = 0$ & $\nu = 0$, the wavenumber is directly proportional to wave frequency, which will give a nondispersive wave behavior (more details are given in ref. [9, 10]).

We will now generate some numerical results and compare the results obtained by the present lateral inertia model with all the other formulated models. This will bring out the effects that lateral inertia has on the wave parameters, namely the wavenumber and the group speeds. For the present analysis, a single-walled carbon nanotube is assumed as a nanorod. The values of the radius, thickness, Young's modulus and density are assumed as 3.5 nm, 0.35 nm, 1.03 TPa, and 2300 kg/m³, respectively.

The present results are compared with the results obtained from the following models, whose summary of equations are as follows :

1. Classical/Local Continuum Model

a. Constitutive relation:

$$\sigma(x) = E\varepsilon(x) \quad (6.72)$$

b. Governing differential equation:

$$\frac{\partial^2 u}{\partial x^2} = \frac{\rho}{E} \frac{\partial^2 u}{\partial t^2} \quad (6.73)$$

c. Dispersion relation:

$$k^2 - \frac{\rho}{E} \omega^2 = 0 \quad (6.74)$$

2. *Second-Order NLSiGM* (See Sect. 6.2)

a. Constitutive relation:

$$\sigma(x) = E \left[\varepsilon(x) + \alpha^2 \frac{\partial^2 \varepsilon(x)}{\partial x^2} \right] \quad (6.75)$$

b. Governing differential equation:

$$\alpha^2 \frac{\partial^4 u}{\partial x^4} + \frac{\partial^2 u}{\partial x^2} = \frac{\rho}{E} \frac{\partial^2 u}{\partial t^2} \quad (6.76)$$

c. Dispersion relation:

$$\alpha^2 k^4 - k^2 + \frac{\rho}{E} \omega^2 = 0 \quad (6.77)$$

3. *Fourth-Order NLSiGM* (See Sect. 6.2)

a. Constitutive relation:

$$\sigma(x) = E \left[\varepsilon(x) + \alpha^2 \frac{\partial^2 \varepsilon(x)}{\partial x^2} + \alpha^4 \frac{\partial^4 \varepsilon(x)}{\partial x^4} \right] \quad (6.78)$$

b. Governing differential equation:

$$\alpha^4 \frac{\partial^6 u}{\partial x^6} + \alpha^2 \frac{\partial^4 u}{\partial x^4} + \frac{\partial^2 u}{\partial x^2} = \frac{\rho}{E} \frac{\partial^2 u}{\partial t^2} \quad (6.79)$$

c. Dispersion relation:

$$-\alpha^4 k^6 + \alpha^2 k^4 - k^2 + \frac{\rho}{E} \omega^2 = 0 \quad (6.80)$$

4. *NLSGM* (See Sect. 6.1)

a. Constitutive relation:

$$\sigma(x) - \alpha^2 \frac{\partial^2 \sigma(x)}{\partial x^2} = E \varepsilon(x) \quad (6.81)$$

b. Governing differential equation:

$$\frac{\partial^2 u}{\partial x^2} + \frac{\rho}{E} \alpha^2 \frac{\partial^4 u}{\partial x^2 \partial t^2} = \frac{\rho}{E} \frac{\partial^2 u}{\partial t^2} \quad (6.82)$$

c. Dispersion relation:

$$-k^2 + \frac{\rho}{E} \alpha^2 \omega^2 k^2 + \frac{\rho}{E} \omega^2 = 0 \quad (6.83)$$

5. Born–Kármán model (Based on Lattice Dynamics) [12]

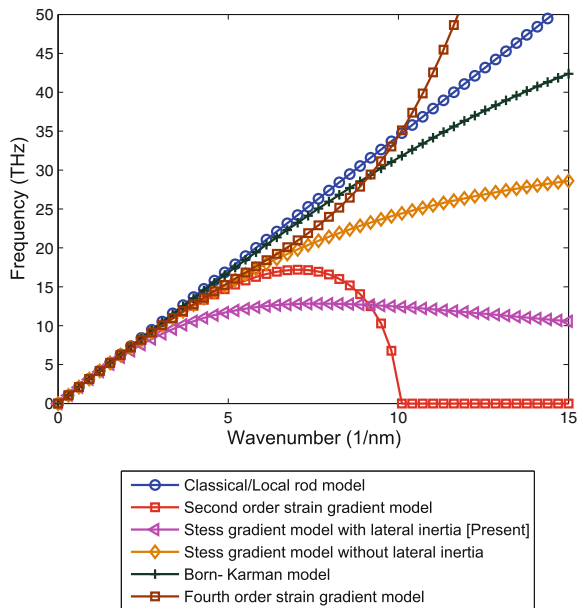
a. Dispersion relation:

$$\omega = \frac{2}{a} \sqrt{\frac{E}{\rho}} \sin\left(\frac{k \times a}{2}\right). \tag{6.84}$$

Figure 6.13 shows the variation of axial wavenumber of a nanorod with wave frequency. From Fig. 6.13, for a nanorod, it can be seen that there is only one mode of wave propagation, i.e., axial or longitudinal. For local or classical models, the wavenumbers for the axial mode have a linear variation with the frequency which is in the tera-hertz (THz) range. The linear variation of the wavenumbers denoted that the waves will propagate nondispersively, i.e, the waves do not change their shapes as they propagate. On the other hand, the wavenumbers obtained from strain gradient/nonlocal stress gradient models have a nonlinear variation with the frequency, which indicates that the waves are dispersive in nature. However, the wavenumbers of this wave mode have a substantial real part starting from the zero frequency. This implies that the mode starts propagating at any excitation frequency and does not have a cut-off frequency (refer Fig. 6.13).

The spectrum curves for nanorod obtained from both second and fourth-order strain gradient models are also shown in Fig. 6.13, for comparison. Both the strain gradient models exhibit dispersive nature of waves. It can also be seen that the fourth-order strain gradient model give improved approximation over the second-order strain gradient model, as compared to the classical continuum model (such observations

Fig. 6.13 A comparison of the wavenumber dispersion with wave frequency in a nanorod obtained from classical/local and nonlocal theories suggested in the literature with the present result, to show the effect of lateral inertia



are also made in Ref. [9]). Also, the results are compared with the Born–Karman model, as well as the nonlocal stress gradient model. It can be concluded that the instability of the second-order strain gradient model can be overcome by considering the inertia gradients used in the fourth-order NLStGM.

The effect of the scaling parameter on the wave dispersion relation in nanorod is shown in Fig. 6.14. As the nonlocal scaling parameter ($\alpha = e_0 a$) increases, the frequency of the wave will decrease with an increase in wavenumber. Here α values are assumed from 0.0 to 1.0 nm. As α tends to larger value, the wave frequency becomes very small at higher values of wavenumber as shown in Fig. 6.14. It can be seen that while dealing with the nonlocal elasticity theory including the effect of lateral inertia, one should not neglect the scaling parameter. Hence, the scaling parameter plays an important role while dealing with the dynamics of nanostructures.

The effect of radius of nanorod, on the wave dispersion relation based on the present formulation, is shown in Fig. 6.15. For the present analysis, we consider three different radii of nanorods i.e., 1.0, 2.0 and 5.0 nm. For comparison, the results obtained from local/classical elasticity are also shown in the same figure. As the radius of the nanorod increases, the wave frequency becomes almost constant for wavenumbers larger than 5.0 1/nm. The effect of the lateral inertia shows that as the radius of the nanorod increases, the wavenumber decreases and will not become constant irrespective of the wavenumber.

It can be concluded that the wave dispersion characteristics in a nanorod is drastically different for local and nonlocal models. The local model predicts that the wave will propagate at all frequencies, but the nonlocal model shows that the wave will propagate only up to certain frequencies depending on the nonlocal scaling parameter. It has also been shown that the unstable second-order strain gradient model can be replaced by considering the inertia gradient terms in the formulations.

Fig. 6.14 Wavenumber dispersion (including the effect of lateral inertia) with wave frequency in a nanorod for various values of the nonlocal scaling parameter (α)

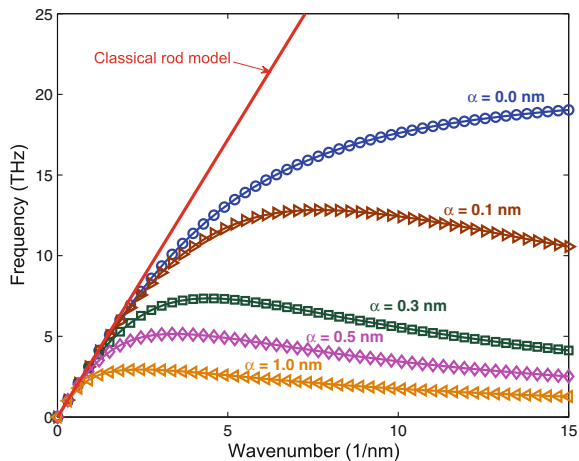
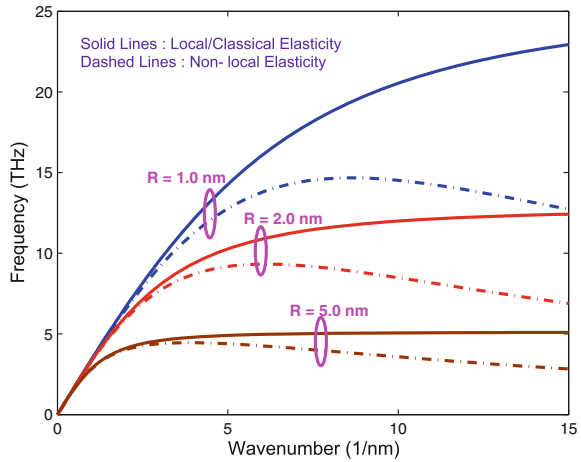


Fig. 6.15 Wavenumber dispersion (including the effect of lateral inertia) with wave frequency in a nanorod obtained from both the local and nonlocal formulations for different radii of nanorods



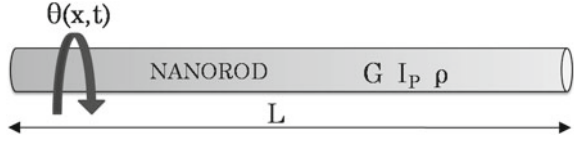
6.4 Torsional Wave Propagation in NLSGM Nan shafts

The majority of the literature on nonlocal elasticity exists pertaining to the free transverse and longitudinal vibration of micro/nanobeams (CNTs), nanoplates (graphene sheets), and nanoshells (carbon nanotubes). This is because the transverse modes are more prone to get excited by common types of external excitations. On the contrary, only limited works on nonlocal elasticity have been devoted to the torsional vibration and wave propagation of nanostructures. Nanorods when used as electromechanical resonator can be externally excited and they exhibit both axial and torsional vibrations. Therefore, there is a strong scientific need to gain an understanding of the torsional wave propagation of complex nan shafts system and the mathematical modeling of such phenomena.

Torsional wave propagation of CNTs is important to the design of different CNT-based torsional devices including but not limited to sensors, oscillators, gyroscopes, and torsional pendulums. It is therefore necessary to have a clear understanding of CNT behavior under torsional vibrations. In this section, a study of the dynamic torsional properties of CNTs is presented and dispersion relations of torsional waves are derived using a nonlocal shaft model and compared with those of classical models and results from molecular dynamics simulations.

Will first derive the governing differential equation. For this, let us consider a nan shafts as shown in Fig. 6.16. The nanorod is assumed to be of length L . General physical model to represent carbon nanotube include the nonlocal shell, nonlocal beam, or nonlocal shaft model. Here we will consider a simple one-dimensional nonlocal shaft model. The present work can also be extended to nonlocal beam and shell models. The nonlocal constitutive relation for shear stress in one-dimensional differential form can be simplified as

Fig. 6.16 A nanoshaft, showing length L , shear modulus G , density ρ , polar moment of inertia I_P , and torsional displacement $\theta(x, t)$



$$\mathcal{L}\sigma_S = G\epsilon_S \quad (6.85)$$

where $\mathcal{L} = 1 - (e_0a)^2\nabla^2$, G is the shear modulus, ϵ_S is the shear strain and σ_S is the shear stress of nanorod. The stress resultant due to shear stress is $Q_S = \int_A \sigma_S dA$ and the torque relation is $T_S = \int_A \sigma_S z dA$. Now using these shear stress resultant and the torque can be written as follows using Eq. (6.85)

$$\mathcal{L}Q_S = Q_S - (e_0a)^2 \frac{\partial^2 Q_S}{\partial x^2} = GA\epsilon_S, \quad (6.86)$$

$$\mathcal{L}T_S = T_S - (e_0a)^2 \frac{\partial^2 T_S}{\partial x^2} = GI_P \frac{\partial \theta}{\partial x} \quad (6.87)$$

where θ is the angular displacement and I_P is the polar moment of inertia of the cross-sections of the nanoshaft. Now considering an element of nanoshaft, the equation of motion can be written as

$$\left(T_S + \frac{\partial T_S}{\partial x} dx \right) - T_S + T_{EXT} dx = \rho I_P \frac{\partial^2 \theta}{\partial t^2} dx \quad (6.88)$$

where T_S and T_{EXT} are the induced torque and the external torque per unit length, respectively. The term $\rho I_P \frac{\partial^2 \theta}{\partial t^2} dx$ on the right hand side of Eq. (6.88) represents the inertia torque acting on the element of nanoshaft. The symbols ρ and t are the density of nanoshaft and time, respectively. Using Eqs. (6.87 and 6.88), we have

$$T_S = GI_P \frac{\partial \theta}{\partial x} + \rho I_P (e_0a)^2 \frac{\partial^3 \theta}{\partial x \partial t^2} - (e_0a)^2 \frac{\partial T_{EXT}}{\partial x} \quad (6.89)$$

Using Eqs. (6.87 and 6.89) ignoring the external torque we get the nonlocal governing equation of motion for torsional wave propagation in nan shafts as

$$GI_P \frac{\partial^2 \theta}{\partial x^2} - \rho I_P \frac{\partial^2 \theta}{\partial t^2} + \rho I_P (e_0a)^2 \frac{\partial^4 \theta}{\partial x^2 \partial t^2} = 0 \quad (6.90)$$

when we neglect the nonlocal small-scale effect (i.e., $e_0a = 0$), we get the conventional scale-free equation for torsional wave propagation in shafts.

Next, we will compute the wave numbers, group speeds and the escape velocities for the present model. For analyzing the ultrasonic wave dispersion characteristics in nanorods, we assume that a harmonic type of wave solution for the displacement

field $u(x, t)$ and it can be expressed in complex form as [10],

$$\theta(x, t) = \sum_{n=0}^{N-1} \hat{\theta}(x, \omega_n) e^{-j(k_\theta x - \omega_n t)} \tag{6.91}$$

where, N is the number of time sampling points. ω_n is the circular frequency at the n th time sample and $j = \sqrt{-1}$. Substituting Eq. (6.91) into the governing partial differential equation Eq. (6.90), we get the dispersion relation as follows. Hereafter, the subscript n in Eq. (6.91) is dropped for simplified notations.

$$-k_\theta^2 + (e_0 a)^2 \eta^2 \omega^2 k_\theta^2 + \eta^2 \omega^2 = 0 \tag{6.92}$$

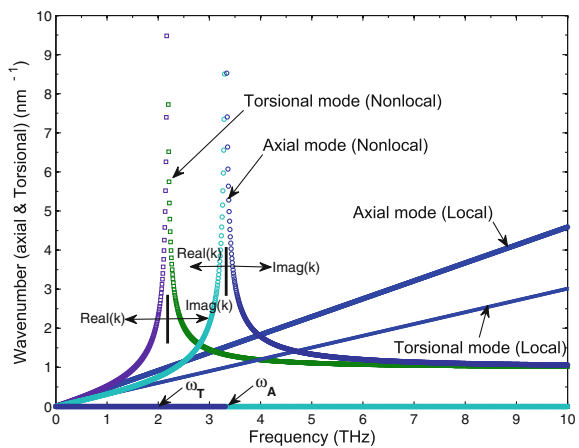
where $\eta = \sqrt{\frac{\rho I_P}{G I_P}}$. This dispersion relation is solved for the wavenumbers as

$$k_{\theta,1,2} = \pm \sqrt{\frac{\eta^2 \omega^2}{1 - (e_0 a)^2 \eta^2 \omega^2}} \tag{6.93}$$

The torsional wavenumber k_θ is a function of the wave frequency ω , the nonlocal scaling parameter $e_0 a$ and the material properties (G & ρ) of the nan shaft. If $e_0 a = 0$, we get the local wave behavior. Rest of the behavior for this model is very similar to the axial wave propagation of the NLSGM nanorods.

Figure 6.17 shows the spectrum relation plot as a function of nonlocal scale parameter $e_0 a$. From the figure, we see that at certain frequencies, the wavenumber is tending to infinity and this frequency value decreases with increase in the scale parameter. Its value can be analytically determined by looking at the wavenumber expression Eq. (6.93) and setting $k_\theta \rightarrow \infty$. Which is given as

Fig. 6.17 Wavenumber dispersion (spectrum relation) for a nan shaft obtained from both local and nonlocal elasticity models



$$\omega_{escape} = \frac{1}{(e_0 a) \eta} = \frac{1}{e_0 a} \sqrt{\frac{G}{\rho}} \quad (6.94)$$

The escape frequency is inversely proportional to the nonlocal scaling parameter and is independent of the diameter of the nanoshaft. The variation of the escape frequency with nonlocal scaling parameter is shown in Fig. 6.18.

Wave velocities can be computed as before. That is,

$$C_{phase} = \frac{\omega}{k_\theta} = \frac{1}{\eta} \left[1 - (e_0 a)^2 \eta^2 \omega^2 \right]^{1/2} \quad (6.95)$$

$$C_{group} = \frac{\partial \omega}{\partial k_\theta} = \frac{1}{\eta} \left[1 - (e_0 a)^2 \eta^2 \omega^2 \right]^{3/2} \quad (6.96)$$

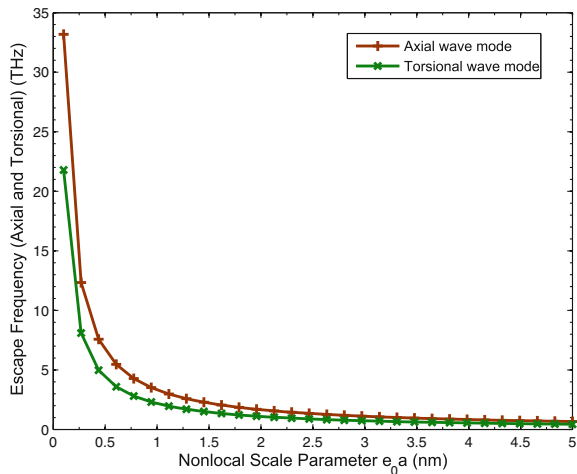
These wave speeds also depend on the nonlocal scaling parameter. When $e_0 a = 0$, both the wave speeds are equal (i.e., $C_{phase} = C_{group} = 1/\eta = \sqrt{G/\rho}$), which is already proved for local or classical bars/rods [10]. The phase speed and group speed dispersion curves with wave frequency are shown in Fig. 6.19a, b, respectively.

6.4.1 Numerical Results and Discussion

For the present analysis, a single-walled carbon nanotube is assumed as a nanoshaft. The values of the radius, thickness, Young's modulus, Poisson's ratio, and density are assumed as 2.0 nm, 0.1 nm, 3.03 TPa, 0.19 and 2300 kg/m³ [28], respectively.

Figure 6.17 shows the real and imaginary parts of the torsional wavenumber of a nanoshaft. The thick lines represent the real part and the thin lines show the imaginary

Fig. 6.18 Escape frequency variation with nonlocal scaling parameter of the axial and torsional waves in nanorod and nanoshaft



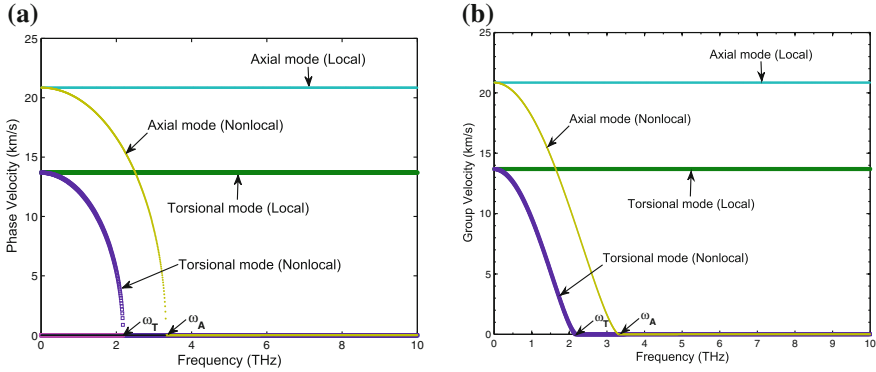


Fig. 6.19 Torsional and axial wave velocities in nanorod and nanoshaft (a) Phase velocity and (b) Group velocity

part of the wavenumbers. From Fig. 6.17, for a nanoshaft, it can be seen that there is only one mode of wave propagation, that is the torsional mode. For local or classical models, the wavenumbers for the torsional mode have a linear variation with the frequency which is in the THz range. As in the case of NLSGM nanorods, the wavenumbers obtained from nonlocal elasticity have a nonlinear variation with the frequency, which indicates that the waves are dispersive in nature. At escape frequency, as in the case of other nanorod models discussed earlier, the wavenumbers tend to infinity as shown in Fig. 6.17, beyond which no propagation occurs. For comparison, the axial wavenumbers in nanorod are also shown in Fig. 6.17. It can be observed that the axial wavenumbers in nanorod are higher than the torsional wavenumbers.

One important outcome of the nonlocal elasticity is the realistic prediction of the dispersion curve that is, frequency-wavenumber/wavevector relation. As shown in Eringen [29], the dispersion relation $\frac{\omega}{C_1 k} = (1 + (e_0 a)^2 k^2)^{-1/2}$, the nonlocal scale parameter $e_0 a$, closely matches with the Born–Karman model dispersion $\frac{\omega a}{C_1} = 2 \sin\left(\frac{ka}{2}\right)$ when $e_0 = 0.39$ is considered. However, among the two natural conditions at the mid-point and end of the first Brillouin zone, we have, $\left.\frac{d\omega}{dk}\right|_{k=0} = C_1$; $\left.\frac{d\omega}{dk}\right|_{k=\frac{\pi}{a}} = 0$ and among these relations, only first one is satisfied. It was suggested that two-parameter approximation of the kernel function will give better results. This is reiterated by Lazar et al. [30] that one parameter (only $e_0 a$) nonlocal kernel function will never be able to model the lattice dynamics relation and it is necessary to use the Bi-Helmholtz type equation with two different coefficients of nonlocality to satisfy all the boundary conditions. It is to be noted that the simple forms of the group and phase velocities that exist for isotropic materials permitted to tune the nonlocality parameters, so that the lattice dispersion relation is matched. Further, by virtue of the Helmholtz decomposition, only one-dimensional Brillouin zone needs to be handled. Although the general form of the boundary conditions, i.e., group speed is equal to phase speed (at $k = 0$) or zero (at $k = \pi/a$), is still

applicable, the expressions are difficult to handle. This is because, the Brillouin zone is really a two-dimensional region where four boundary conditions are involved.

The escape frequencies are purely a function of the nonlocal scaling parameter. The variation of the escape frequency with nonlocal parameter is shown in Fig. 6.18. It can also be observed that, the escape frequencies of axial waves in nanorod are higher than the torsional waves. It shows that, as e_0a increases the escape frequency decreases, such variation can also be observed from Fig. 6.17. For very small values of e_0a , the escape frequencies are very large, and at higher values of e_0a the escape frequencies are very small and approach to a constant value.

Figure 6.19, plots the wave speeds (i.e., both phase and group) for the nanoshaft obtained from both local and nonlocal models. It is now well-known that in nonlocal elasticity, the wavenumber tends to infinity at escape frequencies, so that the phase speeds (see Fig. 6.19a) and group speeds (see Fig. 6.19b) are tending to zero at those frequencies, indicating localization and stationary behavior. Both the wave speeds are higher in axial wave case as compared to the torsional wave case in the nanorod. These predictions are similar to other nonlocal models.

6.5 Spectral Finite Element Formulation

A structure can be thought of as a system of connected waveguides that transmits different types of waves in a system. As we have seen in this chapter, wave propagation analysis is always based on the governing elastodynamic equations. This is best accomplished by performing spectral analysis, which gives the wavenumbers and wave speeds, as was shown in this chapter. The solution of wave equation can be expressed as a combination of different waves, and these are expressed in terms of complex exponentials containing the wavenumbers. Using the variational approach in the frequency domain, by using the exact solution to the wave equation as in interpolation function, we can derive a dynamic stiffness matrix for each waveguide segment. Thus, the response of each and every structural member is described by a stiffness matrix in the frequency space, which is appropriately called a spectral finite element. The classical static stiffness matrix is actually obtained from the spectral stiffness matrix in a zero-frequency limit. By connecting all the elements (or waveguides) according to the spatial geometry, a global stiffness matrix is constructed and a global response due to a specified impulse is studied first by going over all the frequencies and then by transforming to the time domain, which is conveniently done by the fast Fourier transform (FFT). The details of this method are given in [9, 10, 31].

Application of the finite element method (FEM) for wave propagation requires a very fine mesh to capture the mass distribution accurately. The mesh size should be comparable to the wavelengths, which are very small at high frequencies. Hence, the problem size increases enormously. Many applications in smart structure applications, such as structural health monitoring or active wave control in composite structures, require wave-based modeling since one has to use high-frequency inter-

rogating signals. If one needs online diagnostic tools in structures, wave-based modeling is an absolute one. For such problems, the FEM by itself cannot be used as a modeling tool as it is very expensive from the computational viewpoint. Hence, one needs an alternate formulation wherein the frequency content of the exciting signal is not an issue. That is, we need a modeling tool that can give a smaller problem size for high-frequency loading, at the same time retaining the matrix structure of the FEM. Such a technique is feasible through the spectral finite element (SFEM) technique [9, 10].

It is not enough to have the expressions of the wavenumbers or phase speeds with matched dispersion relation. To visualize the manifestation of these speeds, it is necessary to develop a tool for analyzing the nonlocal media subjected to high frequency loading. The convolution integral form of the nonlocal theory of elasticity naturally suggests that integral transform-based method of solving partial differential equation will enjoy superiority as compared to the conventional FEM. One such method is the SFEM.

The SFEM, popularized by the senior author of this book [10], is an integral transform-based method with the matrix structure of FEM. The SFEM is the FEM formulated in the frequency domain and wavenumber space. That is, these elements will have interpolating functions that are complex exponentials or Bessel functions. These interpolating functions are also functions of the wavenumbers. For example, a governing partial 1-D wave equation, when transformed into the frequency domain using DFT, removes the time derivative and reduces the PDE to a set of ODEs, which have complex exponentials as solutions. In the SFEM, we use these exact solutions as the interpolating functions. As a result, the mass is distributed exactly and hence, one single element is sufficient between any two discontinuities to get an exact response, irrespective of the frequency content of the exciting pulse. That is, one SFEM can replace hundreds of FEMs normally required for wave propagation analysis. Hence, the SFEM is an ideal candidate for developing online health monitoring software. In addition to smaller system sizes, other major advantages of the SFEM include the following:

- Since the formulation is based on the frequency domain, system transfer functions are the direct byproduct of the approach. As a result, one can perform inverse problems such as force identification/system identification in a straightforward manner.
- The approach gives the dynamic stiffness matrix as a function of frequency, directly from the formulation. Hence, we have to deal with only one element of dynamic stiffness as opposed to two matrices in the FEM (stiffness and mass matrices).
- Since different normal modes have different amounts of damping at various frequencies, by formulating the elements in the frequency domain one can treat the complex damping mechanisms more realistically.
- The SFEM lets you formulate two sets of elements, one is the finite length element and the other is the infinite element or *throw-off element*. This *throw-off element* acts as a conduit of energy out of the system. There are various uses of this infinite *throw-off element*, such as adding maximum damping, obtaining good resolution

of the responses in the time domains and also in modeling large lengths, which are computationally very expensive to model in the FEM.

- The SFEM is probably the only technique that gives you responses in both the time and frequency domains in a single analysis.

The SFEM can be formulated in a similar manner to the FEM by writing the ‘weak form’ of the governing differential equation and substituting the assumed functions for displacements and integrating the resulting expression. Since the functions involved are much more complex, integration of these functions in the ‘closed form’ takes a longer time. In addition, by this approach we cannot obtain the dynamic stiffness matrix of the ‘throw-off element’, as the latter is normally complex. Hence, we adopt an equilibrium approach of element formulation, which eliminates integration of the complex functions. In this chapter, we show this formulation for a simple isotropic rod element, while the procedure remains the same for other elements.

Formulation of the spectral elements requires determination of the spectrum relation (wavenumber vs. frequency). The SFEM begins with transformation of the governing equation into the frequency domain by using a discrete Fourier transform. The solution of this transformed equation becomes the interpolating function for the spectral element formulation. The procedure of formulating the SFEM for a simple 1-D nanorod is illustrated below.

Figure 6.20 shows a rod subjected to dynamic forces at two ends. The fundamental equation on the longitudinal wave in a nanorod element is obtained first.

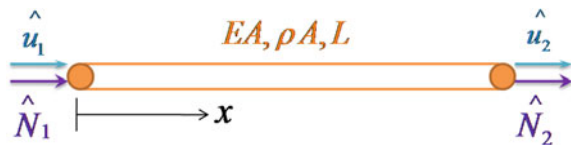
6.5.1 Frequency Dependent Shape Functions

The nonlocal elastodynamic equation governing the axial response of a nanorod (assuming zero external forcing) is given in Eq. (6.9). This time-domain equation is transformed into frequency domain using Discrete Fourier Transform (DFT). Here the main variable that needs transformation is the axial deformation $u(x, t)$ and its DFT can be written as

$$u(x, t) = \sum_n \hat{u}_n(x, \omega_n) e^{i\omega_n t} = \hat{u}(x, \omega) e^{i\omega t} \quad (6.97)$$

where ω_n are the circular frequencies and \hat{u}_n are the spatially dependent Fourier coefficients, often named the spectral components of axial displacement. For short-

Fig. 6.20 Nodal Loads and degree of freedom for the longitudinal spectral element



hand, the summation and subscript n will be omitted in the following, as shown in the last part of Eq. (6.97).

Substituting Eqs. (6.97) into Eq. (6.9) will yield the Helmholtz equation corresponding to the 1-D wave Eq. (6.9) set up over the domain X of size L ,

$$\frac{d^2\hat{u}}{dx^2} + \left(\frac{\omega^2}{\eta - (e_0a)^2\omega^2} \right) \hat{u} = 0, \quad (6.98)$$

where $\eta = \sqrt{\rho/E}$. Then, the spectral matrix expresses a connection between the kinematic and the dynamic quantities, i.e., $\{\hat{u}_1, \hat{u}_2\}$ with $\{\hat{F}_1, \hat{F}_2\}$ at both ends of the rod: 1 and 2. The hat signifies that the quantities are in the frequency space. The derivation of the spectral stiffness matrix is carried out as follows.

The wave solution of Eq. (6.98) for a finite nanorod element with length L can be obtained as

$$\hat{u}(x, \omega) = C_1 e^{-ik_1 x} + C_2 e^{-ik_1(L-x)} = \begin{bmatrix} e^{-ikx} & e^{-ik(L-x)} \end{bmatrix} \begin{Bmatrix} C_1 \\ C_2 \end{Bmatrix} \quad (6.99)$$

where k_1 is the wavenumber of the nanorod defined in Eq. (6.93) with boundary conditions $u(x=0) = \hat{u}_1$, $u(x=L) = \hat{u}_2$. The coefficients C_1 and C_2 can be represented in terms of the nodal displacements \hat{u}_1 and \hat{u}_2 defined at two end nodes 1 and 2 of the rod element, as follows

$$\begin{Bmatrix} C_1 \\ C_2 \end{Bmatrix} = \frac{1}{1 - e^{-i2kL}} \begin{bmatrix} 1 & -e^{-ikL} \\ -e^{-ikL} & 1 \end{bmatrix} \begin{Bmatrix} \hat{u}_1 \\ \hat{u}_2 \end{Bmatrix} \quad (6.100)$$

The spectral displacement $\hat{u}(x)$ of Eq. (6.99) can be rewritten in terms of the nodal displacements \hat{u}_1 and \hat{u}_2 by substituting Eq. (6.100) into Eq. (6.99). That is

$$\hat{u}(x, \omega) = \hat{G}_1(x)\hat{u}_1 + \hat{G}_2(x)\hat{u}_2 \quad (6.101)$$

where

$$\hat{G}_1(x) = \frac{e^{-ikx} - e^{-ik(2L-x)}}{1 - e^{-i2kL}} \quad (6.102)$$

$$\hat{G}_2(x) = \frac{-e^{-ik(L+x)} + e^{-ik(L-x)}}{1 - e^{-i2kL}} \quad (6.103)$$

Functions $\hat{G}_1(x)$ and $\hat{G}_2(x)$ are the frequency dependent rod shape functions or exact shape functions. The significance of these shape functions is that the complete description of the element is captured in the two nodal degree of freedom \hat{u}_1 and \hat{u}_2 .

6.5.2 Dynamic Stiffness Matrix

Since the spectral element can be very long then the ability to compute the response between nodes is necessary. This can be done conveniently using the shape function and the nodal values. Thus, the displacements and membrane forces are obtained simply as

$$\hat{u}(x, \omega) = \hat{G}_1(x)\hat{u}_1 + \hat{G}_2(x)\hat{u}_2 \quad (6.104)$$

$$\hat{N}(x, \omega) = (EA - \rho A(e_0a)^2\omega^2)\frac{d\hat{u}(x)}{dx} = (EA - \rho A(e_0a)^2\omega^2)\left[\frac{d\hat{G}_1(x)}{dx}\hat{u}_1 + \frac{d\hat{G}_2(x)}{dx}\hat{u}_2\right] \quad (6.105)$$

The member loads at each end of the rod are related to the displacements by (see Fig. 6.16)

$$\hat{N}_1 = -\hat{N}(x=0) = -(EA - \rho A(e_0a)^2\omega^2)\left[\frac{d\hat{G}_1(x)}{dx}\Big|_{x=0}\hat{u}_1 + \frac{d\hat{G}_2(x)}{dx}\Big|_{x=0}\hat{u}_2\right] \quad (6.106)$$

$$\hat{N}_2 = +\hat{N}(x=L) = +(EA - \rho A(e_0a)^2\omega^2)\left[\frac{d\hat{G}_1(x)}{dx}\Big|_{x=L}\hat{u}_1 + \frac{d\hat{G}_2(x)}{dx}\Big|_{x=L}\hat{u}_2\right] \quad (6.107)$$

The dynamic stiffness of the two-noded element can now be written in matrix form from Eqs. (6.106, 6.107),

$$\begin{Bmatrix} \hat{N}_1 \\ \hat{N}_2 \end{Bmatrix} = (EA - \rho A(e_0a)^2\omega^2)\begin{bmatrix} -\frac{d\hat{G}_1(x)}{dx}\Big|_{x=0} & -\frac{d\hat{G}_2(x)}{dx}\Big|_{x=0} \\ \frac{d\hat{G}_1(x)}{dx}\Big|_{x=L} & \frac{d\hat{G}_2(x)}{dx}\Big|_{x=L} \end{bmatrix}\begin{Bmatrix} \hat{u}_1 \\ \hat{u}_2 \end{Bmatrix} \quad (6.108)$$

Here, the frequency-dependent dynamic element stiffness matrix for the nanorod is

$$[\hat{K}_{dyn}]_{SFEM} = (EA - \rho A(e_0a)^2\omega^2)\begin{bmatrix} -\frac{d\hat{G}_1(x)}{dx}\Big|_{x=0} & -\frac{d\hat{G}_2(x)}{dx}\Big|_{x=0} \\ \frac{d\hat{G}_1(x)}{dx}\Big|_{x=L} & \frac{d\hat{G}_2(x)}{dx}\Big|_{x=L} \end{bmatrix} = \begin{bmatrix} K_{11} & K_{12} \\ K_{21} & K_{22} \end{bmatrix} \quad (6.109)$$

The simplified dynamic stiffness matrix can be obtained by using Eqs. (6.102 and 6.103), which gives a symmetric matrix. The elements of the dynamic stiffness matrix are function of the nonlocal scaling parameter. In general, the dynamic stiffness is complex but in special case of a simple rod with no damping, the matrix is real only. This is discussed more detail in the next subsection. For comparison, we write the dynamic stiffness of a conventional finite element for a local elasticity model is given by

$$[\hat{K}_{dyn}]_{FEM} = [K] - \omega^2[M] = \frac{EA}{L} \begin{bmatrix} 1 & -1 \\ -1 & 1 \end{bmatrix} - \omega^2 \frac{\rho AL}{6} \begin{bmatrix} 1 & 1 \\ 1 & 2 \end{bmatrix} \quad (6.110)$$

6.5.3 Numerical Results and Discussion

The frequency-dependent exact shape functions ($\hat{G}_1(x)$ and $\hat{G}_2(x)$) of the nanorod obtained from local and nonlocal elasticities are shown in Figs. 6.21 and 6.22 for various frequencies [32]. The $\hat{G}_1(x)$ variation with nondimensional length of nanorod (x/L) is shown for 1, 5, 10, and 15 THz frequencies. These functions occur in pairs, where one member of the pair is the *mirror image* of the other. It has been observed that the shape functions are also affected by the nonlocal scale at higher frequencies (see Figs. 6.21 and 6.22). For $e_0a = 0$ and $e_0a = 0.5$ nm, the difference between shape function variation at various frequencies is negligible. At $e_0a = 1.0$ nm, the difference is not negligible especially at higher frequencies. The effect of e_0a on the frequency-dependent shape functions is considerable at higher frequencies, i.e., for > 10 THz. This effect is same for both the functions, i.e., $\hat{G}_1(x)$ and $\hat{G}_2(x)$. Such effects are helpful in analyzing the wave behavior and the vibration behavior in nanoscale structures very accurately using spectral finite element method. Hence, both the frequency-dependent shape functions and the dynamic stiffness matrix are considerably altered due to scale parameter e_0 .

A special characteristic of two-noded spectral elements is that they have an infinite frequency. That is, all the vibrational modal information is contained in the 2×2 spectral stiffness matrix given by Eq. (6.109). Figure 6.23 gives a comparison of some stiffness coefficients of the SFEM and FEM at very low and medium frequencies. We see that at low frequencies they practically match each other. At medium frequencies, we see that the stiffness coefficients differ substantially. We can make the FEM stiffness match the spectral stiffness if we use many elements to model the rod. This is one of the reasons why the model sizes of the SFEM are very small.

The conventional stiffness is monotonic in frequency and \hat{K}_{11} , for example, goes through zero only once. The spectral dynamic stiffness, on the other hand, has many zeros as seen from broader frequency plot of Figs. 6.24b and 6.25b. The SFEM computer code has many resemblances to the FEM code. That is, as in the FEM, the element dynamic stiffness matrix is generated, assembled, and solved. However, all of these operations have to be performed for each frequency. Since the system sizes are small, these do not pose a major computational problem. The significant difference, from a practical point of view, between the two formulations is that the number of rod segments in the present formulation need only coincide with the number of discontinuities. Thus, only one element needs to be used per uniform segment. This can result in an enormous reduction in the size of the matrices to be solved.

The frequency-dependent dynamic element stiffness is plotted against lower and higher frequencies in Figs. 6.24 and 6.25 for local and nonlocal elasticity theories. It has been observed that there is a perfect matching of the dynamic stiffness elements (\hat{K}_{11} and \hat{K}_{12}) for frequencies $< \sim 1$ THz (clearly seen from Figs. 6.24a and 6.25a),

Fig. 6.21 Frequency-dependent exact shape function $\hat{G}_1(x)$ of the nanorod for (a) local elasticity $e_0a = 0$, (b) nonlocal elasticity $e_0a = 0.5 \text{ nm}$ and (c) $e_0a = 1.0 \text{ nm}$

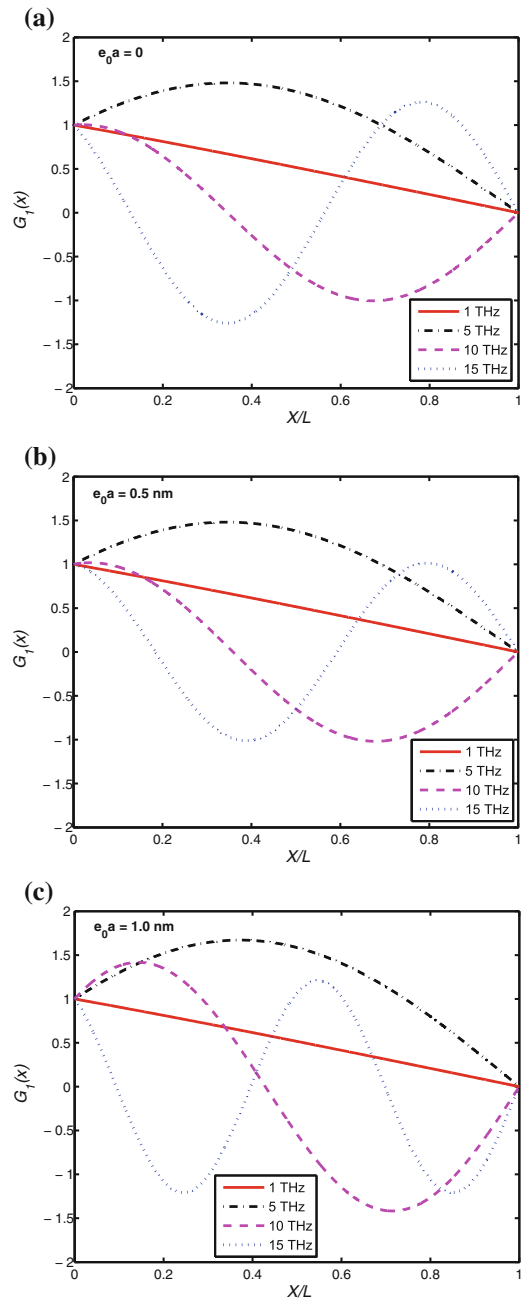
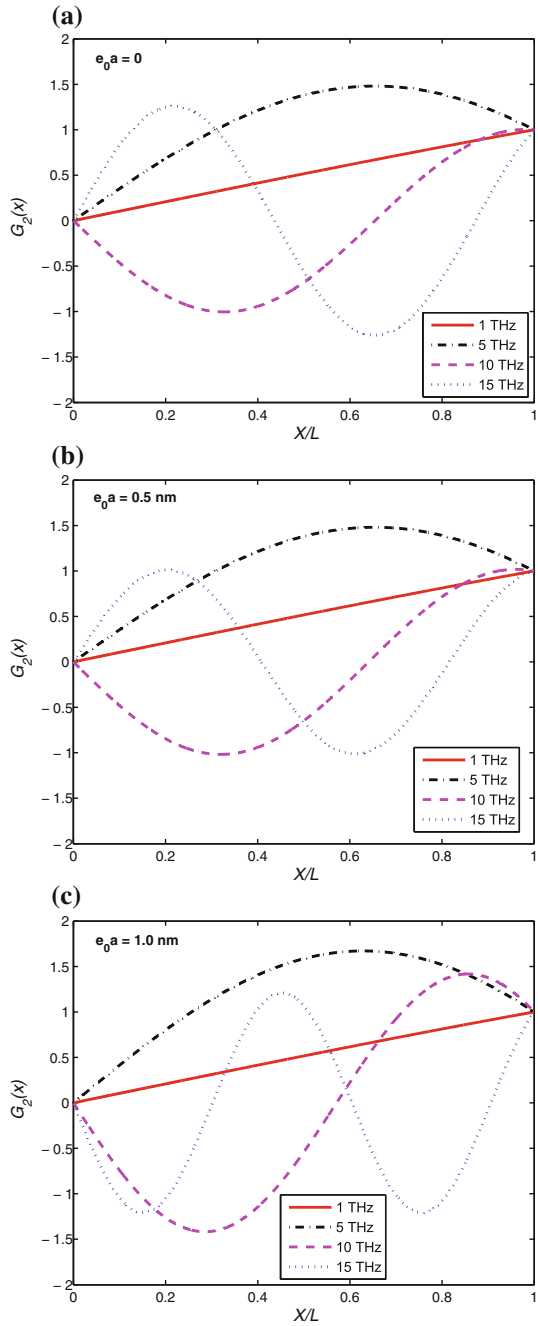


Fig. 6.22 Frequency-dependent exact shape function $\hat{G}_2(x)$ of the nanorod for (a) local elasticity $e_0a = 0$, (b) nonlocal elasticity $e_0a = 0.5$ nm and (c) $e_0a = 1.0$ nm



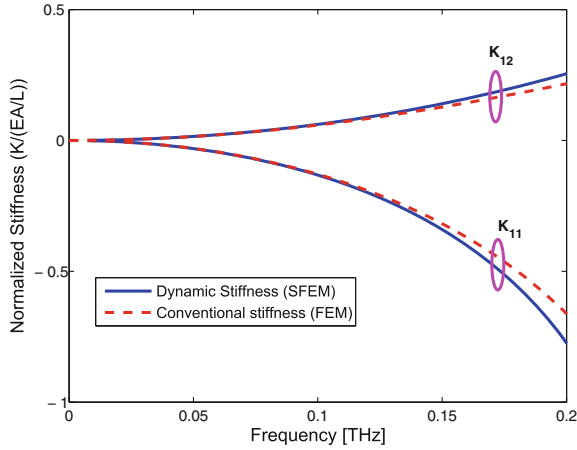


Fig. 6.23 Dynamic stiffness comparison between spectral finite element method (SFEM) and conventional finite element method (FEM)

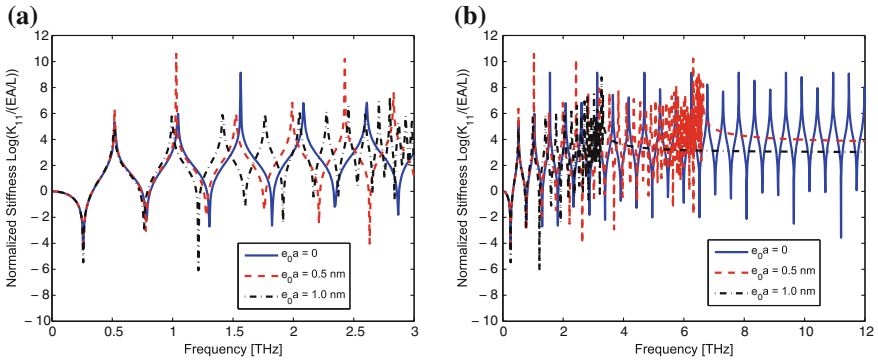


Fig. 6.24 Dynamic stiffness (\hat{k}_{11}) behavior at (a) Lower frequencies and (b) Higher frequencies

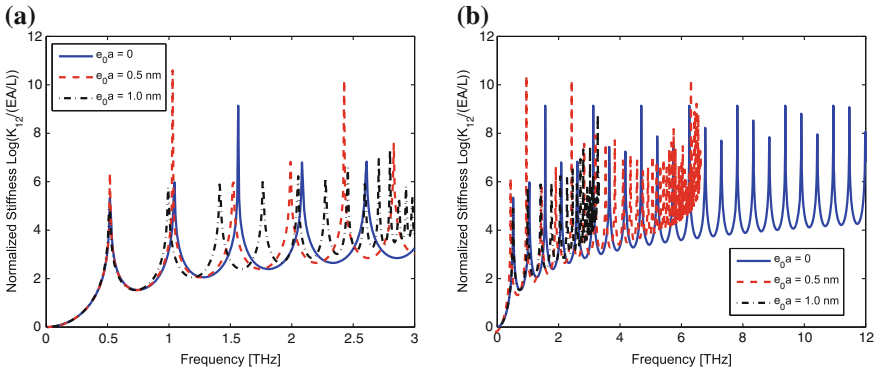


Fig. 6.25 Dynamic stiffness (\hat{k}_{12}) behavior at (a) Lower frequencies and (b) Higher frequencies

for $e_0a = 0, 0.5$ and 1.0 nm. For higher frequencies the effect of e_0a on dynamic stiffness of nanorod is quite considerable. In Fig. 6.24b, it can be seen that the relation between dynamic stiffness and frequency can be seen upto certain frequencies only depending on the values of nonlocal small-scale parameter. Such frequencies are called as escape frequencies. For $e_0a = 0$, the escape frequency occurs at infinite frequency. For $e_0a = 0.5$ nm and 1.0 nm, the escape frequencies are 6.803 THz and 3.338 THz, respectively. Such behavior can also observed from Fig. 6.25b.

Spectral FEM approach is limited to only those waveguides whose governing partial differential equation is exactly solvable. For many complicated nonlocal models, the governing equations are difficult to solve. In such cases, the matrix methodology of the present method enables the coupling of the SFE and the conventional finite element as was done in [33] to model cracks and holes in a macro waveguide with discontinuities.

The governing equation for nonlocal torsional wave propagation is very similar to that of the axial wave propagation model. Hence, the form of the dynamic stiffness for torsional wave propagation in nan shafts is very similar to the axial wave propagation model Eq. (6.109). That is, the same matrix can be used to perform the torsional wave propagation studies in nan shafts with the following substitution:

1. $u(x, t)$ replaced by $\theta(x, t)$ in Eq. (6.97)
2. $\eta = \sqrt{\rho/E}$ in Eq. (6.98) be replaced by $\eta = \sqrt{\rho/G}$ (for more details see [34]).

6.6 Summary

The nonlocal elasticity theory has been incorporated into classical rod model to capture unique features of the nanorods. The strong effect of the nonlocal scale parameter has been obtained, which leads to substantially different axial wave behaviors of nanorods from those of classical rods. Explicit expressions are derived for wavenumbers and wave speeds of nanorods. The studies also show that the nonlocal scale parameter introduces certain band gap region (without any periodicity) in axial wave mode where no wave propagation occurs. This is manifested in the spectrum curves as the region where the wavenumber tends to infinite (or wave speed tends to zero).

Next, the ultrasonic wave dispersion characteristics of a nanorod are analyzed using nonlocal second and fourth-order strain gradient models. It is shown that the second-order strain gradient model can become unstable and uniqueness is not guaranteed. The wave analysis in nanorod shows that the fourth-order strain gradient model gives prediction that is better than the second-order strain gradient model. The second-order strain gradient model gives a critical wavenumber at certain wave frequency, where the wave speed is zero. The ultrasonic wave characteristics of the nanorod obtained from the nonlocal strain gradient models are compared with the classical continuum model. A relation among the number of waves along the nanorod, the nonlocal scaling parameter, and the length of the nanorod is obtained

from the nonlocal second-order strain gradient model. The effect of nonlocal scaling parameter and the length of the nanorod on the number of waves along the nanorod are also captured in this work. Finally, the dynamic response behavior of nanorods is explained from both the strain gradient models. After this, the nonlocal elasticity theory has been incorporated into classical rod model by considering the lateral inertia effect to capture unique features of the nanorods. It is shown that the unstable second-order strain gradient model presented in the literature can be made stable by considering the inertia gradient terms in the formulations. The effect of the nonlocal small-scale parameter and the size of the nanorod on the wavenumber dispersion relation are also investigated in the present chapter.

Toward the end, the SFE formulation of nanorods is presented. The exact shape functions (frequency dependent) and dynamic stiffness matrix are obtained as function of nonlocal scale parameter. It is found that the small scale parameter, considerably alters the exact shape functions and the elements of the dynamic stiffness matrix.

In the next chapter, we will discuss the the flexural wave propagation in one-dimensional nanostructures such as nanobeams as a logical extension of this chapter.

References

1. H.W. Kroto, J.R. Heath, S.C. O'Brien, R.F. Curl, R.E. Smalley, C60—Buckminsterfullerene. *Nature* **318**, 162–163 (1985)
2. B.O. Dabbousi, J. RodriguezViejo, F.V. Mikulec, J.R. Heine, H. Mattoussi, R. Ober, K.F. Jensen, M.G. Bawendi, (CdSe)ZnS core-shell quantum dots: Synthesis and characterization of a size series of highly luminescent nanocrystallites. *J. Phys. Chem. B* **101**, 9463–9475 (1997)
3. J.L. Vossen, W. Kern, *Thin Film Process*. (Academic Press Inc., London, 1978)
4. S.D. Senturia, *Microsystem Design* (Kluwer Academic Publishers, Norwell, 2001)
5. C.R. Martin, Membrane-based synthesis of nanomaterials. *Chem. Mater.* **8**, 1739–1746 (1996)
6. V.A. Fonoberov, A.A. Balandin, Low-frequency vibrational modes of viruses used for nano-electronic self-assemblies. *Phys. Status Solidi B* **241**, R67–R69 (2004)
7. A.C. Eringen, On differential equations of nonlocal elasticity and solutions of screw dislocation and surface waves. *J. Appl. Phys.* **54**, 4703 (1983)
8. A.C. Eringen, *Non-local Polar Field Models* (Academic Press, New York, 1996)
9. J.F. Doyle, *Wave Propagation in structures* (Springer-Verlag Inc., New York, 1997)
10. S. Gopalakrishnan, A. Chakraborty, D.R. Mahapatra, *Spectral Finite Element Method: Wave Propagation, Diagnostics and Control in Anisotropic and Inhomogenous Structures* (Springer-Verlag Landon Ltd, London, 2008)
11. S. Narendar, S. Gopalakrishnan, Nonlocal scale effects on ultrasonic wave characteristics of nanorods. *Phys. E: Low-dimensional Syst. Nanostruct.* **42**, 1601–1604 (2010)
12. X. Zhang, K. Kun, P. Sharma, B.I. Yakobson, An atomistic and non-classical continuum field theoretic perspective of elastic interactions between defects (force dipoles) of various symmetries and application to graphene. *J. Mech. Phys. Solids* **54**, 2304–2329 (2006)
13. H. Askes, A.S.J. Suiker, L.J. Sluys, A classification of higher order strain-gradient models-linear analysis. *Archeive Appl. Mech.* **72**, 171–188 (2002)
14. L.J. Sluys, *Wave propagation, Localisation and Dispersion in Softening Solids* (Delft University of Technology, Dordrecht, 1992)

15. H.B. Mühlhaus, E.C. Aifantis, A variational principle for gradient plasticity. *Int. J. Solids Struct.* **28**, 845–857 (1991)
16. N. Triantafyllidis, S. Bardenhagen, On higher gradient continuum theories in 1-D non-linear elasticity. Derivation from and comparison to corresponding discrete models, *J. Elast.* **33**, 259–293 (1993)
17. C.S. Chang, J. Gao, Second-gradient constitutive theory for granular material with random packing structure. *Int. J. Solids Struct.* **32**, 2279–2293 (1995)
18. H.B. Mühlhaus, F. Oka, Dispersion and wave propagation in discrete and continuous models for granular materials. *Int. J. Solids Struct.* **33**, 2841–2858 (1996)
19. B.S. Altan, E.C. Aifantis, On some aspects in the special theory of gradient elasticity. *J. Mech. Behav. Mater.* **8**, 231–282 (1997)
20. H. Askes, A.S.J. Suiker, L.J. Sluys, Dispersion analysis and element-free Galerkin simulations of higher-order strain gradient models. *Mater. Phys. Mech.* **3**, 12–20 (2001)
21. N.W. Ashcroft, M.N. David, *Solid State Physics* (Rinehart and Winston, New York, 1976)
22. J. Peddieson, G.R. Buchanan, R.P. McNitt, Application of nonlocal continuum models to nanotechnology. *Int. J. Eng. Sci.* **41**, 305–312 (2003)
23. S. Narendar, S. Gopalakrishnan, Ultrasonic wave characteristics of nanorods via nonlocal strain gradient models. *J. Appl. Phys.* **107**, 084312 (2010)
24. A.E.H. Love, *A Treatise on the Mathematical Theory of Elasticity*, 4th edn. (Cambridge University Press, Cambridge, 1927)
25. A. Graff, *Wave Motion in Elastic Solids* (Dover Publications, New York, 1995)
26. T.G. Zhang, T.X. Yu, A note on a velocity sensitive energy-absorbing structure. *Int. J. Impact Eng.* **8**, 43–51 (1989)
27. S. Narendar, Terahertz wave propagation in uniform nanorods: a nonlocal continuum mechanics formulation including the effect of lateral inertia. *Phys. E: Low-dimensional Syst. Nanostruct.* **43**, 1015–1020 (2011)
28. G. Cao, X. Chena, J.W. Kysarb, Thermal vibration and apparent thermal contraction of single-walled carbon nanotubes. *J. Mech. Phys. Solids* **54**, 1206–1236 (2006)
29. A.C. Eringen, Linear theory of non-local elasticity and dispersion of plane waves. *Int. J. Eng. Sci.* **10**, 425–435 (1972)
30. M. Lazar, G. Maugin, E.C. Aifantis, On the theory of nonlocal elasticity of bi-helmholtz type and some applications. *Int. J. Solids Struct.* **43**, 1404–1421 (2006)
31. U. Lee, *Spectral Finite Element Method* (Cambridge University Press, Cambridge, 2009)
32. S. Narendar, S. Gopalakrishnan, Spectral finite element formulation for nanorods via nonlocal continuum mechanics. *J. Appl. Mech.* **78**(6), 061018 (2011)
33. S. Gopalakrishnan, J.F. Doyle, Spectral super-elements for wave propagation in structures with local nonuniformities. *Comput. Methods Appl. Mech. Eng.* **121**, 77–90 (1995)
34. S. Narendar, Spectral finite element and nonlocal continuum mechanics based formulation for torsional wave propagation in nanorods, *Finite. Elem. Anal. Des.* **62**, 65–75 (2012)

Chapter 7

Wave Propagation in 1D-Nanostructures: Nanobeams

Nanobeams are those which undergo flexural or transverse motion in lateral directions. The cross-sections of such nanostructures could be rectangular or circular. Some of the nano thin films, which find applications in Nano Electro Mechanical Systems (NEMS) is normally idealized as nanobeam with rectangular cross-section, while SWCNT undergoing transverse vibration, are normally idealized as nanobeams with circular cross-section. There are two different theories that describe the motion of beams. The first is the Euler–Bernoulli beam theory, which is also called the elementary beam theory. In this theory, rotation of the cross-section is derived from the transverse motion and the plane sections are assumed plane before and after bending. The second theory is called the Timoshenko beam theory, which is also called the First-order shear deformation Theory (FSDT). In this theory, the rotation of the cross-section is considered as independent motion and not derived from transverse deformation. Due to shear deformation effects, the plane sections do not remain plane after the bending of the section. The main aim of this chapter is to study the effect of nonlocal scale parameter on the transverse wave propagation in nanobeams. As before, we will use spectral analysis, outlined in Chap. 2, to perform this study. Some of the analysis performed in this chapter are the following:

- Wave propagation in general 1D nanobeams using NLSGM,
- Wave propagation in rotating nanobeams,
- Wave propagation in SWCNT carrying fluids,
- Wave propagation in nanobeams subjected to magnetic field, and
- Surface effects on flexural wave propagation in nanobeams.

7.1 NLSM for Euler–Bernoulli Nanobeams

Nanobeams such as carbon nanotubes are central elements to new devices. Let us consider a nanobeam under the action of stress resultants shown in Fig. 7.1.

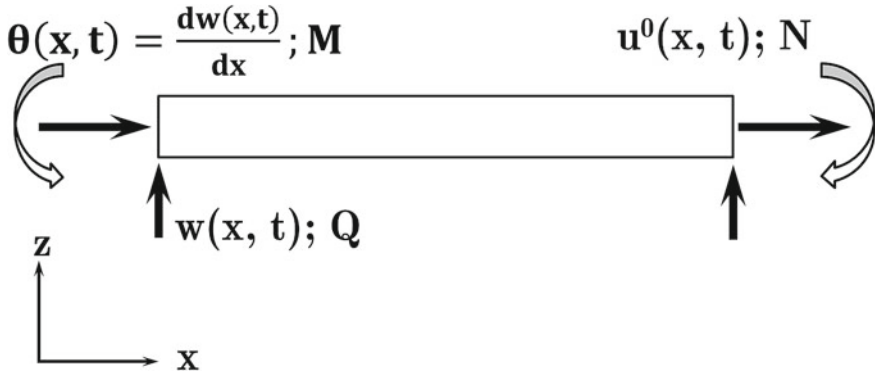


Fig. 7.1 A nanobeam under the action of its stress resultants

Considering the elementary Euler–Bernoulli theory of beams, the axial and transverse displacement fields of a rotating beam can be represented [1]

$$u(x, z, t) = u^0 - z \frac{\partial w}{\partial x} \quad (7.1)$$

$$w(x, z, t) = w(x, t) \quad (7.2)$$

where w is transverse displacements of the point $(x, 0)$ on the middle plane (i.e., $z = 0$) of the beam. The only nonzero strain of the Euler–Bernoulli beam theory, accounting for the strain is the axial strain given by

$$\varepsilon_{xx} = \frac{\partial u}{\partial x} = \frac{\partial u^0}{\partial x} - z \frac{\partial^2 w}{\partial x^2} \quad (7.3)$$

This is also called as bending strain. The equations of motion of the Euler–Bernoulli beam theory in terms of stress resultants are given by

$$\frac{\partial Q}{\partial x} = \rho A \frac{\partial^2 u^0}{\partial t^2} \quad (7.4)$$

$$\frac{\partial^2 M}{\partial x^2} = \rho A \frac{\partial^2 w}{\partial t^2} \quad (7.5)$$

where

$$Q = \int_A \sigma_{xx} dA, \quad M = \int_A z \sigma_{xx} dA \quad (7.6)$$

and σ_{xx} is the axial stress on the yz -section in the direction of x , Q is the axial force and M is the bending moment.

Using the nonlocal constitutive relation, we can express stress resultants of Euler–Bernoulli beam theory in terms of the strains. As opposed to the linear algebraic equations between the stress resultants and strains in a local theory, the nonlocal constitutive relations lead to differential relations involving the stress resultants and the strains. In the following, we assume the nanobeam to be homogeneous and isotropic. The nonlocal constitutive relation take the following special form for one-dimensional beams:

$$\sigma_{(xx)} - (e_0a)^2 \frac{\partial^2 \sigma_{xx}}{\partial x^2} = E \varepsilon_{xx} \quad (7.7)$$

where E is the Young's modulus of the beam. Using Eqs. (7.6) and (7.7), we have

$$Q - (e_0a)^2 \frac{\partial^2 Q_{xx}}{\partial x^2} = EA \frac{\partial u^0}{\partial x} \quad (7.8)$$

$$M - (e_0a)^2 \frac{\partial^2 M_{xx}}{\partial x^2} = EI \kappa_e \quad (7.9)$$

where $I = \int_A z^2 dA$ is the moment of inertia of the beam cross-section and $\kappa_e = -\frac{\partial^2 w}{\partial x^2}$ is the bending strain of the beam.

With the help of the nonlocal constitutive relations and the equations of motion presented, the moment can be expressed in terms of the generalized displacements as, by substituting Eq. (7.9) into Eq. (7.5), we get

$$M = -EI \frac{\partial^2 w}{\partial x^2} + (e_0a)^2 \rho A \frac{\partial^2 w}{\partial t^2} \quad (7.10)$$

Substituting M from Eq. (7.10) into Eq. (7.5), we obtain the equation of motion of nonlocal Euler beam as

$$EI \frac{\partial^4 w}{\partial x^4} + \rho A \frac{\partial^2 w}{\partial t^2} - \rho A (e_0a)^2 \frac{\partial^4 w}{\partial x^2 \partial t^2} = 0 \quad (7.11)$$

where $w = w(x, t)$ is the flexural deflection, ρ is the mass density, A is the cross-sectional area, EI is the bending rigidity of the beam structure, and e_0a is the nonlocal scaling parameter. It is observed that if the internal length scale a is identically zero, then the local Euler–Bernoulli beam model is recovered.

7.1.1 Wave Dispersion Characteristics

Next, we will compute the parameters that describe the wave characteristics of the nanobeams, namely wavenumbers and wave speeds. The time variable can be eliminated from the governing partial differential equation of the nonlocal beam Eq. (7.11) by using the Fourier transformation [1, 2], for transverse displacement given by

$$w(x, t) = \sum_{n=1}^N \widehat{W}(x, \omega_n) e^{i\omega_n t} \quad (7.12)$$

where ω_n the circular frequency of the n th sampling point and N is the Nyquist frequency. The sampling rate and the number of sampling points (N_1) should be sufficiently large to have relatively good resolution of response both at high and low frequencies. Substitution of Eq.(7.12) into Eq.(7.11), we get

$$\sum_{n=1}^N \left[EI \frac{d^4 \widehat{W}}{dx^4} - \rho A \omega_n^2 \widehat{W} + \rho A \omega_n^2 (e_0 a)^2 \frac{d^2 \widehat{W}}{dx^2} \right] e^{i\omega_n t} = 0 \quad (7.13)$$

This equation must be satisfied for each n and hence can be written as the ordinary differential equation (ODE) in single variable x .

$$EI \frac{d^4 \widehat{W}}{dx^4} - \rho A \omega^2 \left(\widehat{W} - (e_0 a)^2 \frac{d^2 \widehat{W}}{dx^2} \right) = 0 \quad (7.14)$$

where \widehat{W} is the amplitude of the wave motion is, k is the wavenumber, and ω is the frequency of the wave motion. Now using the complete solution of this ODE is [1]:

$$\widehat{W}(x) = \widetilde{W} e^{-ik_n x} \quad (7.15)$$

Substitution of Eq.(7.15) into Eq.(7.14) yields

$$\left\{ EI k_n^4 - \rho A \omega^2 (e_0 a)^2 k_n^2 - \rho A \omega^2 \right\} \widetilde{W} = 0 \quad (7.16)$$

For nontrivial solution of the amplitude \widetilde{W} , this implies that

$$EI k^4 - \rho A \omega^2 (e_0 a)^2 k^2 - \rho A \omega^2 = 0 \quad (7.17)$$

this is known as the dispersion or characteristic equation for the assumed nonlocal Euler–Bernoulli beam. The wavenumbers are obtained by solving the characteristic Eq.(7.17) as

$$k_{1,2,3,4} = \pm \sqrt{\frac{\rho A \omega^2 (e_0 a)^2 \pm \sqrt{\rho A \omega^2 (4EI + \rho A \omega^2 (e_0 a)^4)}}{2EI}} \quad (7.18)$$

These wavenumbers are functions of the nonlocal scaling parameter, wave frequency, and other material parameters of the beam. Out of these four wavenumbers two are purely real and the other two are purely imaginary. The real part gives rise to the propagating component while the imaginary part gives rise to the spatially damped

mode. From Eq. (7.14) it is obvious that, there is no possibility for a cut off frequency, above which the spatially damped mode turns to be propagative.

The phase speed which is defined as $C_p = Real\left(\frac{\omega_n}{k_n}\right)$ is different for different ω_n , which is not the case for a local elasticity nanorod model. In addition, it should be noted that the phase speed is defined with respect to real k_n , since the real part represents the propagative component of the wave. As a result, the speeds change with frequencies, which makes the wave highly dispersive.

The group speeds can be evaluated using the expression $C_g = Real\left(\frac{\partial\omega_n}{\partial k_n}\right)$. This is the speed one has to use for calculating the arrival of reflections. The group velocities of waves in nonlocal beams are derived as

$$C_{g\alpha} = \frac{2EI k_\alpha^3 + \rho A \omega^2 (e_0 a)^2 k_\alpha}{\rho A \omega (1 + (e_0 a)^2 k_\alpha^2)} \tag{7.19}$$

where $\alpha = 1, 2, 3, 4$, corresponding to four wave modes . From this expression we can have the dispersion relation, which is a plot of group velocity and wave frequency. This plot will give full description of the wave propagation in beams. Both the speeds are also a function of nonlocal scaling parameter and wave circular frequency.

Next, we will discuss the wave dispersion characteristics of the beams (of cross-section $b \times h$) using the nonlocal Euler–Bernoulli model. The spectrum curves (wavenumber vs. frequency) and dispersion curves (group speed vs. frequency) are shown for both local and nonlocal continuum models in Fig. 7.2a, b.

There is no existence of cut-off frequency as is clear from Eq. (7.14). In local elasticity ($e_0 a = 0$ nm) solution, the wavenumbers for the flexural mode has a nonlinear variation with the frequency which is in the THz range. The nonlinear variation of the wavenumbers denotes that the waves will propagate dispersively, that is, the waves change their shapes as they propagate. However, the wavenumbers of this

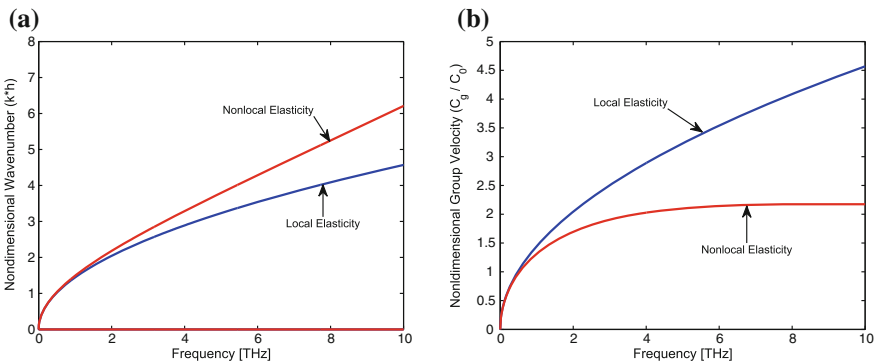


Fig. 7.2 **a** Spectrum curves (wavenumber dispersion), for a nonlocal beam obtained from both local and nonlocal Euler–Bernoulli beam theories. **b** Dispersion curves (group speed dispersion), for a nonlocal beam obtained from both local and nonlocal Euler–Bernoulli beam theories

flexural wave mode have a substantial real part starting from the zero frequency. This implies that the mode starts propagating at any excitation frequency and does not have a cut-off frequency. In nonlocal elasticity ($e_0a = 0.5$ nm) solution, the wavenumbers behave pretty much the same way as local elasticity solution. However, the slopes of the two solutions are quite different indicating the changes in the group speeds. The wavenumbers obtained from nonlocal elasticity calculations are higher as compared to the local elasticity solution. As the nonlocal scale coefficient increases, the wavenumber also increases. At low frequencies, that is, below 1 THz the increasing rate of wavenumber with frequency is very small. However, at higher frequencies the, wavenumber increases at a faster rate compared to wavenumbers at lower frequencies as shown in Fig. 7.2a.

The group speed variation for both local and nonlocal Euler–Bernoulli beam theories is shown in Fig. 7.2b. Slope changes in the wavenumber manifests in the changes in the group speeds. The crucial difference is that the nonlocal speeds are numerically small compared to the speeds computed from the local models and it attains a constant value at higher frequencies.

7.2 NLSGM for Timoshenko Nanobeam

Next, we present the wave characteristics of the nonlocal stress gradient Timoshenko nanobeam model. As stated earlier, these models are also referred to as FSDT models. These models can be used either to model nanothin films (of rectangular cross section) or SWCNT (of hollow circular cross section). For the nonlocal Timoshenko beam theory, the Hook's law of CNT can be expressed as the following partial differential forms:

$$\sigma_{xx} - (e_0a)^2 \frac{\partial^2 \sigma_{xx}}{\partial x^2} = E \varepsilon_{xx} \quad (7.20)$$

$$\tau_{xz} - (e_0a)^2 \frac{\partial^2 \tau_{xz}}{\partial x^2} = G \gamma_{xz} \quad (7.21)$$

where σ_{xx} is the axial stress, τ_{xz} the shear stress, ε_{xx} the axial strain, γ_{xz} the shear strain, E the Young's modulus, and G the shear modulus.

Based on the Timoshenko beam theory, the displacement field at any point can be written as

$$U_1(x, z, t) = u^0(x, t) - z\psi(x, t) \quad (7.22)$$

$$U_2(x, z, t) = 0 \quad (7.23)$$

$$U_3(x, t) = w(x, t) \quad (7.24)$$

where x is the longitude coordinate, z the coordinate measured from the mid-plane of the CNT and $\psi(x, t)$ the rotation of the cross-section. The terms $u^0(x, t)$ and

$w(x, t)$ are the axial and transverse displacements, respectively, of the point $(x, 0)$ on the mid-plane (i.e., $z = 0$) of the CNT. The nonzero strains are expressed as

$$\varepsilon_{xx} = \frac{\partial U_1}{\partial x} = \frac{\partial u^0}{\partial x} - z \frac{\partial \psi}{\partial x} \quad (7.25)$$

$$\varepsilon_{yy} = \frac{\partial U_2}{\partial y} = 0 \quad (7.26)$$

$$\gamma_{xz} = \frac{\partial U_1}{\partial z} + \frac{\partial U_3}{\partial x} = \frac{\partial w}{\partial x} - \psi \quad (7.27)$$

For establishing the dynamic equations of the SWCNT, the bending moment M and the shear force Q are used as

$$M = \int_A z \sigma_{xx} dA \quad (7.28)$$

$$Q = \int_A \tau_{xz} dA \quad (7.29)$$

where σ_{xx} is the normal stress, τ_{xz} is the transverse shear stress, and A_c is the cross-sectional area of the CNT. Using Eqs. (7.20), (7.21) and (7.25)–(7.29) one can obtain the nonlocal constitutive relations for Timoshenko beam as

$$M - (e_0 a)^2 \frac{\partial^2 M}{\partial x^2} = E I_c \frac{\partial \psi}{\partial x} \quad (7.30)$$

$$Q - (e_0 a)^2 \frac{\partial^2 Q}{\partial x^2} = G A_c \kappa \left(\frac{\partial w}{\partial x} - \psi \right) \quad (7.31)$$

where κ is the shear correction factor used to compensate for the error due to constant shear stress assumption. This value varies with the cross-section [3]. A value of $\kappa = 0.877$ was used by Reddy and Pang [4] for analysis of CNTs. I_c represents the moment of area of the cross-section. Note that the bending moment and shear force given in Eqs. (7.30) and (7.31) reduce to that of the local Timoshenko model when the characteristic length is set to zero.

Now consider a small beam element of length dx . The dynamic equations for the beam element subjected to nonlocal bending moment and shear force are given as

$$\frac{\partial Q}{\partial x} dx - \rho_c A_c \frac{\partial^2 w}{\partial t^2} dx = 0 \quad (7.32)$$

$$\frac{\partial M}{\partial x} dx - Q dx - \rho_c I_c \frac{\partial^2 \psi}{\partial t^2} dx = 0 \quad (7.33)$$

Here ρ_c is the density of the CNT. The bending moment M and shear force Q in the Timoshenko beam theory are related to the bending displacements w and ψ by

(from Eqs. (7.30) to (7.33))

$$M = EI_c \frac{\partial \psi}{\partial x} + \rho_c A_c (e_0 a)^2 \frac{\partial^2 w}{\partial t^2} + \rho_c I_c (e_0 a)^2 \frac{\partial^3 w}{\partial x \partial t^2} \quad (7.34)$$

$$Q = GA_c \kappa \left(\frac{\partial w}{\partial x} - \psi \right) + \rho_c A_c (e_0 a)^2 \frac{\partial^3 w}{\partial x \partial t^2} \quad (7.35)$$

Substitution of Eqs. (7.34) and (7.35) into Eqs. (7.32) and (7.33) leads to the following nonlocal governing equations of motion for SWCNT as:

$$GA_c \kappa \left(\frac{\partial \psi}{\partial x} - \frac{\partial^2 w}{\partial x^2} \right) + \rho_c A_c \frac{\partial^2 w}{\partial t^2} - \rho_c A_c (e_0 a)^2 \frac{\partial^4 w}{\partial x^2 \partial t^2} = 0 \quad (7.36)$$

$$EI_c \frac{\partial^2 \psi}{\partial x^2} + GA_c \kappa \left(\frac{\partial w}{\partial x} - \psi \right) - \rho_c I_c \left(\frac{\partial^2 \psi}{\partial t^2} - (e_0 a)^2 \frac{\partial^4 \psi}{\partial x^2 \partial t^2} \right) = 0 \quad (7.37)$$

where $G = \frac{E}{2(1+\nu)}$ is shear modulus of the beam, ν is the Poisson's ratio, κ is the shear adjustment coefficient, vary with the cross-section of the beam [3], I_c is the moment of inertia of the cross-section of the beam, A_c is the cross-sectional area, and ρ_c is the mass density of the beam. It is observed that if the internal length scale a is identically zero, then the local Timoshenko beam model is recovered.

7.2.1 Wave Dispersion Characteristics

Next, we perform spectral analysis to determine the wave characteristics of this model. As in the case of nanorods, we will first transform the governing PDE Eqs. (7.36) and (7.37) to a set of ODE through DFT, which is given by

$$w(x, t) = \sum_{n=1}^N \widehat{W}(x, \omega_n) e^{i\omega_n t} \quad (7.38)$$

$$\psi(x, t) = \sum_{n=1}^N \widehat{\Psi}(x, \omega_n) e^{i\omega_n t} \quad (7.39)$$

Substituting the solutions Eqs. (7.38) and (7.39) into Eqs. (7.36) and (7.37), leads to

$$\sum_{n=1}^N \left[GA_c \kappa \left(\frac{\partial \widehat{\Psi}}{\partial x} - \frac{\partial^2 \widehat{W}}{\partial x^2} \right) - \rho_c A_c \omega_n^2 \left(\widehat{W} - (e_0 a)^2 \frac{\partial^2 \widehat{W}}{\partial x^2} \right) \right] e^{i\omega_n t} = 0 \quad (7.40)$$

$$\sum_{n=1}^N \left[EI_c \frac{\partial^2 \Psi}{\partial x^2} + GA_c \kappa \left(\frac{\partial \widehat{W}}{\partial x} - \widehat{\Psi} \right) + \rho_c I_c \omega_n^2 \left(\widehat{\Psi} - (e_0 a)^2 \frac{\partial^2 \widehat{\Psi}}{\partial x^2} \right) \right] e^{i\omega_n t} = 0 \quad (7.41)$$

These two equations must be satisfied for each n and hence can be written as the ordinary differential equations in single variable x as (note that subscript n is dropped from expressions)

$$GA_c \kappa \left(\frac{d\widehat{\Psi}}{dx} - \frac{d^2 \widehat{W}}{dx^2} \right) - \rho_c A_c \omega^2 \left(\widehat{W} - (e_0 a)^2 \frac{d^2 \widehat{W}}{dx^2} \right) = 0 \quad (7.42)$$

$$EI_c \frac{d^2 \Psi}{dx^2} + GA_c \kappa \left(\frac{d\widehat{W}}{dx} - \widehat{\Psi} \right) + \rho_c I_c \omega^2 \left(\widehat{\Psi} - (e_0 a)^2 \frac{d^2 \widehat{\Psi}}{dx^2} \right) = 0 \quad (7.43)$$

The complete solutions of these ODEs are of the form

$$\widehat{W}(x) = \widetilde{W} e^{-ikx} \quad (7.44)$$

$$\widehat{\Psi}(x) = \widetilde{\Psi} e^{-ikx} \quad (7.45)$$

where \widetilde{W} is the amplitude of deflection of the beam, and $\widetilde{\Psi}$ is the amplitude of the slope of the beam due to bending deformation alone. By substituting the solutions Eqs.(7.44) and (7.45) into Eqs.(7.42) and (7.43), leads to two algebraic equations in \widetilde{W} and $\widetilde{\Psi}$, and rewriting them in matrix form as

$$\begin{bmatrix} GA_c \kappa k^2 - \rho_c A_c \omega^2 (1 + (e_0 a)^2 k^2) & iGA_c \kappa k \\ -iGA_c \kappa k - i(e_0 a)^2 k^3 & \rho_c I_c \omega^2 (1 + (e_0 a)^2 k^2) - GA_c \kappa - EI_c k^2 \end{bmatrix} \begin{Bmatrix} \widetilde{W} \\ \widetilde{\Psi} \end{Bmatrix} = \begin{Bmatrix} 0 \\ 0 \end{Bmatrix} \quad (7.46)$$

By assuming the nontrivial solution for the amplitudes \widehat{W} and $\widehat{\Psi}$, Eq.(7.46) can be rewritten as

$$\mathbf{S}_2 k^2 + \mathbf{S}_1 k + \mathbf{S}_0 = 0 \quad (7.47)$$

where

$$\mathbf{S}_2 = \begin{bmatrix} -GA_c \kappa - \rho_c A_c (e_0 a)^2 \omega^2 & 0 \\ 0 & -EI_c + \rho_c I_c (e_0 a)^2 \omega^2 \end{bmatrix} \quad (7.48)$$

$$\mathbf{S}_1 = \begin{bmatrix} 0 & iGA_c \kappa k \\ -iGA_c \kappa k & 0 \end{bmatrix} \quad (7.49)$$

$$\mathbf{S}_0 = \begin{bmatrix} -\rho_c A_c \omega^2 & 0 \\ 0 & -GA_c \kappa + \rho_c I_c \omega^2 \end{bmatrix} \quad (7.50)$$

The wavenumbers and hence the group speeds are solved from Eq.(7.47) by using Polynomial Eigenvalue Problem (PEP) [1]. Equating the determinant of matrix in Eq.(7.46) to zero (for the nontrivial solution of \widehat{W} , and $\widehat{\Psi}$) will give the charac-

teristic polynomial in terms of wavenumber k of the order 4, solution of which is quite difficult. PEP converts the characteristic polynomial equation into a matrix of size 2×2 , whose eigen values form the solution of the equation. After obtaining the wavenumbers, group speeds are extracted. This form is amenable to solution of wavenumbers through PEP. From Eq. (7.47), we can clearly see the dependence of nonlocal scale parameter e_0a on wavenumber.

Looking at the matrix S_0 in Eq. (7.50), we can clearly see the existence of a cut-off frequency. The cut-off frequencies of this nonlocal beams are obtained by setting $k = 0$ in the dispersion relation (Eq. (7.47)) that is, for the present case of PEP, one can set $|\mathbf{S}_0| = 0$, for the cut-off frequencies as

$$\omega_c^{\text{flexural}} = 0, \quad \omega_c^{\text{shear}} = \sqrt{\frac{GA_c\kappa}{\rho_c I_c}} \quad (7.51)$$

We have seen in Chap. 6 that for the case of nanorods, the nonlocality introduced certain band gaps in the group speed plots at certain frequency, beyond which the group speed goes to zero. We called this frequency as *escape frequency*. In other words, at the escape frequency, the wavenumber tends to infinity. Its value can be analytically determined by looking at the wavenumber expression (Eq. (7.47)) and setting $k \rightarrow \infty$. This amounts to setting the $|\mathbf{S}_2| = 0$, which gives

$$\omega_e^{\text{flexural}} = \frac{1}{(e_0a)} \sqrt{\frac{GA_c\kappa}{\rho_c A_c}}, \quad \omega_e^{\text{shear}} = \frac{1}{(e_0a)} \sqrt{\frac{EI_c}{\rho_c I_c}} \quad (7.52)$$

where $\omega_e^{\text{flexural}}$ and ω_e^{shear} are called “escape frequencies” in flexural and shear modes, respectively. Next, we will derive the expressions for the wave speeds. Differentiating the Eq. (7.47) with respect to the wave frequency (ω), one can obtain the group speeds as

$$2\rho_c\omega(1 + (e_0a)^2k^2)\mathbf{H}C_g + (2k\mathbf{S}_2 + \mathbf{S}_1) = 0 \quad (7.53)$$

$$\mathbf{H} = \begin{bmatrix} -A_c & 0 \\ 0 & I_c \end{bmatrix} \quad (7.54)$$

where $C_g = (\partial\omega/\partial k)$ is the group speed of a wave in the beam and the matrices \mathbf{S}_1 and \mathbf{S}_2 are given in Eqs. (7.48) and (7.49). This is again a PEP in terms of C_g and one can solve it for group speeds of respective modes (That is, for flexural and shear), which is again a function of nonlocal scale parameter. These are discussed next.

The spectrum and dispersion curves obtained from local and nonlocal Timoshenko beam theories are shown in Fig. 7.3a, b. Figure 7.3a shows the variation of the wavenumbers with the wave frequency for both local (or classical) and nonlocal elasticities. This figure shows two modes namely, flexural and shear. Flexural wave mode starts from zero wave frequency and shear wave mode propagates only after shear cut-off frequency, the frequency at which the imaginary part of wavenumber

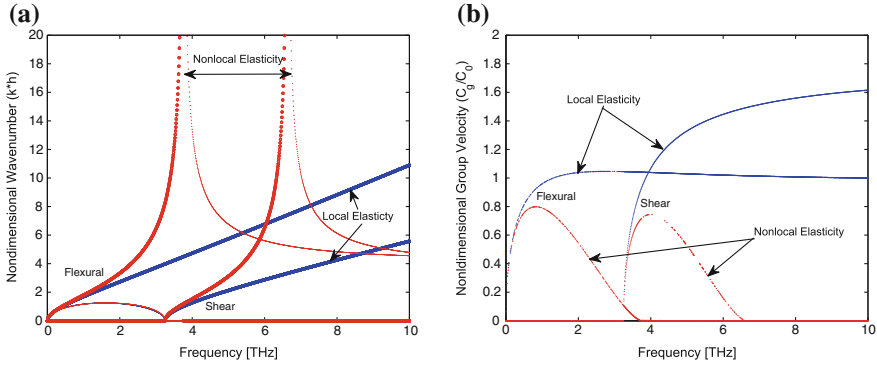


Fig. 7.3 **a** Spectrum curves (wavenumber variation: Real wavenumbers—*thick lines*; Imaginary wavenumbers—*thin lines*). **b** Dispersion curves (group speed variation)

becomes real. The values of the cut-off frequency are calculated from Eq. (7.51). In the present study for a rectangular thin film of area 1×2 nm beam, we have shear cut-off frequency at 3.25 THz. It can be observed from Eq. (7.51) that these frequencies are independent of the nonlocal scaling parameter, and hence same frequencies are obtained from both local and nonlocal theories (see Fig. 7.3a).

For $e_0a = 0$, which is the case of local theory of elasticity solution, wavenumbers increase monotonically with the increase in frequency, which is shown in Fig. 7.3a and correspondingly, the group speeds, shown in Fig. 7.3b increases with increase in wave frequency. However, at higher frequencies, they attain a constant value, which is typical of Timoshenko beam solution. However, with the introduction of nonlocal scale effects, the wave behavior is altered drastically. Both the flexural and shear wave modes escape to infinity at escape frequency, beyond this frequency there is no wave propagation. The value of escape frequency decreases with increase in the scale parameter e_0a , for both wave modes. Equation (7.52) gives the expression for escape frequencies in nonlocal FSDT beam. From this expression it is clear that, escape frequencies are independent of slenderness ratio of the beam (ratio of the width to thickness of the beam), for both wave modes. However, the group speed amplitudes may change. Figure 7.4 shows the variation of escape frequencies of flexural and shear wave modes with the nonlocal scaling parameter. It shows that as e_0a increases, the escape frequency decreases. At higher values of e_0a , escape frequencies approach to very small values. The detailed variation in escape frequency for these beams as a function of nonlocal scale parameter is shown in Fig. 7.5 for $e_0a = 0.5$ nm, 1.0 nm and 2.0 nm, respectively. It shows the effect of b/h and the nonlocal scaling parameter (e_0a) on the escape frequencies of the flexural and shear wave modes, more clearly. The escape frequencies for both flexural and shear modes are constant with various sizes of the beams. The values of escape frequency are decreasing with increase in the nonlocal scale coefficient (see Fig. 7.5) and are still constant with b/h .

Fig. 7.4 Escape frequency variation of nonlocal beams with nonlocal scaling parameter (e_0a)

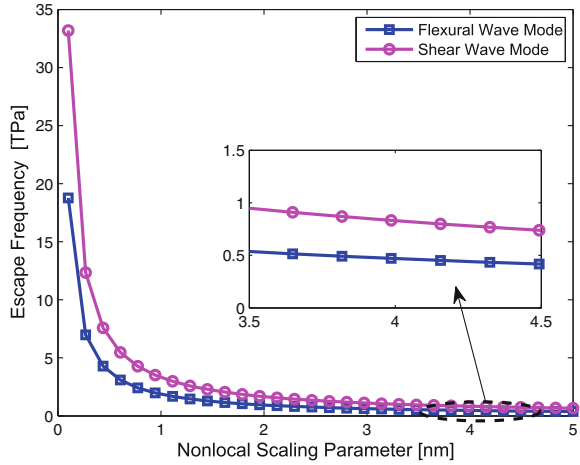
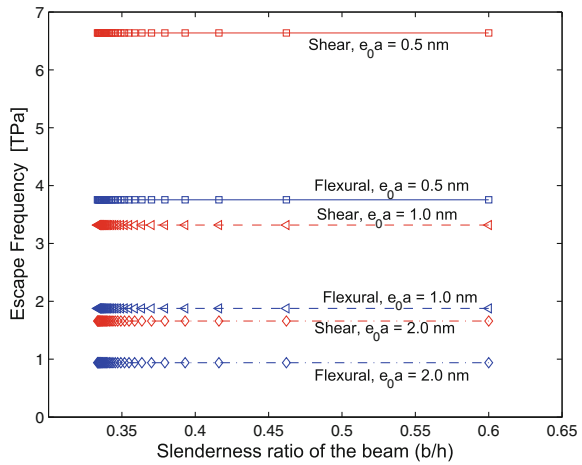


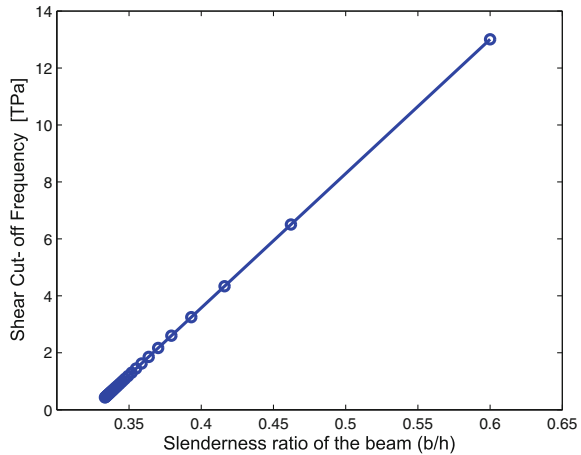
Fig. 7.5 Escape frequency variation of nonlocal beams with slenderness ratio of the beam ($\frac{b}{h}$)



The shear cut-off frequency variation with slenderness ratio of the beam (b/h) is shown in Fig. 7.6. This figure shows that, as the slenderness ratio of the beam increases, the shear cut-off frequency increases and at lower values of b/h , the shear cut-off frequency approaches to very small values. Hence, it can be concluded that for large values of scale parameter, shear deformation on the beam has negligible effect and beam behaves more like elementary beam.

We have limited ourselves with few parametric studies, especially with respect to those Timoshenko beam of rectangular cross-section. Some more studies using this theory is performed in the next chapter, which will address the wave propagation in MWCNT, where in the cross-section will be modeled as hollow circular sections.

Fig. 7.6 Shear cut-off frequency variation of nonlocal beams with slenderness ratio of the beam ($\frac{b}{h}$)



7.3 Rotating Nanotubes: An Introduction

Because of future promising exploration of nanotechnology, focus is being put in the miniaturization of mechanical and electromechanical devices. Attention is sought toward the development of nanodevices and nanomachines [5]. Nanomachines are systems in the nanometer realm with moving parts [6]. Nanostructures undergoing rotation include nanoturbines, nanoscale molecular bearings, shaft and gear, and multiple gear systems. These nanostructure machines are expected to receive considerable attention in the near future. Researchers have thus reported the feasibility of nanoscale rotating structures. Examples include the study of molecular gears [5], fullerene gears [7], and carbon nanotubes gears [8, 9]. Srivastava [10] has reported the rotational dynamics of carbon nanotubes and carbon nanotubes gears under a single applied laser field. A typical carbon nanotubes gear is shown in Fig. 7.7. Lohrasebi and Tabar [11] carried out computational modeling of rotating nanomotor. Dynamics of the rotary nanomotor was simulated using stochastic molecular dynamics method. Zhang et al. [12] carried out atomistic simulations of double-walled carbon nanotubes as rotational bearings. Recently, Fennimore et al. [13] reported the feasibility of rotating nanostructures. They showed the construction and successful operation of a nanoscale electromechanical actuator. The rotating nanostructural system consists of a rotatable metal plate, with a multi-walled carbon nanotube serving as the key motion-enabling element. For efficient design of these rotating nanomachines, proper understanding of its mechanical behavior such as bending, vibration, and buckling is required. The development of simplified models for the dynamics of complex nano-technological systems is thus necessary. This is because for many cases, fully atomistic simulations would be computationally expensive and prohibitive.

Recently, there has been great work done on vibration analysis of CNTs under rotation. Pradhan and Murmu [14] developed a single nonlocal beam model and applied to investigate the flap wise bending-vibration characteristics of a rotating

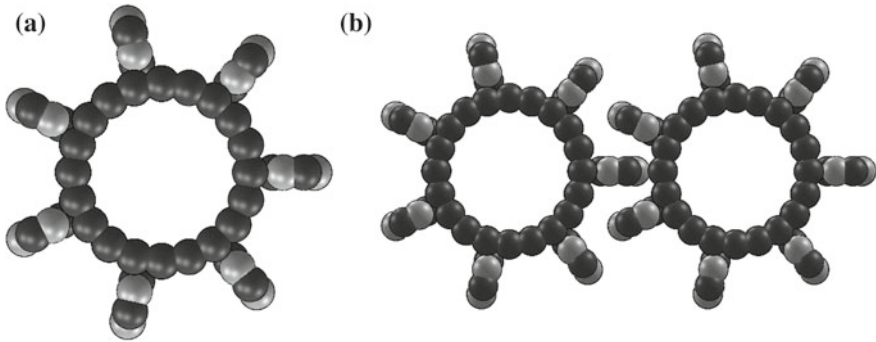


Fig. 7.7 Carbon nanotube gears: A molecular diagram

nanocantilever. Differential quadrature method (DQM) was utilized and nondimensional nonlocal frequencies were obtained. They also discussed the effects of the nonlocal small scale, angular velocity, and hub radius on vibration characteristics of the nanocantilever. Murmu and Adhikari [15] investigated the nonlocal effects in bending vibration of an initially prestressed single-walled carbon nanotube via nonlocal elasticity. The carbon nanotube was assumed to be attached to a molecular hub and was undergoing rotation. They also utilized the differential quadrature method and the nonlocal bending frequencies of the rotating system were determined. The effects of the initial preload on vibration characteristics of rotating carbon nanotube were examined. Further, influence of nonlocal effects, angular velocities, hub radii, and higher mode frequencies were also studied. Hence, it is worth looking in to the wave dispersion characteristics of the nanotubes under rotation, which are found as blades of a nanoturbine and also important for practical development of nanomachines.

In the present section, the wave dispersion characteristics of a rotating nanotube modeled as SWCNT are studied using the spectral analysis. The rotating SWCNT is modeled as a Euler–Bernoulli beam. The governing partial differential equation for a uniform rotating beam is derived incorporating the nonlocal scale effects and the variable coefficient for the centrifugal term is replaced by the maximum centrifugal force. The rotating beam problem is now transformed to a case of beam subjected to an axial force. Even though this averaging seems to be a crude approximation, one can use this as a powerful model for analyzing the wave dispersion characteristics of the rotating CNT.

7.3.1 Governing Equations for Rotating Nanotube

Nanotubes are central to new rotating devices such as miniature motor. A rotating CNT can be represented as a cantilever beam (see Fig. 7.8a) having displacements perpendicular to the plane of rotation. The detailed coordinate system on this rotating beam is shown in Fig. 7.8b. Considering the elementary Euler–Bernoulli theory of beams, the axial and transverse displacement fields of a rotating beam can be

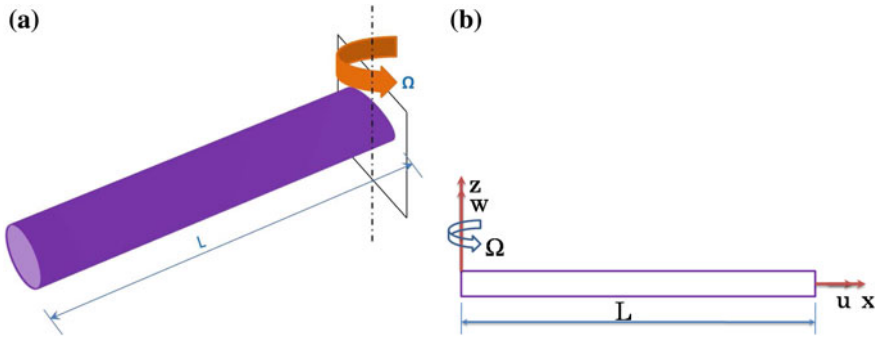


Fig. 7.8 **a** A schematic of rotating carbon nanotube system with mathematical idealization to rotating nanobeam and **b** Coordinate system and degree of freedom

represented

$$u(x, y, z, t) = u^0 - z \frac{\partial w}{\partial x} \quad (7.55)$$

$$w(x, y, z, t) = w(x, t) \quad (7.56)$$

where w is transverse displacements of the point $(x, 0)$ on the middle plane (i.e., $z = 0$) of the beam. The only nonzero strain of the Euler–Bernoulli beam theory, accounting for the von Kármán strain is given by

$$\varepsilon_{xx} = \frac{\partial u}{\partial x} = \frac{\partial u^0}{\partial x} - z \frac{\partial^2 w}{\partial x^2} \quad (7.57)$$

This is also called as bending strain (or curvature).

The equations of motion of the Euler–Bernoulli beam theory are given by

$$\frac{\partial Q}{\partial x} = \rho A \frac{\partial^2 u^0}{\partial t^2} \quad (7.58)$$

$$\frac{\partial^2 M}{\partial x^2} + \frac{\partial}{\partial x} \left(T(x) \frac{\partial w}{\partial x} \right) = \rho A \frac{\partial^2 w}{\partial t^2} \quad (7.59)$$

where

$$Q = \int_A \sigma_{xx} dA, \quad M = \int_A z \sigma_{xx} dA \quad (7.60)$$

and σ_{xx} is the axial stress in the direction of x , Q is the axial force, M is the bending moment and $T(x)$ is the axial force due to centrifugal stiffening due to rotation and is given as

$$T(x) = \int_x^L \rho A \Omega^2 x dx \quad (7.61)$$

Here, ρ is the mass density, A is the beam cross-section area and Ω is the rotation speed. The nonlocal constitutive relations take the following special form for beams:

$$\sigma_{xx} - (e_0 a)^2 \frac{\partial^2 \sigma_{xx}}{\partial x^2} = E \varepsilon_{xx} \quad (7.62)$$

where E is the Young's modulus of the beam. Using Eq. (7.60) in (7.62), we have

$$Q - (e_0 a)^2 \frac{\partial^2 Q}{\partial x^2} = EA \frac{\partial u}{\partial x} \quad (7.63)$$

$$M - (e_0 a)^2 \frac{\partial^2 M}{\partial x^2} = EI \kappa_e \quad (7.64)$$

where $I = \int_A z^2 dA$ is the moment of inertia of the beam cross-section and $\kappa_e = -\frac{\partial^2 w}{\partial x^2}$ is the bending strain of the beam. With the help of the nonlocal constitutive relations and the equations of motion, the moment can be expressed in terms of the generalized displacements as, by substituting Eq. (7.64) into Eq. (7.59), we get

$$M = -EI \frac{\partial^2 w}{\partial x^2} + (e_0 a)^2 \left[\rho A \frac{\partial^2 w}{\partial t^2} - \frac{\partial}{\partial x} \left(T(x) \frac{\partial w}{\partial x} \right) \right] \quad (7.65)$$

Substituting M from Eq. (7.65) into Eq. (7.59), we obtain the equation of motion of rotating nonlocal Euler beams as

$$-EI \frac{\partial^4 w}{\partial x^4} + (e_0 a)^2 \frac{\partial^2}{\partial x^2} \left[\rho A \frac{\partial^2 w}{\partial t^2} - \frac{\partial}{\partial x} \left(T(x) \frac{\partial w}{\partial x} \right) \right] + \frac{\partial}{\partial x} \left(T(x) \frac{\partial w}{\partial x} \right) = \rho A \frac{\partial^2 w}{\partial t^2} \quad (7.66)$$

If we assume a uniform rotating beam, then $T(x)$ can be replaced by the maximum force (at the root, i.e., at $x = 0$) given by

$$T_{\max} = \int_0^L \rho A \Omega^2 x dx = \frac{\rho A \Omega^2 L^2}{2} \quad (7.67)$$

This allows us to represent the governing equation as a constant coefficient nonlocal partial differential equation. Finally, the nonlocal governing differential equation for transverse displacement ($w(x, t)$) of a rotating cantilever beam is derived as

$$EI \frac{\partial^4 w}{\partial x^4} - T_{\max} \frac{\partial^2 w}{\partial x^2} + T_{\max} (e_0 a)^2 \frac{\partial^4 w}{\partial x^4} + \rho A \frac{\partial^2 w}{\partial t^2} - \rho A (e_0 a)^2 \frac{\partial^4 w}{\partial t^2 \partial x^2} = 0 \quad (7.68)$$

7.3.2 Wave Dispersion Analysis

For analyzing the dispersion characteristics of waves in nanotubes, the primary variable in the analysis ($w(x, t)$, the transverse deformation) is transformed into frequency domain using DFT and it is given by [1]

$$w(x, t) = \sum_{n=1}^N \hat{w}(x, \omega_n) e^{-j(kx - \omega_n t)} \quad (7.69)$$

where $\hat{w}(x, \omega_n)$ is the frequency domain amplitude of the flexural deformation of CNTs, k is the wavenumber and ω_n is the angular frequency of the wave motion at n th sampling point, N is the number of samples and $j = \sqrt{-1}$. Eliminating the time variable from Eq. (7.68) using the above spectral approximation of the displacement gives,

$$\sum_{n=1}^N \left[EI \frac{\partial^4 \hat{w}(x, \omega_n)}{\partial x^4} - T_{\max} \frac{\partial^2 \hat{w}(x, \omega_n)}{\partial x^2} + T_{\max} (e_0 a)^2 \frac{\partial^4 \hat{w}(x, \omega_n)}{\partial x^4} - \rho A \omega^2 \hat{w}(x, \omega_n) + \rho A (e_0 a)^2 \omega^2 \frac{\partial^2 \hat{w}(x, \omega_n)}{\partial x^2} \right] e^{j\omega_n t} = 0 \quad (7.70)$$

Equation (7.70) must be satisfied for each n and hence can be written as

$$EI \frac{d^4 \hat{w}}{dx^4} - T_{\max} \frac{d^2 \hat{w}}{dx^2} + T_{\max} (e_0 a)^2 \frac{d^4 \hat{w}}{dx^4} - \rho A \omega^2 \hat{w} + \rho A (e_0 a)^2 \omega^2 \frac{d^2 \hat{w}}{dx^2} = 0 \quad (7.71)$$

For the sake of simplicity in the analysis, we express this equation in a nondimensional form. Now define new variables as

$$\begin{aligned} \tilde{x} &= \frac{x}{L}; & \tilde{w} &= \frac{\hat{w}}{L}; \\ \frac{d\hat{w}}{dx} &= \frac{d\tilde{w}}{d\tilde{x}}; & L \frac{d^2 \hat{w}}{dx^2} &= \frac{d^2 \tilde{w}}{d\tilde{x}^2}; & L^2 \frac{d^3 \hat{w}}{dx^3} &= \frac{d^3 \tilde{w}}{d\tilde{x}^3}; & L^3 \frac{d^4 \hat{w}}{dx^4} &= \frac{d^4 \tilde{w}}{d\tilde{x}^4}; \\ \tau &= \frac{e_0 a}{L} \end{aligned} \quad (7.72)$$

The nondimensional form of the Eq. (7.71) is

$$EI \frac{1}{L^3} \frac{d^4 \tilde{w}}{d\tilde{x}^4} - T_{\max} \frac{1}{L} \frac{d^2 \tilde{w}}{d\tilde{x}^2} + T_{\max} (e_0 a)^2 \frac{1}{L^3} \frac{d^4 \tilde{w}}{d\tilde{x}^4} - \rho A \omega^2 L \tilde{w} + \rho A (e_0 a)^2 \omega^2 \frac{1}{L} \frac{d^2 \tilde{w}}{d\tilde{x}^2} = 0 \quad (7.73)$$

Rearranging and defining a new variable

$$\omega_{\text{str}} = \frac{1}{L^2} \sqrt{\frac{EI}{\rho A}} \quad (7.74)$$

Equation (7.73) changes to

$$\left[1 + \tau^2 \frac{1}{2} \left(\frac{\Omega}{\omega_{\text{str}}} \right)^2 \right] \frac{d^4 \tilde{w}}{d\tilde{x}^4} - \frac{1}{2} \left(\frac{\Omega}{\omega_{\text{str}}} \right)^2 \frac{d^2 \tilde{w}}{d\tilde{x}^2} + \tau^2 \left(\frac{\omega}{\omega_{\text{str}}} \right)^2 \frac{d^2 \tilde{w}}{d\tilde{x}^2} - \left(\frac{\omega}{\omega_{\text{str}}} \right)^2 \tilde{w} = 0 \quad (7.75)$$

Since the differential equation is a constant coefficient one, it has the solution of the form $\tilde{w} = \tilde{W} e^{-jkx}$. On substituting this solution in Eq. (7.75), we get (for $\tilde{W} \neq 0$),

$$\left[1 + \tau^2 \frac{1}{2} \left(\frac{\Omega}{\omega_{\text{str}}} \right)^2 \right] k^4 + \left[\frac{1}{2} \left(\frac{\Omega}{\omega_{\text{str}}} \right)^2 - \tau^2 \left(\frac{\omega}{\omega_{\text{str}}} \right)^2 \right] k^2 - \left(\frac{\omega}{\omega_{\text{str}}} \right)^2 = 0 \quad (7.76)$$

where k is the wavenumber. This is the dispersion/characteristic equation of the rotating uniform beams. One can solve for the wavenumbers as

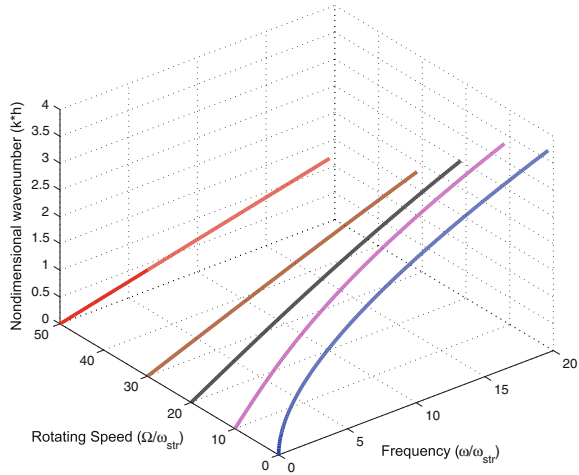
$$k = \pm \sqrt{\frac{-\left[\frac{1}{2} \left(\frac{\Omega}{\omega_{\text{str}}} \right)^2 - \tau^2 \left(\frac{\omega}{\omega_{\text{str}}} \right)^2 \right] \pm \sqrt{\left[\frac{1}{2} \left(\frac{\Omega}{\omega_{\text{str}}} \right)^2 - \tau^2 \left(\frac{\omega}{\omega_{\text{str}}} \right)^2 \right]^2 + 4 \left[1 + \tau^2 \frac{1}{2} \left(\frac{\Omega}{\omega_{\text{str}}} \right)^2 \right] \left(\frac{\omega}{\omega_{\text{str}}} \right)^2}}{2 \left[1 + \tau^2 \frac{1}{2} \left(\frac{\Omega}{\omega_{\text{str}}} \right)^2 \right]}} \quad (7.77)$$

The wavenumbers are mainly a function of the nonlocal scaling parameter ($e_0 a$), rotational speed of the beam (Ω), and the wave circular frequency. The corresponding wave speeds, namely, Phase speed ($C_p = \text{Real}(\frac{\omega}{k})$) and Group speed ($C_g = \text{Real}(\frac{\partial \omega}{\partial k})$), are obtained from Eq. (7.77). A detail discussion on these parameters is presented next.

For Numerical Experiments, a nanobeam is assumed as a (5, 5) SWCNT and the diameter of the SWCNT is $d = 0.675$ nm, length $L = 10d$, Young's modulus $E = 5.5$ TPa, and the density $\rho = 2,300$ kg/m³.

The spectrum curves (that is, nondimensional wavenumber ($k \times h$), h are the thickness of the nanotube versus nondimensional wave frequency ($\omega/\omega_{\text{str}}$) for the rotating SWCNT are shown in Fig. 7.9 for different values of the nondimensional rotational speed $\Omega/\omega_{\text{str}}$ for $\tau = e_0 a/L = 0$ (i.e., local elasticity calculation). It can be seen that for nonrotating CNT (that is, $\Omega/\omega_{\text{str}} = 0$), the nondimensional flexural wavenumber shows a nonlinear variation with wave frequency, i.e., the waves will change their shape as they propagate. As the rotational speed of the CNT increases, the nondimensional wavenumbers tend to become nondispersive in nature as shown in Fig. 7.9. It means that the waves will not change their shape as they propagate in the medium. Also, the wavenumber shows an inverse dependence on rotation speed. For a nonrotating CNT, the spectrum relation is dispersive in nature. However, for a rotating beam, at higher speeds, the above nonlinear relation shifts to a linear nature due to the relatively negligible contribution from the ω term, especially for lower

Fig. 7.9 Wavenumber dispersion in rotating nanotube for $\tau = e_0a/L = 0$ for different values of Ω/ω_{str}



values of ω . That is, the variation of k is dominated by the centrifugal force term at high Ω/ω_{str} .

Figure 7.10 shows the spectrum curves for rotating and nonrotating CNTs for various values of the nonlocal scaling parameter. Figure 7.10a shows that as we move from local elasticity to nonlocal elasticity solution, the spectrum curve becomes linear at higher values of the wave frequency. The wavenumbers also increase as the nonlocal scaling parameter increases. The matching of local and nonlocal solutions is limited only upto < 0.2 THz frequency. After this frequency, the difference between the wavenumbers predicted is very large. If the rotational speed of the CNT increases from $\Omega/\omega_{str} = 0$ to $\Omega/\omega_{str} = 10$ (Fig. 7.10b), the spectrum curve is slightly non-linear as compared to nonrotating case. The wavenumbers obtained from local and nonlocal cases are same upto 0.45 THz frequency. The wavenumbers are showing an increasing tendency as the nonlocal parameter increases. If the rotational speed of the CNT increases to very high values like $\Omega/\omega_{str} = 30, 50$ and 100 , the local and nonlocal calculations are almost similar upto 1 THz, 1.6 THz and 2.5 THz frequencies, respectively (see Fig. 7.10c–e). As the rotational speed of the CNT increases to very high values, the nonlocal scaling parameter effect on the spectrum curves is negligible. It means that if the CNT rotates at very high speeds, the local elasticity and nonlocal elasticity calculations give almost similar spectrum relations. It can also be observed that as the rotational speed of the CNT increases, the wavenumbers become very small and the dispersive nature changes to nondispersive nature (see Fig. 7.10).

The nondimensional phase speed (C_p/C_0) and nondimensional group speed (C_g/C_0), where $C_0 = \sqrt{E/\rho}$, dispersions of the rotating CNT are shown in Fig. 7.11, obtained from the local elasticity calculations (i.e., $\tau = e_0a/L = 0$). Thick lines represent the phase speed variation and the thin lines show the group speed variation. It can be seen that the phase speed of the rotating CNTs is higher than the group

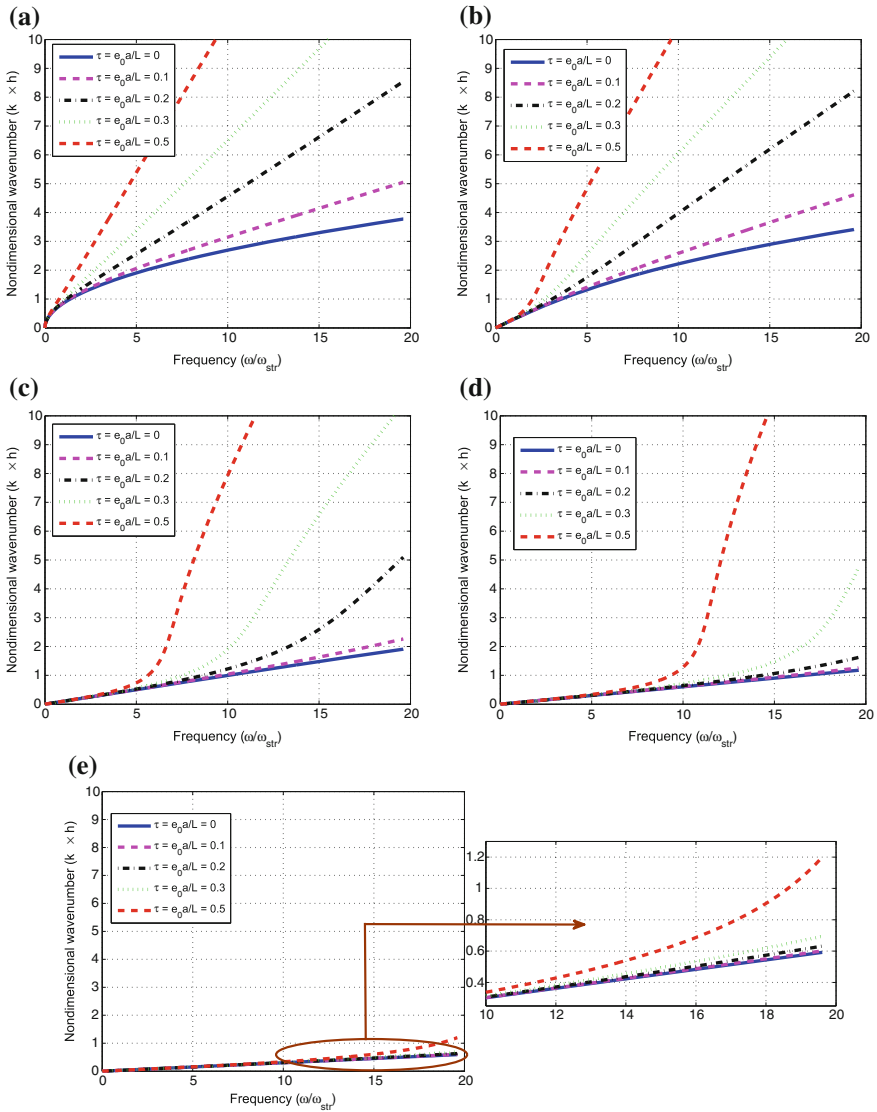
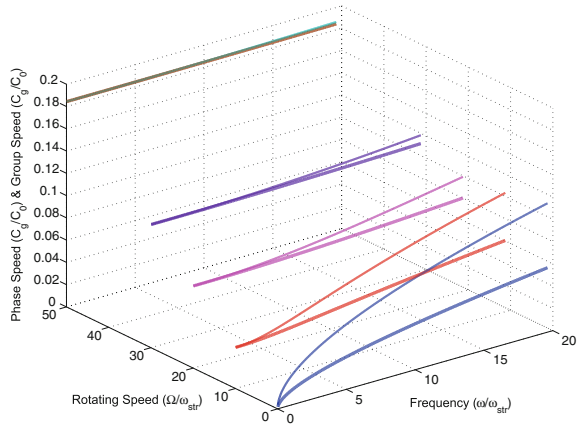


Fig. 7.10 Wave dispersion in rotating nanotube for various values of nonlocal scale $\tau = 0, 0.1, 0.2, 0.3, 0.5$. For (a) $\frac{\Omega}{\omega_{str}} = 0$; (b) $\frac{\Omega}{\omega_{str}} = 10$; (c) $\frac{\Omega}{\omega_{str}} = 30$; (d) $\frac{\Omega}{\omega_{str}} = 50$; (e) $\frac{\Omega}{\omega_{str}} = 100$

speed. Because of the nonlinear relation of the wavenumber with wave frequency, for nonrotating CNT, the phase and group speeds also show a nonlinear variation with frequency. As the rotational speed of the CNT increase to higher values, both the speeds will saturate to a constant velocity, because of the linear variation of

Fig. 7.11 Phase speed (*Thick lines*) and Group speed (*Thin lines*) dispersion in rotating nanotube for $\tau = \frac{e_0 d}{L} = 0$ for different values of $\frac{\Omega}{\omega_{str}}$



the wavenumber with wave frequency. The difference between the phase and group speeds of the rotating CNTs is negligible at higher rotational speeds as shown in Fig. 7.11, which is a characteristic of any nondispersive system. In the limiting case, we can say that they become equal and constant for all wave frequencies. For a non-rotating beam, both phase and group speeds are dispersive and show that the speeds approach infinity for very high frequencies. This unreasonable limit is due to the limitation of Euler–Bernoulli beam theory.

Figure 7.12 shows the nondimensional phase speed and nondimensional group speed variation with both the wave frequency and the nonlocal scaling parameter for rotations and nonrotating CNTs. Figure 7.12a shows that, for nonrotating CNT, the phase and group speeds will decrease as the nonlocal scaling parameter increases, because the wavenumbers are increasing with increase in τ (see Fig. 7.10). Also, the difference between the phase and group speeds dips at higher values of τ . As the rotational speed of the CNT increases, both phase and group speeds will also increase as shown in Fig. 7.12b–e. For small rotational speeds, and large values of τ , both speeds show a decrease in nature at smaller frequencies and they become constant at higher wave frequencies. Such difference will also vanish at higher rotational speeds as shown in Fig. 7.12e. On the other hand, one more interesting feature of the nonlocality is that the difference between both the wave speeds is considerable at smaller rotational speeds and τ as well as at the higher rotational speeds and τ and this aspect can be clearly seen from Fig. 7.12.

The wave propagation analysis procedure illustrated here can be extended to study the wave propagation analysis of rotating graphene sheets. This would be helpful in understanding the wave dispersion characteristics of future rotating nanomachines. One such nanomachine is the nanoturbine. For efficient designing of these nanomachines, proper understanding of its mechanical behavior is required. The nanoturbine is characterized by a rotating blades modeled as a rotating nanotube. Rotating nanocantilever rotates at an angular velocity about the hub axis. The performances of these nanoturbines are extremely dependent on dynamic properties of their beam-

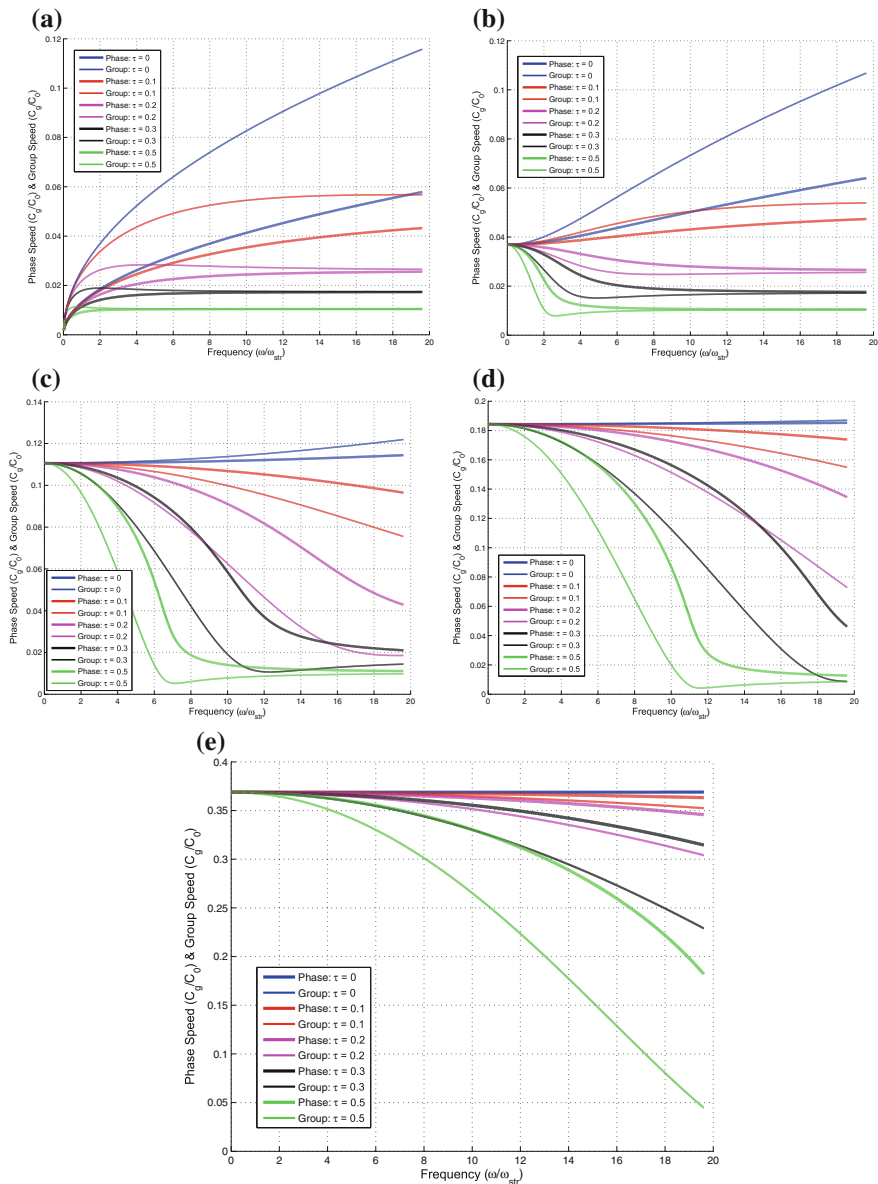


Fig. 7.12 Phase speed (*Thick lines*) and Group speed (*Thin lines*) dispersion in rotating nanotube for different values of $\frac{\Omega}{\omega_{str}}$. Here (a) $\frac{\Omega}{\omega_{str}} = 0$; (b) $\frac{\Omega}{\omega_{str}} = 10$; (c) $\frac{\Omega}{\omega_{str}} = 30$; (d) $\frac{\Omega}{\omega_{str}} = 50$; (e) $\frac{\Omega}{\omega_{str}} = 100$

like elements. In summary, this study would be useful in understanding the scale effects in rotating nanostructures.

7.4 Fluid Carrying SWCNTs

Currently, the study of the CNT filled with fluids is of great interest and is a challenging topic for researchers. This is because CNT promise many new applications in nanobiological devices and nanomechanical systems such as fluid conveyance and drug delivery because of their excellent mechanical properties, chemical and thermal stability, and hollow geometry [16, 17]. Numerous studies of mechanical properties of CNT are available in the literature [18–20], while only a limited amount of work is concerned with the aspect of conveying fluid due to involving of a complicated wave behavior.

The interaction of water with SWCNT is experimentally studied by Babu et al. [21] and demonstrated that the CNT can be used for fabricating nanofluidic devices that involve transport of aqueous fluids. Storage and transport of fluids (or gases) inside CNTs have been the subject of several studies [22–24]. For more details on the topic of fluid inside CNTs, the interested reader is referred to the recent review articles reported by Whitby and Quirke [25] and Mattia and Gogotsi [26]. However, the literature concerning on the study of CNT conveying fluids are relatively scarce.

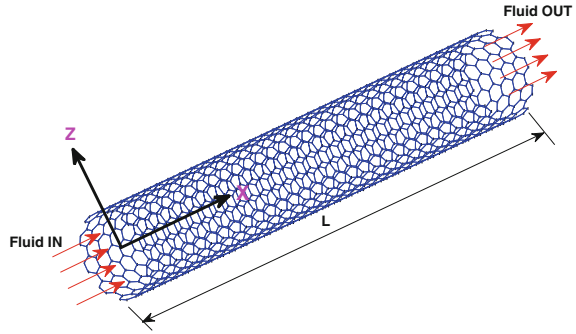
A few studies are reported on wave propagation in CNTs, especially in fluid-filled CNTs with consideration of nonlocal scale effects. Therefore, it is very significant to study the wave propagation of CNTs conveying fluid. The present section presents a theoretical approach to investigate the wave propagation of SWCNTs conveying fluids. The SWCNT is modeled as a Nonlocal Timoshenko beam stress gradient model. The fluid inside the CNT is assumed as water. Using the proposed method, the influence of fluid properties on the wave propagation in CNTs conveying fluid is analyzed the same problem can be modeled differently. That is, the SWCNT can be modeled as long hollow cylindrical shell and to this the fluid loading can be introduced. The wave propagation study of such a model is reported in Chap. 11 of this book.

7.4.1 Nonlocal Governing Equations of Motion

Consider the uniform flow of an inviscid fluid through SWCNT regarded as an elastic hollow cylinder, as shown in Fig. 7.13. The SWCNT has an equivalent Young's modulus E , shear modulus G , Poisson's ratio ν , cross-sectional area A , length L inner radius R , and thick ness t . Let its transverse displacement be $w = w(x, t)$, where time t and the spatial coordinate x .

The Timoshenko beam theory is considered here, and this theory incorporates the effects of rotary inertia and transverse shear deformation on the terahertz wave propagation characteristics of the fluid-conveying SWCNT. In this study, we neglect the gravity effect of the fluid and assume that the SWCNTs are not subjected to an axial load. According to the force and moment balances to a differential element of a CNT and using the procedure adopted in Sect. 7.2, the governing differential

Fig. 7.13 A fluid carrying SWCNT of length L , x and z are the axial and transverse directions, respectively. Coordinate system shown for a (10, 10) SWCNT of 8.147 nm length and consisting of 1340 carbon atoms



equation of motion for CNTs conveying fluid using nonlocal elasticity theory can be written as

$$GA\kappa \left(\frac{\partial \psi}{\partial x} - \frac{\partial^2 w}{\partial x^2} \right) + M_F U_F^2 \frac{\partial^2 w}{\partial x^2} + 2M_F U_F \frac{\partial^2 w}{\partial x \partial t} + (M_C + M_F) \frac{\partial^2 w}{\partial t^2} - M_C (e_0 a)^2 \frac{\partial^4 w}{\partial t^2 \partial x^2} = 0 \quad (7.78)$$

$$EI \frac{\partial^2 \psi}{\partial x^2} - GA\kappa \left(\psi - \frac{\partial w}{\partial x} \right) - (J_C + J_F) \frac{\partial^2 \psi}{\partial t^2} + J_C (e_0 a)^2 \frac{\partial^4 \psi}{\partial t^2 \partial x^2} = 0 \quad (7.79)$$

where I is the second moment of inertia of the SWCNT. $\psi(x, t)$ is the rotation angle of the cross-section perpendicular to the longitudinal axis. M_C and M_F are the mass per unit axial length for SWCNT and fluid, respectively. J_C and J_F are the mass moment of inertia for SWCNT and fluid, respectively. U_F is the uniform mean flow velocity of conveying fluid. κ is the shear correction factor of the SWCNT.

Next, we will perform the wave dispersion analysis. For this we will undertake spectral analysis on Eqs.(7.78) and (7.79) and obtain the relevant equations for wavenumbers and group speeds. For analyzing the dispersion characteristics of waves at terahertz level frequency in fluid filled SWCNT, we assume that a harmonic type of wave solution for the displacement field $w(x, t)$ and $\psi(x, t)$, and they can be expressed in complex form as [1, 2].

$$w(x, t) = \hat{w}(x, \omega) e^{-j(kx - \omega t)} \quad (7.80)$$

$$\psi(x, t) = \hat{\psi}(x, \omega) e^{-j(kx - \omega t)} \quad (7.81)$$

where $\hat{w}(x, \omega)$, $\hat{\psi}(x, \omega)$ are the frequency domain amplitudes of the flexural and the slope of the beam due to bending deformation of CNTs, respectively. k is the wavenumber and ω is the angular frequency of the wave motion and $j = \sqrt{-1}$.

Substituting Eqs.(7.80) and (7.81) into Eqs.(7.78) and (7.79) yields *two* homogeneous equations in terms of \hat{w} and $\hat{\psi}$ as

$$\begin{bmatrix} Q_{11} & Q_{12} \\ Q_{21} & Q_{22} \end{bmatrix} \begin{Bmatrix} \hat{w} \\ \hat{\psi} \end{Bmatrix} = \{0\} \quad (7.82)$$

where

$$\begin{aligned} Q_{11} &= GA\kappa k^2 - M_F U_F^2 k^2 + 2M_F U_F k\omega - (M_C + M_F)\omega^2 - M_C(e_0a)^2 k^2 \omega^2, \\ Q_{12} &= -Q_{21} = -jGA\kappa k, \\ Q_{22} &= -EI k^2 - GA\kappa + (J_C + J_F)\omega^2 + J_C(e_0a)^2 \omega^2 k^2. \end{aligned}$$

The wavenumbers and hence the wave speeds (phase and group speeds) are solved from Eq. (7.82) by using Polynomial Eigenvalue Problem (PEP) [1]. Equating the determinant of matrix $[Q_{ab}]$ ($a, b = 1, 2$) to zero (for the nontrivial solution of \hat{w} , and $\hat{\psi}$) will give the characteristic polynomial in terms of wavenumber k of the order 4, solution of which is quite difficult. PEP converts the characteristic polynomial equation into a matrix of size 2×2 , whose eigenvalues form the solution of the equation. After obtaining the wavenumbers, wave speeds are extracted. The details of computation of wavenumbers using PEP for this SWCNT are given below.

The resultant equation (Eq. (7.82)) can be written in matrix form as

$$\mathbf{S}_2 k^2 + \mathbf{S}_1 k + \mathbf{S}_0 = 0 \quad (7.83)$$

where

$$\mathbf{S}_2 = \begin{bmatrix} GA\kappa - M_C(e_0a)^2 \omega^2 - M_F U_F^2 & 0 \\ 0 & -EI I_1 + J_C(e_0a)^2 \omega^2 \end{bmatrix} \quad (7.84)$$

$$\mathbf{S}_1 = \begin{bmatrix} 2M_F U_F \omega - jGA\kappa & \\ jGA\kappa & 0 \end{bmatrix} \quad (7.85)$$

$$\mathbf{S}_0 = \begin{bmatrix} -(M_C + M_F)\omega^2 & 0 \\ 0 & -GA\kappa + (J_C + J_F)\omega^2 \end{bmatrix} \quad (7.86)$$

Equation (7.83) is the PEP in k for the present problem. This form is amenable to solution of wavenumbers through PEP. From Eq. (7.83), we can clearly see the dependence of nonlocal scale parameter e_0a on wavenumber.

It is well-known that Timoshenko beam model always exhibit cut-off frequency beyond which shear mode starts propagating. The cut-off frequencies of this SWCNTs are obtained by setting $k = 0$ in the dispersion relation (Eq. (7.83)), i.e., for the present case of PEP one can set $|\mathbf{S}_0| = 0$, for the cut-off frequencies as

$$\omega_c^{\text{flexural}} = 0, \quad \omega_c^{\text{shear}} = \sqrt{\frac{GA\kappa}{J_C + J_F}} \quad (7.87)$$

The shear cut-off frequency is a function of the mass moment inertial of the fluid, that is, mass density of the fluid. It will also depend on the SWCNT cross-sectional

properties. Observe that it is independent of the nonlocal scaling parameter. Next, we will investigate the presence of band gaps or in other words the existence of escape frequencies in the group speed plots. The value of escape frequency can be analytically determined by looking at the wavenumber expression and setting $k \rightarrow \infty$. This amounts to setting the $|\mathbf{S}_2| = 0$ in Eq. (7.83), which gives

$$\omega_e^{\text{flexural}} = \frac{1}{(e_0 a)} \sqrt{\frac{EI}{J_C}}, \quad \omega_e^{\text{shear}} = \frac{1}{(e_0 a)} \sqrt{\frac{GA\kappa - M_F U_F^2}{M_C}} \quad (7.88)$$

where $\omega_e^{\text{flexural}}$ and ω_e^{shear} are the escape frequencies in flexural and shear wave mode, respectively. The escape frequencies are inversely related to nonlocal scaling parameter. These frequencies are again a function of the fluid velocity (U_F) in the SWCNT.

The next important parameter in wave dispersion analysis is determination of wave speeds. By definition, phase speed is given as $C_{\text{phase}} = \text{Real}(\frac{\omega}{k})$. Differentiating the Eq. (7.83) with respect to the wave frequency (ω), one can obtain the group speeds ($C_{\text{group}} = \frac{\partial \omega}{\partial k}$) as

$$\left[k^2 \frac{\partial \mathbf{S}_2}{\partial \omega} + \frac{\partial \mathbf{S}_0}{\partial \omega} \right] C_{\text{group}} + 2k\mathbf{S}_2 + \mathbf{S}_1 = 0 \quad (7.89)$$

where the matrices \mathbf{S}_2 , \mathbf{S}_1 and \mathbf{S}_0 are given in Eqs. (7.84) and (7.86). This is again a PEP in terms of C_{group} and one can solve it for group speeds of respective modes (i.e., for flexural and shear), which is again a function of nonlocal scale parameter.

Next, studies on the effect of nonlocal scaling parameter and the fluid density on the terahertz wave propagation in fluid-carrying SWCNT is performed. The radius of the SWCNT is assumed as $R = 3.5$ nm, thickness $t = 0.34$ nm, density $\rho_C = 2,300$ kg/m³ and Young's modulus $E = 1.03$ TPa. In order to know the effect of nonlocal scaling parameter on the wave characteristics of the SWCNT, we assumed that the flow liquid in the SWCNT is water (density $\rho_W = 1,000$ kg/m³).

The spectrum and dispersion curves of the fluid-filled SWCNTs (the uniform velocity of the fluid in SWCNT is assumed as $U_F = 1,000$ m/s) with and without nonlocal effects are shown in Figs. 7.14 and 7.15. Figure 7.14a shows the effect of fluid in SWCNT on the variation of the wavenumbers with the wave frequency for local elasticity. This figure shows the two fundamental modes namely, flexural and shear. Flexural wave mode starts from zero frequency and shear wave mode propagates only after shear cut-off frequency, the frequency at which the imaginary part of wavenumber becomes real. The values of the cut-off frequency are calculated from Eq. (7.87). In the present study for a 3.5 nm radius SWCNT, we have shear cut-off frequency at 0.6256 THz, without fluid and 0.5493 THz, with fluid (water). It can be observed from Eq. (7.87) that these frequencies are independent of the nonlocal scaling parameter, and hence same frequencies are obtained from both local and nonlocal theories (see Fig. 7.14).

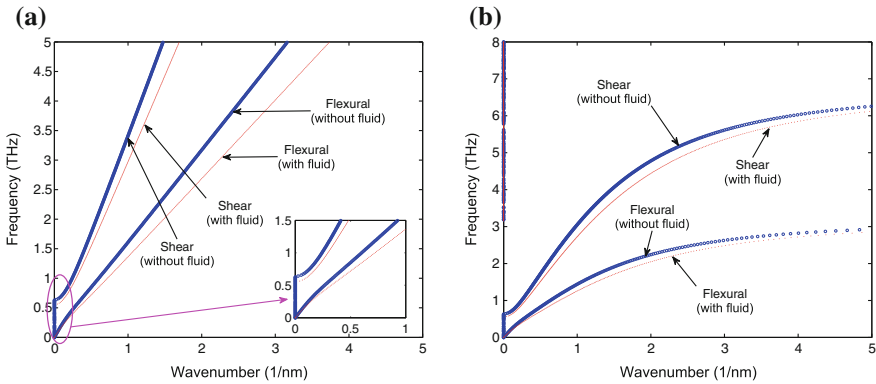


Fig. 7.14 Wavenumber dispersion in SWCNT with and without fluid effect obtained from (a) local elasticity ($e_0a = 0$ nm) and (b) nonlocal elasticity ($e_0a = 0.5$ nm)

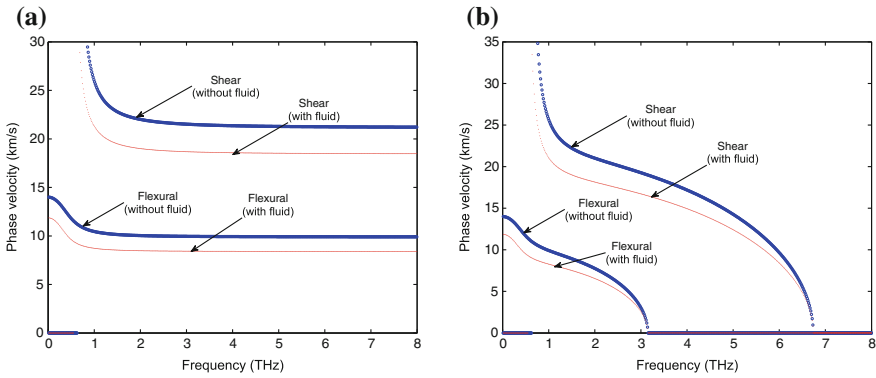


Fig. 7.15 Phase speed dispersion in SWCNT with and without fluid effect obtained from (a) local elasticity ($e_0a = 0$ nm) and (b) nonlocal elasticity ($e_0a = 0.5$ nm)

For $e_0a = 0$, which is the case of local theory of elasticity solution, flexural wavenumbers have a nearly linear variation with frequency, especially at higher frequencies, which is shown in Fig. 7.14a and correspondingly, the phase speeds, shown in Fig. 7.15a, show constant variation. When the fluid loading is considered in the CNT, the wavenumbers increases and the corresponding wave speeds are decreased. Because of the fluid, the shear cut-off frequency also decreased as shown in the inset of Fig. 7.14a.

However, with the introduction of nonlocal scale effects, the wave behavior is altered drastically. Both the flexural and shear wave modes escape to infinity at escape frequency, a phenomenon we are seeing for most of the nonlocal elasticity models. The spectrum and dispersion curves shown in Figs. 7.14b and 7.15b are plotted for $e_0a = 0.5$ nm. The effect of the presence of fluid in SWCNT from nonlocal elasticity is same as the local elasticity. From Figs. 7.14b and 7.15b, it can be observed that the

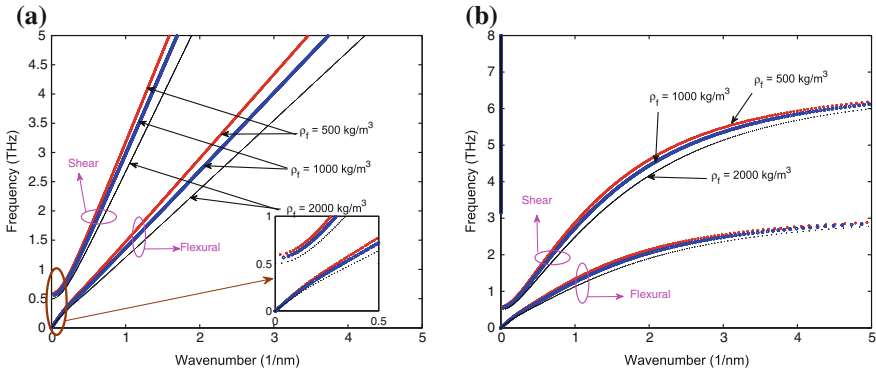


Fig. 7.16 Wavenumber dispersion in SWCNT for different fluids (i.e., different densities) obtained from (a) local elasticity and (b) nonlocal elasticity

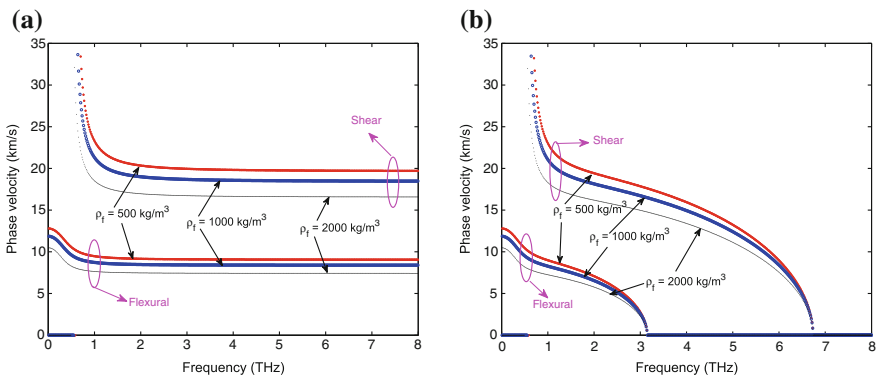


Fig. 7.17 Phase speed dispersion in SWCNT for different fluids (i.e., different densities) obtained from (a) local elasticity and (b) nonlocal elasticity

escape frequencies of the flexural and shear wave mode are not affected by the fluid in SWCNT. The escape frequencies of the flexural and shear wave modes (with and without fluid in SWCNT) are 3.159 and 6.729 THz, for $e_0a = 0.5 \text{ nm}$, respectively.

The effect of the fluid density on the spectrum and dispersion curves of the SWCNT is shown in Figs. 7.16 and 7.17. Here, for observing the effect of nonlocal parameter on the terahertz wave propagation in SWCNT, three different types of fluid are used with densities $\rho_f = 500, 1,000$ and $2,000 \text{ kg/m}^3$, respectively. As the fluid becomes denser, the wavenumbers of the flexural and shear wavenodes are increasing and the corresponding wave velocities are decreasing (see Figs. 7.16 and 7.17). It is clearly seen that from Fig. 7.16 that as the fluid in SWCNT becomes denser, the shear cut-off frequency slightly decreases. The escape frequencies of the flexural and shear wavenodes are not affected by the fluid density as shown in Figs. 7.16b and 7.17b (here $e_0a = 0.5 \text{ nm}$). It can be seen that the escape frequencies of the

shear wavemode are function of fluid density and the fluid velocity in SWCNT (see Eq. (7.88)). It is observed that the effect of the fluid velocity and the density are negligibly small on escape frequencies. The observations made in Figs. 7.14 and 7.15 for $e_0a = 0$ and $e_0a = 0.5$ nm are still valid for Figs. 7.16 and 7.17.

The variation of the shear cut-off frequency with the radius of the SWCNT is shown in Fig. 7.18. We have already discussed that the shear cut-off frequency is affected by the presence of the fluid. Figure 7.18a shows that the shear cut-off frequencies are smaller with the presence of the fluid as compared to the empty SWCNT. For $R < 1$ nm, the difference between the shear cut-off frequencies is negligible. As the radius of the SWCNT increases the shear cut-off frequency decreases as shown in Fig. 7.18a. The effect of the fluid density on the shear cut-off frequency is shown in Fig. 7.18b. As the fluid becomes denser and at higher values of the SWCNT radius, the shear cut-off frequency decreases. We also observe that, as the fluid becomes denser, the shear cut-off frequencies are almost same for $R < 1$ nm. Figure 7.18a shows that, as the radius of the nanotube increases, the shear cut-off frequency decreases and at higher values of R , the cut-off frequency approaches to very small values.

The escape frequency variation with nonlocal scaling parameter e_0a for flexural and shear waves is shown in Fig. 7.19. The value of escape frequency decreases with increase in e_0a , for both wave modes. For very small values of e_0a , the escape frequencies are very high. The escape frequencies of both wave modes are not affected by fluid density and the uniform fluid velocity in CNT. From Eq. (7.88), it is observed that $GA\kappa \gg M_F U_F^2$. Obviously, $\omega_e^{\text{flexural}} < \omega_e^{\text{shear}}$ (see Fig. 7.19).

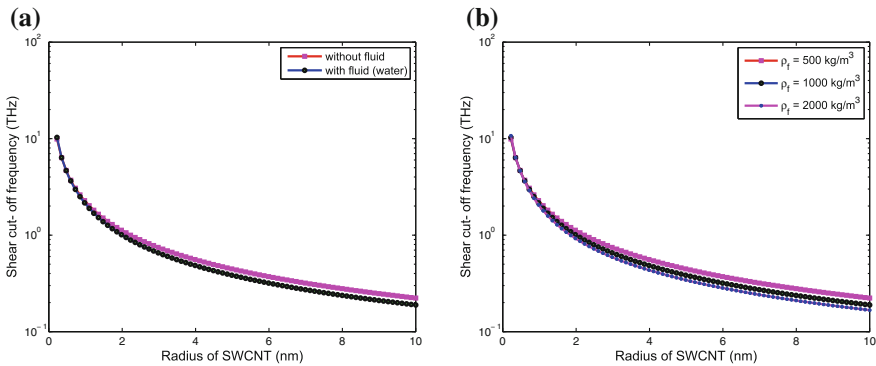
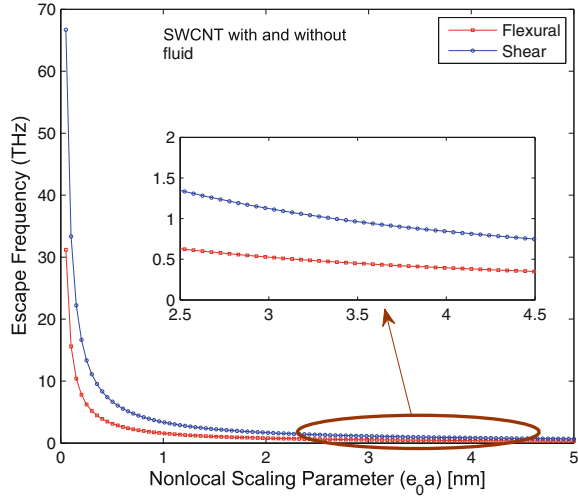


Fig. 7.18 Shear cut-off frequency variation with SWCNT radius (a) with and without fluid effect and (b) for different densities of fluids

Fig. 7.19 Escape frequency variation of flexural and shear waves with SWCNT radius (with and without fluid effect)



7.5 Magnetic Field Effects on SWCNT

Recently, growing interest in terahertz physics of nanoscale materials and devices has drawn more attention to CNTs phonon dispersion relation, especially in the terahertz frequency range. In recent years, the microwave absorbing effect and electromagnetic characteristics of CNTs has also attracted considerable interest for theoretical and practical importance in fundamental science and application [27, 28]. Hence, understanding the effect of magnetic field on the characteristics of wave propagation in CNTs is essential and may give a useful help in applications for nanoengineering. Wang et al. [29] studied the effect of magnetic field on wave propagation in CNTs embedded in elastic matrix. In some applications of nanoengineering, the investigation on dynamic characteristic of CNTs under magnetic field is useful. Slepyan and Maksimenko [30] studied the electromagnetic wave propagation in CNTs. They reported the discrete relation of wave propagation in CNTs by using molecular dynamics theories. Li and Wang [31] studied the different wave modes coupled in longitudinal or transverse magnetic field. More recently, authors [32] published a work on the vibration analysis of nonlocal Flügge shell model for SWCNTs under the longitudinal magnetic field based on wave propagation approach. This work covers axial, circumferential, and radial degree of freedom in the formulations. The analysis here shows that vibration frequencies of CNTs drop dramatically in the presence of the magnetic field for various circumferential wavenumbers. Such effect is also observed for various boundary conditions of the CNT. Through this work, it is observed that the effect of longitudinal magnetic field on ultrasonic vibration of CNTs are useful in the design of nanodrive device, nano-oscillator and actuators and nanoelectron technology, where carbon nanotubes act as basic elements. Except for the above works, the effect of magnetic field on wave propagation in embedded SWCNTs using nonlocal elasticity theory is studied sparsely in the open literature.

The next section studies the effect of longitudinal magnetic field on wave propagation in carbon nanotubes based on nonlocal continuum mechanics theory. The SWCNT is assumed to be embedded in Pasternak type of elastic medium, which is different from the Winkler foundation model. In the former, the foundation considers both the shear and transverse constraints, while in the latter, the shear constraints are not considered. Wave propagation equations in CNTs are derived by considering the Lorentz magnetic forces applied on CNTs induced by a longitudinal magnetic field through Maxwell equations. The wavenumber characteristic curves of CNTs under a longitudinal magnetic field are obtained by solving the governing equation. The effects of longitudinal magnetic field and the elastic matrix on wave propagation in CNTs are discussed through numerical results. The present work mainly focus on the flexural wave properties of the SWCNTs under longitudinal magnetic field using the nonlocal scale effects.

7.5.1 Maxwell's Relations

Let the current density (\mathbf{J}), strength vectors of electric field (\mathbf{e}), disturbing vectors of magnetic field (\mathbf{h}), the vector of displacement (\mathbf{U}), then, the Maxwell equations [33] are given by

$$\mathbf{J} = \nabla \times \mathbf{h} \quad (7.90)$$

$$\nabla \times \mathbf{e} = -\eta \frac{\partial \mathbf{h}}{\partial t} \quad (7.91)$$

$$\nabla \cdot \mathbf{h} = 0 \quad (7.92)$$

$$\mathbf{e} = -\eta \left(\frac{\partial \mathbf{U}}{\partial t} \times \mathbf{H} \right) \quad (7.93)$$

$$\mathbf{h} = \nabla \times (\mathbf{U} \times \mathbf{H}) \quad (7.94)$$

where the Hamilton arithmetic operator is $\nabla = \frac{\partial}{\partial x} \hat{\mathbf{i}} + \frac{\partial}{\partial y} \hat{\mathbf{j}} + \frac{\partial}{\partial z} \hat{\mathbf{k}}$ and η is the magnetic permeability. For simplifying the analysis, we apply a longitudinal magnetic field vector $\mathbf{H} = (H_x, 0, 0)$ exerted on the carbon nanotube. Let the displacement vector $\mathbf{U} = (u, v, w)$, then

$$\mathbf{h} = \nabla \times (\mathbf{U} \times \mathbf{H}) = -H_x \left(\frac{\partial v}{\partial y} + \frac{\partial w}{\partial z} \right) \hat{\mathbf{i}} + H_x \frac{\partial v}{\partial x} \hat{\mathbf{j}} + H_x \frac{\partial w}{\partial x} \hat{\mathbf{k}} \quad (7.95)$$

$$\begin{aligned} \mathbf{J} = \nabla \times \mathbf{h} = & H_x \left(-\frac{\partial^2 v}{\partial x \partial z} + \frac{\partial^2 w}{\partial x \partial y} \right) \hat{\mathbf{i}} - H_x \left(\frac{\partial^2 v}{\partial y \partial z} + \frac{\partial^2 w}{\partial x^2} + \frac{\partial^2 w}{\partial z^2} \right) \hat{\mathbf{j}} \\ & + H_x \left(\frac{\partial^2 v}{\partial x^2} + \frac{\partial^2 v}{\partial y^2} + \frac{\partial^2 w}{\partial y \partial z} \right) \hat{\mathbf{k}} \end{aligned} \quad (7.96)$$

The Lorentz force (\mathbf{f}) induced by the longitudinal magnetic field is

$$\begin{aligned}\mathbf{f} &= f_x \hat{\mathbf{i}} + f_y \hat{\mathbf{j}} + f_z \hat{\mathbf{k}} = \eta(\mathbf{J} \times \mathbf{H}) \\ &= \eta \left[0 \hat{\mathbf{i}} + H_x^2 \left(\frac{\partial^2 v}{\partial x^2} + \frac{\partial^2 v}{\partial y^2} + \frac{\partial^2 w}{\partial y \partial z} \right) \hat{\mathbf{j}} + H_x^2 \left(\frac{\partial^2 w}{\partial x^2} + \frac{\partial^2 w}{\partial y^2} + \frac{\partial^2 v}{\partial y \partial z} \right) \hat{\mathbf{k}} \right]\end{aligned}\quad (7.97)$$

Therefore, Lorentz force along the x , y , and z directions are

$$f_x = 0 \quad (7.98)$$

$$f_y = \eta H_x^2 \left(\frac{\partial^2 v}{\partial x^2} + \frac{\partial^2 v}{\partial y^2} + \frac{\partial^2 w}{\partial y \partial z} \right) \quad (7.99)$$

$$f_z = \eta H_x^2 \left(\frac{\partial^2 w}{\partial x^2} + \frac{\partial^2 w}{\partial y^2} + \frac{\partial^2 v}{\partial y \partial z} \right) \quad (7.100)$$

For the present wave propagation analysis in SWCNT, we assume that $w = w(x, t)$ only, so that the Lorentz force in z -direction is written as

$$f_z = \eta H_x^2 \frac{\partial^2 w}{\partial x^2} \quad (7.101)$$

Here f_z denotes the body force.

7.5.2 Nonlocal Governing Equations of Motion Including Magnetic Field Effects

In the present work, ultrasonic wave dispersion characteristics of single-walled carbon nanotubes embedded in elastic medium are presented. The chemical bonds are assumed to be formed between the carbon nanotube and the elastic medium (see Fig. 7.20). The elastic matrix is described by a Pasternak foundation model, which accounts for both normal pressure and the transverse shear deformation of the surrounding elastic medium. When the shear effects are neglected, the model reduces to Winkler foundation model. The normal pressure or Winkler elastic foundation parameter is approximated as a series of closely spaced, mutually independent, vertical linear elastic springs where the foundation modulus is assumed equivalent to stiffness of the springs. The normal pressure and the incompressible layer that resists transverse shear deformation by Pasternak foundation model is expressed as

$$p(x) = -K_W w + K_S \frac{\partial^2 w}{\partial x^2} \quad (7.102)$$

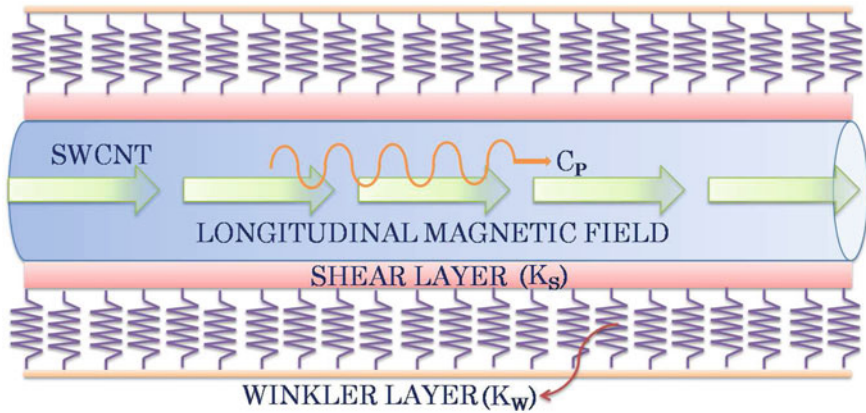


Fig. 7.20 Schematic of single-walled carbon nanotube embedded in Pasternak type elastic medium (consists of both shear layer with stiffness K_S and Winkler layer with stiffness K_W) under the longitudinal magnetic field. Here C_P represents the wave propagation velocity

where the first parameter K_W is the Winkler foundation modulus, the second parameter K_S is the stiffness of the shearing layer. The values of K_W and K_S are per unit area.

A slender SWCNT can be modeled using Euler–Bernoulli beam theory. Considering the elementary Euler–Bernoulli theory of beams, the axial and transverse displacement fields can be represented as

$$u(x, y, z, t) = u^0 - z \frac{\partial w}{\partial x} \quad (7.103)$$

$$w(x, y, z, t) = w(x, t) \quad (7.104)$$

where w is transverse displacement of a point $(x, 0)$ on the middle plane (i.e., $z = 0$) of the beam. The only nonzero strain of the Euler–Bernoulli beam theory is

$$\varepsilon_{xx} = \frac{\partial u}{\partial x} = \frac{\partial u^0}{\partial x} - z \frac{\partial^2 w}{\partial x^2} \quad (7.105)$$

The equations of motion of the Euler–Bernoulli beam theory are given by

$$\frac{\partial Q}{\partial x} - \rho A \frac{\partial^2 u^0}{\partial t^2} = 0 \quad (7.106)$$

$$\frac{\partial^2 M}{\partial x^2} - \rho A \frac{\partial^2 w}{\partial t^2} + f(x) - p(x) = 0 \quad (7.107)$$

where

$$Q = \int_A \sigma_{xx} dA, \quad M = \int_A z \sigma_{xx} dA \quad (7.108)$$

and $p(x)$ is force exerted by the elastic matrix per unit area, σ_{xx} is the axial stress in the direction of x , Q is the axial force, M is the bending moment and $f(x)$ is a function of space to incorporate the longitudinal magnetic force, ρ is the mass density, and A is the beam cross-section area.

The nonlocal constitutive relation takes the following form for beams:

$$\sigma_{xx} - (e_0 a)^2 \frac{\partial^2 \sigma_{xx}}{\partial x^2} = E \varepsilon_{xx} \quad (7.109)$$

where E is the Young's modulus of the beam material. Using Eqs. (7.108) and (7.109), we have

$$Q - (e_0 a)^2 \frac{\partial^2 Q}{\partial x^2} = EA \frac{\partial u}{\partial x} \quad (7.110)$$

$$M - (e_0 a)^2 \frac{\partial^2 M}{\partial x^2} = EI \kappa_e \quad (7.111)$$

where $I = \int_A z^2 dA$ is the moment of inertia of the beam cross-section and $\kappa_e = -\frac{\partial^2 w}{\partial x^2}$ is the curvature of the beam.

With the help of the nonlocal constitutive relations and the equations of motion presented, the moment can be expressed in terms of the generalized displacement as, by substituting Eq. (7.111) into Eq. (7.107), we get

$$M = -EI \frac{\partial^2 w}{\partial x^2} + (e_0 a)^2 \left[\rho A \frac{\partial^2 w}{\partial t^2} - f(x) + p(x) \right] \quad (7.112)$$

Substituting M from Eq. (7.112) into Eq. (7.107), we obtain the equation of motion of nonlocal Euler–Bernoulli beams as

$$-EI \frac{\partial^4 w}{\partial x^4} + (e_0 a)^2 \frac{\partial^2}{\partial x^2} \left[\rho A \frac{\partial^2 w}{\partial t^2} - f(x) + p(x) \right] + f(x) - p(x) - \rho A \frac{\partial^2 w}{\partial t^2} = 0 \quad (7.113)$$

The present problem assumes a longitudinal magnetic field in SWCNT. Here $f(x) \neq f_z$, since f_z is a body force and $f(x)$ denotes the force per length. Hence, $f(x)$ can be written as

$$f(x) = f_z \times A = \eta A H_x^2 \frac{\partial^2 w}{\partial x^2} \quad (7.114)$$

This allows us to represent the Eq. (7.113) as a constant coefficient nonlocal partial differential equation. Finally, the nonlocal governing differential equation for transverse displacement ($w(x, t)$) of a beam is derived as

$$\begin{aligned}
& EI \frac{\partial^4 w}{\partial x^4} - \eta A H_x^2 \frac{\partial^2 w}{\partial x^2} + \eta A H_x^2 (e_0 a)^2 \frac{\partial^4 w}{\partial x^4} + K_W w - K_S \frac{\partial^2 w}{\partial x^2} - K_W (e_0 a)^2 \frac{\partial^2 w}{\partial x^2} \\
& + K_S (e_0 a)^2 \frac{\partial^4 w}{\partial x^4} + \rho A \frac{\partial^2 w}{\partial t^2} - \rho A (e_0 a)^2 \frac{\partial^4 w}{\partial t^2 \partial x^2} = 0
\end{aligned} \quad (7.115)$$

Using the derived governing differential equation (Eq. (7.115)), a spectral analysis needs to be performed to determine the effect of nonlocal parameter and magnetic field on wave dispersion. Equation (7.115) can be transformed into frequency domain using Fourier transform [1],

$$w(x, t) = \sum_{n=1}^N \widehat{w}(x) e^{i\omega_n t} \quad (7.116)$$

where \widehat{w} is the amplitude of the wave motion, ω_n the circular frequency of the n th sampling point and N is the Nyquist frequency. The sampling rate and the number of sampling points should be sufficiently large to have relatively good resolution of both high and low frequencies, respectively. Substitution of Eq. (7.116) into Eq. (7.115), we get

$$\begin{aligned}
& \sum_{n=1}^N \left[EI \frac{d^4 \widehat{w}}{dx^4} - \eta A H_x^2 \frac{d^2 \widehat{w}}{dx^2} + \eta A H_x^2 (e_0 a)^2 \frac{d^4 \widehat{w}}{dx^4} + K_W \widehat{w} - K_S \frac{d^2 \widehat{w}}{dx^2} - K_W (e_0 a)^2 \frac{d^2 \widehat{w}}{dx^2} \right. \\
& \left. + K_S (e_0 a)^2 \frac{d^4 \widehat{w}}{dx^4} - \rho A \omega_n^2 \widehat{w} + \rho A (e_0 a)^2 \omega_n^2 \frac{d^2 \widehat{w}}{dx^2} \right] e^{i\omega_n t} = 0
\end{aligned} \quad (7.117)$$

This equation must be satisfied for each n and hence can be written as the ordinary differential equation in single variable x as

$$\begin{aligned}
& EI \frac{d^4 \widehat{w}}{dx^4} - \eta A H_x^2 \frac{d^2 \widehat{w}}{dx^2} + \eta A H_x^2 (e_0 a)^2 \frac{d^4 \widehat{w}}{dx^4} + K_W \widehat{w} - K_S \frac{d^2 \widehat{w}}{dx^2} - K_W (e_0 a)^2 \frac{d^2 \widehat{w}}{dx^2} \\
& + K_S (e_0 a)^2 \frac{d^4 \widehat{w}}{dx^4} - \rho A \omega^2 \widehat{w} + \rho A (e_0 a)^2 \omega^2 \frac{d^2 \widehat{w}}{dx^2} = 0
\end{aligned} \quad (7.118)$$

where k is the wavenumber, and ω is the frequency of the wave motion. Substituting $\widehat{w}(x) = \widetilde{w} e^{-ik_n x}$ into Eq. (7.118) yields

$$\begin{aligned}
& \left[EI k_n^4 + \eta A H_x^2 k_n^2 + \eta A H_x^2 (e_0 a)^2 k_n^4 + K_W + K_S k_n^2 + K_W (e_0 a)^2 k_n^2 + K_S (e_0 a)^2 k_n^4 \right. \\
& \left. - \rho A \omega^2 - \rho A \omega^2 (e_0 a)^2 k_n^2 \right] \widetilde{w} = 0
\end{aligned} \quad (7.119)$$

For nontrivial solution of the wave amplitude \widetilde{w} , this implies that

$$\begin{aligned}
& \left[EI + \eta A H_x^2 (e_0 a)^2 + K_S (e_0 a)^2 \right] k_n^4 + \left[\eta A H_x^2 + K_S + K_W (e_0 a)^2 - \rho A \omega^2 (e_0 a)^2 \right] k_n^2 \\
& + K_W - \rho A \omega^2 = 0
\end{aligned} \quad (7.120)$$

this is the dispersion or characteristic equation for an equivalent continuum structure (ECS) of an embedded SWCNT. The wavenumbers are obtained by solving the characteristic equation (7.120) as

$$k_n = \pm \sqrt{-\frac{1}{2} \frac{\alpha_2}{\alpha_4} \pm \sqrt{\frac{1}{4} \left(\frac{\alpha_2}{\alpha_4}\right)^2 - \frac{\alpha_0}{\alpha_4}}} \quad (7.121)$$

where $\alpha_4 = EI + \eta AH_x^2(e_0a)^2 + K_S(e_0a)^2$, $\alpha_2 = \eta AH_x^2 + K_S + K_W(e_0a)^2 - \rho A \omega^2(e_0a)^2$ and $\alpha_0 = K_W - \rho A \omega^2$. Note that the above wavenumber can also be obtained by rewriting the above equation in PEP form and solving it. These wavenumbers are functions of the nonlocal scaling parameter, wave frequency, longitudinal magnetic field strength, stiffness of elastic medium, and other material parameters of the beam. Out of these four wavenumbers two are real and the other two are imaginary. The real and imaginary parts correspond to propagating and spatially damped modes, respectively. From Eq. (7.121) if $K_W = 0$, there is no possibility for a cut-off frequency, above which the spatially damped mode becomes propagation mode. From Eq. (7.120), by equating the constant term to zero or substituting $k = 0$, we can get that the cut-off frequency ω_c as

$$\omega_c = \sqrt{\frac{K_W}{\rho A}} \quad (7.122)$$

The flexural wave cut-off frequency is a function of Winkler foundation parameter K_W and the geometrical properties of the CNT. It is also independent of the strength of the magnetic field.

The phase speed is defined as

$$C_p = Re \left(\frac{\omega_n}{k_n} \right) \quad (7.123)$$

It is different for different ω_n . Again, group speeds can be obtained as before, where $C_g = d\omega/dk$.

Based on the formulations obtained above with the nonlocal Euler–Bernoulli beam model, the wave dispersion characteristics of embedded SWCNT under the influence of the longitudinal magnetic field are investigated and discussed here. The discrete model of the SWCNT with the coordinate system is shown in Fig. 7.20. In example calculations, the effective radius of SWCNT $r_e = 3.5$ nm the wall thickness of SWCNT $h = 0.34$ nm ($Eh = 360$ J/m²), and the mass density of SWCNT, $\rho = 2,300$ Kg/m³, are assumed. The properties of the elastic matrix such as Winkler modulus $K_W = 1.13 \times 10^{18}$ Pa/m and polymer matrix shear modulus $K_S = 1.13$ Pa/m are taken from Ref. [34].

The wave speed variation, with frequency for the SWCNT under longitudinal magnetic field without elastic matrix, obtained from both local and nonlocal theories

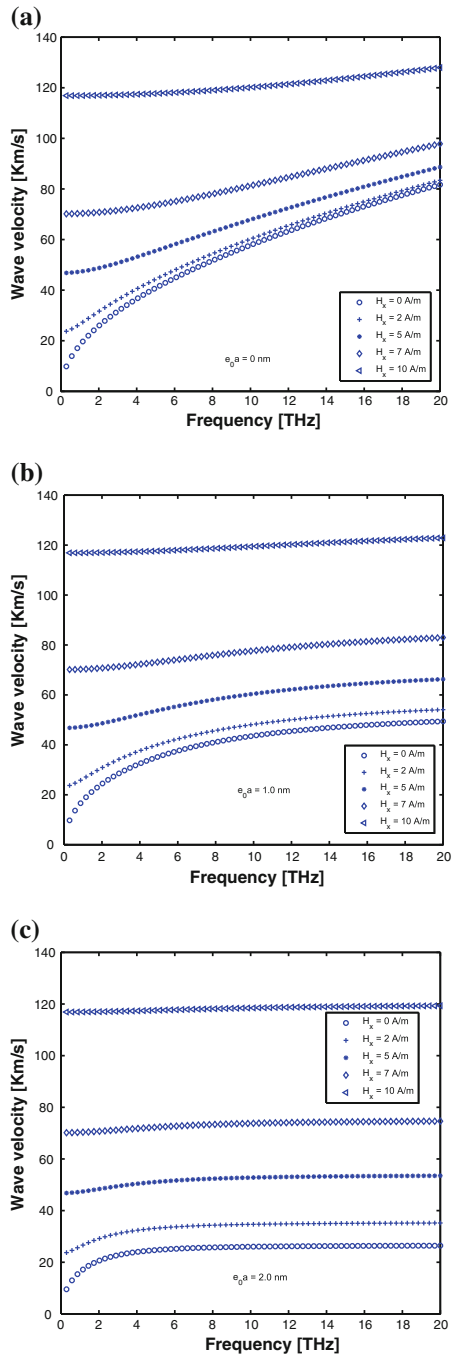
is shown in magnet 1. The local elasticity calculation shows that the wave speed dispersion is nonlinear with frequency at higher frequencies. The nonlocal elasticity calculation shows that the wave speeds are almost constant at higher frequencies as shown in Fig. 7.21b, c. Also wave speeds obtained from the nonlocal elasticity are small as compared to those obtained from the local elasticity calculations. The applied longitudinal magnetic field changes the dynamic characteristic of wave propagation in SWCNT at lower and higher frequency regions (see Fig. 7.21). Such changes are captured in both local and nonlocal elasticity calculations. Over the frequency region studied here, the wave velocity increases with an increase in longitudinal magnetic field strength. However, the longitudinal magnetic field has little influence on wave velocity when its magnitude is very small (< 2.0 A/m) over the entire frequency range. With the increase in the nonlocal parameter, the wave velocity is found to be decreasing as shown in Fig. 7.21. For $e_0a = 2.0$ nm, the magnitude of wave velocity is almost constant for all wave frequencies at higher magnetic field strength (Fig. 7.21c). It means that the application of magnetic field makes the SWCNT stiffer.

For two values of H_x ; 0 and 2 A/m, the effect of the elastic medium (Pasternak foundation) is shown in Fig 7.22 for $e_0a = 0$. The effect of elastic matrix shows that the wave will have a cut-off frequency (see Fig. 7.22a, b). In the presence of the elastic medium, the flexural wave modes are having a frequency band gap region. Within this frequency band gap, the corresponding wavenumbers are imaginary. Thus, the flexural modes are attenuated at frequencies lying within this band. Hence, these wavenumbers have a substantial imaginary part along with the real part, thus these waves attenuate as they propagate. It is found that the presence of the magnetic field will not alter the frequency band gap; however, it will change the shape and magnitude of the wave dispersion curve as shown in Fig. 7.22b. For $H_x = 0$, the dispersion relation is nonlinear whereas it is almost linear for $H_x = 2$ A/m. The effect of the elastic medium for $e_0a = 2.0$ nm is shown in Fig. 7.23 with and without the presence of the longitudinal magnetic field. The presence of magnetic field, the wave dispersion relations is almost constant for higher frequencies. The band gap region is also not affected by the nonlocality (see Fig. 7.23a, b). The cut-off frequency is found to be inversely proportional to the radius of ECS of the SWCNT. So, the cut-off frequency decreases, as the radius of CNT increases. In accordance with Eq. (7.122), the cut-off frequency increases with the stiffness of the Winker foundation parameter.

7.6 Surface Effects on Flexural Wave Propagation in Nanobeams

Surface effects are significant to nanostructure materials and can influence the physical and chemical properties of nanomaterials due to the increase in surface-to-volume ratio. Therefore, many studies have been performed to investigate the surface effects on nanostructures [35–37]. For example, He and Lilley [35] studied the surface effects

Fig. 7.21 Wave speed dispersion with wave frequency in a single-walled carbon nanotube under the influence of longitudinal magnetic field effect obtained from (a) local/classical elasticity ($e_0a = 0$ nm), (b) nonlocal elasticity ($e_0a = 1.0$ nm) and (c) nonlocal elasticity ($e_0a = 2.0$ nm). In this simulations, the elastic matrix is not considered, i.e., $K_W = 0$ and $K_S = 0$



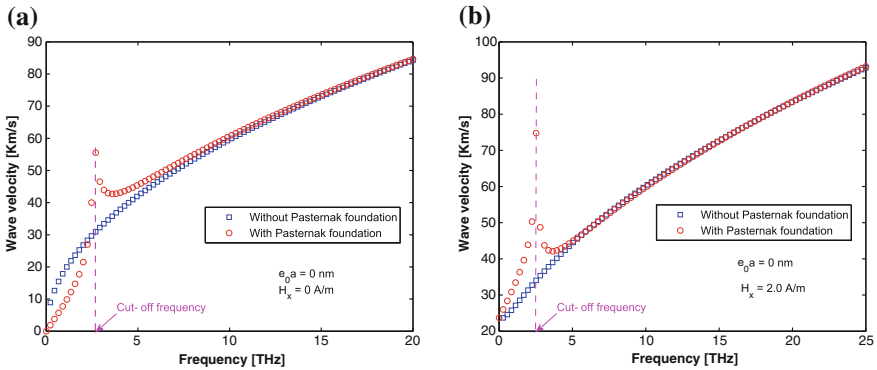


Fig. 7.22 Wave speed dispersion with wave frequency in a single-walled carbon nanotube embedded in Pasternak type elastic medium obtained from local or classical elasticity ($e_0a = 0$ nm) for the longitudinal magnetic field strengths of (a) $H_x = 0$ A/m and (b) $H_x = 2.0$ A/m

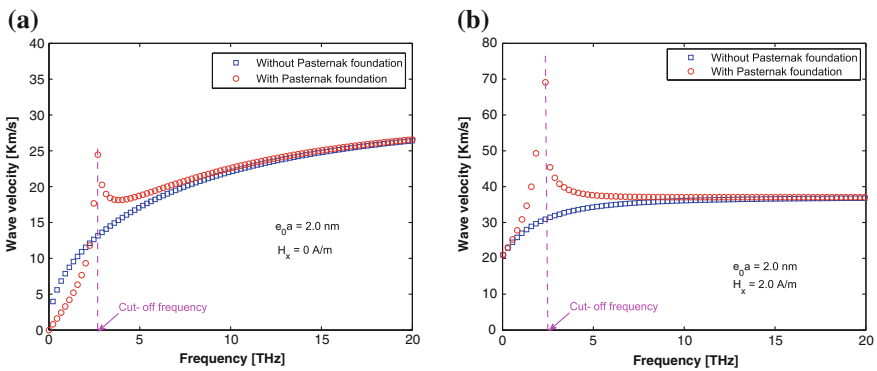


Fig. 7.23 Wave speed dispersion with wave frequency in a single-walled carbon nanotube embedded in Pasternak type elastic medium obtained from nonlocal elasticity ($e_0a = 2.0$ nm) for the longitudinal magnetic field strengths of (a) $H_x = 0$ A/m and (b) $H_x = 2.0$ A/m

on the elastic behavior of static bending nanowires using the Euler–Bernoulli beam theory. Wang and Feng [36] examined the surface effects on axial buckling and the transverse vibration of nanowires using the Timoshenko beam theory. They found that the surface effects with positive surface constants tend to increase the critical axial force and the natural frequency and shear deformation tends to decrease the critical axial compression force and the natural frequency.

Furthermore, classical theories can also be generalized to be able to properly describe the mechanical behavior of thin films at nanoscale [38, 39]. Lu et al. [40] followed this approach to derive the generalized differential equations of static, dynamic, and stability of ultra thin films including surface effects. Assadi et al. [41] modified the laminated plate theory to include the effects of surface properties and temperature on the dynamic behavior of rectangular nanoplates. Farshi et al. [37] studied the

size-dependent flexural vibration of nanotubes with consideration of surface effects using a modified beam theory. Lim and He [39] studied size-dependent nonlinear vibration of thin films based on classical plate theory. Gurtin and Murdoch [42] predicted the presence of surface additional properties for elastic solids based on equilibrium equations. Zhou and Huang [43] demonstrated that the surface excess elasticity can be positive or negative for different materials and their crystal orientations. Molecular dynamics and atomistic calculation methods are frequently used to obtain the magnitudes of surface stresses and surface elasticity effects for different materials. Lee and Chang [44], studied the surface and small-scale effects on vibration analysis of a nonuniform nanocantilever beam.

In the next section, nonlocal beam theory is employed to describe the wave propagation analysis of nanotubes including the surface effects.

7.6.1 Governing Equation of Motion Including Surface Residual Stress

Consider a SWCNT with a cross-section shown in Fig. 7.24. The nonlocal constitutive relations for one-dimensional case (Eq. (7.7)), for moment given in Eq. (7.6) can be rewritten as

$$M - g^2 \frac{\partial^2 M}{\partial x^2} = -\Gamma \frac{\partial^2 w}{\partial x^2} \quad (7.124)$$

where $w = w(x, t)$ is the transverse displacement, which depends on the spatial coordinate along the longitudinal axis X , M the resultant bending moment, Γ the effective flexural rigidity, which includes the surface bending elasticity on the beam and its flexural rigidity, and $g = e_0 a$ is the nonlocal scale parameter, which is used to modify the classical elasticity theory and is limited to application on a device on the nanometer scale. Here a is an internal characteristic length, e.g., length of C–C bond (0.142 nm), granular distance etc., and e_0 is a nonlocal scaling parameter, which has been assumed as a constant appropriate to each material.

In addition, based on the Euler beam theory, the equation of transverse vibrations for a beam is expressed by

$$\frac{\partial \tilde{Q}}{\partial x} = \rho_{nt} A_{nt} \frac{\partial^2 w}{\partial t^2} - H_0 \frac{\partial^2 w}{\partial x^2} \quad (7.125)$$

$$\tilde{Q} = \frac{\partial M}{\partial x} \quad (7.126)$$

where \tilde{Q} is the resultant shear force on the cross-section A , H_0 the surface parameter, which is determined by the residual surface tension, and ρ the density of the beam. Here, the parameters Γ and H_0 are defined as

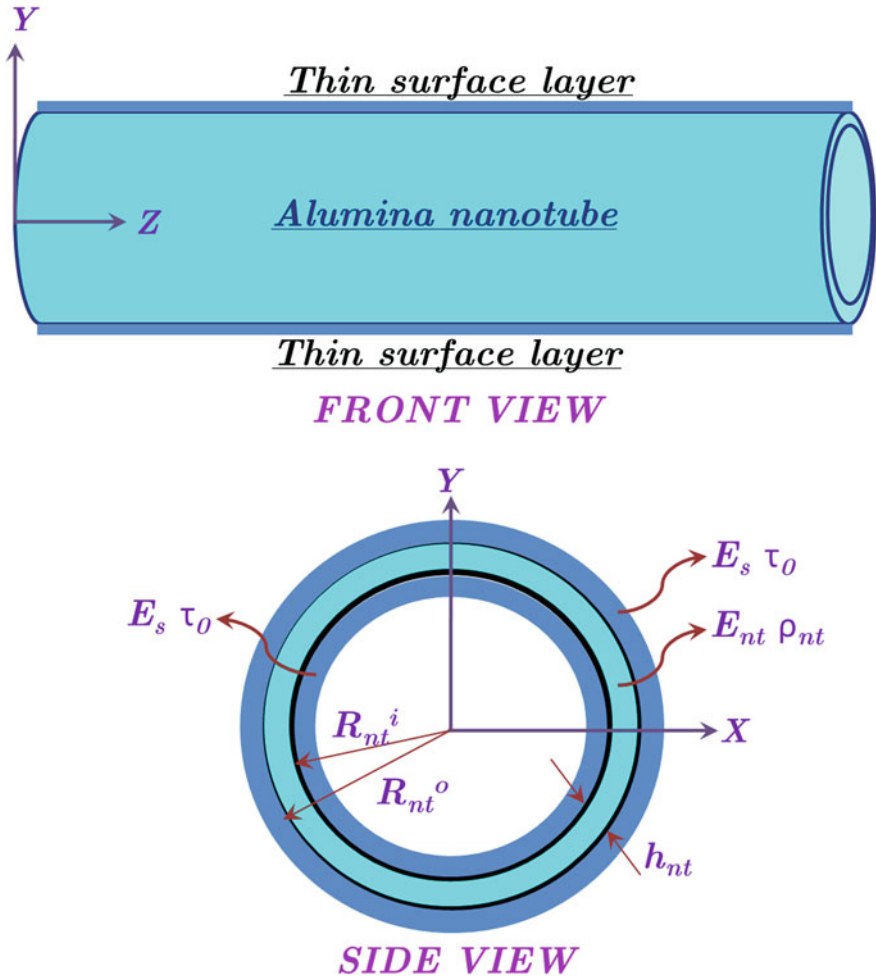


Fig. 7.24 A alumina nanotube with inner and outer thin surface layers and the cross-section of the nanotube

$$\Gamma = E_{nt} I_{nt} + \pi E_s \left(R_{nt}^i{}^3 + R_{nt}^o{}^3 \right) \tag{7.127}$$

$$H_0 = 4\tau_0 \left(R_{nt}^i + R_{nt}^o \right) \tag{7.128}$$

In the above equation, E_{nt} is the Young's modulus of CNT, E_s is the Young's modulus of the surface film, I_{nt} is the area moment of inertia of the CNT, R_{nt}^i is the inner radius of the CNT, R_{nt}^o is the outer radius of the CNT, and τ_0 is the thickness of the CNT. Using Eqs. (7.124)–(7.126), the nonlocal bending moment M can be expressed as

$$M = -\Gamma \frac{\partial^2 w}{\partial x^2} + g^2 \left(\rho_{nt} A_{nt} \frac{\partial^2 w}{\partial t^2} - H_0 \frac{\partial^2 w}{\partial x^2} \right) \quad (7.129)$$

Therefore, substituting Eq. (7.129) into Eq. (7.124), the governing equation of transverse wave propagation for the CNT with consideration of both surface and nonlocal effects can be expressed as

$$\Gamma \frac{\partial^4 w}{\partial x^4} + \rho_{nt} A_{nt} \frac{\partial^2 w}{\partial t^2} - \rho_{nt} A_{nt} g^2 \frac{\partial^4 w}{\partial t^2 \partial x^2} - H_0 \frac{\partial^2 w}{\partial x^2} + H_0 g^2 \frac{\partial^4 w}{\partial x^4} = 0 \quad (7.130)$$

If the nonlocal scaling parameter g is zero, and the surface layer properties are neglected then the above governing differential equation of motion becomes classical governing equation for an Euler–Bernoulli beam.

7.6.2 Wave Propagation Analysis

As before, we first transform the governing differential equation (Eq. (7.130)) to the frequency domain using DFT, which is given by

$$w(x, t) = \sum_{p=0}^{P-1} \sum_{q=0}^{Q-1} \hat{w}(x, \omega_q) e^{-j(k_p x - \omega_q t)} \quad (7.131)$$

where \hat{w} is the amplitude of the wave motion, P and Q are the number of time sampling points and number spatial sampling points respectively. ω_q is the circular frequency at the q^{th} time sample. Similarly, k_p is the wavenumber at the p^{th} spatial sample point and $j = \sqrt{-1}$. Substituting Eq. (7.131) into the governing partial differential equation (Eq. (7.130)), we get the dispersion relation as follows. Hereafter, the subscripts p and q in Eq. (7.131) are dropped for simplified notations.

$$\left(\Gamma + g^2 H_0 \right) k^4 + \left(H_0 - \rho_{nt} A_{nt} \omega^2 \right) k^2 - \rho_{nt} A_{nt} \omega^2 = 0 \quad (7.132)$$

This dispersion relation is solved for the wavenumbers. These wavenumbers are functions of the nonlocal scaling parameter, wave frequency, and other material parameters of the CNT and surface layers. Out of the four wavenumbers, two are purely real and the other two are purely imaginary. The real part gives rise to the propagating component while the imaginary part gives rise to the spatially damped mode. From Eq. (7.132) it is obvious that, there is no possibility for a cut-off frequency, above which the spatially damped mode turns to be propagative. From Eq. (7.132), by equating the constant term to zero or substituting $k = 0$, we can get that the cut-off frequency ω_c , which is zero for the present formulation.

In order to know the effect of relative parameters on the wave propagation analysis of nanotubes, we consider the material properties of an anodic alumina nanotube

with crystallographic of $\langle 111 \rangle$ direction (obtained from Ref. [37]) as follows: $E_{nt} = 70$ GPa, $\rho_{nt} = 2,700$ kg/m³, $E_s = 5.1882$ N/m, $\tau_0 = 0.9108$ N/m.

The surface effects on wavenumber dispersion with wave frequency are shown in Fig. 7.25, obtained from both local/classical and nonlocal calculations. From Fig. 7.25, it can be found that the flexural wavenumbers with surface effects are high as compared to that without surface effects. It can also be observed that, with consideration of surface effects, the flexural wavenumbers are showing a compressive nature. If we consider the small scale effects (nonlocal), the wavenumbers show an increasing tendency (see Fig. 7.25a–c). At higher frequencies, the difference in wavenumbers, obtained by considering with and without the surface effects, increases with the increase of the nonlocal small-scale parameter. With surface effects, the zero wavenumber bands are $0 < k < 5.104 \times 10^8$ m⁻¹, $0 < k < 5.278 \times 10^8$ m⁻¹ and $0 < k < 5.935 \times 10^8$ m⁻¹, respectively, for small-scale parameters of $g = 0.0$ m, 0.5×10^{-9} m and 1.0×10^{-9} m, respectively. As a result, if one employs the wave dispersion relation to determine the nanotube's material properties ignoring surface effects ($E_s = 0$; $\tau_0 = 0$), their values may be significantly underestimated or overestimated. It should be mentioned that the wavenumber size dependence can be different if different material and surface properties are used.

Figure 7.26 shows the surface effects on the wave frequency variation with the nonlocal small-scale parameter for different values of the wavenumber. It can be observed that the wave frequency will decrease with an increase in nonlocal small scale parameter. For $k = 0.5 \times 10^9$ m⁻¹, the surface properties have no effect on the wave frequency for a given small scale parameters (see Fig. 7.26a). As the wavenumber increases, the flexural wave stop band can be observed in the nanotube that has substantial surface effect. For $k = 1.0 \times 10^9$ m⁻¹ and $k = 2.0 \times 10^9$ m⁻¹, the flexural wave propagation region is within the $0 < g < 1.724 \times 10^{-9}$ m and $0 < g < 1.931 \times 10^{-9}$ m scale range, respectively. For scale parameters larger than the above-mentioned range, the angular frequency become imaginary. This means that waves with larger wavenumbers (or, equivalently, with smaller wavelengths) cannot propagate through this medium. Instead, the imaginary frequency implies that the response occurs everywhere in the medium instantaneously. This is physically unrealistic. Therefore, these smaller wavelengths should not be considered. Filtering shorter waves occurs automatically in a discrete medium, where wavelengths smaller than two times the particle size cannot be monitored. However, in a continuous medium, all wavelengths can in principle be present. Especially when shock waves are investigated, all wavelengths are triggered by the loading. From Fig. 7.26a, the most notable feature is that the scale effect is not obvious for smaller wavenumbers and the influence becomes prominent with the wavenumber increasing in Fig. 7.26b–c. Moreover, all of the wave frequencies become smaller with the scale coefficient increasing.

Figure 7.27 shows size-dependent effects on flexural wave propagation in the nanotube with radius of the nanotubes being $R_{nt}^o = h$ and $R_{nt}^o = 2h$. For comparison, the curve for nanotube without the surface effects is also included in Fig. 7.27. Comparing the results with those in Fig. 7.26, similar size and surface effects upon the flexural wave propagation can be observed. It can be observed that as the size of the

Fig. 7.25 The surface effects on spectrum curves (wavenumber dispersion), for a nanotube obtained from (a) local/classical elasticity $g = 0$ m, (b) nonlocal elasticity $g = 0.5 \times 10^{-9}$ m and (c) nonlocal elasticity $g = 1.0 \times 10^{-9}$ m

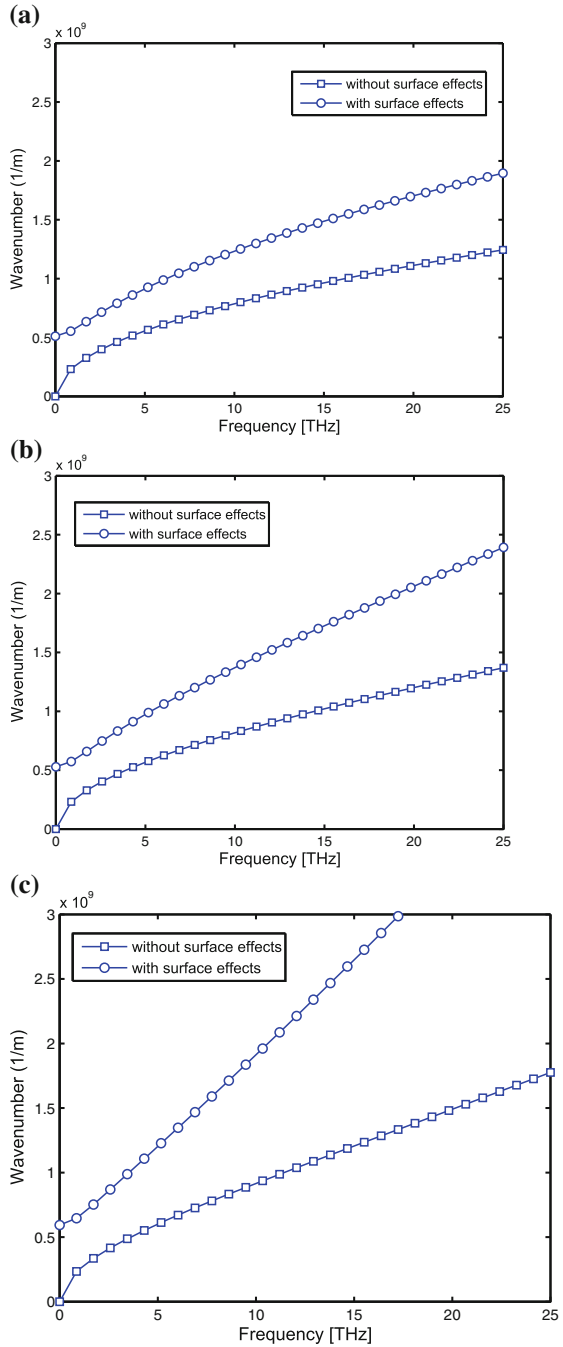


Fig. 7.26 The surface effects on wave frequency dispersion with nonlocal scaling parameter, for a nanotube with wavenumbers **(a)** $k = 0.5 \times 10^9 \text{ m}^{-1}$, **(b)** $k = 1.0 \times 10^9 \text{ m}^{-1}$ and **(c)** $k = 2.0 \times 10^9 \text{ m}^{-1}$

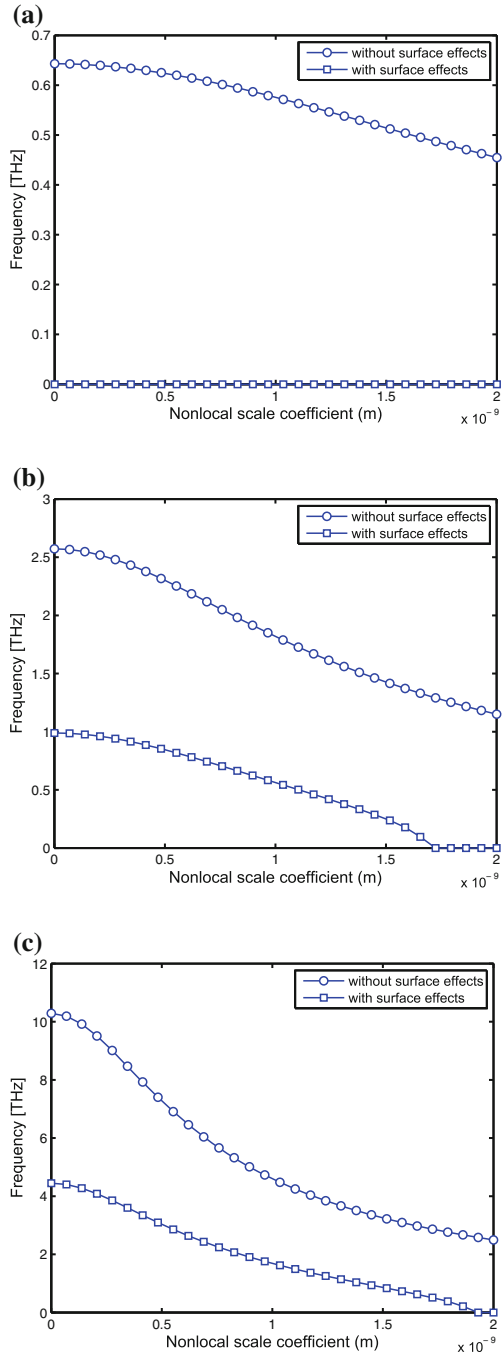
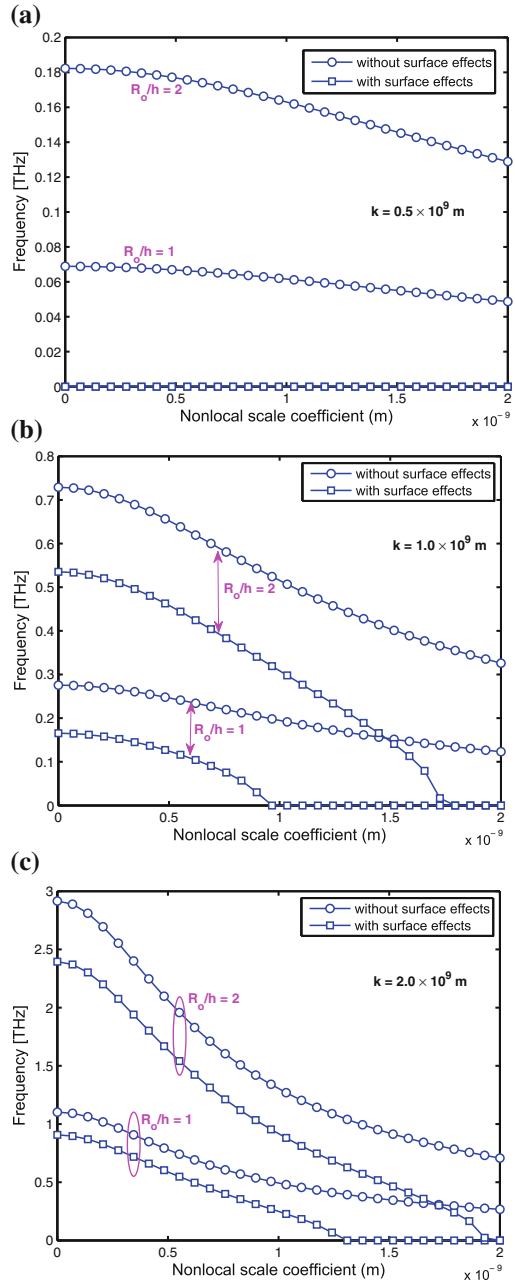


Fig. 7.27 The surface effects on wave frequency dispersion with nonlocal scaling parameter, for different radii of nanotubes with wavenumbers (a) $k = 0.5 \times 10^9 \text{ m}^{-1}$, (b) $k = 1.0 \times 10^9 \text{ m}^{-1}$ and (c) $k = 2.0 \times 10^9 \text{ m}^{-1}$



CNT increase, the wave frequency as well as the scale coefficient range also increase (see Fig. 7.27a–c). It means that when the wavenumber increases or the wavelength decreases, the small-scale effects will be obvious.

7.7 Summary

In the present chapter, the strong effect of nonlocal small scale on wave characteristics of nonlocal beams was studied using both nonlocal Euler–Bernoulli and nonlocal Timoshenko beam models. The governing equations were given for both the beam models and the wave dispersion analysis was performed using spectral analysis. The study shows that, for nonlocal Timoshenko beams, the scale parameter introduces certain band gap region in both flexural and shear wave modes where no wave propagation occurs. This is manifested in the wavenumber plots as the region where the wavenumber tends to infinite and the corresponding group speed tends to be zero. The bandgap region occurs for both flexural and shear wave modes. The strength of the band gap region decreases as the nonlocal small-scale increases. It means that, as we consider very high scale the structure behaves more or like classical behavior. The estimation of the bandgap region can provide useful guidance for the study and design of the next generation of nanodevices that make use of the wave propagation properties of carbon nanotubes.

Next, the wave dispersion characteristics of a rotating nanotube (such as SWCNT) were studied using the spectral analysis and nonlocal scale theory. The rotating nanotube was modeled as a Euler–Bernoulli beam. The governing partial differential equation for a uniform rotating beam was derived incorporating the nonlocal scale effects and a powerful model was derived in analyzing the wave dispersion characteristics of the rotating nanotube. Some of the interesting features of the wave behavior in rotating nanotubes were observed. It has been shown that the dispersive flexural wave tends to behave nondispersively at very high rotation speeds. Understanding the dynamic behavior of rotating nanostructures is important for practical development of nanomachines. At the nanoscale, the nonlocal effects often become more prominent. Such observations are helpful in designing the nanomotors and the other CNT-based rotational nanodevices where CNT acts as a basic element.

The effect of nonlocal scaling parameter on the terahertz wave propagation in fluid-filled single-walled carbon nanotubes (SWCNTs) was also studied in this chapter. The SWCNT was modeled as a Timoshenko beam, including rotary inertia and transverse shear deformation by considering the nonlocal scale effects. The analysis shows that, for a fluid filled SWCNT, the wavenumbers of flexural and shear waves will increase and the corresponding wave speeds will decrease as compared to an empty SWCNT. The nonlocal scale parameter introduces certain band gap region in both flexural and shear wave modes where no wave propagation occurs. The effect of fluid density on the terahertz wave propagation in SWCNT was also studied and the analysis shows that as the fluid becomes denser, the wave speeds will decrease. The escape frequency decreases with the increase in nonlocal scaling parameter, for both

wave modes. We also show that the effect of fluid density and velocity is negligible on the escape frequencies of flexural and shear wave modes.

Next, the effect of longitudinal magnetic field on ultrasonic or terahertz wave dispersion characteristics of an equivalent continuum structure of single-walled carbon nanotubes embedded in elastic medium was studied. Nonlocal governing equation of motion for an ECS of SWCNT under a longitudinal magnetic field was derived by considering the Lorentz magnetic force obtained from Maxwell's relations. The results show that the velocity of flexural waves in SWCNTs increases with the increase in the strength of the longitudinal magnetic field for all frequency bands studied in that particular section. The effect of the magnetic field strength, elastic matrix stiffness, and nonlocal parameter on the ultrasonic wave dispersion properties of SWCNT was also investigated.

Lastly, small-scale/size-dependent wave propagation properties of nanotubes under the effect of surface properties were also investigated. Nonlocal elasticity theory was used to derive the general differential equation based on equilibrium approach to include those scale effects. Scale and surface property-dependent wave characteristic equations were obtained via spectral analysis. It was observed that the effect of surface properties on the flexural waves of nanotubes is more significant. It can be found that the flexural wavenumbers with surface effects were high as compared to that without surface effects. It has been shown that with consideration of surface effects, the flexural wavenumbers were showing a compressive nature. The effect of the small scale and the size of the nanotube on wave dispersion properties was also captured in the present chapter.

References

1. S. Gopalakrishnan, A. Chakraborty, D. Roy Mahapatra, *Spectral Finite Element Method* (Springer, London, 2008)
2. J.F. Doyle, *Wave Propagation in Structures* (Springer, New York, 1997)
3. A. Graff, *Wave Motion in Elastic Solids* (Dover Publications, New York, 1995)
4. J.N. Reddy, S.D. Panga, Nonlocal continuum theories of beams for the analysis of carbon nanotubes. *J. Appl. Phys.* **103**, 023511 (2008)
5. K.E. Drexler, *Nanosystems: Molecular Machinery, Manufacturing, and Computation* (Wiley, New York, 1992)
6. P.V.M. Rao, M. Singh, V. Jain, Carbon nanotubes as machine elements—a critical assessment. *Nanotechnology* **2**, 250–253 (2005)
7. D.H. Robertson, B.L. Dunlap, D.W. Brenner, J.W. Mintmire, C.T. White, Fullerene/Tubule based hollow carbon nano-gears. *Mater. Res. Soc.* **349**, 283 (1994)
8. J. Han, A. Globus, R. Jaffe, G. Deardorff, Molecular dynamics simulation of carbon nanotube based gears. *Nanotechnology* **8**, 95–102 (1997)
9. R. Jaffe, J. Han, A. Globus, Rotor Blade With a Paddle-Type Tip, NASA Technical Report No. NASA-97-006, 1997.
10. D. Srivastava, A phenomenological model of the rotation dynamics of carbon nanotube gears with laser electric fields. *Nanotechnology* **8**, 186–192 (1997)
11. A. Lohrasebi, H. Raffi-Tabar, Computational modeling of an ion-driven nanomotor. *J. Mol. Graphics Model.* **27**, 116–123 (2008)

12. S. Zhang, W.K. Liu, R.S. Ruo, Atomistic simulations of double-walled Carbon nanotubes (DWCNTs) as rotational bearings. *Nanotechnol. Lett.* **4**, 293–297 (2004)
13. A. Fennimore, T.D. Yuzvinsky, W.Q. Han, M.S. Fuhrer, Rotational actuators based on carbon nanotubes. *Nature* **424**, 408–410 (2003)
14. S.C. Pradhan, T. Murmu, Application of nonlocal elasticity and DQM in the flapwise bending vibration of a rotating nanocantilever. *Physica E* **42**(7), 1944–1949 (2010)
15. T. Murmu, S. Adhikari, Scale-dependent vibration analysis of pre-stressed carbon nanotubes undergoing rotation. *J. Appl. Phys.* **108**(12), 123507 (2010)
16. D. Tomanek, R. Enbody, *Science and Application of Nanotubes* (Kuwlar/Plenum, New York, 2000)
17. G. Pastorin, W. Wu, S. Wieckowski, J.P. Briand, K. Kostarelos, M. Prato, A. Bianco, Double functionalization of carbon nanotubes for multimodal drug delivery. *Chem. Commun.* **21**, 1182–1184 (2006)
18. J.R. Xiao, J.W. Gillespie, Nonlinear deformation and progressive failure of multi-walled carbon nanotubes under internal radial pressure. *Phys. Rev. B* **76**, 155404 (2006)
19. S.C. Fang, W.J. Chang, Y.H. Wang, Computation of chirality- and size-dependent surface Young's moduli for single-walled carbon nanotubes. *Phys. Lett. A* **371**, 499–503 (2007)
20. X. Chen, G. Cao, A structural mechanics study of single-walled carbon nanotubes generalized from atomistic simulation. *Nanotechnology* **17**, 1004–1015 (2006)
21. S. Babu, P. Ndungu, J.C. Bradley, M.P. Rossi, Y. Gogotsi, Guiding water into carbon nanopipes with the aid of bipolar electrochemistry. *Microfluid. Nanofluid.* **1**(3), 284–288 (2005)
22. G.E. Gadd, M. Blackford, The world's smallest gas cylinders? *Science* **277**, 933–936 (1997)
23. J. Li, T. Furuta, H. Goto, T. Ohashi, Y. Fujiwara, S. Yip, Theoretical evaluation of hydrogen storage capacity in pure carbon nanostructures. *J. Chem. Phys.* **119**(4), 2376–2385 (2003)
24. A. Skoulidas, D.M. Ackerman, K.J. Johnson, D.S. Sholl, Rapid transport of gases in carbon nanotubes. *Phys. Rev. Lett.* **89**, 185901 (2002)
25. M. Whitby, N. Quirke, Fluid flow in carbon nanotubes and nanopipes. *Nat. Nanotechnol.* **2**, 87–94 (2007)
26. D. Mattia, Y. Gogotsi, Review: static and dynamic behavior of liquids inside carbon nanotubes. *Microfluid. Nanofluid.* **5**(3), 289–305 (2008)
27. G. Fedorova, A. Tselevb, D. Jimenezc, S. Latild, N.G. Kalugine, P. Barbarab, D. Smirnova, S. Rochef, Exploring the magnetically induced field effect in carbon nanotube-based devices. *Physica E* **40**, 1010–1013 (2008)
28. A. Wadhawan, D. Garrett, J.M. Perezb, Nanoparticle-assisted microwave absorption by single-wall carbon nanotubes. *Appl. Phys. Lett.* **83**, 2683–2685 (2003)
29. H. Wang, K. Dong, F. Men, Y.J. Yan, X. Wang, Influences of longitudinal magnetic field on wave propagation in carbon nanotubes embedded in elastic matrix. *Appl. Math. Model.* **34**(4), 878–889 (2010)
30. G.Y. Slepyan, S.A. Maksimenko, Electrodynamics of carbon nanotubes: dynamic conductivity, impedance boundary conditions, and surface wave propagation. *Phys. Rev. B* **60**, 17136–17149 (1999)
31. W. Li, Y.N. Wang, Electromagnetic wave propagation in single-walled carbon nanotube. *Phys. Lett. A* **333**, 303–309 (2004)
32. S. Narendar, S. S. Gupta, S. Gopalakrishnan, Ultrasonic vibration analysis of single-walled carbon nanotubes under longitudinal magnetic field using nonlocal elasticity and wave propagation approach. *Adv. Sci. Lett.* (2011). doi:10.1166/asl.2011.1878
33. K.D. John, *Electromagnetics* (McGrawHill Inc., USA, 1984)
34. S.C. Pradhan, J.K. Phadikar, Small scale effect on vibration of embedded multilayered graphene sheets based on nonlocal continuum models. *Phys. Lett. A* **373**, 1062–1069 (2009)
35. J. He, C.M. Lilley, Surface effect on the elastic behavior of static bending nanowires. *Nano Lett.* **8**, 1798–1802 (2008)
36. G.F. Wang, X.Q. Feng, Timoshenko beam model for buckling and vibration of nanowires with surface effects. *J. Phys. D: Appl. Phys.* **42**, 155411 (2009)

37. B. Farshi, A. Assadi, A. Alinia-ziazi, Frequency analysis of nanotubes with consideration of surface effects. *Appl. Phys. Lett.* **96**, 093105 (2010)
38. D.W. Huang, Size-dependent response of ultra-thin films with surface effects. *Int. J. Solids Struct.* **45**, 568–579 (2008)
39. C.W. Lim, L.H. He, Size-dependent nonlinear response of thin elastic films with nanoscale thickness. *Int. J. Mech. Sci.* **46**, 1715–1726 (2004)
40. P. Lu, L.H. He, H.P. Lee, C. Lu, Thin plate theory including surface effects. *Int. J. Solids Struct.* **43**, 4631–4647 (2006)
41. A. Assadi, B. Farshi, A. Alinia-ziazi, Size dependent dynamic analysis of nanoplates. *J. Appl. Phys.* **107**, 124310 (2010)
42. M.E. Gurtin, A.I. Murdoch, Surface stress in solids. *Int. J. Solids Struct.* **14**, 431–440 (1978)
43. L.G. Zhou, H. Huang, Are surfaces elastically softer or stiffer? *Appl. Phys. Lett.* **84**, 1940 (2004)
44. H.L. Lee, W.J. Chang, Surface and small-scale effects on vibration analysis of a nonuniform nanocantilever beam. *Physica E* **43**, 466469 (2010)

Chapter 8

Wave Propagation in Multi-Walled Carbon Nanotubes

Multi-walled carbon nanotubes consist of multiple layers of graphite rolled in on themselves to form a tube shape. There are two models which can be used to describe the structures of MWCNT. In the Russian Doll model, sheets of graphite are arranged in concentric cylinders, for example, a (0,8) SWCNT within a larger (0,10) single-walled nanotube. In the Parchment model, a single sheet of graphite is rolled in around itself, resembling a scroll of parchment or a rolled newspaper. The interlayer distance in multi-walled nanotubes is close to the distance between graphene layers in graphite, approximately 3.3 \AA (330 pm). While SWCNT can be metallic or semiconductor depending upon its chirality (or diameter), MWCNT is mostly metallic in character. The walls in a MWCNT are held together by *van der Waals force*. A typical MWCNT is shown in Fig. 8.1.

Application of nonlocal continuum theory to nanotechnology problems was initially addressed by Peddison et al. [1], in which the static deformation of a beam structures based on a simplified nonlocal model was analyzed. Ru [2] has presented a work related to the linearized column buckling of a multiple-column model of MWCNT. Yoon et al. [3] presented a work on vibration of MWCNTs, which focused on the resonant frequencies and the associated vibrational modes. Yoon et al. [4] also studied the effects of rotary inertia and shear deformation on transverse wave propagation in individual carbon nanotubes. Chakraborty et al. [5] modeled a MWCNT as an assemblage of cylindrical shell elements connected throughout their lengths by distributed springs to investigate the elastic waves of very high frequency in carbon nanotubes and to give the dispersion relation between the group velocity and the wavenumber. These studies have shown that both elastic models of a beam and a cylindrical shell are valid to describe the vibration or wave propagation of carbon nanotubes in a relatively low-frequency range. Chakraborty et al. [6] have developed spectral element-based model of wave propagation in MWCNTs. Their studies show that a N -walled MWCNT exhibits $N - 1$ cut-off frequencies corresponding to shearing modes which appear at Tera-Hertz scale. Mitra and Gopalakrishnan [7] have studied the characteristics of wave dispersion in MWCNTs using Flugge's shell theory.

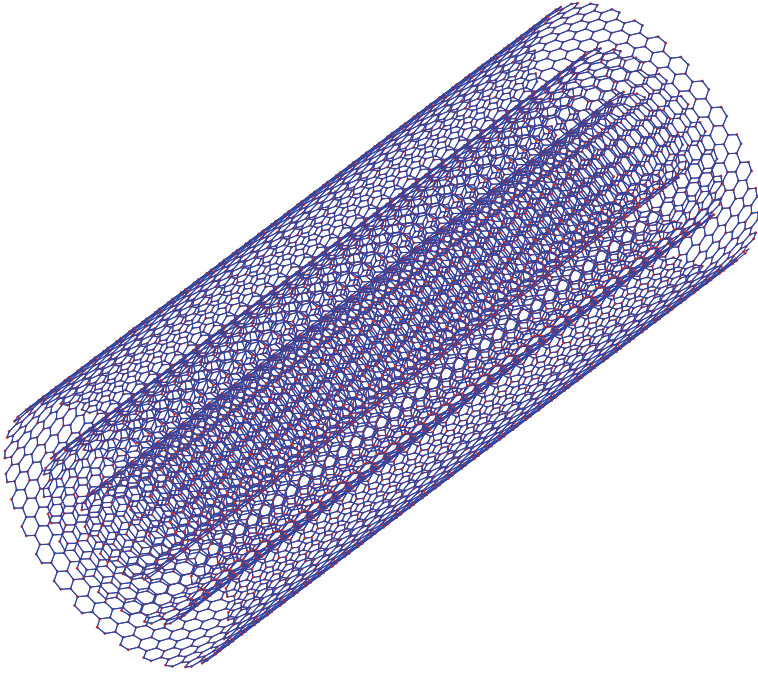


Fig. 8.1 A (10, 10) @ (20, 20) @ (30, 30) multi-walled carbon nanotube (MWCNT) of 10.043 nm length consisting of 1660 @ 3320 @ 4980 carbon atoms (generated in MATLAB)

Several researchers have used non-local elastic models with the second-order gradient of stress to study the vibration and wave propagation of both single- and multi-walled carbon nanotubes in a higher frequency range. These studies have shown that the nonlocal continuum model work as efficiently as molecular dynamics models at high frequencies. From these studies, it is clear that most wave propagation studies performed by various researchers using nonlocal continuum models were limited to SWCNT. The previous wave propagation studies using local continuum models have shown that the wave behavior in a SWCNT is drastically different compared to the behavior of MWCNT. Hence, the main objective of this chapter is to bring out the main effects that the nonlocal scale parameter to the flexural wave propagation in MWCNTs.

In this chapter, a nonlocal multiple Timoshenko beam model is used for analyzing the wave propagation in MWCNTs. Each carbon nanotube in MWCNT is modeled as a Timoshenko beam and the van der Waals interaction is assumed as a distributed spring system. The effect of nonlocal scaling parameter (e_0a) on the wave propagation in MWCNTs and also the variation of the escape and cut-off frequencies with nanotube radius and e_0a is studied in detail. Here $e_0a = 0.5, 1.0$ and 2.0 nm are used in simulation, where $a = 0.142$ nm (C–C bond length).

8.1 van der Waals Forces

Modeling van der Waals forces between the concentric nanotubes is a key component in this study. The principle of modeling this force in the form of distributed springs all along the circumference of each adjacent concentric nanotube is shown in Fig. 8.2. If the interaction pressure per unit area exerted on n th tube by the $(n + 1)$ th tube is denoted by $p_{(n)(n+1)}$ and is given by [2]

$$p_{(n)(n+1)} = c_{(n)(n+1)}(w_{n+1} - w_n) \tag{8.1}$$

where w_n is the inward transverse deflection of the n th tube, van der Waals interaction coefficient $c_{(n)(n+1)}$ is given as [8]

$$c_{(n)(n+1)} = \frac{320(2R_n)}{0.16d^2} \text{ erg/cm}^2 \tag{8.2}$$

where $d = 1.42 \text{ \AA}$ (the length of carbon–carbon (C–C) bond), $n = 1, 2, \dots, N - 1$, R_n is the center line radius of the i th tube.

Let $p_{(n+1)(n)}$ stands for the pressure on $(n + 1)$ th tube due to (n) th tube, we have

$$p_{(n+1)(n)} = -\frac{R_n}{R_{n+1}} p_{(n)(n+1)} \quad n = 1, 2, \dots, N - 1 \tag{8.3}$$

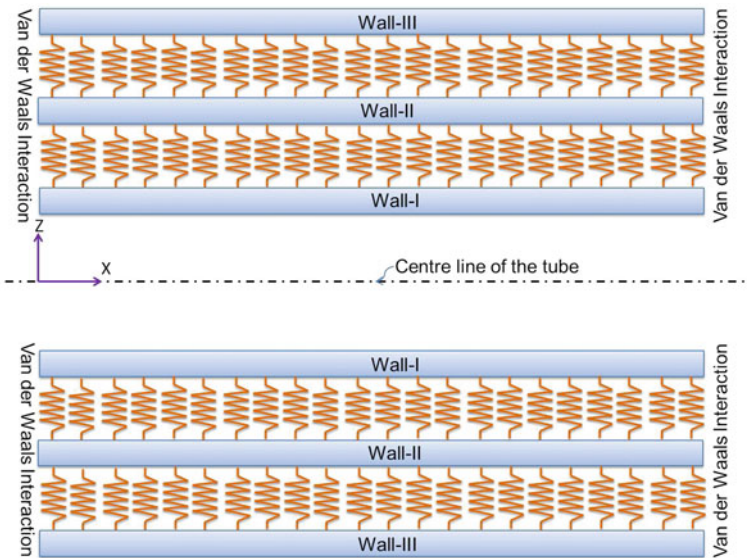


Fig. 8.2 A MWCNT model showing the van der Waals interaction

where R_n is the radius of the n th tube. In the mathematical model for MWCNT discussed in next section, the van der Waals interaction is modeled as distributed springs as shown in Fig. 8.2.

8.2 Governing Equations for NLSGM MWCNT

We consider the modeling of MWCNTs using the Timoshenko beam model for wave propagation analysis.

The consistent basic equations of the nonlocal Timoshenko beam model based on the nonlocal constitutive relations for a single SWCNT are given as (see Sect. 7.2 for derivation of these equations)

$$GA\kappa \left(\frac{\partial^2 w}{\partial x^2} - \frac{\partial \psi}{\partial x} \right) + \rho A \frac{\partial^2}{\partial t^2} \left(w - (e_0 a)^2 \frac{\partial^2 w}{\partial x^2} \right) = 0 \quad (8.4)$$

$$GA\kappa \left(\frac{\partial w}{\partial x} - \psi \right) + EI \frac{\partial^2 \psi}{\partial x^2} - \rho I \frac{\partial^2}{\partial t^2} \left(\psi - (e_0 a)^2 \frac{\partial^2 \psi}{\partial x^2} \right) = 0 \quad (8.5)$$

where x is the longitudinal coordinate measured from the left end of the beam, w is the transverse displacement, ψ is the total section rotation measured on the mean-line of the beam, A is the cross-sectional area of the tube and I is the moment of inertia of the tube. It is assumed that all tubes share the same Young's modulus E , shear modulus G , and Poissons ratio ν . κ is shear correction factor that accounts for the difference in the constant state of shear stress in the Timoshenko beam theory and the parabolic variation of the actual shear stress through the depth of the cross section.

As mentioned earlier, van der Waals interaction between the concentric tubes is modeled as distributed springs as shown in Fig. 8.2. Equations (8.4) and (8.5) will get modified with the introduction of van der Waals pressure $p_{n(n+1)}$, $n = 1, 2, \dots, N$, given by Eqs. (8.1)–(8.3). Note that the van der Waals interaction springs couples the displacements of itself and its immediate neighbor. Equations (8.4) and (8.5) can be extended to N -walled MWCNTs as

$$GA_1\kappa \left(\frac{\partial^2 w_1}{\partial x^2} - \frac{\partial \psi_1}{\partial x} \right) + \rho A_1 \frac{\partial^2}{\partial t^2} \left(w_1 - (e_0 a)^2 \frac{\partial^2 w_1}{\partial x^2} \right) + \left[c_{12}(w_2 - w_1) - (e_0 a)^2 \frac{\partial^2}{\partial x^2} c_{12}(w_2 - w_1) \right] = 0 \quad (8.6)$$

$$GA_1\kappa \left(\frac{\partial w_1}{\partial x} - \psi \right) + EI_1 \frac{\partial^2 \psi_1}{\partial x^2} - \rho I_1 \frac{\partial^2}{\partial t^2} \left(\psi_1 - (e_0 a)^2 \frac{\partial^2 \psi_1}{\partial x^2} \right) = 0 \quad (8.7)$$

$$GA_{2\kappa} \left(\frac{\partial^2 w_2}{\partial x^2} - \frac{\partial \psi_2}{\partial x} \right) + \rho A_2 \frac{\partial^2}{\partial t^2} \left(w_2 - (e_0 a)^2 \frac{\partial^2 w_2}{\partial x^2} \right) + \left[c_{23}(w_3 - w_2) - c_{12}(w_2 - w_1) - (e_0 a)^2 \frac{\partial^2}{\partial x^2} (c_{23}(w_3 - w_2) - c_{12}(w_2 - w_1)) \right] = 0 \quad (8.8)$$

$$GA_{2\kappa} \left(\frac{\partial w_2}{\partial x} - \psi_2 \right) + EI_2 \frac{\partial^2 \psi}{\partial x^2} - \rho I_2 \frac{\partial^2}{\partial t^2} \left(\psi_2 - (e_0 a)^2 \frac{\partial^2 \psi_2}{\partial x^2} \right) = 0 \quad (8.9)$$

⋮
⋮
⋮
⋮

$$GA_{N\kappa} \left(\frac{\partial^2 w_N}{\partial x^2} - \frac{\partial \psi_N}{\partial x} \right) + \rho A_N \frac{\partial^2}{\partial t^2} \left(w_N - (e_0 a)^2 \frac{\partial^2 w_N}{\partial x^2} \right) - \left[c_{(N-1)N}(w_N - w_{N-1}) - (e_0 a)^2 \frac{\partial^2}{\partial x^2} c_{(N-1)N}(w_N - w_{N-1}) \right] = 0 \quad (8.10)$$

$$GA_{N\kappa} \left(\frac{\partial w_N}{\partial x} - \psi_N \right) + EI_N \frac{\partial^2 \psi_N}{\partial x^2} - \rho I_N \frac{\partial^2}{\partial t^2} \left(\psi_N - (e_0 a)^2 \frac{\partial^2 \psi_N}{\partial x^2} \right) = 0 \quad (8.11)$$

It is worth pointing out that when the van der Waals interaction coefficients are infinitely large, all the differences of the deflections between any adjacent tubes should be infinitely small to make the interaction terms bounded in Eqs. (8.6)–(8.11). This indicates that all the deflections are equal to each other and then $w_n = w$ for $n = 1, 2, \dots, N$. For this extreme case, the deflection of MWCNTs can be described by a single deflection curve and therefore a single beam model can be used for MWCNTs instead of a multibeam one. One can substitute $e_0 = 0$ in the Eqs. (8.6)–(8.11), to recover the local or classical Timoshenko beam model for the MWCNTs.

8.2.1 Generalized Wave Dispersion Analysis in MWCNTs

For analyzing the dispersion characteristics of waves in MWCNTs, we assume that a harmonic type of wave solution for the displacement field $w_n(x, t)$ and $\psi_n(x, t)$ ($n = 1, 2, \dots, N$), and they can be expressed in complex form as

$$w_n(x, t) = \sum_{n=1}^N \hat{w}_n(x, \omega) e^{-i(kx - \omega t)}, \quad n = 1, 2, \dots, N, \quad (8.12)$$

$$\psi_n(x, t) = \sum_{n=1}^N \hat{\psi}_n(x, \omega) e^{-i(kx - \omega t)}, \quad n = 1, 2, \dots, N. \quad (8.13)$$

where $\hat{w}_n(x, \omega)$, $\hat{\psi}_n(x, \omega)$ are the frequency domain amplitudes of the flexural and the bending deformation of CNTs, respectively. k is the wavenumber and ω is the angular frequency of the wave motion and $i = \sqrt{-1}$.

Substituting Eqs. (8.12) and (8.13) in Eqs. (8.6)–(8.11) yields $2N$ homogeneous equations in terms of \hat{w}_n and $\hat{\psi}_n$ ($n = 1, 2, \dots, N$) as

$$\begin{bmatrix} Q_{11} & Q_{12} & \dots & \dots & Q_{1N} \\ Q_{21} & Q_{22} & \dots & \dots & Q_{2N} \\ Q_{31} & Q_{32} & \dots & \dots & Q_{3N} \\ \vdots & \vdots & \dots & \dots & \vdots \\ \vdots & \vdots & \dots & \dots & \vdots \\ Q_{2N-2,1} & Q_{2N-2,2} & \dots & \dots & Q_{2N-2,2N-2} \\ Q_{2N-1,1} & Q_{2N-1,2} & \dots & \dots & Q_{2N-1,2N-1} \\ Q_{2N,1} & Q_{2N,2} & \dots & \dots & Q_{2N,2N} \end{bmatrix}_{2N \times 2N} \begin{Bmatrix} \hat{w}_1 \\ \hat{\psi}_1 \\ \hat{w}_2 \\ \vdots \\ \hat{\psi}_{N-1} \\ \hat{w}_N \\ \hat{\psi}_N \end{Bmatrix}_{2N \times 1} = \{\mathbf{0}\}_{2N \times 1} \quad (8.14)$$

where the detailed expressions for Q_{ab} ($a = 1, 2, \dots, 2N$; $b = 1, 2, \dots, 2N$) are shown below for single, double, and three-walled CNTs.

(a) For single-walled carbon nanotubes: (Note this was studied in Chap. 7)

$$Q_{11} = -GA_1\kappa k^2 + \rho A_1\omega^2 \left(1 + (e_0a)^3 k^2\right), \quad (8.15)$$

$$Q_{12} = -Q_{21} = iGA_1\kappa, \quad (8.16)$$

$$Q_{22} = -EI_1k^2 + \rho I_1\omega^2 \left(1 + (e_0a)^3 k^2\right) - GA_1\kappa. \quad (8.17)$$

(b) For double-walled carbon nanotubes:

$$Q_{11} = -GA_1\kappa k^2 - c_{12} \left(1 + (e_0a)^2 k^2\right) + \rho A_1\omega^2 \left(1 + (e_0a)^2 k^2\right), \quad (8.18)$$

$$Q_{12} = -Q_{21} = iGA_1\kappa, \quad (8.19)$$

$$Q_{13} = Q_{31} = c_{12} \left(1 + (e_0a)^2 k^2\right), \quad (8.20)$$

$$Q_{22} = -EI_1k^2 + \rho I_1\omega^2 \left(1 + (e_0a)^2 k^2\right) - GA_1\kappa, \quad (8.21)$$

$$Q_{33} = -GA_2\kappa k^2 - c_{12} \left(1 + (e_0a)^2 k^2\right) + \rho A_2\omega^2 \left(1 + (e_0a)^2 k^2\right), \quad (8.22)$$

$$Q_{34} = -Q_{43} = iGA_2\kappa, \quad (8.23)$$

$$Q_{44} = -EI_2k^2 + \rho I_2\omega^2 \left(1 + (e_0a)^2 k^2\right) - GA_2\kappa, \quad (8.24)$$

$$Q_{14} = Q_{23} = Q_{24} = Q_{32} = Q_{41} = Q_{42} = 0.$$

(c) For three-walled carbon nanotube:

$$Q_{11} = -GA_1\kappa k^2 - c_{12} \left(1 + (e_0a)^2k^2\right) + \rho A_1\omega^2 \left(1 + (e_0a)^2k^2\right), \quad (8.25)$$

$$Q_{12} = -Q_{21} = iGA_1\kappa k, \quad (8.26)$$

$$Q_{13} = Q_{31} = c_{12} \left(1 + (e_0a)^2k^2\right), \quad (8.27)$$

$$Q_{22} = -EI_1k^2 + \rho I_1\omega^2 \left(1 + (e_0a)^2k^2\right) - GA_1\kappa, \quad (8.28)$$

$$Q_{33} = -GA_2\kappa k^2 - c_{12} \left(1 + (e_0a)^2k^2\right) + \rho A_2\omega^2 \left(1 + (e_0a)^2k^2\right), \quad (8.29)$$

$$Q_{34} = -Q_{43} = iGA_2\kappa k, \quad (8.30)$$

$$Q_{35} = Q_{53} = c_{23} \left(1 + (e_0a)^2k^2\right), \quad (8.31)$$

$$Q_{44} = -EI_2k^2 + \rho I_2\omega^2 \left(1 + (e_0a)^2k^2\right) - GA_2\kappa, \quad (8.32)$$

$$Q_{55} = -GA_3\kappa k^2 - c_{23} \left(1 + (e_0a)^2k^2\right) + \rho A_3\omega^2 \left(1 + (e_0a)^2k^2\right), \quad (8.33)$$

$$Q_{56} = -Q_{65} = iGA_3\kappa k, \quad (8.34)$$

$$Q_{66} = -EI_3k^2 + \rho I_3\omega^2 \left(1 + (e_0a)^2k^2\right) - GA_3\kappa, \quad (8.35)$$

$$\begin{aligned} Q_{14} = Q_{15} = Q_{16} = Q_{23} = Q_{24} = Q_{25} = Q_{26} = Q_{32} = Q_{36} = Q_{41} = \\ Q_{42} = Q_{45} = Q_{46} = Q_{51} = Q_{52} = Q_{54} = Q_{61} = Q_{62} = Q_{63} = Q_{64} = 0. \end{aligned} \quad (8.36)$$

The wavenumbers and hence the group speeds are solved from Eq. (8.14) by using Polynomial Eigenvalue Problem (PEP) [6, 9]. Equating the determinant of matrix $[Q_{ab}]$ to zero (for the non-trivial solution of \hat{w}_n , and $\hat{\psi}_n$) will give the characteristic polynomial in terms of wavenumber k of the order $2N$, solution of which is quite difficult. PEP converts the characteristic polynomial equation into a matrix of size $2N \times 2N$, whose Eigen values form the solution of the equation. After obtaining the wavenumbers, group speeds are extracted. The details of computation of wavenumbers using PEP for single, double, and three-walled CNT is shown in the later part of this section.

In the later part of this section, some numerical examples are given to observe the effect nonlocal scaling parameter (e_0) on wave propagation in MWCNTs. We consider double-walled carbon nanotubes (DWCNT) and triple-walled carbon nanotubes (TWCNTs) in the next section to analyze the wave behavior with respect to the nonlocal scaling parameter. The properties of the CNTs assumed for the for the present analysis are shown in Table 8.1.

Table 8.1 Properties of CNTs used in this chapter

Property	Value
Young's modulus (E)	1.03 TPa
Density (ρ)	2700 kg/m ³
Inner tube radius (R_{in})	3.5 nm
Thickness (t)	0.35 nm
Poisson ratio (ν)	0.25
Shear correction factor (κ)	0.8
Shear modulus (G)	0.4 TPa

8.2.2 Wave Dispersion in SWCNTs

We studied Timoshenko beam theory in the context of 1-D nanobeams of rectangular cross section in Sect. 7.2. Its adaptation for SWCNT is straight forward by replacing the area of cross section of area moment of inertia in all its expression with the hollow circular area and area moment of inertia of SWCNT. In this chapter, we will deduce the SWCNT equations from MWCNT equations (Eqs. (8.6)–(8.11)). The main difference here in this chapter is that we will perform parametric studies on wave characteristics pertaining to SWCNT. By setting $N = 1$ in the nonlocal governing partial differential equations (Eqs. (8.6)–(8.11)) of MWCNTs, one can derive the nonlocal governing equations for SWCNTs as

$$GA_1\kappa \left(\frac{\partial^2 w_1}{\partial x^2} - \frac{\partial \psi_1}{\partial x} \right) + \rho A_1 \frac{\partial^2}{\partial t^2} \left(w_1 - (e_0 a)^2 \frac{\partial^2 w_1}{\partial x^2} \right) = 0 \quad (8.37)$$

$$GA_1\kappa \left(\frac{\partial w_1}{\partial x} - \psi_1 \right) + EI_1 \frac{\partial^2 \psi_1}{\partial x^2} - \rho I_1 \frac{\partial^2}{\partial t^2} \left(\psi_1 - (e_0 a)^2 \frac{\partial^2 \psi_1}{\partial x^2} \right) = 0 \quad (8.38)$$

where $w_1 = w_1(x, t)$ and $\psi_1 = \psi_1(x, t)$ are the flexural deflection and the slope of the bending deformation of the beam, A_1 and I_1 are the cross-sectional area and the moment of inertia of the SWCNT. Equations (8.37) and (8.38) are transformed into frequency domain by assuming the displacement field to be harmonic (see Eqs. (8.12) and (8.13)). Substituting Eqs. (8.12) and (8.13) into Eqs. (8.37) and (8.38) and rearranging, the resultant equations can be written in matrix form as

$$\mathbf{S}_2 k^2 + \mathbf{S}_1 k + \mathbf{S}_0 = 0 \quad (8.39)$$

where \mathbf{S}_2 , \mathbf{S}_1 and \mathbf{S}_0 are given by Eqs. (7.48)–(7.50), respectively.

This form is amenable to solution of wavenumbers through PEP. From Eq. (8.39), we can clearly see the dependence of nonlocal scale parameter $e_0 a$ on wavenumber. The expressions for cut-off frequency, the escape frequencies and wave speeds were already derived in Chap. 7 (see Eqs. (7.51)–(7.53)) and hence not repeated here.

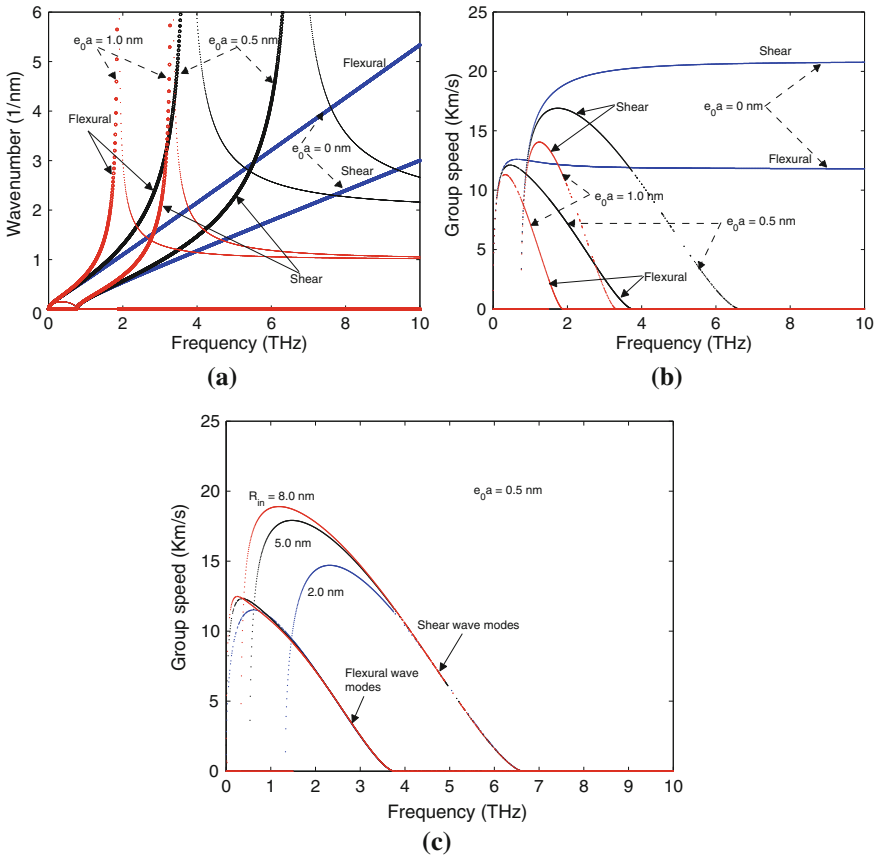


Fig. 8.3 **a** Spectrum curves (Real wavenumbers—*thick lines*; Imaginary wavenumbers—*thin lines*), **b** Dispersion curves for SWCNTs for various nonlocal scaling parameters for $R_{in} = 3.5$ nm (wall-1) and **c** Dispersion curves for SWCNTs for various inner tube radii ($e_0a = 0.5$ nm)

Here, we will study some key observation that were not highlighted in Sect. 7.2 is presented. The spectrum and dispersion curves of the SWCNTs with nonlocal effects are shown in Fig. 8.3. Figure 8.3a shows the variation of the wavenumbers with the wave frequency for both local (or classical) and nonlocal elasticity. This figure clearly shows the two modes namely, flexural and shear. Flexural wave mode starts from zero wave frequency and shear wave mode propagates only after shear cut-off frequency, the frequency at which the imaginary part of wavenumber becomes real. The values of the cut-off frequency are calculated from Eq. (7.51). In the present study for a 3.5 nm radius SWCNT (other properties of CNT are given in Table 8.1), we have shear cut-off frequency at 0.7585 THz. It can be observed from Eq. (7.51) that these frequencies are independent of the nonlocal scaling parameter, and hence same frequencies are obtained from both local and nonlocal theories.

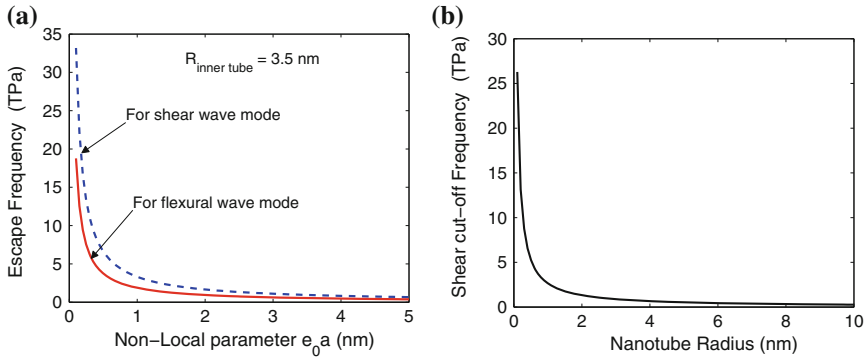


Fig. 8.4 a Escape (or asymptotic) frequency variation of SWCNTs with nonlocal scaling parameter (e_0a). b Cut-off frequency variation of SWCNTs with nanotube radius

For $e_0a = 0$, which is the case of local theory of elasticity solution, wavenumbers increase monotonically with the increase in frequency, which is shown in Fig. 8.3a and correspondingly, the group speeds, shown in Fig. 8.3b increases with increase in wave frequency. However, at higher frequencies, they attain a constant value, which is typical of Timoshenko beam solution. These results are similar to what is presented in Sect. 7.2. However, with the introduction of scale effects, the wave behavior is altered drastically. Both the flexural and shear wave modes escapes to infinity at escape frequency, beyond this frequency there is no wave propagation. The value of escape frequency decreases with increase in the scale parameter e_0a , for both wave modes. The spectrum and dispersion curves shown in Fig. 8.3 are plotted for $e_0a = 0, 0.5, \text{ and } 1.0$ nm, for a 3.5 nm radius SWCNT.

Equation (7.52) gives the expression for escape frequencies in SWCNT. From this expression it is clear that, escape frequency values are independent of SWCNT diameter, for both wave modes. However, the group speed amplitudes may change. Figure 8.3c shows the group speed plots for $e_0a = 0.5$ nm for different radii of SWCNT. From this figure, one can see that the increase in radius yields higher wave speeds. Figure 8.4a shows the variation of escape frequencies of flexural and shear wave modes with the nonlocal parameter. It shows that as e_0a increases, the escape frequency decreases. At higher values of e_0a , escape frequencies approach to very small values. The shear cut-off frequency variation with radius (R) of SWCNT is shown in Fig. 8.4b. This figure shows that, as the radius of the nanotube increases, the shear cut-off frequency decreases and at higher values of R , the cut-off frequency approaches to very small values. Hence, it can be concluded that for large values of scale parameter, shear deformation on CNT has negligible effect and beam behaves like more like elementary beam. Although the wave behavior of SWCNT is similar to the wave behavior of 1-D nanobeams presented in Chap 7, the occurrence of band gap or escape frequencies in these two cases are quite different.

8.2.3 Wave Dispersion in DWCNTs

When we substitute $N = 2$ in the nonlocal governing partial differential equations of MWCNTs (Eqs. (8.6)–(8.11)), one can get the nonlocal governing differential equation of motion for double-walled carbon nanotubes as

$$GA_1\kappa \left(\frac{\partial^2 w_1}{\partial x^2} - \frac{\partial \psi_1}{\partial x} \right) + \rho A_1 \frac{\partial^2}{\partial t^2} \left(w_1 - (e_0 a)^2 \frac{\partial^2 w_1}{\partial x^2} \right) + \left[c_{12}(w_2 - w_1) - (e_0 a)^2 \frac{\partial^2}{\partial x^2} c_{12}(w_2 - w_1) \right] = 0 \quad (8.40)$$

$$GA_1\kappa \left(\frac{\partial w_1}{\partial x} - \psi_1 \right) + EI_1 \frac{\partial^2 \psi_1}{\partial x^2} - \rho I_1 \frac{\partial^2}{\partial t^2} \left(\psi_1 - (e_0 a)^2 \frac{\partial^2 \psi_1}{\partial x^2} \right) = 0 \quad (8.41)$$

$$GA_2\kappa \left(\frac{\partial^2 w_2}{\partial x^2} - \frac{\partial \psi_2}{\partial x} \right) + \rho A_2 \frac{\partial^2}{\partial t^2} \left(w_2 - (e_0 a)^2 \frac{\partial^2 w_2}{\partial x^2} \right) + \left[-c_{12}(w_2 - w_1) - (e_0 a)^2 \frac{\partial^2}{\partial x^2} (-c_{12}(w_2 - w_1)) \right] = 0 \quad (8.42)$$

$$GA_2\kappa \left(\frac{\partial w_2}{\partial x} - \psi_2 \right) + EI_2 \frac{\partial^2 \psi_2}{\partial x^2} - \rho I_2 \frac{\partial^2}{\partial t^2} \left(\psi_2 - (e_0 a)^2 \frac{\partial^2 \psi_2}{\partial x^2} \right) = 0 \quad (8.43)$$

where the subscripts 1 and 2 in Eqs. (8.40)–(8.43) represents for wall-1 (inner) and wall-2 (outer) of the DWCNT (see Fig. 8.2), respectively. Here $w_1 = w_1(x, t)$, $\psi_1 = \psi_1(x, t)$ and $w_2 = w_2(x, t)$, $\psi_2 = \psi_2(x, t)$ are the flexural deflections, cross-section rotations of the inner and the outer walls, respectively and c_{12} is the van der Waals interaction coefficient between wall-1 and wall-2 of a DWCNT (calculated from Eq. (8.2)). A_1 , A_2 and I_1 , I_2 are the cross-sectional area and moment of inertia of the wall-1 and wall-2, respectively.

For analyzing the wave behavior in DWCNTs, we again assume that the harmonic type of wave solution for the displacement field as

$$w_p(x, t) = \sum_{n=1}^N \hat{w}_p(x, \omega) e^{-i(kx - \omega t)}, \quad p = 1, 2, \quad (8.44)$$

$$\psi_p(x, t) = \sum_{n=1}^N \hat{\psi}_p(x, \omega) e^{-i(kx - \omega t)}, \quad p = 1, 2. \quad (8.45)$$

where $\hat{w}_p(x, \omega)$ ($p = 1, 2$) and $\hat{\psi}_p(x, \omega)$ ($p = 1, 2$) are the frequency domain amplitudes of deflection of the beam and the slope of the beam due to bending defor-

mation, respectively. Substitution of the displacement field (Eqs. (8.44) and (8.45)) in the nonlocal governing differential equation of motion of DWCNTs (Eqs. (8.40)–(8.43)) leads to the following polynomial eigenvalue problem

$$\mathbf{D}_2 k^2 + \mathbf{D}_1 k + \mathbf{D}_0 = 0 \quad (8.46)$$

where

$$\mathbf{D}_2 = \begin{bmatrix} D_2^{(11)} & 0 & c_{12}(e_0 a)^2 & 0 \\ 0 & D_2^{(22)} & 0 & 0 \\ c_{12}(e_0 a)^2 & 0 & D_2^{(33)} & 0 \\ 0 & 0 & 0 & D_2^{(44)} \end{bmatrix} \quad (8.47)$$

$$\mathbf{D}_1 = \begin{bmatrix} 0 & iGA_1\kappa & 0 & 0 \\ -iGA_1\kappa & 0 & 0 & 0 \\ 0 & 0 & 0 & iGA_2\kappa \\ 0 & 0 & -iGA_2\kappa & 0 \end{bmatrix} \quad (8.48)$$

$$\mathbf{D}_0 = \begin{bmatrix} D_0^{(11)} & 0 & c_{12} & 0 \\ 0 & D_0^{(22)} & 0 & 0 \\ c_{12} & 0 & D_0^{(33)} & 0 \\ 0 & 0 & 0 & D_0^{(44)} \end{bmatrix} \quad (8.49)$$

The diagonal elements of the matrices \mathbf{D}_2 and \mathbf{D}_0 are given below.

$$D_2^{(11)} = -GA_1\kappa + (-c_{12} + \rho A_1 \omega^2)(e_0 a)^2, \quad (8.50)$$

$$D_2^{(22)} = -EI_1 + \rho I_1 (e_0 a)^2 \omega^2, \quad (8.51)$$

$$D_2^{(33)} = -GA_2\kappa + (-c_{12} + \rho A_2 \omega^2)(e_0 a)^2, \quad (8.52)$$

$$D_2^{(44)} = -EI_2 + \rho I_2 (e_0 a)^2 \omega^2. \quad (8.53)$$

$$D_0^{(11)} = -c_{12} + \rho A_1 \omega^2, \quad (8.54)$$

$$D_0^{(22)} = -GA_1\kappa + \rho I_1 \omega^2, \quad (8.55)$$

$$D_0^{(33)} = -c_{12} + \rho A_2 \omega^2, \quad (8.56)$$

$$D_0^{(44)} = -GA_2\kappa + \rho I_2 \omega^2. \quad (8.57)$$

This dispersion relation, which is also in the form of PEP (Eq. (8.46)) is solved for wavenumbers, which is a function of material properties of the CNTs and the nonlocal parameter ($e_0 a$). For a DWCNT, the nonlocal Timoshenko beam model gives four cut-off frequencies and four escape frequencies in wave dispersion analysis. These cut-off frequencies are obtained by substituting $k = 0$ in the dispersion relation of DWCNTs

(Eq. (8.46)) or by solving $|\mathbf{D}_0(\omega)| = 0$, which gives four cut-off frequencies as

$$\omega_{c1} = 0, \quad \omega_{c2} = \sqrt{\frac{GA_1\kappa}{\rho I_1}}, \quad \omega_{c3} = \sqrt{\frac{GA_2\kappa}{\rho I_2}}, \quad \omega_{c4} = \sqrt{\frac{c_{12}(A_1 + A_2)}{\rho A_1 A_2}} \quad (8.58)$$

One can observe that these cut-off frequencies are independent of the nonlocal scaling parameter (e_0a). The escape (or asymptotic) frequencies are obtained by substituting $k \rightarrow \infty$ in the dispersion relation (Eq. (8.46)), that implies $|\mathbf{D}_2(\omega)| = 0$, which gives

$$\omega_{E1} = \frac{1}{e_0a} \sqrt{\frac{EI_1}{\rho I_1}}, \quad \omega_{E2} = \frac{1}{e_0a} \sqrt{\frac{EI_2}{\rho I_2}} \quad (8.59)$$

$$\omega_{E3} = \frac{1}{\sqrt{2}A_*(e_0a)} \sqrt{A_*(2H_1 + H_2) + \sqrt{(2H_1^2 + H_2^2) + (H_3 - H_4)}} \quad (8.60)$$

$$\omega_{E4} = \frac{1}{\sqrt{2}A_*(e_0a)} \sqrt{A_*(2H_1 + H_2) - \sqrt{(2H_1^2 + H_2^2) + (H_3 - H_4)}} \quad (8.61)$$

where the parameters A_* and H_p ($p = 1, 2, 3, 4$) are given below.

$$H_1 = G\rho\kappa A_*, \quad (8.62)$$

$$H_2 = c_{12}\rho A_+(e_0a^2), \quad (8.63)$$

$$H_3 = 2G\kappa\rho^2 c_{12}(e_0a)^2 A_*A_-, \quad (8.64)$$

$$H_4 = 2G\kappa\rho^2 A_*(G\kappa A_* + c_{12}(e_0a)^2 A_-), \quad (8.65)$$

$$A_* = A_1 A_2, \quad (8.66)$$

$$A_+ = A_1 + A_2, \quad (8.67)$$

$$A_- = A_2 - A_1. \quad (8.68)$$

These escape frequencies are function of the material properties of CNTs and are inversely proportional to the nonlocal scaling parameter. Differentiating the dispersion relation of DWCNTs (Eq. (8.46)) with respect to the wave frequency (ω), we get the PEP for group speeds as

$$\left[k^2 \frac{\partial \mathbf{D}_2}{\partial \omega} + \frac{\partial \mathbf{D}_0}{\partial \omega} \right] C_{g2} + 2k\mathbf{D}_2 + \mathbf{D}_1 = 0 \quad (8.69)$$

where $C_{g2} = (\partial\omega/\partial k)_2$ is the group speed of a wave in DWCNTs and the matrices \mathbf{D}_2 , \mathbf{D}_1 and \mathbf{D}_0 are given in Eqs. (8.47)–(8.49).

The spectrum and dispersion plots for DWCNTs are shown in Fig. 8.5. In the case of DWCNT, most of the observations made for the SWCNT are still valid, That is, as expected, scale parameter introduces the escape frequency where the wavenumber

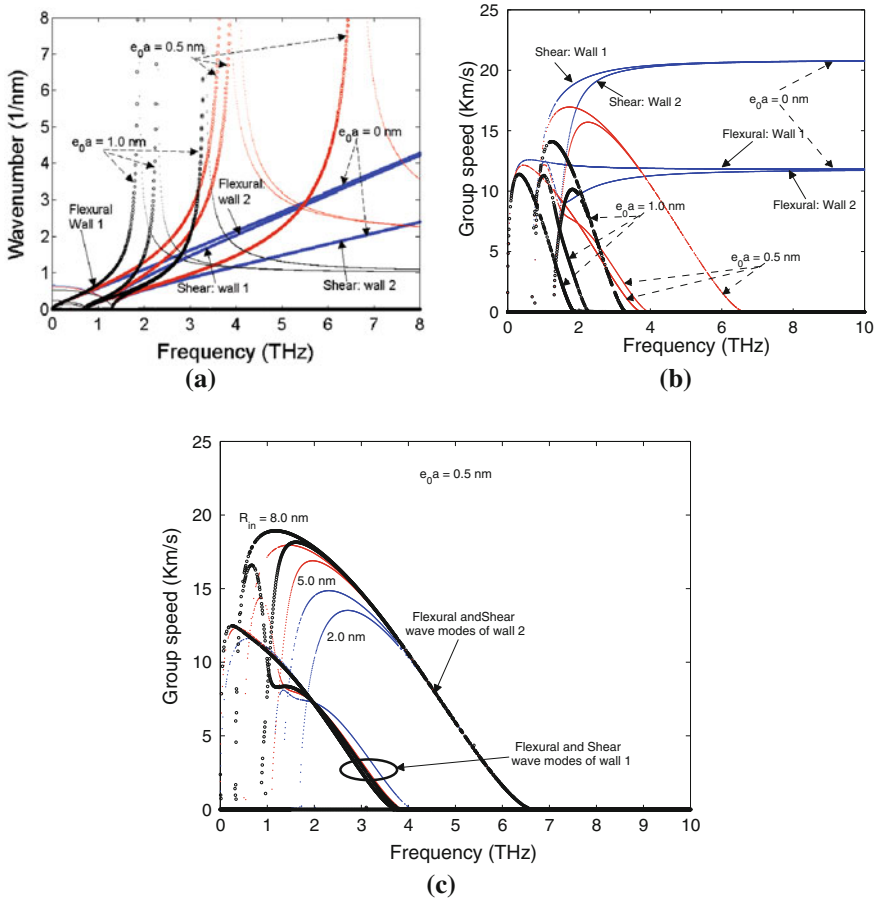


Fig. 8.5 **a** Spectrum curves (Real wavenumbers—*thick lines*; Imaginary wavenumbers—*thin lines*), **b** Dispersion curves for DWCNTs for various nonlocal scaling parameters for wall-1 radius $R_{in} = 3.5$ nm and **c** Dispersion curves for DWCNTs for various radii of wall-1 (for $e_0a = 0.5$ nm)

k tends to infinity and the group speed tends to zero and the values of the escape frequencies decreases with the increase in scale parameter. In addition, when $e_0a = 0$ nm, the flexural speeds of the second wall slightly decreases at low frequencies and slightly increases and attains the speeds of the first wall. This phenomenon is clearly shown in Fig. 8.5b. The value of the cut-off frequency does not change appreciably with the increase in scale parameter. For $e_0a = 0$ the shear mode group speeds at high frequencies remain almost constant.

Figure 8.5c shows the dispersion plots for various inner radii of the CNTs for a given scale parameter ($e_0a = 0.5$ nm). From the figure, it is clear that the escape frequencies for various modes does not change with the increase in the inner radius. The only change in escape frequency is observed in the shear wave mode of the wall 1.

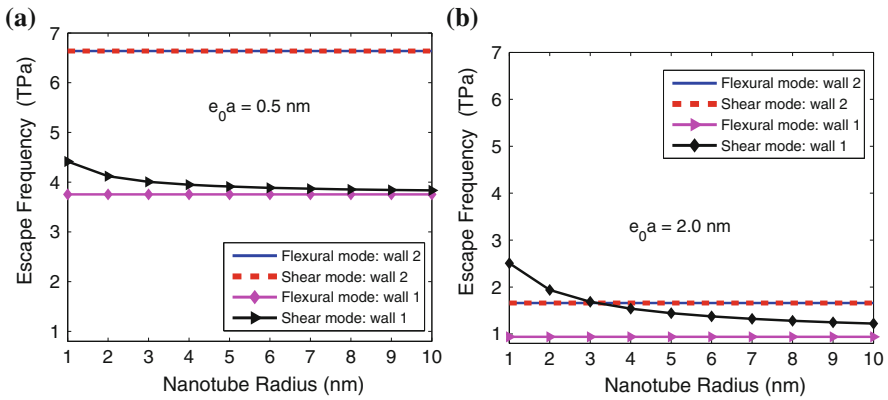


Fig. 8.6 Variation of escape (or asymptotic) frequency with wall-1 radius for (a) $e_0a = 0.5$ nm and (b) $e_0a = 2.0$ nm

The detailed variation in escape frequency for both the walls as a function of nonlocal scale parameter is shown in Fig. 8.6 for $e_0a = 0.5$ and 2.0 nm. It shows the effect of the radius of the nanotube (wall-1) and nonlocal scaling parameter (e_0) on the escape frequency of DWCNTs more clearly. The escape frequencies for both flexural and shear modes of the wall-2 are same and are constant with respect to the radius of the tube. These values of escape frequency are decreasing with the nonlocal scale coefficient e_0a (see Fig. 8.6a, b). As in the wall-2, the escape frequencies of the flexural modes of wall-1 are constant with nanotube radius and they also decrease with increase in nonlocal scaling parameter. The escape frequencies of the shear wave modes of the wall-1 are decreasing with the increase in radius of the tube and also with the increase in nonlocal scaling parameter (see Fig. 8.6).

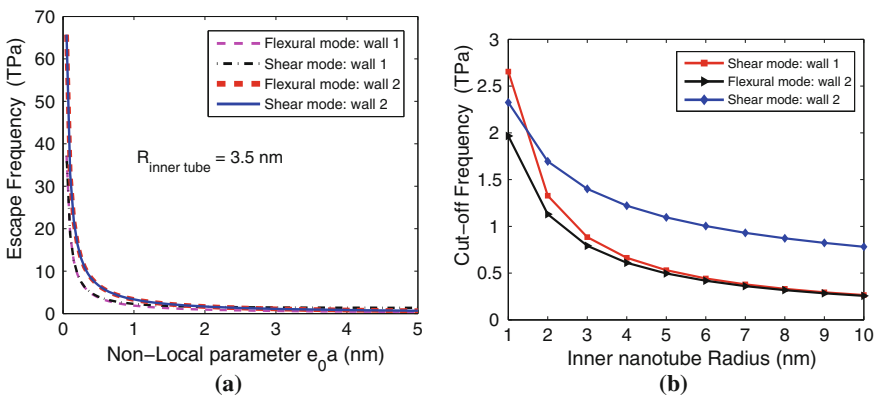


Fig. 8.7 a Escape (or asymptotic) frequency variation of DWCNTs with nonlocal scaling parameter (e_0a), b Cut-off frequency variation of DWCNTs with inner nanotube (wall-1) radius

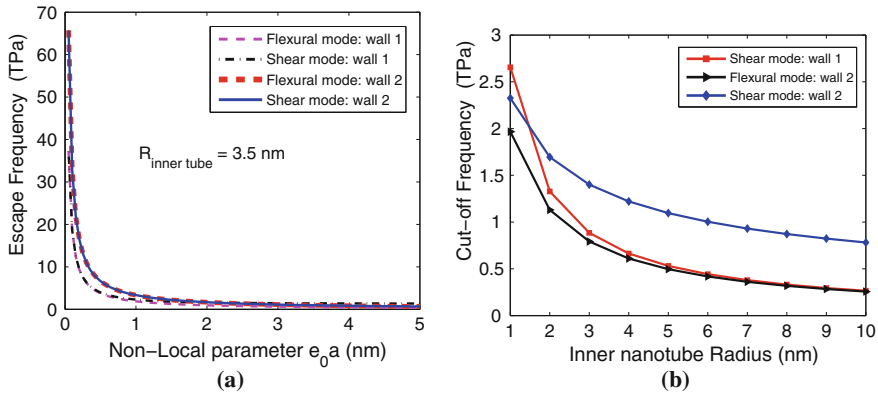


Fig. 8.8 **a** Spectrum curves (Real wavenumbers—*thick lines*; Imaginary wavenumbers—*thin lines*), **b** Dispersion curves for a DWCNT of wall-1 radius $R_{\text{in}} = 3.5 \text{ nm}$ and two SWCNTs of radii 3.5 and 3.85 nm, to observe the van der Waals interaction in DWCNTs, for $e_0 a = 0.5 \text{ nm}$

The variation of escape frequency (for all modes of both walls) with nonlocal scaling parameter (for wall-1 radius of 3.5 nm) is shown in Fig. 8.7a. It shows that the escape frequencies of the flexural and shear wave modes of both walls are decreasing with increase in $e_0 a$. At small values of $e_0 a$ ($< \sim 0.5$), the escape frequencies are very high and are saturating to smaller values of frequency at large values of $e_0 a$ (see Fig. 8.7a). The cut-off frequency variation with inner nanotube (wall-1) radius is shown in Fig. 8.7b, where the cut-off frequencies are decreasing with the increase in nanotube radius. For higher values of tube radius, the cut-off frequencies of the shear mode of wall-2 and that of the flexural mode of wall-1 are almost same (see Fig. 8.7b).

The spectrum and dispersion curves for a DWCNT of inner wall radius of $R_{\text{in}} = 3.5 \text{ nm}$ and two SWCNTs of radii equal to the inner and outer wall radius of the DWCNT (that is, SWCNT₁: $R_1 = 3.5 \text{ nm}$ and SWCNT₂: $R_2 = 3.85 \text{ nm}$), are shown in Fig. 8.8. Here these curves are shown for $e_0 a = 0.5 \text{ nm}$. Here, the flexural and shear wavenumbers of the wall-1 of the DWCNT are in between the values of the SWCNT₁ and SWCNT₂. SWCNT₂ has higher wavenumbers and lower wave group speeds as compared to the wall-1 of DWCNT and SWCNT-1. This variation is clearly shown in the insets of Fig. 8.8a, b. The vdW interaction in DWCNT, will be there only on the outer wall (wall-2) wave modes (both flexural and shear). The outer wall wave modes of the DWCNT are not affected by the two individual SWCNTs as mentioned above.

8.2.4 Wave Dispersion in TWCNTs

Substituting $N = 3$ in the nonlocal governing differential equations of TWCNTs (Eqs. (8.6) to (8.11)) one can obtain the nonlocal governing differential equations of motion for the TWCNTs as

$$GA_1\kappa \left(\frac{\partial^2 w_1}{\partial x^2} - \frac{\partial \psi_1}{\partial x} \right) + \rho A_1 \frac{\partial^2}{\partial t^2} \left(w_1 - (e_0 a)^2 \frac{\partial^2 w_1}{\partial x^2} \right) + \left[c_{12}(w_2 - w_1) - (e_0 a)^2 \frac{\partial^2}{\partial x^2} c_{12}(w_2 - w_1) \right] = 0 \quad (8.70)$$

$$GA_1\kappa \left(\frac{\partial w_1}{\partial x} - \psi \right) + EI_1 \frac{\partial^2 \psi_1}{\partial x^2} - \rho I_1 \frac{\partial^2}{\partial t^2} \left(\psi_1 - (e_0 a)^2 \frac{\partial^2 \psi_1}{\partial x^2} \right) = 0 \quad (8.71)$$

$$GA_2\kappa \left(\frac{\partial^2 w_2}{\partial x^2} - \frac{\partial \psi_2}{\partial x} \right) + \rho A_2 \frac{\partial^2}{\partial t^2} \left(w_2 - (e_0 a)^2 \frac{\partial^2 w_2}{\partial x^2} \right) + \left[c_{23}(w_3 - w_2) - c_{12}(w_2 - w_1) - (e_0 a)^2 \frac{\partial^2}{\partial x^2} (c_{23}(w_3 - w_2) - c_{12}(w_2 - w_1)) \right] = 0 \quad (8.72)$$

$$GA_2\kappa \left(\frac{\partial w_2}{\partial x} - \psi_2 \right) + EI_2 \frac{\partial^2 \psi_2}{\partial x^2} - \rho I_2 \frac{\partial^2}{\partial t^2} \left(\psi_2 - (e_0 a)^2 \frac{\partial^2 \psi_2}{\partial x^2} \right) = 0 \quad (8.73)$$

$$GA_3\kappa \left(\frac{\partial^2 w_3}{\partial x^2} - \frac{\partial \psi_3}{\partial x} \right) + \rho A_3 \frac{\partial^2}{\partial t^2} \left(w_3 - (e_0 a)^2 \frac{\partial^2 w_3}{\partial x^2} \right) + \left[-c_{23}(w_3 - w_2) - (e_0 a)^2 \frac{\partial^2}{\partial x^2} (-c_{23}(w_3 - w_2)) \right] = 0 \quad (8.74)$$

$$GA_3\kappa \left(\frac{\partial w_3}{\partial x} - \psi_3 \right) + EI_3 \frac{\partial^2 \psi_3}{\partial x^2} - \rho I_3 \frac{\partial^2}{\partial t^2} \left(\psi_3 - (e_0 a)^2 \frac{\partial^2 \psi_3}{\partial x^2} \right) = 0 \quad (8.75)$$

where the subscripts 1, 2 and 3 in Eqs. (8.70)–(8.75) represents for wall-1 (inner), wall-2, and wall-3 (outer) of the TWCNT (see Figs. 8.1 and 8.2), respectively. Here $w_p = w_p(x, t)$, $\psi_p = \psi_p(x, t)$ ($p = 1, 2, 3$) are the flexural deflections and cross-section rotations of the three walls (1, 2, and 3), respectively. c_{12} and c_{23} are the van der Waals interaction coefficients between the walls 1-2 and 2-3, respectively, and are calculated from Eq. (8.2). A_p and I_p ($p = 1, 2, 3$) are the cross-sectional areas and the moment of inertias of three walls, respectively.

For analyzing the wave dispersion in TWCNTs, we assume a harmonic type of wave solution for the displacement field in complex form as

$$w_p(x, t) = \sum_{n=1}^N \hat{w}_p(x, \omega) e^{-i(kx - \omega t)}, \quad p = 1, 2, 3, \quad (8.76)$$

$$\psi_p(x, t) = \sum_{n=1}^N \hat{\psi}_p(x, \omega) e^{-i(kx - \omega t)}, \quad p = 1, 2, 3. \quad (8.77)$$

where $\hat{w}_p(x, \omega)$ ($p = 1, 2, 3$) and $\hat{\psi}_p(x, \omega)$ ($p = 1, 2, 3$) are the frequency domain amplitudes of deflection and the slope of the beam for the three walls, respectively. Substitution of the displacement field (Eqs. (8.76) and (8.77)) in the nonlocal governing differential equation of motion of TWCNTs (Eqs.(8.70)–(8.75)) leads to the following polynomial eigenvalue problem

$$\mathbf{T}_2 k^2 + \mathbf{T}_1 k + \mathbf{T}_0 = 0 \quad (8.78)$$

where

$$\mathbf{T}_2 = \begin{bmatrix} T_2^{(11)} & 0 & c_{12}(e_0 a)^2 & 0 & 0 & 0 \\ 0 & T_2^{(22)} & 0 & 0 & 0 & 0 \\ c_{12}(e_0 a)^2 & 0 & T_2^{(33)} & 0 & c_{23}(e_0 a)^2 & 0 \\ 0 & 0 & 0 & T_2^{(44)} & 0 & 0 \\ 0 & 0 & c_{23}(e_0 a)^2 & 0 & T_2^{(55)} & 0 \\ 0 & 0 & 0 & 0 & 0 & T_2^{(66)} \end{bmatrix} \quad (8.79)$$

$$\mathbf{T}_1 = \begin{bmatrix} 0 & iGA_1\kappa & 0 & 0 & 0 & 0 \\ -iGA_1\kappa & 0 & 0 & 0 & 0 & 0 \\ 0 & 0 & 0 & iGA_2\kappa & 0 & 0 \\ 0 & 0 & -iGA_2\kappa & 0 & 0 & 0 \\ 0 & 0 & 0 & 0 & 0 & iGA_3\kappa \\ 0 & 0 & 0 & 0 & -iGA_3\kappa & 0 \end{bmatrix} \quad (8.80)$$

$$\mathbf{T}_0 = \begin{bmatrix} T_0^{(11)} & 0 & c_{12} & 0 & 0 & 0 \\ 0 & T_0^{(22)} & 0 & 0 & 0 & 0 \\ c_{12} & 0 & T_0^{(33)} & 0 & c_{23} & 0 \\ 0 & 0 & 0 & T_0^{(44)} & 0 & 0 \\ 0 & 0 & c_{23} & 0 & T_0^{(55)} & 0 \\ 0 & 0 & 0 & 0 & 0 & T_0^{(66)} \end{bmatrix} \quad (8.81)$$

where the diagonal elements of the matrices \mathbf{T}_2 and \mathbf{T}_0 are given below.

$$T_2^{(11)} = -GA_1\kappa + (-c_{12} + \rho A_1 \omega^2)(e_0 a)^2, \quad (8.82)$$

$$T_2^{(22)} = -EI_1 + \rho I_1 (e_0 a)^2 \omega^2, \quad (8.83)$$

$$T_2^{(33)} = -GA_2\kappa + (-c_{12} + \rho A_2\omega^2)(e_0a)^2, \quad (8.84)$$

$$T_2^{(44)} = -EI_2 + \rho I_2(e_0a)^2\omega^2, \quad (8.85)$$

$$T_2^{(55)} = -GA_3\kappa + (-c_{23} + \rho A_3\omega^2)(e_0a)^2, \quad (8.86)$$

$$T_2^{(66)} = -EI_3 + \rho I_3(e_0a)^2\omega^2. \quad (8.87)$$

$$T_0^{(11)} = -c_{12} + \rho A_1\omega^2, \quad (8.88)$$

$$T_0^{(22)} = -GA_1\kappa + \rho I_1\omega^2, \quad (8.89)$$

$$T_0^{(33)} = -c_{12} + \rho A_2\omega^2, \quad (8.90)$$

$$T_0^{(44)} = -GA_2\kappa + \rho I_2\omega^2, \quad (8.91)$$

$$T_0^{(55)} = -c_{23} + \rho A_3\omega^2, \quad (8.92)$$

$$T_0^{(66)} = -GA_3\kappa + \rho I_3\omega^2. \quad (8.93)$$

This polynomial eigenvalue problem is solved for the wavenumbers. As before, the cut-off frequencies are obtained by setting $k = 0$ in the dispersion relation (Eq. (8.78)). In the present case one can get the cut-off frequencies by solving $|\mathbf{T}_0(\omega)| = 0$. The closed form expressions of cut-off frequency are very big, so we are not elaborating those expressions here. One can derive those expressions by solving $|\mathbf{T}_0(\omega)| = 0$. The escape frequencies can be obtained by setting $k \rightarrow \infty$ in Eq. (8.78) or by solving the $|\mathbf{T}_2(\omega)| = 0$.

Differentiating the dispersion relation (Eq. (8.78)) with respect to the wave frequency (ω) for obtaining group speeds as

$$\left[k^2 \frac{\partial \mathbf{T}_2}{\partial \omega} + \frac{\partial \mathbf{T}_0}{\partial \omega} \right] C_{g3} + 2k\mathbf{T}_2 + \mathbf{T}_1 = 0 \quad (8.94)$$

where $C_{g3} = (\partial\omega/\partial k)_3$ is the group speed of a waves in TWCNTs and the matrices \mathbf{T}_2 , \mathbf{T}_1 and \mathbf{T}_0 are given in Eqs. (8.79)–(8.81). This is also a PEP, one can solve it for group speeds of respective modes (that is, for flexural and shear) of all the three walls.

The spectrum and dispersion curves for TWCNTs are shown in Fig. 8.9a, b, respectively. The wave behavior is similar to DWCNT case and all the observations made are also valid here. For a given nonlocal parameter (say $e_0a = 0.5$ nm) the group speed dispersion curves are shown for various radii of the CNTs in Fig. 8.9c. The escape frequency variation of the flexural and shear modes of the three walls can be clearly seen from Figs. 8.9c and 8.10. The escape frequencies are inversely proportional to the nonlocal parameter, so as the nonlocal parameter increases the escape frequencies decrease as shown in Fig. 8.10a, b. The escape frequencies of the flexural and shear modes of the wall-3 for a given nonlocal parameter are constant for all radii of the CNT. The similar phenomena is observed for the flexural modes

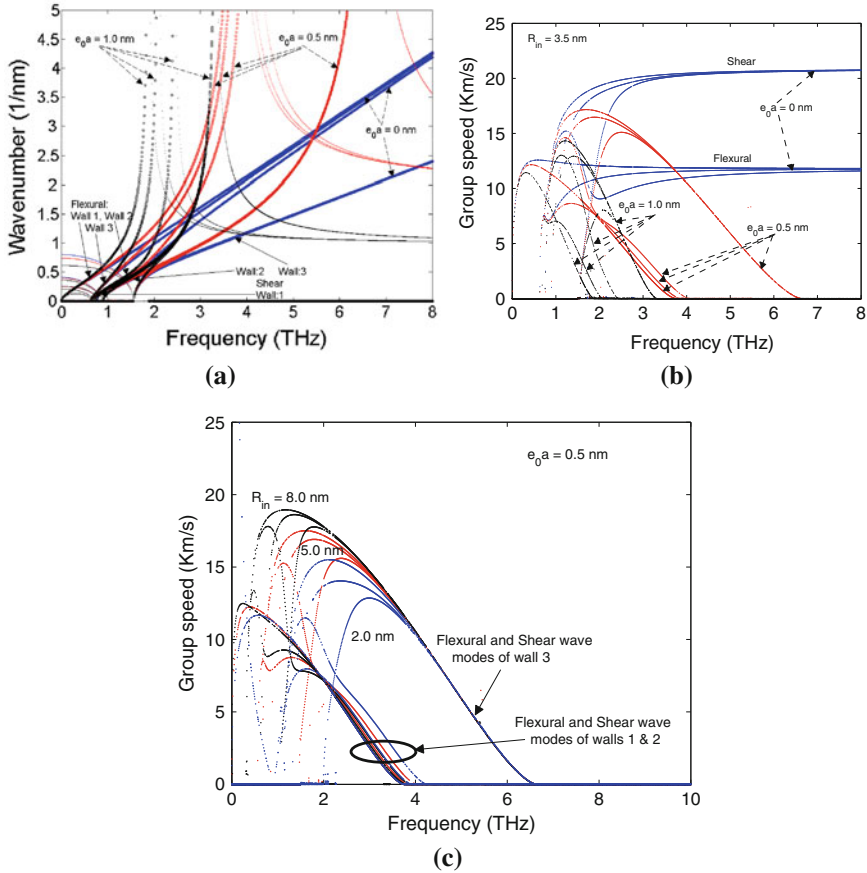


Fig. 8.9 **a** Spectrum curves (Real wavenumbers—*thick lines*; Imaginary wavenumbers—*thin lines*), **b** Dispersion curves for TWCNTs for various nonlocal scaling parameters for wall-1 radius $R_{in} = 3.5$ nm, and **c** Dispersion curves for TWCNTs for various inner tube (wall-1) radii (for $e_0a = 0.5$ nm)

of wall-1 and wall-2 (see Fig. 8.10). The only escape frequencies of the shear wave modes of the walls-1 and 2 are decreasing with the wall radii.

As in the cases of SWCNTs and DWCNTs, the escape frequencies of flexural and shear wave modes of the three walls are decreasing with the nonlocal scaling parameter.

The variation of the cut-off frequencies of all modes of TWCNTs are plotted in Fig. 8.11. These cut-off frequencies are independent of the nonlocal scaling parameter. As the radius of the CNTs increases the cut-off frequencies show a decrease in nature. For higher values of the tube radius the cut-off frequencies of the shear mode of wall-1 and the flexural modes of walls 2 and 3 are almost same as shown in Fig. 8.11.

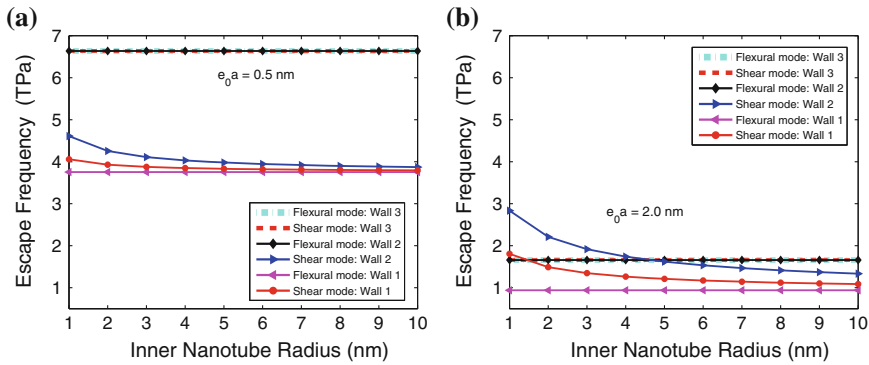
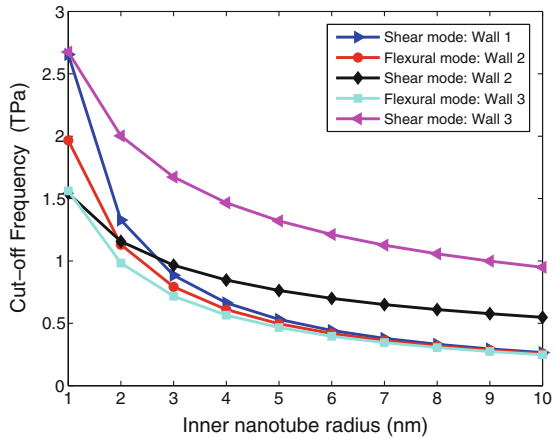


Fig. 8.10 Variation of escape (or asymptotic) frequency with inner nanotube radius for (a) $e_0a = 0.5$ nm and (b) $e_0a = 2.0$ nm

Fig. 8.11 Cut-off frequency variation of TWCNTs with nanotube radius



According to the spectrum and dispersion results of the SWCNTs, DWCNTs and TWCNTs, one can generalize the effect of nonlocal scaling parameter on wave propagation in MWCNTs as explained below. When we consider the wave propagation in N -walled CNT (modeled as N -layered Timoshenko beams connected by distributed springs) with nonlocal scale effects, based the study performed sofar, it leads to the following conclusions.

1. For a given nonlocal parameter (e_0a) the flexural and shear the wave modes of N th wall of the N -walled CNT have same escape frequencies, which are constant for all the radii of the CNT, and decreases with the increase in nonlocal scaling parameter.
2. The flexural wave modes of the remaining $N - 1$ walls (1, 2, . . . , $N - 1$) will also have a fixed escape frequency for different radii of the tubes. As e_0a increases

this frequency decreases. For a given e_0a this frequency is smaller than that of the N th wall.

3. The escape frequencies, for a given e_0a , of the shear wave modes of these $N - 1$ walls have different frequencies for different nanotube radii. As the tube radius and/or e_0a increases these escape frequencies decreases.
4. Because of the van der Waals interaction among the tubes, nonlocal effect is found only on the escape frequencies of the shear wave modes of the $N - 1$ walls.
5. For a N -walled CNT, the cut-off frequencies of flexural and shear wave modes are independent of the nonlocal scaling parameter.

8.3 Summary

In this chapter, a nonlocal Timoshenko beam model was developed for a multi-walled carbon nanotube by modeling the van der Waals interaction between the tubes as the distributed spring system. Effect of nonlocal elasticity on the wave dispersion in multi-walled carbon nanotubes (MWCNTs) was studied using single, double and three walled CNTs, and the results were generalized for MWCNTs. We have shown that the escape frequencies of the flexural and shear wave modes of the N th wall of a N -walled CNT were constant with increase in radius of the CNT. These frequencies decreases with the nonlocal scaling parameter. The flexural wave modes of the remaining $N - 1$ walls were also having a constant escape frequency and it will not vary with the radius of CNT and also decreases with increase in e_0a . The shear wave modes of the $N - 1$ walls show different escape frequencies and they decreases with the increase in radius of CNT and also nonlocal scaling parameter. This variation is because of the van der Waals interaction between the tubes. The significant influence of nonlocal effects were observed only on the shear wave modes of the $N - 1$ walls. We also show that the cut-off frequencies of the N -walled CNTs are independent of e_0a .

All the problems studied in this chapter will provide the reader a clear methodology of using spectral analysis to obtain wave behavior in MWCNT. In the next chapter, we will extend the spectral analysis method to study the wave dispersion characteristics of coupled one-dimensional nanosystems based on nonlocal continuum mechanics theory.

References

1. J. Peddieson, G.R. Buchanan, R.P. McNitt, Application of nonlocal continuum models to nanotechnology. *Int. J. Eng. Sci.* **41**, 305-312 (2003)
2. C.Q. Ru, Column buckling of multiwalled carbon nanotubes with interlayer radial displacements. *Phys. Rev. B* **62**, 16962-16967 (2000)
3. J. Yoon, C.Q. Ru, A. Mioduchowski, Sound wave propagation in multiwall carbon nanotubes. *J. Appl. Phys.* **93**, 4801 (2003)

4. J. Yoon, C.Q. Ru, A. Mioduchowski, Timoshenko-beam effects on transverse wave propagation in carbon nanotubes. *Compos. Part B: Eng.* **35**, 87–93 (2004)
5. A. Chakraborty, Shell element based model for wave propagation analysis in multi-wall carbon nanotubes. *Int. J. Solids Struct.* **44**, 1628–1642 (2006)
6. A. Chakraborty, M.S. Shivakumar, S. Gopalakrishnan, Spectral finite element based model for wave propagation analysis in multi-wall carbon nanotubes. *Int. J. Solids Struct.* **43**, 279–294 (2006)
7. M. Mitra, S. Gopalakrishnan, Wave characteristics of multi-walled carbon nanotubes, 49th AIAA/ASME/ASCE/AHS/ASC Structures, Structural Dynamics and Material Conference, Schaumburg, IL, April, 2008, Paper No. AIAA-2008-1782
8. L. Vaccarini, C. Goze, L. Henrard, E. Hernandez, P. Bernier, A. Rubio, Mechanical and electronics properties of carbon and boron-nitride nanotubes. *Carbon* **38**, 1681–1690 (2000)
9. S. Gopalakrishnan, A. Chakraborty, D.R Mahapatra, *Spectral Finite Element Method* (Springer, London 2008)

Chapter 9

Wave Propagation in Coupled 1D-Nanosystems

The wave propagation in 1-D nanorods was studied in detail in Chap. 6, while 1-D nanobeams (both Euler-Bernoulli and Timoshenko beam models) were discussed in Chap. 7. In Chap. 8, the wave propagation in connected 1-D beams was studied (MWCNT), where the connection is along the circumference of multiple nanotube walls through van der Waals forces. In this chapter, we will study the wave propagation in 1-D nanorods/nanobeams, which are explicitly connected elastically all along the length through a series of distributed springs. Such structures are prevalent in nano electro mechanical systems (NEMS), nano opto-mechanical systems, nano oscillators etc. Again, we will use non local elasticity formulation and the main objective here is to study the effect of non local scale parameter and coupling stiffness on the wave behavior of such nano systems. It should be said here that the literature available on this important topic is not large. There are a few works reported on coupled nano rod systems. Murmu and Adhikari [1], studied the longitudinal vibration of a double-nanorod system (DNRS) based on nonlocal elasticity theory. Their study highlights that the nonlocal effect considerably influences the axial vibration of DNRS. Zhang and Sharma [2], studied the size dependency of strain in arbitrary shaped anisotropic embedded quantum dots due to nonlocal dispersive effects. The size dependency of strain in lattice-mismatched embedded quantum dots based on the mechanism of nonlocal interactions (included in the form of higher-order strain gradients). They concluded that, qualitatively, their nonlocal solutions exhibit strain profiles that are more physical than those obtained from classical elasticity, that is, discontinuities across interfaces are smoothed out and singularities in the cases of corners in polyhedral shapes are eliminated. Although there are a number of works on the dynamics of couple continuum beams, the works reported on the vibration and wave propagation in a doubly coupled nano beam (DNBS) is quite scarce. Some of these are reviewed under the section dealing with double nanobeam system.

9.1 Governing Equations of Motion for Double Nanorod System

In the present section, the small-scale effects on the DNRS are investigated by employing nonlocal continuum mechanics. The effect of nonlocal scaling parameter (e_0a) on the wave propagation in DNRS and also the variation of the escape frequency with e_0a is studied in detail in this section. Here, $e_0a = 1.0$ nm and 2.0 nm are used, where $a = 0.142$ nm (C–C bond length). Wave propagation analysis in DNRS is also carried out after deriving the nonlocal governing equations. The explicit expressions for the wavenumbers as a function of wave frequency for the coupled nanorod system are derived. Also the relation between the escape frequency and nonlocal scaling parameter is derived. Important numerical results are presented on the wave dispersion in DNRS.

Figure 9.1 schematically describes a double nanorod system coupled by springs under discussion and serves to introduce the axial coordinate x , the axial displacement $u = u(x, t)$, the length L , the Young’s modulus E , and the density ρ . This topic was discussed in detail in Chap. 6. The governing differential equation for a single nanorod system is given by

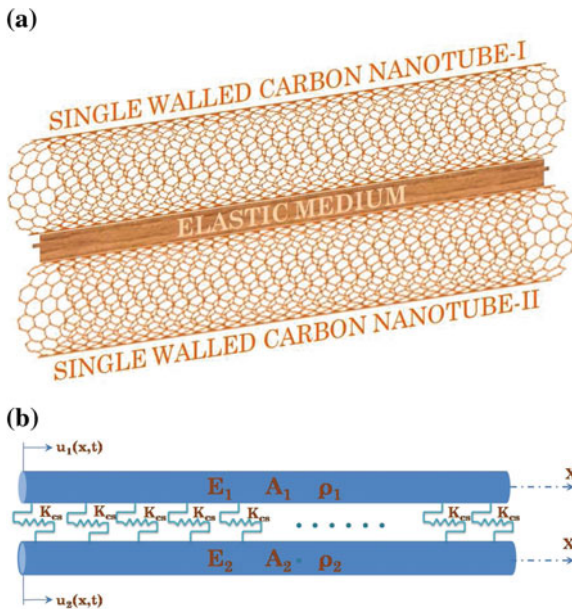


Fig. 9.1 A Coupled single walled carbon nanotube system modeled as a coupled nanorod system: **a** Discrete model **b** Equivalent continuum model, here K_{cs} denote the stiffness of coupled spring, Young’s modulus E , density ρ , cross-sectional area A , and longitudinal displacement $u = u(x, t)$ along X –direction

$$EA \frac{\partial^2 u}{\partial x^2} + g^2 \rho A \frac{\partial^4 u}{\partial x^2 \partial t^2} - \rho A \frac{\partial^2 u}{\partial t^2} + f - g^2 \frac{\partial^2 f}{\partial x^2} = 0 \quad (9.1)$$

We will use Eq. (9.1) for the development of coupled double-nanorod system.

Consider a double-nanorod system (DNRS) as shown in Fig. 9.1. Here we assumed that the coupled SWCNT (see Fig. 9.1a) as double-nanorod. Both nanorods are separated by axially distributed springs. The springs are used to substitute the effect of elastic medium forces due to nano-optomechanical effect or van der Waals forces (vdW) between the two nanorods. The coupled springs are assumed to have a stiffness K_{cs} . In general, the two nanorods have different Young's modulus, cross sectional area, and density. These parameters are assumed to be constant along each nanorod.

The longitudinal displacements over the two nanorods are denoted by $u_1(x, t)$ and $u_2(x, t)$ (see Fig. 9.1b). Based on Eq. (9.1), the governing equations of motion for the axial wave propagation of DNRS can be expressed as

$$E_1 A_1 \frac{\partial^2 u_1}{\partial x^2} + g^2 \rho_1 A_1 \frac{\partial^4 u_1}{\partial x^2 \partial t^2} - \rho_1 A_1 \frac{\partial^2 u_1}{\partial t^2} + f_1 - g^2 \frac{\partial^2 f_1}{\partial x^2} = 0 \quad (9.2)$$

$$E_2 A_2 \frac{\partial^2 u_2}{\partial x^2} + g^2 \rho_2 A_2 \frac{\partial^4 u_2}{\partial x^2 \partial t^2} - \rho_2 A_2 \frac{\partial^2 u_2}{\partial t^2} + f_2 - g^2 \frac{\partial^2 f_2}{\partial x^2} = 0 \quad (9.3)$$

Here the distributed forces on nanorod-1 and nanorod-2 are given as

$$f_1 = K_{cs} (u_2 - u_1) \quad (9.4)$$

$$f_2 = K_{cs} (u_1 - u_2) \quad (9.5)$$

substituting f_1 and f_2 in Eqs. (9.2) and (9.3) gives

$$E_1 A_1 \frac{\partial^2 u_1}{\partial x^2} + g^2 \rho_1 A_1 \frac{\partial^4 u_1}{\partial x^2 \partial t^2} - \rho_1 A_1 \frac{\partial^2 u_1}{\partial t^2} + K_{cs} (u_2 - u_1) - g^2 K_{cs} \left(\frac{\partial^2 u_2}{\partial x^2} - \frac{\partial^2 u_1}{\partial x^2} \right) = 0 \quad (9.6)$$

$$E_2 A_2 \frac{\partial^2 u_2}{\partial x^2} + g^2 \rho_2 A_2 \frac{\partial^4 u_2}{\partial x^2 \partial t^2} - \rho_2 A_2 \frac{\partial^2 u_2}{\partial t^2} - K_{cs} (u_2 - u_1) + g^2 K_{cs} \left(\frac{\partial^2 u_2}{\partial x^2} - \frac{\partial^2 u_1}{\partial x^2} \right) = 0 \quad (9.7)$$

The above equations revert to the equations of classical rod theory [3], if nonlocal scale coefficient is ignored, that is, $g = 0$.

9.1.1 Wave Propagation Analysis in DNRS

For analyzing the ultrasonic wave dispersion characteristics in nanorods, we will perform spectral analysis. That is, we assume that a harmonic type of wave solution for the displacement fields $u_1(x, t)$ and $u_2(x, t)$ it can be expressed in complex form as [3]

$$u_1(x, t) = \sum_{m=0}^{M-1} \sum_{n=0}^{N-1} \hat{u}_1(x, \omega_n) e^{-j(k_m x - \omega_n t)} \quad (9.8)$$

$$u_2(x, t) = \sum_{m=0}^{M-1} \sum_{n=0}^{N-1} \hat{u}_2(x, \omega_n) e^{-j(k_m x - \omega_n t)} \quad (9.9)$$

where, M and N are the number of time sampling points and number spatial sampling points, respectively. ω_n is the circular frequency at the n th time sample. Similarly, k_m is the axial wavenumber at the m th spatial sample point and $j = \sqrt{-1}$. Substituting Eqs. (9.8) and (9.9) into the governing partial differential Eqs. (9.6) and (9.7), we get the dispersion relation as follows. Hereafter, the subscripts m and n are dropped for simplified notations. That is,

$$\begin{bmatrix} Z_{11} & Z_{12} \\ Z_{21} & Z_{22} \end{bmatrix} \begin{Bmatrix} \hat{u}_1 \\ \hat{u}_2 \end{Bmatrix} = \begin{Bmatrix} 0 \\ 0 \end{Bmatrix} \quad (9.10)$$

where,

$$\begin{aligned} Z_{11} &= -E_1 A_1 k^2 + \rho_1 A_1 \omega^2 (1 + g^2 k^2) - K_{cs} (1 + g^2 k^2), \\ Z_{12} &= Z_{21} = K_{cs} (1 + g^2 k^2), \\ Z_{22} &= -E_2 A_2 k^2 + \rho_2 A_2 \omega^2 (1 + g^2 k^2) - K_{cs} (1 + g^2 k^2). \end{aligned} \quad (9.11)$$

Assuming nontrivial solution for \hat{u}_1 and \hat{u}_2 , one can solve the following equation for wavenumbers

$$\begin{vmatrix} Z_{11} & Z_{12} \\ Z_{21} & Z_{22} \end{vmatrix} = 0 \quad (9.12)$$

Solving Eq. (9.12), we get an algebraic equation in wavenumber (known as dispersion relation) as

$$(C_1 C_5 - C_3^2) k^4 + (C_1 C_6 + C_2 C_5 - 2C_3 C_4) k^2 + C_2 C_6 - C_4^2 = 0 \quad (9.13)$$

where

$$\begin{aligned}
C_1 &= -E_1 A_1 + \rho_1 A_1 g^2 \omega^2 - K_{cs} g^2, \\
C_2 &= \rho_1 A_1 \omega^2 - K_{cs}, \\
C_3 &= K_{cs} g^2, \\
C_4 &= K_{cs}, \\
C_5 &= -E_2 A_2 + \rho_2 A_2 g^2 \omega^2 - K_{cs} g^2, \\
C_6 &= \rho_2 A_2 \omega^2 - K_{cs}.
\end{aligned} \tag{9.14}$$

The wavenumber is a function of wave frequency, the nonlocal scaling parameter g , and the material and geometrical properties of the nanorod.

For the present analysis, we are considering the phase speeds of the wave and as before. its expression is given by

$$C_P = \frac{\omega}{k} \tag{9.15}$$

This wave speed also depends on the nonlocal scaling parameter. When $g = 0$, the wave speed is equal (i.e., $C_P = \sqrt{E/\rho}$), which is already proved for local or classical bars/rods (for more details refer [3]).

From Eq. (9.13), we can clearly see the existence of cut-off frequency. The expression for frequency band gap is obtained by setting $k = 0$ in dispersion relation (Eq. 9.13). For the present problem, one can solve the dispersion relation (Eq. 9.13) by setting $k = 0$, i.e., solving $C_2 C_6 - C_4^2 = 0$, we get the cut-off frequency as

$$\omega_{cut} = \sqrt{K_{cs} \left[\frac{1}{\rho_1 A_1} + \frac{1}{\rho_2 A_2} \right]} \tag{9.16}$$

The frequency band gap ($0 - \omega_{cut}$, cut-off frequency) for axial wave mode depends on the material properties of the nanorods and also the coupling spring stiffness.

Figure 9.2a shows the spectrum relation plot as a function of nonlocal scale parameter $e_0 a$. From the figure, we can clearly see the existence of escape frequency and this frequency value decreases with increase in the scale parameter. Its value can be analytically determined by looking at the dispersion relation (Eq. 9.13) and setting $k \rightarrow \infty$ (that is, we get $C_1 C_5 - C_3^2 = 0$), which gives escape frequency as

$$\omega_{escape} = \sqrt{\frac{-H_2 \pm \sqrt{H_2^2 - 4H_4 H_0}}{2H_4}} \tag{9.17}$$

where

$$\begin{aligned}
H_4 &= \rho_1 \rho_2 A_1 A_2 g^4, \\
H_2 &= -E_1 A_1 \rho_2 A_2 g^2 - E_2 A_2 \rho_1 A_1 g^2 - K_{cs} g^4 (\rho_1 A_1 + \rho_2 A_2), \\
H_0 &= E_1 E_2 A_1 A_2 + K_{cs} g^2 (E_1 A_1 + E_2 A_2).
\end{aligned} \tag{9.18}$$

The only solution giving positive value of the escape frequency is admissible. We will discuss more on escape frequency next.

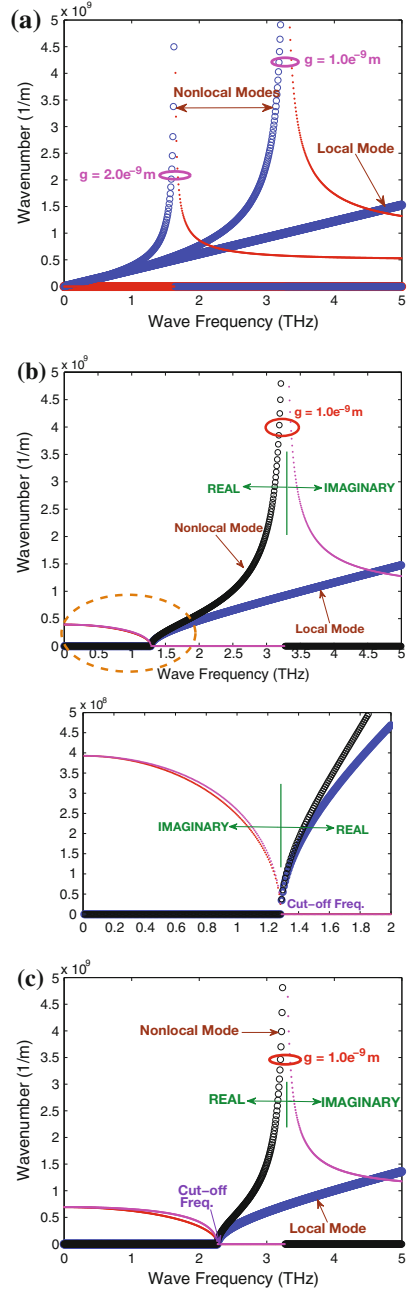
For the present study, we consider the properties of the nanorod (SWCNT) [4]. An armchair SWCNT with chirality (5, 5) is considered. The radius of each individual nanorod (SWCNT) is assumed as $R = 0.34 \text{ nm}$. Young's modulus, E , is considered as 0.971 TPa . The stiffness of the coupling springs is assumed to be in between the low and high stiffness values, that is, $K_{cs} = 8 \text{ N/nm}$ and 80 N/nm , respectively. Here the term DNRS would denote the case of double-carbon-nanotube-rod system. Here, we also assume that both the nanorods/SWCNTs have same properties as mentioned above.

We have assumed the unit of coupling stiffness as N/nm . Hence, all the dimensions in the Eqs. (9.6) and (9.7) as well as Eqs. (9.10)–(9.17) will not match. Generally, it is assumed that the system under consideration is composed of two parallel, and homogeneous rods continuously joined by a Winkler type of elastic layer. This elastic layer stiffness has the units of N/nm^2 , which means that the stiffness K_{cs} is N/nm per unit nm thickness of the Winkler layer. Here, in the present formulation, the rods are joined by the distributed springs, so that the stiffness is $K_{cs} \text{ N/nm}$ per nm thickness of the layer (hence the units of K_{cs} should be read as N/nm^2). In the present calculation, the thickness of this layer is neglected.

Figure 9.2a shows the real and imaginary parts of the axial wavenumber of a nanorod obtained from both local ($g = 0$) and nonlocal elasticity ($g = 1.0 \times 10^{-9} \text{ m}$ and $g = 2.0 \times 10^{-9} \text{ m}$) theories for $K_{cs} = 0$. The thick lines represent the real part and the thin lines show the imaginary part of the wavenumbers. From Fig. 9.2a, for a nanorod, it can be seen that there is only one mode of wave propagation i.e., axial or longitudinal. For local or classical model, the wavenumbers for the axial mode has a linear variation with the frequency which is in the THz range. The linear variation of the wavenumbers denote that the waves will propagate nondispersively, that is, the waves do not change their shapes as they propagate. On the other hand, the wavenumbers obtained from nonlocal elasticity have a nonlinear variation with the frequency, which indicates that the waves are dispersive in nature. However, the wavenumbers of this wave mode have a substantial real part starting from the zero frequency. This implies that the mode starts propagating at any excitation frequency and does not have a cut-off frequency. From Fig. 9.2, we can clearly see the existence of escape frequency).

For a given coupling stiffness (say $K_{cs} = 8 \text{ N/nm}$), the spectrum curve is plotted in Fig. 9.2b. However, the wavenumbers of axial wave mode does not have a substantial real part starting from the zero frequency. This implies that the mode starts propagating only after the cut-off frequency, where the imaginary part of the wavenumber becomes real as shown in Fig. 9.2b. The behavior of the axial wave obtained from local and nonlocal theories is same as observed for the case of $K_{cs} = 0$. The enlarged portion at the cut-off frequency is also shown in Fig. 9.2b. Now, we increase the coupled spring stiffness further to $K_{cs} = 25 \text{ N/nm}$. The resulting spectrum curves are shown in Fig. 9.2c. It can be seen the cut-off frequency is increased from 1.282 THz to 2.274 THz as K_{cs} increases from 8 N/nm to 25 N/nm , respectively. This is a significance difference and one has to consider this variation

Fig. 9.2 Wavenumber dispersion in a double nanorod system **a** $K_{cs} = 0$ N/nm **b** $K_{cs} = 8$ N/nm **c** $K_{cs} = 25$ N/nm



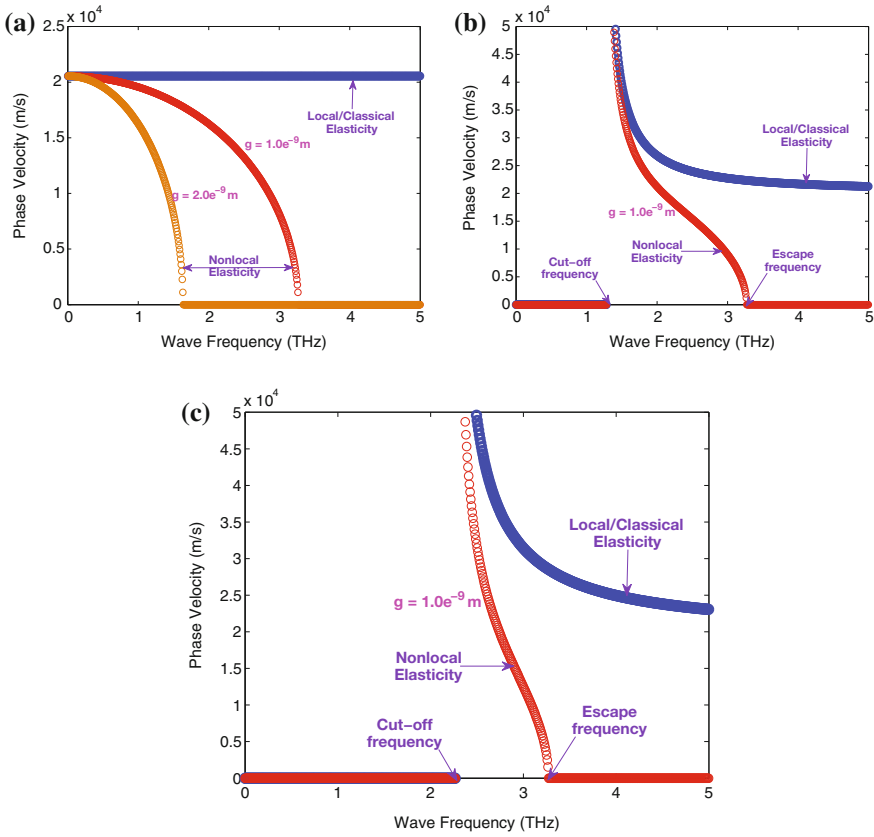


Fig. 9.3 Phase velocity dispersion in a double nanorod system **a** $K_{cs} = 0$ N/nm **b** $K_{cs} = 8$ N/nm **c** $K_{cs} = 25$ N/nm

at small scales. However, there is no significant change in escape frequency as the stiffness of the coupled spring increase. It can be seen that the frequency band gap increases with the stiffness of the coupled spring between nanorods.

Figure 9.3a plots the wave speed for the nanorod obtained from both local and nonlocal models for $K = 0$. Because of the linear variation of wavenumber with wave frequency from local elasticity (see Fig. 9.2a), the phase speed ($C_p = Real(\frac{\omega}{k})$) for the axial mode has a constant value for all the frequencies and hence, the wave does not change its shape as it propagate. It can also be observed, that the axial wave speed behavior is similar for local and nonlocal cases at zero frequency. In nonlocal elasticity, the wavenumber tends to infinity at escape frequencies (see Fig. 9.2a), which results in phase speed tending to zero at these frequencies.

The phase speed variations are shown with respect to wave frequency in Fig. 9.3b, c, respectively for coupling stiffness values of 8 N/nm and 25 N/nm. It can be seen that the cut-off frequency increases as the stiffness of the coupled spring increases. The spring stiffness has no effect on escape frequency of the axial wave mode. The

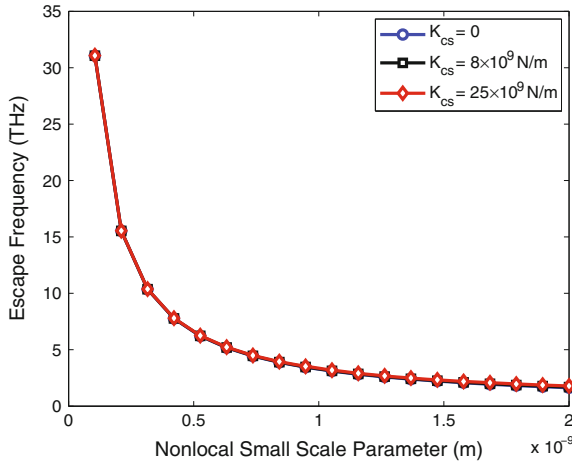


Fig. 9.4 Variation of escape frequency with nonlocal scaling parameter

phase speeds are tending to zero at the escape frequencies. It can be also stated that, as in the case of single nanorod, the wave dispersion characteristics in a coupled nanorod system is drastically different for local and nonlocal models. Where local model predicts that the wave will propagate at all frequencies, but the nonlocal model shows that the wave will propagate up to certain frequencies only depending on the nonlocal scaling parameter (refer Fig. 9.3a–c).

The escape frequencies are purely a function of the nonlocal scaling parameter and the stiffness of the coupled spring. The variation of the escape frequency with nonlocal scaling parameter (g) is shown in Fig. 9.4. It shows that, as g increases the escape frequency decreases, such variation can also be observed from Fig. 9.2. For very small values of g , the escape frequencies are very large, and at higher values of g the escape frequencies are very small and approach to a constant value. We also see that the coupled spring stiffness has very little influence on the escape frequency. Such effect is also observed in Fig. 9.2a–c.

The cut-off frequency of the axial wave mode is a function of the stiffness of the coupled spring and the material and geometrical properties of the nanorod. This cut-off frequency is independent of the nonlocal scaling parameter (see Eq. 9.16). Such variation is also observed in spectrum and dispersion curves. The variation of the cut-off frequency with various sizes of the nanorod is shown in Fig. 9.5 for different values of the coupled spring stiffness. As the diameter of the nanorod increases, the cut-off frequency decreases. For smaller diameter of nanorod, the cut-off frequency is higher and for larger diameters, the cut-off frequency is very small. For diameters higher than 5 nm, the cut-off frequency is almost constant. For high stiffness of the coupled spring and small diameter of nanorod, the cut-off frequency is very high and will decrease drastically for larger diameter nanorods (see Fig. 9.5). The present study may bring in helpful insights while investigating multiple-nanorod-system-models for future NOMS applications.

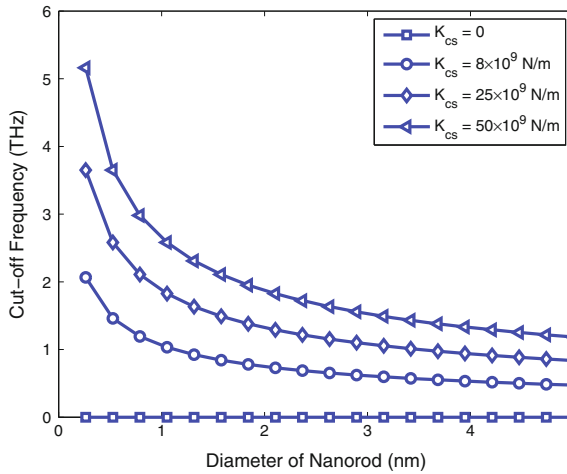


Fig. 9.5 Variation of cut-off frequency with diameter of the nanorods with various values of coupled spring stiffness

9.2 Coupled Nano-Beam System

An important technological extension of the concept of the single beam is that of the complex coupled-beam systems. One such simple coupled beam system is the double-beam system. The double-beam system is a continuous system consisting of two one-dimensional beams joined by an elastic medium represented by distributed vertical springs. Employing beam theories, several important works on vibration and buckling of elastically connected double-beam systems are reported. Vu et al. [5] studied the vibration of homogenous double-beam system subjected to harmonic excitation. Erol and Gurgoz [6] extended the analysis of [5] to axially vibrating double-rod system coupled by translational springs and dampers. Oniszcuk [7] studied the free vibrations of two parallel simply supported beams continuously joined by a Winkler elastic layer. Undamped forced transverse vibrations of an elastically connected simply supported double-beam system were analyzed. Free and forced vibration of double-string complex system was also investigated by Oniszcuk [8, 9]. Hilal [10] investigated the dynamic response of a double Euler-Bernoulli beam due to moving constant load. The effects of the speed of the moving load, the damping and the elasticity of the coupling viscoelastic layer on the dynamic responses of the beam system were presented. Vibration analysis of double-beam systems interconnected only at discrete points was reported by Hamada et al. [11] and Gurgoz and Erol [12]. Buckling and the effect of a compressive load on the free and forced vibration on double-beam systems were reported by Zhang et al. [13, 14]. Kelly and Srinivas [15] carried out vibrations of elastically connected stretched beam systems. Analyses of double-beam systems by numerical techniques were also reported. Rosa and Lippiello [16] presented non-classical boundary conditions and differential

quadrature method for vibrating double beams. Li and Hua [17] presented spectral finite element analysis of elastically connected double-beam systems.

From the above discussion, it can be observed that the vibration theory of double-beam systems is well developed and studied in details. However, there are only few contributions dealing with the vibrations of beam-systems which are scale-dependent. As mentioned earlier, the understanding of dynamics of single-nanobeam (carbon nanotubes, nanowires) is important. The vibration characteristics of nanobeams can be employed for NEMS/MEMS applications. Parallel to vibration of single nanobeam, the study of vibrating multiple-nanobeam system is also relevant for nanosensors and nanoresonators applications. The recent development of nano-optomechanical systems (NOMS) necessitates the use of vibrating double-nanobeam systems.

Frank et al. [18] presented a dynamically reconfigurable photonic crystal nanobeam cavity. Their work involved two closely situated parallel vibrating clamped double-nanobeam systems. Eichenfield et al. [19] described the design, fabrication, and measurement of a cavity nano-optomechanical system (NOMS). The NOMS consisting of two closely separated coupled nanobeams. The researchers fabricated the low dimension double-beam system by depositing stoichiometric silicon nitride using low-pressure-chemical-vapor-deposition on a silicon wafer. Deotare et al. [20] studied the coupled photonic crystal nanobeam cavities consisting of two parallel suspended nanobeams separated by a small gap. The use of vibration properties in double-nanobeam system has also been reported by Lin et al. [21]. The authors studied the coherent mixing of mechanical excitations in nano-optomechanical structures. Most of the works reported here are experimental works. It is understood that controlling every parameter in experiments at nanoscale is difficult. Further, since molecular dynamics simulations are computationally expensive, analysis of nanostructures had been carried out by classical continuum theory. Extensive research over the past decade has shown that classical continuum models are able to predict the performance of 'large' nanostructures reasonably well. Classical continuum models are scale-free theory and it lacks the accountability of the effects arising from the size effects.

Experimental studies [22–25] and atomistic simulations [26] have shown a significant 'size-effect' in the mechanical properties when the dimensions of the nanostructures become small. Size effects are related to atoms and molecules that constitute the materials. As mentioned earlier, nonlocal elasticity accounts for the small-scale effects arising at the nanoscale level. For double-nanobeam system, Murmu and Adhikari [27] studied the nonlocal effects in the longitudinal vibration of double-nanorod systems. Further, using nonlocal elasticity Murmu and Adhikari [28] have proposed nonlocal transverse vibration analysis of coupled double-nanobeam systems. Author's work on coupled nanorod systems is reported in [29].

Therefore, there is a strong motivation to gain an understanding of the entire subject of vibration of complex-nanobeam system and the mathematical modeling of such phenomena. In this chapter, an investigation is carried out to understand the small-scale effects in the wave propagation of nonlocal double-nanobeam system. Here, for analyzing single beam, both Euler-Bernoulli beam and Timoshenko beam

models are considered and the wave characteristics based on these two models are studied in the following sections.

9.2.1 Wave Propagation in Double Euler-Bernoulli Nanobeam System

We will first derive the governing differential equation for the coupled nanobeam system. The one-dimensional equation of motion of a nonlocal Euler-Bernoulli beam (Eq. 7.11) with consideration of distributed transverse load ($q(x)$) can be written as

$$EI \frac{\partial^4 w(x, t)}{\partial x^4} + \rho A \frac{\partial^2 w(x, t)}{\partial t^2} - \rho A (e_0 a)^2 \frac{\partial^4 w(x, t)}{\partial x^2 \partial t^2} - q(x) + (e_0 a)^2 \frac{\partial^4 q(x)}{\partial x^4} = 0 \tag{9.19}$$

where w denotes the deflection of the beam. The terms E , I , and ρA are the Young’s modulus, second moment of inertia, and mass of the nonlocal beam, respectively.

Consider a nonlocal double-nanobeam system (DNBS) as shown in Fig. 9.6. The two nanobeams are denoted as nanobeam-I and nanobeam-II. Vertically distributed springs attach the two nanobeams. The stiffness of the springs is equivalent to the Winkler constant in a Winkler foundation model [7]. The springs can be used to substitute elastic medium forces due to nano-optomechanical effects (see [19–21]) or van der Waals forces between the two nanobeams. These forces arise when the dimension of system approaches nanoscale. Generating a potential difference directly across the nanobeams an attractive electrostatic force can be induced between the two nanobeams [18]. The spring stiffness can be varied between the nanobeams. The springs are considered to have stiffness, K_{cs} . The two nanobeams are different where the length, mass per unit length, and bending rigidity of the i th beam are L_i , $m_i = \rho_i A_i$, and $E_i I_i$ ($i = 1, 2$), respectively. These parameters are assumed to be constant along each nanobeam.

The bending displacements over the two nanobeams are denoted by $w_1(x, t)$ and $w_2(x, t)$, respectively (Fig. 9.6). Based on Eq. (9.19), the governing equations of motion for the flexural wave propagation of DNBS can be expressed as

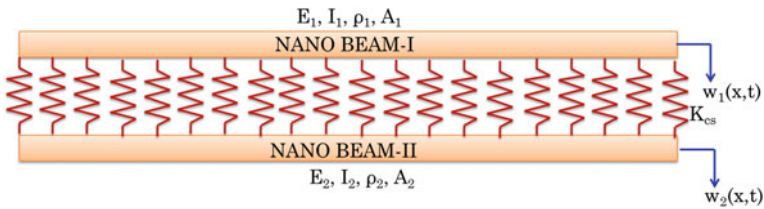


Fig. 9.6 Schematic diagram of elastically connected double-nanobeam system

$$E_1 I_1 \frac{\partial^4 w_1}{\partial x^4} + \rho_1 A_1 \frac{\partial^2 w_1}{\partial t^2} - \rho_1 A_1 (e_0 a)^2 \frac{\partial^4 w_1}{\partial x^2 \partial t^2} - q_1 + (e_0 a)^2 \frac{\partial^4 q_1}{\partial x^4} = 0 \quad (9.20)$$

$$E_2 I_2 \frac{\partial^4 w_2}{\partial x^4} + \rho_2 A_2 \frac{\partial^2 w_2}{\partial t^2} - \rho_2 A_2 (e_0 a)^2 \frac{\partial^4 w_2}{\partial x^2 \partial t^2} - q_2 + (e_0 a)^2 \frac{\partial^4 q_2}{\partial x^4} = 0 \quad (9.21)$$

Here the distributed forces on nanobeam-I and nanobeam-II are given as

$$q_1 = K_{cs} (w_2 - w_1) \quad (9.22)$$

$$q_2 = K_{cs} (w_1 - w_2) \quad (9.23)$$

substituting q_1 and q_2 in Eqs. (9.20) and (9.21), gives

$$\begin{aligned} E_1 I_1 \frac{\partial^4 w_1}{\partial x^4} + \rho_1 A_1 \frac{\partial^2 w_1}{\partial t^2} - \rho_1 A_1 (e_0 a)^2 \frac{\partial^4 w_1}{\partial x^2 \partial t^2} + K_{cs} (w_1 - w_2) \\ + K_{cs} (e_0 a)^2 \left(\frac{\partial^4 w_2}{\partial x^4} - \frac{\partial^4 w_1}{\partial x^4} \right) = 0 \end{aligned} \quad (9.24)$$

$$\begin{aligned} E_2 I_2 \frac{\partial^4 w_2}{\partial x^4} + \rho_2 A_2 \frac{\partial^2 w_2}{\partial t^2} - \rho_2 A_2 (e_0 a)^2 \frac{\partial^4 w_2}{\partial x^2 \partial t^2} + K_{cs} (w_2 - w_1) \\ + K_{cs} (e_0 a)^2 \left(\frac{\partial^4 w_1}{\partial x^4} - \frac{\partial^4 w_2}{\partial x^4} \right) = 0 \end{aligned} \quad (9.25)$$

The above equations revert to the equations of classical beam theory [3], if nonlocal scale coefficient is ignored, i.e., $e_0 a = 0$.

For analyzing the ultrasonic wave dispersion characteristics in coupled nanobeam system, we assume that a harmonic type of wave solution for the displacement field $w_1(x, t)$ and $w_2(x, t)$ it can be expressed in complex form as [3]

$$w_1(x, t) = \sum_{m=0}^{M-1} \sum_{n=0}^{N-1} \hat{w}_1(x, \omega_n) e^{-j(k_m x - \omega_n t)} \quad (9.26)$$

$$w_2(x, t) = \sum_{m=0}^{M-1} \sum_{n=0}^{N-1} \hat{w}_2(x, \omega_n) e^{-j(k_m x - \omega_n t)} \quad (9.27)$$

where, M and N are the number of time sampling points and number of spatial sampling points, respectively. ω_n is the circular frequency at the n^{th} time sample. Similarly, k_m is the wavenumber at the m^{th} spatial sample point and $j = \sqrt{-1}$. Substituting Eqs. (9.26) and (9.27) into the governing partial differential Eqs. (9.24) and (9.25), we get the dispersion relation as follows. Hereafter the subscript m and n are dropped for simplified notations.

$$\left[\mathbf{P}_4 k^4 + \mathbf{P}_2 k^2 + \mathbf{P}_0 \right] \mathbf{d} = \mathbf{0} \quad (9.28)$$

where,

$$\mathbf{P}_4 = \begin{bmatrix} E_1 I_1 & 0 \\ 0 & E_2 I_2 \end{bmatrix} \quad (9.29)$$

$$\mathbf{P}_2 = \begin{bmatrix} -\rho_1 A_1 (e_0 a)^2 \omega^2 + K_{cs} (e_0 a)^2 & -K_{cs} (e_0 a)^2 \\ -K_{cs} (e_0 a)^2 & -\rho_2 A_2 (e_0 a)^2 \omega^2 + K_{cs} (e_0 a)^2 \end{bmatrix} \quad (9.30)$$

$$\mathbf{P}_0 = \begin{bmatrix} -\rho_1 A_1 \omega^2 + K_{cs} & -K_{cs} \\ -K_{cs} & -\rho_2 A_2 \omega^2 + K_{cs} \end{bmatrix} \quad (9.31)$$

$$\mathbf{d} = \begin{Bmatrix} \hat{w}_1 \\ \hat{w}_2 \end{Bmatrix} \quad (9.32)$$

Assuming nontrivial solution for the wave amplitude vector \mathbf{d} , the Eq. (9.28) becomes

$$\mathbf{P}_4 k^4 + \mathbf{P}_2 k^2 + \mathbf{P}_0 = \mathbf{0} \quad (9.33)$$

The above equation is the dispersion relation for double nanobeam system in polynomial eigenvalue form in wavenumbers. Solving Eq. (9.33), we get wavenumbers. The wavenumbers are as a function of wave frequency, the nonlocal scaling parameter $e_0 a$, and the material and geometrical properties of the nanobeams.

Next, we will evaluate the phase and group speeds of the wave and are defined as

$$C_p = \text{real} \left(\frac{\omega}{k(\omega)} \right) \quad (9.34)$$

This wave speed is also depend on the nonlocal scaling parameter. The group speed of the wave can be computed from the following PEP

$$\frac{\partial \mathbf{P}_0}{\partial \omega} C_g + \frac{\partial \mathbf{P}_2}{\partial \omega} k^2 + 2\mathbf{P}_2 k + 4\mathbf{P}_4 k^3 = \mathbf{0} \quad (9.35)$$

where C_g is defined as

$$C_g = \text{real} \left(\frac{\partial \omega}{\partial k} \right) \quad (9.36)$$

A more detail discussion on the variation of these two wave speeds in coupled-nanobeam system is discussed in the upcoming sections.

In the wavenumber dispersion curves, the frequency at which the imaginary part of the wavenumber becomes real is called as the frequency band gap region ($0 - \omega_c$). The expression for frequency band gap is obtained by setting $k = 0$ in dispersion relation (Eq. 9.33). For the present problem, one can solve the dispersion relation (Eq. 9.33) by setting $k = 0$, i.e., solving $|\mathbf{P}_0| = \mathbf{0}$, we get the cut-off frequency as

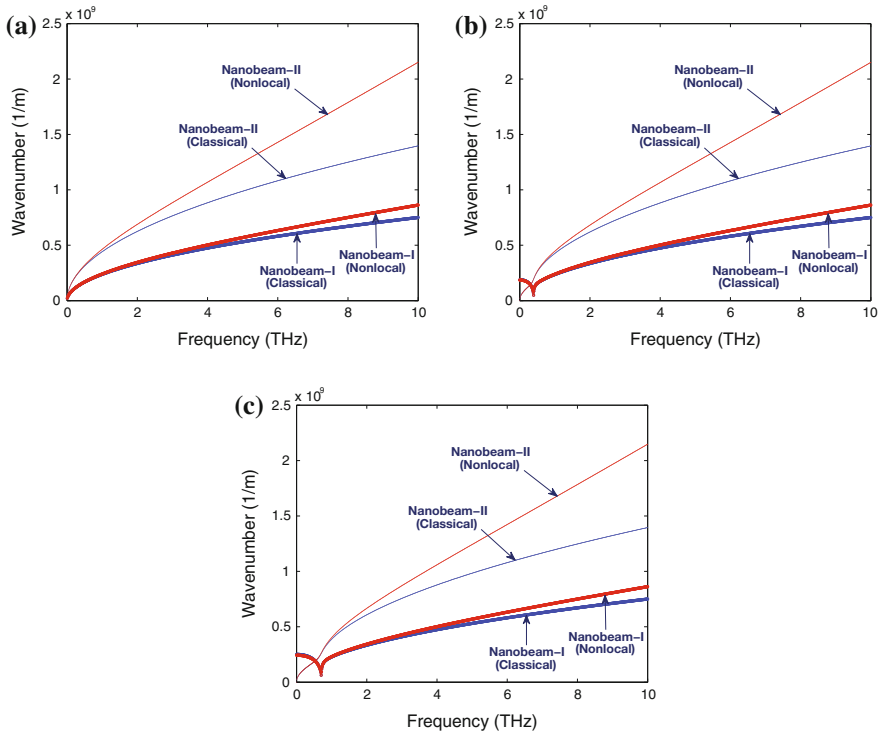


Fig. 9.7 Wavenumber dispersion in a double nanobeam system **a** $K_{cs} = 0$ N/nm **b** $K_{cs} = 8$ N/nm **c** $K_{cs} = 25$ N/nm

$$\omega_c = \sqrt{K_{cs} \left[\frac{1}{\rho_1 A_1} + \frac{1}{\rho_2 A_2} \right]} \tag{9.37}$$

The frequency band gap ($0 - \omega_c$, cut-off frequency) for flexural wave mode depends on the material properties of the nanobeams and also the coupling spring stiffness between the nanobeams. The expression is indeed the same for the cut-off frequency for the coupled nanorod systems obtained earlier in Eq. (9.16).

The spectrum curves for coupled Euler-Bernoulli beam system are plotted in Fig. 9.7a–c, respectively for coupled spring stiffness of 0, 8, and 25 N/nm, respectively. Wavenumber dispersion is similar to that observed in Chap. 7. Here our main aim is to study the effect of coupled spring on the spectrum and dispersion curves of DNBS. Each nanobeam is assumed as a single walled carbon nanotube.

The wavenumber dispersion with frequency shown in Fig. 9.7a is for zero coupled spring stiffness. In this case, wavenumbers of nanobeam-I are small as compared to the nanobeam-II. Also, the wavenumbers obtained from classical or local elasticity are smaller than that of the nonlocal elasticity. The flexural wavenumber shows a nonlinear variation with wave frequency, that is, the waves will change their shape

as they propagate. If we consider a coupled nanobeam system with coupled spring stiffness of 8 N/nm, the wavenumber dispersion looks as shown in Fig. 9.7b. It can be observed that the variation is still nonlinear and a cut-off frequency is observed in wavenumber dispersion of nanobeam-I. Flexural wave mode of nanobeam-II starts from zero wave frequency and flexural wave mode of nanobeam-I propagates only after cut-off frequency, the frequency at which the imaginary part of wavenumber becomes real. The values of the cut-off frequency are calculated from Eq. (9.37). This cut-off frequency purely depends on the coupled spring stiffness. At cut-off frequency, the wavenumber dispersion of nanobeam-II is slightly affected due to the coupled spring effect (see Fig. 9.7b). As the stiffness of the coupled spring increases, the cut-off frequency also increases. This effect is captured in Fig. 9.7c. Also it can be directly observed for Eq. (9.37) as $\omega_c \propto \sqrt{K_{cs}}$. It can also be observed that at higher frequencies the wavenumbers in nonlocal calculations are approximately linear with the wave frequency. Such observation also appears in Fig. 9.7a–c.

The wave speed (both phase and group speed) dispersion with frequency for various spring stiffness are shown in Figs. 9.8a–c and 9.9a–c. The phase speed variation obtained from both local and nonlocal theories are shown in Fig. 9.8a–c for spring stiffness of 0, 8, and 25 N/nm, respectively. The local elasticity calculation shows that the wavenumber is nonlinear with frequency even at higher frequencies and so are the phase and group speed variation with frequency. The nonlocal elasticity calculation shows that the phase speeds are almost constant at higher wave frequencies because of the linear variation of the wavenumber at higher frequencies. Similar observations are made in group speed variation as shown in Fig. 9.9a–c.

9.2.2 Wave Propagation in Coupled Timoshenko Nanobeam System

The consistent basic equations of the nonlocal Timoshenko beam model based on the nonlocal constitutive relations for a SWCNT were derived in Chaps. 7 and 8 are given by

$$GA\kappa \left(\frac{\partial^2 w}{\partial x^2} - \frac{\partial \psi}{\partial x} \right) + \rho A \frac{\partial^2}{\partial t^2} \left(w - (e_0 a)^2 \frac{\partial^2 w}{\partial x^2} \right) = 0 \quad (9.38)$$

$$GA\kappa \left(\frac{\partial w}{\partial x} - \psi \right) + EI \frac{\partial^2 \psi}{\partial x^2} - \rho I \frac{\partial^2}{\partial t^2} \left(\psi - (e_0 a)^2 \frac{\partial^2 \psi}{\partial x^2} \right) = 0 \quad (9.39)$$

where x is the longitudinal coordinate measured from the left end of the beam, w is the transverse displacement, ψ is the total section rotation measured on the mean-line of the beam, A is the cross-sectional area of the tube, and I is the moment of inertia of the tube. It is assumed that all tubes share the same Young's modulus E , shear modulus G , and Poisson's ratio ν . κ is shear correction factor that accounts for the difference in the constant state of shear stress in the Timoshenko beam theory and the parabolic variation of the actual shear stress through the depth of the cross section.

Fig. 9.8 Phase speed dispersion in a double nanobeam system **a** $K_{cs} = 0$ N/nm **b** $K_{cs} = 8$ N/nm **c** $K_{cs} = 25$ N/nm

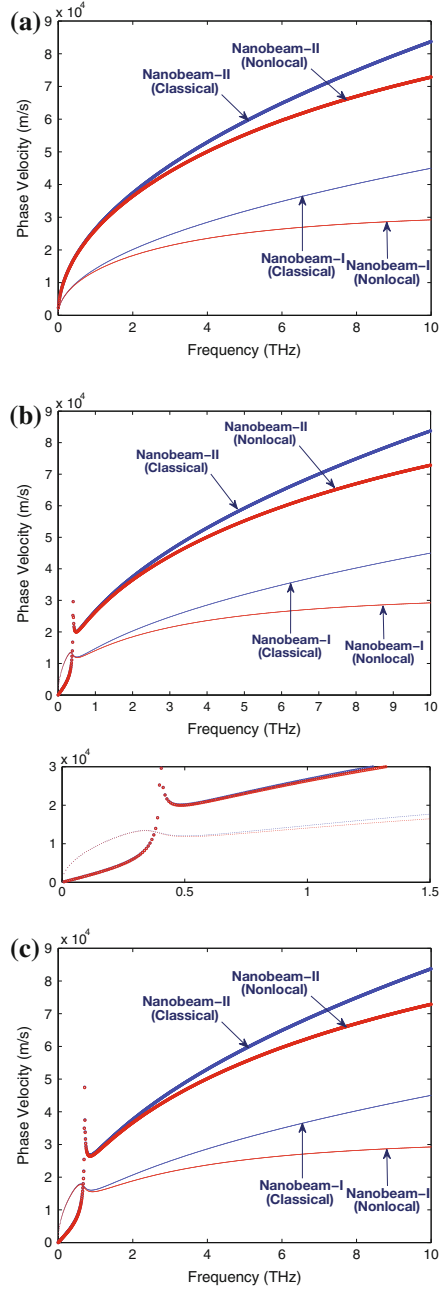
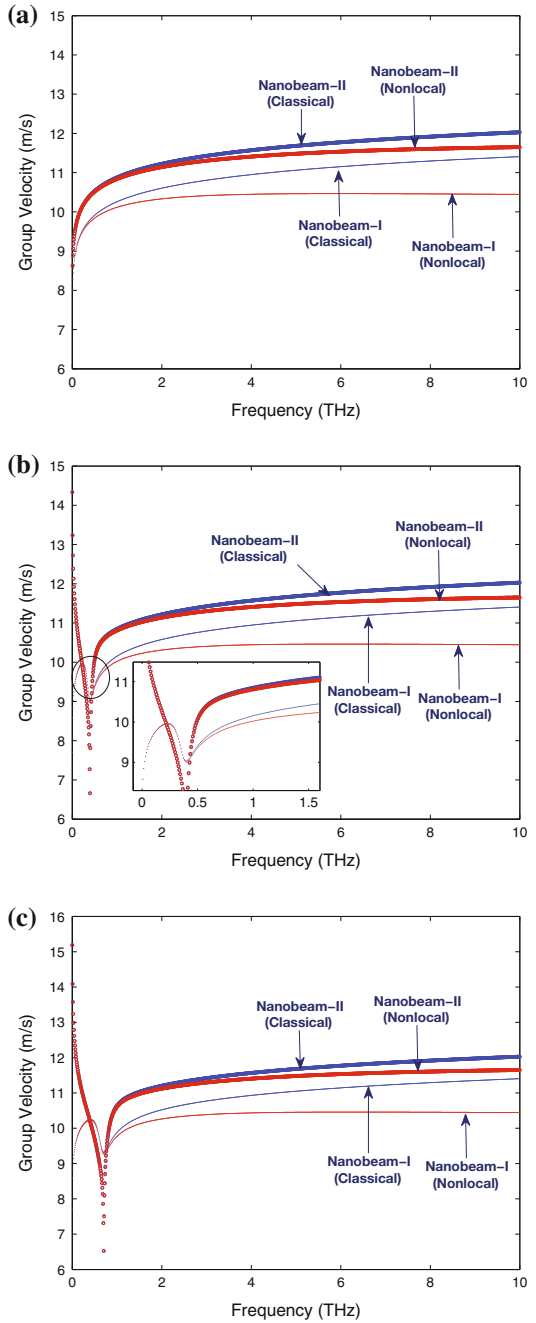


Fig. 9.9 Group speed dispersion in a double nanobeam system **a** $K_{cs} = 0$ N/nm
b $K_{cs} = 8$ N/nm
c $K_{cs} = 25$ N/nm



Consider a nonlocal Timoshenko DNBS. As before, the two nanobeams are denoted as nanobeam-I and nanobeam-II. Vertically distributed springs attach the two nanobeams. The stiffness of the springs is equivalent to the Winkler constant in a Winkler foundation model. The springs can be used to substitute elastic medium forces due to nano-optomechanical effects or van der Waals forces between the two nanobeams. These forces arise when the dimension of system approaches nanoscale. Generating a potential difference directly across the nanobeams, an attractive electrostatic force can be induced between the two nanobeams [18]. As in the Euler-Bernoulli beam case, the spring stiffness can be varied between the nanobeams. The springs are considered to have stiffness, K_{cs} . The two nanobeams are different where the length, shear modulus, mass per unit length, and bending rigidity of the i th beam are L_i , G_i , $\rho_i A_i$, $\rho_i I_i$, and $E_i I_i$ ($i = 1, 2$), respectively. These parameters are assumed to be constant along each nanobeam.

The bending and shear displacements over the two nanobeams are denoted by $w_1(x, t)$, $\psi_1(x, t)$, and $w_2(x, t)$, $\psi_2(x, t)$, respectively. Based on Eqs.(9.38) and (9.39), the governing equations of motion for the wave propagation of Timoshenko double nanobeam system can be expressed as

$$GA_1\kappa \left(\frac{\partial^2 w_1}{\partial x^2} - \frac{\partial \psi_1}{\partial x} \right) + \rho A_1 \frac{\partial^2}{\partial t^2} \left(w_1 - (e_0 a)^2 \frac{\partial^2 w_1}{\partial x^2} \right) - q_1 + (e_0 a)^2 \frac{\partial^2 q_1}{\partial x^2} = 0 \quad (9.40)$$

$$GA_1\kappa \left(\frac{\partial w_1}{\partial x} - \psi_1 \right) + EI_1 \frac{\partial^2 \psi_1}{\partial x^2} - \rho I_1 \frac{\partial^2}{\partial t^2} \left(\psi_1 - (e_0 a)^2 \frac{\partial^2 \psi_1}{\partial x^2} \right) = 0 \quad (9.41)$$

$$GA_2\kappa \left(\frac{\partial^2 w_2}{\partial x^2} - \frac{\partial \psi_2}{\partial x} \right) + \rho A_2 \frac{\partial^2}{\partial t^2} \left(w_2 - (e_0 a)^2 \frac{\partial^2 w_2}{\partial x^2} \right) - q_2 + (e_0 a)^2 \frac{\partial^2 q_2}{\partial x^2} = 0 \quad (9.42)$$

$$GA_2\kappa \left(\frac{\partial w_2}{\partial x} - \psi_2 \right) + EI_2 \frac{\partial^2 \psi_2}{\partial x^2} - \rho I_2 \frac{\partial^2}{\partial t^2} \left(\psi_2 - (e_0 a)^2 \frac{\partial^2 \psi_2}{\partial x^2} \right) = 0 \quad (9.43)$$

In the above equations, the distributed forces on nanobeam-I and nanobeam-II are given as

$$q_1 = K_{cs} (w_2 - w_1) \quad (9.44)$$

$$q_2 = K_{cs} (w_1 - w_2) \quad (9.45)$$

substituting q_1 and q_2 in Eqs. (9.38) and (9.39) gives

$$GA_1\kappa \left(\frac{\partial^2 w_1}{\partial x^2} - \frac{\partial \psi_1}{\partial x} \right) + \rho A_1 \frac{\partial^2}{\partial t^2} \left(w_1 - (e_0 a)^2 \frac{\partial^2 w_1}{\partial x^2} \right) + K_{cs} (w_1 - w_2)$$

$$+ (e_0a)^2 K_{cs} \left(\frac{\partial^2 w_2}{\partial x^2} - \frac{\partial^2 w_1}{\partial x^2} \right) = 0 \quad (9.46)$$

$$GA_1 \kappa \left(\frac{\partial w_1}{\partial x} - \psi_1 \right) + EI_1 \frac{\partial^2 \psi_1}{\partial x^2} - \rho I_1 \frac{\partial^2}{\partial t^2} \left(\psi_1 - (e_0a)^2 \frac{\partial^2 \psi_1}{\partial x^2} \right) = 0 \quad (9.47)$$

$$GA_2 \kappa \left(\frac{\partial^2 w_2}{\partial x^2} - \frac{\partial \psi_2}{\partial x} \right) + \rho A_2 \frac{\partial^2}{\partial t^2} \left(w_2 - (e_0a)^2 \frac{\partial^2 w_2}{\partial x^2} \right) + K_{cs} (w_2 - w_1) \\ + (e_0a)^2 K_{cs} \left(\frac{\partial^2 w_1}{\partial x^2} - \frac{\partial^2 w_2}{\partial x^2} \right) = 0 \quad (9.48)$$

$$GA_2 \kappa \left(\frac{\partial w_2}{\partial x} - \psi_2 \right) + EI_2 \frac{\partial^2 \psi_2}{\partial x^2} - \rho I_2 \frac{\partial^2}{\partial t^2} \left(\psi_2 - (e_0a)^2 \frac{\partial^2 \psi_2}{\partial x^2} \right) = 0 \quad (9.49)$$

The above equations completely describe a nonlocal coupled Timoshenko nanobeam system.

For analyzing the ultrasonic wave dispersion characteristics in coupled Timoshenko nanobeam system, we will need to perform spectral analysis by transforming the field variables to frequency domain. That is,

$$w_1(x, t) = \sum_{m=0}^{M-1} \sum_{n=0}^{N-1} \hat{w}_1(x, \omega_n) e^{-j(k_m x - \omega_n t)} \quad (9.50)$$

$$\psi_1(x, t) = \sum_{m=0}^{M-1} \sum_{n=0}^{N-1} \hat{\psi}_1(x, \omega_n) e^{-j(k_m x - \omega_n t)} \quad (9.51)$$

$$w_2(x, t) = \sum_{m=0}^{M-1} \sum_{n=0}^{N-1} \hat{w}_2(x, \omega_n) e^{-j(k_m x - \omega_n t)} \quad (9.52)$$

$$\psi_2(x, t) = \sum_{m=0}^{M-1} \sum_{n=0}^{N-1} \hat{\psi}_2(x, \omega_n) e^{-j(k_m x - \omega_n t)} \quad (9.53)$$

Substituting Eqs. (9.50) and (9.53) into the governing partial differential Eqs. (9.46) and (9.49), we get the dispersion relation as follows. Hereafter the subscript m and n are dropped for simplified notations, leads to the following polynomial eigenvalue problem

$$\mathbf{Z}_2 k^2 + \mathbf{Z}_1 k + \mathbf{Z}_0 = 0 \quad (9.54)$$

where

$$\mathbf{Z}_2 = \begin{bmatrix} -GA_1\kappa + (-K_{cs} + \rho A_1\omega^2)(e_0a)^2 & 0 \\ 0 & -EI_1 + \rho I_1(e_0a)^2\omega^2 \\ -K_{cs}(e_0a)^2 & 0 \\ 0 & 0 \\ K_{cs}(e_0a)^2 & 0 \\ 0 & 0 \\ -GA_2\kappa + (K_{cs} + \rho A_2\omega^2)(e_0a)^2 & 0 \\ 0 & -EI_2 + \rho I_2(e_0a)^2\omega^2 \end{bmatrix} \quad (9.55)$$

$$\mathbf{Z}_1 = \begin{bmatrix} 0 & iGA_1\kappa & 0 & 0 \\ -iGA_1\kappa & 0 & 0 & 0 \\ 0 & 0 & 0 & iGA_2\kappa \\ 0 & 0 & -iGA_2\kappa & 0 \end{bmatrix} \quad (9.56)$$

$$\mathbf{Z}_0 = \begin{bmatrix} K_{cs} + \rho A_1\omega^2 & 0 & -K_{cs} & 0 \\ 0 & -GA_1\kappa + \rho I_1\omega^2 & 0 & 0 \\ -K_{cs} & 0 & K_{cs} + \rho A_2\omega^2 & 0 \\ 0 & 0 & 0 & -GA_2\kappa + \rho I_2\omega^2 \end{bmatrix} \quad (9.57)$$

This dispersion relation, which is in the form of PEP (Eq. 9.54) is solved for wavenumbers, which is a function of material properties of the CNTs and the nonlocal parameter (e_0a). For a coupled nanobeam system, the nonlocal Timoshenko beam model gives four cut-off frequencies and four escape frequencies in wave dispersion analysis. These cut-off frequencies are obtained by substituting $k = 0$ in the dispersion relation (Eq. 9.54) or by solving $|\mathbf{Z}_0(\omega)| = 0$, which gives four cut-off frequencies as

$$\omega_{c1} = 0, \quad \omega_{c2} = \sqrt{\frac{GA_1\kappa}{\rho I_1}}, \quad \omega_{c3} = \sqrt{\frac{GA_2\kappa}{\rho I_2}}, \quad \omega_{c4} = \sqrt{\frac{K_{cs}}{\rho}} \sqrt{\frac{1}{A_1} + \frac{1}{A_2}} \quad (9.58)$$

One can observe that these cut-off frequencies are independent of the nonlocal scaling parameter (e_0a). The escape (or asymptotic) frequencies are obtained by substituting $k \rightarrow \infty$ in the dispersion relation (Eq. 9.54), that implies $|\mathbf{Z}_2(\omega)| = 0$, which gives

$$\omega_{e1, e2} = \frac{1}{e_0a} \sqrt{\frac{E}{\rho}}, \quad \omega_{e3, e4} = \frac{G\kappa \sqrt{2A_1A_2}}{e_0a} \quad (9.59)$$

These escape frequencies are function of the material properties of CNTs and are inversely proportional to the nonlocal scaling parameter.

Differentiating the dispersion relation of DNBS (Eq. 9.54) with respect to the wave frequency (ω), we get the PEP for group speeds as

$$\left[k^2 \frac{\partial \mathbf{Z}_2}{\partial \omega} + \frac{\partial \mathbf{Z}_0}{\partial \omega} \right] C_g + 2k \mathbf{Z}_2 + \mathbf{Z}_1 = 0 \tag{9.60}$$

where $C_g = (d\omega/dk)$ is the group speed of a wave in DNBS and the matrices \mathbf{Z}_2 , \mathbf{Z}_1 and \mathbf{Z}_0 are given in Eqs. (9.55)–(9.57).

The spectrum and dispersion plots for coupled double Timoshenko nanobeam system are shown in Figs. 9.10–9.12. In the case of Timoshenko beam, most of the observations made for the SWCNT in Chap. 7 are still valid, that is, scale parameter introduces the escape frequency where the wavenumber k tends to infinite and the group/phase speed tends to zero and the values of the escape frequencies decreases with the increase in scale parameter.

Figure 9.10 shows the variation of the wavenumbers with the wave frequency for both local (or classical) and nonlocal elasticity. This figure shows only two modes namely, flexural and shear for both the nanobeams. Flexural wave mode starts from zero wave frequency and shear wave mode propagates only after shear cut-off frequency, the frequency at which the imaginary part of wavenumber becomes real. The values of the shear cut-off frequency are calculated from Eq. (9.58). It can be observed from Eq. (9.58) that these frequencies are independent of the nonlocal

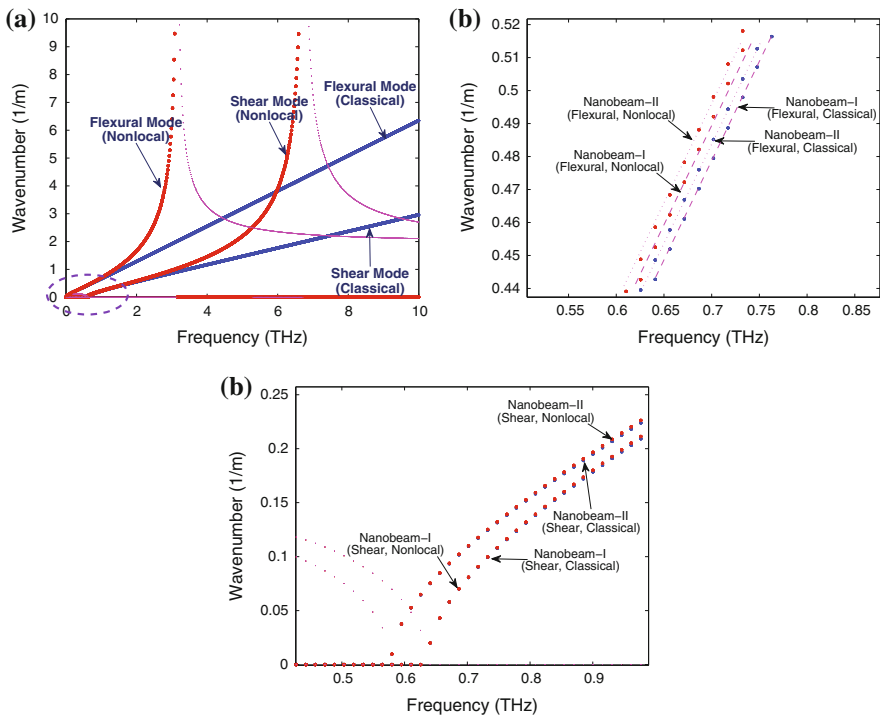
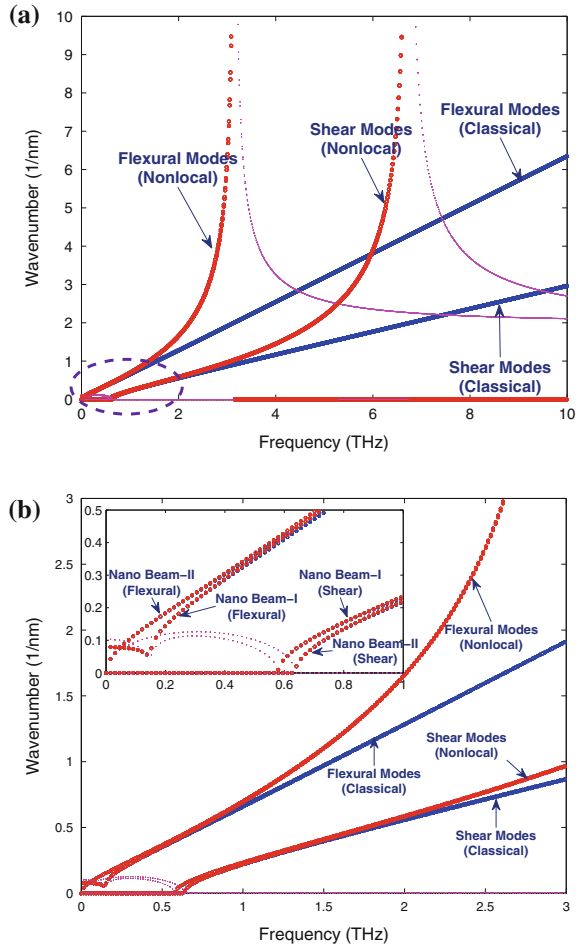


Fig. 9.10 Wavenumber dispersion with wave frequency for a coupled Timoshenko nanobeam system obtained from local and nonlocal elasticity theories for coupled spring stiffness of $K_{cs} = 0$ N/nm

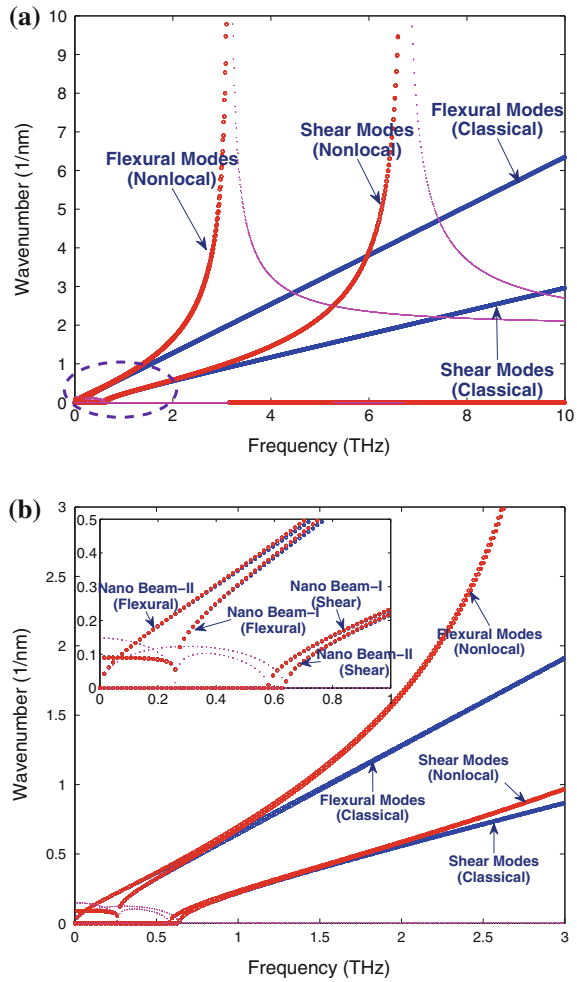
Fig. 9.11 Wavenumber dispersion with wave frequency for a coupled Timoshenko nanobeam system obtained from local and non-local elasticity theories for coupled spring stiffness of $K_{cs} = 8 \text{ N/nm}$



scaling parameter, and hence same frequencies are obtained from both local and nonlocal theories for all the cases (see Figs.9.10–9.12). It can also be noted that the shear cut-off frequency of nanobeam-I is higher than that of the nanobeam-II. However, with the introduction of nonlocal scale effects, the wave behavior is altered drastically. Both the flexural and shear wave modes escape to infinity at a particular frequency called the escape frequency, beyond this frequency there is no wave propagation. The value of escape frequency decreases with increase in the scale parameter e_0a , for both wave modes. Equation (9.59) gives the expression for escape frequencies in coupled nanobeams. From this expression it is clear that, escape frequencies are purely function of nonlocal scale parameter.

Due to the coupling effect, it has been observed that a new cut-off frequency in the flexural wave mode of nanobeam-I (see Figs.9.11 and 9.12) can be seen. It is

Fig. 9.12 Wavenumber dispersion with wave frequency for a coupled Timoshenko nanobeam system obtained from local and non-local elasticity theories for coupled spring stiffness of $K_{cs} = 25 \text{ N/nm}$



clear that the cut-off frequency of the flexural mode of nanobeam-I depends on the coupled spring stiffness (see Eq. 9.58, where, ω_{c_4} is the cut-off frequency of flexural mode of nanobeam-I). Escape frequencies of all the wavemodes remain constant. As the magnitude of coupled spring stiffness increases, the flexural wave mode cut-off frequency of nanobeam-I increases and all other variable is constant (refer Fig. 9.12).

The wave speed variation with frequency is plotted in Figs. 9.13a–c and 9.14a–c. The observations in these plots directly depend on the discussions of the previous section. For all the wave modes, due to nonlocality, wave speeds are tending to zero at escape frequencies. As the magnitude of the coupled spring increases, the cut-off frequency of the flexural mode of nanobeam-I increases. The effect of the coupled spring stiffness on cut-off frequencies is plotted in Fig. 9.15. This figure shows that,

Fig. 9.13 Phase speed dispersion with in a coupled Timoshenko nanobeam system **a** $K_{CS} = 0$ N/nm
b $K_{CS} = 8$ N/nm
c $K_{CS} = 25$ N/nm

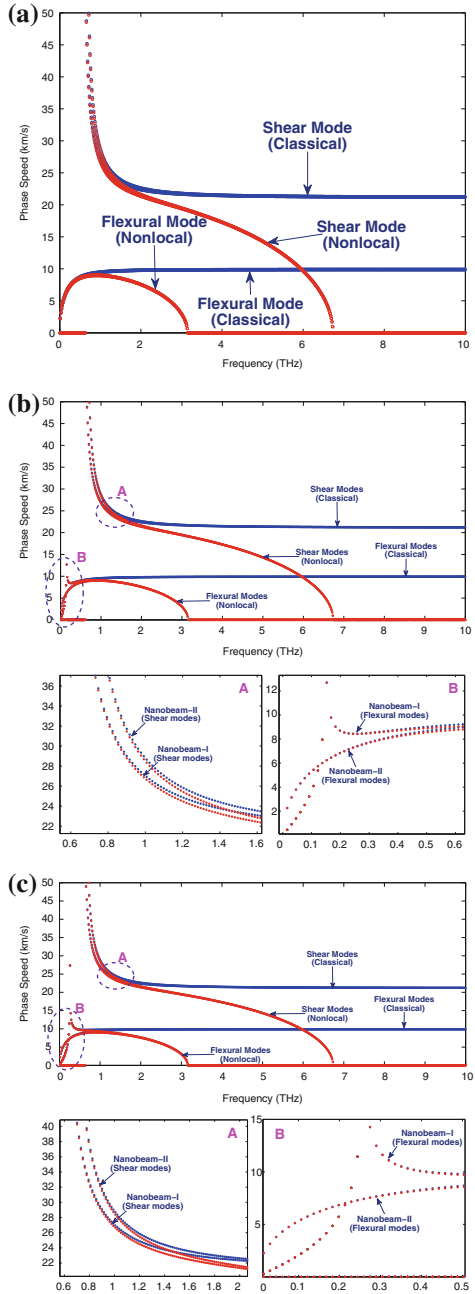
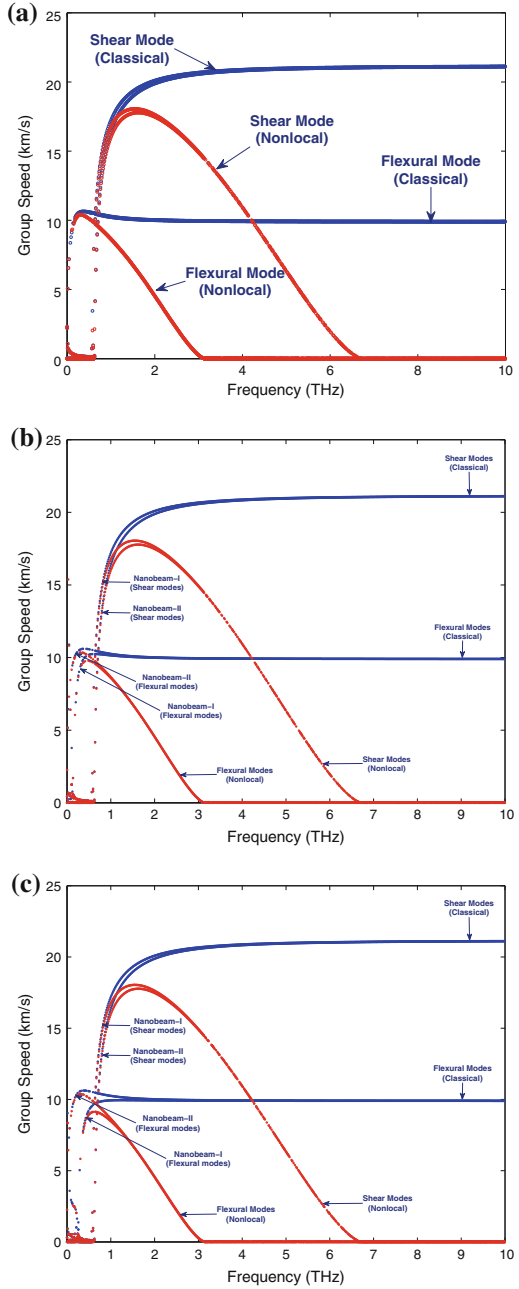


Fig. 9.14 Group speed dispersion with in a coupled Timoshenko nanobeam system **a** $K_{CS} = 0$ N/nm
b $K_{CS} = 8$ N/nm
c $K_{CS} = 25$ N/nm



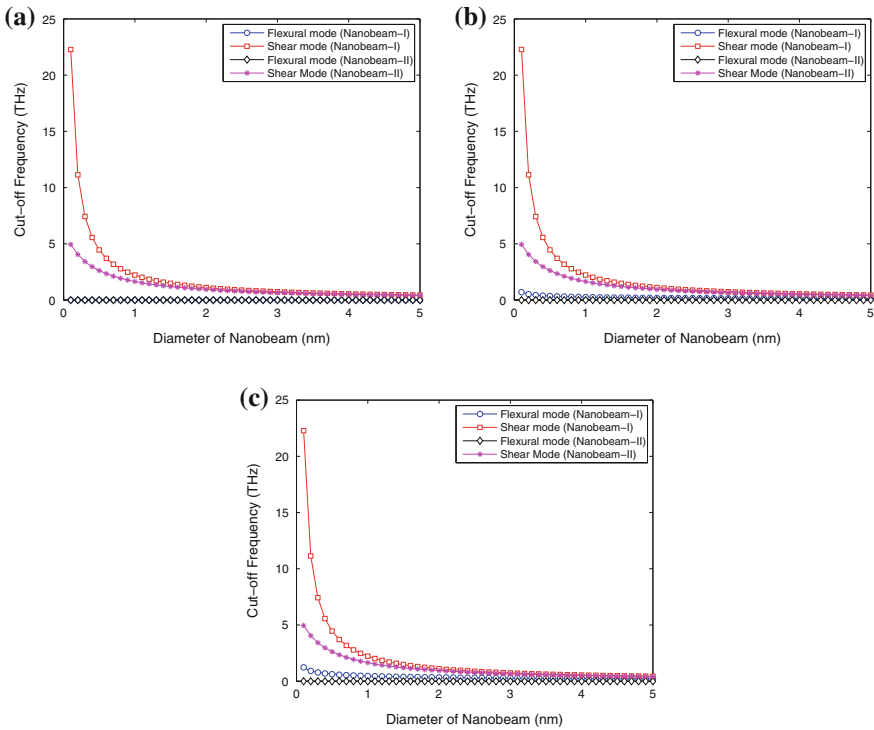
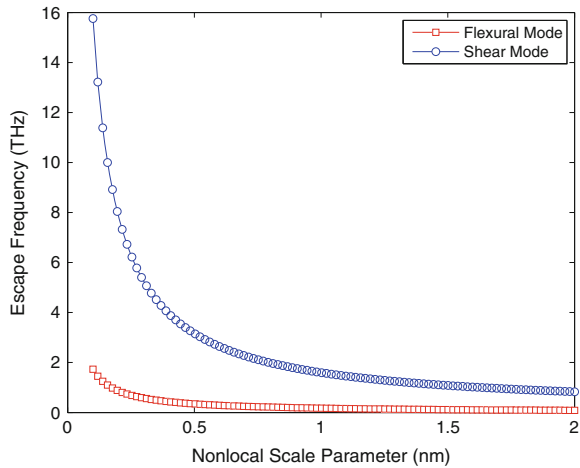


Fig. 9.15 Cut-off frequency variation with various diameters in a coupled Timoshenko nanobeam system **a** $K_{CS} = 0$ N/nm **b** $K_{CS} = 8$ N/nm **c** $K_{CS} = 25$ N/nm

as the diameter of the nanobeam increases, the shear cut-off frequency increases and at small values of diameter, the shear cut-off frequency approaches to very small values (Fig. 9.15a). Hence, it can be concluded that for large values of scale parameter, shear deformation on the beam has negligible effect and beam behaves like more like elementary beam. With the consideration of the coupled spring stiffness, one more cut-off frequency variation is observed in Fig. 9.15b. This cut-off frequency is for flexural wavemode of nanobeam-I. As the value of the spring stiffness increases, the magnitude of this cut-off frequency increases.

Finally, Fig. 9.16 shows the variation of escape frequencies of flexural and shear wave modes with the nonlocal scaling parameter. It shows that as e_0a increases, the escape frequency decreases. At higher values of e_0a , escape frequencies approach to very small values.

Fig. 9.16 Variation of escape frequency of flexural and shear wave modes with the nonlocal scale parameter



9.3 Summary

The present chapter deals with axial, flexural, and shear wave propagation in double nanorod/nanobeam system with consideration of small scale properties. The nonlocal elasticity theory has been incorporated into classical rod/Euler-Bernoulli beam/Timoshenko beam model to capture unique features of the double nanorods or nanobeams. The strong effect of the nonlocal scale has been obtained, which leads to substantially different wave behaviors of nanorods/nanobeams from those of macroscopic rods. The analysis shows that the wave characteristics are highly over estimated by the classical rod/beam model, which ignores the effect of small-length scale. The studies also show that the nonlocal scale parameter introduces certain band gap region in axial/flexural/shear wave modes where no wave propagation occurs. This is manifested in the spectrum curves as the region where the wavenumber tends to infinite or wave speed tends to zero. The effect of the coupled spring stiffness on the wave propagation behavior is well captured in the present analysis. It has been also shown that the cut-off frequency increases as the stiffness of the coupled spring increases and the spring stiffness has no effect on escape frequency of the axial/flexural/shear wave mode. The present study may bring in helpful insights while investigating multiple-nanorod/nanobeam system models for future nano-optomechanical systems (NOMS) applications.

References

1. T. Murmu, S. Adhikari, Nonlocal effects in the longitudinal vibration of double-nanorod systems. *Physica E* **43**(1), 415422 (2010)

2. X. Zhang, P. Sharma, Size dependency of strain in arbitrary shaped anisotropic embedded quantum dots due to nonlocal dispersive effects. *Phys. Rev. B* **72**, 195345 (2005)
3. S. Gopalakrishnan, A. Chakraborty, D. Roy Mahapatra, *Spectral Finite Elem. Method* (Springer-Verlag Landon Ltd., Verlag Landon, 2008)
4. J.P. Lu, Elastic properties of carbon nanotubes and nanoropes. *Phys. Rev. Lett.* **79**(7), 1297–1300 (1997)
5. H.V. Vu, A.M. Ordonez, B.H. Karnopp, Vibration of a double-beam system. *J. Sound Vib.* **229**, 807–822 (2000)
6. H. Erol, M. Gurgoz, Longitudinal vibrations of a double-rod system coupled by springs and dampers. *J. Sound Vib.* **276**, 419–430 (2004)
7. Z. Oniszczuk, Free transverse vibrations of elastically connected simply supported double-beams complex system. *J. Sound Vib.* **232**, 387–403 (2000)
8. A. Oniszczuk, Transverse vibrations of elastically connected double-string complex system—part I: free vibrations. *J. Sound Vib.* **232**, 355–366 (2000)
9. Z. Oniszczuk, Transverse vibrations of elastically connected double-string complex system—part II: forced vibrations. *J. Sound Vib.* **232**, 367–386 (2000)
10. M.A. Hilal, Dynamic response of a double EulerBernoulli beam due to a moving constant load. *J. Sound Vib.* **297**, 477–491 (2006)
11. T.R. Hamada, H. Nakayama, K. Hayashi, Free and forced vibration of elastically connected double-beam systems. *Bull. J. Soc. Mech. Eng.* **26**, 1936–1942 (1983)
12. M. Gurgoz, H. Erol, On laterally vibrating beams carrying tip masses, coupled by several double springmass systems. *J. Sound Vib.* **269**, 431–438 (2004)
13. Y.Q. Zhang, Y. Lu, G.W. Ma, Effect of compressive axial load on forced transverse vibrations of a double-beam system. *Int. J. Mech. Sci.* **50**, 299–305 (2008)
14. Y.Q. Zhang, Y. Lu, S.L. Wang, X. Liu, Vibration and buckling of a doublebeam system under compressive axial loading. *J. Sound Vib.* **318**, 341–352 (2008)
15. S.G. Kelly, S. Srinivas, Free vibrations of elastically connected stretched beams. *J. Sound Vib.* **326**, 883–893 (2009)
16. M.A.D. Rosa, M. Lippiello, Non-classical boundary conditions and DQM for double-beams. *Mech. Res. Commun.* **34**, 538–544 (2007)
17. J. Li, H. Hua, Spectral finite element analysis of elastically connected doublebeam systems. *Finite Elem. Anal. Des.* **43**, 1155–1168 (2007)
18. I.W. Frank, P.B. Deotare, M.W. McCutcheon, M. Loncar, Programmable photonic crystal nanobeam cavities. *Opt. Express* **18**, 8705–8712 (2010)
19. M. Eichenfield, R. Camacho, J. Chan, K.J. Vahala, O. Painter, A picogramand nanometre-scale photonic-crystal optomechanical cavity. *Nature* **459**, 550–555 (2009)
20. P.B. Deotare, M.W. Mc Cutcheon, I.W. Frank, M. Khan, M. Loncar, Coupled photonic crystal nanobeam cavities. *Appl. Phys. Lett.* **95**, 031102 (2009)
21. Q. Lin, J. Rosenberg, D. Chang, R. Camacho, M. Eichenfield, K.J. Vahala, O. Painter, Coherent mixing of mechanical excitations in nano-optomechanical structures. *Nat. Photonics* **4**, 236–242 (2010)
22. J.A. Ruud, T.R. Jervis, F. Spaepan, Nanoindentation of Ag/Ni multilayered thin films. *J. Appl. Phys.* **75**, 4969–4974 (1994)
23. T.G. Sorop, L.J. Jongh, Size-dependent anisotropic diamagnetic screening in super conducting Sn nanowires. *Phys. Rev. B* **75**, 014510 (2007)
24. J.A. Juhasz, S.M. Best, R. Brooks, M. Kawashita, N. Miyata, T. Kokubo, T. Nakamura, W. Bonfield, Mechanical properties of glass-ceramic AeW-polyethylene composites: effect of filler content and particle size. *Biomaterials* **25**, 949–955 (2004)
25. A. Kasuya, Y. Sasaki, Y. Saito, K. Tohji, Y. Nishina, Evidence for sizedependent discrete dispersions in single-wall nanotubes. *Phys. Rev. Lett.* **78**, 4434–4437 (1997)
26. R. Chowdhury, S. Adhikari, C.W. Wang, F. Scarpa, A molecular mechanics approach for the vibration of single walled carbon nanotubes. *Comput. Mater. Sci.* **48**, 730–735 (2010)
27. T. Murmu, S. Adhikari, Nonlocal effects in the longitudinal vibration of double-nanorod systems. *Physica E* **43**, 415–422 (2010)

28. T. Murmu, S. Adhikari, Nonlocal transverse vibration of double-nanobeamsystems. *J. Appl. Phys.* **108**, 083514 (2010)
29. S. Narendar, S. Gopalakrishnan, Axial wave propagation in coupled nanorod system with nonlocal small scale effects, *Compos.: Part B Eng.* **42**, 2013–2023 (2011)

Chapter 10

Wave Propagation in 2D-Nanostructures

The discovery of a new material brings with it some of the most exciting and fruitful periods of scientific and technological research. With a new material come new opportunities to reexamine old problems as well as pose new ones. The discovery of graphene, atomically thin layers of graphite, brought such a period [1]. Graphenes are 2-D nanostructures and as the name suggest, these structures, unlike CNTs, exhibit behavior in the two coordinate directions. That is, a load in the direction of one of the coordinates will give rise to deformations in both the coordinate directions. In wave propagation terminology, an incident wave in one of the coordinate directions will cause circularly crested waves that can be resolved in two coordinate directions. This means, we will have two different wavenumbers corresponding to two coordinate directions and the corresponding phase or group speeds.

Although the existence of graphene in different forms was known, there was difficulty in extracting its pristine form. For the first time, it was possible to isolate single two-dimensional atomic layers of atoms [1]. These are among the thinnest objects imaginable. The strongest bond in nature, the C–C bond covalently locks these atoms in place giving them remarkable mechanical properties. A single layer of graphene is one of the stiffest known materials characterized by a remarkably high Young's modulus of ~ 1 TPa [2]. Graphene is a new class of two-dimensional carbon nanostructure, which holds great promise for the vast applications in many technological fields. After graphene sheets are reported to be successfully extracted from graphite, the researchers have realized the volume of potential applications. It would be one of the prominent new materials for the next generation nanoelectronic devices. Reports related to its applications as strain sensor, mass and pressure sensors, atomic dust detectors, and enhancer of surface image resolution are observed. In addition, graphene structures find application such as atomic-force microscopes, composite nanofibers, nanobearings, and nanoactuators, etc. Consequently, interest is drawn toward research of graphene in the field of physics, material science, and engineering [3]. Therefore, the importance of these structures is realized, and both theoretical and experimental works are carried out by various researchers all over the world. With the difficulty for the controlled experiments at the nanometer scale, the

numerical simulation has been performed widely to understand the behavior of these structures. In this chapter, we will use continuum modeling using nonlocal elasticity to model these 2-D nanostructures to understand the wave propagation behavior in these structures.

In contrast to the investigations on CNTs, it is surprising to find that very few studies have been reported on the theoretical modeling of graphene structures (GS) in the literature. Recently, Behfar and Naghdabadi [4] investigated the nanoscale vibration of a multilayered graphene sheet embedded in an elastic medium, in which the natural frequencies as well as the associated modes were determined using a continuum-based model. The influence of carbon-carbon and carbon-polymer van-der-Waals forces are considered in their work. They [5] further studied the bending modulus of a MLGS using a geometrically based analytical approach. The bending energy in their analysis is based on the vdW interactions of atoms belonging to two neighboring sheets. Their calculations are performed for a double-layered GS, but the derived bending modulus is generalized to a MLGS composed of many double-layered GSs along its thickness, in which the double-layered GSs are alternately the same in configuration. In addition, it should be mentioned that graphite is composed of multilayered sheets, but it was recently reported [6] that single-layered sheet are detectable in carbon nanofilms. Sakhaee et al. [7], have studied the free vibrational behavior of the single layered graphene sheets (SLGS) while considering the effects of chirality and aspect ratio as well as boundary conditions, and have developed predictive models for computing natural frequencies. The potential applications of the SLGSs as mass sensors and atomistic dust detectors have further been investigated [8]. Also, the promising usage of the SLGS as strain sensor has been examined [9]. The importance of size effects and need for nonlocal theories need not be elaborated or emphasized again here and it is implicit that these effects are again important in the context of modeling 2-D nanostructures.

Most of the studies on vibration and buckling of nanoplates are carried out on single-layered graphene sheets (SLGS) and multilayered graphene sheets (MLGS). Some vibration studies on graphene nanosheets are reported recently [10, 11]. However, studies on wave propagation aspect of graphene sheets are minuscule in numbers. GSs can have interesting waveguide properties at very high frequencies in the order of Tera-Hertz (THz). At such high frequencies, continuum model-based finite element type methods cannot be adopted due to their limitation of the element size with respect to the wavelength, which is very small at such frequencies.

In this chapter, the first paper suggesting shell-model for nanotubes [12] is cited here. Yakobson et al. [12] demonstrated that elastic shell theory matches molecular dynamics (MD) simulations if the elastic constants are chosen such that $E = 5.5$ TPa, $\nu = 0.19$, and $t = 0.066$ nm, where E is Young's modulus, ν is the Poisson ratio, and t is the shell thickness. This chapter mainly focus on the flexural wave properties of the graphene sheet using the nonlocal scale effects.

10.1 Flexural Wave Propagation in Monolayer Graphene Sheets

Wave propagation in graphene sheets has been a topic of great interest in nanomechanics, where the equivalent continuum models are widely used. In this section, we will examine this issue by incorporating the nonlocal theory into the classical plate theory model.

10.1.1 Governing Equations for Graphene Structures

Figure 10.1a shows a rectangular graphene sheet and Fig. 10.1b shows its equivalent continuum model. Liew et al. [11] considered graphene as isotropic material in their continuum model. Here, such continuum plate model is assumed. The coordinate system used for the graphene sheet is shown in the same figure. Here, z coordinate is taken along the thickness of the plate. The displacement field according to classical plate theory (CLPT) can be written as

$$u_1(x, y, z, t) = u(x, y, t) - z \frac{\partial w(x, y, t)}{\partial x} \quad (10.1)$$

$$u_2(x, y, z, t) = v(x, y, t) - z \frac{\partial w(x, y, t)}{\partial y} \quad (10.2)$$

$$u_3(x, y, z, t) = w(x, y, t) \quad (10.3)$$

Here u , v and w denote displacement along x , y and z directions, respectively (see Fig. 10.1).

The strains can be calculated as

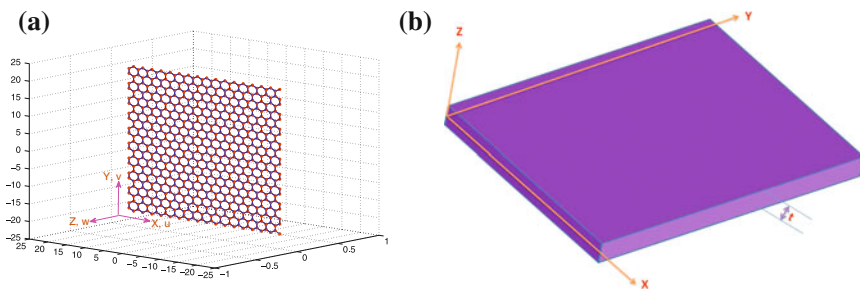


Fig. 10.1 Single-layered graphene sheet: **a** Discrete model (a monolayer graphene of $40 \text{ \AA} \times 40 \text{ \AA}$, consists of 680 carbon atoms arranged in hexagonal array). **b** Equivalent continuum model

$$\varepsilon_{xx} = \frac{\partial u_1}{\partial x} = \frac{\partial u}{\partial x} - z \frac{\partial^2 w}{\partial x^2} \quad (10.4)$$

$$\varepsilon_{yy} = \frac{\partial u_2}{\partial y} = \frac{\partial v}{\partial y} - z \frac{\partial^2 w}{\partial y^2} \quad (10.5)$$

$$\gamma_{xy} = \frac{\partial u_1}{\partial y} + \frac{\partial u_2}{\partial x} = \frac{\partial u}{\partial y} + \frac{\partial v}{\partial x} - 2z \frac{\partial^2 w}{\partial x \partial y} \quad (10.6)$$

$$\varepsilon_{zz} = 0, \quad \gamma_{xz} = 0, \quad \gamma_{yz} = 0 \quad (10.7)$$

It can be noted that nonlocal behavior enters through the constitutive relations. Principle of virtual work is independent of constitutive relations. Hence, this can be applied to derive the equilibrium equations of the nonlocal plates.

Using this principle, following equilibrium equation expressed in terms of stress resultants and transverse displacement $w(x, y, t)$ can be obtained as [13]

$$\frac{\partial^2 M_{xx}}{\partial x^2} + 2 \frac{\partial^2 M_{xy}}{\partial x \partial y} + \frac{\partial^2 M_{yy}}{\partial y^2} = J_0 \frac{\partial^2 w}{\partial t^2} - J_2 \left(\frac{\partial^4 w}{\partial x^2 \partial t^2} + \frac{\partial^4 w}{\partial y^2 \partial t^2} \right) \quad (10.8)$$

where J_0 and J_2 are mass moments of inertia and are defined as follows

$$J_0 = \int_{-\frac{h}{2}}^{+\frac{h}{2}} \rho z dz, \quad (10.9)$$

$$J_2 = \int_{-\frac{h}{2}}^{+\frac{h}{2}} \rho z^2 dz \quad (10.10)$$

Here h denotes the thickness of the plate and the moment resultants are given by

$$M_{xx} = \int_{-\frac{t}{2}}^{+\frac{t}{2}} z \sigma_{xx} dz \quad (10.11)$$

$$M_{xy} = \int_{-\frac{t}{2}}^{+\frac{t}{2}} z \tau_{xy} dz \quad (10.12)$$

$$M_{yy} = \int_{-\frac{t}{2}}^{+\frac{t}{2}} z \sigma_{yy} dz \quad (10.13)$$

The plane stress constitutive relation of a nonlocal plate becomes

$$\begin{Bmatrix} \sigma_{xx} \\ \sigma_{yy} \\ \tau_{xy} \end{Bmatrix} - (e_0 a)^2 \left[\frac{\partial^2}{\partial x^2} + \frac{\partial^2}{\partial y^2} \right] \begin{Bmatrix} \sigma_{xx} \\ \sigma_{yy} \\ \tau_{xy} \end{Bmatrix} = \begin{bmatrix} C_{11} & C_{12} & 0 \\ C_{21} & C_{22} & 0 \\ 0 & 0 & C_{66} \end{bmatrix} \begin{Bmatrix} \varepsilon_{xx} \\ \varepsilon_{yy} \\ \gamma_{xy} \end{Bmatrix} \quad (10.14)$$

where, σ_{xx} and σ_{yy} are the normal stresses in x and y directions respectively and τ_{xy} is the in-plane shear stress. For the case of an isotropic plate, the expressions for C_{ij}

in terms of Young's modulus E and Poisson's ratio ν are given as $C_{11} = C_{22} = \frac{E}{1-\nu^2}$, $C_{12} = C_{21} = \frac{\nu E}{1-\nu^2}$ and $C_{66} = \frac{E}{2(1+\nu)}$.

Using strain displacement relationship Eq. (10.7), stress-strain relationship Eq. (10.14) and stress resultants definition Eq. (10.13), we can express stress resultants in terms of displacements as follows

$$M_{xx} - (e_0a)^2 \left(\frac{\partial^2 M_{xx}}{\partial x^2} + \frac{\partial^2 M_{xx}}{\partial y^2} \right) = -C_{11}I_2 \frac{\partial^2 w}{\partial x^2} - C_{12}I_2 \frac{\partial^2 w}{\partial y^2} \quad (10.15)$$

$$M_{xy} - (e_0a)^2 \left(\frac{\partial^2 M_{xy}}{\partial x^2} + \frac{\partial^2 M_{xy}}{\partial y^2} \right) = -2C_{66}I_2 \frac{\partial^2 w}{\partial x \partial y} \quad (10.16)$$

$$M_{yy} - (e_0a)^2 \left(\frac{\partial^2 M_{yy}}{\partial x^2} + \frac{\partial^2 M_{yy}}{\partial y^2} \right) = -C_{21}I_2 \frac{\partial^2 w}{\partial x^2} - C_{22}I_2 \frac{\partial^2 w}{\partial y^2} \quad (10.17)$$

where

$$I_2 = \int_{-\frac{t}{2}}^{+\frac{t}{2}} z^2 dz \quad (10.18)$$

Using Eqs. (10.8) and (10.15–10.17) we get the following nonlocal governing partial differential equation in terms of flexural displacement w

$$\begin{aligned} & C_{11}I_2 \frac{\partial^4 w}{\partial x^4} + 2(C_{12} + 2C_{66})I_2 \frac{\partial^4 w}{\partial x^2 \partial y^2} + C_{22}I_2 \frac{\partial^4 w}{\partial y^4} - J_0(e_0a)^2 \left(\frac{\partial^4 w}{\partial x^2 \partial t^2} + \frac{\partial^4 w}{\partial y^2 \partial t^2} \right) \\ & + J_2(e_0a)^2 \left(\frac{\partial^6 w}{\partial x^4 \partial t^2} + 2 \frac{\partial^6 w}{\partial x^2 \partial y^2 \partial t^2} + \frac{\partial^6 w}{\partial y^4 \partial t^2} \right) + J_0 \frac{\partial^2 w}{\partial t^2} - J_2 \left(\frac{\partial^4 w}{\partial x^2 \partial t^2} + \frac{\partial^4 w}{\partial y^2 \partial t^2} \right) = 0 \end{aligned} \quad (10.19)$$

It can be seen that corresponding local elasticity equation [13] can be recovered by putting $e_0a = 0$ in the above equation.

10.1.2 Wave Dispersion Analysis

The wave dispersion formulation begins by assuming a solution of the displacement field. In particular, time harmonic waves are sought, and it is assumed that the model is unbounded in Y -direction (although bounded in X -direction). Thus, the assumed form is a combination of Fourier transform in Y -direction and Fourier transform in time, which is written as

$$w(x, y, t) = \sum_{n=1}^N \sum_{m=1}^M \hat{w}(x) e^{-j\eta_m y} e^{j\omega_n t}, \quad (10.20)$$

The ω_n and the η_m are the circular frequency at n^{th} sampling point and the wavenumber in y -direction at the m^{th} sampling point, respectively. The N is the index corresponding to the Nyquist frequency in fast Fourier transform (FFT), which is used for computer implementation of the Fourier transform and $j = \sqrt{-1}$.

Substituting Eq. (10.20) in Eq. (10.19), an ordinary differential equation is obtained for the unknown $\hat{w}(x)$ as

$$H_4 \frac{d^4 \hat{w}}{dx^4} + H_2 \frac{d^2 \hat{w}}{dx^2} + H_0 \hat{w} = 0 \quad (10.21)$$

where

$$H_4 = C_{11} I_2 - J_2 (e_0 a)^2 \omega_n^2, \quad (10.22)$$

$$H_2 = -2(C_{12} + 2C_{66}) I_2 \eta_m^2 + J_0 (e_0 a)^2 \omega_n^2 - 2J_2 (e_0 a)^2 \eta_m^2 \omega_n^2 + J_2 \omega_n^2, \quad (10.23)$$

$$H_0 = C_{22} I_2 \eta_m^2 - J_0 (e_0 a)^2 \omega_n^2 \eta_m^2 - J_2 (e_0 a)^2 \omega_n^2 \eta_m^2 - J_0 \omega_n^2 - J_2 \omega_n^2 \eta_m^2. \quad (10.24)$$

Since this ODE is having constant coefficients, its solution can be written as $\hat{w}(x) = \tilde{w} e^{jkx}$, where k is the wavenumber in x -direction, yet to be determined and \tilde{w} is an unknown constant. Substituting this assumed form of \hat{w} in the ODE gives for $\tilde{w} \neq 0$

$$H_4 k^4 + H_2 k^2 + H_0 = 0 \quad (10.25)$$

which is a quadratic equation in k and can be solved for wavenumbers as

$$k = \pm \sqrt{\frac{-H_2 \pm \sqrt{H_2^2 - 4H_4 H_0}}{2H_4}} \quad (10.26)$$

We can see clearly that the dependence of nonlocal scale parameter $e_0 a$ on wavenumber. The group speed of the flexural wave ($C_g = d\omega/dk$) is obtained as

$$C_g = -\frac{4H_4 k^3 + 2H_2 k}{G_4 k^4 + G_2 k^2 + G_0} \quad (10.27)$$

where

$$G_4 = -2J_2 (e_0 a)^2 \omega_n, \quad (10.28)$$

$$G_2 = 2J_0 (e_0 a)^2 \omega_n - 4J_2 (e_0 a)^2 \eta_m^2 \omega_n + 2J_2 \omega_n, \quad (10.29)$$

$$G_0 = -2J_0 (e_0 a)^2 \omega_n \eta_m^2 - 2J_2 (e_0 a)^2 \omega_n \eta_m^2 - 2J_0 \omega_n - 2J_2 \omega_n \eta_m^2. \quad (10.30)$$

The group speed of the wave is also a function of the nonlocal scaling parameter and the y -directional wavenumber.

In the spectrum relations curve, the frequency at which the imaginary part of wavenumber becomes real is called as cut-off frequency. Looking at Eq. (10.26), the term H_0 indicates the possibility of a waveguide having cut-off frequencies. This is obtained by setting $k = 0$ in the dispersion relation Eq. (10.25), i.e., for the present case one can set $H_0 = 0$, which gives the cut-off frequency expression as

$$\omega_c^{flexural} = \sqrt{\frac{C_{22}I_2\eta_m^4}{(J_0 + J_2\eta_m^2)(1 + (e_0a)^2\eta_m^2)}} \quad (10.31)$$

The cut-off frequency is directly proportional to the y -directional wavenumber (η_m) and also depends on the nonlocal scaling parameter. For $\eta_m = 0$, the wavenumbers of the flexural wave mode have a substantial real part starting from the zero frequency, which implies that the mode starts propagating at any excitation frequency and does not have a cut-off frequency. For $\eta_m \neq 0$, the flexural wave mode, however, has a certain frequency band within which the corresponding wavenumbers are purely imaginary. Thus, the wave mode does not propagate at frequencies lying within this band. These wavenumbers have a substantial imaginary part along with the real part, thus these waves attenuate as they propagate.

In this case, the term H_4 in Eq. (10.26) indicates the possibility of a waveguide having escape frequencies. Its value can be analytically determined by looking at the wavenumber expression and setting $k \rightarrow \infty$. This accounts to setting the $H_4 = 0$, which gives

$$\omega_e^{flexural} = \frac{1}{e_0a} \sqrt{\frac{C_{11}I_2}{J_2}} \quad (10.32)$$

where ω_e is called escape frequency of the flexural mode.

Next, we will investigate the relations derived above and investigate the wave behavior in the monolayer graphene sheet. For the present wave propagation analysis, the material properties of the graphene are assumed as: Young's modulus $E = 1.06$ TPa and density $\rho = 2300$ kg/m³. The choice of effective wall thickness t of nanostructures such as CNT, graphene, etc., is a longstanding issue in nanomechanics. One of the best approaches to estimate the thickness of CNT (i.e., rolled graphene sheet) is to model single-wall CNTs as linear elastic thin shells [14]. The shell thickness t is determined by fitting the atomistic simulation results of tensile rigidity and bending rigidity of single-wall CNTs. Such an approach gives the CNT thickness t much smaller than the graphite inter-layer spacing 0.34 nm, ranging from 0.06 to 0.09 nm. The scattered CNT thickness 0.06 – 0.09 nm depends on the interatomic potential as well as simulation details. We have chosen the thickness of the graphene as $t = 0.089$ nm, obtained by Kudin et al. [14] via *Ab initio* computations. They defined the effective thickness of graphene or CNTs as $t = \sqrt{\frac{12 \times \text{Bending Rigidity}}{\text{Tension Rigidity}}}$.

The flexural wavenumber dispersion with wave frequency in the graphene is shown in Figs. 10.2a, b, respectively, obtained from both local and nonlocal elasticity theories. For the present analysis, the nonlocal scaling parameter is assumed as

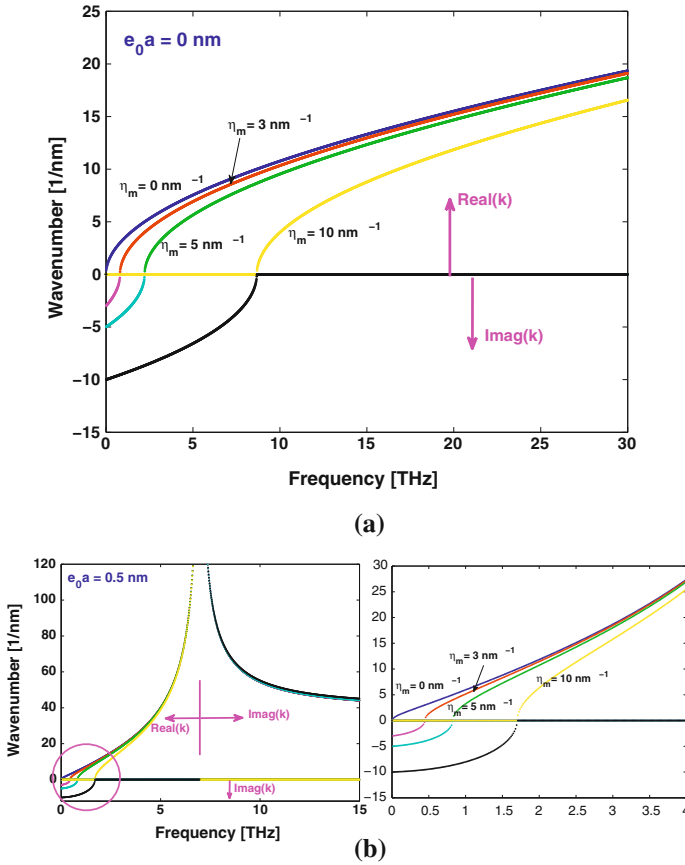


Fig. 10.2 Wavenumber dispersion in monolayer graphene sheets (a) local elasticity ($e_0a = 0 \text{ nm}$) (b) nonlocal elasticity ($e_0a = 0.5 \text{ nm}$). Wavenumber variation at lower frequencies is shown separately for clear visibility

$e_0a = 0.5 \text{ nm}$. The spectrum curves shown in Fig. 10.2a is for $\eta_m = 0$ (represents 1D wave propagation), 3, 5, 10 nm^{-1} . The local elasticity calculation shows that the flexural wavenumber follow a nonlinear variation at low values of wave frequency; and at higher frequencies it varies linearly as shown in Fig. 10.2a. This nonlinear variation indicates that the waves are dispersive in nature, that is, the waves will change their shape as they propagate. The linear variation indicates that the waves are in nondispersive nature. For $\eta_m = 0$, the wavenumbers of the flexural wave mode does not have a cut-off frequency. As η_m increases all the waves are still dispersive in nature as shown in Fig. 10.2a. As the y -directional wavenumber increases from 0 to 10 nm^{-1} , the wave modes are having a frequency band gap region. The frequency band within which the corresponding wavenumbers are purely imaginary. Thus, the flexural mode does not propagate at frequencies lying within this band.

Hence, these wavenumbers have a substantial imaginary part along with the real part, thus these waves attenuate as they propagate. It can also be seen that from Fig. 10.2a, the frequency band also increases with increase in η_m .

The wavenumber dispersion with frequency obtained from nonlocal elasticity ($e_0a = 0.5$ nm) is shown in Fig. 10.2b. The observations made in local elasticity are still valid in nonlocal elasticity also. The only difference is that, because of nonlocal elasticity, the wavenumbers of the flexural wave become highly nonlinear and tends to infinity at escape frequency or asymptotic frequency. It can be seen that the wavenumbers before escape frequency are real and after that imaginary (see Fig. 10.2b). The cut-off frequency of the flexural wave for $\eta_m = 3, 5$ and 10 nm^{-1} , respectively, occurs at 0.8087, 2.2280, and 8.6820 THz in local/classical elasticity, and at 0.4578, 0.8392, and 1.7090 THz in nonlocal elasticity ($e_0a = 0.5$ nm). The nonlocal scale highly affects the frequency band gap of the flexural waves in graphene sheet. The escape frequency of this flexural wave is 6.9580 THz for $e_0a = 0.5$ nm. It has also been observed that the escape frequencies are independent of η_m from Fig. 10.2b.

The local/classical elasticity calculation shows that, the wave will propagate even at higher frequencies. However, nonlocal elasticity predicts that the waves can propagate only up to escape frequency and this behavior, we also saw in 1-D nanostructures.

The phase speed and group speed dispersions with the wave frequency are shown in Figs. 10.3, 10.4, obtained from local and nonlocal elasticity. Figure 10.3a shows that the flexural wave speeds are increasing from low frequency to higher values of wave frequency (local elasticity calculation, $e_0a = 0$). As η_m increases from 0 to 10 nm^{-1} , the wave speeds tends to a constant value at higher values of wave frequency. As we move to nonlocality ($e_0a \neq 0$), the flexural wave stops propagating at certain escape frequency as shown in Fig. 10.3b, which is due to the imaginary part of the wavenumber after the escape frequency. For any value of the η_m , the escape frequency of all flexural waves is same. The group speed dispersion in graphene is shown in Fig. 10.4a, b, respectively obtained from local and nonlocal elasticity theories. The

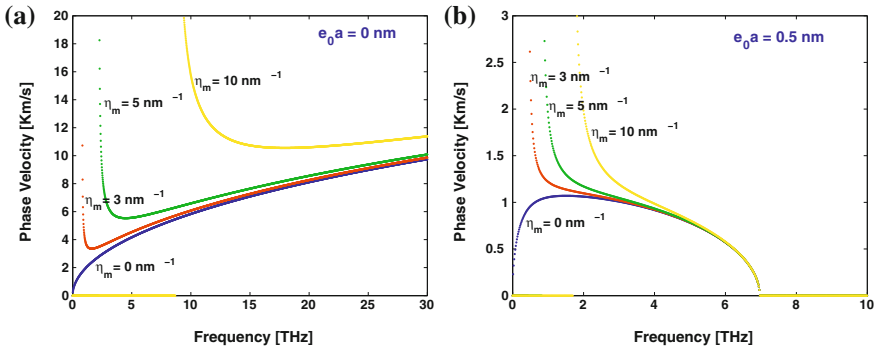


Fig. 10.3 Phase speed dispersion in monolayer graphene sheets (a) local elasticity ($e_0a = 0$ nm) (b) nonlocal elasticity ($e_0a = 0.5$ nm)

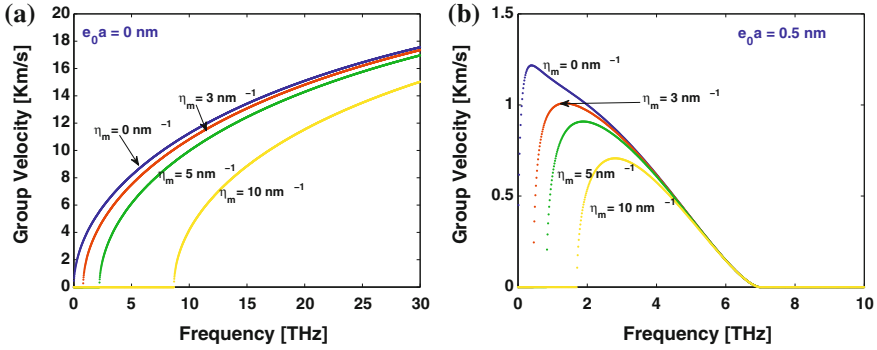


Fig. 10.4 Group speed dispersion in monolayer graphene sheets (a) local elasticity ($e_0a = 0$ nm) (b) nonlocal elasticity ($e_0a = 0.5$ nm)

group speed of the flexural wave is almost constant at higher values of the wave frequencies. The local elasticity calculation shows that the group speed of the wave will be nonzero even at higher values of the frequency (Fig. 10.4a), and that is zero at escape frequency (Fig. 10.4b) in nonlocal elasticity. The magnitude of the group speed is decreasing with an increase in the η_m .

The variation of the cut-off frequency of flexural wave with nonlocal scaling parameter and y -directional wavenumber (η_m) are shown in Fig. 10.5a, b, respectively. The cut-off frequency variation shown in Fig. 10.5a is for $\eta_m = 2, 5$ and 8 nm^{-1} . It shows that for a given η_m , as we increase the nonlocal scaling parameter, the cut-off frequency of flexural wave mode decreases. It has been found that at higher values of the nonlocal scaling parameter, the cut-off frequencies of the flexural wave will depend on the y -directional wavenumber, such difference is clearly seen from Fig. 10.5a inset. The cut-off frequency variation of flexural wave with η_m is shown in

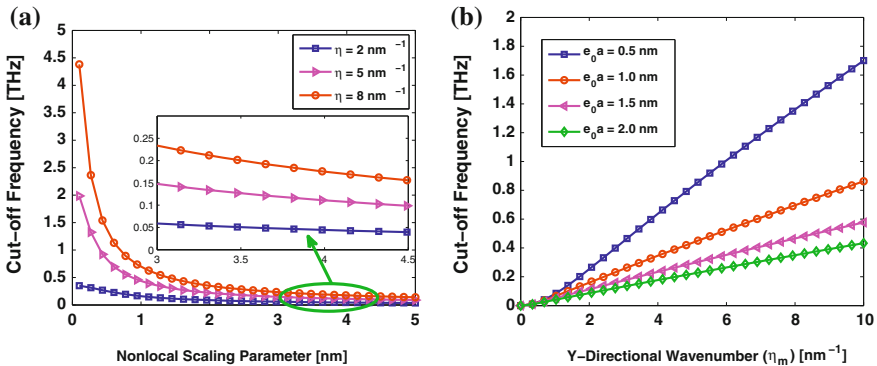


Fig. 10.5 Cut-off frequency variation in monolayer graphene sheets (a) For different nonlocal scale parameter (b) For different y directional wavenumber η_m

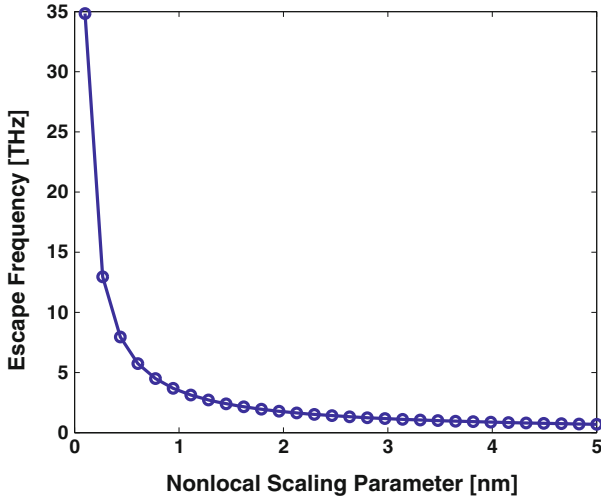


Fig. 10.6 Escape frequency variation of flexural wave of a monolayer graphene sheet with nonlocal scaling parameter

Fig. 10.5b. For a given e_0a , the cut-off frequency will increase as with increase in η_m . As the nonlocal scaling parameter decreases, the cut-off frequency also decreases with η_m (see Fig. 10.5b).

The escape frequency variation with nonlocal scaling parameter is shown in Fig. 10.6. It shows that as e_0a increases, the escape frequency decreases. At higher values of e_0a , escape frequencies approach to very small value.

Toward this end, it would be appropriate to discuss about some physics of graphene related to the nonlocal elasticity. Good example is the recent study of ballistic thermal transport of graphene ribbons by Munoz et al. [15]. The authors of this paper presented an elastic shell-based theory for calculating the thermal conductance of graphene ribbons of arbitrary width b . Their analysis of vibrational modes of a continuum thin plate lead to a general equation for ballistic conductance ρ . At low temperature, it yielded a power law $\rho \sim T^\beta$, where the exponent β varied with the ribbon width b from $\beta = 1$ for a narrow ribbon ($\rho \sim T$, as a four-channel quantum wire) to $\beta = \frac{3}{2}$ ($\rho = bT^{\frac{3}{2}}$) in the limit of wider graphene sheets [15]. They augmented the ballistic results by the phenomenological value of a phonon mean free path to account for scattering and it agreed well with the reported experimental observations. If one introduces nonlocality into the continuum elastic shell model of the graphene, referring to Fig. 10.1 of Ref. [15], the first and second lowest branches are displayed for transverse acoustic mode, longitudinal acoustic mode, and bending mode, plus a single branch for torsion mode. As compared to the calculations of nonlocality, the branches obtained from classical elastic shell model of the graphene were smaller than that of the nonlocal calculations (refer Figs. 10.2, 10.3 of this article). Also the cut-off frequencies of all the vibrational modes of the dispersion curves

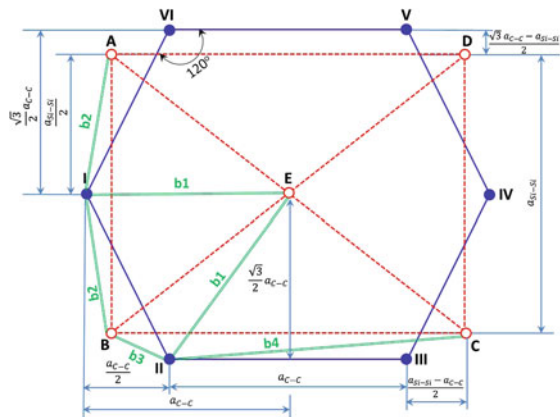
of graphene sheet obtained from classical elasticity calculations are higher than the nonlocal elasticity calculations.

Incorporating the nonlocal elasticity theory in the graphene elastic shell model, one can also estimate the thermal conductance of the graphene sheet. Here one can also obtain the exact values of the nonlocal scale parameter (e_0a) by matching the nonlocal elasticity calculations of thermal conductivity of graphene sheet at room temperature as a function of length with the molecular dynamics (MD) results presented in [16, 17].

10.2 Modeling of Graphene Layer on Silicon Substrate

Graphene is a two-dimensional monolayer of carbon atoms bonded together like a honeycomb fashion and is of one atom thick in size. These bonds are hybridized into a sp^2 configuration. There are three in-plane (σ) bonds per atom. These bonds are extremely strong and form the rigid backbone of the hexagonal structure. It is the partially filled p_z orbitals (π orbitals) perpendicular to the plane that are responsible for electron conduction. Due to the out-of-plane π orbitals, interactions between graphene and a substrate or between graphene layers influence the electronic structure of graphene [18]. The hexagonal honeycomb crystal lattice in graphene contains two atoms per unit cell. A single parameter characterizes this structure, that is, the distance a between two equivalent atoms in the lattice (which is also the distance between the atom and its second nearest neighbor). In this section, we consider a monolayer graphene resting on silicon substrate. This hybrid system consists of a single hexagonal cell of graphene and a cell of silicon structure. These two are separated vertically by distance r_h . Here the graphene cell is resting over the silicon cell as shown in Fig. 10.7 (top view).

Fig. 10.7 Hybrid system: A single graphene hexagonal cell consisting of six carbon atoms and a single cell in silicon structure interaction, a_{C-C} and a_{Si-Si} are the bond lengths of $C - C$ and $Si - Si$, (● - Carbon atoms and ○ - Si atoms in figure)



10.2.1 Potential Energy, Equilibrium and Force Constants

For a system of N particles, in general, the total potential energy may be expanded as [19]

$$\Gamma = \gamma_2 + \gamma_3 + \dots \quad (10.33)$$

$$\gamma_2 = \frac{1}{2!} \sum_i^N \sum_{i \neq j}^N U(\mathbf{r}_i, \mathbf{r}_j) \quad (10.34)$$

$$\gamma_3 = \frac{1}{3!} \sum_i^N \sum_{i \neq j \neq k}^N \sum_k^N U(\mathbf{r}_i, \mathbf{r}_j, \mathbf{r}_k) \quad (10.35)$$

where $U(\mathbf{r}_i, \mathbf{r}_j)$ and $U(\mathbf{r}_i, \mathbf{r}_j, \mathbf{r}_k)$ represent the two- and three-body interactions, respectively. The position of the i^{th} particle is denoted by \mathbf{r}_i . In this study, the two-body part is represented by a Mie-type potential [20] as

$$U(\mathbf{r}_{ij}) = \frac{\varepsilon}{m-n} \left[n \left(\frac{r_0}{r_{ij}} \right)^m - m \left(\frac{r_0}{r_{ij}} \right)^n \right] \quad (10.36)$$

where $r_{ij} = |\mathbf{r}_i - \mathbf{r}_j|$, r_0 represents the equilibrium distance and ε denotes the two body energy at $r_{ij} = r_0$. The exponents m and n account for the repulsive and attractive terms, respectively. In order for the potential energy given by Eqs. (10.33–10.35) to be used in calculation for a specific system, the parameters ε and r_0 must be first evaluated. In accordance with [20], on the stability of the diamond cubic structure, the values of the exponents m and n were taken as 12 and 6, respectively. The evaluation process is basically a simple fitting procedure, however, due to the nonlinear nature of the potential function, it often becomes quite cumbersome. The parameters in the Mie-type potential are given for $Si-Si$, $C-C$, and $Si-C$ systems in Table 10.1, which are obtained from [20]. Substituting $m = 12$ and $n = 6$ in the potential energy expression given in Eq. (10.36), one has

$$U(\mathbf{r}_{ij}) = U(r) = \varepsilon \left[\left(\frac{r_0}{r} \right)^{12} - 2 \left(\frac{r_0}{r} \right)^6 \right] \quad (10.37)$$

This two-body interaction energy variation with the interatomic distance is shown in Fig. 10.8a. The modified Mie potential for the present hybrid lattice is shown in

Table 10.1 Potential energy parameters for two-body system (Mie-type potential)

Two-body parameters	ε (eV)	r_0 (\AA)
Si-Si	2.187	2.2951
C-C	5.437	1.4806
Si-C	3.895	1.74

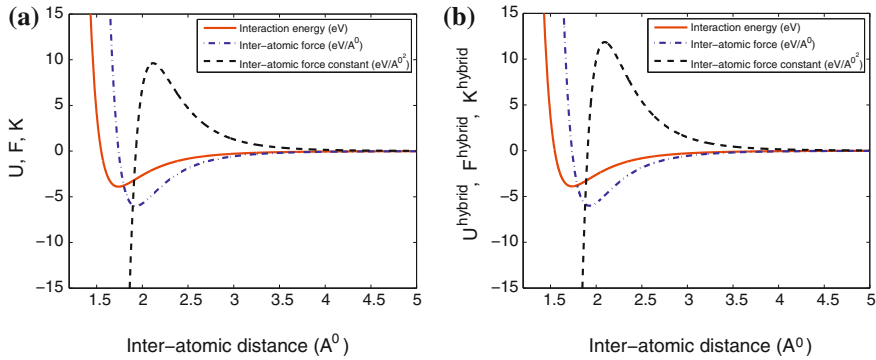


Fig. 10.8 Inter-atomic Energy, Force and Force constant obtained from (a) Mie potential and (b) Hybrid lattice

Fig. 10.7 and this is obtained from the following relation:

$$U^{hybrid}(r_h) = \varepsilon \left[\left(\frac{r_0}{f(r_h)} \right)^{12} - 2 \left(\frac{r_0}{f(r_h)} \right)^6 \right] \quad (10.38)$$

where $f(r_h) = \sqrt{r_h^2 + a_{C-C}^2 + 0.5a_{Si-Si}^2 - a_{C-C}a_{Si-Si}}$. Here r_h is the vertical distance between the graphene layer and the silicon substrate and a_{C-C} , a_{Si-Si} are the bond lengths of C – C and Si – Si, respectively.

The minimum potential energy requires that,

$$\frac{dU^{hybrid}(r_h)}{dr_h} = 0 \quad (10.39)$$

This gives $r_h^e = 1.7359 \text{ \AA}$ as the equilibrium distance for the hybrid lattice. The bond force is obtained by differentiating the potential energy with respect to the equilibrium distance r_h as

$$F(r_h) = -\frac{dU^{hybrid}(r_h)}{dr_h} = \frac{12\varepsilon r_h}{r_0^2} \left[\left(\frac{r_0}{f(r_h)} \right)^{14} - \left(\frac{r_0}{f(r_h)} \right)^8 \right] \quad (10.40)$$

The bond force constant is the second derivative of the potential with respect to r_h or the first derivative of the bond force F with respect to r_h and is written as

$$K^{sub}(r_h) = \frac{d^2U^{hybrid}(r_h)}{dr_h^2} = \frac{dF(r_h)}{dr_h} = -\frac{12\varepsilon r_h^2}{r_0^4} \left[14 \left(\frac{r_0}{f(r_h)} \right)^{16} - 8 \left(\frac{r_0}{f(r_h)} \right)^{10} \right] \quad (10.41)$$

The nonlinear variation of the potential energy, interatomic force, and force constants of the present graphene-silicon hybrid lattice arrangement are shown in Fig. 10.8b.

Now we need to obtain a closed form expression for the force constant of the C–Si bond. Let us consider a single cell in graphene and a single cell in pure silicon substrate as shown in Fig. 10.7. The vertical distance between the graphene cell and the silicon cell is r_h . First consider that carbon atom I and this is connected to silicon atoms A , B , and E as shown in Fig. 10.7. The bonds between I and A , B , E are labeled as b_2 , b_2 , and b_1 , respectively. The sum of the total vertical components of the bond forces is

$$F_{hybrid}^{(I)} = F_1 \sin \theta_1 + 2F_2 \sin \theta_2 \quad (10.42)$$

where F_1 is the force between carbon atom I and Si-atom E , and F_2 is the force between carbon atom I and Si-atom E , and also similar force between atoms I and B . Now consider a corner carbon atom II and this is connected to Si-atoms B , E and C . These bonds are labeled as b_3 , b_1 , and b_4 , respectively as shown in Fig. 10.7. The sum of the total vertical components of these bond forces is

$$F_{hybrid}^{(II)} = F_2 \sin \theta_2 + F_3 \sin \theta_3 + F_4 \sin \theta_4 \quad (10.43)$$

where F_2 , F_3 , and F_4 are the bond forces between atoms II & B ; II & E and II & C , respectively and the bond angles are defined as

$$\theta_1 = \tan^{-1} \left(\frac{r_h}{D_1} \right) \quad (10.44)$$

$$\theta_2 = \tan^{-1} \left(\frac{r_h}{D_2} \right) \quad (10.45)$$

$$\theta_3 = \tan^{-1} \left(\frac{r_h}{D_3} \right) \quad (10.46)$$

$$\theta_4 = \tan^{-1} \left(\frac{r_h}{D_4} \right) \quad (10.47)$$

$$\theta_5 = \tan^{-1} \left(\frac{r_h}{D_5} \right) \quad (10.48)$$

where

$$D_1 = D_3 = a_{C-C} \quad (10.49)$$

$$D_2 = \frac{1}{2} \sqrt{(2a_{C-C} - a_{Si-Si})^2 + (a_{Si-Si})^2} \quad (10.50)$$

$$D_4 = \frac{1}{2} \sqrt{(\sqrt{3}a_{C-C} - a_{Si-Si})^2 + (a_{Si-Si} - a_{C-C})^2} \quad (10.51)$$

$$D_4 = \frac{1}{2} \sqrt{(\sqrt{3}a_{C-C} - a_{Si-Si})^2 + (a_{Si-Si} + a_{C-C})^2} \quad (10.52)$$

In the above expressions a_{C-C} and a_{Si-Si} are the bond lengths of carbon in graphene and silicon in pure Si-substrate, respectively. The total bond force is expressed as the sum of the bond forces $F_{hybrid}^{(I)}$ and $F_{hybrid}^{(II)}$:

$$F_{hybrid}^{total} = 2F_{hybrid}^{(I)} + 4F_{hybrid}^{(II)} \quad (10.53)$$

The total bond force constant is expressed as

$$K^{sub}(r_h) = \frac{1}{r_h} \left(2K^{(I)}(r_h) + 4K^{(II)}(r_h) \right), \quad (10.54)$$

where

$$K^{(I)}(r_h) = K_1(r_h)D_1 \sin \theta_1 + 2K_2(r_h)D_2 \sin \theta_2, \quad (10.55)$$

$$K^{(II)}(r_h) = K_2(r_h)D_2 \sin \theta_2 + K_3(r_h)D_3 \sin \theta_3 + K_4(r_h)D_4 \sin \theta_4. \quad (10.56)$$

Here K_i is the force constant of the bond i and D_i is the corresponding bond length. The total bond force constant of the bond between the graphene and silicon substrate at equilibrium distance r_h^e is obtained as $K^{sub}(r_h^e) = K^{sub}(r_h) \Big|_{r_h=r_h^e} = 6.3584 \times 10^4$ N/m. This value should be multiplied by the number of atoms per unit area, which is equal to the ratio of the total number of atoms in a graphene sheet to the area of the sheet. This value is expected to be independent of the size of the sheet.

10.3 Wave Propagation in Single Graphene Layer on Silicon Substrate

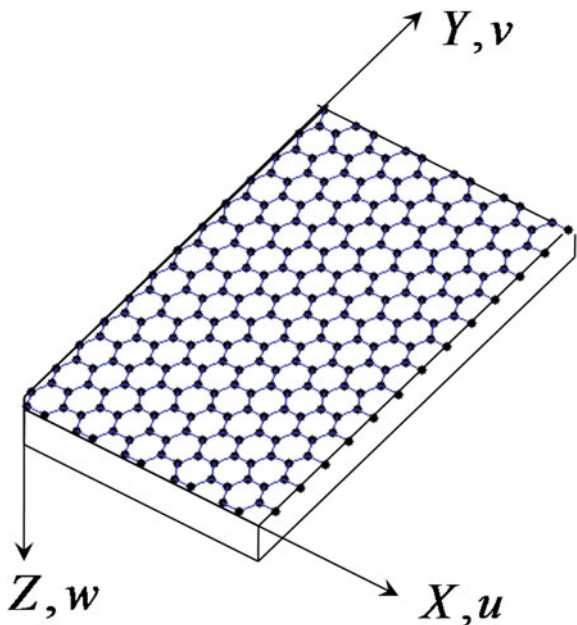
We will first outline a detail derivation of the nonlocal governing differential equations of motion for the graphene-silicon system. This system is modeled as a one atom thick nanoplate on linearly distributed vertical springs.

The displacement field for this nanoplate is assumed as [21]

$$\begin{aligned} u(x, y, z, t) &= u^o(x, y, t) - z \frac{\partial w}{\partial x} \\ v(x, y, z, t) &= v^o(x, y, t) - z \frac{\partial w}{\partial y} \\ w(x, y, z, t) &= w(x, y, t) \end{aligned} \quad (10.57)$$

where, $u^o(x, y, t)$, $v^o(x, y, t)$, and $w(x, y, t)$ are the axial (inplane-longitudinal and lateral) and transverse displacements, respectively along the mid-plane as shown in Fig. 10.9. The mid-plane of the plate is at $z = 0$. The associated nonzero strains are

Fig. 10.9 A single layer of graphene on a crystalline substrate



$$\begin{Bmatrix} \varepsilon_{xx} \\ \varepsilon_{yy} \\ \varepsilon_{xy} \end{Bmatrix} = \begin{Bmatrix} \frac{\partial u^o}{\partial x} \\ \frac{\partial v^o}{\partial y} \\ \frac{\partial u^o}{\partial y} + \frac{\partial v^o}{\partial x} \end{Bmatrix} + \begin{Bmatrix} -\frac{\partial^2 w}{\partial x^2} \\ -\frac{\partial^2 w}{\partial y^2} \\ -2\frac{\partial^2 w}{\partial x \partial y} \end{Bmatrix} \quad (10.58)$$

where, ε_{xx} and ε_{yy} are the normal strains in x and y directions respectively, while, ε_{xy} is the in-plane shear strain.

The nonlocal constitutive relation for isotropic materials is given as

$$\left(1 - (e_0 a)^2 \left[\frac{\partial^2}{\partial x^2} + \frac{\partial^2}{\partial y^2} \right] \right) \begin{Bmatrix} \sigma_{xx} \\ \sigma_{yy} \\ \sigma_{xy} \end{Bmatrix} = \begin{bmatrix} C_{11} & \nu C_{11} & 0 \\ \nu C_{22} & C_{22} & 0 \\ 0 & 0 & C_{66} \end{bmatrix} \begin{Bmatrix} \varepsilon_{xx} \\ \varepsilon_{yy} \\ \varepsilon_{xy} \end{Bmatrix} \quad (10.59)$$

where, σ_{xx} and σ_{yy} are the normal stresses in x and y directions respectively and σ_{xy} is the in-plane shear stress. For the case of an isotropic plate, the expressions for material constants C_{ij} in terms of Young's modulus E and Poisson's ratio ν are given as $C_{11} = C_{22} = E/(1 - \nu^2)$ and $C_{66} = E/(2(1 + \nu))$.

The total strain energy (Π) and kinetic energy (Γ) of the present graphene-silicon system are expressed as

$$\Pi = \frac{1}{2} \int_{-h/2}^{+h/2} \int_A \left(\sigma_{xx} \varepsilon_{xx} + \sigma_{yy} \varepsilon_{yy} + \sigma_{xy} \varepsilon_{xy} + K^{sub} w^2 \right) dz dA \quad (10.60)$$

$$\Gamma = \frac{1}{2} \int_{-h/2}^{+h/2} \int_A \rho \left(\dot{u}^2 + \dot{v}^2 + \dot{w}^2 \right) dz dA \quad (10.61)$$

The governing equations are derived based on Hamilton's principle. The Hamilton's principle is stated as

$$\int_{t_1}^{t_2} (\delta \Pi - \delta \Gamma) dt = 0 \quad (10.62)$$

Substituting Eqs. (10.60) and (10.61) into Eq. (10.62), we obtain

$$\begin{aligned} \frac{1}{2} \int_{t_1}^{t_2} \int_{-h/2}^{+h/2} \int_A \left(\delta \sigma_{xx} \varepsilon_{xx} + \sigma_{xx} \delta \varepsilon_{xx} + \delta \sigma_{yy} \varepsilon_{yy} + \sigma_{yy} \delta \varepsilon_{yy} + \delta \sigma_{xy} \varepsilon_{xy} \right. \\ \left. + \sigma_{xy} \delta \varepsilon_{xy} + 2K^{sub} w \delta w - 2\rho \{ \dot{u} \delta \dot{u} + \dot{v} \delta \dot{v} + \dot{w} \delta \dot{w} \} \right) dA dz dt = 0 \end{aligned} \quad (10.63)$$

The minimization of this functional with respect to the three degrees of freedom (u^o , v^o , w) will give three nonlocal governing partial differential equations of motion for the assumed system (graphene on Si-substrate) as

$$\begin{aligned} \delta u^o : -J_0 \frac{\partial^2 u^o}{\partial t^2} + J_0 (e_0 a)^2 \left(\frac{\partial^4 u^o}{\partial x^2 \partial t^2} + \frac{\partial^4 u^o}{\partial y^2 \partial t^2} \right) - I_0 \left(C_{11} \frac{\partial^2 u^o}{\partial x^2} + C_{66} \frac{\partial^2 u^o}{\partial y^2} \right) + \\ I_0 (C_{12} + C_{66}) \frac{\partial^2 v^o}{\partial x \partial y} + J_1 \frac{\partial^3 w}{\partial x \partial t^2} - J_1 (e_0 a)^2 \left(\frac{\partial^5 w}{\partial x^3 \partial t^2} + \frac{\partial^5 w}{\partial x \partial y^2 \partial t^2} \right) - \\ C_{11} I_1 \frac{\partial^3 w}{\partial x^3} - I_1 (C_{12} + 2C_{66}) \frac{\partial^3 w}{\partial x \partial y^2} = 0 \end{aligned} \quad (10.64)$$

$$\begin{aligned} \delta v^o : -J_0 \frac{\partial^2 v^o}{\partial t^2} + J_0 (e_0 a)^2 \left(\frac{\partial^4 v^o}{\partial x^2 \partial t^2} + \frac{\partial^4 v^o}{\partial y^2 \partial t^2} \right) - I_0 \left(C_{22} \frac{\partial^2 v^o}{\partial y^2} + C_{66} \frac{\partial^2 v^o}{\partial x^2} \right) + \\ I_0 (C_{12} + C_{66}) \frac{\partial^2 u^o}{\partial x \partial y} + J_1 \frac{\partial^3 w}{\partial y \partial t^2} - J_1 (e_0 a)^2 \left(\frac{\partial^5 w}{\partial x^2 \partial y \partial t^2} + \frac{\partial^5 w}{\partial y^3 \partial t^2} \right) - \\ C_{22} I_1 \frac{\partial^3 w}{\partial y^3} - I_1 (C_{12} + 2C_{66}) \frac{\partial^3 w}{\partial x^2 \partial y} = 0 \end{aligned} \quad (10.65)$$

$$\begin{aligned}
\delta w : & -J_0 \frac{\partial^2 w}{\partial t^2} + J_2 \left(\frac{\partial^4 w}{\partial x^2 \partial t^2} + \frac{\partial^4 w}{\partial y^2 \partial t^2} \right) + J_0 (e_0 a)^2 \left(\frac{\partial^4 w}{\partial x^2 \partial t^2} + \frac{\partial^4 w}{\partial y^2 \partial t^2} \right) - \\
& J_2 (e_0 a)^2 \left(\frac{\partial^6 w}{\partial x^4 \partial t^2} + 2 \frac{\partial^6 w}{\partial x^2 \partial y^2 \partial t^2} + \frac{\partial^6 w}{\partial y^4 \partial t^2} \right) + K^{sub} (e_0 a)^2 \left(\frac{\partial^2 w}{\partial x^2} + \frac{\partial^2 w}{\partial y^2} \right) - \\
& K^{sub} w - I_2 \left(C_{11} \frac{\partial^4 w}{\partial x^4} + C_{22} \frac{\partial^4 w}{\partial y^4} \right) - 2I_2 (C_{11} + 2C_{66}) \frac{\partial^4 w}{\partial x^2 \partial y^2} - J_1 \frac{\partial^3 u^o}{\partial x \partial t^2} + \\
& J_1 (e_0 a)^2 \left(\frac{\partial^5 u^o}{\partial x^3 \partial t^2} + \frac{\partial^5 u^o}{\partial x \partial y^2 \partial t^2} \right) + C_{11} I_1 \frac{\partial^3 u^o}{\partial x^3} + I_1 (C_{12} + 2C_{66}) \frac{\partial^3 u^o}{\partial x \partial y^2} - \\
& J_1 \frac{\partial^3 v^o}{\partial y \partial t^2} + J_1 (e_0 a)^2 \left(\frac{\partial^5 v^o}{\partial x^2 \partial y \partial t^2} + \frac{\partial^5 v^o}{\partial y^3 \partial t^2} \right) + I_1 (C_{12} + 2C_{66}) \frac{\partial^3 v^o}{\partial x^2 \partial y} + C_{22} I_1 \frac{\partial^3 v^o}{\partial y^3} = 0
\end{aligned} \tag{10.66}$$

where K^{sub} is the force constant of the bonds between the graphene sheet and the Si substrate and the parameters I_p and J_p are defined as follows:

$$I_p = \int_{-h/2}^{h/2} z^p dz, \quad J_p = \int_{-h/2}^{h/2} \rho z^p dz, \quad p = 0, 1, 2. \tag{10.67}$$

It should be observed that when the nonlocal scaling parameter $e_0 a$ is set to zero, the classical governing equations of motion for the plate are recovered.

10.3.1 Wave Dispersion Analysis

For harmonic wave propagation in graphene sheet, the displacement field can be expressed in complex form as [22, 23]

$$u^o(x, t) = \sum_{n=1}^N \sum_{m=1}^M \hat{u}_{mn} e^{-jk_n x} e^{-j\eta_m y} e^{j\omega t}, \tag{10.68}$$

$$v^o(x, t) = \sum_{n=1}^N \sum_{m=1}^M \hat{v}_{mn} e^{-jk_n x} e^{-j\eta_m y} e^{j\omega t}, \tag{10.69}$$

$$w^o(x, t) = \sum_{n=1}^N \sum_{m=1}^M \hat{w}_{mn} e^{-jk_n x} e^{-j\eta_m y} e^{j\omega t} \tag{10.70}$$

where \hat{u}_{mn} , \hat{v}_{mn} , \hat{w}_{mn} are the frequency amplitudes, k_n and η_m are the wavenumbers in x - and y -directions, respectively, ω is the frequency of the wave motion and $j = \sqrt{-1}$. In the equations that follow, we will drop the subscripts m and n and for

more brevity, we will denote the x direction wavenumber $k_n = k_x$ and the y direction wavenumber $\eta_m = k_y$.

The nonlocal governing equations for the graphene and Si-substrate model are given in Eqs. (10.64–10.66). Our next step is to analyze the ultrasonic type of wave propagation in this system. Substituting the displacement Eqs. (10.68–10.70) in the nonlocal governing equations of the graphene-Si system and after simplifying, the resultant equations expressed in matrix form as:

$$\mathbf{S}_4 k_x^4 + \mathbf{S}_3 k_x^3 + \mathbf{S}_2 k_x^2 + \mathbf{S}_1 k_x + \mathbf{S}_0 = 0 \quad (10.71)$$

where

$$\mathbf{S}_4 = \begin{bmatrix} 0 & 0 & 0 \\ 0 & 0 & 0 \\ 0 & 0 & J_2(e_0a)^2\omega^2 - C_{11}I_2 \end{bmatrix} \quad (10.72)$$

$$\mathbf{S}_3 = \begin{bmatrix} 0 & 0 & jJ_1\omega^2(e_0a)^2 - jC_{11}I_1 \\ 0 & 0 & 0 \\ -jJ_1\omega^2(e_0a)^2 + jC_{11}I_1 & 0 & 0 \end{bmatrix} \quad (10.73)$$

$$\mathbf{S}_2 = \begin{bmatrix} J_0\omega^2(e_0a)^2 - C_{11}I_0 & 0 & 0 \\ 0 & J_0\omega^2(e_0a)^2 - C_{66}I_0 & S_2^{(23)} \\ 0 & S_2^{(32)} & S_2^{(33)} \end{bmatrix} \quad (10.74)$$

$$\mathbf{S}_1 = \begin{bmatrix} 0 & -(C_{11} + C_{66})I_0k_y & S_1^{(13)} \\ -(C_{11} + C_{66})I_0k_y & 0 & 0 \\ S_1^{(31)} & 0 & 0 \end{bmatrix} \quad (10.75)$$

$$\mathbf{S}_0 = \begin{bmatrix} S_0^{(11)} & 0 & 0 \\ 0 & S_0^{(22)} & S_0^{(23)} \\ 0 & S_0^{(32)} & S_0^{(33)} \end{bmatrix} \quad (10.76)$$

where the elements $S_r^{(pq)}$ ($p, q = 1, 2, 3$, and $r = 0, 1, 2$) are given below.

$$S_2^{(23)} = jJ_1k_y(e_0a)^2\omega^2 - j(C_{11} + 2C_{66})I_1k_y, \quad (10.77)$$

$$S_2^{(32)} = -jJ_1k_y(e_0a)^2\omega^2 + j(C_{11} + 2C_{66})I_1k_y, \quad (10.78)$$

$$S_2^{(33)} = J_2\omega^2 \left(1 + (e_0a)^2k_y^2 \right) - J_0\omega^2(e_0a)^2 - (C_{11} + 2C_{66})I_2k_y^2 - K^{sub}(e_0a)^2, \quad (10.79)$$

$$S_1^{(13)} = jJ_1\omega^2 \left(1 + (e_0a)^2k_y^2 \right) - j(C_{11} + 2C_{66})I_1k_y^2, \quad (10.80)$$

$$S_1^{(31)} = -jJ_1\omega^2 \left(1 + (e_0a)^2k_y^2 \right) + j(C_{11} + 2C_{66})I_1k_y^2, \quad (10.81)$$

$$S_0^{(11)} = J_0\omega^2 \left(1 + (e_0a)^2k_y^2\right) - C_{66}I_0k_y^2, \quad (10.82)$$

$$S_0^{(22)} = J_0\omega^2 \left(1 + (e_0a)^2k_y^2\right) - C_{22}I_0k_y^2, \quad (10.83)$$

$$S_0^{(23)} = jJ_1k_y\omega^2 \left(1 + (e_0a)^2k_y^2\right) - jC_{22}I_1k_y^3, \quad (10.84)$$

$$S_0^{(32)} = -jJ_1k_y\omega^2 \left(1 + (e_0a)^2k_y^2\right) + jC_{22}I_1k_y^3, \quad (10.85)$$

$$S_0^{(33)} = J_2\omega^2k_y^2 \left(1 + (e_0a)^2k_y^2\right) + J_0\omega^2 \left(1 + (e_0a)^2k_y^2\right) - C_{22}I_2k_y^4 \\ - K^{sub} \left(1 + (e_0a)^2k_y^2\right). \quad (10.86)$$

The Eq. (10.71) is in the form of polynomial eigenvalue problem in wavenumber k_x , which can be solved to obtain the dispersion relations. The dispersion of the wavenumbers with wave frequency is shown in Figs. 10.10, 10.11, respectively calculated based on local and nonlocal elasticity theories. The figure also shows the effect of silicon substrate on ultrasonic wave characteristics of graphene at $k_y = 0, 2$ and 5 nm^{-1} .

In the previous section, we had shown in the analysis of monolayer graphene sheets that the cut-off frequency shifting happens when the values of horizontal wavenumber is varied. We will examine this here for the case of monolayer graphene on silicon substrate. Note that, unlike the previous case, here the in-plane and out-of-plane waves are coupled and hence cut-off frequency can exist for both these waves. The expressions for frequency band gap are obtained by setting $k_x = 0$ in dispersion relation Eq. (10.71). For the present case of PEP, one can solve $|\mathbf{S}_0| = 0$ to obtain the cut-off frequencies of all the fundamental wave modes in the graphene-Si system as

$$\omega_c^{inplane} = k_y \sqrt{\frac{I_0C_{66}}{J_0 \left(1 + (e_0a)^2k_y^2\right)}}, \quad (10.87)$$

$$\omega_c^{flexural} = \sqrt{\frac{1}{2H_0} \sqrt{H_1 + H_2}} \quad (10.88)$$

where H_0, H_1 and H_2 are given as

$$H_0 = (J_0J_2 - J_1^2)k_y^4(e_0a)^2 + J_0^2(1 + (e_0a)^2k_y^2) + (J_0J_2 - J_1^2)k_y^2 \quad (10.89)$$

$$H_1 = J_0K^{sub}(1 + (e_0a)^2k_y^2) + (J_0 + J_2)C_{22}I_2k_y^4 + (I_0J_0 - 2I_1J_2)C_{22}k_y^4 \quad (10.90)$$

$$H_2 = [J_0^2(e_0a)^4k_y^4 + 2J_0^2(e_0a)^2k_y^2 + J_0^2]K^{sub2} + \\ [(2J_0^2I_2 - 2J_0I_0J_2 - 4J_0J_1I_1 + 4J_1^2I_0)C_{22}(e_0a)^2k_y^6 - \\ (2J_0^2(e_0a)^2I_0 + 2J_0^2I_2 - 2J_0I_0J_2 - 4J_0J_1I_1 + 4J_1^2I_0)C_{22}k_y^4 - 2C_{22}I_0J_0^2k_y^2]K^{sub} + \quad (10.91)$$

$$[J_0^2 I_2^2 + I_0^2 J_2^2 - 4J_0 I_2 J_1 I_1 - 2J_0 I_2 I_0 J_2 - 4J_1 I_1 I_0 J_2 + 4J_0 J_2 I_1^2 + 4J_1^2 I_0 I_2] C_{22}^2 k_y^8 + [4J_0^2 I_1^2 - 2J_0^2 I_2 I_0 - 4I_0 J_0 J_1 I_1 + 2I_0^2 J_0 J_2] C_{22}^2 k_y^6 + I_0^2 J_0^2 C_{22}^2 k_y^4.$$

The above two expressions for the frequency band gap reveals that, for all the fundamental wave modes (longitudinal, lateral, and flexural) the cut-off frequencies are mainly function of y -direction wavenumber (k_y) and the nonlocal scaling parameter ($e_0 a$) only. The wave speeds (phase speed $C_p = \omega/k_x$, and group speed $C_g = d\omega/dk_x$) can be computed from the dispersion relation that is, Eq. (10.71) This is done by differentiating the PEP in wavenumber (k_x) with respect to wave frequency as:

$$\mathbf{G}_1 C_g + \mathbf{G}_0 = 0 \quad (10.92)$$

where

$$\mathbf{G}_1 = \left[k_x^4 \frac{\partial \mathbf{S}_4}{\partial \omega} + k_x^3 \frac{\partial \mathbf{S}_3}{\partial \omega} + k_x^2 \frac{\partial \mathbf{S}_2}{\partial \omega} + k_x \frac{\partial \mathbf{S}_1}{\partial \omega} + \frac{\partial \mathbf{S}_0}{\partial \omega} \right] \quad (10.93)$$

$$\mathbf{G}_0 = 4\mathbf{S}_4 k_x^3 + 3\mathbf{S}_3 k_x^2 + 2\mathbf{S}_2 k_x + \mathbf{S}_1 \quad (10.94)$$

where $C_g = (\partial\omega/\partial k_x)$ is the group speed of a waves in graphene and the matrices \mathbf{S}_4 , \mathbf{S}_3 , \mathbf{S}_2 , \mathbf{S}_1 and \mathbf{S}_0 are given in Eqs. (10.72–10.76), respectively. The Eq. (10.92) is also a PEP in group speed, one can solve it for group speeds (as a function of wave frequency, wavenumbers and nonlocal scaling parameter) of respective modes (that is, for axial- u , v , and flexural- w) of the graphene-Si system. The group speed dispersion in graphene-Si system with wave frequency is shown in Figs. 10.12, 10.13, calculated based on local and nonlocal elasticity theories, respectively. The effect of the silicon substrate on group speed dispersion can also be clearly seen from these plots for y -directional wavenumber $k_y = 0, 2$, and 5 nm^{-1} .

In this section, the effect of the substrate as well as the nonlocal scale on the wave dispersion properties of the graphene are presented through numerical simulations. For the sake of analysis, the material properties of the graphene are assumed as: Young's modulus $E = 1.06 \text{ TPa}$ and density $\rho = 2300 \text{ kg/m}^3$. As mentioned earlier, the choice of effective wall thickness t of nanostructures such as CNT, graphene, etc., is a longstanding issue in nanomechanics. We have chosen the thickness of the graphene as $t = 0.089 \text{ nm}$, obtained by Kudin et al. [14] via *Ab initio* computations.

The wavenumber dispersion with wave frequency in the graphene-Si system is shown in Figs. 10.10, 10.11, obtained from local and nonlocal elasticity theories, respectively. The Fig. 10.10 shows the wavenumber dispersion obtained from local elasticity theory, where $e_0 = 0 \text{ nm}$. The Fig. 10.10a, b are plotted for $k_y = 0$ (represents 1D wave propagation); Fig. 10.10c, d are plotted for $k_y = 2 \text{ nm}^{-1}$ and Fig. 10.10e, f are plotted for $k_y = 5 \text{ nm}^{-1}$. The frequency band gap of the flexural waves is small as compared to that of the longitudinal and lateral (in-plane) waves for the case of without substrate effect. As the y -directional wavenumber k_y increases the frequency band gap of all the three fundamental modes increases. If we consider the substrate effect, then the flexural wave starts propagating after a large frequency

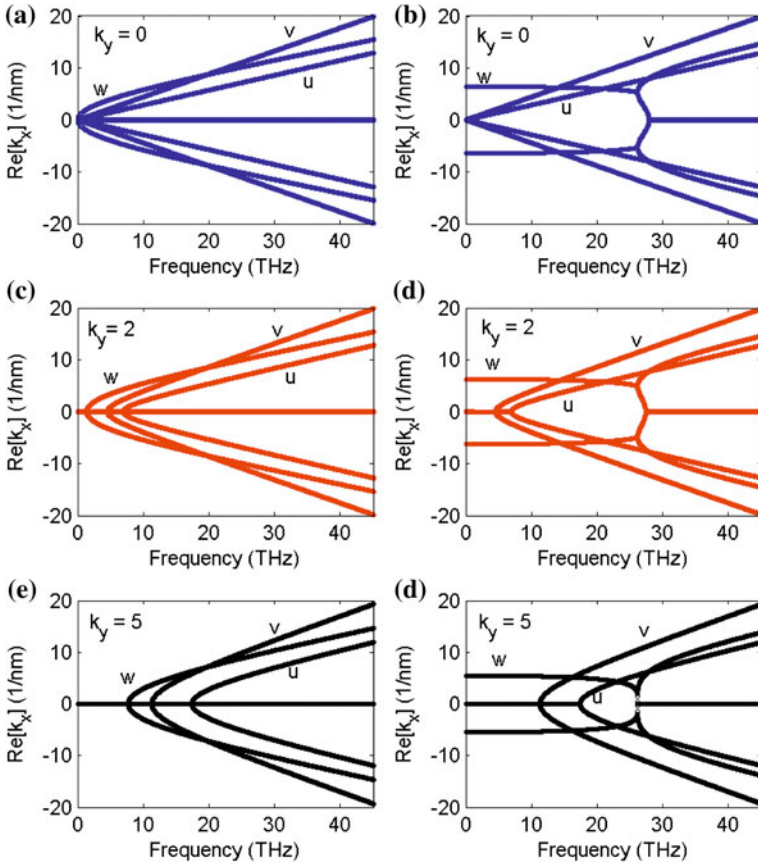


Fig. 10.10 Wavenumber (k_x) dispersion with wave frequency of graphene on Si-substrate obtained by using local elasticity theory ($e_0 = 0$). Figures (a), (c) and (e) are without substrate and (b), (d) and (f) are with substrate, Here y-direction wavenumber is assumed as $k_y = 0, 2, \text{ and } 5 \text{ nm}^{-1}$

band gap as compared to that of the inplane waves. The local elasticity shows that a linear variation of the axial wavenumbers with frequency for $k_y = 0$, that is, the longitudinal and lateral wavenumbers are nondispersive in nature. For $k_y = 0$, the flexural wavenumber shows a nonlinear variation at low values of wave frequency and at higher values of wave frequency it varies linearly as shown in Fig. 10.10. As k_y increases, all the wavenumbers are dispersive in nature. According to Fig. 10.10b, d, and f, one can observe that the substrate effect on flexural waves.

The wavenumber dispersion with frequency for nonlocal elasticity ($e_0 = 0.39$) is shown in Fig. 10.11. The observations made in local elasticity are still valid in nonlocal elasticity also. The only difference is that, because of nonlocal elasticity, the wavenumbers (for both in-plane and flexural) becomes highly nonlinear at higher

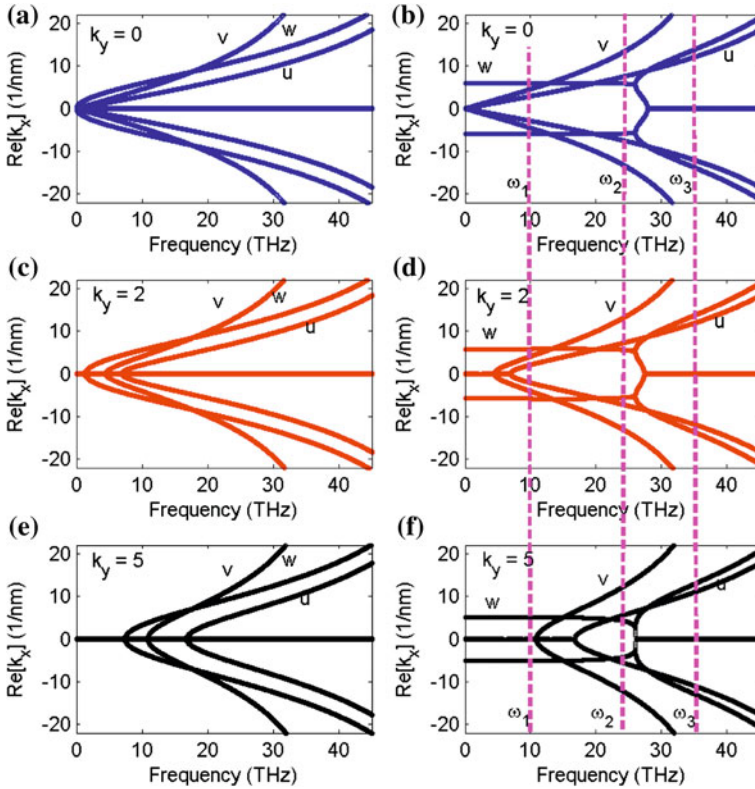


Fig. 10.11 Wavenumber (k_x) dispersion with wave frequency (shown up to nonlocality limit) of graphene on Si-substrate obtained by using nonlocal elasticity theory ($e_0 = 0.39$). Figures (a), (c) and (e) are without substrate (b), (d) and (f) are with substrate. Here y-direction wavenumber is assumed as $k_y = 0, 2$, and 5 nm^{-1} . Here $\omega_1 = 10$, $\omega_2 = 25$ and $\omega_3 = 35 \text{ THz}$

wave frequencies as shown in Fig. 10.11. The frequency band gap variation is same as we move from local to nonlocal elasticity with and without substrate effects.

Local elasticity shows that, the wave will propagate even at higher frequencies. However, nonlocal elasticity predicts that the waves can propagate up to certain frequencies only, after that it will stand, that is, no propagation. The wavenumber dispersion curves obtained from nonlocal elasticity are shown upto the nonlocal limit only. The phenomena discussed in the beginning of this paragraph, occurs above the nonlocal limit.

The group speed dispersion with the wave frequency is shown in Figs. 10.12 and 10.13 for local and nonlocal elasticity, respectively. Figure 10.12a, b shows that (for $k_y = 0$), the in-plane (u, v) wave speeds are constant with wave frequency and the flexural wave speeds are increasing from low frequency and after that they are constant at higher values of wave frequency. The magnitude of the flexural group speeds are higher compared to the axial wave group speeds. As k_y increases from 0

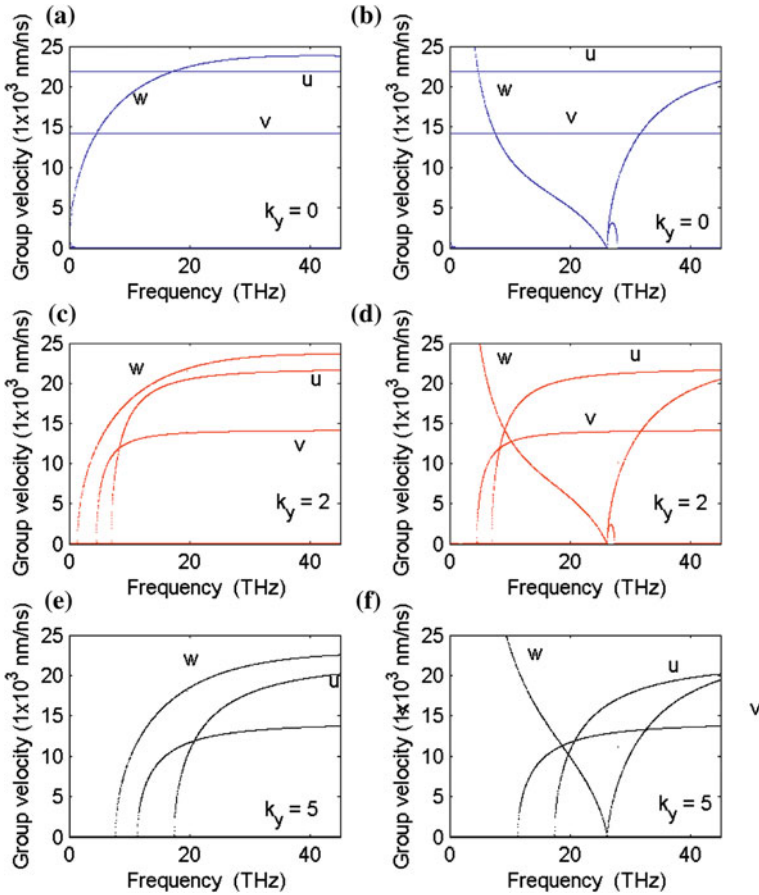


Fig. 10.12 Group speed dispersion of graphene on Si-substrate obtained from local elasticity theory ($\epsilon_0 = 0$). Figures (a), (c) and (e) are without substrate (b), (d) and (f) are with substrate. Here y-direction wavenumber is assumed as $k_y = 0, 2, \text{ and } 5 \text{ nm}^{-1}$

to 5 nm^{-1} , the axial wave group speeds also shows dispersive nature. We can also clearly observe the effect of substrate on the flexural wave group speeds.

In the nonlocal case, the group speeds of the in-plane and flexural waves stop propagating at certain frequencies as shown in Fig. 10.13. The group speeds of the in-plane waves are same for with and without substrate effect. The effect is observed only on the flexural wave speeds. There are two cut-off frequencies for the flexural waves with substrate effect. As k_y increases, the flexural wave group speeds retain the shape as shown in local elasticity and the extra frequency band gap also vanishes. From these results, we can observe that only flexural waves are affected by the substrate whether it is local or nonlocal elasticity.

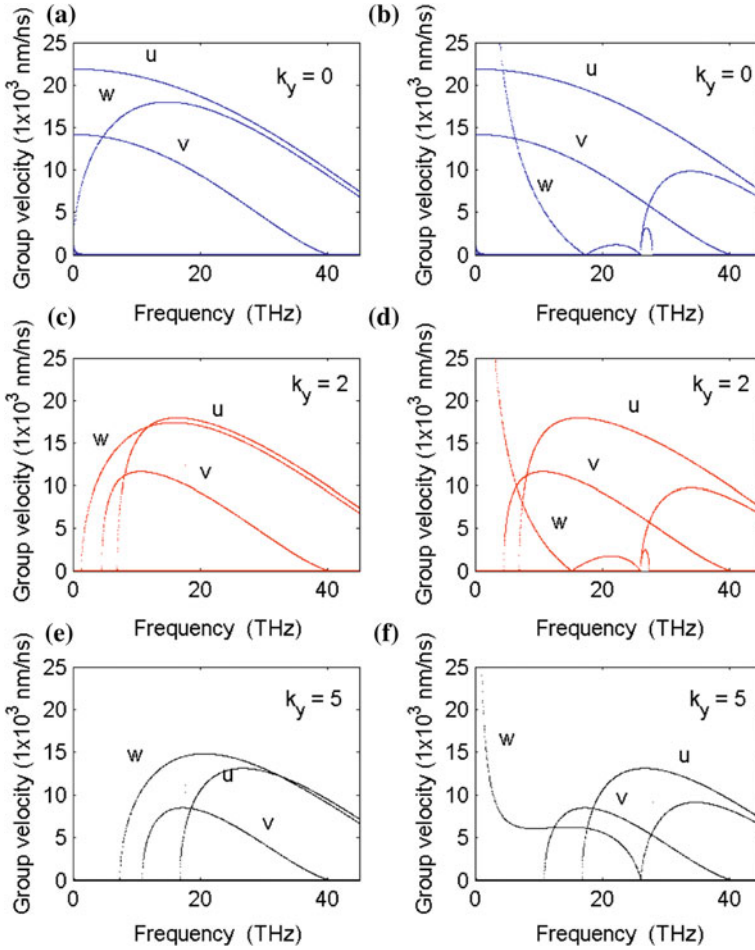


Fig. 10.13 Group speed dispersion of graphene on Si-substrate obtained from nonlocal elasticity theory ($e_0 = 0.39$). Figures (a), (c) and (e) are without substrate (b), (d) and (f) are with substrate. Here y-direction wavenumber assumed as $k_y = 0, 2, \text{ and } 5 \text{ nm}^{-1}$

The variation of the cut-off frequencies of in-plane and flexural waves are shown in Fig. 10.14a, b, without and with substrate effect respectively. Local elasticity (solid lines) shows a linear variation of the cut-off frequencies with wavenumber k_y with and without substrate effects. Nonlocal elasticity (dash lines) predicts smaller values of cut-off frequencies at high values of k_y as compared to local elasticity. Because of the substrate effect at $k_y = 0$, the flexural wave has nonzero cut-off frequency, axial waves have zero cut-off frequency as shown in Fig. 10.14a.

The deformed wave modes of the graphene with and without substrate effect are shown in Figs. 10.15–10.17 at the wave frequencies ω_1, ω_2 and ω_3 as marked in

Fig. 10.14 Variation of cut-off frequency (edge of frequency band gap) for varying wavenumber k_y , $k_x = 0$. Individual branches correspond to inplane modes (u, v) and flexural (w) modes are shown. Both local and nonlocal frequency band gap variations are shown **a** Without silicon substrate **b** With silicon substrate

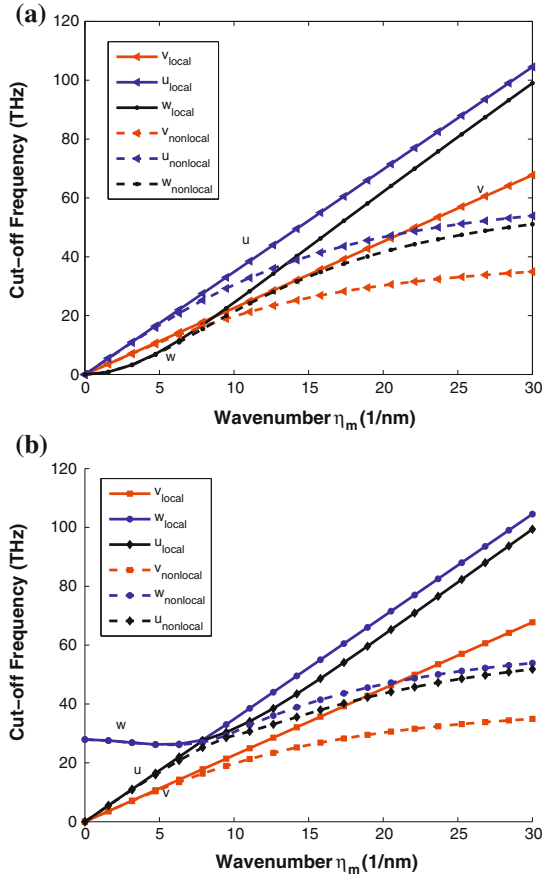


Fig. 10.11. These figures clearly shows the nature of wave propagation in graphene (see Figs. 10.15–10.17). The deformed wave modes is shown for $k_y = 5.0 \text{ nm}^{-1}$.

The contours of k_y versus k_x are shown in Figs. 10.18, 10.19 for local and nonlocal elasticity, respectively, for ω_1 , ω_2 and ω_3 . Because of substrate effect, the flexural wavenumbers are showing a different phenomena for both from local and nonlocal case.

10.4 Temperature Effects on Wave Propagation in Nanoplates

We have seen from the last section that the mono layer graphene, modeled as covlantly bonded honeycomb carbon atoms nanoplates, exhibited some very interesting waveguide properties at very high frequencies in the order of terahertz. In this section,

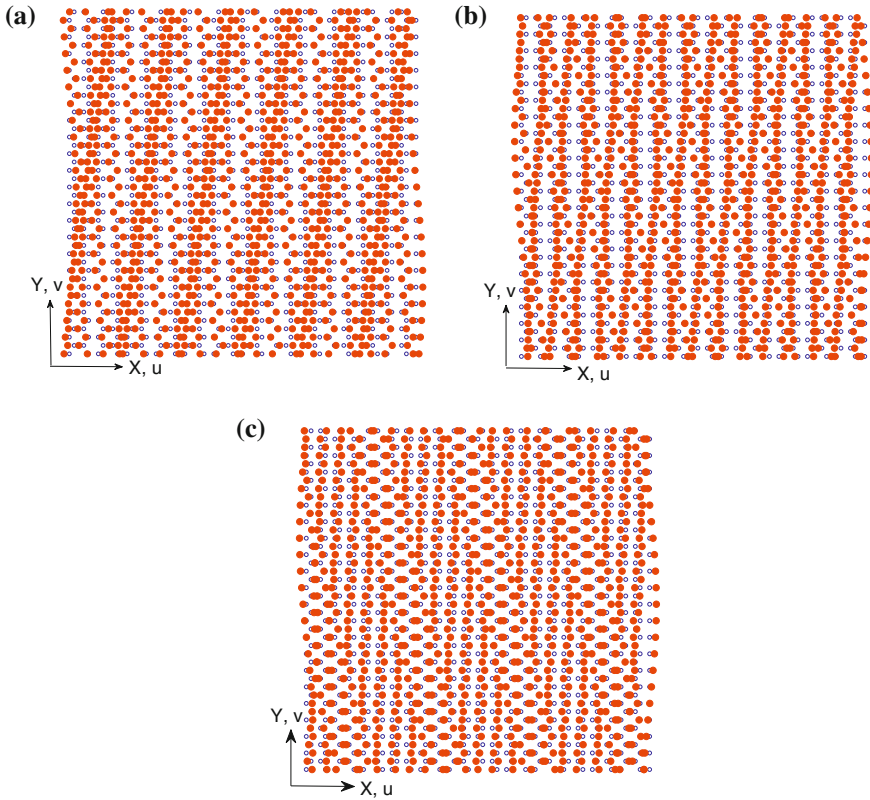


Fig. 10.15 Deformed wave modes in x-direction (u) for **a** $\omega_1 = 10$ THz, **b** $\omega_2 = 25$ THz and **c** $\omega_3 = 35$ THz, as indicated in Fig. 10.11. Blue circles are the initial positions of atoms and the red faced dots are the displaced positions of atoms

we will study the effect of temperature on the wave behavior of a nanoplate. As said before, the work regarding this topic that is reported in the literature is minimal.

Lately, some researches indicated that the thermal effects on the mechanical behaviors of the carbon nanotubes are obvious. Jiang et al. [24] developed a method to determine the thermal expansion coefficient for the nanotubes. In their research, it is concluded that the thermal expansion coefficient is negative for the low or room temperature but positive for the high temperature. Then some works on the mechanical characteristics of the carbon nanotubes with thermal effects are reported in the literature [25, 26]. Recently, Wang et al. [27], studied the thermal effects on the vibration properties of the double-layered nanoplates. They have shown that the vibration properties can be obviously tuned by the thermal effects and the influences on the vibration behaviors are usually different for different modes.

Due to the lack of the study on the ultrasonic wave dispersion properties of the nanoplates, this section is motivated on the use of nonlocal continuum mechanics to

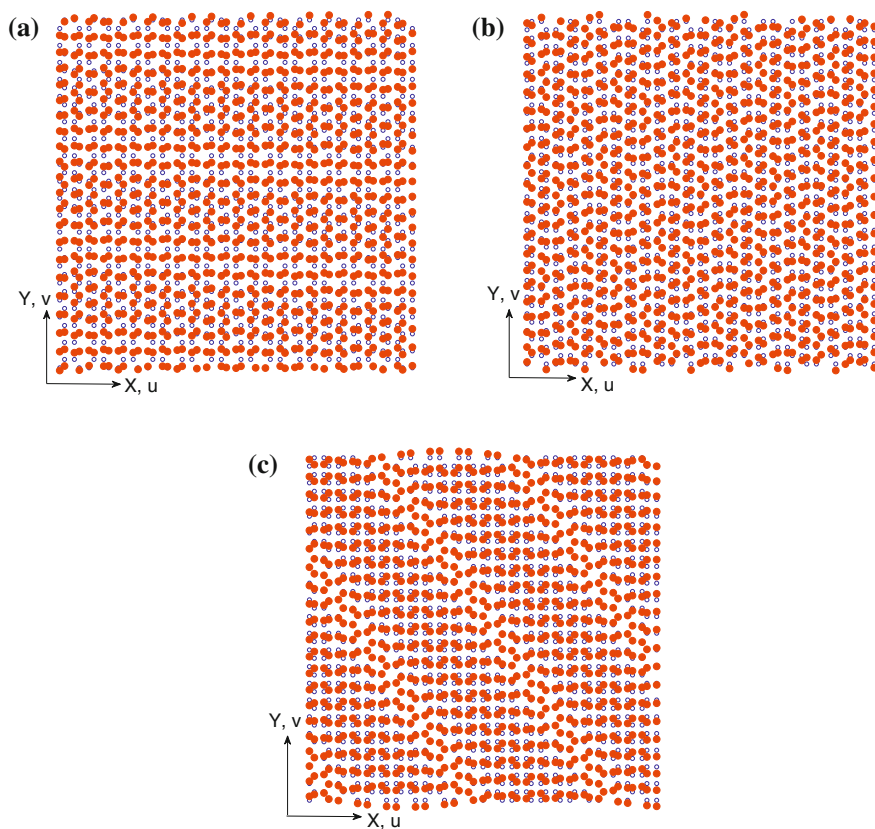


Fig. 10.16 Deformed wave modes in y -direction (v) for **a** $\omega_1 = 10$ THz, **b** $\omega_2 = 25$ THz and **c** $\omega_3 = 35$ THz, as indicated in Fig. 10.11. Blue circles are the initial positions of atoms and the red faced dots are the displaced positions of atoms

study the wave dispersion properties of the nanoplates due to the axial stress caused by thermal effects. The thermal effects and the nonlocal scale influences on the wave dispersion properties are discussed in detail.

10.4.1 Governing Equations of Motion Including Thermal Effects

We have said earlier that the constitutive relation for any nonlocal elastic solid may be simplified to

$$\left(1 - g^2 \nabla^2\right) t_{ij} = c_{ijkl} \varepsilon_{kl} \quad (10.95)$$

where $g = e_0 a$ is the nonlocal scale parameter.

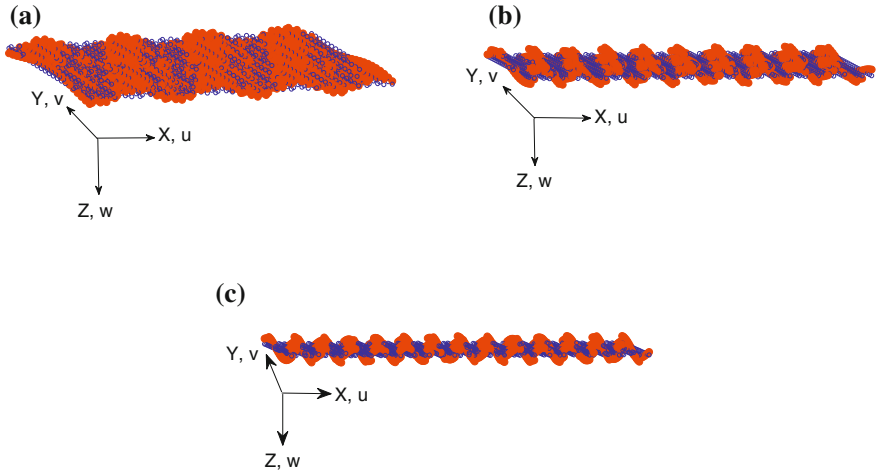


Fig. 10.17 Deformed wave modes in z-direction (flexural - w) for **a** $\omega_1 = 10$ THz, **b** $\omega_2 = 25$ THz and **c** $\omega_3 = 35$ THz, as indicated in Fig. 10.11. Blue circles are the initial positions of atoms and the red faced dots are the displaced positions of atoms

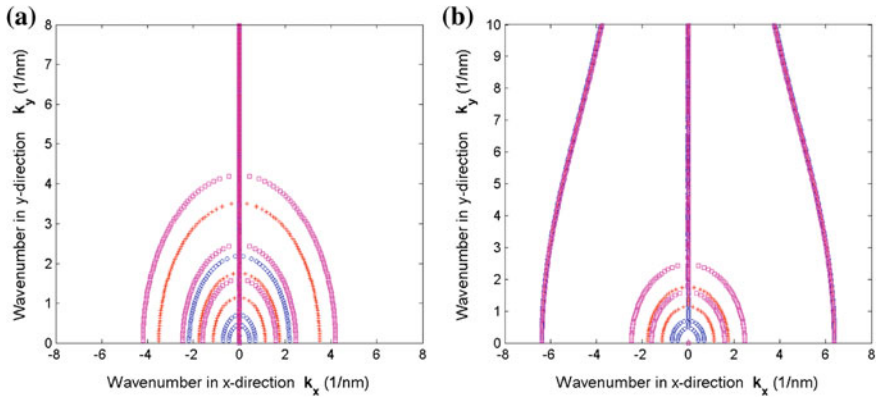


Fig. 10.18 Wavenumber (k_x vs. k_y) contours obtained from local elasticity at wave frequencies of (i) $\omega_1 = 10$ THz (blue o), (ii) $\omega_2 = 25$ THz (red +) and (iii) $\omega_3 = 35$ THz (magenta □) for **(a)** without substrate and **(b)** with substrate

Expanding the terms in the Eq. (10.95), the two-dimensional nonlocal constitutive equation with the partial differential form will be

$$\sigma_{xx} - g^2 \left(\frac{\partial^2 t_{xx}}{\partial x^2} + \frac{\partial^2 t_{xx}}{\partial y^2} \right) = C_{11} \varepsilon_{xx} + C_{12} \varepsilon_{yy} \tag{10.96}$$

$$\sigma_{yy} - g^2 \left(\frac{\partial^2 t_{yy}}{\partial x^2} + \frac{\partial^2 t_{yy}}{\partial y^2} \right) = C_{21} \varepsilon_{xx} + C_{22} \varepsilon_{yy} \tag{10.97}$$

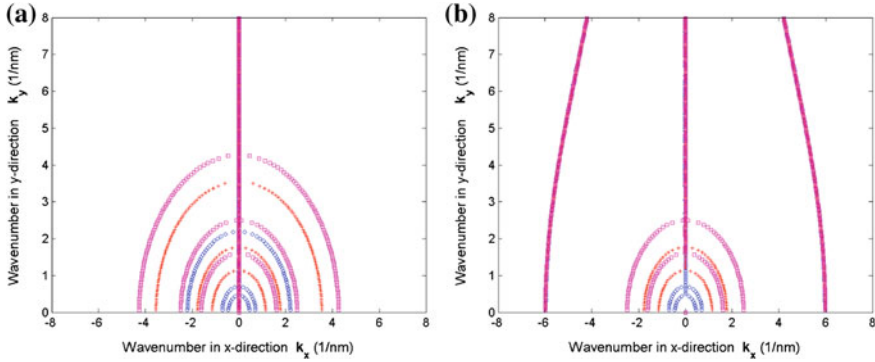


Fig. 10.19 Wavenumber (k_x vs. k_y) contours obtained from nonlocal local elasticity at wave frequencies of (i) $\omega_1 = 10$ THz (blue \circ), (ii) $\omega_2 = 25$ THz (red $+$) and (iii) $\omega_3 = 35$ THz (magenta \square) for (a) without substrate and (b) with substrate

$$\tau_{xy} - g^2 \left(\frac{\partial^2 t_{xy}}{\partial x^2} + \frac{\partial^2 t_{xy}}{\partial y^2} \right) = C_{66} \gamma_{xy} \tag{10.98}$$

where, σ_{xx} and σ_{yy} are the normal stresses in x and y directions respectively and τ_{xy} is the in-plane shear stress. For the case of an isotropic plate, the expressions for C_{ij} in terms of Young’s modulus E and Poisson’s ratio ν are given as $C_{11} = C_{22} = \frac{E}{1-\nu^2}$, $C_{12} = C_{21} = \frac{\nu E}{1-\nu^2}$ and $C_{66} = \frac{E}{2(1+\nu)}$.

The above constitution relations with consideration of thermal effects will be written as

$$\sigma_{xx} - g^2 \left(\frac{\partial^2 t_{xx}}{\partial x^2} + \frac{\partial^2 t_{xx}}{\partial y^2} \right) = C_{11} \varepsilon_{xx} + C_{12} \varepsilon_{yy} - \frac{E \alpha T}{1 - \nu} \tag{10.99}$$

$$\sigma_{yy} - g^2 \left(\frac{\partial^2 t_{yy}}{\partial x^2} + \frac{\partial^2 t_{yy}}{\partial y^2} \right) = C_{21} \varepsilon_{xx} + C_{22} \varepsilon_{yy} - \frac{E \alpha T}{1 - \nu} \tag{10.100}$$

$$\tau_{xy} - g^2 \left(\frac{\partial^2 t_{xy}}{\partial x^2} + \frac{\partial^2 t_{xy}}{\partial y^2} \right) = C_{66} \gamma_{xy} \tag{10.101}$$

where α is the thermal conductivity of the nanoplate and T is the temperature. The vibration equation for the nanoplates is expressed as [28, 29]

$$\frac{\partial^2 M_{xx}}{\partial x^2} + 2 \frac{\partial^2 M_{xy}}{\partial x \partial y} + \frac{\partial^2 M_{yy}}{\partial y^2} + N_{TH} \left(\frac{\partial^2 w}{\partial x^2} + 2 \frac{\partial^2 w}{\partial x \partial y} + \frac{\partial^2 w}{\partial y^2} \right) = \rho h \frac{\partial^2 w}{\partial t^2} \tag{10.102}$$

where w is the deflection, N_{TH} is the thermal stress due to the temperature change, ρ is the mass density, h is the thickness of nanoplate and t is the time.

The bending moment in Eq. (10.102) (i.e. M_{xx} , M_{yy} and M_{xy}) can be given as

$$M_{xx} = \int_{-\frac{h}{2}}^{+\frac{h}{2}} z t_{xx} dz, \quad (10.103)$$

$$M_{xy} = \int_{-\frac{h}{2}}^{+\frac{h}{2}} z t_{xy} dz, \quad (10.104)$$

$$M_{yy} = \int_{-\frac{h}{2}}^{+\frac{h}{2}} z t_{yy} dz \quad (10.105)$$

Based on Eqs. (10.99–10.101) and (10.103–10.105), the bending moments are given as the following form:

$$M_{xx} - g^2 \left(\frac{\partial^2 M_{xx}}{\partial x^2} + \frac{\partial^2 M_{xx}}{\partial y^2} \right) = -D \left(\frac{\partial^2 w}{\partial x^2} + \nu \frac{\partial^2 w}{\partial y^2} \right) - \frac{M_{TH}}{1 - \nu} \quad (10.106)$$

$$M_{xy} - g^2 \left(\frac{\partial^2 M_{xy}}{\partial x^2} + \frac{\partial^2 M_{xy}}{\partial y^2} \right) = -D(1 - \nu) \frac{\partial^2 w}{\partial x \partial y} - \frac{M_{TH}}{1 - \nu} \quad (10.107)$$

$$M_{yy} - g^2 \left(\frac{\partial^2 M_{yy}}{\partial x^2} + \frac{\partial^2 M_{yy}}{\partial y^2} \right) = -D \left(\frac{\partial^2 w}{\partial y^2} + \nu \frac{\partial^2 w}{\partial x^2} \right) \quad (10.108)$$

where $D = Eh^3/[12(1 - \nu^2)]$ is the bending stiffness of the nanoplate and $M_{TH} = \int_{-\frac{h}{2}}^{+\frac{h}{2}} E\alpha T z dz$. Furthermore, the thermal stress can be expressed as

$$N_{TH} = -\frac{E\alpha T}{1 - \nu} \times h \quad (10.109)$$

where α is the thermal expansion coefficient and T the temperature change.

According to Eqs. (10.102), (10.108), and (10.109), we can obtain the nonlocal governing equation for the nanoplate with thermal effects as

$$\begin{aligned} & D \left(\frac{\partial^4 w}{\partial x^4} + 2 \frac{\partial^4 w}{\partial x^2 \partial y^2} + \frac{\partial^4 w}{\partial y^4} \right) - N_{TH} \left(\frac{\partial^2 w}{\partial x^2} + \frac{\partial^2 w}{\partial y^2} \right) \\ & + N_{TH} g^2 \left(\frac{\partial^4 w}{\partial x^4} + 2 \frac{\partial^4 w}{\partial x^2 \partial y^2} + \frac{\partial^4 w}{\partial y^4} \right) + \rho h \frac{\partial^2 w}{\partial t^2} - \rho h g^2 \left(\frac{\partial^4 w}{\partial x^2 \partial t^2} + \frac{\partial^4 w}{\partial y^2 \partial t^2} \right) = 0 \end{aligned} \quad (10.110)$$

10.4.2 Thermo-Elastic Flexural Wave Dispersion Analysis

The wave dispersion formulation begins by assuming a solution of the displacement field. In particular, time harmonic waves are sought and it is assumed that the model is unbounded in Y -direction (although bounded in x -direction). Thus, the assumed

form is a combination of Fourier transform in Y -direction and Fourier transform in time

$$w(x, y, t) = \sum_{n=1}^N \sum_{m=1}^M \hat{w}(x) e^{j\eta_m y} e^{-j\omega_n t}, \quad (10.111)$$

The ω_n and the η_m are the circular frequency at n^{th} sampling point and the wavenumber in y -direction at the m^{th} sampling point, respectively. The N is the index corresponding to the Nyquist frequency in fast Fourier transform (FFT), which is used for computer implementation of the Fourier transform and $j = \sqrt{-1}$. Substituting Eq. (10.111) in Eq. (10.110), an ordinary differential equation is obtained for the unknown $\hat{w}(x)$.

Since the governing equation is having constant coefficients, its solution can be written as $\hat{w}(x) = \tilde{w}e^{jkx}$, where k is the wavenumber in x -direction, yet to be determined and \tilde{w} is an unknown constant. Substituting this assumed form of \hat{w} in the ODE gives for $\tilde{w} \neq 0$

$$T_1 \lambda^2 + T_2 \lambda + T_3 = 0 \quad (10.112)$$

where $T_1 = D + g^2 N_{TH}$, $T_2 = 2\eta_m^2 (D + g^2 N_{TH}) - \rho h \omega^2 g^2 + N_{TH}$, $T_3 = \eta_m^4 (D + g^2 N_{TH}) - \rho h \omega^2 (1 + g^2 \eta_m^2) + N_{TH} \eta_m^2$ and $\lambda = k^2$. We can see clearly that the dependence of nonlocal scale parameter g on wavenumber.

The phase speed of the flexural wave is obtained as

$$C_p = \text{Real} \left(\frac{\omega}{\sqrt{\lambda}} \right) \quad (10.113)$$

The phase speed of the wave will also a function of the nonlocal scaling parameter and the y -directional wavenumber.

The cut-off frequencies of flexural wave mode is obtained by setting $\sqrt{\lambda} = 0$ in the dispersion relation Eq. (10.112) that is, for the present case one can set $T_3 = 0$. The cut-off frequency is obtained as

$$\omega_c = \sqrt{\frac{1}{\rho h} \left(\frac{D\eta_m^2}{1 + (e_0 a)^2 \eta_m^2} + N_{TH} \eta_m^2 \right)} \quad (10.114)$$

The cut-off frequency is directly proportional to the y -directional wavenumber (η_m) and also depends on the nonlocal scaling parameter. For $\eta_m = 0$, the wavenumbers of the flexural wave mode have a substantial real part starting from the zero frequency. This implies that the mode starts propagating at any excitation frequency and does not have a cut-off frequency. For $\eta_m \neq 0$, the flexural wave mode, however, has a certain frequency band within which the corresponding wavenumbers are purely imaginary, where the wave does not propagate. These wavenumbers have a substantial imaginary part along with the real part, thus these waves attenuate as they propagate.

Next, using the derived dispersion Eq. (10.112), the thermal as well as the nonlocal scale effects on the ultrasonic wave dispersion properties of the nanoplates are

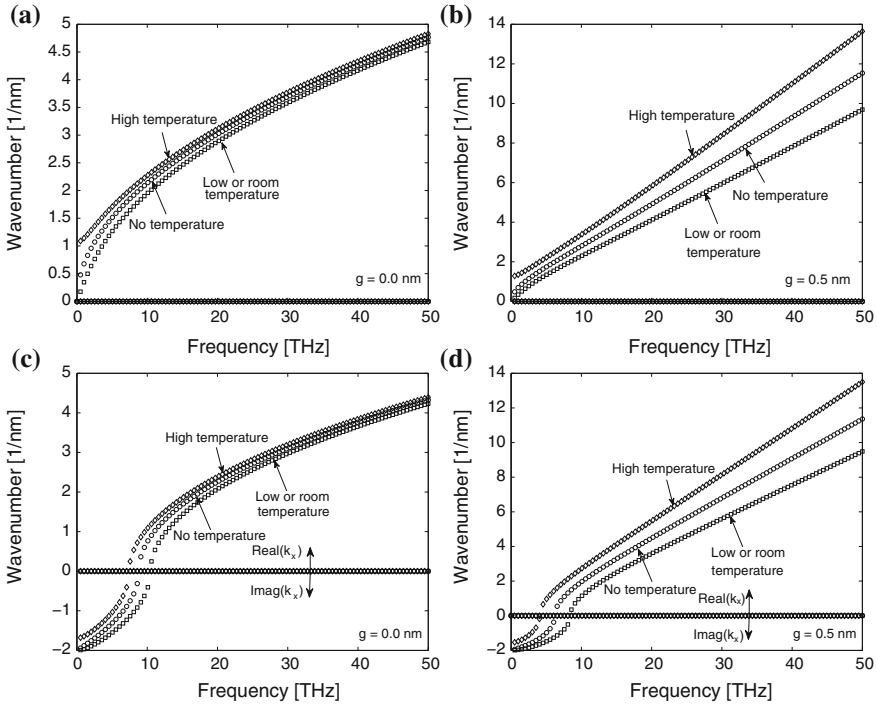


Fig. 10.20 Ultrasonic wave dispersion characteristics of nanoplate: Wavenumber dispersion with frequency obtained from **a** local elasticity (for $\eta_m = 0$), **b** nonlocal elasticity (for $\eta_m = 0$), **c** local elasticity (for $\eta_m = 2 \text{ nm}^{-1}$) and **d** nonlocal elasticity (for $\eta_m = 2 \text{ nm}^{-1}$). Here η_m is the axial half wavenumber in y -direction

studied. The material constants for the nanoplate assumed are the Young’s modulus $E = 1.06 \text{ TPa}$, the mass density $\rho = 2250 \text{ kg/m}^3$ and the Poisson’s ratio $\nu = 0.25$. The room or low temperature (i.e., thermal conductivity $\alpha = -1.6 \times 10^{-6} \text{ K}^{-1}$) and high temperature (i.e., thermal conductivity $\alpha = 1.1 \times 10^{-6} \text{ K}^{-1}$) used for the nanostructures are considered [30, 31]. The temperature change is assumed in the range of $T = 0$ to 90 K .

The flexural wavenumber dispersion with wave frequency is shown in Fig. 10.20, obtained from both local and nonlocal elasticity theories. The figure also shows the effects of the low and high temperature on the flexural wavenumber in nanoplate. For the present analysis, the nonlocal scaling parameter is assumed as $e_0a = 0, 0.5 \text{ nm}$. The spectrum curves shown in Fig. 10.20a, b are for $\eta_m = 0$ (represents 1D wave propagation), Fig. 10.20c, d are for $\eta_m = 2 \text{ nm}^{-1}$. The local elasticity calculation shows that the flexural wavenumber follow a nonlinear variation at lower values of wave frequency; and at higher frequencies it varies linearly as shown in Fig. 10.20. For $\eta_m = 0$, the wavenumbers of the flexural wave mode have a substantial real part starting from the zero frequency. As η_m increases, all the waves are still dispersive in

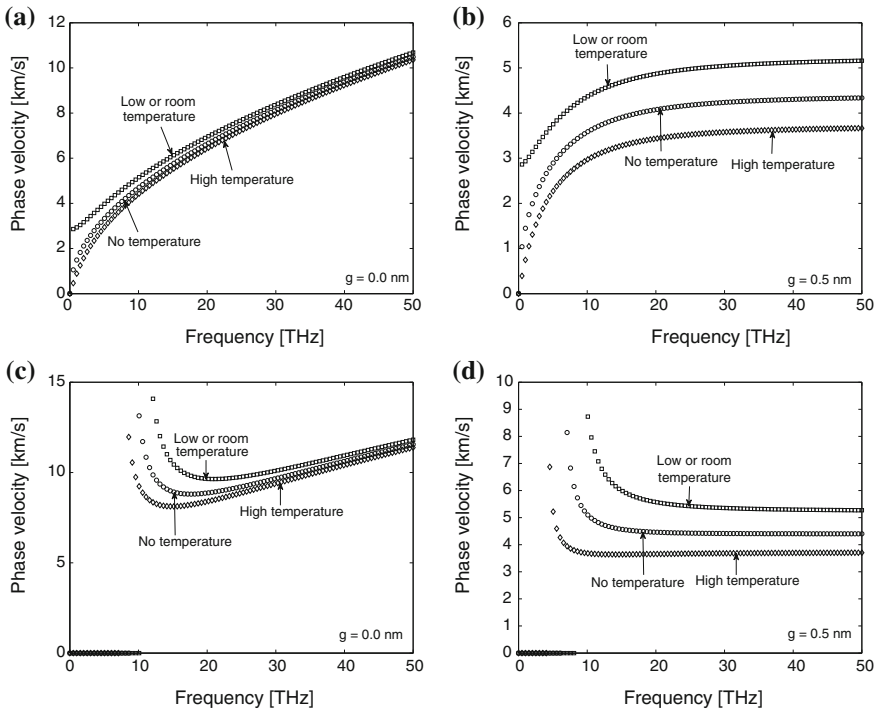


Fig. 10.21 Ultrasonic wave dispersion characteristics of nanoplate: Phase speed dispersion with frequency obtained from **a** local elasticity (for $\eta_m = 0$), **b** nonlocal elasticity (for $\eta_m = 0$), **c** local elasticity (for $\eta_m = 2 \text{ nm}^{-1}$) and **d** nonlocal elasticity (for $\eta_m = 2 \text{ nm}^{-1}$). Here η_m is the axial half wavenumber in y -direction

nature as shown in Fig. 10.20c, d. As the y -directional wavenumber increases from 0 to 2 nm^{-1} , the wave modes exhibit a frequency band gap region. The frequency band within which the corresponding wavenumbers are purely imaginary. Thus, the flexural mode does not propagate at frequencies lying within this band. Hence, these wavenumbers have a substantial imaginary part along with the real part, thus these waves attenuate as they propagate. It can also be seen that from Fig. 10.21, the frequency band also increases with increase in η_m .

The effect of temperature on the flexural waves in nanoplate are also significant (see Fig. 10.20). The magnitude of the flexural wavenumber will be higher in the case of higher temperature as compared to the low or room temperature. The temperature plays an important on the frequency band gap of the flexural wave mode. As the temperature increases for lower values to higher, the magnitude of the frequency band gap of the flexural waves decreases as shown in Fig. 10.20c, d. Due to nonlocality, the flexural wavenumber variation become highly linear over a range of frequencies as shown in Fig. 10.20b, d. The linear variation of the wavenumber with frequency is mainly due to the consideration of atom-atom interaction at nanoscale level based on

nonlocal elasticity. The local elasticity calculations show that, at higher frequencies the effect of temperature on the wavenumbers is not significant (see Fig. 10.20a, c). However, nonlocal elasticity calculations show that, the temperature effect will be more significant on the wavenumber at higher frequencies (see Fig. 10.20b, d). Hence, the results show that one has to consider the effect of temperature at higher frequency analysis.

The effect of the nonlocal scale parameter and the lower and higher temperatures on the wave speed are captured in Fig. 10.21. It shows that the flexural wave speeds are increasing from low frequency to higher values of wave frequency (local elasticity calculation, $e_0a = 0$). As we move to nonlocality ($e_0a \neq 0$), the flexural wave speed becomes constant at higher values of frequency as shown in Fig. 10.21b, d, which is due to the linear variation of the wavenumber with frequency. It can also be observed that, the magnitude of phase speed is higher for the case of low temperature as compared to the higher temperatures. Over a given frequency range, the magnitude of the wave speed predicted by the nonlocal elasticity is small as compared to the local elasticity calculations.

The variation of cut-off frequency with respect to y -directional wavenumber is shown in Fig. 10.22. The effect of nonlocal scale parameter on the cut-off frequency is shown in Fig. 10.22a, for zero temperature case. It can be seen that as the nonlocal scale parameter increases, the cut-off frequency decreases over the given range of the y -directional wavenumber. It means that, the classical elasticity predicts the over estimated values for the cut-off frequency. The effect of the lower and higher temperatures on the cut-off frequency are shown in Fig. 10.22b. For high temperature case, the cut-off frequencies are smaller and this become significant as the nonlocal scale coefficient increases. The cut-off frequency difference between low and high temperature will increase as the y -directional wavenumber increases (see Fig. 10.22b). At higher modenumbers, the temperature effect on the cut-off frequency is very significant and cannot be omitted. The effect of various temperatures on the flexural

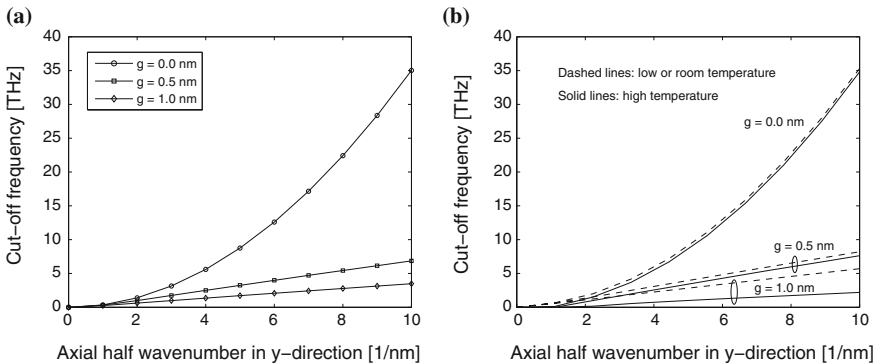


Fig. 10.22 Cut-off frequency variation with axial half wavenumber in y -direction for various nonlocal scaling parameters: **a** the effect of zero temperature and **b** the effect of low and high temperature

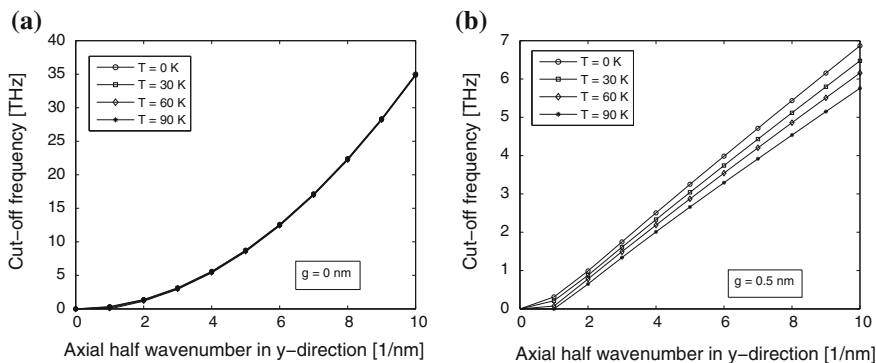


Fig. 10.23 Cut-off frequency variation with axial half wavenumber in y -direction for various temperatures obtained from (a) local/classical elasticity theory and (b) nonlocal elasticity theory

wave cut-off frequency are shown in Fig. 10.22. Here temperature range is assumed between 0 – 90 K. The local/classical elasticity calculations show that, the cut-off frequency will not change with temperature (Fig. 10.23a). The nonlocal calculations show that, the magnitude of the cut-off frequency will decrease with the increase in temperature (Fig. 10.23b). Over a given wavenumber range, the cut-off frequency predicted by the nonlocal elasticity are smaller than that of the classical elasticity.

10.5 Surface Effects on Wave Propagation in Nanoplates

We have seen in the previous chapter on nanobeams, the surface effects had pronounced effect on the wave dispersion. In this section, we will explore its effects on the ultrasonic wave behavior in nanoplates. In macroscopic and even microscopic structural elements, such as beams and plates, surface effects can be neglected and classical theories [32] are sufficient. As the structural size decreases toward the nanoscale regime, the surface-to-bulk energy ratio increases and surface effects must be taken into account. It is a well-known fact that the classical continuum theory does not take into account the so-called size effect.

Some of the work reported on surface effects are summarized below. Gurtin and Murdoch [33] developed a mathematical framework for elastic material surfaces for calculation of surface parameters of nanomaterials. In another work, Shenoy [34] used an atomistic calculation approach based on crystals lattice energies to characterize the nanosurface effects. Many other attempts have also been made to describe both static and dynamic behavior of nanoscale structure with consideration of surface effects [35–37].

Propagation of surface and bulk waves in the presence of surface elasticity has profound importance in the area of thin film applications, for example, microelectronic and micro-electro-mechanical systems. The widespread application of micro

and nanostructured thin film materials has resulted in the need for advanced measurement techniques to characterize their mechanical properties. Both bulk waves and Lamb waves can be used for this purpose [38]. However, the excitation frequency in these applications is on the order of GHz-THz and as a result the wavelengths are comparable to the film thickness or even smaller.

An important area of nanotechnology where surface effects are very important, and that has received increasing interests in recent years is the design and fabrication of nanomechanical and nanoelectromechanical systems. These are devices integrating electrical and mechanical functionality at nanoscale. In this regime, NEMS offer a number of unique attributes such as small size, low mass, high mechanical resonance frequencies, and high sensitivity. Application of NEMS includes actuators, sensors, machines and electronics at nanoscales [39]. NEMS can be used to measure extremely small displacements and forces that lead to new developments for applications in medicine, computers, communications, etc. The principal components of NEMS are mechanical elements that either deflect or vibrate in response to the external excitations, and a transducer that can convert mechanical energy to electrical or optical signals. Nanostructures such as nanobeams, nanoplates, and nanomembranes are the common components of NEMS mechanical parts, while the electrical parts are accounted through the surface effects. Structural integrity, reliability, and durability of NEMS are important issues in practical applications. Therefore, understanding the mechanical properties, response, and stability of NEMS structural elements is crucial to the exploitation of NEMS technology.

Due to the surface energy effects at nanoscale, the investigation of the mechanical behavior of nanostructures with surface energy effects remains a topic of substantial interest. Lagowski et al. [40] carried out an experiment to measure the natural frequencies of GaAs wafers in the configuration of cantilever beams within a small-scale region. They found that the natural frequencies substantially depend on the surface stress, which cannot be explained by classical theory of vibration. To investigate this experimental phenomenon, Gurtin et al. [41] developed a simple one-dimensional beam model to illustrate that the beam resonant frequency is independent of the surface stress and therefore the experimental results require a different explanation. Wang and Feng [42] developed a sandwich-beam model to study the effects of surface elasticity and surface tension on the natural frequencies of micro or nanosized beams and revealed that when the thickness of beams reduces to microns or nanometers, both the surface elasticity and surface tension have significant effects on its vibration frequency. Yang et al. [43] and Ekinci and Roukes [44] have fabricated nanometer scale electromechanical beam resonators and examined their response experimentally. Wang et al. [45] studied the surface buckling of a microbeam due to surface energy effects. Sadeghian et al. [46] studied the effects of surface stress on resonance frequency of nanocantilevers. Recently, Lachut and Sader [47] proposed a three-dimensional model to examine the surface stress effects on the stiffness of cantilever plates. Lim and He [48] analyzed the deformations of nanofilms under bending by incorporating the surface elasticity effects into Von Karman plate theory. Lu et al. [49] complemented Lim and He's model [50] by considering the normal stress variation along the thickness direction and presented a general model for static

and dynamic analysis of thin film structures. He and Lilley [51], [52] studied the surface energy effects on static bending and bending resonance of nanowires with different boundary conditions.

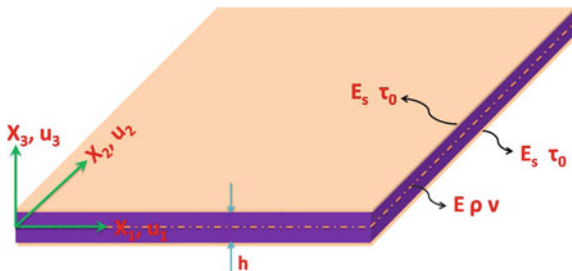
Based on the above introduction and literature survey, it can be seen that understanding the size-dependent behavior of beam-like structures at nanoscale is essential for effective NEMS design. The nonlocal continuum modeling approach accounting for surface energy effects is considered to be attractive due to its simplicity and computational efficiency. In this section, we study the surface effects on the wave behavior of nanoplates. Again using the spectral analysis, several interesting wave propagation properties are captured in this study.

10.6 Mathematical Modeling of Nanoplate with the Surface Effects

The present surface effect model of a nanoplate is the extension of the beam model presented in Chap. 7. That is, the surface effect model consists of a heterogeneous nanoplate composed of three layers: a *bulk layer* (middle) and two finite thickness *surface layers* (upper and lower). The geometry of the nanoplate with degree of freedom and its elastic properties (E , ν and ρ) are illustrated in Fig. 10.24. The elastic properties of the bulk part are E , ν , ρ which are, respectively, its elasticity modulus, Poisson’s ratio, and mass density. To simulate the upper and lower surface effects, two thin layers with surface elasticity modulus of E_u , E_l , respectively are considered. Thickness of the surface layers are taken as h_u and h_l for upper and lower layers. Surface residual stress is shown by τ_0 while $\tilde{Q}(x)$ indicates the transverse distributed loading induced by the residual surface tension. In order to deal with the problem of zero thickness of surface layers, the model is idealized to possess the property of $E_u h_u$ and $E_l h_l$ of a constant magnitude equal to E_s as a material property. Surface residual stress effects, which act due to transverse loads can be calculated by Laplace Young equations. Stress jump across each surface [53] is related to the curvature tensor by

$$\langle \sigma_{ij}^+ - \sigma_{ij}^- \rangle n_i n_j = \sigma_{\alpha\beta}^s \kappa_{\alpha\beta} \tag{10.115}$$

Fig. 10.24 Configuration of nanoplate (material properties: Young’s modulus E , Poisson’s ratio ν and density ρ) with two thin surface layers of surface elasticity modulus E_s and surface residual stress τ_0



where κ is the surface curvature describing both the singly- and doubly-curved surfaces. In addition, $\sigma_{\alpha\beta}^s$ stands for surface stresses ($\alpha, \beta = 1, 2$) with n_i being the components of the surface unit normal vector where $i = 1, 2, 3$. Thus, Laplace-Young equation below describes the transverse load on the plate undergoing lateral displacement

$$\tilde{Q}(x_1, x_2) = 2\tau_0 \nabla^2 u_3 \quad (10.116)$$

In the above equations, $u_3 = u_3(x_1, x_2)$ represents transverse displacement along x_3 axis. As mentioned earlier in this investigation, Kirchhoff plate theory is modified to include surface effect parameters. To derive the fundamental equation of motion of nanoplates, principle of virtual work is applied. As the first step, the surface potential energy Π_{pe}^S can be expressed as

$$\Pi_{pe}^S = \tilde{Q}(x_1, x_2) \times u_3(x_1, x_2) = 2\tau_0 u_3 \nabla^2 u_3 \quad (10.117)$$

The constitutive relation is obtained from nonlocal elasticity to capture the nanoscale size effects. The nonlocal constitutive relation is written as

$$\left(1 - \vartheta^2 \nabla^2\right) t_{ij} = c_{ijkl} \varepsilon_{kl} \quad (10.118)$$

where $\vartheta = e_0 a$, which is same as g used in the earlier chapters and a is an internal characteristic length (lattice parameter, granular size, or molecular diameters) and e_0 is a constant appropriate to each material for adjusting the model to match some reliable results by experiments or other theories.

Using all the appropriate assumptions and nonlocal constitutive relation, the nonlocal governing differential equation of wave propagation of the nanoplate with consideration of scale effects is given by

$$z_1 \nabla^4 u_3 + z_2 \ddot{u}_3 - z_2 \vartheta^2 \nabla^2 \ddot{u}_3 - z_3 \nabla^2 \ddot{u}_3 + z_3 \vartheta^2 \nabla^4 \ddot{u}_3 - \tilde{Q} + \vartheta^2 \nabla^2 \tilde{Q} = 0 \quad (10.119)$$

where $\nabla^2 = \partial^2/\partial x_1^2 + \partial^2/\partial x_2^2$. The parameters involved in the above governing equation are described as follows

$$z_1 = \frac{E_s h^2}{2(1 - \nu^2)} + \frac{E h^3}{12(1 - \nu^2)} = D \left(1 + \frac{6 E_s}{h E}\right), \quad (10.120)$$

$$z_2 = \rho h, \quad (10.121)$$

$$z_3 = \frac{\rho h^3}{12} \quad (10.122)$$

where D is the flexural rigidity of the nanoplate.

10.6.1 Dispersion Characteristics

For a harmonic wave propagation in a nanoplate, the displacement field can be written in complex form as

$$u_3(x_1, x_2, t) = \sum_{n=1}^N \sum_{m=1}^M \hat{u}_3(x_1) e^{-jk_{2m}x_2} e^{j\omega_n t}, \quad (10.123)$$

The ω_n and the k_{2m} are the circular frequency at n^{th} sampling point and the wavenumber in x_2 -direction at the m^{th} sampling point, respectively.

Substituting Eq. (10.123) in Eq. (10.119), an ordinary differential equation is obtained for the unknown $\hat{u}_3(x_1)$. Since this ODE will have constant coefficients, its solution can be written as $\hat{u}_3(x_1) = \tilde{u}_3 e^{jk_1 x_1}$, where k_1 is the wavenumber in x_1 -direction, yet to be determined and \tilde{u}_3 is an unknown constant. Substituting this assumed form of \hat{u}_3 in the ODE and assuming $\tilde{u}_3 \neq 0$ gives

$$H_4 k_1^4 + H_2 k_1^2 + H_0 = 0 \quad (10.124)$$

where

$$H_4 = z_1 + 2\tau_0 \vartheta^2 - z_3 \vartheta^2 \omega^2, \quad (10.125)$$

$$H_2 = 2z_1 k_2^2 + (2\tau_0 - z_3 \omega^2)(1 + 2\vartheta^2 k_2^2) - z_2 2\tau_0 \omega^2, \quad (10.126)$$

$$H_0 = z_1 k_2^4 + (2\tau_0 k_2^2 - z_2 \omega^2 - z_3 \omega^2 k_2^2)(1 + \vartheta^2 k_2^2). \quad (10.127)$$

Note that the subscript m is dropped from the y directional wave number for convenient notation. The wavenumber is a function of wave frequency, the nonlocal scaling parameter g , the x_2 -directional wavenumber, and the material properties (E & ρ) of the nanorod as well as the surface properties. Equation (10.124) is solved to obtain x directional wavenumber as a function of nonlocal scale parameter g , surface effect parameter τ_0 , and the y directional wavenumber η_m .

Next, we will compute the wave speeds, namely the phase and group speeds, with the usual expressions. These wave speeds, it will be seen, also depend on the nonlocal scaling parameter, the x_2 -directional wavenumber and material properties of the surface layer and nanoplate. These expressions are quite long and hence the explicit expressions are not given here. These can be easily computed from the wavenumber equation Eq. (10.124).

The cut-off frequencies of flexural wave mode is obtained by setting $k_1 = 0$ in the dispersion relation Eq. (10.124) that is, for the present case one can set $H_0 = 0$. The cut-off frequency is obtained as

$$\omega_{cut} = k_2 \sqrt{\frac{\frac{z_1 k_2^2}{1 + \vartheta^2 k_2^2} + 2\tau_0}{z_2 + z_3 k_2^2}} \quad (10.128)$$

The cut-off frequency is directly proportional to the x_2 -directional wavenumber (k_2) and also depends on the nonlocal scaling parameter and material properties of the surface layer and nanoplate. For $k_2 = 0$, the wavenumbers of the flexural wave mode have a substantial real part starting from the zero frequency.

Next, we will examine the existence of escape frequency, which is one of the fundamental property of the system modeled by nonlocal elasticity. Its value can be analytically determined by looking at the wavenumber expression and setting $k_1 \rightarrow \infty$. This amounts to setting the $H_4 = 0$, which gives

$$\omega_{escape} = \frac{1}{\vartheta} \sqrt{\frac{z_1 + 2\tau_0 \vartheta^2}{z_3}} \quad (10.129)$$

It can be seen that the escape frequency of the flexural wavemode is highly dependent on both the nonlocal scale parameter and the surface stress.

Next, the scale-dependent wave propagation characteristics of a nanoplate is studied through illustrative plots. We consider the material properties of an anodic alumina with crystallographic orientation in $\langle 111 \rangle$ direction (obtained from Ref. [54, 55]) as follows: $E = 70$ GPa, $\rho = 2700$ kg/m³, $E_s = 5.1882$ N/m, $\tau_0 = 0.9108$ N/m.

A comparison of dispersion relations of a graphene sheet (nanoplate) with a size of 3.62 nm \times 15.03 nm obtained from molecular dynamics (MD) simulations [56], the nonlocal finite element plate model [56], and the present nonlocal model is shown in Fig. 10.25. All these simulations are done without considering the surface effects. It can be seen that the present model results matches with the MD simulation results for a nonlocal scale parameter values of 0.15 nm. It can be observed that the phase speed increases with the wavenumber in this nanoplate.

The effect of the surface properties on the flexural wavenumber dispersion with wave frequency in the nanoplate is shown in Fig. 10.26, obtained from both local and nonlocal elasticity theories. For the present analysis, the nonlocal scaling parameter is assumed as $\vartheta = 0.5 \times 10^{-9}$ m. The spectrum curves shown in Fig. 10.26 is plotted for the case of $k_2 = 0$ (represents 1D wave propagation). The local elasticity calculation (Fig. 10.26a) shows that the flexural wavenumber follows a nonlinear variation at low values of wave frequency; and at higher frequencies it varies linearly. It is clear that, in the presence of the surface effects, the wavenumber will decrease compared to the surface stress-free case. It means that the surface properties are significant at nanoscale and cannot be neglected. For $k_2 = 0$, the wavenumbers of the flexural wave mode have a substantial real part starting from the zero frequency.

The wavenumber dispersion with frequency obtained from nonlocal elasticity ($\vartheta = 0.5 \times 10^{-9}$ m) is shown in Fig. 10.27b. The observations made in local elasticity are also valid for nonlocal elasticity case. The only difference is that, because of nonlocal elasticity, the wavenumbers of the flexural wave become highly nonlinear

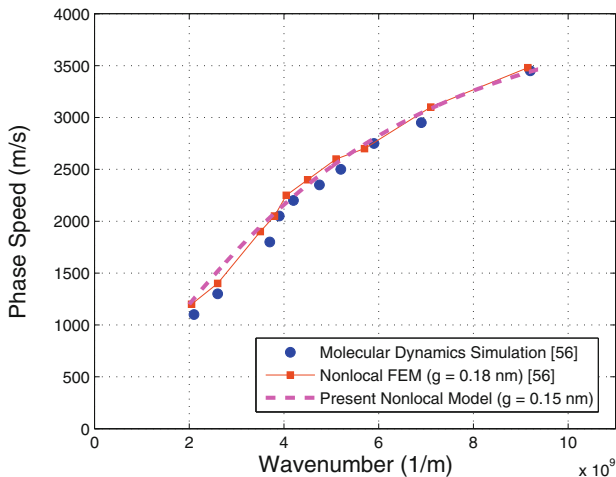


Fig. 10.25 Comparison of dispersion relations of a graphene sheet as nanoplate with a size of 3.62 nm × 15.03 nm obtained from MD simulations, the nonlocal finite element plate model, and the present nonlocal model. All these simulations are done without considering the surface effects

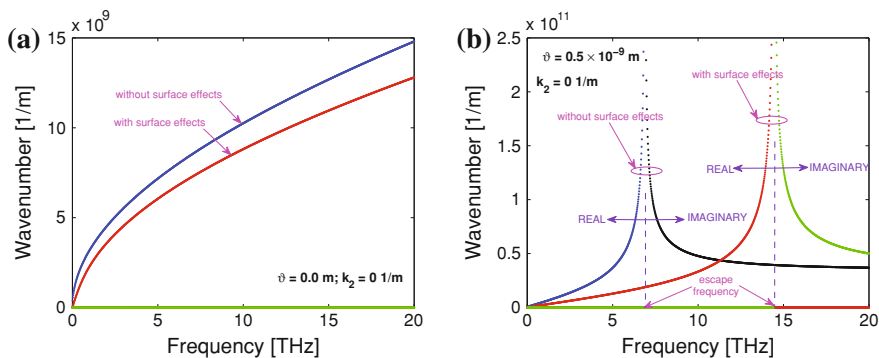


Fig. 10.26 The effect of surface effects on wavenumber dispersion with wave frequency in nanoplate obtained from (a) local elasticity and (b) nonlocal elasticity, for $k_2 = 0$

and tend to infinity at escape frequency. It can be seen that the wavenumbers before escape frequency are real and after that it is imaginary (see Fig. 10.27b). In the presence of surface effects, the escape frequencies are higher. This means that, in the presence of surface effects, the flexural wave will propagate to higher frequencies as compared to stress-free surface case (see Fig. 10.27b).

The effect of surface properties on corresponding phase speed and group speed dispersions with the wave frequency are shown in Figs. 10.28 and 10.29, respectively, obtained from local and nonlocal elasticity. Figure 10.28 shows that the flexural wave speeds are increasing from lower frequency to higher values of wave frequency (local elasticity calculation, $\vartheta = 0$). The surface stress will increase the flexural

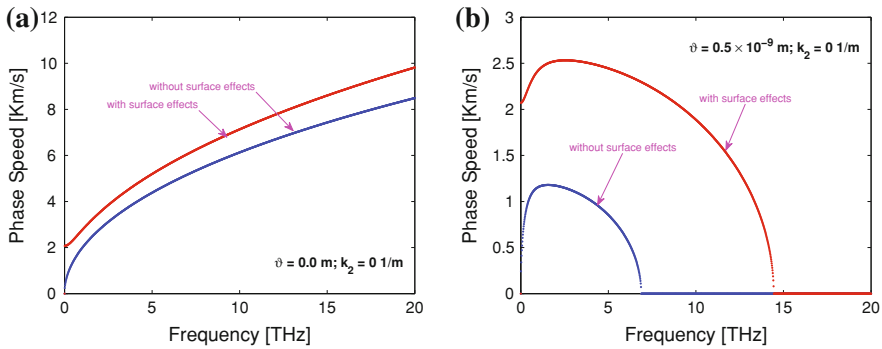


Fig. 10.27 The effect of surface effects on phase speed variation with wave frequency in nanoplate obtained from (a) local elasticity and (b) nonlocal elasticity, for $k_2 = 0$

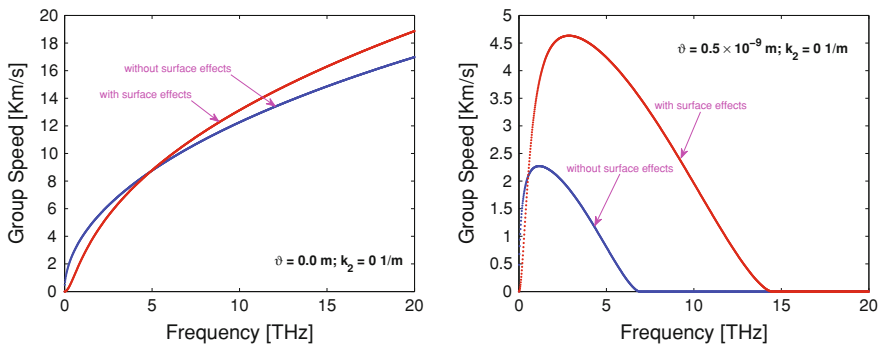


Fig. 10.28 The effect of surface effects on group speed variation with wave frequency in nanoplate obtained from (a) local elasticity and (b) nonlocal elasticity, for $k_2 = 0$

wave phase and group velocities (see Fig. 10.28, 10.29). As we move to nonlocality ($\vartheta \neq 0$), the flexural wave stops propagating as before at escape frequency as shown in Figs. 10.28a and 10.29a. The local elasticity calculation shows that the phase and group speed of the wave will be nonzero even at higher values of the frequency (Figs. 10.28a and 10.29a), and it is zero at escape frequency (Figs. 10.28b and 10.29b) in the nonlocal elasticity case. The magnitude of the phase and group speed will increase in the presence of the surface effects.

The effect of the surface properties and the x_2 direction half wavenumber k_2 on the wave propagation properties of the nanoplate are shown in Figs. 10.30, 10.31, and 10.32. For the present analysis k_2 is assumed as $2 \times 10^9 \text{ m}^{-1}$. As k_2 increases from 0 to $2 \times 10^9 \text{ m}^{-1}$, the flexural waves are still dispersive in nature as shown in Fig. 10.30. As the x_2 -directional wavenumber increases, the wave modes are having a frequency band gap region. The frequency band within which the corresponding wavenumbers are purely imaginary. Thus, the flexural mode does not propagate at frequencies lying within this band. It can also be seen that from Fig. 10.30, the frequency band also

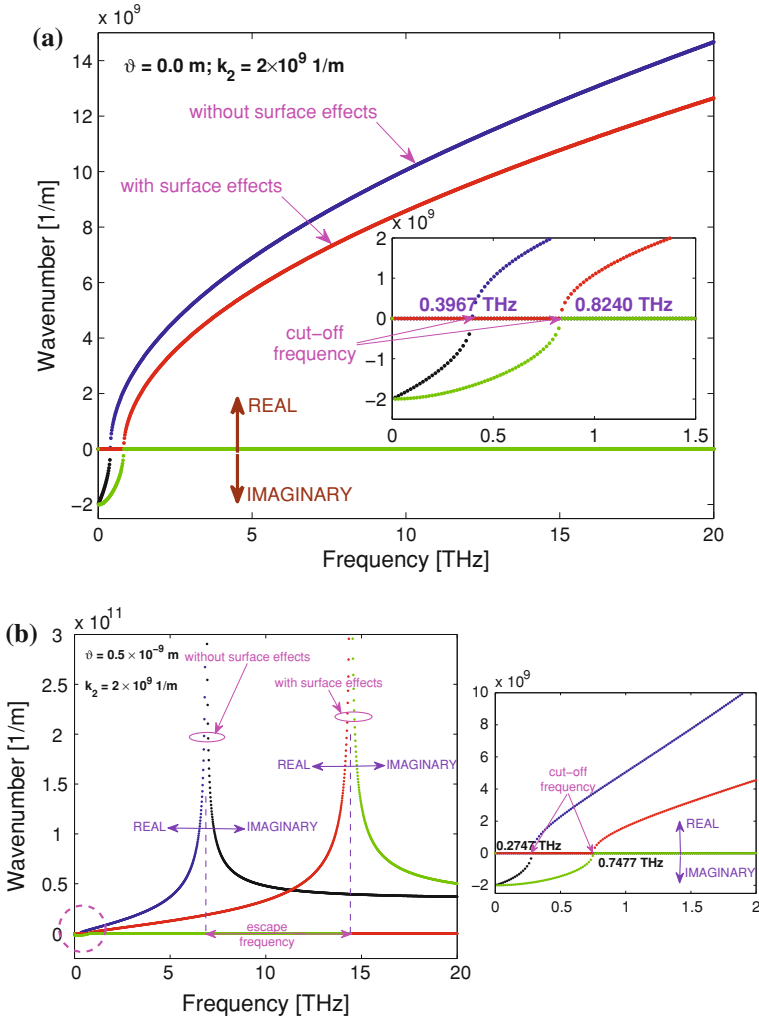


Fig. 10.29 The effect of surface effects on wavenumber dispersion with wave frequency in nanoplate obtained from (a) local elasticity and (b) nonlocal elasticity, for $k_2 = 2 \times 10^9 \text{ 1/m}$

increase with increase in k_2 . The effects observed in Fig. 10.27 are still valid for this case also. The surface effects will increase the cut-off and escape frequencies of the flexural wave as shown in Fig. 10.30a, b. It can also be observed that the cut-off frequencies will decrease with an increase in scale parameter (observe inset figures of Fig. 10.30). It means that, the nonlocal scale highly affects the frequency band gap of the flexural waves in nanoplate. It has also been observed that the escape frequencies are independent of k_2 from Figs. 10.30 to 10.32.

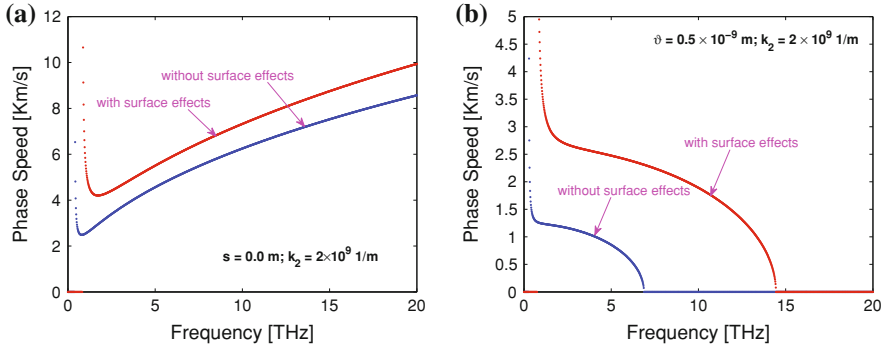


Fig. 10.30 The effect of surface effects on phase speed variation with wave frequency in nanoplate obtained from (a) local elasticity and (b) nonlocal elasticity, for $k_2 = 2 \times 10^9$ 1/m

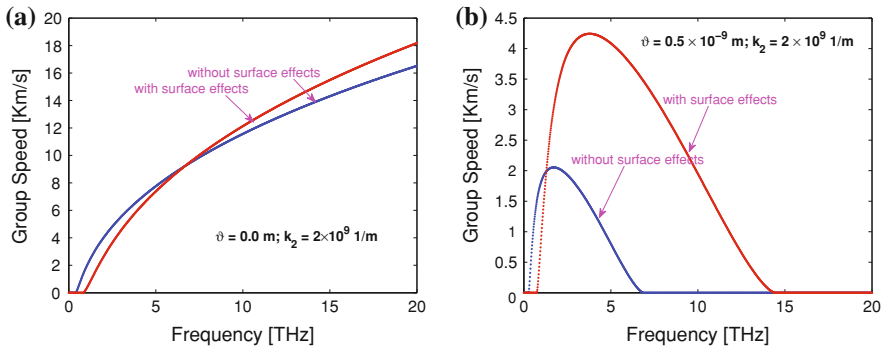


Fig. 10.31 The effect of surface effects on group speed variation with wave frequency in nanoplate obtained from (a) local elasticity and (b) nonlocal elasticity, for $k_2 = 2 \times 10^9$ 1/m

As we move to nonlocality ($\vartheta \neq 0$), the flexural wave stops propagating at escape frequency as shown in Figs. 10.30 and 10.31. For any value of the k_2 , the escape frequency of all flexural waves is same. The local elasticity calculation shows that the wave speeds of the flexural wave will be nonzero even at higher values of the frequency (Figs. 10.30a and 10.31a), and it is zero at escape frequency (Figs. 10.30b and 10.31b) in the nonlocal elasticity case. The magnitude of the group speed is decreasing with an increase in the k_2 (see Figs. 10.29 and 10.32 a). In the presence of the surface effects, the wave speeds increase drastically. The local/classical elasticity calculation shows that, the wave will propagate even at higher frequencies.

The variation of the cut-off frequency of flexural wave with nonlocal scaling parameter and x_2 -directional wavenumber (k_2) are shown in Figs. 10.32, 10.33, respectively. The cut-off frequency variation shown in Fig. 10.32b is for $k_2 = 1 \times 10^9$, 2×10^9 and 3×10^9 m^{-1} . It shows that for a given k_2 , as we increase the nonlocal scaling parameter the cut-off frequency of flexural wave mode decreases. The surface effects increase the cut-off frequencies of the flexural wave drastically

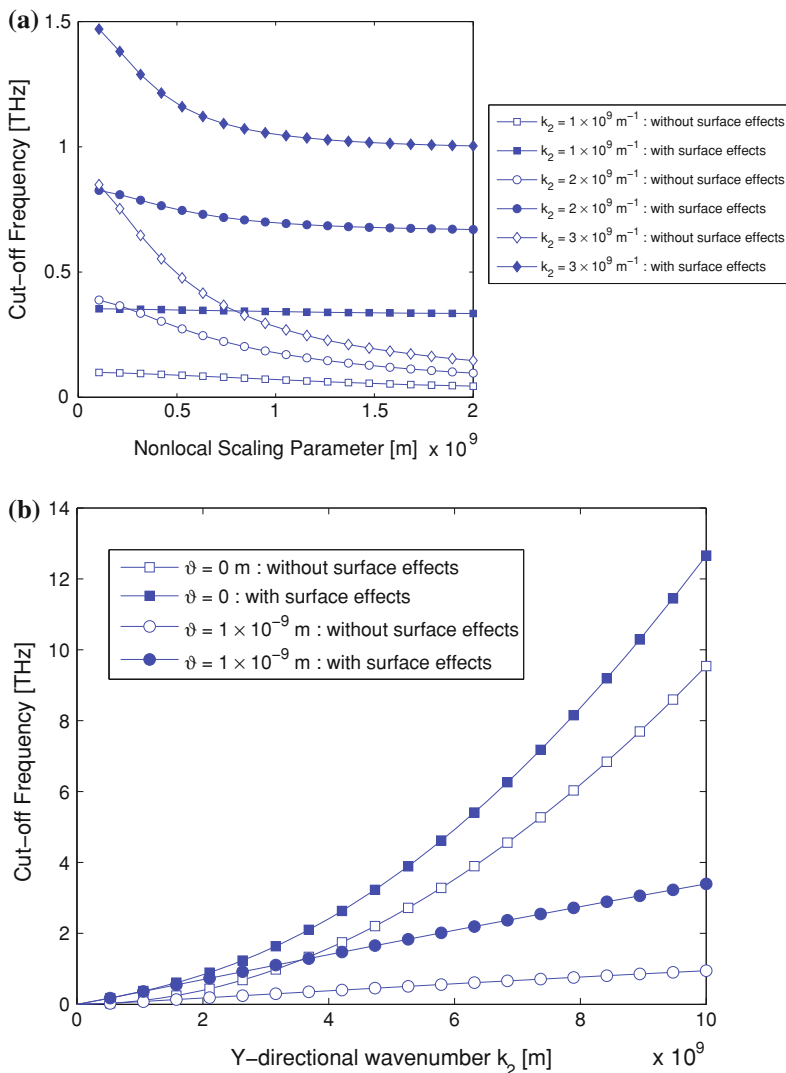


Fig. 10.32 Surface Effect on cut-off frequency on flexural mode (a) Nonlocal scaling parameter for various wavenumbers (b) wavenumbers for various scale coefficients

and this effect is more prominent for smaller values of the nonlocal scale coefficients. It has been found that at higher values of the nonlocal scaling parameter, the cut-off frequencies of the flexural wave will depend on the x_2 -directional wavenumber, such difference is clearly seen from Fig. 10.32b. With the consideration of surface effects, it can be observed that, there is a significant of difference in the cut-off frequency variation at higher values of the nonlocal scaling parameter. As small-

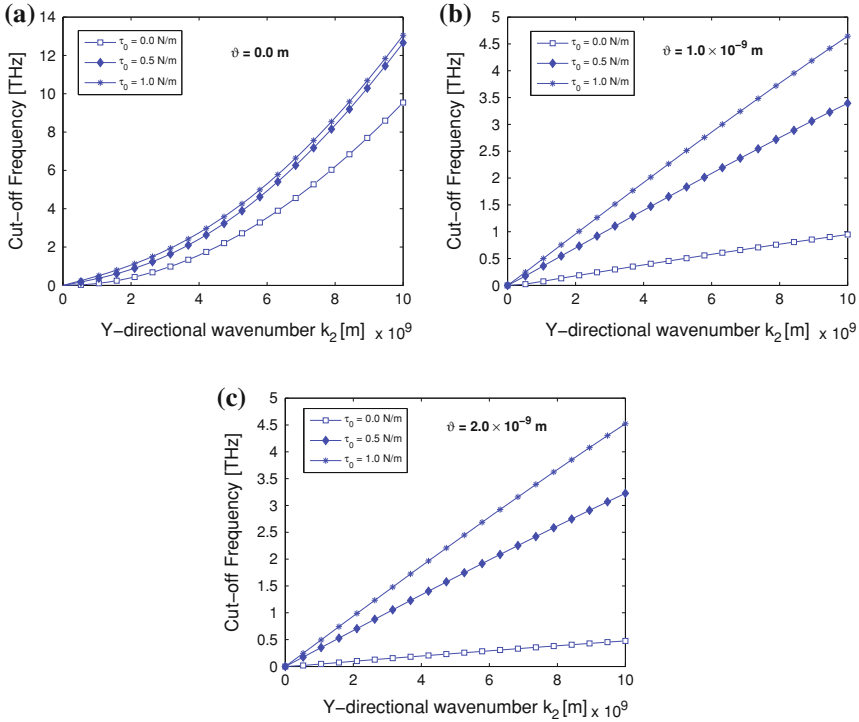


Fig. 10.33 Surface effects on cut-off frequency variation of flexural wave mode with wavenumbers for various surface stresses **a** $\vartheta = 0$, **b** $\vartheta = 1$ nm and **c** $\vartheta = 2$ nm

scale parameter increases, the cut-off frequencies tend to approach a smaller value and this effect can be overcome by considering the surface layers over the nanoplate. The cut-off frequency variation of flexural wave with k_2 is shown in Fig. 10.33. For a given ϑ , the cut-off frequency will increase as with increase in k_2 . For a given k_2 , the local elasticity gives higher values of cut-off frequencies than the nonlocal elasticity. The surface effects tend to decrease in cut-off frequency. In the nonlocal case, the relation between the cut-off frequency and the k_2 is almost linear (see Fig. 10.33).

The effect of different values surface residual stresses (τ_0) on the cut-off frequency variation is shown in Fig. 10.34a. Here τ_0 is assumed as 0 N/m, 0.5 N/m and 1.0 N/m. The effect of the small-scale parameter is also shown in Fig. 10.33. For $\vartheta = 0$, as the surface residual stress τ_0 increases, the cut-off frequency also increases nonlinearly with k_2 (Fig. 10.33a). For $\nu = 1.0 \times 10^{-9}$ m and $\nu = 2.0 \times 10^{-9}$ m, the cut-off frequency variation with k_2 is shown in Fig. 10.33b, c, respectively. The difference between the cut-off frequency variation for $\tau_0 = 0$ and $\tau_0 \neq 0$ will increase drastically as we move from local to nonlocal elasticity. This variation is more prominent for higher values of the wavenumber k_2 . If there is a small variation in the surface stress, then the cut-off frequency difference is very small and can be neglected for

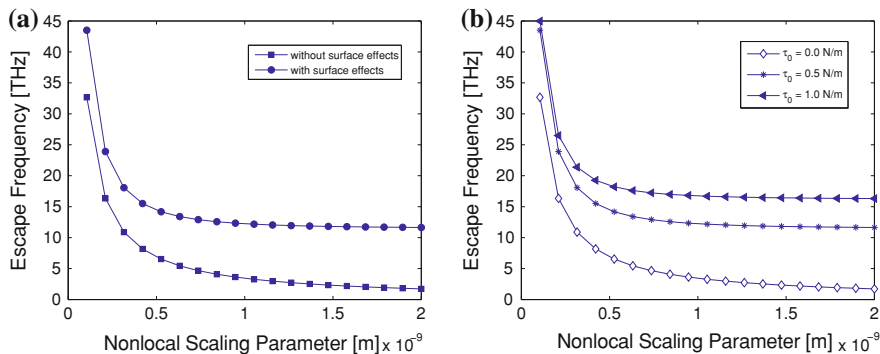


Fig. 10.34 Surface effects on escape frequency of flexural wave mode (a) variation with nonlocal scaling parameter (b) Variation with surface stresses

$\vartheta = 0$. As ϑ increases, this difference is more and cannot be neglected. It means that the surface stress is more effective for small-scale nanoplate.

The escape frequency variation with nonlocal scaling parameter is shown in Fig. 10.34b. It shows that as ϑ increases, the escape frequency decreases. For surface stress-free nanoplate, at higher values of ϑ , escape frequencies approach to very small value. If surface effects are considered, the escape frequency will increase for given ϑ . As ϑ increase, the escape frequency decreases but will not approach to smaller value, and it becomes constant with ϑ (see Fig. 10.34b). The effect of the various surface residual stresses on the escape frequency of the flexural wave is captured in Fig. 10.34b. As τ_0 increase, the escape frequency will also increase and this effect is more pronounced for smaller values of ϑ . For $\tau_0 = 0$, the escape frequency decreases drastically with ϑ and approaches to very small value. For $\tau_0 \neq 0$, the escape frequency decreases and approaches to a constant value and it will not have effect on the variation of scale parameter

10.7 Summary

Wave propagation in graphene sheets (GSs) has been a topic of great interest in nanomechanics, where the equivalent continuum models are widely used. In this chapter, we examined this issue by incorporating the nonlocal theory into the classical plate model. The influence of the nonlocal effects has been thoroughly investigated in detail for wave propagation behavior. The results are qualitatively different from those obtained based on the local plate theory and thus, are important for the development of GS-based nanodevices such as strain sensor, mass and pressure sensors, atomic dust detectors, enhancer of surface image resolution, etc.

In this chapter, an ultrasonic type of flexural wave propagation model is derived for a single layer graphene sheet. The nonlocal scale parameter introduces certain

band gap region in flexural wave mode where no wave propagation occurs. This is manifested in the wavenumber plots as the region where the wavenumber tends to infinite or wave speed tends to zero. It has been shown that the cut-off frequency is a function of nonlocal scaling parameter and the y -directional wavenumber, the escape frequency is purely a function of nonlocal scaling parameter only.

In addition, the ultrasonic wave propagation in graphene on silicon substrate, is studied using both local and nonlocal elasticity theories. In our formulation, the graphene sheet is modeled as an isotropic plate of one-atom thick (h) and the silicon (Si) substrate is modeled as distributed springs. The nonlocal governing differential equations are derived for this system from minimization of total potential energy. An expression for the force constant of C-Si bond is derived as a function of the distance between graphene and substrate by modifying the Mie-type potential for hybrid system. After that an ultrasonic type of wave propagation model is also derived and the results of the wave dispersion analysis are shown for both local and nonlocal elasticity. From this analysis, we show that the substrate affects the flexural wave mode only and the frequency band gap of flexural mode is significantly affected by the substrate. We also show that the cut-off frequencies of inplane (longitudinal and lateral) and flexural waves depends not only on the y -direction wavenumber, material properties of graphene and substrate but also on nonlocal scaling parameter. The frequency band gap of all the fundamental wave modes considered in this chapter are decreases at higher values of y directional wavenumber in nonlocal elasticity.

Next, an ultrasonic analysis of flexural wave propagation model is derived for a nanoplate with the consideration of thermal effects. The nanoplate is modeled as an isotropic plate of one atom thick. For this model, the nonlocal governing differential equation of motion is derived from the minimization of the total potential energy. The effect of the nonlocal scale and the low/high temperature effects on the wave propagation in nanoplates are captured and discussed in detail.

Lastly, the terahertz wave dispersion characteristics of a nanoplate are studied with consideration of the surface effecters as well as the nonlocal small-scale effects. Non-local elasticity theory of plate is used to derive the general differential equation based on equilibrium approach to include those scale effects. Scale and surface property-dependent wave characteristic equations are obtained via spectral analysis. For the present study, the material properties of an anodic alumina with crystallographic of $\langle 111 \rangle$ direction are considered. The present analysis shows that the effect of surface properties on the flexural waves of nanoplates are more significant. It can be found that the flexural wavenumbers with surface effects are high as compared to that without surface effects. The scale effects shows that, the wavenumbers of the flexural wave become highly nonlinear and tend to infinite at certain frequency. After that frequency, the wave will not propagate and the corresponding wave velocities tend to zero at that frequency (escape frequency). The effects of surface stresses on the terahertz wave propagation properties of nanoplate are also captured in this chapter. At the end of this chapter, reader can clearly see the difference in the wave behavior due to surface effects between the 2-D nanostructure (studied in this Chapter) and the 1-D nanostructure (studied in Chap. 7).

References

1. K.S. Novoselov, A.K. Geim, Electric field effect in atomically thin carbon films. *Science* **306**(5696), 666–669 (2004)
2. M. Poot, H.S.J. van der Zant, Nanomechanical properties of few-layer graphene membranes. *Appl. Phys. Lett.* **92**, 6 (2008)
3. X.X. Luo, D.D.L. Chung, Vibration damping using flexible graphite, *Carbon* **38**, 1510–1512 (2000)
4. K. Behfar, R. Naghdabadi, Nanoscale vibrational analysis of a multi-layered graphene sheet embedded in an elastic medium. *Compos. Sci. Technol.* **65**, 1159–1164 (2005)
5. K. Behfar, P. Seifi, R. Naghdabadi, J. Ghanbari, An analytical approach to determination of bending modulus of a multi-layered graphene sheet. *J. Thin Solid Films* **496**(2), 475–480 (2005)
6. S. Horiuchi, T. Gotou, M. Fujiwara, Single graphene sheet detected in a carbon nanofilm. *Appl. Phys. Lett.* **84**, 2403 (2004)
7. A. Sakhaee-Pour, M.T. Ahmadian, R. Naghdabadi, Vibrational analysis of single-layered graphene sheets. *Nanotechnology* **19**, 085702 (2008)
8. A. Sakhaee-Pour, M.T. Ahmadian, A. Vafai, Applications of single-layered graphene sheets as mass sensors and atomistic dust detectors. *Solid State Commun.* **4**, 168–172 (2008)
9. A. Sakhaee-Pour, M.T. Ahmadian, Potential application of single-layered graphene sheet as strain sensor. *Solid State Commun.* **147**, 336–340 (2008)
10. A. Sakhaee-Pour, M.T. Ahmadian, R. Naghdabadi, Vibrational analysis of single-layered graphene sheets. *Nanotechnology* **19**, 085702 (2008)
11. K.M. Liew, X.Q. He, S. Kitipornchai, Predicting nanovibration of multi-layered graphene sheets embedded in an elastic matrix. *Acta Mater.* **54**, 4229–4236 (2006)
12. B.I. Yakobson, C.J. Brabec, J. Bernholc, Nanomechanics of carbon tubes: instabilities beyond linear response. *Phys. Rev. Lett.* **76**, 2511–2514 (1996)
13. J.N. Reddy, *Mechanics of Laminated Composite Plates: Theory and Analysis* (Chemical Rubber Company, Boca Raton, 1997)
14. K.N. Kudin, G.E. Scuseria, B.I. Yakobson, C₂F₂BN, and C nanoshell elasticity from ab initio computations. *Phys. Rev. B* **64**, 235406 (2001)
15. E. Munoz, J. Lu, B.I. Yakobson, Ballistic thermal conductance of graphene ribbons. *Nano Lett.* **10**, 1652–1656 (2010)
16. S. Ghosh, I. Calizo, D. Teweldebrhan, E.P. Pokatilov, D.L. Nika, A.A. Balandin, W. Bao, F. Miao, C.N. Lau, Extremely high thermal conductivity of graphene: prospects for thermal management applications in nanoelectronic circuits. *Appl. Phys. Lett.* **92**, 151911 (2008)
17. S. Balandin, S. Ghosh, W. Bao, I. Calizo, D. Teweldebrhan, F. Miao, C.N. Lau, Superior thermal conductivity of single-layer graphene. *Nano Lett.* **8**, 902–907 (2008)
18. M.C. Schabel, J.L. Martins, Energetics of interplanar binding in graphite. *Phys. Rev. B* **46**, 7185–7188 (1992)
19. T. Taka, T. Halicioğlu, D.W.A. Tiller, A parametric study of crystal stability and surface energy for diamond cubic structures. *Phys. Status Solidi B* **130**, 131 (1985)
20. T. Taka, T. Halicioğlu, D.W.A. Tiller, Calculation of potential energy parameters for the silicon-carbon system. *Phys. Status Solidi B* **130**, 475–481 (1985)
21. A.H. Nayfeh, P.F. Pai, *Linear and Non-linear Structural Analysis* (John Wiley and Sons, New Jersey, 2004)
22. J.F. Doyle, *Wave Propagation in Structures* (Springer-Verlag Inc., New York, 1997)
23. S. Gopalakrishnan, A. Chakraborty, D.R. Mahapatra, *Spectral Finite Element Method* (Springer-Verlag London Ltd, London, 2008)
24. H. Jiang, B. Liu, Y. Huang, K.C. Hwang, Thermal expansion of single wall carbon nanotubes. *J. Eng. Mater. Technol.* **126**, 265–270 (2004)
25. X.H. Yao, Q. Han, Investigation of axially compressed buckling of a multi-walled carbon nanotube under temperature field. *Compos. Sci. Technol.* **67**, 125–134 (2007)

26. S. Narendar, S. Gopalakrishnan, Critical buckling temperature of single-walled carbon nanotubes embedded in a one-parameter elastic medium based on nonlocal continuum mechanics. *Phys. E: Low Dimensional Syst. Nanostruct.* **43**, 1185–1191 (2011)
27. Y.Z. Wang, F.M. Li, K. Kishimoto, Thermal effects on vibration properties of double-layered nanoplates at small scales. *Compos.: Part B Eng.* **42**(5), 1311–1317 (2011)
28. T. Murmu, S.C. Pradhan, Buckling of biaxially compressed orthotropic plates at small scales. *Mech. Res. Commun.* **36**, 933–938 (2009)
29. S. Narendar, S. Gopalakrishnan, Strong nonlocalization induced by small scale parameter on terahertz flexural wave dispersion characteristics of a monolayer graphene. *Phys. E: Low Dimensional Syst. Nanostruct.* **43**, 423–430 (2010)
30. Y.Q. Zhang, X. Liu, G.R. Liu, Thermal effect on transverse vibrations of double-walled carbon nanotubes. *Nanotechnology* **18**, 445701 (2007)
31. A. Benzair, A. Tounsi, A. Bessèghier, H. Heireche, N. Moulay, L. Boumia, The thermal effect on vibration of single-walled carbon nanotubes using nonlocal Timoshenko beam theory. *J. Phys. D: Appl. Phys.* **41**, 225404 (2008)
32. J.N. Reddy, *Theory and Analysis of Elastic Plates* (Taylor & Francis, Philadelphia, 1999)
33. M.E. Gurtin, A.I. Murdoch, A continuum theory of elastic material surfaces. *Arch. Ration. Mech. Anal.* **57**, 291–323 (1974)
34. V.B. Shenoy, Atomistic calculations of elastic properties of metallic fcc crystal surfaces. *Phys. Rev. B* **71**, 094104 (2005)
35. M.J. Lachut, J.E. Sader, Effect of surface stress on the stiffness of cantilever plates. *Phys. Rev. Lett.* **99**, 206102 (2007)
36. P. Lu, H.P. Lee, C. Lu, S.J.O. Shea, Surface stress effects on the resonance properties of cantilever sensors. *Phys. Rev. B* **72**, 085405 (2005)
37. Z. Wang, Y. Zhao, Self-instability and bending behaviors of nano plates. *Acta Mech. Solida Sin.* **22**, 630–643 (2009)
38. F. Zhang, S. Krishnaswamy, C.M. Lilley, Bulk-wave and guided-wave photoacoustic evaluation of the mechanical properties of aluminum/silicon nitride double-layer thin films. *Ultrasonics* **45**, 66–76 (2006)
39. H.G. Craighead, Nanoelectromechanical systems. *Science* **290**, 1532–1535 (2000)
40. J. Lagowski, H.C. Gatos, E.S. Sproles Jr, Surface stress and normal mode of vibration of thin crystal: GaAs. *Appl. Phys. Lett.* **26**, 493 (1975)
41. M.E. Gurtin, X. Markenscoff, R.N. Thurston, Effect of surface stress on the natural frequency of thin crystals. *Appl. Phys. Lett.* **29**, 529 (1976)
42. G.F. Wang, X.Q. Feng, Effects of surface elasticity and residual surface tension on the natural frequency of microbeams. *Appl. Phys. Lett.* **90**, 231904 (2007)
43. Y.T. Yang, K.L. Ekinci, M.H. Huang, Monocrystalline silicon carbide nanoelectromechanical systems. *Appl. Phys. Lett.* **78**, 162–164 (2001)
44. K.L. Ekinci, M.L. Roukes, Nanoelectromechanical systems. *Rev. Sci. Instrum.* **76**, 061101 (2005)
45. G.F. Wang, X.Q. Feng, S.W. Yu, Surface buckling of a bending microbeam due to surface elasticity. *Europhys. Lett.* **77**, 44002 (2007)
46. H. Sadeghian, C.K. Yang, K.B. Gavan, J.F.L. Goosen, E.W.J. van der Drift, H.S.J. van der Zant, P.J. French, A. Bossche, F. van Keulen, Effects of surface stress on nanocantilevers. *Surf. Sci. Nanotechnol.* **7**, 161–166 (2009)
47. M.J. Lachut, J.E. Sader, Effect of surface stress on the stiffness of cantilever plates. *Phys. Rev. Lett.* **99**, 206102 (2007)
48. C.W. Lim, L.H. He, Size-dependent nonlinear response of thin elastic films with nano-scale thickness. *Int. J. Mech. Sci.* **46**(11), 1715–1726 (2004)
49. P. Lu, L.H. He, H.P. Lee, Thin plate theory including surface effects. *Int. J. Solids Struct.* **43**(16), 4631–4647 (2006)
50. L.H. He, C.W. Lim, B.S. Wu, A continuum model for size-dependent deformation of elastic films of nano-scale thickness. *Int. J. Solids Struct.* **41**(3–4), 847–857 (2004)

51. J. He, C.M. Lilley, Surface effect on the elastic behavior of static bending nanowires. *Nano Lett.* **8**(7), 1798–1802 (2008)
52. J. He, C.M. Lilley, Surface stress effect on bending resonance of nanowires with different boundary conditions. *Appl. Phys. Lett.* **93**, 263108 (2008)
53. M.E. Gurtin, A.I. Murdoch, Surface stress in solids. *Int. J. Solids Struct.* **14**(6), 431–440 (1978)
54. B. Farshi, A. Assadi, A. Alinia-ziazi, Frequency analysis of nanotubes with consideration of surface effects. *Appl. Phys. Lett.* **96**, 093105 (2010)
55. A. Assadi, B. Farshi, Vibration characteristics of circular nanoplates. *J. Appl. Phys.* **108**, 074312 (2010)
56. B. Arash, Q. Wang, K.M. Liew, Wave propagation in graphene sheets with nonlocal elastic theory via finite element formulation. *Comput. Methods Appl. Mech. Eng.* **223–224**, 1–9 (2012)

Chapter 11

Wave Propagation in Nanoshells

Wave propagation analysis of nanoshells such as CNTs are relevant due to their various applications, which include sensing superconductivity, transport and optical phenomena. Both atomistic models as well as continuum models have been reported in the literature and applied to such applications. The CNTs can have interesting waveguide properties at very high frequencies in the order of up to terahertz. This we have seen in earlier chapters. At such high frequencies, continuum model-based finite element type methods cannot be adopted due to their limitation of the element size with respect to the wavelength, which is very small at such frequencies. Lattice dynamics for direct observation of phonons and spectral finite element type method are more efficient and consistent to analyze such situation. With these theories and method of analysis, this chapter brings out several interesting features of high frequency ultrasonic wave propagation in CNTs modeled as cylindrical shells, using nonlocal elasticity theory, which are not observed in macroscale structures.

The analysis here is one order complex than what was presented in Chap. 10, that is, we bring in all the three motion in the analysis, although the problem can still be construed as 2-D. In this chapter, we will perform analysis in polar coordinates since it is natural for shell-type geometry.

Wang and Varadan [1] studied the wave propagation in CNTs based on the proposed nonlocal elastic shell theory. The applicability of the proposed nonlocal elastic shell theory was especially explored and analyzed based on the differences between the wave solutions from local and nonlocal theories in numerical simulations. It was found that the newly proposed nonlocal shell theory is indispensable in predicting CNT phonon dispersion relations at larger longitudinal and circumferential wavenumbers and smaller wavelength in the circumferential direction when the small-scale effect becomes dominant. They have not captured the wave properties of SWCNT at all frequencies.

11.1 Wave Propagation in Circular Cylindrical Nanoshells

In this section, the carbon nanotubes are modeled as nonlocal cylindrical shells. So, for the case of cylindrical shells, the nonlocal constitutive relations are expressed in polar coordinate systems (R, θ) and are given by

$$\left(1 - (e_0a)^2 \left[\frac{\partial^2}{\partial x^2} + \frac{1}{R^2} \frac{\partial^2}{\partial \theta^2} \right] \right) \{\sigma\} = [C] \{\varepsilon\} \tag{11.1}$$

where

$$\{\sigma\} = \{\sigma_{xx}, \sigma_{\theta\theta}, \tau_{x\theta}, \tau_{\theta x}\}^T \tag{11.2}$$

$$\{\varepsilon\} = \{\varepsilon_{xx}, \varepsilon_{\theta\theta}, \gamma_{x\theta}, \gamma_{\theta x}\}^T \tag{11.3}$$

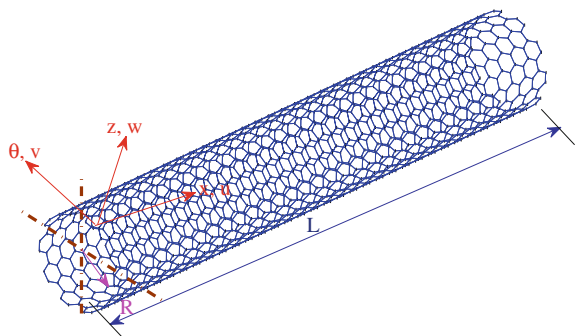
and

$$[C] = \begin{bmatrix} \frac{E}{1-\nu^2} & \frac{\nu E}{1-\nu^2} & 0 & 0 \\ \frac{\nu E}{1-\nu^2} & \frac{E}{1-\nu^2} & 0 & 0 \\ 0 & 0 & \frac{E}{2(1+\nu)} & 0 \\ 0 & 0 & 0 & \frac{E}{2(1+\nu)} \end{bmatrix} \tag{11.4}$$

where $\sigma_{xx}, \sigma_{\theta\theta}$ are the normal stresses, $\tau_{x\theta}, \tau_{\theta x}$ are the shear stresses, $\varepsilon_{xx}, \varepsilon_{\theta\theta}$ are the normal strains, $\gamma_{x\theta}, \gamma_{\theta x}$ are the shear strains, R is the radius measured from the mid-plane of the cross section in the following CNT analysis, E is the Young’s modulus of the material, ν is the Poisson ratio, and the parameter e_0a is the scale coefficient that captures the small scale or nonlocal effect on the response of structures in nano-size.

The polar coordinate system employed for analysis is shown in Fig. 11.1, with θ as the coordinate in the circumferential direction and v as the corresponding displacement variable. In the nonlocal elastic shell theory, the stress and moment resultants are defined based on the stress components in Eq. (11.1), and thus can be expressed as follows by referencing the kinematic relations in Flügge’s shell theory [2, 3]:

Fig. 11.1 Degree of freedom defined on a (10,10) single-walled carbon nanotube (with 8.147 nm length and consisting of 1,340 carbon atoms)



The stress resultants are given as

$$\{N\} = \int_{-h/2}^{+h/2} \{\sigma\}[H]dz \quad (11.5)$$

$$\{M\} = - \int_{-h/2}^{+h/2} \{\sigma\}[H]zdz \quad (11.6)$$

where

$$\{N\} = \{N_{xx}, N_{\theta\theta}, N_{x\theta}, N_{\theta x}\}^T \quad (11.7)$$

$$\{M\} = \{M_{xx}, M_{\theta\theta}, M_{x\theta}, M_{\theta x}\}^T \quad (11.8)$$

and

$$[H] = \begin{bmatrix} 1 + \frac{z}{R} & 0 & 0 & 0 \\ 0 & 1 + \frac{z}{R} & 0 & 0 \\ 0 & 0 & 1 & 0 \\ 0 & 0 & 0 & 1 \end{bmatrix} \quad (11.9)$$

Substituting Eq. (11.1) in Eqs. (11.5) and (11.6), we get

$$\left(1 - (e_0a)^2 \left[\frac{\partial^2}{\partial x^2} + \frac{1}{R^2} \frac{\partial^2}{\partial \theta^2} \right]\right) \{N\} = [Z_1]\{d\} + [Z_2]\{d\} \quad (11.10)$$

$$\left(1 - (e_0a)^2 \left[\frac{\partial^2}{\partial x^2} + \frac{1}{R^2} \frac{\partial^2}{\partial \theta^2} \right]\right) \{M\} = [Z_3]\{d\} \quad (11.11)$$

where

$$[Z_1] = \begin{bmatrix} hC(1, 1) \frac{\partial}{\partial x} & \frac{h}{R} C(1, 2) \frac{\partial}{\partial \theta} & -\frac{h}{R} C(1, 2) \\ -hC(2, 1) \frac{\partial}{\partial x} & \frac{h}{R} C(2, 2) \frac{\partial}{\partial \theta} & -\frac{h}{R} C(2, 2) \\ \frac{h}{R} C(3, 3) \frac{\partial}{\partial \theta} & \frac{h}{R} \left(\frac{1-\nu}{2}\right) C(1, 2) \frac{\partial}{\partial x} & 0 \\ \frac{h}{R} C(3, 3) \frac{\partial}{\partial \theta} & \frac{h}{R} \left(\frac{1-\nu}{2}\right) C(1, 2) \frac{\partial}{\partial x} & 0 \end{bmatrix} \quad (11.12)$$

$$[Z_2] = \begin{bmatrix} 0 & 0 & \frac{h^3}{12R} C(1, 1) \frac{\partial^2}{\partial x^2} \\ 0 & 0 & -\frac{h^3}{12R^3} C(2, 2) \left(1 + \frac{\partial^2}{\partial \theta^2}\right) \\ 0 & \frac{h^3}{12R^2} \left(\frac{1-\nu}{2}\right) C(1, 1) \frac{\partial}{\partial x} & \frac{h^3}{12R^2} \left(\frac{1-\nu}{2}\right) C(1, 1) \frac{\partial^2}{\partial x \partial \theta} \\ \frac{h^3}{12R^2} \left(\frac{1-\nu}{2}\right) C(2, 2) \frac{\partial}{\partial x} & 0 & -\frac{h^3}{12R^2} \left(\frac{1-\nu}{2}\right) C(2, 2) \frac{\partial^2}{\partial x \partial \theta} \end{bmatrix} \quad (11.13)$$

$$[Z_3] = \begin{bmatrix} -\frac{h^3}{12R}C(1,1)\frac{\partial}{\partial x} & +\frac{h^3}{12R^2}C(1,2)\frac{\partial}{\partial\theta} & -\frac{h^3}{12R^2}C(1,2)\frac{\partial^2}{\partial\theta^2} - hC(1,1)\frac{\partial^2}{\partial x^2} \\ 0 & 0 & -\frac{h^3}{12R^2}C(2,2)\left(1 + \frac{\partial^2}{\partial\theta^2}\right) - hC(2,1)\frac{\partial^2}{\partial x^2} \\ 0 & -\frac{h^3}{12R^2}(1-\nu)C(1,1)\frac{\partial}{\partial x} & -\frac{h^3}{12R^2}(1-\nu)C(1,1)\frac{\partial^2}{\partial x\partial\theta} \\ \frac{h^3}{24R^2}(1-\nu)C(2,2)\frac{\partial}{\partial\theta} & -\frac{h^3}{24R}(1-\nu)C(2,2)\frac{\partial}{\partial x} & -\frac{h^3}{12R}(1-\nu)C(2,2)\frac{\partial^2}{\partial x\partial\theta} \end{bmatrix} \quad (11.14)$$

and

$$\{d\} = \{u, v, w\}^T \quad (11.15)$$

where $C(i, j)$ ($i, j = 1, 2, 3$) are the elements of the matrix $[C]$. Here u, v , and w are the axial, circumferential and radial displacements of the SWCNT wall respectively (see Fig. 11.1). These displacements are function of x, θ , and t . R is the centerline radius of the SWCNT and h is the thickness of the CNT wall, as shown in Fig. 11.1.

The dynamic equilibrium equations of stress resultant $\{N\}$ and moment resultant $\{M\}$ are given as [3]

$$[Z_4]\{N\} + [Z_5]\{M\} = [Z_6]\{d\} \quad (11.16)$$

where

$$[Z_4] = \begin{bmatrix} R\frac{\partial}{\partial x} & 0 & \frac{\partial}{\partial\theta} & 0 \\ 0 & R\frac{\partial}{\partial\theta} & R^2\frac{\partial}{\partial x} & 0 \\ 0 & R & 0 & 0 \end{bmatrix} \quad (11.17)$$

$$[Z_5] = \begin{bmatrix} 0 & 0 & 0 & 0 \\ 0 & -\frac{\partial}{\partial\theta} & -R\frac{\partial}{\partial x} & 0 \\ R^2\frac{\partial^2}{\partial x^2} & \frac{\partial^2}{\partial\theta^2} & R\frac{\partial^2}{\partial x\partial\theta} & R\frac{\partial^2}{\partial x\partial\theta} \end{bmatrix} \quad (11.18)$$

$$[Z_6] = \rho h R^2 \begin{bmatrix} \frac{\partial^2}{\partial t^2} & 0 & 0 \\ 0 & \frac{\partial^2}{\partial t^2} & 0 \\ 0 & 0 & \frac{\partial^2}{\partial t^2} \end{bmatrix} \quad (11.19)$$

Substituting Eqs. (11.10) and (11.11) into Eq. (11.16) leads to following governing partial differential equations including the nonlocal effects for SWCNT

$$\begin{aligned} & \frac{\partial^2 u}{\partial x^2} + \frac{(1-\nu)}{2R^2} \frac{\partial^2 u}{\partial\theta^2} + \frac{(1+\nu)}{2R} \frac{\partial^2 v}{\partial x\partial\theta} + \frac{\nu}{R} \frac{\partial w}{\partial x} \\ & + \Lambda \left[\frac{(1-\nu)}{2R^2} \frac{\partial^2 u}{\partial\theta^2} - R \frac{\partial^3 w}{\partial x^3} + \frac{(1-\nu)}{2R} \frac{\partial^3 w}{\partial x\partial\theta^2} \right] \\ & = \Gamma \left[\frac{\partial^2 u}{\partial t^2} - (e_0 a)^2 \frac{\partial^4 u}{\partial t^2 \partial x^2} - \frac{1}{R^2} (e_0 a)^2 \frac{\partial^4 u}{\partial t^2 \partial\theta^2} \right] \end{aligned} \quad (11.20)$$

$$\begin{aligned}
& \frac{(1+\nu)}{2R} \frac{\partial^2 u}{\partial x \partial \theta} + \frac{(1-\nu)}{2} \frac{\partial^2 v}{\partial x^2} + \frac{1}{R^2} \frac{\partial^2 v}{\partial \theta^2} + \frac{1}{R^2} \frac{\partial w}{\partial \theta} \\
& + \Lambda \left[\frac{3(1-\nu)}{2} \frac{\partial^2 v}{\partial x^2} - \frac{(3-\nu)}{2} \frac{\partial^3 w}{\partial x^2 \partial \theta} \right] \\
& = \Gamma \left[\frac{\partial^2 v}{\partial t^2} - (e_0 a)^2 \frac{\partial^4 v}{\partial t^2 \partial x^2} - \frac{1}{R^2} (e_0 a)^2 \frac{\partial^4 v}{\partial t^2 \partial \theta^2} \right] \quad (11.21)
\end{aligned}$$

$$\begin{aligned}
& \frac{\nu}{R} \frac{\partial u}{\partial x} + \frac{1}{R^2} \frac{\partial v}{\partial \theta} - \frac{w}{R^2} + \Lambda \left[R^2 \frac{\partial^4 w}{\partial x^4} + 2 \frac{\partial^4 w}{\partial x^2 \partial \theta^2} + \frac{1}{R^2} \frac{\partial^4 w}{\partial \theta^4} \right. \\
& \left. - R \frac{\partial^3 u}{\partial x^3} + \frac{(1-\nu)}{2R} \frac{\partial^3 u}{\partial x \partial \theta^2} - \frac{(3-\nu)}{2} \frac{\partial^3 v}{\partial x^2 \partial \theta} - \frac{2}{R^2} \frac{\partial^2 w}{\partial \theta^2} - \frac{w}{R^2} \right] \\
& = \Gamma \left[\frac{\partial^2 w}{\partial t^2} - (e_0 a)^2 \frac{\partial^4 w}{\partial t^2 \partial x^2} - \frac{1}{R^2} (e_0 a)^2 \frac{\partial^4 w}{\partial t^2 \partial \theta^2} \right] \quad (11.22)
\end{aligned}$$

where $\Lambda = \frac{(1-\nu^2)D}{EhR^2}$, $\Gamma = \frac{\rho h(1-\nu^2)}{Eh}$; E , ρ , ν and D are the Young's modulus, mass density, Poisson's ratio, and the effective bending stiffness, respectively.

11.1.1 Wave Dispersion Analysis

The displacements u , v , and w for the SWCNT wall is approximated as general solution form of the wave propagation can be given by [4, 5],

$$u(x, \theta, t) = \sum_{m=0}^{M-1} \sum_{n=0}^{N-1} \widehat{U} \cos(k\theta) e^{-j(\xi_m x - \omega_n t)} \quad (11.23)$$

$$v(x, \theta, t) = \sum_{m=0}^{M-1} \sum_{n=0}^{N-1} \widehat{V} \sin(k\theta) e^{-j(\xi_m x - \omega_n t)} \quad (11.24)$$

$$w(x, \theta, t) = \sum_{m=0}^{M-1} \sum_{n=0}^{N-1} \widehat{W} \cos(k\theta) e^{-j(\xi_m x - \omega_n t)} \quad (11.25)$$

where \widehat{U} , \widehat{V} , and \widehat{W} represent the longitudinal, circumferential and radial amplitudes of displacements of the SWCNT, respectively. ω_n is the circular frequency at the n^{th} time sample, ξ_m is the axial wavenumber at m^{th} spatial sample point and k is the circumferential wavenumber. Substituting Eqs. (11.23)–(11.25) into the governing wave equations (Eqs. (11.20)–(11.22)), we get the reduced equations as follows (Hereafter the subscript n and m are dropped for simplified notations). Writing them in matrix form, we get the Polynomial Eigenvalue Problem as

$$\mathbf{A}^4 k^4 + \mathbf{A}^3 k^3 + \mathbf{A}^2 k^2 + \mathbf{A}^1 k + \mathbf{A}^0 = 0 \quad (11.26)$$

where

$$\mathbf{A}^4 = \begin{bmatrix} 0 & 0 & 0 \\ 0 & 0 & 0 \\ 0 & 0 & \frac{\Lambda}{R^2} \end{bmatrix} \quad (11.27)$$

$$\mathbf{A}^3 = \begin{bmatrix} 0 & 0 & 0 \\ 0 & 0 & 0 \\ 0 & 0 & 0 \end{bmatrix} \quad (11.28)$$

$$\mathbf{A}^2 = \begin{bmatrix} -\frac{(1+\Lambda)(1-\nu)}{2R} + \Gamma(e_0 a)^2 \omega^2 & 0 \\ 0 & -1 + \Gamma(e_0 a)^2 \omega^2 \\ \frac{j\Lambda\xi(1-\nu)}{2R} & 0 \\ \frac{j\Lambda\xi(1-\nu)}{2R} & \\ 0 & \\ 2\Lambda\xi^2 - 2\frac{\Lambda}{R^2} + \Gamma(e_0 a)^2 \omega^2 \end{bmatrix} \quad (11.29)$$

$$\mathbf{A}^1 = \begin{bmatrix} 0 & -\frac{\xi(1+\nu)}{2R} & 0 \\ -\frac{\xi(1+\nu)}{2R} & 0 & \frac{j\Lambda\xi^2(3-\nu)}{2} + j \\ 0 & -\frac{j\Lambda\xi^2(3-\nu)}{2} - j & 0 \end{bmatrix} \quad (11.30)$$

$$\mathbf{A}^0 = \begin{bmatrix} -\xi^2 + \Gamma\omega^2(1 + (e_0 a)^2 \xi^2) & 0 \\ 0 & -\frac{\xi^2(3\Lambda+1)(1-\nu)}{2} + \Gamma\omega^2(1 + (e_0 a)^2 \xi^2) \\ -j\Lambda\xi^3 R - \frac{j\xi\nu}{R} & 0 \\ -j\Lambda\xi^3 R - \frac{j\xi\nu}{R} & \\ 0 & \\ \Lambda\xi^4 R^2 - j\Lambda\xi^3 R + (1 - \Lambda) + \Gamma(1 + (e_0 a)^2 \xi^2) \omega^2 \end{bmatrix} \quad (11.31)$$

The wavenumbers can be computed by solving the PEP (Eq.(11.26)). The solution is done for the wavenumbers in circumferential direction k . As said earlier, these wavenumbers are function of frequency, nonlocal scaling parameter, and axial wavenumber. The corresponding wave speed or phase speed is calculated as $C_p = \text{Real}\left(\frac{\omega}{k}\right)$. It should be mentioned here that, to obtain the wavenumbers in axial direction, the Fourier transform should be performed in the circumferential direction.

As before, the cut-off frequencies of the SWCNTs are obtained by setting $k = 0$ in the dispersion relation (Eq. (11.26)) that is, for the present case of PEP, one can set $|\mathbf{A}^0| = 0$, for the cut-off frequencies of the fundamental wave modes are obtained as

$$\omega_c^1 = \frac{\xi}{R} \sqrt{\frac{(\nu - 1)(1 + 3\Lambda)}{2\Gamma(1 + (e_0a)^2\xi^2)}} \quad (11.32)$$

$$\omega_c^2 = \frac{1}{R} \sqrt{\frac{1 + \xi^2(1 + \Lambda) + \sqrt{\chi}}{2\Gamma(1 + (e_0a)^2\xi^2)}} \quad (11.33)$$

$$\omega_c^3 = \frac{1}{R} \sqrt{\frac{1 + \xi^2(1 + \Lambda) - \sqrt{\chi}}{2\Gamma(1 + (e_0a)^2\xi^2)}} \quad (11.34)$$

where $\chi = 1 - 2\xi^2(1 - 2\nu^2) + \xi^4(1 + 2\Lambda + 8\nu\Lambda) - 2\Lambda\xi^6(1 - 2\Lambda) + \Lambda^2\xi^8$. Here suffix ' c ' stands for *cut-off*. These cut-off frequencies are dependent on the nonlocal scaling parameter and the axial wavenumber. It has been shown that the nonlocal scale effects does not change the cut-off frequencies of all the wave modes where as the axial wavenumber shows a significant variation in cut-off frequencies.

As already mentioned, k is obtained for a given value of ξ . Hence, here unknown value is ξ . After solving $|\mathbf{A}^0| = 0$, the cut-off frequencies are obtained as function of ξ , e_0a and material properties of the structure. The local elasticity theory, which does not consider the internal length scale, the dispersion behavior will be markedly different compared to the results of nonlocal elasticity case.

The escape frequency value can be analytically determined by looking at the wavenumber expression and setting $k \rightarrow \infty$ in Eq. (11.26), which gives

$$\omega_e^1 = \frac{1}{(e_0a)\sqrt{\Gamma}} \quad (11.35)$$

$$\omega_e^2 = \frac{1}{(e_0a)} \sqrt{\frac{(1 + \Lambda)(\nu - 1)}{2\Gamma}} \quad (11.36)$$

Here suffix ' e ' stands for *escape*. These escape frequencies are inversely proportional to the nonlocal scaling parameter and are also a function of the material properties of the SWCNT. These frequencies are independent of the axial wavenumbers (ξ). The nonlocal scale coefficient introduced significant variation in escape frequencies of all the fundamental wavemodes.

Next, numerical experiments are presented to analyze the effect of nonlocal elasticity on ultrasonic wave properties of SWCNTs modeled as nanoshell. A major difference in modeling SWCNT as a Beam (in Chap. 7) and nanoshell is that in the later, the breathing wave modes or optical modes can be effectively captured. The material properties of SWCNT assumed for the present analysis are as follows,

Young’s modulus, $Eh = 360 \text{ J/m}^2$, mass density, $\rho = 2700 \text{ kg/m}^3$ and Poisson’s ratio, $\nu = 0.27$. The SWCNT wall thickness $h = 0.34 \text{ nm}$. The effective bending stiffness, D is taken as $D = 2 \text{ eV}$ ($1 \text{ eV} = 1.6021 \times 10^{-19} \text{ N/m}^2$). The diameter of SWCNT is assumed as 2.0 nm . The nonlocal scale coefficient (e_0a) is taken as 0 and 0.3 nm , for the present analysis.

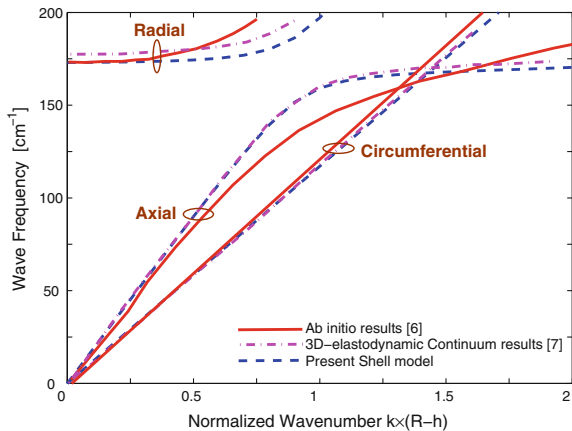
The developed SWCNT shell model is validated by comparing the simulated results with those available in the literature. In Fig. 11.2, the acoustic phonon dispersion relation of a (10,10) SWCNT with $R = 0.678 \text{ nm}$ and $h = 0.045 \text{ nm}$ are presented.

The present results are compared with the corresponding results (for first mode) obtained from ab initio [6] and 3-D elastodynamic continuum [7] models. In the figure (Fig. 11.2), the frequencies in optical unit are presented for varying axial wavenumber k normalized as $k \times (R - h)$ (Note: In this work, the Young’s modulus (assumed as constant) is considered to be independent of the radius. The radius R of (N, N) SWCNT is calculated as $R = \frac{3Nac-c}{2\pi}$, where a_{C-C} is carbon bond length and equal to 0.142 nm . In the Fig. 11.2, the frequencies are expressed in optical units cm^{-1} , where the conversion is given as, $1 \text{ Hz} = 3.336 \times 10^{-11} \text{ cm}^{-1}$). It can be seen, that the acoustic phonon dispersion relation predicted by the present model is in good agreement with that obtained from references [6, 7].

The derived polynomial eigenvalue problem for the present SWCNT shell is given in Eq. (11.26). This PEP is obtained by substituting the spectral form of displacement field (Eqs. (11.23)–(11.25)) into the governing differential equations (Eqs. (11.20)–(11.22)). The PEP is solved for the eigenvalues. Once assuming $\{\widehat{U} \neq 0, \widehat{V} = 0, \widehat{W} = 0\}$, we obtain eigenvalues (i.e., wavenumbers) of the longitudinal/axial wave mode. Likewise we obtain for the remaining wave modes. Once these are identified, we solve for the entire PEP for all the eigenvalues/wavenumbers. This is the easiest way to identify the type of wave in a given structures.

Figure 11.3a shows the real and imaginary parts of the circumferential wavenumber of a SWCNT obtained from both local/classical and nonlocal shell theories for

Fig. 11.2 A Comparison of acoustic phonon dispersion relation for a (10,10) single-walled carbon nanotube ($R = 0.678 \text{ nm}$ and $h = 0.045 \text{ nm}$) obtained from ab initio results and 3D-elastodynamic continuum models with the present continuum shell model



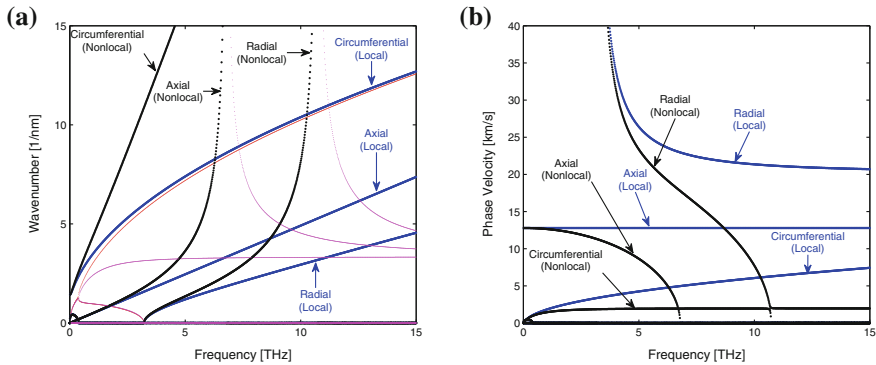


Fig. 11.3 Dispersion relations for a SWCNT obtained from both local and nonlocal Flügge shell theories for axial wavenumber $\xi R = 0$ (a) Wavenumber variation (b) Phase speed variation

zero axial wavenumber. These wavenumbers are obtained assuming variation only in the circumferential direction. Thick lines represent the real part and the thin lines show the imaginary part of the wavenumbers. From Fig. 11.3a, for SWCNT, for local elasticity solution, it can be seen that there are three modes of wave propagation, namely, axial circumferential and radial. The wavenumbers for the axial mode has a linear variation with the frequency, which is in the THz range. On the other hand, the circumferential wavenumbers have a nonlinear variation with the frequency, which indicates that the waves are dispersive in nature. However, the wavenumbers of this circumferential wave mode have a substantial real part starting from the zero frequency. The radial mode, however, has a certain frequency band within which the corresponding wavenumbers are purely imaginary. Thus, the radial mode does not propagate at frequencies lying within this band. Both the circumferential and radial wavenumbers have a substantial imaginary part and hence, these waves attenuate as they propagate.

Figure 11.3a also shows the wavenumber dispersion obtained from nonlocal elasticity. It can be seen that because of nonlocality, as in the most nonlocal models, the wavenumber tends to reach infinity at escape frequencies and the correspondingly, the wave velocity tends to zero at these frequencies indicating localization and stationary behavior (shown in Fig. 11.3b). Observe that the circumferential waves are not following the nonlocal elasticity behavior that is, the wavenumbers are not tending to infinity and the corresponding wave speeds are not zero. It shows that the circumferential waves will propagate at any frequencies whereas the axial and radial waves will propagate up to the respective escape frequencies only. The nonlocal elasticity does not affect the cut-off frequencies of these waves. Figure 11.3b clearly shows the nonlocal elastic effects on wave velocities in SWCNT. The local elasticity calculation shows that all the three wave will propagate at any frequencies. The nonlocal elasticity calculation shows that the axial and radial waves will stop propagating at their respective escape frequencies whereas the circumferential wave will propagate dispersively at higher frequencies. The magnitudes of wave veloci-

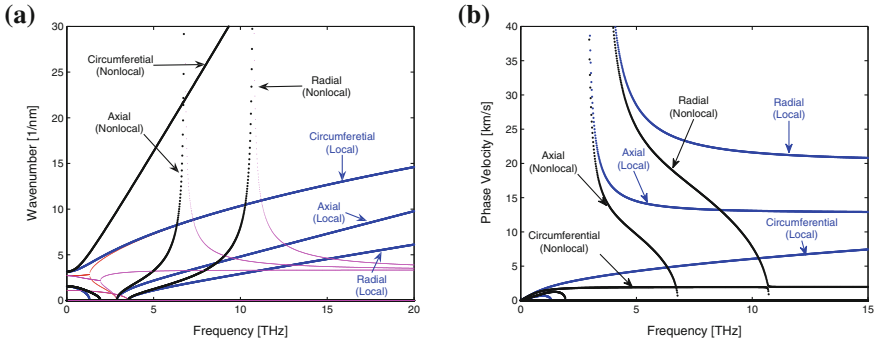


Fig. 11.4 Dispersion relations for a SWCNT obtained from both local and nonlocal Flügge shell theories for axial wavenumber $\xi R = 1$ (a) Wavenumber variation (b) Phase speed variation

ties of circumferential waves are smaller in nonlocal elasticity as compared to local elasticity (see Fig. 11.3b).

Figure 11.4a shows the variation of circumferential wavenumbers obtained from both local and nonlocal elastic shell models, for an axial wavenumber of $\xi R = 1$. Here, coupling exists between the axial, circumferential, and radial wave modes. It can be seen that the axial mode has a nonlinear variation with frequency unlike of what is shown in Fig. 11.3a. This nonlinear variation occur due to the coupling arising from the coupled displacement fields. Thus, here, the axial modes are dispersive in nature. Next, the real part of the wavenumbers for the axial mode exists after cut-off frequency. This implies that the mode start propagating only after the cut-off frequency. In Fig. 11.3a, where $\xi R = 0$, such cut-off frequency does not exist for the axial mode. The radial mode, however, shows similar pattern as in Fig. 11.3a and has a frequency band within which the waves do not propagate. The circumferential mode also shows similar pattern as in Fig. 11.3a and does not have a frequency band. The importance of this figure is to check the effect of axial wavenumber on the wave behavior in SWCNT. For $\xi R \neq 0$, the wavenumbers for the axial mode exists after a certain frequency band. The phase speed variation obtained from both local and nonlocal elastic models for $\xi R = 1$ is shown in Fig. 11.4b.

Equations (11.35) and (11.36) gives the expression for escape frequencies of radial and axial wave modes, respectively. From these expressions, it is clear that escape frequency values are independent of SWCNT diameter, for both wave modes. However, the phase speed amplitudes may change. Figure 11.5 shows the variation of escape frequencies of axial and radial wave modes with the nonlocal scaling parameter. It shows that as $e_0 a$ increases, the escape frequency decreases. At higher values of $e_0 a$, escape frequencies approach to very small values. Figure 11.6 shows the dependence of the escape frequency on the CNT radius and the nonlocal scaling parameter. From this figure, it is clear that the escape frequency does not vary with the radius of SWCNT. As the nonlocal scaling parameter increases the magnitude of the escape frequency decreases for both the wave modes as shown in Fig. 11.6a–d.

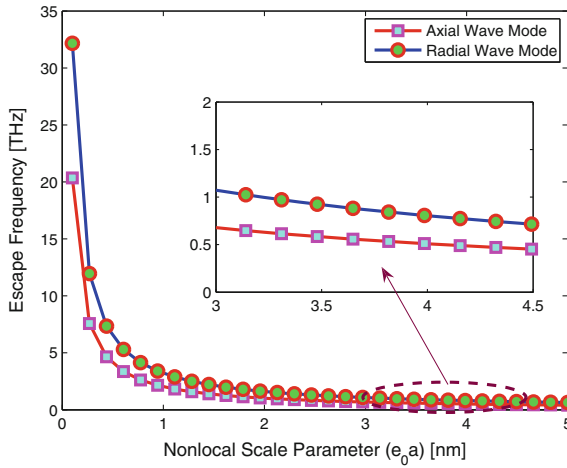


Fig. 11.5 Escape frequency variation of SWCNTs with nonlocal scaling parameter (e_0a)

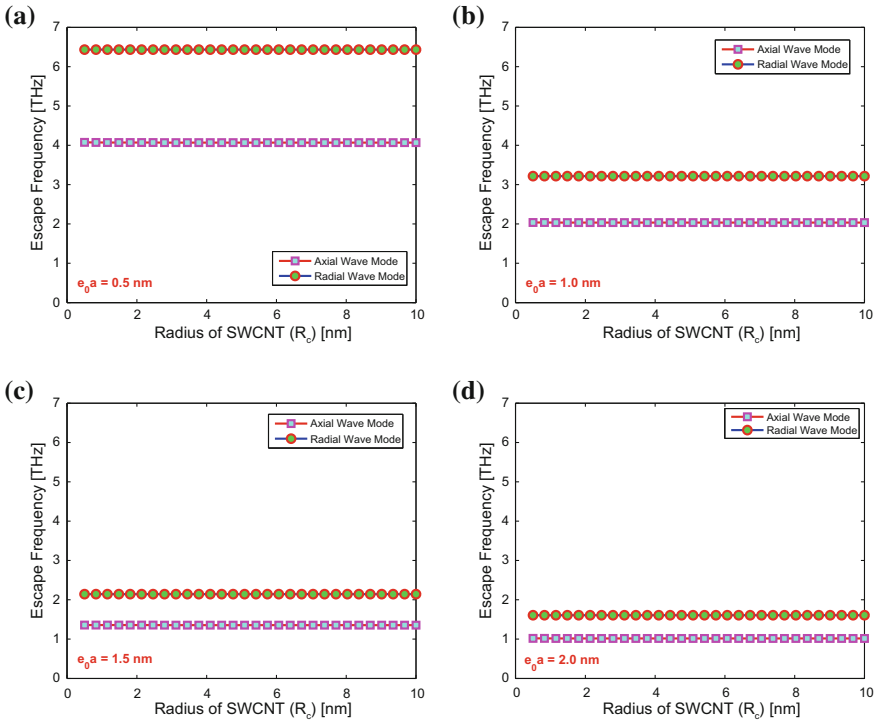


Fig. 11.6 Effect of radius of SWCNT and nonlocal scaling parameter on the escape frequencies of axial and radial wave modes

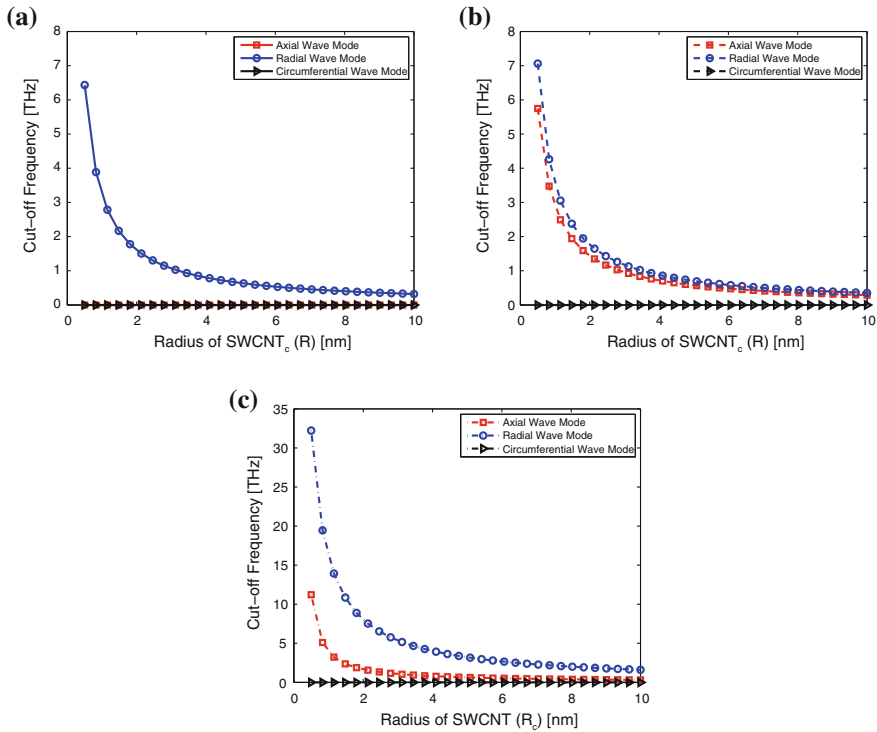


Fig. 11.7 Cut-off frequency variation with radius of carbon nanotube for (a) $\xi R = 0$, (b) $\xi R = 1$ and (c) $\xi R = 5$ (For any value of nonlocal-scaling parameter)

The cut-off frequency variation with radius (R) of SWCNT is shown in Fig. 11.7. Figure 11.7a, b, and c are shown for $\xi R = 0$, 1 and 5, respectively. When $\xi R = 0$, the cut-off frequencies exist for only radial wavemodes. As the radius of the nanotube increases, the cut-off frequency decreases and at higher values of R the cut-off frequency approaches to very small values. The cut-off frequency of the radial wave for different values of nonlocal scaling parameter is given in Table 11.1. It has been found that the cut-off frequency will not vary with the nonlocal scaling parameter. Figure 11.7b, c (when $\xi R \neq 0$), shows that the cut-off frequencies exist for both the axial and radial wave modes. As the radius of the nanotube increases, the cut-off frequencies of axial and radial waves will decrease and at higher values of R the cut-off frequencies approach to very small values. These cut-off frequencies will also not vary with the nonlocal scaling parameter as given in Tables 11.2 and 11.3.

Table 11.1 Radial wave cut-off frequencies (ω_c^R) in THz for $\xi R = 0$

R_{cnt} (nm)	ω_c^R @ $e_0a = 0.0$ nm	ω_c^R @ $e_0a = 1.0$ nm	ω_c^R @ $e_0a = 10.0$ nm
0.5000	6.4335	6.4335	6.4335
1.5556	2.0679	2.0679	2.0679
2.6111	1.2319	1.2319	1.2319
3.6667	0.8773	0.8773	0.8773
4.7222	0.8773	0.8773	0.8773
5.7778	0.5567	0.5567	0.5567
6.8333	0.4707	0.4707	0.4707
7.8889	0.4078	0.4078	0.4078
8.9444	0.3596	0.3596	0.3596
10.0000	0.3217	0.3217	0.3217

Table 11.2 Radial wave cut-off frequencies (ω_c^R) in THz for $\xi R = 1$

Radius of CNT (nm)	ω_c^R @ $e_0a = 0.0$ nm	ω_c^R @ $e_0a = 1.0$ nm	ω_c^R @ $e_0a = 10.0$ nm
0.5000	7.0626	7.0626	7.0626
1.5556	2.2658	2.2658	2.2658
2.6111	1.3496	1.3496	1.3496
3.6667	0.9611	0.9611	0.9611
4.7222	0.7462	0.7462	0.7462
5.7778	0.6099	0.6099	0.6099
6.8333	0.5157	0.5157	0.5157
7.8889	0.4467	0.4467	0.4467
8.9444	0.3940	0.3940	0.3940
10.0000	0.3524	0.3524	0.3524

Table 11.3 Axial wave cut-off frequencies (ω_c^A) in THz for $\xi R = 1$

Radius of CNT (nm)	ω_c^A @ $e_0a = 0.0$ nm	ω_c^A @ $e_0a = 1.0$ nm	ω_c^A @ $e_0a = 10.0$ nm
0.5000	5.7481	5.7481	5.7481
1.5556	1.8494	1.8494	1.8494
2.6111	1.1018	1.1018	1.1018
3.6667	0.7847	0.7847	0.7847
4.7222	0.6093	0.6093	0.6093
5.7778	0.4980	0.4980	0.4980
6.8333	0.4210	0.4210	0.4210
7.8889	0.3647	0.3647	0.3647
8.9444	0.3217	0.3217	0.3217
10.0000	0.2877	0.2877	0.2877

11.2 Fluid-Filled Nanoshells

Fluid-filled nanotubes modeled as hollow SWCNT beam using both local and non-local theory was presented in Chap. 7. It was shown that the fluid loading on the walls of the nanobeam had significantly influenced the dispersion characteristics of the nanobeam. In this chapter, we will model the same problem, wherein the SWCNT will be modeled as a nanoshell containing the fluid. The major feature of such modeling is that in addition to the regular axial and transverse modes (acoustic phonon modes), we will be able to capture the cross-sectional breathing modes (optical modes). Analysis based on both local and nonlocal elasticity models will be presented and in particular, the effect of fluid on the circumferential or breathing modes will be investigated in detail. The modeling of SWCNT will again be based on Flügge's thin shell theory [3]. The three degree of freedom nanoshell is shown in Fig. (11.1). The governing differential equations including the nonlocal effects for the fluid-filled SWCNT are given as

$$\begin{aligned} & \frac{\partial^2 u}{\partial x^2} + \frac{(1-\nu)}{2R^2} \frac{\partial^2 u}{\partial \theta^2} + \frac{(1+\nu)}{2R} \frac{\partial^2 v}{\partial x \partial \theta} + \frac{\nu}{R} \frac{\partial w}{\partial x} \\ & + \Lambda \left[\frac{(1-\nu)}{2R^2} \frac{\partial^2 u}{\partial \theta^2} - R \frac{\partial^3 w}{\partial x^3} + \frac{(1-\nu)}{2R} \frac{\partial^3 w}{\partial x \partial \theta^2} \right] \\ & = \Gamma \left[\frac{\partial^2 u}{\partial t^2} - (e_0 a)^2 \frac{\partial^4 u}{\partial t^2 \partial x^2} - \frac{1}{R^2} (e_0 a)^2 \frac{\partial^4 u}{\partial t^2 \partial \theta^2} \right] \end{aligned} \quad (11.37)$$

$$\begin{aligned} & \frac{(1+\nu)}{2R} \frac{\partial^2 u}{\partial x \partial \theta} + \frac{(1-\nu)}{2} \frac{\partial^2 v}{\partial x^2} + \frac{1}{R^2} \frac{\partial^2 v}{\partial \theta^2} + \frac{1}{R^2} \frac{\partial w}{\partial \theta} \\ & + \Lambda \left[\frac{3(1-\nu)}{2} \frac{\partial^2 v}{\partial x^2} - \frac{(3-\nu)}{2} \frac{\partial^3 w}{\partial x^2 \partial \theta} \right] \\ & = \Gamma \left[\frac{\partial^2 v}{\partial t^2} - (e_0 a)^2 \frac{\partial^4 v}{\partial t^2 \partial x^2} - \frac{1}{R^2} (e_0 a)^2 \frac{\partial^4 v}{\partial t^2 \partial \theta^2} \right] \end{aligned} \quad (11.38)$$

$$\begin{aligned} & \frac{\nu}{R} \frac{\partial u}{\partial x} + \frac{1}{R^2} \frac{\partial v}{\partial \theta} - \frac{w}{R^2} + \Lambda \left[R^2 \frac{\partial^4 w}{\partial x^4} + 2 \frac{\partial^4 w}{\partial x^2 \partial \theta^2} + \frac{1}{R^2} \frac{\partial^4 w}{\partial \theta^4} \right. \\ & \left. - R \frac{\partial^3 u}{\partial x^3} + \frac{(1-\nu)}{2R} \frac{\partial^3 u}{\partial x \partial \theta^2} - \frac{(3-\nu)}{2} \frac{\partial^3 v}{\partial x^2 \partial \theta} - \frac{2}{R^2} \frac{\partial^2 w}{\partial \theta^2} - \frac{w}{R^2} \right] \\ & = \Gamma \left[\frac{\partial^2 w}{\partial t^2} - (e_0 a)^2 \frac{\partial^4 w}{\partial t^2 \partial x^2} - \frac{1}{R^2} (e_0 a)^2 \frac{\partial^4 w}{\partial t^2 \partial \theta^2} \right. \\ & \left. - \frac{1}{\rho h} \left(\frac{\partial^2 p^f}{\partial t^2} - (e_0 a)^2 \frac{\partial^4 p^f}{\partial t^2 \partial x^2} - \frac{1}{R^2} (e_0 a)^2 \frac{\partial^4 p^f}{\partial t^2 \partial \theta^2} \right) \right] \end{aligned} \quad (11.39)$$

where $\Lambda = \frac{(1-\nu^2)D}{EhR^2}$, $\Gamma = \frac{\rho h(1-\nu^2)}{Eh}$

where u , v , and w are the axial, circumferential and radial displacements of the SWCNT wall, respectively. These displacements are function of x , θ , and t . R is the centerline radius of the SWCNT and h is the thickness of the wall. E , ρ , ν and D are the Young’s modulus, mass density, Poisson’s ratio, and the effective bending stiffness, respectively. The equation of motion of fluid in the cylindrical shell is given by [8]

$$\frac{1}{R} \frac{\partial}{\partial R} \left[R \frac{\partial p^f}{\partial R} \right] + \frac{1}{R^2} \left[\frac{\partial^2 p^f}{\partial \theta^2} \right] + \frac{\partial^2 p^f}{\partial x^2} = \frac{1}{C_f^2} \frac{\partial^2 p^f}{\partial t^2} \tag{11.40}$$

where p^f is the acoustic pressure and C_f is the sound speed of the fluid.

11.2.1 Wave Dispersion Analysis

The displacements u , v , and w for the SWCNT wall is approximated as general solution form of the wave propagation can be given by,

$$u(x, \theta, t) = \hat{U} \exp\{-j(k^a x - \omega t)\} \cos(k^c \theta) \tag{11.41}$$

$$v(x, \theta, t) = \hat{V} \exp\{-j(k^a x - \omega t)\} \sin(k^c \theta) \tag{11.42}$$

$$w(x, \theta, t) = \hat{W} \exp\{-j(k^a x - \omega t)\} \cos(k^c \theta) \tag{11.43}$$

where \hat{U} , \hat{V} , and \hat{W} represent the longitudinal, circumferential, and radial amplitudes of displacements of the SWCNT, respectively. ω is the circular frequency, k^a and k^c are the axial and circumferential wavenumbers, respectively. Substituting Eqs. (11.41)–(11.43) into the governing wave equations (see Eqs. (11.37)–(11.39)), we get the reduced equations as follows. Writing it in matrix form, we get the Polynomial Eigenvalue Problem as,

$$A^4 k^{c^4} + A^3 k^{c^3} + A^2 k^{c^2} + A^1 k^c + A^0 = 0 \tag{11.44}$$

where,

$$A^4 = \begin{bmatrix} 0 & 0 & 0 \\ 0 & 0 & 0 \\ 0 & 0 & \frac{\Lambda}{R^2} \end{bmatrix} \quad A^3 = \begin{bmatrix} 0 & 0 & 0 \\ 0 & 0 & 0 \\ 0 & 0 & 0 \end{bmatrix} \tag{11.45}$$

$$A^2 = \begin{bmatrix} -\frac{(1+\Lambda)(1-\nu)}{2R} + \Gamma(e_0 a)^2 \omega^2 & 0 \\ 0 & -1 + \Gamma(e_0 a)^2 \omega^2 \\ \frac{j\Lambda k^a (1-\nu)}{2R} & 0 \end{bmatrix}$$

$$\left. \begin{array}{c} \frac{j\Lambda k^a(1-\nu)}{2R} \\ 0 \\ 2\Lambda k^{a^2} - 2\frac{\Lambda}{R^2} + \Gamma(e_0a)^2(P_0^a + \omega^2) \end{array} \right] \quad (11.46)$$

$$A^1 = \begin{bmatrix} 0 & -\frac{k^a(1+\nu)}{2R} & 0 \\ -\frac{k^a(1+\nu)}{2R} & 0 & \frac{j\Lambda k^{a^2}(3-\nu)}{2} + j \\ 0 & -\frac{j\Lambda k^{a^2}(3-\nu)}{2} - j & 0 \end{bmatrix} \quad (11.47)$$

$$A^0 = \begin{bmatrix} -k^{a^2} + \Gamma\omega^2\chi & 0 \\ 0 & -\frac{k^{a^2}(3\Lambda+1)(1-\nu)}{2} + \Gamma\omega^2\chi \\ -j\Lambda k^{a^3}R - \frac{jk^{a^2}\nu}{R} & 0 \\ -j\Lambda k^{a^3}R - \frac{jk^{a^2}\nu}{R} & 0 \\ 0 & 0 \\ \Lambda k^{a^4}R^2 - j\Lambda k^{a^3}R + (1-\Lambda) + \Gamma\chi(\omega^2 + P_0^a) \end{bmatrix} \quad (11.48)$$

where $\chi = 1 + (e_0a)^2k^{a^2}$. The wavenumbers can be computed by solving the PEP (Eq. 11.44). The phase speed is calculated from the definition of phase speed as $C_p = \text{Real}[\omega/k^c]$.

Based on the displacement modes (Eqs. (11.41)–(11.43)) of dynamic response to a fluid-filled SWCNTs, the pressure caused by a fluid liquid in the CNT should satisfy the acoustic wave equation (Eq. (11.40)) in cylindrical co-ordinates, which can be expressed as

$$p^f = P_0^a Z_n(k^r R) \exp\{-j(k^a x - \omega t)\} \cos(k^c \theta) \quad (11.49)$$

where

$$P_0^a = \frac{\rho_f \omega^2}{k^r Z_n'(k^r R)} \hat{W}, \quad k^r = \pm \left[\frac{\omega^2}{C_f^2} - k^{a^2} \right]^{1/2} \quad (11.50)$$

where ρ_f is the density of the fluid, where Z_n denotes a Bessel function J_n of order n when $k^{r^2} > 0$, and the modified Bessel function I_n when $k^{r^2} < 0$. Here k^r represent the radial wavenumber.

Next, numerical experiments are presented to analyze the ultrasonic wave properties of fluid-filled SWCNTs including nonlocal scale effects.

The material properties of SWCNT are as follows, Young's modulus, $Eh = 360 \text{ J/m}^2$, mass density, $\rho = 2700 \text{ kg/m}^3$ and Poisson's ratio, $\nu = 0.27$. The SWCNT wall thickness $h = 0.34 \text{ nm}$. The effective bending stiffness, D is taken as $D = 2 \text{ eV}$ ($1 \text{ eV} = 1.6021 \times 10^{-19} \text{ N/m}^2$). The SWNTs have a diameter of 2.0 nm.

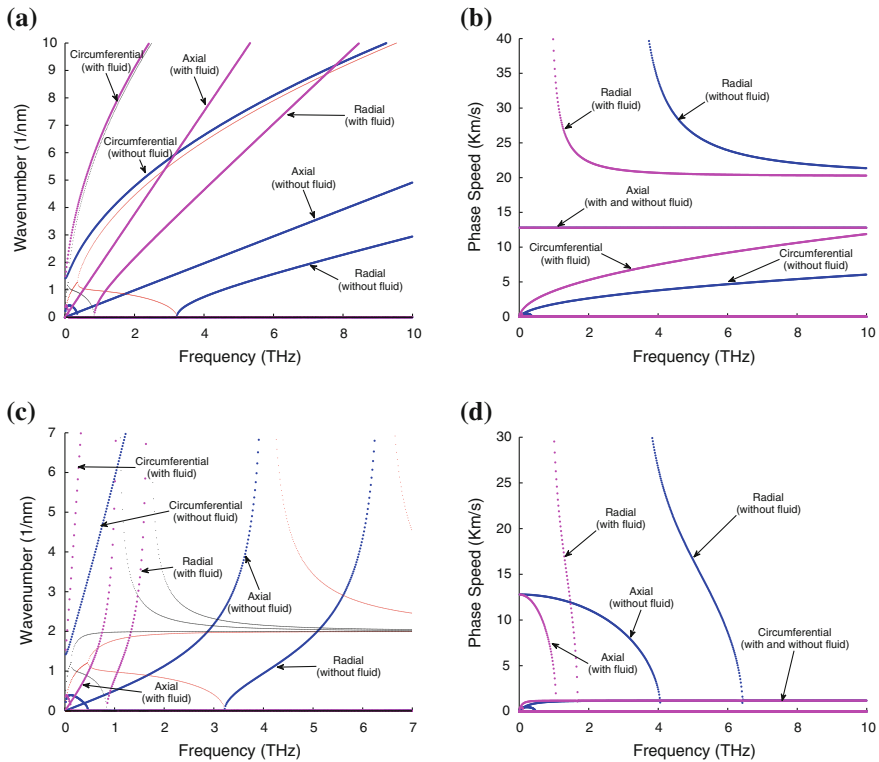


Fig. 11.8 Wavenumber [thin lines-imaginary; thick lines-real] and phase speed dispersion in fluid-filled SWCNTs: (a) & (b) local elasticity, (c) & (d) nonlocal elasticity

The property of water fluid has the density of 1000 kg/m^3 and the free wave speed of 1500 m/s .

Figure 11.8a and c show the real and imaginary parts of the circumferential wavenumber of fluid-filled SWCNT for local elasticity and nonlocal elasticity, respectively. These wavenumbers are obtained by assuming variation only in the circumferential direction. The thick lines represent the real part and the thin lines show the imaginary part of the wavenumbers. From Fig. 11.8a, it can be seen that there are three modes of wave propagation, namely, axial, circumferential, and radial. The wavenumbers for the axial mode has a linear variation with the frequency. The linear variation of the wavenumbers denote that the waves will propagate nondispersively (see Fig. 11.8b). On the other hand, the circumferential wavenumbers are dispersive in nature. However, the wavenumbers of this circumferential wave mode have a substantial real part starting from the zero frequency. The radial mode, however, has a certain frequency band within which the corresponding wavenumbers are purely imaginary. Thus, the radial mode does not propagate at frequencies lying within this frequency band. The presence of fluid (water) in SWCNT alters the ul-

trasonic wave dispersion behavior. The wavenumber and wave velocity are smaller in the presence of fluid as compared to the empty SWCNT as shown in Fig. 11.8.

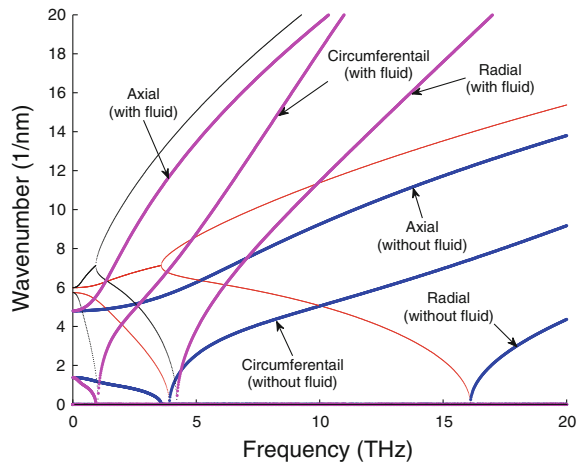
Figure 11.8b shows the wavenumber dispersion obtained from nonlocal elasticity. It can be seen that because of nonlocality, the wavenumber tends to reach the continuum limit at escape frequencies. Observe that the circumferential waves are not following the nonlocal elasticity behavior, that is, the wavenumbers do not tend to infinity and the corresponding wave speeds are not zero. It shows that the circumferential waves will propagate at any frequencies.

Figure 11.9 shows the variation of circumferential wavenumbers with and without fluid in SWCNT for an axial wavenumber of $k^a = 5 \text{ nm}^{-1}$. Here, coupling exists between the axial, circumferential and radial wave modes. It can be seen that the axial mode has a nonlinear variation with frequency unlike that shown in Fig. 11.8a. This nonlinear variation occur due to the coupling of degrees of freedom. Thus, here, the axial modes are dispersive in nature. Next, the real part of the wavenumbers for the circumferential mode exists after a certain frequency referred as the cut-off frequency. This implies that the mode start propagating only after the cut-off frequency. In Fig. 11.8a and c, where $k^a = 0$, such cut-off frequency does not exist for the circumferential mode. The radial mode, however, shows similar pattern as in Fig. 11.8 and has a frequency band within which the waves do not propagate.

Figure 11.10 shows the effect of fluid density on ultrasonic wave propagation in fluid-filled SWCNTs. It has been observed that the wavenumber of all the three modes will increase as the fluid in CNT becomes denser (see Fig. 11.10a) and the corresponding wave speeds will decrease (see Fig. 11.10b). The other observation is that the cut-off frequencies of the radial waves will decrease as the fluid becomes denser. That implies the cut-off frequencies of the radial waves will depend on the density of the fluid in SWCNT.

The effect of the axial wavenumber (k^a) on the ultrasonic wave behavior in fluid-filled SWCNTs is also observed in Fig. 11.11. The effect of axial wavenumber on total

Fig. 11.9 Wavenumber [thin lines-imaginary; thick lines-real] dispersion in fluid-filled SWCNTs for axial wavenumber $k^a = 5 \text{ nm}^{-1}$ (local elasticity)



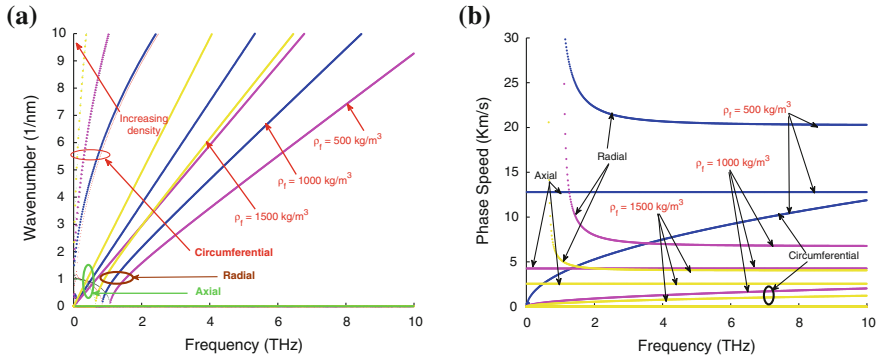


Fig. 11.10 Variation of (a) wavenumber [thin lines-imaginary; thick lines-real] and (b) phase speed dispersion in fluid-filled SWCNTs for different fluid densities (ρ_f)

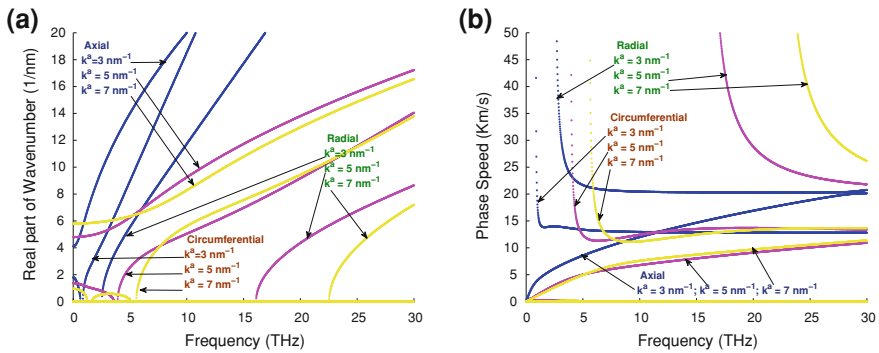


Fig. 11.11 Variation of wavenumber [only real part is shown] and phase speed dispersion in water-filled SWCNTs for different axial wavenumbers of $k^a = 3, 5$ and 7 nm^{-1}

ultrasonic wave behavior on SWCNTs is already explained in Fig. 11.9. Similar type of behavior is also observed in Fig. 11.11. As we increase k^a , the cut-off frequencies of the radial and circumferential modes will also increase. The axial waves in this case are dispersive in nature as shown in Fig. 11.11a. The effect of k^a on the wave velocity of fluid-filled SWCNTs is shown in Fig. 11.11b. For smaller frequencies, the wave velocities decrease as k^a increase, and at higher frequencies the velocities are almost constant (see Fig. 11.11b).

11.3 Wave Propagation in Higher Order Nanoshells

In this section, first order shear deformation theory (FSDT) is used, that includes the contribution of stiffness and inertial coupling for studying the characteristic wave propagation in carbon nanotubes is presented. The model uses lateral con-

traction caused by Poisson's ratio effect . Appearance of higher order Lamb wave modes above certain cut-off frequencies have been studied for bulk metallic beams by Mindlin and Harrmann [9], Doyle [4] and Gopalakrishnan [10] and for laminated composite plates by Karim et al. [11]. In this section, the contribution of a contractional mode along with shear mode is studied for their effects on the wave behavior of cylindrical SWCNTs. Expression of cut-off frequencies and escape frequencies in shear mode and contractional mode are also derived.

11.3.1 Governing Nanoshell Equations Including Shear and Contraction Effects

The displacement field for axial and transverse motion based on FSDT and thickness contraction is given by

$$u(x, y, z, t) = u^0(x, t) - z\phi(x, t) \quad (11.51)$$

$$w(x, y, z, t) = w^0(x, t) + z\psi(x, t) \quad (11.52)$$

where u and w are the axial and transverse displacements, respectively, at a material point. u^0 is the beam axial displacement along the reference plane, w^0 is the transverse displacement on the reference plane, ϕ is the curvature- independent rotation of the beam cross-section about Y -axis and $\psi = \varepsilon_{zz}$ is the contraction/elongation parallel to Z -axis (shown in Fig. 11.12).

The strains are obtained as

$$\varepsilon_{xx} = \frac{\partial u^0(x, t)}{\partial x} - z \frac{\partial \phi(x, t)}{\partial x} \quad (11.53)$$

$$\varepsilon_{zz} = \psi(x, t) \quad (11.54)$$

$$\varepsilon_{xz} = -\phi(x, t) + \frac{\partial w^0(x, t)}{\partial x} + z \frac{\partial \psi(x, t)}{\partial x} \quad (11.55)$$

The nonlocal constitutive relation for isotropic materials is given as

$$\begin{Bmatrix} \sigma_{xx} \\ \sigma_{zz} \\ \tau_{xz} \end{Bmatrix} - (e_0 a)^2 \frac{\partial^2}{\partial x^2} \begin{Bmatrix} \sigma_{xx} \\ \sigma_{zz} \\ \tau_{xz} \end{Bmatrix} = \begin{bmatrix} C_{11} & \nu C_{12} & 0 \\ \nu C_{12} & C_{22} & 0 \\ 0 & 0 & C_{66} \end{bmatrix} \begin{Bmatrix} \varepsilon_{xx} \\ \varepsilon_{zz} \\ \gamma_{xz} \end{Bmatrix} \quad (11.56)$$

where, σ_{xx} and σ_{zz} are the normal stresses in x and z directions respectively and τ_{xz} is the in-plane shear stress. For the case of an isotropic plate, the expressions for C_{ij} in terms of Young's modulus E and Poisson's ratio ν are given as $C_{11} = C_{12} = C_{22} = E/(1 - \nu^2)$ and $C_{66} = E/(2(1 + \nu))$.

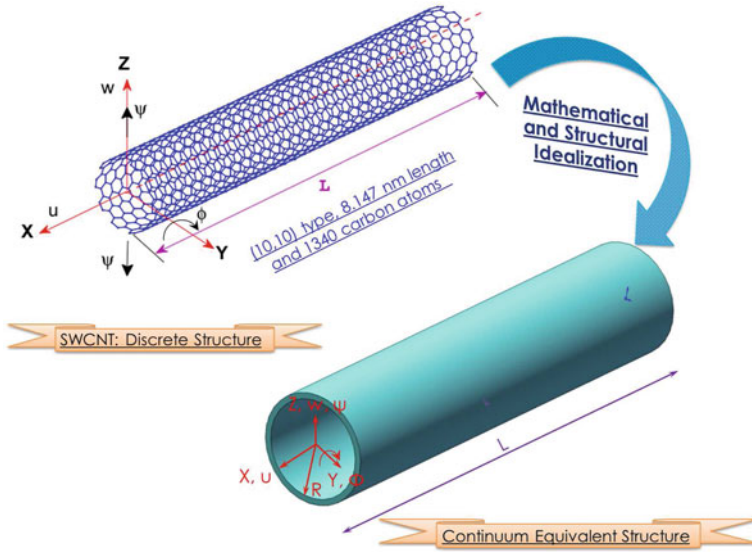


Fig. 11.12 Mathematical and structural idealization of the single-walled carbon nanotube (SWCNT) showing the degree of freedom defined on both the discrete structure and its equivalent continuum structure

The potential and kinetic energies are given as

$$\begin{aligned} \Pi^E &= \frac{1}{2} \int_V (\sigma_{xx}\epsilon_{xx} + \sigma_{zz}\epsilon_{zz} + \tau_{xz}\gamma_{xz}) dV \\ &= \frac{1}{2} \int_0^L \int_A (\sigma_{xx}\epsilon_{xx} + \sigma_{zz}\epsilon_{zz} + \tau_{xz}\gamma_{xz}) dx dA \end{aligned} \quad (11.57)$$

$$\begin{aligned} \Gamma^E &= \frac{1}{2} \rho \int_V (\dot{u}^2 + \dot{w}^2) dV \\ &= \frac{1}{2} \rho \int_0^L \int_A ([\dot{u}^0(x, t) - z\dot{\phi}(x, t)]^2 + [\dot{w}^0(x, t) + z\dot{\psi}(x, t)]^2) dx dA \end{aligned} \quad (11.58)$$

assuming constant cross-sectional area of SWCNT,

$$\Pi^E = \frac{1}{2} A \int_0^L (\sigma_{xx}\epsilon_{xx} + \sigma_{zz}\epsilon_{zz} + \tau_{xz}\gamma_{xz}) dx \quad (11.59)$$

$$\Gamma^E = \frac{1}{2} \rho A \int_0^L ([\dot{u}^0(x, t) - z\dot{\phi}(x, t)]^2 + [\dot{w}^0(x, t) + z\dot{\psi}(x, t)]^2) dx \quad (11.60)$$

Using Hamilton's principle,

$$\int_{t_1}^{t_2} \delta \mathcal{L}^E dt = \int_{t_1}^{t_2} \left(\delta \Gamma^E - \delta \Pi^E \right) dt = 0 \quad (11.61)$$

and Eqs. (11.53)–(11.55) and (11.56), and the fundamental lemma of calculus of variations, the nonlocal governing equations of motion are derived as:

$$\begin{aligned} \delta u^0 : \quad & I_0 \frac{\partial^2 u^0}{\partial t^2} - I_0 (e_0 a)^2 \frac{\partial^4 u^0}{\partial t^2 \partial x^2} - I_1 \frac{\partial^2 \phi}{\partial t^2} + I_1 (e_0 a)^2 \frac{\partial^4 \phi}{\partial t^2 \partial x^2} - C_{11} J_0 \frac{\partial^2 u^0}{\partial x^2} \\ & + C_{11} J_1 \frac{\partial^2 \phi}{\partial x^2} - C_{12} J_0 \frac{\partial \psi}{\partial x} = 0 \end{aligned} \quad (11.62)$$

$$\begin{aligned} \delta \psi : \quad & I_2 \frac{\partial^2 \psi}{\partial t^2} - I_2 (e_0 a)^2 \frac{\partial^4 \psi}{\partial t^2 \partial x^2} + I_1 \frac{\partial^2 w^0}{\partial t^2} + I_1 (e_0 a)^2 \frac{\partial^4 w^0}{\partial t^2 \partial x^2} + C_{12} J_0 \frac{\partial u^0}{\partial x} \\ & - C_{12} J_1 \frac{\partial \phi}{\partial x} + C_{22} J_0 \psi - C_{66} J_1 \left(\frac{\partial^2 w^0}{\partial x^2} - \frac{\partial \phi}{\partial x} \right) - C_{66} J_2 \frac{\partial^2 \psi}{\partial x^2} = 0 \end{aligned} \quad (11.63)$$

$$\begin{aligned} \delta w^0 : \quad & I_0 \frac{\partial^2 w^0}{\partial t^2} - I_0 (e_0 a)^2 \frac{\partial^4 w^0}{\partial t^2 \partial x^2} + I_1 \frac{\partial^2 \psi}{\partial t^2} - I_1 (e_0 a)^2 \frac{\partial^4 \psi}{\partial t^2 \partial x^2} \\ & - C_{66} J_0 \left(\frac{\partial^2 w^0}{\partial x^2} - \frac{\partial \phi}{\partial x} \right) - C_{66} J_1 \frac{\partial^2 \psi}{\partial x^2} = 0 \end{aligned} \quad (11.64)$$

$$\begin{aligned} \delta \phi : \quad & I_2 \frac{\partial^2 \phi}{\partial t^2} - I_2 (e_0 a)^2 \frac{\partial^4 \phi}{\partial t^2 \partial x^2} - I_1 \frac{\partial^2 u^0}{\partial t^2} + I_1 (e_0 a)^2 \frac{\partial^4 u^0}{\partial t^2 \partial x^2} - C_{66} J_0 \left(\frac{\partial w^0}{\partial x} - \phi \right) \\ & - C_{66} J_1 \frac{\partial \psi}{\partial x} + C_{11} J_1 \frac{\partial^2 u^0}{\partial x^2} - C_{11} J_2 \frac{\partial^2 \phi}{\partial x^2} + C_{11} J_1 \frac{\partial \psi}{\partial x} = 0 \end{aligned} \quad (11.65)$$

where

$$J_p = \int_0^{2\pi} \int_{R-h}^{R+h} z^p r dr d\theta, \quad (11.66)$$

$$I_p = \int_0^{2\pi} \int_{R-h}^{R+h} \rho z^p r dr d\theta \quad (11.67)$$

Here $z = r \sin \theta$ and $p = 0, 1, 2$. One can substitute $e_0 a = 0$ in the Eqs. (11.62)–(11.65), to recover the local or classical coupled equations for the SWCNTs.

11.3.2 Wave Dispersion Analysis

Using discrete Fourier transformation (DFT) for the temporal field, the spectral solution for primary displacement field variables can be expressed as

$$\mathbf{d}(x, t) = \hat{\mathbf{d}}(x, \omega) e^{-j(kx - \omega t)} \quad (11.68)$$

where $\mathbf{d} = \{u^0 \ \psi \ w^0 \ \phi\}^T$ is the generic displacement vector as a function of (x, t) and $\hat{\mathbf{d}} = \{\hat{u}^0 \ \hat{\psi} \ \hat{w}^0 \ \hat{\phi}\}^T$ represents the the spectral amplitude vector corresponding to generic displacement vector as a function of (x, ω) . k is the wavenumber and ω is the angular frequency of the wave motion and $j = \sqrt{-1}$.

Substituting Eqs. (11.68) in the governing equations of motion of SWCNT (see Eqs. (11.62)–(11.65)) yields four homogeneous equations in terms of \hat{u} , $\hat{\psi}$, \hat{w} and $\hat{\phi}$ as

$$\begin{bmatrix} Q_{11} & Q_{12} & Q_{13} & Q_{14} \\ Q_{21} & Q_{22} & Q_{23} & Q_{24} \\ Q_{31} & Q_{32} & Q_{33} & Q_{34} \\ Q_{41} & Q_{42} & Q_{43} & Q_{44} \end{bmatrix} \begin{Bmatrix} \hat{u}^0 \\ \hat{\psi} \\ \hat{w}^0 \\ \hat{\phi} \end{Bmatrix} = \begin{Bmatrix} 0 \\ 0 \\ 0 \\ 0 \end{Bmatrix} \quad (11.69)$$

where

$$\begin{aligned} Q_{11} &= -C_{11}J_0k^2 + I_0\omega^2 + I_0\omega^2(e_0a)^2k^2; \\ Q_{12} &= -Q_{21} = -jC_{12}J_0k; \\ Q_{13} &= Q_{31} = 0; \\ Q_{14} &= Q_{41} = C_{11}J_1k^2 - I_1\omega^2 - I_1(e_0a)^2\omega^2k^2; \\ Q_{22} &= -C_{55}J_2k^2 - C_{12}J_0 + I_2\omega^2 + I_2\omega^2(e_0a)^2k^2; \\ Q_{23} &= Q_{32} = -C_{55}J_1k^2 + I_1\omega^2 + I_1\omega^2(e_0a)^2k^2; \\ Q_{24} &= -Q_{42} = j(C_{55} - C_{12})J_1k; \\ Q_{33} &= -C_{55}J_0k^2 + I_0\omega^2 + I_0\omega^2(e_0a)^2k^2; \\ Q_{34} &= -Q_{43} = jC_{55}J_0k; \\ Q_{44} &= -C_{11}J_2k^2 - C_{55}J_0 + I_2\omega^2 + I_2\omega^2(e_0a)^2k^2. \end{aligned} \quad (11.70)$$

The wavenumbers and hence the wave speeds (i.e., phase and group speeds) are solved from Eq. (11.69) by using Polynomial Eigenvalue Problem. Equating the determinant of matrix $[Q_{ab}]$ to zero (for the nontrivial solution of $\hat{\mathbf{d}}$ will give the characteristic polynomial in terms of wavenumber k of the order 8, solution of which is quite difficult. PEP converts the characteristic polynomial equation into a matrix of size 4×4 , whose eigen values form the solution of the equation. After obtaining the wavenumbers, the wave speeds are extracted. The details of compu-

tation of wavenumbers using PEP are as follows. We write characteristic equation (Eq. (11.69)) of the form given by

$$[\mathbf{S}_2]k^2 + [\mathbf{S}_1]k + [\mathbf{S}_0] = 0 \quad (11.71)$$

where

$$[\mathbf{S}_2] = \begin{bmatrix} S_2^{(11)} & 0 & 0 & S_2^{(14)} \\ 0 & S_2^{(22)} & S_2^{(23)} & 0 \\ 0 & S_2^{(32)} & S_2^{(33)} & 0 \\ S_2^{(41)} & 0 & 0 & S_2^{(44)} \end{bmatrix} \quad (11.72)$$

$$[\mathbf{S}_1] = \begin{bmatrix} 0 & -jC_{12}J_0 & 0 & 0 \\ jC_{12}J_0 & 0 & 0 & -j(C_{12} - C_{66})J_1 \\ 0 & 0 & 0 & jC_{66}J_0 \\ 0 & j(C_{12} - C_{66})J_1 & -jC_{66}J_0 & 0 \end{bmatrix} \quad (11.73)$$

$$[\mathbf{S}_0] = \begin{bmatrix} I_0\omega^2 & 0 & 0 & -I_1\omega^2 \\ 0 & -C_{22}J_0 + I_2\omega^2 & I_1\omega^2 & 0 \\ 0 & I_1\omega^2 & I_0\omega^2 & 0 \\ -I_1\omega^2 & 0 & 0 & -C_{66}J_0 + I_2\omega^2 \end{bmatrix} \quad (11.74)$$

Here

$$\begin{aligned} S_2^{(11)} &= -C_{11}J_0 + I_0\omega^2(e_0a)^2 \\ S_2^{(14)} &= S_2^{(41)} = C_{11}J_1 - I_1(e_0a)^2\omega^2 \\ S_2^{(22)} &= -C_{66}J_2 + I_2\omega^2(e_0a)^2 \\ S_2^{(23)} &= S_2^{(32)} = -C_{66}J_1 + I_1\omega^2(e_0a)^2 \\ S_2^{(33)} &= -C_{66}J_0 + I_0\omega^2(e_0a)^2 \\ S_2^{(44)} &= -C_{11}J_2 + I_2\omega^2(e_0a)^2 \end{aligned} \quad (11.75)$$

This form is amenable to solution of wavenumbers through PEP. From Eq. (11.71), we can clearly see the dependence of nonlocal scale parameter e_0a on wavenumber. The cut-off frequencies of this SWCNTs are obtained by setting $Det([\mathbf{S}_0]) = 0$, which gives

$$\omega_c^{axial} = 0, \quad \omega_c^{flexural} = 0 \quad (11.76)$$

$$\omega_c^{contraction} = \sqrt{\frac{C_{22}I_0J_0}{I_0I_2 - I_1^2}}, \quad \omega_c^{shear} = \sqrt{\frac{C_{66}I_0J_0}{I_0I_2 - I_1^2}} \quad (11.77)$$

Next, we will set $Det[\mathbf{S}_2] = 0$ and determine the escape frequencies, which are given by

$$\omega_e^{axial} = \frac{1/e_0a\sqrt{C_{66}}}{[2(I_0I_2 - I_1^2)\sqrt{X_2 - 4I_1J_1X_1 + 4X_0 - 2I_0I_2J_0J_2} + X_1 - 2I_1J_1]^{1/2}} \quad (11.78)$$

$$\omega_e^{flexural} = \frac{\sqrt{C_{66}}}{e_0a} \left[\frac{\sqrt{X_2 - 4I_1J_1X_1 + 4X_0 - 2I_0I_2J_0J_2} - X_1 + 2I_1J_1}{2(I_1^2 - I_0I_2)} \right]^{1/2} \quad (11.79)$$

$$\omega_e^{shear} = \frac{1/e_0a\sqrt{C_{11}}}{[2(I_0I_2 - I_1^2)\sqrt{X_2 - 4I_1J_1X_1 + 4X_0 - 2I_0I_2J_0J_2} + X_1 - 2I_1J_1]^{1/2}} \quad (11.80)$$

$$\omega_e^{contraction} = \frac{\sqrt{C_{11}}}{e_0a} \left[\frac{\sqrt{X_2 - 4I_1J_1X_1 + 4X_0 - 2I_0I_2J_0J_2} - X_1 + 2I_1J_1}{2(I_1^2 - I_0I_2)} \right]^{1/2} \quad (11.81)$$

where

$X_2 = I_0^2J_2^2 + I_2^2J_0^2$; $X_1 = I_0J_2 + I_2J_0$; $X_0 = I_0I_2J_1^2 + I_1^2J_0J_2$. Here ω_e is the escape frequency or sometimes called the asymptotic frequency. Differentiating the Eq. (11.71) with respect to the wave frequency (ω), one can obtain the group speeds as

$$2\omega \left((e_0a)^2k^2 + 1 \right) [\mathbf{H}]C_g + 2k[\mathbf{S}_2] + [\mathbf{S}_1] = 0 \quad (11.82)$$

Here

$$[\mathbf{H}] = \begin{bmatrix} I_0 & 0 & 0 & -I_1 \\ 0 & I_2 & I_1 & 0 \\ 0 & I_1 & I_0 & 0 \\ -I_1 & 0 & 0 & I_2 \end{bmatrix} \quad (11.83)$$

where $C_g = (\partial\omega/\partial k)$ is the group speed of a wave in SWCNT and the matrices $[\mathbf{S}_2]$, and $[\mathbf{S}_1]$ are given in Eqs. (11.72) and (11.73), respectively. This is again a PEP in terms of C_g and one can solve it for group speeds of respective modes (i.e., for axial, flexural, shear, and contraction), which is again a function of nonlocal scale parameter.

The phase speed is next calculated from the usual definition as

$$C_p = Re \left(\frac{\omega}{k} \right) \quad (11.84)$$

The detail effect of the nonlocality on wave speeds of single-walled carbon nanotubes will be discussed in the later part of this section.

We will now present the numerical results for the wave properties of higher order SWCNTs. First, the wavenumber, phase and group speeds are obtained for SWCNT

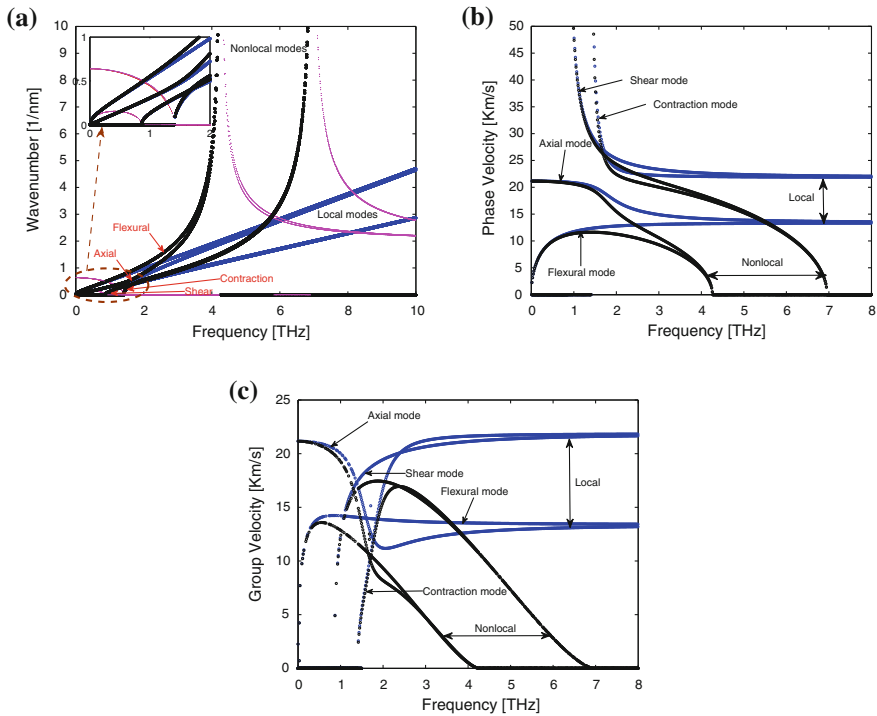


Fig. 11.13 Dispersion Analysis of Fluid-Filled Higher order SWCNT (Both local and nonlocal models) (a) Wavenumber variation (b) Phase speed variation (c) Group speed variation

from local and nonlocal elastic theories. Following Wang [12], the nonlocal parameter e_0a should be less than 2.0 nm, hence, here in the simulation procedure, we choose $e_0a = 0$ nm and 0.5 nm, respectively.

Figure 11.13a shows the real and imaginary parts of the wavenumber of SWCNT obtained from both local and nonlocal models. These wavenumbers are obtained by solving the PEP given in Eq. (11.71). Thick lines represent the real part and the thin lines show the imaginary part of the wavenumbers. From Fig. 11.13a, it can be seen that there are four modes of wave propagation, namely, axial, flexural, shear, and contractional. For local/classical elasticity ($e_0a = 0$), the wavenumbers for the axial mode has a linear variation with the frequency which is in the tera hertz (THz) range. On the other hand, the flexural wavenumbers have a nonlinear variation with the frequency at low frequencies, while at high frequencies, the flexural waves show a linear variation with frequency. The shear and contractional wave modes, however, have certain frequency band within which the corresponding wavenumbers are purely imaginary. Thus, these modes do not propagate at frequencies lying within this band. Both the shear and contraction wavenumbers have a substantial imaginary part along with the real part, thus these waves attenuate as they propagate. In the present study for a 3.5 nm radius SWCNT, we have shear cut-off frequency at 0.8545 THz and

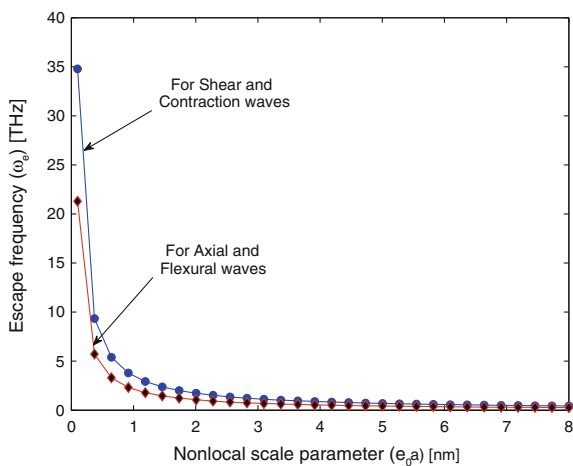
contraction cut-off frequency at 1.404 THz. The values of the cut-off frequency are calculated from Eq. (11.77). It can be observed from Eq. (11.77) that these frequencies are independent of the nonlocal scaling parameter, and hence same frequencies are obtained from both local and nonlocal theories.

For $e_0a = 0$, which is the case of local theory of elasticity solution, wavenumbers increase monotonically with the increase in frequency, which is shown in Fig. 11.13a and correspondingly, the wave speeds, shown in Figs. 11.13b and c increases with increase in wave frequency. However, at higher frequencies, they attain a constant value. However, with the introduction of scale effects (for present analysis $e_0a = 0.5$ nm), the wave behavior is altered drastically. All the wave modes escapes to infinity (as shown in Fig. 11.13a), at escape frequency, and beyond this frequency there is no wave propagation. These are shown in Figs. 11.13b and c.

Effect of nonlocal scaling parameter and radius of SWCNT on the escape frequencies of axial, flexural, shear, and contraction wave modes as shown in Figs. 11.14 and 11.15 a-d, respectively.

Figure 11.14 shows the variation of escape frequencies of flexural and shear wave modes with the nonlocal parameter. The value of escape frequency decreases with increase in the scale parameter e_0a , for all the wave modes. The escape frequencies of the axial and flexural waves are same and that of the shear and contraction waves are also same. It shows that as e_0a increases, the escape frequency decreases. At higher values of e_0a , escape frequencies approach to very small values as shown in Fig. 11.14. Equations (11.78)–(11.81) gives the expressions for escape frequencies of all waves in SWCNT. From these expressions it is clear that escape frequency values are independent of SWCNT diameter (see Fig. 11.3.2), for all wave modes. The detailed variation in escape frequency for SWCNTs as a function of nonlocal scale parameter is shown in Figs. 6.8a-d for $e_0a = 0.5$ nm, 1.0 nm, 1.5 nm and 2.0 nm, respectively. It shows the effect of the radius of the nanotube and nonlo-

Fig. 11.14 Effect of small-scale parameter on the escape frequencies of axial, flexural, shear, and contractional waves



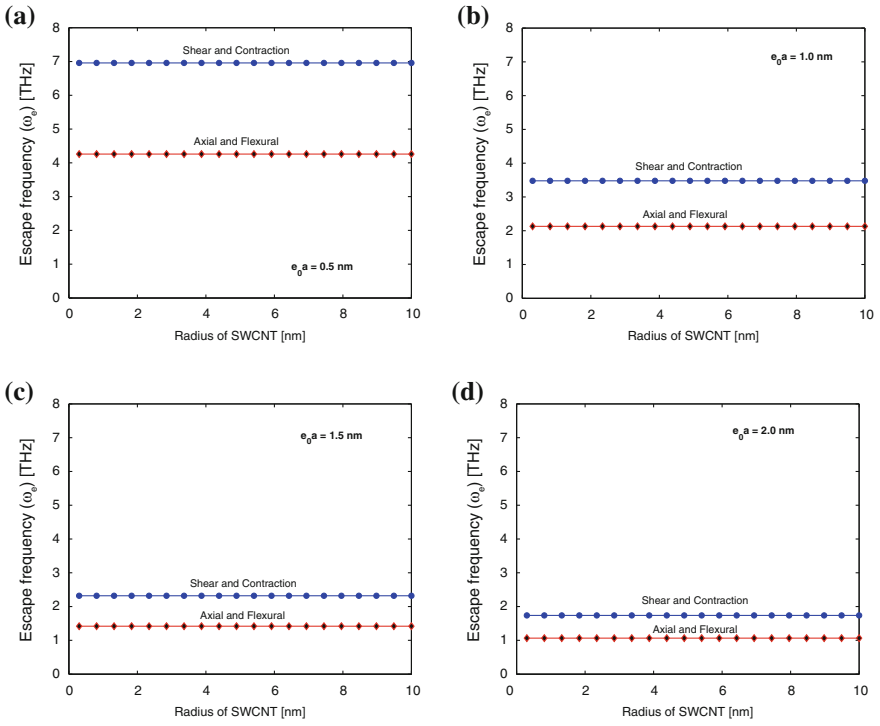
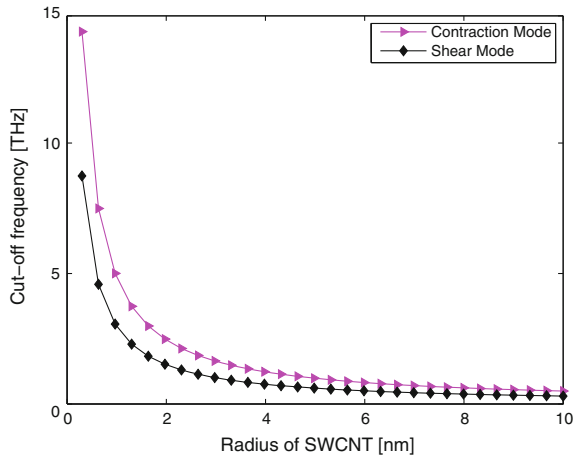


Fig. 11.15 Escape frequency variation with radius of SWCNT

Fig. 11.16 Cut-off frequency variation of the shear and contraction wave modes



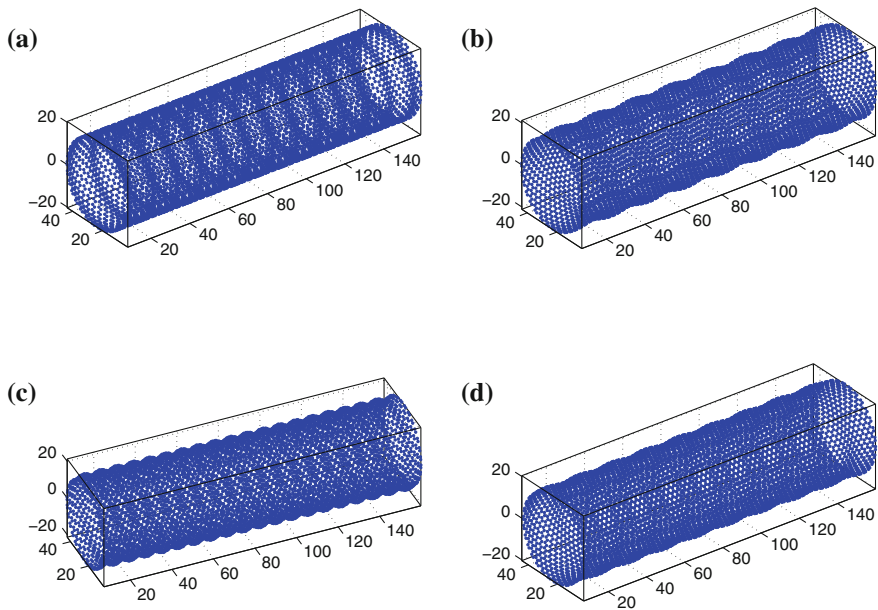


Fig. 11.17 (a) Axial, (b) contraction, (c) flexural and (d) shear wave modes (at 10.067-THz wave frequency) for a (30,30) SWCNT of length 15.282 nm consisting of 7,500 carbon atoms

cal scaling parameter (e_0) on the escape frequency of SWCNTs more clearly. The escape frequencies for both axial and flexural modes are same that of the shear and contraction waves is also same and these are constant with respect to the radius of the CNT. These values of escape frequency are decreasing with the nonlocal scale coefficient e_0a (see Fig. 11.15a–d) and are still constant with radius of CNT.

The variation of the cut-off frequencies of shear contraction wavemodes with radius (R) of SWCNT are shown in Fig. 11.16. This figure shows that, as the radius of the nanotube increases, the cut-off frequencies decrease and at higher values of R , the cut-off frequencies approach to a very small values. Hence, it can be concluded that for large values of scale parameter, shear deformation on CNT has negligible effect and CNT behaves like more like elementary beam (for more details see Refs. [13–16]).

Figure 11.17 shows the wave modes at 10.067-THz wave frequency of a (30,30) SWCNT of length 15.282 nm consisting of 7,500 carbon atoms. Figure 11.17a is for axial wave mode case, Fig. 11.17b is for contraction, Fig. 11.17c is for flexural and Fig. 11.17d is for shear wave modes of this SWCNT. From these figures, one can clearly visualize the type of wave mode and its effect on the CNT.

11.4 Summary

This chapter began with a study of the ultrasonic wave propagation analysis in SWCNT using nonlocal elasticity theory via nonlocal Flügge's shell theory. Nonlocal governing equations for this system are derived and wave propagation analysis is also carried out. The nonlocal elasticity calculation shows that the wavenumber tends to infinity at escape frequency and the corresponding wave velocity tends to zero at those frequencies indicating localization and stationary behavior. This behavior is observed only for axial and radial waves in SWCNT. It has been shown that the circumferential waves will propagate dispersively at higher frequencies in nonlocal elasticity. We also show that the cut-off frequencies depend on the axial wavenumber and not on the nonlocal scaling parameter.

Next, the ultrasonic wave characteristics of fluid-filled SWCNTs are studied by modeling it as a thin shell based on Flügge's shell theory incorporating nonlocal scale effects. The ultrasonic wave propagation analysis is also carried out. The presence of fluid in SWCNT alters the ultrasonic wave dispersion behavior. The wavenumber and wave velocity are smaller in the presence of fluid as compared to the empty SWCNT. The nonlocal elasticity calculation shows that the wavenumber tends to reach the continuum limit at certain frequencies and the corresponding wave velocity tends to zero at those frequencies indicating localization and stationary behavior. The effect of density and axial wavenumber on the ultrasonic wave behavior in SWCNTs filled with water is also discussed in this section.

Finally, the effect of nonlocal scaling parameter on the coupled (axial, flexural, shear, and contraction) wave propagation in SWCNTs is studied. The axial and transverse motion of SWCNT is modeled based on FSDT and thickness contraction. The governing equations are derived based on nonlocal constitutive relations and the wave dispersion analysis is also carried out. The nonlocal elasticity calculation shows that the wavenumber tends to infinite at certain frequencies and the corresponding wave velocity tends to zero at those frequencies indicating localization and stationary behavior. A polynomial eigenvalue problem in wavenumbers is obtained as a function of wave frequency, nonlocal scale parameter, and the material properties of the SWCNT. Explicit expressions are derived for cut-off and escape frequencies of all waves in SWCNT. It is also shown that the cut-off frequencies of shear and contraction mode are independent of the nonlocal scale parameter.

At the end of this book, the reader will now be in a position to understand the effects of various nanostructure parameters on its wave propagation. Some of the observations may be same for some cases discussed in this book (such as existence of escape frequencies for all cases of nonlocal elasticity waveguides), while many new phenomenon are seen in certain nonlocal waveguides. This book has shown the complex nature of wave propagation in many different nanostructures and it has unified the whole wave propagation analysis concepts under one major analysis tool, that is the spectral analysis of motion.

References

1. Q. Wang, V.K. Varadan, Application of nonlocal elastic shell theory in wave propagation analysis of carbon nanotubes. *Smart Mater. Struct.* **16**, 178–190 (2007)
2. S. Markus, *The Mechanics of Vibration of Cylindrical Shells* (Elsevier, Amsterdam, 1988)
3. W. Flugge, *Stresses in Shells* (Springer, Berlin/Heidelberg, 1960)
4. J.F. Doyle, *Wave Propagation in Structures* (Springer-Verlag Inc., New York, 1997)
5. S. Gopalakrishnan, A. Chakraborty, D. Roy Mahapatra, *Spectral Finite Element Method* (Springer-Verlag Landon Ltd, Roy Mahapatra, Spectral Finite Element Method, 2008)
6. L.H. Ye, B.G. Liu, D.S. Wang, R. Han, Ab initio phonon dispersions of single-wall carbon nanotubes. *Phys. Rev. B* **69**, 235409 (2004)
7. L. Chico, R. Perez-Alvarez, C. Cabrillo, Low-frequency phonons in carbon nanotubes: a continuum approach. *Phys. Rev. B* **73**, 075425 (2006)
8. P.M. Morse, K.U. Ingard, *Theoretical Acoustics* (McGraw-Hill, New York, 1969)
9. R.D. Mindlin, G. Harrmann, A one dimensional theory of compressional waves in an elastic rod. In: *Proceedings of First US National Congress of Applied Mechanics*, 187–191 (1950)
10. S. Gopalakrishnan, A deep rod finite element for structural dynamics and wave propagation problems. *Int. J. Numer. Meth. Eng.* **48**, 731–744 (2000)
11. M.R. Karim, M.A. Awal, T. Kundu, Elastic wave scattering by cracks and inclusions in plates: in-plane case. *Int. J. Solids Struct.* **29**(19), 2355–2367 (1992)
12. Q. Wang, Wave propagation in carbon nanotubes via nonlocal continuum mechanics. *Journal of Applied Physics* **98**, 124301 (2005)
13. S. Narendar, S. S. Gupta, S. Gopalakrishnan, Longitudinal magnetic field effect on nonlocal ultrasonic vibration analysis of single-walled carbon nanotubes based on wave propagation approach. *Adv. Sci. Let.* **4**(11/12), 3382–3389 (2011)
14. S. Narendar, S. Gopalakrishnan, A revisit to capture the entire behavior of ultrasonic wave dispersion characteristics of single walled carbon nanotubes based on nonlocal elasticity theory and Flugge shell model. *J. Comput. Theor. Nanos.* **8**(10), 1933–1944 (2011)
15. S. Narendar, S. Gopalakrishnan, Ultrasonic wave dispersion characteristics of fluid-filled single-walled carbon nanotubes based on nonclassical shell model. *Adv. Sci. Let.* **4**(11/12), 3480–3485 (2011)
16. S. Narendar, S. Gopalakrishnan, Nonlocal continuum mechanics formulation for axial, flexural, shear and contraction coupled wave propagation in single walled carbon nanotubes. *Lat. Am. J. Sol. Struct.* **4**, 421–437 (2012)

Index

A

Ab initio pseudopotentials, 35
Acoustic phonon dispersion, 330, 336
Acoustic pressure, 337
Anodic alumina, 206
Armchair CNT
 chirality, 93
Asymptotic stiffness, 83

B

Band gap, 174, 190, 201, 211, 243, 252, 290, 303
Bessel function, 338
Bi-Helmholtz equation, 151
Born-Karman model, 61, 85, 143, 151
Boussinesq problem, 51
Breathing modes, 336
Brillouin zone, 85, 151, 152
Buckling load, 74, 76
Bulk waves, 305

C

Carbon nanotube, 3
 armchair, 8, 71, 80, 86
 chiral, 8, 71, 80, 101
 chiral angle, 8
 chirality, 40
 in plane stiffness, 72
 material property estimation, 71
 multi-Wall, 3, 8
 nanoresonator, 38
 properties, 10
 roll-up vector, 8
 rotating, 177

 single-wall, 4, 7, 38
 structure, 8
 zigzag, 8, 71, 80, 94
Centrifugal stiffening, 179
Circumferential displacement, 326, 337
Circumferential wavenumber, 327, 331, 339
Classical elasticity theory, 123, 143, 205, 314
 constitutive relation, 143
Classical plate theory, 271
COMPASS, 39
Contractional wave mode, 348
Coupling stiffness, 239, 262
Critical wavenumber, 134, 136
Crystal lattice, 66, 280
Crystallographic direction, 206, 310
Current density, 195
Cut-off frequency, 23, 28, 294
 DNBS, 252
 DNRS, 243, 246, 247
 DWCNT, 226
 fluid carrying SWCNT, 193
 fluid filled nanoshell, 340
 graphene, 275, 277, 278
 graphene on silicon substrate, 289
 higher order nanoshell, 346
 magnetic field effects, 200
 nanoplate with surface effects, 309, 314
 nanoplate with temperature effects, 301, 304
 nanoshell, 329, 331, 332
 SWCNT Timoshenko beam, 223
 Timoshenko DNBS, 259, 261
 Timoshenko nanobeam, 174
 TWCNT, 233
Cylindrical nanoshell, 324

D

- Density functional theory, 34
- Dispersion relation
 - DNBS, 251
 - DWCNT, 225
 - fluid filled nanoshell, 337
 - fourth order PDE, 26
 - graphene, 273
 - graphene on silicon substrate, 287
 - higher order nanoshell, 345
 - lateral inertia effects, 142
 - MWCNT, 219
 - nanoplate with surface effects, 309
 - nanoplate with temperature effects, 300
 - nanoshell, 327
 - NLSGM nanorod, 124
 - NLStGM nanorods, 135
 - second order PDE, 24
 - SWCNT, 222
 - TWCNT, 231
- DNBS
 - Euler-Bernoulli beam theory, 250
 - governing equations, 257
 - Timoshenko beam theory, 254
- Double nanobeam system, 239, 248
 - governing equations, 250
- Double nanorod system, 239
 - governing equations, 240
- DWCNT, 220, 221
 - governing equation, 225
- Dynamic stiffness, 153

E

- Effective density, 139
- Eigenvalue problem, 92, 98, 113
- Electric field, 195
- Equivalent continuum structure, 200
- Escape frequency
 - DNRS, 243, 247
 - DWCNT, 227, 228
 - fluid carrying SWCNT, 193
 - fluid carrying SWCNT, 190
 - graphene, 275, 277
 - higher order nanoshell, 347, 349
 - nanoplate with surface effects, 310, 312, 317
 - nanoshaft, 149, 151, 152
 - nanoshell, 329, 332
 - NLGSM rod, 126
 - NLSGM nanorods, 124
 - SWCNT Timoshenko beam, 224
 - Timoshenko beam theory, 174
 - Timoshenko DNBS, 259, 261

Timoshenko nanobeam, 174, 175

TWCNT, 233, 234

- Euler-Bernoulli beam theory, 72, 81, 165, 185, 203, 211, 239, 248, 249, 266
 - dispersion relation, 167

F

- First order shear deformation theory, 341
- Flügge's shell theory, 324, 336, 352
- Flexural wave
 - graphene on silicon substrate, 290
 - nanoplate with surface effects, 312
 - Timoshenko DNBS, 260
- Fluid carrying SWCNT, 187, 189
 - dispersion relation, 188
 - effect of fluid density, 192
 - governing equations, 187
 - Timoshenko beam theory, 189
- Fluid filled nanoshell
 - governing equations, 336
- Fourier transform, 20, 168, 273
 - DFT, 21, 24, 153, 154, 172, 181, 199, 206, 274, 301, 345
 - FFT, 152, 274, 301

G

- Graphene, 60, 121, 269, 270, 289, 317
 - elastic shell model, 280
 - governing equations, 271, 273
- Graphene on silicon substrate, 280
 - equilibrium & force constants, 281
 - force constant, 282, 287
 - governing equations, 284, 286
- Graphite, 8
- Green's function, 65
- Group speeds, 22
 - DNBS, 252, 254
 - DWCNT, 227
 - fluid carrying SWCNT, 190
 - graphene, 274, 277
 - graphene on silicon substrate, 290, 292
 - higher order nanoshell, 347
 - magnetic field effects, 200
 - nanoplate with surface effects, 309, 312
 - nanorods, 125
 - nanoshaft, 150, 152
 - NLGSM nanobeams, 169
 - NLStGM nanorods, 134
 - rotating nanotubes, 185
 - second order NLStGM nanorods, 133
 - Timoshenko beam theory, 174
 - TWCNT, 233

H

- Hamilton's principle, 130, 286
- Helmholtz decomposition, 151
- Hexagonal lattice, 8
- Higher order nanoshell
 - governing equations, 342
- Hybrid lattice, 282
 - bond force, 282
- Hyperbolic partial differential equation, 50

I

- In-plane stiffness, 71, 74, 77, 83
- Integro-partial differential equations, 62
- Inter-atomic repulsion, 39
- Interatomic potentials, 31
 - AIREBO, 40
 - Mie, 281
 - Morse, 85
 - REBO, 39
- Interpolation functions, 45
- Inviscid fluid, 187

K

- Kirchhoff plate theory, 308

L

- Lagrange's equation, 140
- Lamb waves, 306, 342
- Laplace Young equation, 307
- Laplacian operator, 122
- Lattice dynamics, 62, 65, 85, 145, 323
 - dispersion relation, 145
- Lattice parameter, 67
- Length scales, 47, 60, 121
- Lorentz force, 196
- Love's equation, 140

M

- Magnetic field, 195
- Magnetic field effects, 199
 - Euler-Bernoulli beam theory, 197
 - governing equation, 196
 - SWCNT, 194
- Maxwell's relations, 195
- MEMS, 121, 249
- Metropolis algorithms, 42
- Microcontinuum, 59
- Micro-polar theory, 59
- Modeling
 - ab initio* methods, 32, 290, 330

- continuum modeling, 43, 60
- 3-D elastodynamic continuum model, 330
- finite element method, 44, 47, 152, 157, 310
- integral type non local elasticity, 52
- kinetic Monte Carlo simulations, 42
- mixed spatial-temporal derivatives, 51
- molecular dynamics, 36, 280
- Monte Carlo methods, 42
- multiscale modeling, 46
 - non local continuum mechanics, 49
- Molecular dynamics simulations, 82, 270, 310
- Molecular mechanics model, 84
- Multi-layered graphene sheets, 270
- MWCNT, 215, 239

N

- Nanoplate, 284
 - surface effect, 305
- Nanoplate with surface effects
 - governing equations, 307
- Nanoplate with temperature effects
 - governing equations, 297
- Nanorods
 - dynamic stiffness, 156
- Nanoshaft
 - governing equation, 147
 - torsional wavenumber, 148
- Nanoshell
 - governing equations, 326
- Nanostructures, 41, 81, 121, 201, 249
 - fullerenes, 3, 121
 - hybridization, 4
 - hybridization index, 5
 - linear hybridization, 7
 - modeling
 - nanofiber, 121
 - nanotube, 7, 40, 121
 - nanowire, 7, 121, 203
 - one-dimensional, 121
 - tetrahedral hybridization, 6
 - tridiagonal hybridization, 6
 - two-dimensional, 121, 280
 - wave propagation, 13
 - zero-dimensional, 121
- Nanotechnology, 2
- NEMS, 13, 165, 239, 249, 306
- NLSGM, 122
- NLSGM MWCNT
 - governing equations, 218
- NLSGM nanobeam
 - constitutive relation, 170
 - dispersion relation, 172

- NLSGM nanobeam (*cont.*)
 Euler Bernoulli beam theory, 165, 169
 flexural wave, 170
 Timoshenko beam theory, 170
- NLSGM nanorod, 137, 143
 constitutive relation, 144
 dispersion relation, 144
 effect of lateral inertia, 139
 governing equation, 122, 124
- NLSGM SWCNT
 governing equations, 218
- NLStGM, 122, 129
- NLStGM fourth order nanorod, 144
 constitutive relation, 144
 dispersion relation, 144
 governing equation, 144
- NLStGM nanorod, 137
 constitutive relation, 129
 fourth order, 143
 fourth order nanorods, 134
 governing equation, 129
 second order nanorods, 133
 uniqueness and stability, 131
- NLStGM second order nanorod, 144
 constitutive relation, 144
 dispersion relation, 144
 governing equation, 144
- NOMS, 239, 249
- Non local theory
 constitutive relation, 60, 73, 86, 91, 111, 147, 205, 218, 272
 cylindrical shell problem, 68
 introduction, 60
 Kernel function, 69
 mixed nonlocality, 63
 need, 59
 non local modulus, 61, 65
 nonlocal scale parameter, 71
 one dimensional modulus, 66
 properties of kernels, 65
 scale parameter estimation, 84
 spatial nonlocality, 63
 temporal nonlocality, 63
 three dimensional modulus, 67
 two dimensional modulus, 66
 types, 63
- Nonlocal continuum mechanics, 85, 101
- Nyquist frequency, 168, 274, 299
- P**
- Pasternak foundation model, 196, 201
- Phase speed, 22
 DNBS, 252, 254
- DNRS, 243, 246
- fluid carrying SWCNT, 190
- fluid filled nanoshell, 338
- graphene, 277
- graphene on silicon substrate, 290
- higher order nanoshell, 347
- magnetic field effects, 200
- nanoplate with surface effects, 309, 312
- nanoplate with temperature effects, 301
- nanorods, 125
- nanoshaft, 150, 152
- NLGSM nanobeams, 169
- NLStGM nanorods, 134, 136
- rotating nanotube, 183
- second order NLStGM nanorods, 133
- Phonon, 323
- Poisson's ratio effect, 139, 342
- Polynomial eigenvalue problem, 29, 174, 189, 190, 200, 221, 226, 232, 233, 252, 258, 259, 289, 290, 327, 330, 337, 345
- Potential functions, 37
- Principle of virtual work, 308
- Q**
- Quantum
 coherence, 1
 confinement, 1
 dots, 121
 mechanical potentials, 37
 surface effects, 2
- R**
- Radial displacement, 326, 337
- Residual surface tension, 307
- Rotating nanomotor, 177
- Rotating nanotubes
 dispersion relation, 181
 Euler-Bernoulli theory, 179
 governing equations, 178
- S**
- Scale effect, 41
- Schrödinger equation, 34, 36
- Shape functions, 154, 155, 157
- Shear wave mode, 349
- Single-layered graphene sheets, 270
- Singular value decomposition, 28
- Sound speed, 337
- Spectral analysis, 21
- Spectral finite element, 20, 152, 156, 161, 249, 323

- Spectral stiffness matrix, 152
 - Stick-spiral system, 87, 94
 - Strain-gradient elasticity, 50
 - Structural dynamics, 19
 - Surface effects in nanobeam, 201
 - governing equations, 205
 - Surface residual stress, 316
 - SWCNT, 126, 135, 1433, 220, 244, 254
 - governing equations, 72, 222
 - bond angle, 86, 106
 - bond length, 86, 110
 - chiral angle, 101
 - chiral vector, 101
 - in plane stiffness estimation, 75
 - material property estimation, 79
 - nanobeam, 170
 - properties, 115
 - shell model, 330
 - solution of equations, 74
- T**
- Thermal expansion coefficient, 300
 - Thermal stress, 297
 - Three-body interaction, 281
 - Throw-off element, 153
 - Timoshenko beam theory, 165, 203, 211, 216, 218, 222, 236, 239, 250, 254, 259, 266
 - fluid carrying SWCNT, 187
 - governing equations, 254
 - Translation vector, 102
 - Transverse inertia, 140
 - TWCNT, 221
 - governing equations, 231
- U**
- Universal force field, 39
- V**
- Van der Waals force, 102, 215–219, 239, 241, 250, 257, 270
- W**
- Wave propagation
 - coupled systems, 239
 - 2-D nanostructures, 269
 - DNBS, 248
 - DNRS, 242
 - double nanobeam system, 251
 - fluid filled nanoshell, 336
 - graphene, 271
 - graphene on silicon substrate, 284
 - higher order nanoshell, 341
 - introduction, 19, 20
 - molecular dynamics for CNT, 38
 - molecular dynamics for graphene, 41
 - nanobeam with surface effects, 206
 - nanobeams, 165
 - nanoplate with surface effects, 305
 - nanoplate with temperature effects, 295
 - nanorod with lateral inertia effects, 139, 142
 - nanorods, 121
 - nanoshaft, 147
 - NLSGM nanorods, 122
 - NLStGM nanorods, 128
 - terminologies, 21
 - TWCNT, 231
 - Waveguide, 21
 - Wavenumber, 21, 86
 - characteristic equation, 24
 - DNBS, 252, 253
 - DNRS, 242, 244
 - DWCNT, 226
 - evanescent mode, 27
 - fluid carrying SWCNT, 189
 - fluid filled nanoshell, 337
 - fourth order NLStGM nanorod, 134
 - graphene, 274, 275
 - graphene on silicon substrate, 287, 289
 - higher order nanoshell, 345, 346, 348
 - magnetic field effects, 199
 - nanobeam with surface effects, 206
 - nanoplate with surface effects, 309, 310
 - nanoplate with temperature effects, 301, 303
 - nanorod with lateral inertia effects, 143
 - nanoshell, 327, 330
 - NLGSM nanobeams, 168
 - NLSGM nanorods, 124
 - NLStGM nanorod, 133, 134
 - propagating mode, 28
 - rotating nanotubes, 185
 - SWCNT Timoshenko beam, 222
 - Timoshenko DNBS, 258
 - Timoshenko beam theory, 173
 - TWCNT, 233
 - Weak form of the governing equation, 154
 - Winkler foundation model, 196, 250, 257
 - Winkler foundation parameter, 200, 244
- Z**
- Zigzag CNT
 - chirality, 100